POLITECHNIKA WARSZAWSKA

Automatyka, Elektronika, Elektrotechnika i Technologie Kosmiczne

Dziedzina nauk inżynieryjno-techniczna

Rozprawa doktorska

mgr inż. Sebastian Łapczyński

Analiza zjawisk fizycznych w układach stykowych i torach prądowych podczas przepływu prądu znamionowego oraz zwarciowego

Promotor
dr hab. inż. Łukasz Kolimas, profesor uczelni

WARSZAWA 2024

Streszczenie

Analiza zjawisk fizycznych w układach stykowych i torach prądowych podczas przepływu prądu znamionowego oraz zwarciowego

Niniejsza rozprawa dotyczy modelowania zjawisk fizycznych w aparatach elektrycznych podczas przepływu prądu znamionowego oraz zwarciowego. W pracy skupiono się na zjawiskach fizycznych występujących w układach stykowych oraz torach wielkoprądowych takich jak: zjawiska termiczne – nagrzewanie elementów aktywnych oraz pasywnych aparatów elektrycznych; zjawiska elektryczne – odziaływania elektrodynamiczne, gęstość prądu, rozkłady pola elektrycznego, ładunku elektrycznego i potencjału elektrycznego oraz na zjawiskach mechanicznych. Zjawiska fizyczne przeanalizowano na podstawie szczegółowo sporządzonych modeli symulacyjnych 3D. Do badań symulacyjnych wykorzystano Metodę Elementów Skończonych (MES). Wyniki z badań symulacyjnych poddano ewaluacji poprzez ich porównanie z wynikami badań eksperymentalnych uzyskanych na podstawie prac własnych oraz tych dostępnych w literaturze. Autor w niniejszej pracy proponuje nowatorski sposób prototypowania, który ma na celu: lepsze zrozumienie zjawisk fizycznych (w niektórych przypadkach tylko w zaproponowany sposób jest to możliwe); rozwijanie nie tylko ulepszonych konstrukcji urządzeń elektrycznych, ale budowę nowych; przyspieszyć proces projektowania, znacząco ograniczyć koszty produkcyjne i czas wdrożenia aparatu elektrycznego oraz wykazać skutki jego ekspozycji na wymienione zjawiska fizyczne. Ważnym aspektem pracy jest przedstawienie w sposób nowatorski symulacji oddziaływań elektrodynamicznych w aparatach elektrycznych niskiego i wysokiego napięcia. W pracy zaproponowano również szereg modyfikacji konstrukcji w celu analizy działania badanych aparatów elektrycznych i wyjaśniono ich sens fizyczny. Na podstawie przeprowadzonych badań autor wraz z zespołem zgłosił rozwiązania patentowe nowatorskich urządzeń takich jak: mikropompa magnetomotoryczna, wyzwalacz elektromagnetyczny, reluktancyjny mechanizm udarowy ze stabilizacją drgań, mufa elektrotechniczna, urządzenie do pomiaru rezystywności gruntu oraz urządzenie pozwalające na zmniejszenie czasu wyłączania łuku elektrycznego.

Słowa kluczowe: układy stykowe; prototypowanie; metoda elementów skończonych; symulacje zjawisk fizycznych; przepływ prądu; aparaty elektryczne

Abstract

Analysis of physical phenomena in contact systems and current paths during the flow of rated and short-circuit current

This thesis concerns the modelling of physical phenomena in electrical apparatuses during the flow of rated and short-circuit current. The work focused on physical phenomena occurring in contact systems and high-current circuits, such as: thermal phenomena – heating of active and passive elements of electrical devices; electrical phenomena – electrodynamic interactions, current density, distribution of electric field, electric charge and electric potential as well as mechanical phenomena. The physical phenomena were analyzed on the basis of detailed 3D simulation models. The Finite Element Method (FEM) was used for simulation procurement. The results from the simulation tests were evaluated by comparing them with the results of experimental tests obtained on the basis of authors own work and those available in the literature. In this work, the author proposes an innovative prototyping method that aims to: better understand physical phenomena (in some cases it is only possible in the proposed way); developing not only improved designs of electrical devices, but building new ones; speed up the design process, significantly reduce production costs and implementation time of the electrical device, and demonstrate the effects of its exposure to the mentioned physical phenomena. An important aspect of the work is the innovative presentation of the simulation of electrodynamic interactions in low- and high-voltage electrical devices. The work also proposes a number of modifications to analyze the operation of the tested electrical devices and explains their physical meaning. Based on the research executed, the author and his team submitted patent solutions for innovative devices such as: a magnetomotive micropump, an electromagnetic trigger, a reluctance impact mechanism with vibration stabilization, an electrotechnical coupler, a device for measuring soil resistivity, and a device allowing to reduce the switching off time of an electric arc.

Keywords: contact systems; prototypes; finite element method; simulations of physical phenomena; current flow; electric apparatus

Spis treści

1. Wstęp

1.1. Zjawiska fizyczne występujące w torach prądowych, zestykach aparatów elektrycznych i urządzeniach rozdzielczych podczas przepływu prądu znamionowego oraz zwarciowego

Styki aparatów elektrycznych należą do najbardziej obciążonych elementów obwodów prądowych [1, 2]. Dlatego powinny być projektowane, konstruowane i eksploatowane w taki sposób, aby dopuszczalne ograniczenia ich parametrów technicznych, wynikające z odpowiednich przepisów i norm były nieprzekroczone [3]. Parametry procesu łączenia aparatury elektrycznej ściśle zależą od parametrów i właściwości kinematycznych, dynamicznych i strukturalnych mechanizmu napędowego odpowiedzialnego za ruch styków elektrycznych.

Układy stykowe oraz tory prądowe umożliwiają przewodzenie prądów roboczych oraz zwarciowych, zaś układy zestykowe łączników elektrycznych służą do dokonywania łączeń w obwodach elektrycznych. Szynoprzewody, to przewody elektryczne w postaci sztywnych lub giętkich szyn prądowych na ogół zamkniętych we wspólnej obudowie (mogą być też gołe), o odpowiednio zaprojektowanej długości, kształcie i przekroju, łączonych w ciągi zestawianych modułów, montowanych wzdłuż wytyczonych tras – od rozdzielnicy do odbiorników.

Zestykiem nazywamy część toru prądowego, w której przepływ prądu jest umożliwiony dzięki styczności dwóch przewodników, zwanych stykami. Zadaniem układu zestykowego jest mechaniczne wymuszenie stanu zwarcia styków ruchomych i nieruchomych w zamierzony sposób i utrzymywanie ich docisku w tym stanie [4]. Mechanizm układu zestykowego powinien w sposób niezawodny załączać i wyłączać prądy niezależnie od parametrów znamionowych aparatu. Temperatura całej konstrukcji musi być utrzymywana na poziomie umożliwiającym stabilne warunki pracy, które również określają odpowiednie normy. Mechanizm układu stykowego powinien być odporny na szczepienie się styków przy łączeniu, pracy w warunkach znamionowych i przeciążeniowych, a także przy pracy podczas przepływu prądów zwarciowych [5]. Jest to bezpośrednio związane ze zjawiskami fizycznymi takimi jak temperatura pracy styków oraz zjawiskiem odskoku ze względu na powstające siły elektrodynamiczne. Ważne jest również, aby zminimalizować zużycie układu zestykowego w momencie załączania – podczas tego procesu na styki oddziałuje szereg sił, które powodują uszkodzenia mikro powierzchni elementów mechanicznych napędu oraz elementów aktywnych [6, 7]. Oddziaływanie wspomnianych sił jest efektem różnicy potencjałów elektrycznych pomiędzy stykami.

Zestyki i tory prądowe ze względu na konieczność przewodzenia dużych wartości prądów ciągłych i znacznie większych chwilowych zwarciowych są zwykle budowane jako zgrupowany układ wielu pojedynczych, równoległych torów prądowych. Celem projektowania takich układów jest zapewnienie jak największej obciążalności prądowej. Przepływ prądu przez każdy z torów jest zawsze w jakimś stopniu nierównomierny, co może nastręczać pewnych trudności podczas analizy układów tego typu. Niesymetryczne obciążenie jest bezpośrednio spowodowane przez zjawisko naskórkowości i efektu zbliżenia.

Przy badaniach układów stykowych aparatów elektrycznych oraz torów prądowych w szczególności należy zwrócić uwagę na zjawiska fizyczne związane z:

1. rozpływem prądu elektrycznego w badanym układzie,
2. nagrzewaniem się elementów aktywnych oraz pasywnych,
    a. dopuszczalnymi granicami przyrostu temperatury,
    b. bilansem cieplnym,
    c. rozkładem temperatury podczas pracy aparatu,
    d. drogami oddawania ciepła oraz sposobami oddawania ciepła takimi jak konwekcja, promieniowanie oraz przewodnictwo,
3. siłami elektrodynamicznymi oddziaływującymi na układ,
4. odziaływaniami elektromagnetycznymi w aparatach elektrycznych,
5. parametrami mechanicznymi projektowanego układu stykowego,
    a. kształtem styku oraz jego wpływem na parametry mechaniczne oraz elektryczne,
    b. eliminacją awarii oraz występowania nieporządnych zjawisk fizycznych lub ich ograniczenia podczas pracy aparatu,

najkorzystniejszym ułożeniem i kształtem torów prądowych.

1.2. Przegląd stanu techniki na podstawie kluczowych publikacji dla pracy autora

Analizą i badaniami torów prądowych zajmowało się dotychczas wielu autorów. Istotnymi pozycjami jest opracowanie [8] R. Holma, z roku 2000 (reedycja) oraz referaty prezentowane na cyklicznych naukowych konferencjach międzynarodowych. W pracach przedstawiona została analiza zjawisk zachodzących w zestykach. Zagadnienia rezystancji zestykowej, oddziaływania elektrodynamiczne w zestykach, nagrzewanie zestyków oraz odskoki styków i wiele innych zostały w tych pracach dokładnie omówione.

Istotnymi pozycjami są publikacje E. Walczuka poświęcone odskokom styków, zjawiskami szczepienia styków oraz zjawiskom ich erozji. Tematyka monografii [9] została poświęcona obciążalności prądowej.

Analizie zjawisk fizycznych w układach stykowych, a zwłaszcza badaniu właściwości dynamicznych układów zestykowych poświęcona została monografia B. Miedzińskiego [10] oraz inne publikacje [11, 12, 13], gdzie omówiono zagadnienia związane z właściwościami zestyków, wyborem materiałów stykowych, a także wytyczne dotyczące zasad modelowania torów wielkoprądowych.

Zagadnienia dotyczące zjawisk fizycznych zachodzących w łącznikach elektrycznych oraz zasad obliczeń urządzeń elektroenergetycznych, przede wszystkim, w odniesieniu do obliczeń cieplnych torów prądowych, dynamiki ruchu styków, analizy mechanizmów napędowych i wytrzymałości układów izolacyjnych, a także analizy statystycznej wyników badań zostały przedstawione przez S. Kulasa w licznych książkach i publikacjach naukowych [14, 15, 16, 17].

W zakresie nagrzewania się torów wielkoprądowych płaskich istotna jest publikacja M. Pawłota [18]. Autor omówił połączenia śrubowe szyn płaskich stosowane w układach szyn zbiorczych stacji elektroenergetycznych. W pracy przedstawiono analizę wpływu siły docisku połączenia śrubowego, na wartość temperatur osiąganych w zestyku przy przepływie prądów zakłóceniowych, na przykładzie płaskich szyn miedzianych. W publikacjach [19, 20] J. Maksymiuk opisał obliczenia aparatów elektroenergetycznych, przede wszystkim, w odniesieniu do obliczeń cieplnych torów prądowych, dynamiki ruchu styków, analizy mechanizmów napędowych, a także zagadnienia dotyczące zjawisk fizycznych zachodzących w łącznikach elektrycznych. Opis zjawisk fizycznych w aparatach elektrycznych i rozdzielnicach średnich i wysokich napięć przedstawił J. Maksymiuk wraz z J. Nowickim w publikacji [21].

Inną istotną referencją literaturową jest pozycja pod redakcją P. Slade [22] zawiera teoretyczne i praktyczne informacje na temat zjawisk fizycznych zachodzących w zestykach. W pozycji zostały omówione zagadnienia dotyczące obliczania rezystancji zestykowej, erozji, sczepiania styków, odskoków styków, a także przedstawiony został problem wyboru materiałów wykorzystywanych do budowania układów stykowych. W książce znajduje się również szczegółowy opis wiodących układów stykowych w zależności od techniki łączenia – niskiego, średniego lub wysokiego napięcia.

Monografia Piotra Borkowskiego [23] w wyczerpujący sposób przedstawia przegląd nowoczesnych metod badań zestyków z naciskiem na występujące w zestykach zjawiska fizyczne dla prądów w zakresie od 2 A do 20 kA oraz różnego rodzaju badania modelowe. Przedstawiono przykładowe wyniki badań laboratoryjnych różnych zestyków oraz zjawisk fizycznych zachodzących w zestykach. W monografii autor skupił się głównie na zestykach rozłącznych aparatów elektrycznych.

Problematyka procesów łączeniowych związanych z załączaniem i wyłączaniem prądu w obwodach elektrycznych jest wnikliwie omawiana w pozycjach napisanych przez Z. Cioka [24, 25, 26]. Zwrócono tam szczególną uwagę na opis teoretyczny zjawiska łuku łączeniowego i teorię zestyków, a także na charakterystyki zapłonowe łączników elektrycznych.

W publikacji [27] autorzy zajęli się zwiększonymi obciążeniami aktualnie istniejących systemów przesyłowych. Przedsiębiorstwa energetyczne i operatorzy systemów poszukują możliwości zwiększenia przepustowości istniejących linii napowietrznych bez zwiększenia ryzyka dla sprzętu lub awarii systemu. Autor poruszył również tematykę diagnostyki istniejących zestyków i połączeń.

W publikacjach [28, 29] autorzy pokazali, jak istotne cechy mechaniczne i elektryczne mają wpływ na ogólną niezawodność i wydajność układu stykowego. Publikacje podzielono na trzy części, z których pierwsza koncentruje się na mechanice, materiałach, przepływie ciepła oraz podstawowych zagadnień niezawodności styków elektrycznych. Kolejny rozdział stanowią zagadnienia, takie jak układy energetyczne i elektroniczne. W ostatnim rozdziale przedstawiono możliwości diagnostyki zestyków.

Liczne inne publikacje przedmiotowe, obejmujące referaty konferencyjne, wydawnictwa periodyczne oraz książki, zostały przytoczone w poszczególnych rozdziałach niniejszej pracy.

W literaturze dotyczącej procesu przewodzenia prądu przez tory wielkoprądowe i zestyki brakuje wnikliwego, jednolitego opracowania poświęconego zjawiskom fizycznym zachodzącym w szynoprzewodach i zestykach, podczas przepływu dużego zakresu prądów znamionowych i zwarciowych, uwzględniającego wyniki analizy tych zjawisk metodami numerycznymi, analitycznymi, a także rezultatów wyników częściowych badań eksperymentalnych. Istnieje również stosunkowo mało publikacji w dziedzinie układów stykowych pokazujących ewaluację układów rzeczywistych za pomocą metod numerycznych oraz na odwrót – modeli numerycznych za pomocą dedykowanych eksperymentów.

1.3. Numeryczna analiza zjawisk fizycznych – wykorzystanie MES

Numeryczne metody obliczeniowe, takie jak MES (Metoda Elementów Skończonych), pozwoliły na wykonywanie wielu iteracji obliczeń równolegle. Pozwala to na przyspieszenie całego procesu projektowania wybranych urządzeń elektrycznych oraz ich komponentów. Techniki cyfrowe są również wykorzystywane przy projektowaniu konstrukcji aparatury elektrycznej. Za pomocą oprogramowania CAD (Projektowanie Wspomagane Komputerowo) możliwe jest projektowanie urządzeń od pojedynczego elementu po całe złożone zespoły. Symulacje dla tych konstrukcji są również możliwe w dalszym etapie, w ramach projektu przy użyciu specjalistycznego oprogramowania. Można je wykorzystać w celu symulacji ruchu elementów względem siebie, wykluczenia kolizji poszczególnych elementów, a na koniec obserwacji opracowanego układu w warunkach symulujących naturalne środowisko pracy. Wykorzystanie sprzężonych symulacji MES jest bardzo efektywne przy przeprowadzaniu wielokrotnych analiz dotyczących aspektów elektrycznych, mechanicznych, termicznych i tych dotyczących trwałości materiałów. Ogromną zaletą MES jest możliwość sprawdzenia skomplikowanych scenariuszy z zastosowaniem różnych warunków brzegowych [30, 31].

Warto odnieść się do przełomowego i ważnego dokumentu „Grid 2030". Stany Zjednoczone, za pośrednictwem Departamentu Energii (DOE), wyobrażają sobie przyszłą sieć energetyczną jako w pełni zautomatyzowaną sieć przesyłu energii. Z możliwością monitorowania i sterowania każdym węzłem sieci, zapewniając dwukierunkowy przepływ informacji i energii pomiędzy wszystkimi węzłami w procesie przesyłu i dystrybucji od elektrowni do użytkownika końcowego [32]. Obecnie prowadzona jest analiza działania wyłącznika powietrznego (MCB) oraz kompaktowego (MCCB) [33]. Wiele badań koncentruje się na optymalizacji komór gaszeniowych [34]. Rzadziej badania dotyczą jedno i dwupunktowych układów stykowych, zmniejszających rezystancję przejścia [35, 36]. Aby móc w pełni przygotować modułowe urządzenia elektryczne do digitalizacji rozumianej jako powiązanie funkcji z inteligencją w działaniu, konieczne jest zbudowanie modeli MES oraz urządzeń elektronicznych o odpowiedniej, specyficznej funkcjonalności [37, 38].

Jak wspomniano, prowadzone są prace badawcze w zakresie modułowych urządzeń elektrycznych, niektóre z nich zaawansowane. Autorzy przedstawiają dynamiczne modele zjawisk fizycznych [39] w tym modele CFD, termiczne, mechaniczne [40 – 42].

1.4. Cel badań oraz tezy badawcze

Głównym celem niniejszej pracy było zbudowanie modeli oraz wykonanie symulacji w celu badania zjawisk fizycznych związanych z przepływem prądu znamionowego i zwarciowego. Wykonane modele oraz symulacje miały wiernie odtwarzać warunki rzeczywiste eksperymentów. Głównymi obiektami badań były układy stykowe, tory prądowe aparatów elektrycznych i urządzeń rozdzielczych.

W oparciu o krytyczny przegląd literatury, zrealizowane badania i analizy wykonane przez autora tej rozprawy formułuje się następujące tezy:

Istnieje możliwość badania zjawisk fizycznych związanych z przepływem prądu znamionowego i zwarciowego przez aparaty elektryczne i urządzenia rozdzielcze z wykorzystaniem szczegółowych, wiarygodnych modeli 3D oraz symulacji wykorzystujących metodę elementów skończonych. Istnieje możliwość badania zjawisk fizycznych związanych z techniką łączenia realizowaną przez aparaty elektryczne i urządzenia rozdzielcze na drodze symulacyjnej z dużą zbieżnością wyników.

Na główną tezę rozprawy składają się następujące, bardziej szczegółowe tezy:

A. Istnieje możliwość badania sił elektrodynamicznych w układach stykowych i torach prądowych aparatów elektrycznych i urządzeń rozdzielczych z wykorzystaniem szczegółowych modeli 3D i zaawansowanych symulacji MES (A5, A9, A10, A11, P1). Dotyczy to również przypadków, w których obliczenia analityczne są uproszczone, a pomiary eksperymentalne niemożliwe.

B. Istnieje możliwość badania zjawisk termicznych w torach prądowych aparatów elektrycznych i urządzeń rozdzielczych z dużą zbieżnością wyników już na wstępnymi etapie projektowania tychże urządzeń z wykorzystaniem modeli 3D i metody elementów skończonych (A6, A7, A8).

C. Istnieje możliwość budowania wiarygodnych modeli 3D do analizy zjawisk fizycznych elektromagnetycznych w urządzeniach elektrofizycznych (A2, A4, P2, P3, P4, P6).

D. Istnieje możliwość budowania wiarygodnych modeli 3D do analizy zjawisk elektromechanicznych i mechanicznych związanych z pracą układów stykowych aparatów elektrycznych na różnych poziomach napięć (A1, A3).

E. Istnieje możliwość prototypowania wiarygodnych konstrukcji urządzeń elektromechanicznych, elektrycznych oraz elektronicznych na podstawie otrzymanych wyników eksperymentalnych oraz z symulacji wykonanych za pomocą oprogramowania wykorzystującego metodę elementów skończonych (P1 – P6).

1.5. Publikacje oraz patenty składające się na niniejszą rozprawę

Rozprawa zawiera 11 publikacji oraz 5 patentów, których współtwórcą jest autor niniejszej rozprawy doktorskiej. Publikacje oraz patenty zostały wymienione poniżej wraz z zaznaczeniem co było wkładem doktoranta w daną pracę badawczą:

A1. Łukasz Kolimas, **Sebastian Łapczyński.**, "*Currents of contact welding in a static layout: A laboratory exercise*", International Journal of Electrical Engineering Education, I, ISSN 0020-7209, 2022, s. 3 – 19, (**40 pkt. wg. wykazu MNiSW, IF= 0,938**).

Wkład doktoranta w powstanie tej pracy polegał na:

- opracowaniu stanowiska do prób eksperymentalnych oraz zajęć dydaktycznych,
- agregacji wyników oraz ich statystycznemu opracowaniu,
- weryfikacji metody dydaktycznej przedstawionej w publikacji,
- opracowaniu koncepcji artykułu
- współpracy przy pisaniu artykułu.

Procentowy udział doktoranta: 40%

A2. Łukasz Kolimas, **Sebastian Łapczyński**, Michał Szulborski, Michał Świetlik, "*Low Voltage Modular Circuit Breakers: FEM Employment for Modelling of Arc Chambers*", Bulletin of the Polish Academy of Sciences-Technical Sciences, 68, ISSN 0239-7528, s. 61-70, 2020, (**100 pkt. wg. wykazu MNiSW, IF=1,38**).

Wkład doktoranta w powstanie tej pracy polegał na:

- budowaniu modelu 3D komory gaszeniowej wyłącznika nadprądowego,
- wykonaniu symulacji rozkładu potencjału, termicznych oraz pomocy w wykonaniu symulacji CFD (Computational Fluid Dynamics),
- porównaniu zjawisk fizycznych w dwóch wariantach komór gaszeniowych,
- współpracy w przygotowaniu stanowiska badawczego i realizacji pomiarów,
- współpracy przy pisaniu artykułu.

Procentowy udział doktoranta: 20%

A3. **Sebastian Łapczyński**, Michał Szulborski, Karol Golota, Łukasz Kolimas, Łukasz Kozarek, "*Mechanical and Electrical Simulations of Tulip Contact System*", Energies, I, ISSN 1996-1073, s. 1-28, 2020, (**140 pkt. wg. wykazu MNiSW, IF=3,2**).

Wkład doktoranta w powstanie tej pracy polegał na:

- budowie modelu 3D układu stykowego tulipanowego,
- analizie zjawisk fizycznych w układzie stykowym,
- sporządzenie symulacji dynamiki ruchu styków,
- ocenie wykorzystania wyników w aspekcie aplikacyjnym,
- sporządzeniu koncepcji artykułu,
- współpracy przy pisaniu artykułu.

Procentowy udział doktoranta: 10%

A4. Łukasz Kolimas, Krzysztof Bieńkowski, **Sebastian Łapczyński**, Michał Szulborski, Łukasz Kozarek, Karol Birek, "*Control System and Measurements of Coil Actuators Parameters for Magnetomotive Micropump Concept*", Bulletin of the Polish Academy of Sciences-Technical Sciences, 68, ISSN 0239-7528, s. 893-901, 2020, (**100 pkt. wg. wykazu MNiSW, IF=1,38**).

Wkład doktoranta w powstanie tej pracy polegał na:

- opracowaniu koncepcji artykułu,
- opracowaniu metody badawczej,
- zbudowaniu modelu 3D siłownika elektrodynamicznego,
- porównaniu dwóch mechanizmów (reluktancyjnego oraz elektrodynamicznego) działania siłownika dla mikropompy,
- opracowaniu budowy dwóch wariantów siłowników,
- przygotowaniu stanowiska do badań oraz pomocy w pomiarach,
- ocenie parametrów siłowników o różnych mechanizmach działania w odniesieniu do wykorzystania w docelowym wynalazku (mikropompa),
- przygotowaniu symulacji

- korekcie pracy przed wprowadzeniem do druku.

Procentowy udział doktoranta: 40%

A5. Michał Szulborski, **Sebastian Łapczyński**, Łukasz Kolimas, Łukasz Kozarek, Desire Rasolomampionona, "*Calculations of Electrodynamic Forces in Three-phase Asymmetric Busbar System with the use of FEM*", Energies, I, ISSN 1996-1073, s. 1-25, 2020, (**140 pkt. wg. wykazu MNiSW, IF=3,2**).

Wkład doktoranta w powstanie tej pracy polegał na:

- opracowaniu modelu 3D rozdzielnicy oraz torów prądowych,
- wykonaniu części symulacji dotyczących sił elektrodynamicznych,
- analizie wyników symulacji,
- współpracy przy pisaniu artykułu.

Procentowy udział doktoranta: 10%

A6. Michał Szulborski, **Sebastian Łapczyński**, Łukasz Kolimas, Łukasz Kozarek, Desire Rasolomampionona, Tomasz Żelaziński, Adam Smolarczyk, "*Transient Thermal Analysis of NH000 gG 100A Fuse Link Employing Finite Element Method*", Energies, 14(5), ISSN 1996-1073, s. 1-17, 2021, (**140 pkt. wg. wykazu MNiSW, IF=3,2**)

Wkład doktoranta w powstanie tej pracy polegał na:

- współpracy przy budowie stanowiska badawczego,
- wykonaniu części modelu 3D wkładki topikowej,
- współpracy przy wykonaniu symulacji termicznych,
- współpracy przy pisaniu artykułu,
- wykonaniu materiałów graficznych,
- porównaniu wyników eksperymentalnych oraz symulacyjnych.

Procentowy udział doktoranta: 15%

A7. Michał Szulborski, **Sebastian Łapczyński**, Łukasz Kolimas, Daniel Zalewski, "*Transient Thermal Analysis of the Circuit Breaker Current Path with the use of FEA Simulation*", Energies, I, ISSN 1996-1073, s. 1-24, 2021, (**140 pkt. wg. wykazu MNiSW, IF=3,2**).

Wkład doktoranta w powstanie tej pracy polegał na:

- opracowaniu modelu 3D toru prądowego wyłącznika nadprądowego,
- wykonaniu symulacji termicznych,
- współpracy przy zbudowaniu stanowiska pomiarowego,
- analizie wyników symulacji nagrzewania toru prądowego wyłącznika w odniesieniu do badań eksperymentalnych,
- współpracy przy pisaniu artykułu.

Procentowy udział doktoranta: 15%

A8. Michał Szulborski, **Sebastian Łapczyński**, Łukasz Kolimas, "*Thermal analysis of heat distribution in busbars during rated current flow in low-voltage industrial switchgear*", Energies, 14, ISSN 1996-1073, s. 1-23, 9, 2021, (**140 pkt. wg. wykazu MNiSW, IF=3,2**).

Wkład doktoranta w powstanie tej pracy polegał na:

- zbudowanie modelu 3D rozdzielnicy oraz torów prądowych,
- współpracy przy budowaniu modelu symulacyjnego,
- współpracy przy wykonaniu symulacji rozkładu temperatury,
- współpracy przy analizie wyników symulacji w odniesieniu do eksperymentu,
- współpracy przy pisaniu artykułu.

Procentowy udział doktoranta: 20%

A9. Michał Szulborski, **Sebastian Łapczyński**, Łukasz Kolimas, "*Increasing magnetic blowout force by using ferromagnetic side plates inside MCB*", Energies, I, ISSN 1996-1073, s. 1-17, 2022, (**140 pkt. wg. wykazu MNiSW, IF=3,2**).

Wkład doktoranta w powstanie tej pracy polegał na:

- opracowaniu koncepcji artykułu,
- opracowaniu metody badawczej,
- zbudowaniu modeli symulacyjnych,
- wykonaniu symulacji łuku elektrycznego na płytkach dejonizacyjnych komory gaszeniowej,
- analizie i ewaluacji symulacji łuku elektrycznego na płytkach dejonizacyjnych komory gaszeniowej,
- ocenie rozpływu ładunku elektrycznego,
- formułowaniu wniosków badawczych,
- opracowaniu treści artykułu,
- korekcie pracy przed wprowadzeniem do druku.

Procentowy udział doktoranta: 40%

A10. Michał Szulborski, **Sebastian Łapczyński**, Łukasz Kolimas, Mykhailo Tyryk, "*Electrodynamic Forces in a High Voltage Circuit Breakers with Tulip Contact System – FEM simulations*", IEEE Access, I, ISSN 2169-3536, s. 1-22, 2022, (**100 pkt. wg. wykazu MNiSW, IF= 3,9**).

Wkład doktoranta w powstanie tej pracy polegał na:

- opracowaniu koncepcji artykułu,
- zbudowaniu modeli 3D,
- zbudowaniu modeli symulacyjnych,
- wykonaniu symulacji sił elektrodynamicznych w układzie stykowym tulipanowym,
- analizie i ewaluacji symulacji sił elektrodynamicznych w układzie stykowym tulipanowym,
- formułowaniu wniosków badawczych,
- opracowaniu treści artykułu,
- korekcie pracy przed wprowadzeniem do druku.

Procentowy udział doktoranta: 40%.

A11. Michał Szulborski, **Sebastian Łapczyński**, Łukasz Kolimas, Łukasz Kozarek, Hubert Cichecki, Przemysław Sul, Maciej Owsiński, Przemysław Berowski, Dariusz Baczyński, Marcin Wesołowski, "*Examination of Electrodynamic Forces in High Voltage Disconnector Related to the Short-Circuit Current Using the Digital Twin Technology*", IEEE Access, s. (99):1-1, 2024, (**100 pkt. wg. wykazu MNiSW, IF= 3,56**).

Wkład doktoranta w powstanie tej pracy polegał na:

- opracowaniu koncepcji artykułu,
- zbudowaniu modelu 3D,
- zbudowaniu modeli symulacyjnych,
- wykonaniu symulacji sił elektrodynamicznych w rozłączniku wysokiego napięcia,
- analizie i ewaluacji symulacji sił elektrodynamicznych za pomocą technologii Digital Twin,
- formułowaniu wniosków badawczych,
- opracowaniu treści artykułu,
- korekcie pracy przed wprowadzeniem do druku.

Procentowy udział doktoranta: 10%.

P1. Łukasz Kolimas, **Sebastian Łapczyński**, Michał Szulborski, Łukasz Kozarek, „*Urządzenie i sposób zmniejszania czasu wyłączenia łuku elektrycznego w wyłącznikach wysokiego napięcia*”, P.234768 UP RP, data udzielenia prawa 18.07.2023.

Mój wkład w powstanie tej pracy polegał na:

- opracowaniu koncepcji wynalazku na podstawie badań z publikacji A3,
- przygotowaniu rysunków technicznych,
- przygotowaniu zgłoszenia patentowego.

Procentowy udział doktoranta: 25%.

P2. Łukasz Kolimas, Krzysztof Bieńkowski, **Sebastian Łapczyński**, Michał Szulborski, Łukasz Kozarek, Karol Birek, "*Pompa oraz sposób sterowania pompy*", PAT.243768 UP RP, data udzielenia prawa: 17.08.2021.

Mój wkład w powstanie tej pracy polegał na:

- opracowaniu koncepcji wynalazku na podstawie badań z publikacji A4,
- przygotowaniu rysunków technicznych,
- przygotowaniu zgłoszenia patentowego.

Procentowy udział doktoranta: 17%.

P3. Łukasz Kolimas, Krzysztof Bieńkowski, **Sebastian Łapczyński**, Michał Szulborski Łukasz Kozarek, Karol Birek, „*Wyzwalacz elektromagnetyczny*", PAT.239158 UP RP, data udzielenia prawa 10.08.2021.

Mój wkład w powstanie tej pracy polegał na:

- opracowaniu koncepcji wynalazku na podstawie badań z publikacji A4,
- przygotowaniu rysunków technicznych,
- przygotowaniu zgłoszenia patentowego.

Procentowy udział doktoranta: 17%.

P4. Łukasz Kolimas, Krzysztof Bieńkowski, **Sebastian Łapczyński**, Michał Szulborski, Łukasz Kozarek, Karol Birek, "*Reluktancyjny mechanizm udarowy ze stabilizacją drgań*", PAT.241143 UP RP, data nadania prawa 06.05.2022.

Mój wkład w powstanie tej pracy polegał na:

- opracowaniu koncepcji wynalazku na podstawie badań z publikacji A4,
- przygotowaniu rysunków technicznych,
- przygotowaniu zgłoszenia patentowego.

Procentowy udział doktoranta: 17%.

P5. Łukasz Kolimas, Krzysztof Bieńkowski, **Sebastian Łapczyński**, Michał Szulborski, Łukasz Kozarek, Karol Birek, „*Mufa elektrotechniczna*", PAT.241142 UP RP, data udzielenia prawa 12.05.2022.

Mój wkład w powstanie tej pracy polegał na:

- opracowaniu koncepcji wynalazku na podstawie badań z publikacji A7,
- przygotowaniu rysunków technicznych,
- przygotowaniu zgłoszenia patentowego.

Procentowy udział doktoranta: 17%.

P6. Łukasz Kolimas, **Sebastian Łapczyński**, Michał Szulborski, Łukasz Kozarek, "*Urządzenie do pomiaru rezystywności gruntu*",, PAT.244861 UP RP, data udzielenia prawa 12.12.2023.

Mój wkład w powstanie tej pracy polegał na:

- opracowaniu koncepcji wynalazku na podstawie badań z publikacji A8,
- przygotowaniu rysunków technicznych,
- przygotowaniu zgłoszenia patentowego.

Procentowy udział doktoranta: 25%.

Sumaryczny Impact Factor na rok 2023 cyklu 10 publikacji składających się na osiągnięcie naukowe wynosi: 25,802.

Sumaryczna liczba punktów MNiSW cyklu 11 publikacji naukowych oraz 6 patentów składających się na osiągnięcie naukowe wynosi: a) publikacje naukowe – 1240; b) patenty – 450.

Wskaźniki biometryczne doktoranta wyniosły – indeks Hirscha: 5; sumaryczna liczba cytowań: 72 (baza *Web of Science Core Collection*) oraz 87 (baza *Scopus*). Dane pochodzą z biblioteki głównej Politechniki Warszawskiej i zostały potwierdzone.

Oświadczenia wszystkich współautorów o udziale procentowym w publikacjach A1 – A11 oraz patentach P1 – P6 oraz zgoda na włączenie tych prac do cyklu publikacji powiązanych tematycznie, stanowiących osiągnięcie naukowe przedstawione do oceny w postępowaniu zamieszczono w osobnym załączniku (załącznik 1).

2. Wkład autora rozprawy

2.1. Publikacje dotyczące analizy oddziaływań elektrodynamicznych

Modelowanie oddziaływania sił elektrodynamicznych zostało przedstawione w pracach [A4, A5, A9, A10, A11]. Badania dotyczą układu stykowego tulipanowego wysokiego napięcia oraz torów prądowych w rozdzielnicy niskiego napięcia. Zostały również rozpatrzone mechanizmy pozwalające na wykorzystanie oddziaływań elektrodynamicznych w celu uzyskania ruchu posuwisto – zwrotnego i implementacji tego rozwiązania w patentach [P2 – P4].

Powstawanie sił elektrodynamicznych w zestykach aparatów elektrycznych związane jest z przepływem prądów o dużej wartości – prądy zakłóceniowe. W zależności od konstrukcji układu stykowego zjawisko występowania sił elektrodynamicznych jest niepożądane, gdyż może prowadzić do sczepiania się styków podczas odskoków elektrodynamicznych lub do ich rozerwania i zniszczenia. Zjawisko odrzutu elektrodynamicznego wykorzystywane jest również do zwiększenia prędkości rozchodzenia się styków w wyłącznikach ograniczających poprzez odpowiednie pętlowe ukształtowanie torów prądowych zestyku. Wyniki analiz numerycznych oddziaływań elektrodynamicznych jest niezwykle trudno ewaluować eksperymentalnie. Stąd konieczność przeprowadzania obliczeń analitycznych, które zakładają bardzo duże uproszczenia.

W pracy [A4] zaproponowano budowę oraz pomiary siłowników elektrodynamicznego oraz reluktancyjnego. Powyżej wymienione elementy wykonawcze miały zostać wykorzystane jako napędy nowatorskiej koncepcji mikropompy magnetomotorycznej. Artykuł porusza różne aspekty wyznaczania wartości parametrów, układu sterowania, odziaływania sił elektrodynamicznych i optymalizacji podstawowych elementów zespołów cewek, które zostały poruszone w literaturze [43 – 47]. Przeprowadzona praca opisuje system pomiarowy i analizę uzyskanych wartości. Porównano wykonane siłowniki i wskazano zalety i wady budowy koncepcyjnego urządzenia. Na podstawie pomiarów, aspektów konstrukcyjnych, kontroli układu oraz kluczowych parametrów, takich jak prędkość tłoka, energia zmagazynowana w kondensatorach i sprawności, wybrano najlepsze rozwiązanie do wdrożenia w przyszłych pracach nad konstrukcją mikropompy magnetomotorycznej.

W literaturze opisuje się konstrukcje siłowników o dużych masach własnych i ograniczonej częstotliwości pracy, które mogłyby zostać porównane do zaproponowanego przez autora rozwiązania [48]. Jeżeli chodzi o obliczenia i metodologię, dobrze przedstawioną metodykę opisano w publikacji [49]. W artykule przedstawiono studium konstrukcyjne lekkiego siłownika bezwładnościowego ze zintegrowanym czujnikiem prędkości do realizacji sterowania ze sprzężeniem zwrotnym prędkości, czyli aktywnego tłumienia. W literaturze nie przedstawiono jednak modelu, który jednoznacznie łączyłby obliczenia analityczne i numeryczne dla siłowników o liniowym przepływie płynu. Nie udało się zawrzeć w cytowanej pracy przejrzystego sposobu projektowania i testowania takich elementów wykonawczych poprzez budowę powtarzalnego stanowiska badawczego. Nadal istnieją konstrukcje o dużych masach własnych i ograniczonej częstotliwości pracy na przykład w publikacji [50]. Półpraktyczne rozwiązanie zaproponował zespół chińskich badaczy [51]. Autorzy w wielu publikacjach przedstawiają metody prowadzenia obliczeń dla podobnych maszyn elektrycznych w porównaniu do pompy magnetomotorycznej zaprezentowanej przez autora w niniejszej pracy [52 – 56]. Żadna z wymienionych prac dostępnych w literaturze nie opisuje takiego rozwiązania jakie proponuje autor – należy wskazać skalę jak i sposób wykonania w tym zaproponowanie mechanizmu pracy elementów wykonawczych pompy bez tarcia.

Zaprezentowany przez autora model pokazuje także, jak sterować przepływem, aby był on liniowy, co często ma kluczowe znaczenie w zastosowaniach w przemyśle medycznym i chemicznym. Autor samodzielnie opracował koncepcję publikacji [A4] oraz samodzielnie zbudował artykuł. Doktorant samodzielnie zbudował model 3D siłownika elektrodynamicznego, który był przedmiotem patentów [P2 – P4] w wariantach zmodyfikowanych. Autor był odpowiedzialny za prace analityczne polegające na porównaniu mechanizmów oraz wyników symulacyjnych jak i empirycznych dla siłownika reluktancyjnego oraz elektrodynamicznego w celu doboru odpowiedniego rozwiązania do zastosowaniu w pompie magnetomotorycznej. Autor również uczestniczył w budowie obiektów empirycznych oraz przygotowania stanowiska do badań eksperymentalnych w tym również wykonywaniu pomiarów.

W pracy [A5] przeprowadzono obliczenia analityczne trójfazowego układu szyn zbiorczych. Obliczono kluczowe parametry, takie jak maksymalna wartość siły elektrodynamicznej, wartość wytrzymałości mechanicznej, częstotliwość drgań własnych szyn zbiorczych. Obliczenia wykonano również za pomocą modelu równoległego układu szyn zbiorczych w programie ANSYS, co potwierdziło uzyskane wyniki z obliczeń analitycznych. Zaproponowany model umożliwiał: obserwację działania sił, energii działających na izolatory wsporcze, realizację doboru i modelowania torów prądowych ze względu na zagrożenia związane z przepływem prądu zwarciowego, obserwację skutków działania sił elektrodynamicznych od prądu zwarciowego niesymetrycznego. Wykazano, że model oparty na elementach skończonych jest bardzo pomocny w doborze szynoprzewodów o nietypowych kształtach. W prowadzonych rozważaniach przedstawiono model 3-D z uwzględnieniem wszystkich zagrożeń elektromechanicznych (naprężenia izolatorów wsporczych, częstotliwość drgań własnych układu i sił elektrodynamicznych).

Wielu uczonych badało stabilność termiczną EIPB (*Enclosed Isolated Phase Busbar*) przy prądzie zwarciowym [57 – 58]. Autorzy w wykazanych publikacjach zaproponowali metodę obliczania temperatury przewodu magistrali z wykorzystaniem analizy sieci cieplnej. Przeanalizowali oni rezystancję styku części szyn zbiorczych i obliczali wzrost temperatury generowany przez rezystancję.

W publikacjach [59 – 62] autorzy wykonali badania eksperymentalne do sprawdzenia niezawodności styków szyn zbiorczych i przewidywali stan zestyku na podstawie modeli teoretycznych. Rozważali oddziaływanie sił elektrodynamicznych, wzrostu temperatury i innych czynników, takich jak wytrzymałość mechaniczna oraz wpływ stanu zwarcia na przewód magistrali. Jednak większość z tych metod dotyczy bardzo małych rozmiarów szyn prostych, które nie są dłuższe niż 5 m. Praca [A5] dotyczyła bardziej kompleksowych wariantów szyn o dłuższych odcinkach oraz analizy oddziaływania sił elektrodynamicznych na izolatory wsporcze.

Pracę [A5] można uznać za nowatorską wymieniając jej następujące atuty: odniesienie się do projektowania rozdzielnic pod kątem obliczania sił elektrodynamicznych, nie tylko obciążalności prądowej szyn zbiorczych (jest to rzadko spotykane podejście w literaturze); publikacja przedstawia całościową analizę sił elektrodynamicznych w rozdzielnicach; rozpatrywany jest przypadek asymetrii, który analitycznie jest trudno opisać i wyznaczyć – wykorzystanie MES pozwala na rozpatrzenie takiego scenariusza; ograniczenie przewymiarowań i częstych niedoszacowań w obliczeniach ze względu na konieczność przyjęcia uproszczeń oraz niekorzystnych założeń wpływających na dokładność otrzymywanych wyników.

W wykonanej pracy [A5] autor był odpowiedzialny za opracowanie modelu 3D badanej rozdzielnicy oraz jej torów prądowych. Doktorant wykonał część symulacji dotyczących badań sił elektrodynamicznych – symulacje deformacji torów prądowych. Autor uczestniczył w analizie wyników oraz budowie publikacji.

W pracy [A9] przedstawiono metodę numerycznego modelowania komór gaszeniowych niskiego napięcia stosowanych w aparatach modułowych. Skupiono się na przedstawieniu zjawiska zwiększania wydmuchu poprzez zastosowanie płytek ferromagnetycznych dzielących łuk elektryczny wewnątrz aparatu elektrycznego. Zastosowanie materiału ferromagnetycznego do produkcji komór gaszeniowych powoduje zniekształcenie pola magnetycznego generowanego przez łuk elektryczny. Prowadzi to do wytworzenia siły magnetycznej, która przyciąga łuk w stronę obszaru płytek dejonizacyjnych komory gaszeniowej. Autorzy zaprezentowali nowoczesne narzędzia do analizy zjawisk fizycznych wewnątrz komory gaszeniowej. Zaprezentowany materiał pozwala zbadać wpływ zmian geometrii i materiałów elementów toru prądowego na proces wyłączania prądu. Zastosowane podejście może być wykorzystane do analizy zjawisk fizycznych w urządzeniach nie tylko dla prądu przemiennego, ale także dla prądu stałego.

W referencyjnej pracy [63] zaproponowano zastosowanie magnesów trwałych wewnątrz komory łukowej w celu poprawy wydajności gaszenia łuku. Magnesy trwałe wytwarzają pole magnetyczne, w którym łuk elektryczny zachowuje się inaczej w porównaniu z płytkami dejonizacyjnymi. Autorzy w badaniach przedstawiają porównanie danych testowych wyłączników z konfiguracją płytki dejonizacyjnej i magnesów trwałych z uwzględnieniem różnych polaryzacji i rozmieszczenia. Celem tej pracy było zrozumienie zachowania łuku elektrycznego wewnątrz wyłączników, gdy magnesy stałe są używane do gaszenia łuku elektrycznego w komorze łukowej. Jest to istotne zagadnienie dla badań przeprowadzonych przez doktoranta. Praca [64] dotyczyła problemu łuku plazmowego. Artykuł koncentruje się na wpływie różnych par polimerów, takich jak PA66, POM, PTFE, PMMA, na zachowanie się łuku i wpływ odpowietrzania na rozkład ciśnienia. Ulegające ablacji pary polimeru, które są generowane przez silne promieniowanie łuku, zmieniają właściwości termodynamiczne i transportowe plazmy łukowej. Jest to szczególnie ważne przy rozważaniach dotyczących aparatów modułowych.

Przeprowadzone symulacje obliczeniowe w pracy [A9] potwierdziły, że wykonywanie analiz numerycznych na dokładnych modelach konstrukcyjnych 3D może stanowić istotne ułatwienie podczas budowy i prototypowania komór gaszeniowych. Dzięki tego typu analizom projektanci aparatury elektrycznej są w stanie stworzyć urządzenia bardziej dopracowane już na etapie projektowania. Dokonując odpowiednich zmian konstrukcyjnych. Przeprowadzone badania zwarciowe potwierdziły założenia teoretyczne zawarte w literaturze. Dodatkowo wyniki symulacji są spójne z wynikami uzyskanymi z przeprowadzonych badań eksperymentalnych. Przeprowadzone symulacje obliczeniowe potwierdziły, że wykonywanie analiz numerycznych na dokładnych modelach konstrukcyjnych 3D może stanowić istotne ułatwienie podczas budowy i prototypowania komór gaszeniowych. Dzięki tego typu analizom projektanci aparatury elektrycznej są w stanie stworzyć urządzenia bardziej dopracowane już na etapie projektowania. Dokonując odpowiednich zmian konstrukcyjnych, takich jak dopracowanie kształtu wycięć w płytach komory gaśniczej, możliwe jest zwiększenie wydajności elektrod łukowych. Istotną zaletą pracy jest możliwość zmiany parametrów symulacji w tym geometrii elementów oraz analiza zjawisk fizycznych (szczególnie oddziaływań elektrodynamicznych) na bieżąco.

Autor samodzielnie opracował koncepcję publikacji [A9] oraz zbudował artykuł. Autor był w sposób znaczący odpowiedzialny za opracowanie metody badawczej wykorzystanej w tej pracy. Autor zbudował w stopniu znaczącym modele symulacyjne komory gaszeniowej oraz płytek dejonizacyjnych – symulacje łuku elektrycznego. Również w stopniu znaczącym wykonał symulacje dla wyżej wymienionych obiektów. Autor brał udział w ocenie analitycznej dotyczącej rozpływu ładunku elektrycznego oraz sformułował wnioski badawcze. Autor współpracował przy korekcie publikacji przed wprowadzeniem do druku.

Praca [A10] dotyczyła wpływu sił elektrodynamicznych działających na styczki układu tulipanowego, często stosowanych w wyłącznikach wysokiego napięcia [65, 66]. Głównym problemem faktycznej ewaluacji poprzez pomiary dynamiczne (siły elektrodynamiczne) jest specyfika pracy wyłącznika. Układ stykowy znajduje się bezpośrednio w komorze wyłącznika wypełnionej gazem CO_2 lub SF_6 [67 – 69]. Dlatego badania w normalnych warunkach pracy są bardzo trudne, wręcz niemożliwe. Autorzy zaproponowali zastosowanie metody MES (metody elementów skończonych) w celu uzyskania wartości sił elektrodynamicznych działających na układ styków poprzez wykonanie szczegółowej symulacji sprzężonej 3D. Analiza wyników dała istotne wnioski dotyczące działania takich układów styków w warunkach zwarciowych.

Autor przeprowadził gruntowne badania literatury, które potwierdzają brak informacji na temat badania sił elektrodynamicznych w układach stykowych wysokiego napięcia. W działach B+R producentów układów stykowych i wyłączników można znaleźć badania statyczne. Prace dotyczą wyłącznie układu stykowego zbudowanego z jednego ponacinanego elementu. W takim wypadku poza komorą wyłącznika możliwe stają się badania poprzez odciąganie jednej ze styczek i statyczne wyznaczanie siły elektrodynamicznej. Nie jest to siła związana z przepływem prądu, a tym bardziej prądu zwarciowego. Jest to siła mechaniczna uzyskana poprzez sprężystość materiału, niekiedy również sprężyny dociskającej.

Badania autora publikacji [A10] dotyczą oddziaływań sił elektrodynamicznych na poszczególne styczki układu stykowego tulipanowego w wyłącznikach wysokiego napięcia. Autor w swojej pracy wykazuje, że styczki nie są równomiernie obciążone elektrodynamicznie podczas przepływu prądu zwarciowego, a tym samym bada wiele punktów oddziaływań rozmieszczonych na poszczególnych styczkach. Nie jest to ograniczony układ statyczny jednej styczki (tak jak zwykle było to realizowane w literaturze). Nowatorskim aspektem tej pracy jest analiza oddziaływań elektrodynamicznych na badany układ w sposób kompleksowy i dynamiczny biorąc pod uwagę cały mechanizm stykowy aparatu.

Autor samodzielnie opracował koncepcję publikacji oraz zbudował artykuł. Autor był w sposób znaczący odpowiedzialny za opracowanie metody badawczej wykorzystanej w tej pracy. Autor zbudował w stopniu znaczącym modele symulacyjne zestyku tulipanowego. Również w stopniu znaczącym wykonał symulacje sił elektrodynamicznych dla wyżej wymienionego obiektu. Autor brał udział w ocenie analitycznej dotyczącej wartości sił elektrodynamicznych jakie uzyskano podczas przeprowadzania symulacji i odniesienia ich do wartości rzeczywistych oraz analitycznych, które są dostępne w literaturze. Autor sformułował samodzielnie wnioski badawcze. Autor współpracował przy korekcie publikacji przed wprowadzeniem do druku.

Praca [A11] dotyczyła nowatorskiej technologii modelowania obiektów zwanej Digital Twin (DT) w aspekcie analizy symulacyjnej zjawisk fizycznych. Zaprezentowano, zweryfikowano i omówiono model Digital Twin przedstawiający analizę sił elektrodynamicznych w trójfazowym rozłączniku wysokiego napięcia. Doświadczenia związane z pracą laboratoryjną i pomiarami sił elektrodynamicznych wyraźnie pokazały, że często pomimo stosowania nowoczesnych maszyn obliczeniowych proces badawczy jest trudny, bardzo kosztowny, a wartości sił elektrodynamicznych są prawie niemożliwe do zmierzenia w warunkach rzeczywistych. Stąd pomysł wykorzystania bardzo zaawansowanych modeli aparatów elektrycznych zminimalizowanych do modelu zredukowanego. Tego typu operacja możliwa była z wykorzystaniem technologii Digital Twin. Ze względu na dużą liczbę urządzeń elektrycznych (dławików, transformatorów, odłączników) w sieciach wysokiego napięcia przeprowadzenie symulacji całościowej dla skomplikowanego, wieloelementowego układu jest często czasochłonne lub wręcz niemożliwe. Zaproponowane podejście badawcze pozwoliło uzyskać wyniki z bardzo złożonych modeli w znacznie korzystniejszym czasie i o porównywalnej jakości w odniesieniu do klasycznych metod symulacyjnych MES (Model klasyczny MES – 12 godzin, model zredukowany DT – 2 minuty). Model zredukowany może być stosowany nie tylko przez badaczy, ale także w działach rozwoju przedsiębiorstw. Wyniki modelowania MES za pomocą technologii Digital Twin porównano i zweryfikowano z wartościami eksperymentalnymi uzyskanymi z badań zwarciowych przeprowadzonych w Instytucie Energetyki.

W publikacjach [105 – 108] autorzy w ciekawy sposób przedstawili technologię Digital Twin. Autorzy pokazują, że wraz z nadejściem ery cyfrowej technologia Digital Twin stała się nową potencjalną technologią numeryczną modelowania i badania obiektów. Cieszy się rosnącym zainteresowaniem zarówno w środowisku akademickim, jak i przemysłowym. Technologia DT toruje drogę opłacalnym próbom odtworzenia warunków rzeczywistych i optymalnemu zarządzaniu wydajnością poprzez tworzenie cyfrowej reprezentacji wirtualnej sieci fizycznej na potrzeby symulacji i prognoz.

Kolejni autorzy z zakresu elektroenergetyki przedstawiali kompleksowy model inteligentnych elektrowni [109 – 110]. W publikacjach przedstawiono wielopoziomową metodę budowy DT stacji elektroenergetycznej. W tej metodzie technologia DT zapewnia ramy struktury do zarządzania podstacją, a system wieloczynnikowy realizuje inteligentne funkcje podstacji. W pierwszej kolejności szczegółowo opisano architekturę technologii DT stacji elektroenergetycznej. Następnie zaproponowano szkielet systemu wieloczynnikowego dla szczegółowo przedstawionych funkcji modelu. Należy zwrócić uwagę na ogromny poziom skomplikowania i szczegółowości tego typu modeli, który byłby trudny do symulowania wykorzystując klasyczną MES.

Autor samodzielnie opracował koncepcję publikacji oraz zbudował artykuł. Autor był w sposób znaczący odpowiedzialny za opracowanie metody badawczej wykorzystanej w tej pracy. Autor współpracował przy budowie modelu symulacyjnego rozłącznika wysokiego napięcia. Również współpracował przy wykonywaniu symulacji sił elektrodynamicznych dla wyżej wymienionego obiektu. Autor brał udział w ocenie analitycznej dotyczącej wartości sił elektrodynamicznych jakie uzyskano podczas przeprowadzania symulacji i odniesienia ich do wartości rzeczywistych oraz analitycznych, które są dostępne w literaturze. Autor sformułował wnioski badawcze. Autor współpracował przy korekcie publikacji przed wprowadzeniem do druku.

2.2. Publikacje dotyczące analizy zjawisk termicznych

Modelowanie zjawisk termicznych zostało przedstawione w pracach [A6, A7, A8]. Na podstawie badań wykonanych w publikacjach [A7, A8] opracowano patenty [P5, P6].

W pracy [A6] zaproponowano szczegółowy, trójwymiarowy, przejściowy model wkładki bezpiecznikowej NH000 gG 100A wykonany metodą elementów skończonych. Głównym przedmiotem przeprowadzonych analiz były właściwości termiczne bezpieczników podczas pracy w warunkach znamionowych (100 A) i niestandardowych (110 A i 120 A). Prace dotyczą zarówno elementów zewnętrznych wkładki bezpiecznikowej (korpus ceramiczny), jak i elementów wewnętrznych (obwód prądowy). Opisano zarówno rozkład gęstości prądu elektrycznego, jak i jego wpływ na temperaturę elementów konstrukcyjnych bezpieczników w czasie ich pracy. Rozkład temperatury, straty mocy i rozpraszanie energii mierzono za pomocą modelu numerycznego. W celu weryfikacji i walidacji modelu przeprowadzono badania eksperymentalne, podczas których mierzono temperaturę w różnych częściach urządzenia przy wykorzystaniu prądu znamionowego.

Ważnym nurtem badań jest zbudowanie uniwersalnego modelu numerycznego bezpiecznika jako elementu zabezpieczającego urządzenia elektryczne. O wadze tych badań świadczą liczne publikacje [70 – 76].

Zaproponowany model można określić jako nowatorski pod względem powtarzalności wyników analizy termicznej wkładek bezpiecznikowych dla zakresu prądów (80 A, 90 A, 100 A, 110 A, 120 A). Można zatem stwierdzić, że proponowany model jest cennym atutem, który może obniżyć koszty oraz uprościć i przyspieszyć prace nad badaniami nowych typów wkładek topikowych. Ważnym aspektem był fakt, że ewaluację eksperymentalną modelu uzyskano z dwóch niezależnych źródeł, co czyni tę pracę znaczącą.

Autor był odpowiedzialny za prace dotyczące budowy stanowiska eksperymentalnego oraz wykonanie niektórych elementów modelu 3D wkładki topikowej do złożenia na podstawie danych inżynierskich – element topikowy. Autor współpracował przy wykonaniu symulacji termicznych MES wkładki topikowej i był odpowiedzialny za analizę materiałową oraz dobór odpowiednich dla symulacji parametrów. Autor opracował materiały graficzne oraz współpracował przy powstawaniu publikacji.

W pracy [A7] zaproponowano oryginalne, nowe sposoby modelowania zjawisk fizycznych aparatów modułowych niskiego napięcia. Opracowano dokładny model 3D oraz wykonano analizy pól sprzężonych. Model wykorzystano podczas konstruowania i prototypowania nowych konstrukcji modułowych aparatów elektrycznych. Na etapie modelowania uzyskano szczegółowy i wiernie odzwierciedlający rzeczywistość model konstrukcyjny. Analiza zjawisk fizycznych pozwoliła na szczegółowe zrozumienie i poznanie procesów związanych z przepływem prądu przez tory prądowe aparatów elektrycznych.

Istotnym elementem konstrukcji wyłącznika jest tor prądowy. Podczas wyłączania prądu zwarciowego tor prądowy narażony jest na oddziaływanie termiczne i mechaniczne, które mogą doprowadzić do trwałego uszkodzenia elementów toru prądowego lub nawet całego wyłącznika nadprądowego [77, 78]. Podczas procesu gaszenia łuku elektrycznego w wyłączniku zachodzą złożone zjawiska fizyczne, takie jak wydzielanie się ciepła w kanale łuku elektrycznego oraz powstawanie sił elektrodynamicznych powodujących naprężenia oddziałujące na styki wyłącznika [79]. Ścieżki prądowe różnią się kształtem i wielkością styków elektrycznych. Im większy prąd znamionowy wyłącznika, tym większe (masywniejsze) są styki elektryczne w torze prądowym [80]. W literaturze nie porusza się często zagadnień związanych ze zorganizowanym i sformalizowanym podejściem do budowy modeli termicznych aparatów elektrycznych w tym wyłączników nadprądowych. Zaproponowane opracowanie [A7] może być wykorzystywane do prac badawczo-rozwojowych, w procesie projektowania lub ulepszania konstrukcji urządzeń elektrycznych i jest uzupełnieniem literatury pod względem sposobu prowadzenia takich prac.

Aspektem nowatorskim w wykonanej pracy było szczegółowe i kompleksowe podejście do analizy termicznej oraz analizy parametrów elektrycznych biorąc pod uwagę dokładne odwzorowanie toru prądowego modułowego wyłącznika nadprądowego. Uzyskano powtarzalne wyniki, które zostały ewaluowane eksperymentalnie.

Autor był odpowiedzialny za opracowanie dokładnego modelu 3D toru prądowego wyłącznika nadprądowego oraz wykonaniu symulacji termicznych dla tego aparatu. Ponadto autor współpracował przy zbudowaniu stanowiska pomiarowego. Autor brał udział w współpracy przy analizie wyników symulacji w odniesieniu do badań eksperymentalnych oraz współpracował przy sporządzaniu publikacji.

W pracy [A8] przedstawiono analizę sprzężoną: Maxwell 3D, Transient Thermal oraz Fluent CFD, w momencie pojawienia się prądu znamionowego na szynach głównych rozdzielnicy niskiego napięcia. W analizie przedstawiono przepływ prądu znamionowego w szynach rozdzielnicy, co umożliwiło określenie ich wartości temperaturowych. Wyniki symulacji zostały potwierdzone badaniami eksperymentalnymi. Przedstawiono sposób odprowadzania ciepła w szynach zbiorczych i obudowie rozdzielnicy poprzez konwekcję powietrzną. Uwzględniono rozkład temperatur izolatorów. Wyniki uzyskane w trakcie symulacji pozwoliły na szczegółową analizę konstrukcji rozdzielnicy i wyciągnięcie właściwych wniosków w aspekcie praktycznym i teoretycznym. Pomogło to we wprowadzeniu zmian konstrukcyjnych w przygotowanym prototypie rozdzielnicy na etapie projektowania i budowy.

Podczas eksperymentów laboratoryjnych badane były określone punkty w rozdzielnicy, w których spodziewany był wzrost temperatury [81]. Nie oddaje to jednak w pełni całego zakresu temperatur obserwowanych w torach prądowych występujących wewnątrz rozdzielnicy [82]. W pracy omówiono pomiary temperatury w miejscu łączenia szyn zbiorczych na podstawie rezystancji zestyku i materiału galwanicznego w odniesieniu do wartości rezystancji zestyku. Badania miały na celu zapobieganie awariom podczas łączenia szyn zbiorczych, co z powodzeniem wykazano. Wyniki pomiarów i symulacji pokazują, że prawidłowe połączenie szyn zbiorczych jest bardzo ważne z punktu widzenia budowy i eksploatacji urządzeń rozdzielczych [83]. Ponadto wykonywanie tego typu testów jest operacją skomplikowaną, kosztowną i czasochłonną. Wymaga kilku testów przed opracowaniem gotowego produktu. W celu obniżenia kosztów tego typu badań [84] istnieje możliwość wykonania szczegółowego modelu 3D rozdzielnicy oraz wykonania symulacji komputerowej w środowisku MES – co jest pomysłem nowatorskim i znacząco ograniczającym koszty analizy oraz zużycia materiałów. Wykorzystano również analizy sprzężone bazujące na modułach *ANSYS*: *Maxwell 3D*, *Fluent CFD*, *Transient Thermal*, pozwalające na symulacje dokładnego rozkładu temperatury na szynach zbiorczych oraz wewnątrz rozdzielnicy [85].

Autor był odpowiedzialny za opracowanie modelu 3D rozdzielnicy oraz jej torów prądowych. Ponadto autor współpracował przy zbudowaniu stanowiska pomiarowego. Autor brał udział w współpracy przy wykonaniu symulacji numerycznych dla sporządzonego modelu 3D w tym głównie przy symulacjach termicznych dla obiektu. Autor współpracował przy porównywaniu wyników uzyskanych z symulacji do tych uzyskanych z eksperymentu oraz zajmował się budowaniem publikacji.

2.3. Publikacje dotyczące analizy zjawisk łukowych

Modelowanie zjawisk łukowych zostało przedstawione w publikacjach [A1, A2]. Ponad to w wymienionych pracach zostały zbadane zjawiska elektryczne takie jak rozkład potencjału, straty mocy na torach prądowych oraz układach stykowych aparatów, drogi oraz szybkości jakie przemierzały ładunki podczas gaszenia łuku elektrycznego w komorze gaszeniowej, rozkład pola elektromagnetycznego oraz magnetycznego. Analizy zostały wykonane z wykorzystaniem narzędzi MES i stanowiły graficzną reprezentację wyników symulacji numerycznych. Na podstawie badań zjawisk elektrycznych pochodzących z publikacji [A2] sporządzono patent [P1].

W pracy [A1] zaproponowano nową metodę dydaktyczną bazującą na analizie zjawisk fizycznych w układzie stykowym wysokiego napięcia.

Pomysł zbudowania statycznego układu stykowego powstał aby studenci mogli ćwiczyć swoje umiejętności i dzięki temu lepiej rozumieć zachodzące zjawiska fizyczne dotyczące prądów szczepienia i zjawisk łukowych. Nowatorski system zadań został sformułowany z myślą o skupieniu się na podstawowych umiejętnościach i zakresie wiedzy, który jest najważniejszy dla młodego inżyniera elektryka [85 – 94].

Doktorant w tej pracy opracował stanowisko do prób eksperymentalnych oraz badań dydaktycznych zarówno sporządzając odpowiedni schemat jak i pracując fizycznie przy powstawaniu tego stanowiska. Autor był również odpowiedzialny za agregację wyników pracy oraz ich obróbkę statystyczną co stanowiło weryfikację zaproponowanej metody dydaktycznej. Autor również przyczynił się do powstania koncepcji artykułu i uczestniczył bezpośrednio w jego sporządzeniu.

W pracy [A2] zaproponowano nowe sposoby modelowania zjawisk łukowych w aparatach niskiego napięcia. W publikacji rozpatrywany był model komory gaszeniowej wyłącznika nadprądowego niskiego napięcia. Zaproponowany model umożliwiał: obserwację gradientu napięcia w komorach gaszeniowych aparatów elektrycznych, analizę pola przepływowego w komorach gaszeniowych aparatów elektrycznych, realizację twórczych badań eksperymentalnych w obszarze aparatów modułowych niskiego napięcia, badań w obszarze wytrzymałości elektrycznej i mechanicznej kluczowych elementów aparatów elektrycznych niskiego napięcia oraz możliwość prognozowania miejsca wystąpienia łuku elektrycznego na elektrodach bieżnikowych.

W celu weryfikacji założeń konstrukcyjnych i konieczności wybranych rozwiązań – przeprowadza się wiele testów i symulacji, które pozwalają na wykrycie defektów i optymalizację efektywności komory łukowej już na etapie projektu. Środki te są niezbędne do ograniczenia zużycia materiałów konstrukcyjnych i pomagają poprawić właściwości komory łukowej. Wykorzystanie symulacji MES (Metody Elementów Skończonych) jest bardzo skuteczne w przeprowadzaniu wielu analiz dotyczących aspektów elektrycznych, mechanicznych i tych dotyczących trwałości materiałów. Ogromną zaletą tej metody jest możliwość sprawdzenia skomplikowanych scenariuszy, w których stosuje się różne warunki brzegowe. Dobrym przykładem jest symulacja rozkładu ciśnienia gazu na powierzchni komory łukowej FSI przeprowadzona w publikacji [2]. We wspomnianym przypadku symulację wykorzystano do zachowania dodatkowych informacji poddanych pomiarom odkształceń obudowy komory łukowej [1 – 6].

Przedstawiony model oraz procedura w pracy [A2] zostały zweryfikowane badaniami empirycznymi, które potwierdzają zasadność takiego postępowania. Ważną cechą wynikającą z tej pracy jest możliwość rekonstrukcji modeli komór łukowych i w przypadku zmian konstrukcyjnych, uniknięcie kosztownych i czasochłonnych badań laboratoryjnych lub przynajmniej ograniczenie nakładów. Podejście to jest zgodne z panującym obecnie trendem redukcji czasu i kosztów w projektowaniu i wytwarzaniu aparatów elektrycznych. Optymalizację można zastosować do istniejących rozwiązań z wykorzystaniem proponowanej procedury. Taki proces może nie tylko zwiększyć bezpieczeństwo użytkowników, ale także ograniczyć zużycie materiałów, pozytywnie wpływając na środowisko. Poza tym modelowanie MES w tym modelowanie za pomocą CFD (Computational Fluid Dynamics) może być wykorzystane do projektowania aparatury dla różnych warunków, zakresów napięć i zastosowań [95 – 98]. Powyższe stwarza ogromne możliwości bezpiecznego, szybkiego i wysoce ekonomicznego kreowania nowych trendów i rozwiązań w inżynierii aparatury elektrycznej. Wadą modelowania MES jest nadal konieczność przeprowadzenia badań eksperymentalnych w celu ewaluacji modelu, tak jak jest to określone we wszystkich obowiązujących normach.

Autor w tej pracy był odpowiedzialny za zbudowanie modelu 3D komory gaszeniowej, który w dalszych etapach posłużył do wykonania symulacji MES za pomocą programów takich jak ANSYS oraz COMSOL. Autor był również odpowiedzialny za samodzielne wykonanie symulacji termicznych dla komór gaszeniowych badanych wyłączników nadprądowych oraz uczestniczył w wykonaniu symulacji CFD dla tych aparatów. Doktorant zajmował się również pracą analityczną polegającą na porównaniu wyników oraz ich interpretacją porównawczą. Celem było odniesienie rezultatów pochodzących z symulacji MES do rezultatów empirycznych. Autor brał również udział w przygotowywaniu stanowiska do badań eksperymentalnych oraz współpracy przy sporządzeniu publikacji.

2.4. Publikacje dotyczące analizy zjawisk mechanicznych

Modelowanie zjawisk mechanicznych zostało przedstawione w pracy [A3]. W publikacji przedstawiono dynamikę ruchu zestyku tulipanowego, modyfikację konstrukcji styczek zestyku.

W pracy [A3] zaproponowano model układu stykowego tulipanowego. Zaproponowany model bazuje na pomierzonych wielkościach fizycznych i umożliwia: obserwację działania sił działających na styczki układu stykowego, energii wszystkich styczek zestyku nieruchomego, obserwacja wpływu mimośrodu zamocowania styku ruchomego na możliwość załączania, wyznaczania wartości parametrów elektrycznych podczas operacji łączeniowych.

Połączenie dwóch rodzajów analiz – analizy ruchu zestyku i analizy rozkładu pola elektrycznego, daje obraz najbliższy rzeczywistemu działaniu układu styku wieńcowego. Pozwala to zaprojektować cały zestyk w optymalny sposób. Analiza dotyczyła zarówno czasu projektowania, jak i kosztów oraz kwestii materiałowych związanych z budową prototypu. Wykonano szereg symulacji dotyczących tych elementów, aby udowodnić, że odpowiednie symulacje mogą wspomóc proces projektowania styków elektrycznych, wykrywania uszkodzeń i analizy konstrukcji podczas pracy układu [99, 100].

Liczni autorzy w dostępnej literaturze koncentrowali się głównie na symulowaniu układu stykowego wieńcowego tak jakby model był zbudowany z jednolitego materiału [1, 31, 101]. W rzeczywistości przy niewielkiej liczbie nacięć styk nieruchomy jest masywny i ogólna analiza mechaniczna całego styku może nie mieć sensu, ze względu na nakład pracy i możliwość otrzymania wystarczających wyników podczas przeprowadzenia symulacji dla jednej styczki [82]. Dlatego w niektórych przypadkach analizę zjawisk fizycznych można sprowadzić tylko do pojedynczej styczki [102]. Niemniej jednak zbudowanie modelu pozwalającego na symulowanie zachowania wielu styczek podczas badań pozwala na uchwycenie ich wzajemnych interakcji, co może być kluczowe w celu dogłębnego zrozumienia zjawisk mechanicznych i elektrycznych podczas eksploatacji układu [103]. W niniejszej pracy zaobserwowano znaczenie wzajemnych przemieszczeń styczek względem siebie i ich wzajemne oddziaływania. Powodują one zmianę całkowitej energii momentu obrotowego i naprężeń mechanicznych, które należy wziąć pod uwagę podczas analizy. Warto zauważyć, że wysokoprądowe układy styków tulipanowych są również powszechnie stosowane w technice próżniowej. W technice próżniowej układy styków wielolstyczkowych są zawsze zamykane w warunkach beznapięciowych. Jednakże obciążenia mechaniczne i związane z nimi zagrożenia, w tym uszkodzenia, awarie, a nawet scenariusze, w których dochodzi do zniszczenia aparatury są bardzo podobne do systemów z ośrodkiem gaszeniowym jakim jest SF6 [104].

Praca [A3] jest nowatorska, gdyż skupia się na analizie działania styku nieruchomego. Niemniej jednak podczas omawiania wyników symulacji wzięto pod uwagę i przeprowadzono analizę styków ruchomych (wszystkich). Następujące zdania podkreślają znaczenie wykonanej pracy: możliwość obserwacji zachowania, działania, sił i energii wszystkich styczek styku nieruchomego (stałego); obserwacja wpływu mimośrodu mocowania styku ruchomego na możliwość załączenia; analiza mechaniczna styku jak dla rzeczywistego układu fizycznego; wyznaczanie wartości parametrów elektrycznych podczas operacji łączeniowych; potencjalny rozwój konstrukcji styków w innych środowiskach gaszeniowych (przyszłe prace nad sporządzonym modelem).

Autor był odpowiedzialny za zbudowanie modelu 3D układu stykowego, które w kolejnych etapach posłużył do przeprowadzenia symulacji MES dynamiki ruchu tego zestyku. Autor współpracował przy wykonaniu symulacji dynamiki ruchu zestyku oraz analizie parametrycznej, która pozwolił na obserwację wielkości elektrycznych. Autor pracował nad ewaluacją sporządzonego modelu i odniesieniu wyników z symulacji do dostępnych danych inżynierskich uzyskanych w Laboratorium Zwarciowym Politechniki Warszawskiej. Autor uczestniczył w sporządzeniu koncepcji publikacji jak i bezpośrednim budowaniu artykułu.

2.5. Patenty

Autor niniejszej pracy jest współautorem patentów [P1 – P6] sporządzonych na podstawie publikacji wymienionych w podrozdziałach rozdziału 2. Wkład autora rozprawy niniejszej pracy.

Przedmiotem patentu [P1] jest urządzenie zmniejszające czas wyłączenia łuku elektrycznego w wyłącznikach wysokiego napięcia. Urządzenie zabezpieczające zawiera zbiornik z czynnikiem gaszącym, przy czym do zbiornika poprzez przepustnice wylotową oraz przepustnice wlotową dołączony jest układ odpływowy sterująco-zabezpieczający. Przepustnica wlotowa dołączona jest do układu odpływowego sterująco-zabezpieczającego poprzez układ sprężarki. Układ odpływowo sterująco-zabezpieczający dołączony jest do miejsca styku elektrody ruchomej z elektrodą nieruchomą wyłącznika wysokiego napięcia. Przedmiotem zgłoszenia jest również sposób zmniejszania czasu wyłączenia łuku elektrycznego w wyłącznikach wysokiego napięcia. Praca powiązana z publikacją [A3]. Autor był odpowiedzialny za opracowanie koncepcji wynalazku, przygotowywanie rysunków technicznych oraz przygotowywanie treści zgłoszenia patentowego.

Przedmiotem patentu [P2] była pompa zawierająca sekcje (A, B) obejmującą korpus z uzwojeniem pierwotnym, wyposażony w pierwszy wlot i pierwszy wylot, mieszczący ruchomy ruchem posuwistym, dwukierunkowym szczelny tłok, cechuje się tym, że tłok jest wyposażony w uzwojenie wtórne, zaś pierwszy wlot i pierwszy wylot są rozmieszczone z pierwszej strony korpusu i zamykane odpowiednio pierwszym zaworem wlotowym i pierwszym zaworem wylotowym, a po drugiej, przeciwnej względem tłoka stronie korpus jest zaopatrzony w drugi wlot zamykany drugim zaworem wlotowym i drugi wylot zamykany drugim zaworem wylotowym. Zgodnie ze zgłoszeniem pracą pompy steruje się podając zmienne napięcie na uzwojenie pierwotne każdej sekcji. Praca powiązana z publikacją [A4]. Autor był odpowiedzialny za opracowanie koncepcji wynalazku, przygotowywanie rysunków technicznych oraz przygotowywanie treści zgłoszenia patentowego. Wynalazek powstał ściśle na podstawie pomysłu autora (budowa siłownika).

Przedmiotem patentu [P3] był wyzwalacz elektromagnetyczny którego budowa została przedstawiona na Rysunku 1.

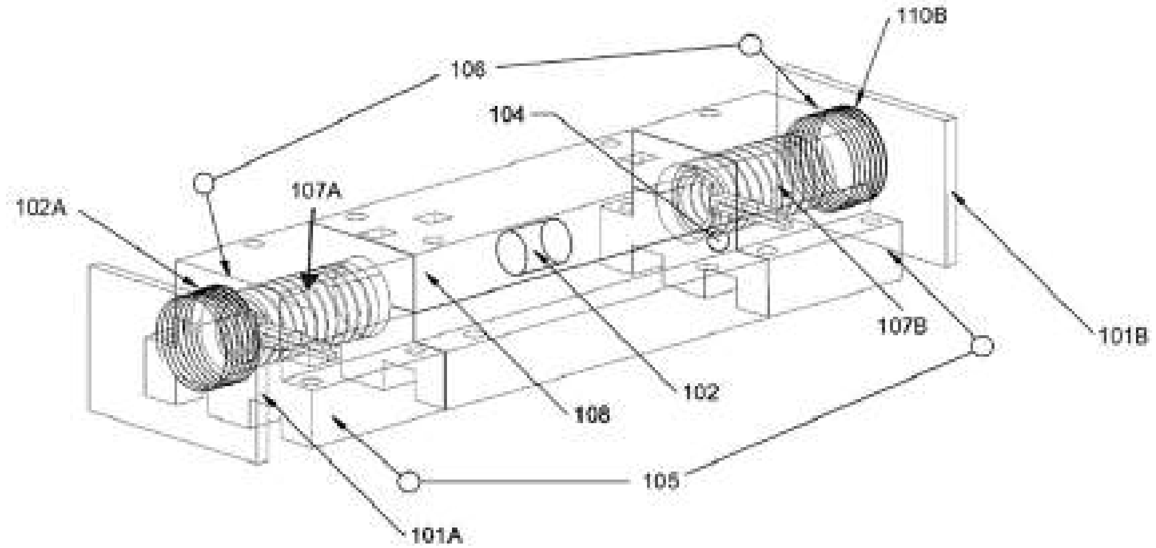

Rys. 1. Schemat wynalazku zaczerpnięty z PAT.239158 UP RP, data udzielenia prawa 10.08.2021.

Wyzwalacz był zaopatrzony w korpus (108) wewnątrz którego przy jego pierwszym końcu znajduje się pierwsza cewka (107A), i który ma z przeciwnych stron pierwszą ruchomą zworę elektromagnetyczną (101A) i drugą ruchomą zworę elektromagnetyczną (101B) zgodnie z wynalazkiem cechuje się tym, że korpus (108) jest diamagnetyczny lub paramagnetyczny, i ma drugi koniec przy którym wewnątrz korpusu (108) znajduje się druga cewka (107B), współosiowa z pierwszą cewką (107A). Pierwsza (107A) i druga (107B) cewka częściowo otaczają współosiową z cewkami pustą przestrzeń korpusu (108) wewnątrz której przemieszcza się ruchomy rdzeń (102). Pierwsza (101A) i druga (101B) zwora są namagnesowane, a przy pustej przestrzeni korpusu (102) w sąsiedztwie zwór są rozmieszczone czujniki optyczne (104). Praca powiązana z publikacją [A4]. Autor był odpowiedzialny za opracowanie koncepcji wynalazku, przygotowywanie rysunków technicznych oraz przygotowywanie treści zgłoszenia patentowego. Wynalazek powstał ściśle na podstawie pomysłu autora (budowa siłownika).

Przedmiotem patentu [P4] był reluktancyjny mechanizm udarowy ze stabilizacją drgań, znajdujący zastosowanie w elektronarzędziach, zawierający blok roboczy i połączony z nim blok stabilizatora drgań. Blok roboczy zawiera roboczy układ zasilania zawierający sekcję pierwszą i dołączoną do niej szeregowo sekcję drugą, przy czym między sekcją pierwszą a sekcją drugą umiejscowiony jest ferromagnetyczny trzpień roboczy umieszczony przesuwnie wzdłuż osi obudowy. Blok stabilizatora drgań zawiera podłużną obudowę, o osi podłużnej równoległej do osi podłużnej obudowy bloku roboczego, przy czym w obudowie bloku stabilizatora drgań znajdują się: układ zasilania stabilizatora drgań, sprężyna odbojowa oraz ferromagnetyczny trzpień stabilizatora drgań umiejscowiony między sekcją stabilizatora drgań a sprężyną odbojową, zamocowany przesuwnie wzdłuż osi obudowy. Praca powiązana z publikacją [A4]. Autor był odpowiedzialny za opracowanie koncepcji wynalazku, przygotowywanie rysunków technicznych oraz przygotowywanie treści zgłoszenia patentowego. Wynalazek powstał ściśle na podstawie pomysłu autora (budowa siłownika).

Przedmiotem patentu [P5] była mufa elektrotechniczna do łączenia dwóch odcinków kabli lub przewodów, zawierającą wałek sprzęgający, pierwszą głowicę i drugą głowicę. Wałek sprzęgający zawiera umiejscowione po przeciwnych stronach osiowe otwory: pierwszy otwór z gwintem lewoskrętnym i drugi otwór z gwintem prawoskrętnym. Pierwsza głowica zawiera z jednej strony gwintowany trzpień łączący z gwintem lewoskrętnym, a z przeciwnej strony współosiowy z trzpieniem otwór gwintowany z gwintem stożkowym lewoskrętnym. Druga głowica zawiera z jednej strony gwintowany trzpień łączący z gwintem prawoskrętnym, a z przeciwnej strony współosiowy z trzpieniem otwór gwintowany z gwintem stożkowym prawoskrętnym. Pierwsza głowica jest wkręcalna trzpieniem łączącym w pierwszy otwór wałka sprzęgającego, a druga głowica jest wkręcalna trzpieniem łączącym w drugi otwór wałka sprzęgającego. Autor był odpowiedzialny za opracowanie koncepcji wynalazku, przygotowywanie rysunków technicznych oraz przygotowywanie treści zgłoszenia patentowego.

Przedmiotem patentu [P6] było urządzenie do pomiaru rezystywności gruntu zawierające przewodzące elektrody, amperomierz i woltomierz charakteryzuje się tym, że zawiera korpus z komorą wewnętrzną, w której na przeciwległych ściankach bocznych umieszczono płytki przewodzące, a dno korpusu zawiera wsuwaną płytkę, przy czym do płytki przewodzącej dołączone jest wzorcowe źródło energii elektrycznej połączone szeregowo ze stabilizatorem napięcia poprzez rezystancję wejściową i włącznik, następnie stabilizator napięcia połączony jest z amperomierzem i włącznikiem pomiaru prądu kolejno podłączony ponownie do wzorcowego źródła energii elektrycznej poprzez rezystencją zastępczą badanej próbki, przy czym pomiędzy stabilizatorem, a amperomierzem umieszczony jest woltomierz wraz z włącznikiem. Autor był odpowiedzialny za opracowanie koncepcji wynalazku, przygotowywanie rysunków technicznych oraz przygotowywanie treści zgłoszenia patentowego.

3. Podsumowanie i wnioski końcowe

3.1. Podsumowanie

Rozprawa składa się z jedenastu publikacji [A1 – A11] i sześciu udzielonych patentów [P1 – P6], w których zaproponowano:

W pracach [A5, A9, A10, A11, P1] zaproponowano oryginalne, nowe podejście do modelowania zjawisk fizycznych w torach wielkoprądowych. Zaproponowane modele umożliwiały: obserwację działania sił, energii działających na izolatory wsporcze, realizację doboru i modelowania torów prądowych ze względu na zagrożenia związane z przepływem prądu zwarciowego, obserwację skutków działania sił elektrodynamicznych od prądu zwarciowego niesymetrycznego i symetrycznego, realizację twórczych badań eksperymentalnych w obszarze: prądów sczepienia, rezystancji przejścia, sił docisku, torów prądowych wraz z zestykami płaskimi. W pracy [A10] zaproponowano oryginalne, nowe sposoby modelowania zjawisk fizycznych w zestykach aparatów elektrycznych wysokiego napięcia. Opracowany właściwy i skuteczny sposób projektowania styków elektrycznych został osiągnięty poprzez połączenie badań teoretycznych i praktycznych. Zaproponowano również oryginalne, nowe sposoby modelowania zjawisk fizycznych zaproponowano oryginalne, nowe sposoby modelowania zjawisk fizycznych w torach wielkoprądowych. Zaproponowany model umożliwia: obserwację działania sił, energii działających na izolatory wsporcze, realizację doboru i modelowania torów prądowych ze względu na zagrożenia związane z przepływem prądu zwarciowego, obserwację skutków działania sił elektrodynamicznych od prądu zwarciowego niesymetrycznego, realizację twórczych badań eksperymentalnych w obszarze: prądów sczepienia, rezystancji przejścia, sił docisku, torów prądowych wraz z zestykami płaskimi. W pracach [A4, A5] zaproponowano oryginalne, nowe sposoby modelowania zjawisk fizycznych w zestykach aparatów elektrycznych wysokiego napięcia. Opracowany właściwy i skuteczny sposób projektowania styków elektrycznych został osiągnięty poprzez połączenie badań teoretycznych i praktycznych.

W pracach [A6, A7, A8] zaproponowano oryginalne, nowe sposoby modelowania zjawisk fizycznych w torze i stykach bezpiecznika topikowego niskiego napięcia. Zaproponowane modele bazują na pomierzonych wielkościach fizycznych i umożliwiają: obserwację pól temperaturowych, realizację twórczych badań eksperymentalnych: w obszarze bezpieczników topikowych, prądów przeciążeniowych i skutków ich przepływu. Zaproponowano szczegółowy trójwymiarowy model wkładki topikowej. W przeprowadzonych analizach skupiono się głównie na właściwościach termicznych podczas pracy bezpieczników w warunkach nominalnych (100 A) i niestandardowych (110 A i 120 A). Opisano zarówno rozkład prądu elektrycznego, jak i jego wpływ na temperaturę elementów konstrukcyjnych bezpieczników w czasie ich pracy. Wyznaczono rozkład temperatury, straty mocy i rozpraszanie energii. W celu weryfikacji i walidacji modelu przeprowadzono badania eksperymentalne, podczas których mierzono temperaturę na różnych częściach urządzenia przy użyciu prądu znamionowego. Na koniec oba zestawy wyników zestawiono i porównano z wynikami uzyskanymi w badaniach symulacyjnych. Podkreślono możliwą istotną korelację między wynikami badań empirycznych a pracami symulacyjnymi. Zaproponowano również oryginalne, nowe sposoby modelowania zjawisk fizycznych w urządzeniach rozdzielczych. Przedstawiono zaawansowaną analizę sprzężoną: indukcji, temperatury i przepływu w momencie wystąpienia prądu znamionowego występującego na szynach głównych rozdzielnicy niskiego napięcia. Model symulacyjny był dokładnym odwzorowaniem rzeczywistego prototypu rozdzielnicy. Badania symulacyjne potwierdzono badaniami eksperymentalnymi. Przedstawiono odprowadzanie ciepła w szynach zbiorczych i obudowie rozdzielnicy - poprzez konwekcję powietrza. Uwzględniono rozkład temperatury dla izolatorów mostu szynowego wykonanych z materiału ognioodpornego: poliestru bezhalogenowego. Wyniki pozwoliły na szczegółową analizę konstrukcji rozdzielnicy i wyciągnięcie wniosków w aspekcie teoretycznym i praktycznym. Dodatkowo wykonano i zaprezentowano badani dla prądu zwarciowego.

W pracach [A2, A4, P2, P3, P4, P6] zaproponowano oryginalne, nowe sposoby modelowania zjawisk fizycznych w aparatach elektrycznych niskiego napięcia. Zaproponowane modele bazują na pomierzonych wielkościach fizycznych i umożliwiają: obserwację pola elektromagnetycznego, indukcji magnetycznej, obserwację gradientu napięcia w komorach gaszeniowych aparatów elektrycznych, analizę pola przepływowego w komorach gaszeniowych aparatów elektrycznych, realizację twórczych badań eksperymentalnych w obszarze aparatów modułowych niskiego napięcia, badań w obszarze wytrzymałości elektrycznej i mechanicznej kluczowych elementów aparatów elektrycznych niskiego napięcia.

W pracach [A1, A3] zaproponowano oryginalne, nowe sposoby modelowania zjawisk fizycznych aparatów modułowych niskiego napięcia. Opracowano dokładny model 3D oraz wykonano zaawansowane analizy pól sprzężonych. Model wykorzystano podczas konstruowania i prototypowania nowych konstrukcji modułowych aparatów elektrycznych. Już na etapie modelowania uzyskano akceptowalny model konstrukcyjny. Analiza zjawisk fizycznych pozwala na szczegółowe zrozumienie i poznanie procesów związanych z przepływem prądu przez tory prądowe aparatów elektrycznych.

3.2. Wnioski końcowe

Autor dokonał przeglądu literatury w zakresie zjawisk fizycznych występujących w układach stykowych i torach prądowych aparatów elektrycznych niskiego oraz wysokiego napięcia. Autor w swoich pracach wnikliwie omówił zjawiska fizyczne występujące podczas przepływu prądów znamionowych oraz zwarciowych przez wspomniane w pracach [A1 – A11] oraz [P1 – P6] aparaty, a dokładnie ich układy stykowe oraz tory prądowe. Duży nacisk został położony na omówienie oddziaływania sił elektrodynamicznych w aparatach niskiego i wysokiego napięcia oraz procesów termicznych, a w szczególności nagrzewania torów prądowych podczas przepływu prądu o różnych wartościach, zjawisk elektrycznych w tym zjawisk łukowych oraz zjawisk mechanicznych. Ponadto przedstawiono prace pokazujące próby konstruowania modeli MES przez innych autorów dla różnych aparatów elektrycznych. Prace te dotyczyły zarówno zjawisk elektrycznych, termicznych oraz mechanicznych. Po przeanalizowaniu omówionych w literaturze dotychczasowych obszarów zastosowań rozwiązań modelowych autor zdecydował się na zbudowanie modeli MES wybranych aparatów elektrycznych, a następnie symulacji zjawisk fizycznych w tych aparatach w celu otrzymania wyników jak najbliższych rzeczywistym warunkom eksperymentalnym. Opracowane zostały modele numeryczne, w których określono warunki brzegowe, warunki symulacyjne oraz geometrię poszczególnych symulowanych elementów tworzących aparat elektryczny.

Autor za istotny swój wkład w dyscyplinę uznaje:

- **wykonanie badań eksperymentalnych rzeczywistych obiektów, w tym badań zwarciowych;**
- **opracowanie szczegółowych reprezentacji graficznych w środowisku 3D wybranych elementów aparatów elektrycznych;**
- **opracowanie numerycznych modeli symulacyjnych zjawisk fizycznych (oddziaływania termiczne, oddziaływania elektrodynamiczne, oddziaływania mechaniczne, oddziaływania łukowe) generujących rozwiązania zbieżne z wynikami uzyskanymi z badań eksperymentalnych dla różnych warunków;**

- **analizę otrzymanych wyników z numerycznych modeli symulacyjnych oraz ich dyskusję w porównaniu do wartości rezultatów otrzymanych eksperymentalnie oraz odniesienie do wyników dostępnych w literaturze;**
- **opracowanie wynalazków na podstawie modeli symulacyjnych, oraz wyników eksperymentalnych uzyskanych podczas wykonywania przedstawionych prac naukowych w formie patentów.**

Autor tym samym odpowiedział na wszystkie postawione tezy badawcze sformułowane w rozdziale *1.4. Cel badań oraz tezy badawcze*.

4. Literatura

1. Bini, R.; Galletti, B.; Iordanidis, A.; Schwinne, M., *Arc-induced Turbulent Mixing in a Circuit Breaker Model*, In Proceedings of the 1st International Conference on Electric Power Equipment–Switching Technology, Xi'an, Chinyx, 23–27 Październik 2011; s. 375–378

2. Wang, L.; Liu, H.; Zheng, W.; Ge, C.; Guan, R.; Chen, L.; Jia, S., *Numerical Simulation of Impact Effect of Internal Gas Pressure on Chamber Housing in Low-Voltage Circuit Breaker*, IEEE Trans. Compon. Packag. Manuf. Technol. 2014, 4, s. 632–640

3. Ye, X.; Dhotre, M.T.; Mantilla, J.D.; Kotilainen, S., *CFD Analysis of the Thermal Interruption Process of Gases with Low Environmental Impact in High Voltage Circuit Breakers*, In Proceedings of the 2015 Electrical Insulation Conference (EIC), Seattle, WA, USA, 7–10 Czerwiec 2015

4. Dhotre, M.T.; Ye, X.; Seeger, M.; Schwinne, M.; Kotilainen, S., *CFD Simulation and Prediction of Breakdown Voltage in High Voltage Circuit Breakers*, In Proceedings of the 2017 Electrical Insulation Conference (EIC), Baltimore, MD, USA, 11–14 Czerwiec 2017

5. Chen, D.G.; Li, Z.P.; Li, X.W., *Simulation of pressure rise in arc chamber of MCCB during its interruption process*, In Proceedings of the 53rd IEEE Holm Conference on Electrical Contacts, Pittsburgh, PA, USA, 16–19 Wrzesień 2007; s. 43–47

6. Rumpler, C.; Stammberger, H.; Zacharias, A., *Low-voltage arc simulation with outgassing polymers*, In Proceedings of the IEEE 57th Holm Conference on Electrical Contacts, Minneapolis, MN, USA, 11–14 Wrzesień 2011; s. 1–8

7. Li, Z. *Research of Gas Dynamic Problems in Arc Chamber of Low-Voltage Circuit Breaker*, Ph.D. Dissertation, Department Electrical Engineering, Xi'an Jiaotong University, Xi'an, Chiny, 2006

8. Holm, R., *Electric Contacts, Theory and Applications*, Springer-Verlag, Berlin, 2000.

9. Walczuk, E.: *Wpływ odskoków sprężystych na sczepianie się zestyków łącznika*, Zeszyty Naukowe Politechniki Łódzkiej „Elektryka", Łódź 1972, nr 37

10. Iordanidis, A.; Franck, C.M. *Self-consistent radiation based simulation of electric arcs*. *Part II: Application to gas circuit breakers*. J. Phys. D Appl. Phys. 2008, 41, 135206

11. Miedziński B., Okraszewski Z., Żołnierczyk T.: *The effect of contact surface conditions on reed bouncing*, IEEE Trans. Comp. Hybrits and Manuf. Tech. Nr 1, 1985

12. Miedziński, B., Zawiślński, J., Shoffa, V.: *The influence of a displacement current on dynamics of a H.V. reed*, Proceedings of ICEC 2000, Sztokholm

13. Miedziński B., Szymański A., Wiśniewski G., Grodziński A.: *Transformation of low power arc to glowing under inductive load DC*, Proceedings of Switching Arc Phenomena – SAP, Łódź 2001

14. Kulas, S., Kolimas, Ł., *Badania symulacyjne wielkoprądowego układu stykowego załącznika zwarciowego*, Przegląd Elektrotechniczny 2007, nr 3, s. 137–140

15. Kulas, S., Kolimas, Ł.: *Analysis of the electric Fidel strength In the contact system*, XX Symposium Electromagnetic Phenomena in Nonlinear Circuits, Conference Proceedings – CD, Lille, Francja, 2–4 Lipiec 2008

16. Kulas, S., Kolimas, Ł.: *Optimization of Electric Field in Contacts on Example of Making Switch*, Proceedings of the 42th International Universities Power Engineering Conference, University of Brighton, Brighton, UK 2007, s. 491–495

17. Kulas, S.: *Podstawy konstrukcji elektromechanicznych*, OWPW, 2012

18. Pawłota, M.: *Nagrzewanie się zestyków szynoprzewodów płaskich łączonych przez docisk w warunkach zakłóceniowych*, Mechanizacja i Automatyzacja Górnictwa 2011, nr 8, s. 57–66

19. Maksymiuk, J.: *Aktualne problemy budowy i eksploatacji wyłączników wysokonapięciowych*, Przegląd Elektrotechniczny, nr 3, Warszawa 1998.

20. Maksymiuk J.: *Aparaty elektryczne*, WNT, Warszawa 1977, 1992

21. Maksymiuk, J., Nowicki, J.: *Aparaty elektryczne i rozdzielnice wysokich i średnich napięć*, OWPW, ISBN 9788378141754, 2014

22. Slade, P. G., *Electrical Contacts, Priniciples and Applications*, CRC Press, Warszawa, 2008

23. Borkowski, P.: *Nowoczesne metody badań zestyków elektrycznych*, Akademicka Oficyna Wydawnicza EXIT, Warszawa, 2013

24. Ciok, Z.: *Ochrona środowiska w elektroenergetyce*, PWN, Warszawa 2001.

25. Ciok, Z., Maksymiuk, J., Pochanke, Z., Zdanowicz, L.: *Badanie urządzeń energoelektrycznych*, WNT, Warszawa 1992

26. Ciok, Z.: *Procesy łączeniowe w układach elektroenergetycznych*. Warszawa, WNT 1976

27. Löbel, H., Grossmann, S., Golletz F.: *Thermal behaviour of nework components depending on outdoor weather conditions*, Electricity Distribution – Part 1, 20th International Conference and exhibition on, ISBN 978-1-84919126-5, 2009

28. Braunovic, M., Myshkin, N., Konchits, V.: *Electrical Contacts: Fundamentals, Applications and Technology (Electrical and Computer Engineering)*, 2006

29. Braunovic, M.: *Characterization Techniques for Nanostructured Contact Materials*, Proceedings of the 56th IEEE Holm Conference on, DOI:10.1109/HOLM 2010.5619531 Conference: Electrical Contacts (HOLM), 2010
30. Basse, N. T. P., Bini, R., Seeger, M., *Measured turbulent mixing in a small-scale circuit breaker model*, Appl. Optics, vol. 48, nr 32, 2009, s. 6381–6391
31. Incropera, F. P., DeWitt, D. P., Bergman, T. L., Lavine, A. S., *Introduction to Heat Transfer*, V Edycja. Hoboken, NJ, USA, Wiley, 2006
32. Li, D., Qi, L., *Energy based fuse modeling and simulation*, 2013 IEEE Electric Ship Technologies Symposium (ESTS), Arlington, VA, 2013; s. 487–492, doi: 10.1109/ESTS.2013.6523781
33. Kumar, P., Kale, A., "*3-Dimensional CFD simulation of an internal arc in various compartments of LV/MV Switchgear*", Ansys Convergence Conference, Wrzesień 2016.
34. Hartland, D. J., *Electric contact systems - passing power to the trains*, IET Professional Development Course on Electric Traction Systems, 2010, s. 25–37
35. Gómez, J.C., Tourn, D.H., *gPV fuse: Special characteristics for photo voltaic cells protection*, In Proceedings of the 9th International Conference on Electrical Fuses and their Applications (ICEFA), Maribor, Slovenia, 12–14 Wrzesień 2011; s. 1–9.
36. Gomez, J. C., Tourn, D., Nesci, S., Zamarillo, G.R., *PV cells protection by using class PV fuses*, IEEE Lat. Am. Trans. 2013; 11, s. 531–537
37. Zhang, Y., Su, J., Zheng, L., Li, R., Yu, B., Shang, W., *Analysis of high-voltage DC fuse's ageing characteristics under the overload pulse current carrying mode and the caused short-circuit failure in series-resonant converter power source*, Int. J. Elec. Power, vol. 117, 2020, s. 1–10
38. Kumar, A., *Electro-thermal Characterizations, Compact Modeling and TCAD based De-vice Simulations of advanced SiGe:C BiCMOS HBTs and of nanometric CMOS FET*, Micro and nanotechnologies/Microelectronics, Université Bordeaux 1 Sciences et Technologie, 2012
39. Plesca A., Mihet-Popa L., *Thermal Analysis of Power Rectifiers in Steady-State Conditions*, Energies 2020, 13(8), 1942; Kwiecień, 2020, doi.org/10.3390/en13081942
40. Di Napoli, F., Magnani, A., Copola, M., Guerriero, P., D'Alessandro, V., Codecasa L., Tricoli, P., Daliento, S., *On-Line Junction Temperature Monitoring of Switching Devices with Dynamic Compact Thermal Models Extracted with Model Order Re-duction*, Energies, 10(2), 189, 2017

41. De Tommasi, L., Magnani, A., De Magistris M., *Advancements in the identification of passive RC networks for compact modeling of thermal effects in electronic devices and systems,* International Journal of Numerical Modelling: Electronic Networks, Devices and Fields, 31.3, 2018
42. Kühnel Ch., Schlegel S., Großmann S., *Investigations on the long-term behavior and switching function of fuse-elements for NH-fuse-links (gG) at higher thermal stress,* 2017 6th International Youth Conference on Energy (IYCE), Budapeszt, Węgry, 21–24 Czerwiec 2017
43. An Y., Liu G., Wang P., Wen H., Meng Z., *Magnetic force analysis and experiment of novel permanent magnet axial thrust balance structure in canned motor pump,* IEEE 2nd International Conference on Advanced Computer Control, vol. 1, 2010
44. Cai J., Deng Y., *Initial Rotor Position Estimation and Sensorless Control of SRM Based on Coordinate Transformation*, IEEE Trans. Instrum. Meas., vol. 64, no. 4, s. 1004-1018, Kwiecień 2015
45. Masi A., Danisi A., Losito R., Perriard R. *Characterization of magnetic immunity of an ironless inductive position sensor,* IEEE Sensors Journal. vol. 13, no. 3, s. 941–948, 2013
46. Yongdae K., Choi H.Y., CH Y., Lee, *Design and preliminary evaluation of high-temperature position sensors for aerospace applications*, IEEE Sensors Journal. vol. 14, no. 11, s. 4018–4025, 2014
47. Khoshnoud F., Silva C.W., *Recent advances in MEMS sensor technology-mechanical applications, IEEE Instrumentation & Measurement Magazine*, vol 15, no. 2, s. 14–24, Kwiecień 2012
48. Loussert G., *An Efficient and Optimal Moving Magnet Actuator for Active Vibration Control*, 15 th International Conference on New Actuators, Bremen, Germany, s. 1390142, 13–15 Czerwca 2016
49. Paulitsch C., Gardonio P., Elliott S.J., Sas P., Boonen R., *Design of a Lightweight, Electrodynamic, Inertial Actuator with Integrated Velocity Sensor for Active Vibration Control of a Thin Lightly-Damped Panel*, Proceedings of ISMA, s. 239–251, 2004
50. Paulitsch C., Gardonio P., Elliott S.J., *Active vibration damping using an interial, electrodynamic actuator,* Journal of vibration and acoustics, vol. 129, s. 39–47, Luty 2007.

51. Li X., Tian K., Zhou Y., *Linear Electromagnetic Oil Pumping Unit Based on the Principle of Coil Gun*, IEEE Conference, Chiny, 2008.
52. Fang P., Ding F., Li Q., *Novel High-Response Electromagnetic Actuator for Electronic Engraving System*, IEEE Transactions on Magnetics, vol. 42, no. 3, s. 460–464, Marzec 2006.
53. Nakanishi Y., Honda T., Kasamura K., Nakashima Y., Nakano K., Kondo K., Higaki H., *Bio-inspired shaft seal in coolant pump for electric vehicles*, IEEE International Conference on Renewable Energy Research and Applications (ICRERA), 2016
54. Clark R. E., Jewell G. W., Forrest S. J., Rens J., Maerky J., *Design Features for Enhancing the Performance of Electromagnetic Valve Actuation Systems*, IEEE Trans. Magn., vol. 41, no. 3, s. 692–696, Marzec 2005
55. Hoshi H., Shinshi T., Takatani S., *Third- generation blood pumps with mechanical noncontact magnetic bearings*, Artificial Organs, vol. 30, no. 5, s. 324–338, 2006.
56. Antaki J.F., Paden B., Burgreen G., Groom N.J., *Blood pump having a magnetically suspended rotor*, America Patent, No: 6447266 B2, Wrzesień 2002
57. Popa I. C., Dolan A.I., *Numerical modeling of three-phase busbar systems: Calculation of the thermal field and electrodynamic forces*, in Proc. Int. Conf. Appl. Theor. Electr. (ICATE), Craiova, Rumunia, Październik 2016, s. 1–9
58. Jiaxin Y., Ruichao W., Huimin L., Longqing B., Hongjian W., *Research on the calculation methods of enclosed isolated phase busbar in short-circuit condition*, in Proc. IEEE 62nd Holm Conf. Electr. Contacts (Holm), Clearwater Beach, FL, USA, Październik 2016, s. 111–114
59. Gatherer J., Jackson R. L., A multi-variable parametric study on the performance of bolted busbar contacts, in Proc. IEEE 61st Holm Conf. Elect. Contacts (Holm), San Diego, CA, USA, Październik 2015, s. 124–131
60. Kadkhodaei G., Sheshyekani K., Hamzeh M., Tavakoli S. D., *Multiphysics analysis of busbars with various arrangements under short-circuit condition* Elect. Syst. Transp., vol. 6, no. 4, s. 237–245, 2016
61. Kadkhodaei G., Sheshyekani K., and Hamzeh M., *Coupled electric– magnetic–thermal–mechanical modelling of busbars under shortcircuit conditions* Generat., Transmiss. Distrib., vol. 10, no. 4, s. 955–963, 2016

62. J.-Y. Zhong, S.-J. Wu, Z. Wang, Y.-J. Guo, and X.-Y. Qin, *A 3-D steady-state analysis of thermal behavior in EHV GIS busbar* J. Elect. Eng. Technol., vol. 11, no. 3, s. 781–789, 2016
63. Galvan E., Rodrigues J.J., *Study of the influence of permanent magnets in the interruption process of the electrical arc in MCB*, 2017 IEEE Holm Conference Electrical Contacts, IEEE, Denver, CO, USA, 10–13, Wrzesień 2017
64. Mahesh S. R., Kale A., Kumar S., *A Three Dimensional CFD Analysis to Investigate the Effect of Ablative Materials and Venting Arrangement on Arc Characteristics in Low Voltage Circuit Breakers*, IEEE, 2013 IEEE 59th Holm Conference on Electrical Contacts (Holm 2013), Newport, RI, USA, 22–25, Wrzesień 2013.
65. Ł. Kolimas, S. Łapczyński, M. Szulborski, *Tulip contacts: Experimental studies of electrical contacts in dynamic layout with the use of FEM software*" Int. J. Electr. Eng. Educ. 2019, vol. 1, s. 1–4.
66. International Electrotechnical Commission, *High-Voltage Switchgear and Controlgear—Part 102: Alternating Current Disconnectors and Earthing Switches*; *IEC 62271-102:2012*; International Electrotechnical Commission: Geneva, Switzerland, 2018.
67. Iwata M., Tanaka S., and Ohtaka T., *CFD calculation of pressure rise due to internal AC and DC arcing in a closed container*, IEEE Trans. Power Deliv. 26 1700–9, 2011 2016
68. Y. Wu, M. Li, M. Rong, F. Yang, A.B. Murhpy, Y. Wu, Y.D. Yuan, D. "*Experimental and theoretical study of internal fault arc in a closed container*", J. Phys. D Appl. Phys. vol. 47, 2014
69. M. Farhana, M.K.M. Jamil, I. Dahaman, M. Syafrudin, *Study on the electromagnetic force affected by short-circuit current in vertical and horizontal arrangement of busbar system*, In Proceedings of the International Conference on Electrical, Control and Computer Engineering 2011 (InECCE), Pahany, Malezja, 21–22 Czerwiec 2011; s. 1–8
70. Demir, M., Kahramanoğlu, G., Yıldız, A.B., *Calculating of fuse melting point for power electronics circuits by inrush energy and determination of the eligibility*, 2016 18th European Conference on Power Electronics and Applications (EPE'16 ECCE Europe), Karlsruhe, 2016, s. 1–6, doi: 10.1109/EPE.2016.7695322

71. Tong, J., Zou, Y., *Design of a Fuse-Time Testing System on STM32*, 2013 International Conference on Computer Sciences and Applications, Wuhan, Chiny 2013, 406–409, doi: 10.1109/CSA.2013.102
72. Farahani, H.F., Asadi, M., Kazemi, A., *Analysis of thermal behavior of power system fuse using finite element method*, 2010 4th International Power Engineering and Optimization Conference (PEOCO), Shah Alam, 2010, s. 189–195, doi: 10.1109/PEOCO.2010.5559169
73. Tanaka, T., Yamasaki, M., *Modeling of fuses for melting time and fusing current analysis*, INTELEC 2004. 26th Annual International Telecommunications Energy Conference, Chicago, IL, USA, 2004, s. 671–675, doi: 10.1109/INTLEC.2004.1401542
74. Pihler, J., Stegne, M., Kitak, P., Glotic, A., Fluher, B., Tiˇcar, I., Voršiˇc, J., *Fuse application in medium voltage switchgear*, In Proceedings of the 9th International Conference on Electric Fuses and their Applications (ICEFA), Maribor, Słowenia, 12–14 Września 2011, s. 110–118
75. Grass, N., *Protection of Power Electronic Multi Converter Systems in AC and DC Applications*, In Proceedings of the 10th International Conference on Electric Fuses and their Applications, Frankfurt and Menem, Niemcy, s. 1–5
76. Qi, B., Zhao, X., Zhang, Sh., Huang, M., Li, Ch., *Measurement of the electric field strength in transformer oil under impulse voltage*, IEEE Transactions on Dielectrics and Electrical Insulation, Kwiecień 2017, vol. 24, s. 1256–1262
77. Rumpler, C., Stammberger, H., Zacharias, A., *Low-voltage arc simulation with out-gassing polymers*, in Proc. IEEE 57th Holm Conf. Electr. Contacts, Wrzesień 2011, s. 1–8
78. Ye, X., Dhotre, M. T., Mantilla, J. D., Kotilainen, S., *CFD Analysis of the Thermal Interruption Process of Gases with Low Environmental Impact in High Voltage Circuit Breakers*, 2015 Electrical Insulation Conference (EIC), Seattle, Washington, USA, 7–10 Czerwca, 2015
79. Ryzhov, V.V., Molokanov, O. H., Dergachev, P. A., Vedechenkov, N. A., Kurbatova, E. P., Kurbatov, P. A., *Simulation of the Low – Voltage DC Arc*, Intenational Youth Conference on Radio Electronics, Electrical and Power Engineering (REEPE), Rosja, 14–15 Marzec 2019

80. Geetha, N.D., Rasilo, P., Arkkio, A., *Sensitivity Analysis of Inverse Thermal Modeling to Determine Power Losses in Electrical Machines*, IEEE Transactions on Magnetics, vol. 54, nr 11, 2018
81. Muhammood, M., Kamarol, M., Ishak, D., Masri, S., *Temperature rise prediction in 3-phase busbar system at 20 °C ambient temperature*, In Proceedings of the 2012 IEEE International Conference on Power and Energy (PECon), Kota Kinabalu, Malezja, 2–5 Grudzień 2012; s. 736–740
82. Risdiyanto, A., Arifin, M., Khayam, U., *Study on temperature distribution at busbar connection based on contact resistance of dierent plating contact surface*, In Proceedings of the 2013 Joint International Conference on Rural Information Communi-cation Technology and Electric-Vehicle Technology (rICT & ICeV-T), Bandung, Indonezja, 26–28 Listopad 2013; s. 1–6
83. Jung, H.S., *Study for temperature rise on busbar of the switchgear and controlgear assemblies*, Korea Inst. Inf. Commun. Eng. 2017, 21, s. 379–385
84. Park, S.W., Cho, H., *A practical study on electrical contact resistance and temperature rise at at the connections of the copper busbars in switchgears*, In Proceedings of the 2014 IEEE 60th Holm Conference on Electrical Contacts (Holm), Nowy Orlean, LA, USA, 12–15 Październik 2014; s. 1–7, doi:10.1109/HOLM.2014.7031066
85. Thompson, M.K., Thompson, J.M., *ANSYS Mechanical APDL for Finite Element Analysis*, 2017; 978-0-12-812981-4
86. Tovar E., Piedra N., *Guest editorial: Open educational resources in engineering education: Various perspectives opening the education of engineers*, IEEE Trans. Educ., 2014, vol. 57, no. 4, s. 213 – 219
87. Margaryan A., *Work-Based Learning: A Blend of Pedagogy and Technology, Saarbrücken, Germany: AV Akademikerverlag*, 2008
88. Ros S. et al., *UNED OER experience: From OCW to Open UNED*, IEEE Trans. Educ., 2014, vol. 57, no. 4, s. 248–254
89. Lundquist C., Skoglund M. A., Granstrom K., Glad T., *Insights from implementing a system for peer review,* IEEE Trans. Educ.,2013, vol. 56, no. 3, s. 261–267
90. Li, H. et al., *Peer assessment in the digital age: A meta-analysis comparing peer and teacher ratings*, Assess. Eval. Higher Educ., 2015, vol. 41, no. 2, s. 245–264
91. Fernandes M. A. C., *Problem-based learning applied to the artificial intelligence course*. Computer Applications in Engineering Education, 2016, 24(3):388-399

92. Lee C. S., Su J. H., Lin K. E., et al, *A project-based laboratory for learning embedded system designs with support from the industry*. IEEE Trans. Educ., 2008, 53(2):173–181

93. Ionescu C. M., Fabregas E., Cristescu S. M., Dormido S., Keyser R. D., *A remote laboratory as an innovative educational tool for practicing control engineering concepts*, IEEE Trans. Educ., 2013, vol. 56, no. 4, pp. 436 – 442

94. Jong B.S., Lai C.H., Hsia Y.T., Lin T.W., *Effects of anonymity in group discussion on peer interaction and learning achievement*, IEEE Trans. Educ., 2013, vol. 56, no. 3, s. 292–299

95. Zhang X, Zhang J, Gockenbach E., *Calculation of pressure and temperature in medium-voltage electrical installations due to fault arcs*, J. Phys. D: Appl. Phys. 41, 105206, 2008

96. Friberg G, Pietsch G. J., *Calculation of pressure rise due to arcing faults*, IEEE Trans. Power Deliv. 14 365–70, 1999

97. El Ouadhane, H., et. al, *Solutions For Internal Arc Protection Acc., Iec 62271-200 With Pressure Relief Into The Switchgear Room For Gas And Air Insulated Medium Voltage Switchgears*, 21st International Conference on Electricity Distribution, Frankfurt, 6–9 Czerwiec 2011

98. Kale A., Ranade M., *Study and simulation of pressure loss characteristics of venting arrangements in switchgear products*, ieema Journal, Swicon Listopad 2015.

99. Geng, C., He, F., Zhang, J., Hu, H., *Partial stray inductance modeling and measuring of asymmetrical parallel branches on the bus-bar of electric vehicles*, Energies 2017, 10, 1519.

100. Shing, A. W. C., Pascoschi, G., *Contact wire wear measurement and data management*, IET International Conference on Railway Condition Monitoring, 2006, s. 182 – 187.

101. Christen, T., *Radiation and nozzle ablation models for CFD simulations of gas circuit breakers*, In Proceedings of the 1st International Conference on Electric Power Equipment–Switching Technologies, Xi'an, Chiny, 23 – 27 Październik 2011.

102. Biao, W., Yanyan, L., Xiaojun, Z., *Study on detection technology of the contact pressure on the electrical contacts of relays*, 26th International Conference on Electrical Contacts (ICEC 2012), 2012, s. 161 – 164.

103. Kolimas, Ł., Sul, P., *Modelowanie i analiza dynamiki ruchu styków na przykładzie styku tulipanowego*, Przegląd Elektrotechniczny, ISSN 0033-2097, 2015.

104. Kolimas, Ł., *Analiza rozpływu prądu w sąsiadujących torach wielkoprądowych i zestykach*, Przegląd Elektrotechniczny, ISSN 0033-2097, 2012.

105. Bun R., Krzyszkowski A., ‘*Mathematical models of electrodynamic influences on an example of the flat inductor*, in Proc. Modern Problems Radio Eng., Telecommun. Comput. Sci., Luty 2002, s. 24–25.

106. Triantafyllidis, D. G., Dokopoulos P. S., Labridis D. P., *Parametric short-circuit force analysis of three-phase busbars-a fully automated finite element approach*, IEEE Trans. Power Del., vol. 18, no. 2, Kwiecień 2003, s. 531–537.

107. Shen B., Zhang X., Zhou D., *Analysis and calculation of short-circuit electro-dynamic forces on rectangular bus bars*, in Proc. IEEE 6th Int. Power Electron. Motion Control Conf., Maj 2009, s. 2618–2621

108. Yusop F. M., Jamil M. K. M., Ishak D., Masri, S., *Study on the electromagnetic force affected by short-circuit current in vertical and horizontal arrangement of busbar system*, in Proc. Int. Conf. Electr., Control Comput. Eng. (InECCE), Czerwiec 2011, s. 196–200.

109. Zhu Y., Chen D., Zhou C., Lu L., Duan X., *A knowledge graph based construction method for digital twin network*, in Proc. IEEE 1st Int. Conf. Digit. Twins Parallel Intell. (DTPI), Lipiec 2021, s. 362–365.

110. Liu Y., *Research on the design of digital twin system for construction safety*, in Proc. 2nd Int. Signal Process., Commun. Eng. Manage. Conf. (ISPCEM), Listopad. 2022, s. 254–258

5. Kopie publikacji oraz patentów składających się na niniejszą rozprawę

A1. *Currents of contact welding in a static layout: A laboratory exercise*

Original Article

IJEEE

International Journal of Electrical Engineering & Education
2022, Vol. 59(1) 45–59

DOI: 10.1177/0020720919840986
journals.sagepub.com/home/ije
SAGE

Currents of contact welding in a static layout: A laboratory exercise

Łukasz Kolimas and Sebastian Łapczyński

Abstract

The purpose of the proposed course is to enhance students' knowledge, engineering skills and understanding in the field of electrical contacts power engineering – the currents of contact welding. The main goal for students is to acquire brief skills concerning measurements of certain parameters using static layout: currents that cause contact welding, clamping force of contacts joints and breaking force. Moreover, students are encouraged to obtain soft skills like confidence in the mentioned field and creativity. Student work during the exercise is evaluated on the basis of report from laboratory work and test. Essential aspect is safety training while working with HV and MV switchgears – that is another obligatory feature which participants will obtain from this course. Course results were evaluated as significant on the basis of concluded statistical analysis and comparison to previous formula employed during the classes.

Keywords

Contact welding, short circuit current, electrical measurements, laboratory setup, electrical contacts

Introduction

The phenomena of contacts welding in the short circuit conditions is essential for the proper understanding of operations on medium and high voltage power systems. In order to broaden students' knowledge involving medium and high voltage

Electrical Faculty, Electrical Power Engineering Institute, Warsaw University of Technology, Warsaw, Poland

Corresponding author:
Sebastian Łapczyński, Warsaw University of Technology, Koszykowa 75, Warsaw 00-662, Poland.
Email: seb.lapczynski@gmail.com

engineering skills, the course was reformed and based on laboratory practice. Till 2015, the course was in the form of lecturing which was based on running calculations with use of supporting software like Matlab or Excel. Learning curve was high and that was caused by the lack of phenomena presentation. The grades distribution was not satisfactory and students were complaining about the formula of the classes. Therefore, idea of building static layout has arisen on which students can train their skills and then better understand ongoing phenomena. New form of exercise was drilled in with the start of 2017. The workout idea was also guessed around working in teams for acquiring soft skills and confidence. Moreover, the novel tasking system was formulated with the objective to target essential skills and scope of knowledge that is most important for a young electrical engineer.[1–17]

Technical aspects of the education formula

In the case of sufficiently large currents, permanent changes in the physical condition of the contacts surfaces are expected. Electrical processes concerning welding of contacts by short-circuit currents are complex and demand to be explained thoroughly. The main goal for the tutors is to explain theory and show its practical implementation to help students cope with electrical engineering problems related, e.g., to the occurrence of currents of contact welding and other parameters alongside them. With high values of current running through contacts (e.g. in short circuit conditions), such key parameters as softening and melting temperatures of contact surfaces are increased successively. The exemplary 3D model of contacts layout made in SolidWorks is shown in Figure 1.

Exceeding the melting point of the material of which contacts are made leads to the brief enlargement of its surface. Furthermore, what happens next is the reduction of the narrowing resistance, temperature fluctuations in the relation with changes of current values and finally the contacts welding. The definition of the current of contact welding is described as a current value which causes contacts to weld. Force value approximately higher than 2 Newtons is required to break joint contacts. Different types of convertible contacts can be used during the laboratory work e.g. flat, linear and point contacts. Those are shown on schematic in Figure 2.

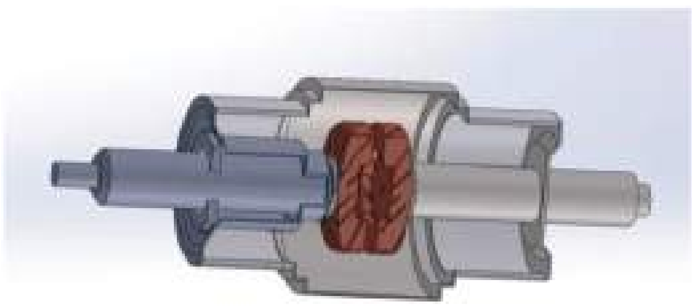

Figure 1. Exemplary 3D model of flat contacts layout.

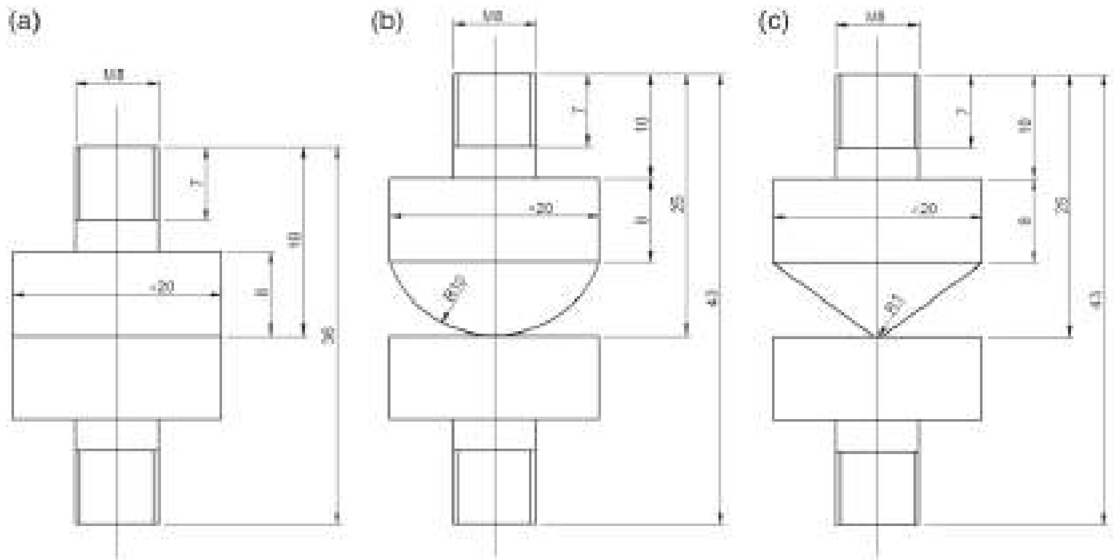

Figure 2. Different types of electrical convertible contacts: (a) flat; (b) linear; (c) point. Given dimensions are in millimeters.

Assumptions and equations

The melting of the contact surface, with sufficiently large current amplitude, appears only during the first half of the current period. The reason for this is the increase in the contact region due to the flow of the first half-wave of the current, which leads to a reduction in the contact resistance at the moment of the second wave and subsequent half-wave currents. Therefore, the maximum temperature in the contact occurs during the first half-current, and the number of the next half-waves does not affect the value of the welding current limit.[18,19]

Following the fact mentioned above in order to conduct experiments, restraints were formulated:

- the dimensions of the transverse cross-section of the contact were assumed to be much larger than the contact surface area of the contact with the radius r_p;
- electrodynamic forces in the contacts are not taken into account; a constant value of the radius of the contact surface, r_p, was assumed;
- it is assumed that the coefficient of thermal conductivity and specific heat of the material (c) do not depend on the temperature and are similar at all contact points to the heating of the contact surface.
- for calculations concerning currents of contact welding (i_s) model involving short sine shaped pulses ($<10^{-3}$ s) is used

$$i_s = \sqrt{\frac{192 c_0 \ln\left(1+\frac{2}{3}\alpha\vartheta_s\right)}{\pi^4 \alpha H^2 \rho_0}}\,\frac{F_{doc}}{\sqrt{t}} \tag{1}$$

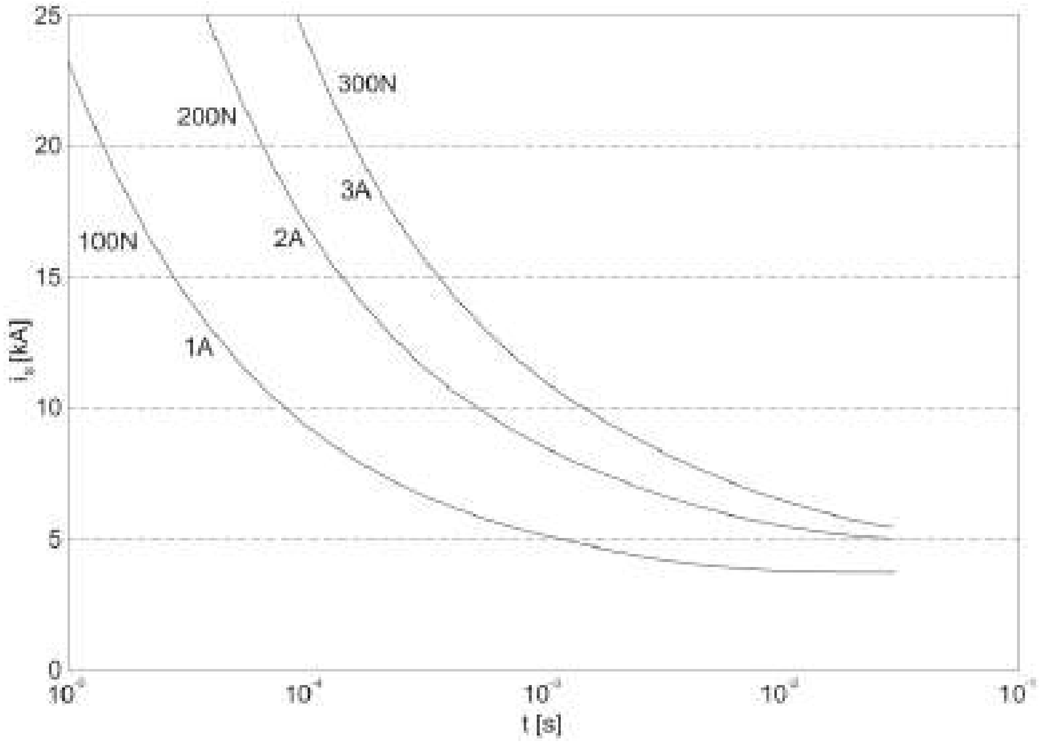

Figure 3. Trends in the values of currents of contact welding starting from half period of current wave. Markers 1A, 2A and 3A represent points at which values of clamping force and short-circuit current rendered welding of contacts possibility.

where c_0 is the thermal conductivity at the reference temperature in $[\text{Ws m}^{-1}{}^{\circ}\text{C}^{-1}]$; α is the temperature resistivity coefficient in $[{}^{o}\text{C}^{-1}]$; ϑ_s is the melting temperature in $[{}^{o}\text{C}]$; H is the material hardness in $[\text{Nm}^{-2}]$; ρ is the specific resistance in reference temperature in $[\Omega\text{m}]$; F_{doc} is contact clamping force in [N]; t is time of current flow in [s].

Trends in the values of short-circuit currents of the contact welding starting from half period of the current wave for chosen model are shown in Figure 3.

The skin effect, resulting from the steepness of the short circuit current rise, is not taken into account in a significant way. That is noticeable especially in the analysis of exponential currents with significant steepness. Such waveforms occur while switching short circuit currents with generator switches and also while switching pulse currents with high values. Determining the value of currents of contact welding from the above equation (1) is not simple and it caused problems for students. Thus, important aspect for studying currents of contact welding is by experiment not only by sole calculations.[20–23]

Laboratory setup

Tests concerning measurements of current of contact welding are conducted using designed station. Figure 4 presents the schematic diagram of such station for measuring currents of contact welding.

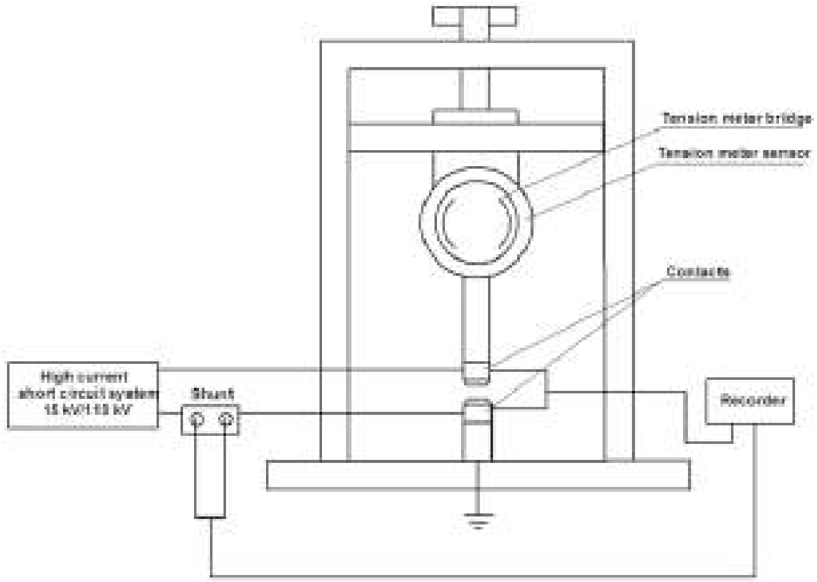

Figure 4. Schematic diagram of station constructed for measuring currents of contact welding.

The main components of the testing station are:

- stiffener for fixing contacts, sets of convertible contacts;
- copper, flexible wire for station powering;
- special ring with strained tension meters – for measuring the clamping force (F_{doc}) and breaking force;
- knob and guideway system for setting the clamping force value (F_{doc}).

Clamping and breaking force of the contacts were measured by a tension meter bridge and a digital voltmeter. Current registration (shunt: 10 kA, 79.2 μΩ, 1 s) and voltage drop across the contact are carried out on a 12-channel HIOKI recorder, type 8626. The voltage drop on the contact is measured by a voltage divider with overvoltage protection diode installed. The measurements of the contact resistance, before and after the test, are conducted with a special resistance bridge, called the micro ohmmeter type MO 2A. The photographs of described layout are presented in Figure 5.

Sets of convertible contacts made of different materials were tested. The main three types were contacts made of copper (Cu) and copper-tungsten (Cu-W) sintered powder composites and skeletal composites (aluminum; brass).

The laboratory stand is located in the building of Warsaw University of Technology, Electrical Department in Warsaw, Poland. This exercise is one of eight exercises performed during the course of Electrical Apparatuses for engineering course students on their third year. The laboratory is mandatory for all that want to finish the basic course of electrical apparatuses.

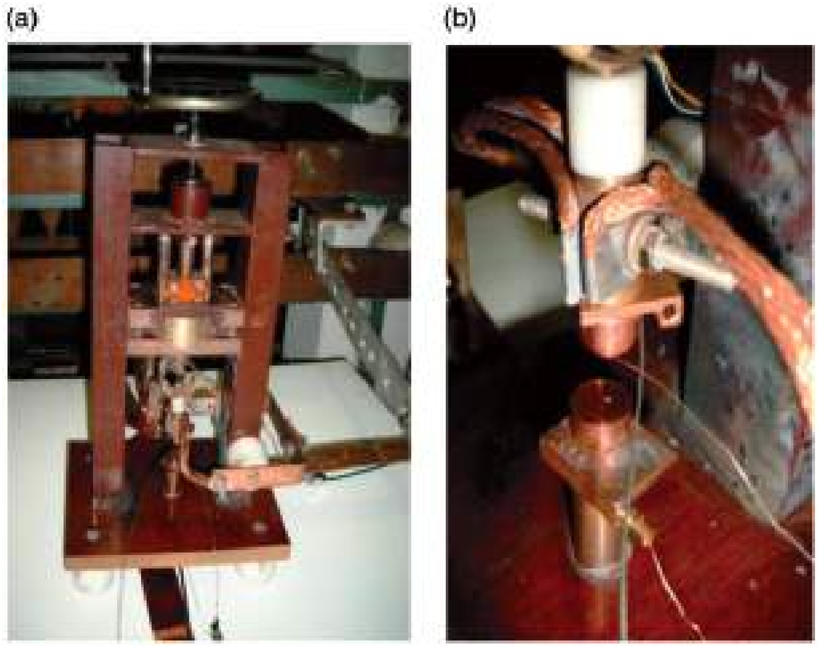

Figure 5. The photographs showing the designed station for measuring currents of contact welding: (a) overlook of the entire layout; (b) contacts in the open position before the measurement run.

Laboratory classes

Students' are obliged to read and accustom with instruction which is available in the script prepared for the laboratory operations. In the script, students' will find data about experimental scenarios and input parameters values needed for exercise procurement. Script can be borrowed from University of Technology Library which is situated in the main building.

Exercise execution

Exercise is conducted by group of three students supervised by two tutors (obligatory condition). Firstly, students need to be informed about hazards during execution of the exercise. The occupational safety training opens the task. All elements of the short-circuit system are fenced and protected against electric shock in a direct manner. The students during the laboratory have to get familiar with the setup by drawing the equivalent circuit and the nameplates of all used devices. Especially with the equipment designated for measuring electrical and dynamical parameters:

- Measurements of the contact clamping force and welding force (force needed to separate tacked contacts) are conducted using a tension meter bridge and a digital voltmeter.

- The data concerning current and voltage drop values on the contacts are stored by the digital recorder, equipped with a probe wired with protection diodes.
- Measurements of the contact resistance before and after the test are measured by a special resistance measuring bridge.

The students under the supervision of the teacher begin their work by checking the short-circuit system supplied from the 15 kV switchgear. The switch and disconnector of 15 kV switchgear should be placed in the open position. The students under the supervision of the tutor review the state of connections of high-current busbars, shunt and divider.

In the first phase of the task, two students, under the supervision of the third colleague are required to attach samples (contacts) of their choice in the holders of the test bench. The students use different types of contacts. The first types of contacts are tungsten-copper composite flat, point and linear contacts. The second types are aluminum and brass flat, point and linear contacts (shown in Figure 2). The contacts should be steadily attached. For every trail, students should use a new pair of contacts. The students set the clamping force of the contacts using a graduated tension meter bridge. Next group should measure the contact resistance and connect the wires to measure the voltage drop across the contact during current flow. Then, by choosing the number of choke coils, students adjust the value of the expected current in the short circuit system.

The second phase of the exercise is to establish the current flow in the short circuit system. In this part of the exercise, all participants (teachers and students) must be located in the control room of the short-circuit laboratory, insulated with reinforced glazing from the test stand. The tutors perform with caution switching operations on the short circuit (closing the disconnector, closing the circuit breaker and switching on the current from short circuit system). Waveforms and current parameters data are stored in the recorder memory during the tests.

In the third phase of the exercise, students after checking the system safety (turning off the power, establishing a visible break – open disconnector – supervision of the tutors is critically required) make a reading of current and voltage measurements. The contacts should be inspected, if necessary, some of the contacts should be photographed (those with a significant contact point surface degradation). On the basis of the measurements and above-mentioned equations, students must determine the contact resistance, the force needed to separate the contacts (welding force) and the clamping force after the test.

Exemplary laboratory results validation protocol

Results which students derived are validated on the basis of prepared tables showing proper ranges for results. Table 1 shows juxtaposed results for copper, aluminum and brass flat contacts – incoming and out coming data (input-result relation). Validation tables are clear indicator of proper values set by the students

Table 1. Validation tables for experiment concluded using flat contacts made of copper, aluminum and brass composites.

Validation table for exercise results validation purposes – Copper flat contact			Validation table for exercise results validation purposes – Aluminum flat contact			Validation table for exercise results validation purposes – Brass flat contact		
Measur. parameter	Valid values	Critical values	Measur. parameter	Valid values	Critical values	Measur. parameter	Valid values	Critical values
Clamping force [N] (input)	100–150	80–140 or 200 –300	Clamping force [N] (input)	200–400	80–180 or 450 –600	Clamping force [N] (input)	300–500	500–700
Welding current [kA] (input)	16–19	Less than 16 or 20 –25 kA	Welding current [kA] (input)	4–6	Less than 4 or more than 6	Welding current [kA] (input)	5–7	Less than 5 or more than 8
Time [ms] (input)	5	Less than 5 or more than 10	Time [ms] (input)	4	Less than 4 more than 10	Time [ms] (input)	4	Less than 4 or more than 7
Breaking force [N] (result)	88–134	–	Breaking force [N] (result)	20–180	–	Breaking force [N] (result)	20–80	–

for obtaining correct results. Tables are also essential for troubleshooting when experiment is not going accordingly to the intentions.

Values showed in tables are describing the ranges which indicate chance for proper outcome from the experiment. For valid values bracket, welding of contacts will probably occur. For critical values, welding will not probably occur. There is always a slight possibility that welding will not occur for the valid values or will occur for the critical values. That is due to the complex mechanism of the current of contact welding phenomena (multiple parameters and conditions involved – not only that in Table 1). Inter alia the current range sufficient for evaporation of metal, by which contacts are made, is very hard for precise pinpoint. Flat contact was presented because it is the most successful at receiving the welding (recommended for students). The scenario involving copper and its composites is the most difficult for obtaining the weld. Even setting the proper values is leaving a gap in the probability of success. Case concerning aluminum and brass is much more accurate in result prediction (it is also recommended for students to start from these experimental scenarios).

Student evaluation

The students' progress is evaluated on the basis of project report (10% of the total points), concluding test (90% of the total points).

Project report

Project report is prepared by the students after concluding the laboratory part of the exercise. Measurement results need to be devised and concluded. Report contents are the findings, juxtapositions, valid calculations being evidence of derived results, diagrams, and the most importantly aimed conclusions. The form of the report, the calculation results and overall understanding of the merit are being evaluated by checking tutor.

Concluding test

Concluding test is the ultimate effort that student must complete for passing the course. The test is composed of open and test questions concerning the topic of the exercise. Test questions are of multiple choices. In order to pass the concluding test student needs to score 50% of the total points available from it. The total points count is 14. The exemplary test questions are presented below:

1. *Which physical parameters affect the boundary welding current? What are the dependencies between them? (4 points)*
2. *What physical phenomena should be analyzed in the aspect of limiting the welding current? (4 points)*
3. *In which contact the transition resistance will have the greatest value? (2 points)*
   a) Point; b) Flat; c) Linear; d) Multipoint;

4. *In which contact layout the probability of welding is not likely possible? (2 points)*
   a) Point; b) Flat; c) Tulip; d) Linear
5. *In which constructions of switchgears the phenomenon of welding may occur? (2 points)*
   a) LV; b) MV; c) HV; d) CCTV Rack Cabinets

Results and statistical analysis

Results

For the results presentation, the grades distribution from three semesters before employing new formula and three semesters that already employed new formula was compared. Old formula – winter semester of 2014 and both semesters of 2015; total number of students participated during this period was 120. New formula – both semesters of 2017 and spring semester of 2018; total number of students participated during this period was 140. Grade distributions from mentioned semesters are juxtaposed in Figure 6. In order to show that presented data are a

(a)

Old formula average results		
Total number of students : 120		
Grade	Number of students	Percentage
5	1	1%
4,5	6	5%
4	7	6%
3,5	24	20%
3	36	29%
2	46	39%

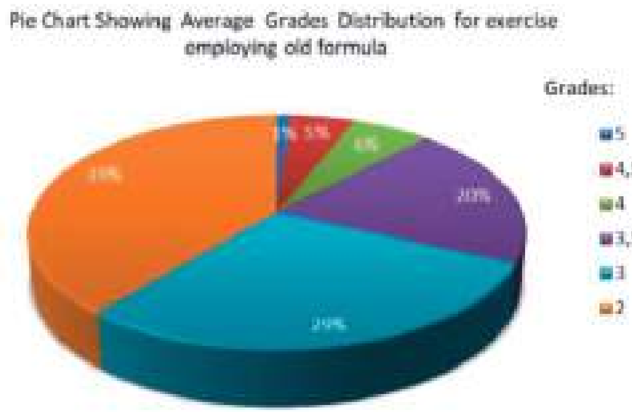

(b)

New formula average results		
Total number of students : 143		
Grade	Number of students	Percentage
5	5	3%
4,5	10	7%
4	32	22%
3,5	39	27%
3	34	24%
2	23	16%

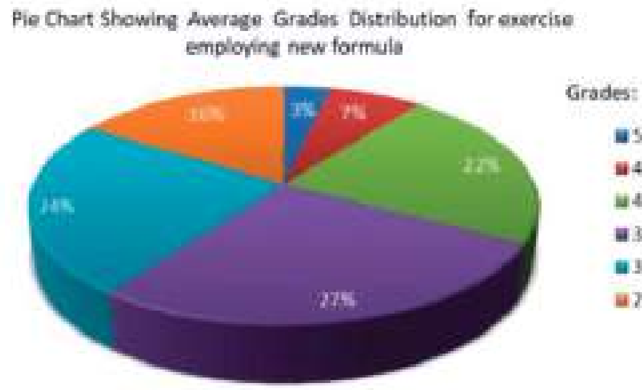

Figure 6. Juxtaposition of grades distribution old formula/new formula: (a) old formula – aggregated data from winter semester of 2014 and both semesters of 2015; (b) aggregated data from both semesters of 2017 and spring semester of 2018.

significant proof for educational effect achieved, proper statistical analysis was carried out. The gap between educational semesters was due to the time needed for station establishment and start-up of the new formula.

Statistical analysis

In order to obtain an answer to the question whether the new teaching formula gave a significant improvement in results, a statistical analysis was carried out using the STATISTICA program. It was used to analyze the basic descriptive statistics and verify the appropriate statistical hypotheses. Accepted level of significance was equal to: $\alpha = 0.05$. For the old method, the average of grades was equal to 2.867 with the standard deviation equal to 0.791. For the new method, the average grade was equal to 3.374 with the standard deviation equal to 0.784. The average difference was 0.507 to the benefit of the new teaching formula. At that point statistical significance is viable for checking.

Verification whether the samples come from a normal distribution is obligatory. This will settle which statistical model should be used – the parametric t-student test or its non-parametric equivalent: the Mann–Whitney test. The graphical presentation of the Shapiro–Wilk test used for verifying the normality of the distributions is shown in Figure 7. For both the old and the new formula $p < 0.05$, the hypothesis concerning normality of distribution is rejected. Distributions are not normal.

Mann–Whitney test is viable for employment at this point. Two hypotheses are formulated: Null hypothesis (H0): The averages in groups are equal. The average for the old teaching formula is the same as for the new one. No significant differences between the old and the new formula.

Alternative hypothesis (H1): The averages in groups are different. The average for the old teaching formula is different from the new one. There is a significant difference between the old and the new formula.

The significance is $p < 0.05$; therefore, the null hypothesis is rejected for an alternative one. The average is different.

This means that the differences between teaching methods are statistically significant. There is a significant difference between the old and the new method. The average difference was equal to 0.507 to the benefit of the new teaching formula. This is a significant difference, and therefore it can be stated that the new teaching formula gives better results. Verification table and the box diagram showing the significant difference is depicted in Figure 8.

Evaluation and conclusions

Course evaluation

The course formula is majorly influencing students engineering skills and offers them the chance for preparation in terms of work as designer/power engineer of

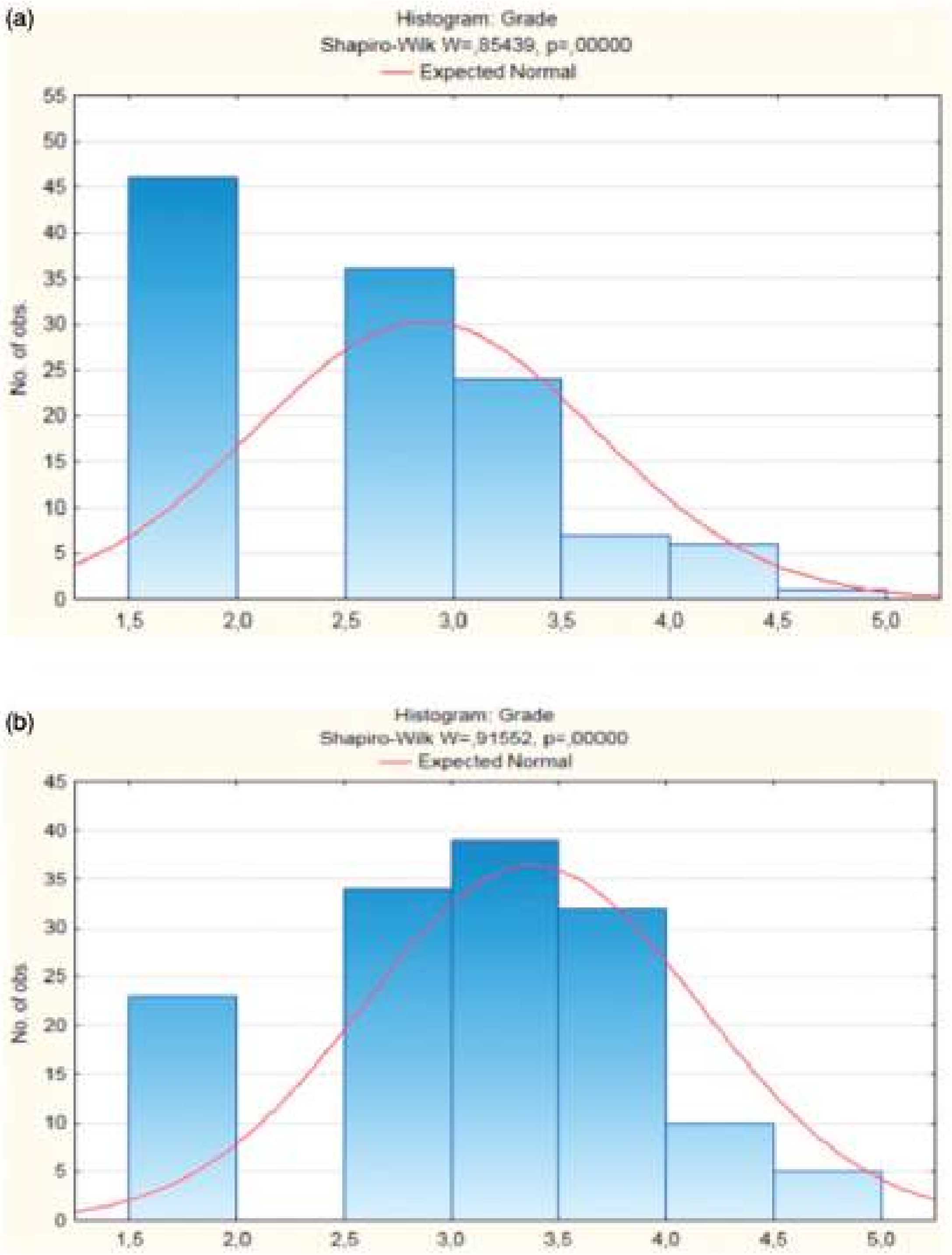

Figure 7. Graphical presentation of Shapiro–Wilk's test: (a) old formula; (b) new formula.

electrical contacts. Not only knowledge but most importantly the interfacing with high power devices, shifting the elements, understanding the values measured, choosing scenarios and making the work more effective is what this course offers. That is also the key to gain the confidence as the engineer – to experiment. Students are accustomed with difficult tasks that involve and require creativity,

(a)

Mann - Whitney U-Test; By variable method; Marked tests are significant at $p < 0{,}5000$									
Variable	Rank Sum Old Method	Rank Sum New Method	U	Z	p-value	Z adjusted	p-value	Valid N Old Method	Valid N New Method
Grade	12787,50	21928, 50	5527,500	-4,96723	0,000001	-5,10742	0,000000	120	143

(b)

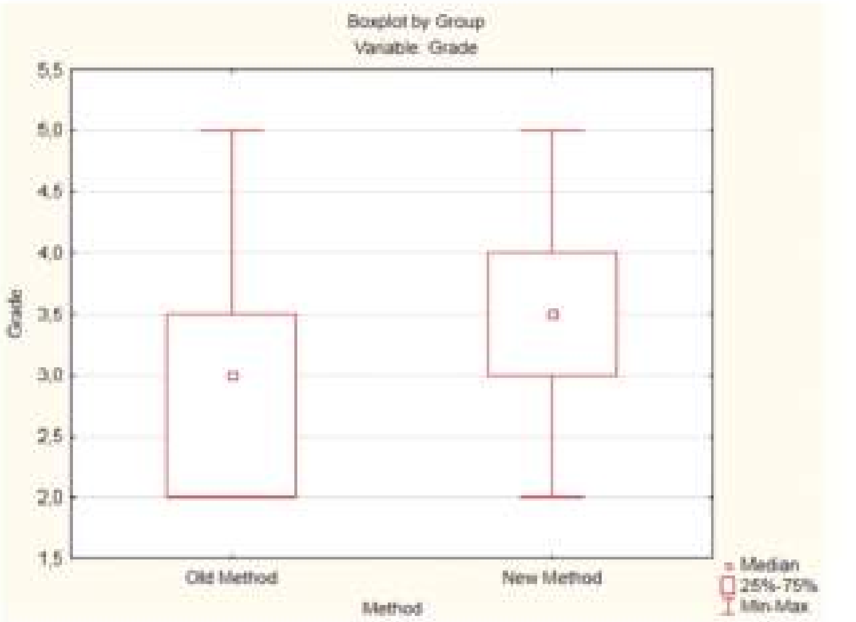

Figure 8. Graphical presentation of new education formula significance: (a) numerical result from Mann–Whitney's test; (b) box diagram showing difference for the benefit of the new educational formula.

team work and awareness. Very important aspect is safety training and proper etiquette while working in conditions in which high voltage occurs. Students are also taught how to process obtained data in the form of reports. Proper data processing is crucial in every engineering and scientific work for yield of valuable conclusions. The Laboratory of Short Circuits is also the place where students' can learn how to solve real engineering problems in safe environment under supervision of the best specialist in the country and learn basics about the electrical equipment. The theory is mixed with practice which gives students possibility to understand much more and get them closer to their career goals.

Conclusions

The proposed formula was successfully employed with the start of the year 2017. Many concerns were solved in order to construct measuring station and implement new formula that majorly raised the quality of transferring the knowledge in mentioned branch of electro-technology. Before the change, the course was in form of lecturing which were very hard to comprehend without seeing the full picture concerning the studied phenomena. Therefore, new formula was proposed that employed not only lecturing's but also engineering work. It was well accepted by the students that were simply expressing boredom concerning the old ways of education (old formula). The overall threshold of requirements was raised but also the learning curve seemed to be reduced. Test questions that were described in one of the previous chapters tend to be quite difficult but with proper education techniques students are coping with them well. That is what the results showed. The sheer idea was to make students more active during classes and force them to witness effects of work they are doing. Another aspect is tightening the contact with tutor. Participants were forced to ask questions, be aware of what the tutor is showing them because they knew that in a few moments they would need to do the same.

The science concerning electrical contacts is complex – full of long equations, solving tedious computing's and hard experimental work. Nevertheless, it is critically needed and it is in our interest (as tutors) to provide the course that will help in understanding this knowledge which is not easily accessible.

Declaration of conflicting interests

The author(s) declared no potential conflicts of interest with respect to the research, authorship, and/or publication of this article.

Funding

The author(s) received no financial support for the research, authorship, and/or publication of this article.

ORCID iD

Sebastian Łapczyński http://orcid.org/0000-0002-3238-6513

References

1. Abdulwahed M and Nagy ZK. The impact of different preparation modes on enhancing the undergraduate process control engineering laboratory: a comparative study. *Comput Appl Eng Educ* 2014; 22: 110–119.
2. Regalado A. The most important education technology in 200 years. *MIT Technol Rev* 2012; 116: 61–62.
3. Feisel LD and Rosa AJ. The role of the laboratory in undergraduate engineering education. *J Eng Educ* 2005; 94: 121–130.
4. Balamuralithara B and Woods PC. Virtual laboratories in engineering education: the simulation lab and remote lab. *Comput Appl Eng Educ* 2009; 17: 108–118.
5. Núñez JLM, Caro ET, López JS, et al. Education quality enhancement through open education adaptation. In: *Proceedings of frontiers in education conference*, Madrid, Spain, 22 October-25 October 2014, pp.1–4. IEEE.
6. Carstensen A-K and Bernhard J. Bode plots not only a tool of engineers, but also a key to facilitate students learning in electrical and control engineering. In: *Proceedings of*

physics teaching in engineering education Leuven, Belgium, 20 July-24 July 2002, pp.5–7. IJEEE.

7. Johansson M, Gafvert M and Astrom KJ. Interactive tools for education in automatic control. *IEEE Control Syst* 1998; 18: 33–40.
8. Kumar A, Fernando S and Panicker RC. Project-based learning in embedded systems education using an FPGA platform. *IEEE Trans Educ* 2013; 56: 407–415.
9. Tovar E and Piedra N. Guest editorial: open educational resources in engineering education: various perspectives opening the education of engineers. *IEEE Trans Educ* 2014; 57: 213–219.
10. Margaryan A. *Work-based learning: a blend of pedagogy and technology*. Saarbrücken, Germany: AV Akademikerverlag, 2008.
11. Ros S, et al. UNED OER experience: from OCW to Open UNED. *IEEE Trans Educ* 2014; 57: 248–254.
12. Lundquist C, Skoglund MA, Granstrom K, et al. Insights from implementing a system for peer review. *IEEE Trans Educ* 2013; 56: 261–267. no.
13. Li H, et al. Peer assessment in the digital age: a meta-analysis comparing peer and teacher ratings. *Assess Eval Higher Educ* 2015; 41: 245–264.
14. Fernandes MAC. Problem-based learning applied to the artificial intelligence course. *Comput Appl Eng Educ* 2016; 24: 388–399.
15. Lee CS, Su JH, Lin KE, et al. A project-based laboratory for learning embedded system designs with support from the industry. *IEEE Trans Educ* 2008; 53: 173–181.
16. Ionescu CM, Fabregas E, Cristescu SM, et al. A remote laboratory as an innovative educational tool for practicing control engineering concepts. *IEEE Trans Educ* 2013; 56: 436–442.
17. Jong B-S, Lai C-H, Hsia Y-T, et al. Effects of anonymity in group discussion on peer interaction and learning achievement. *IEEE Trans Educ* 2013; 56: 292–299.
18. Cabecinhas D, Naldi R, Silvestre C, et al. Robust landing and sliding maneuver hybrid controller for a quadrotor vehicle. *IEEE Trans Contr Syst Technol* 2016; 24: 400–412.
19. Gonzalez D, Berger F, Hopfeld M, et al. Model switch experiments for determining the evolution of contact resistance of electrical contacts in contactors. In: *IEEE 62nd Holm conference on electrical contacts* (Holm), Clearwater Beach, FL, USA, 9 October-12, October 2016, pp.129–134. IEEE.
20. Meyer P and Perriard Y. Skin and proximity effects for coreless transformers. *Int Conf Electric Mach Syst*, Beijing, China, 20 August–23 August 2011, pp. 1–5. IEEE.
21. Kim JS, Im SH and Park GS. A study on the skin effect and eddy current distributions in conductive media. In: *20th international conference on electrical machines and systems (ICEMS)*, Sydney, NSW, Australia, 11 August–14 August 2017, pp.1–4. IEEE.
22. Braunovic M, Myshkin N and Konchits V. *Electrical contacts: fundamentals, applications and technology (electrical and computer engineering)*. Chicago, IL, USA: IEEE, 2006.
23. Slade P. *Electrical contacts: principles and applications*. 2nd ed. Boca Raton: CRC Press, 2017.

A2. *Low Voltage Modular Circuit Breakers: FEM Employment for Modelling of Arc Chambers*

BULLETIN OF THE POLISH ACADEMY OF SCIENCES
TECHNICAL SCIENCES, Vol. 68, No. 1, 2020
DOI: 10.24425/bpasts.2020.131837

POWER SYSTEMS & POWER ELECTRONICS

Low voltage modular circuit breakers: FEM employment for modelling of arc chambers

Ł. KOLIMAS, S. ŁAPCZYŃSKI, M. SZULBORSKI*, and M. ŚWIETLIK

Institute of Electrical Power Engineering, Warsaw University of Technology, 75 Koszykowa St., 00-662 Warsaw, Poland

Abstract. FEM (finite element method) is an essential and powerful numerical method that can explicitly optimize the design process of electrical devices. In this paper, the employment of FEM tools such as SolidWorks, COMSOL and ANSYS is proposed in order to aid electrical apparatuses engineering and modeling – those are arc chambers of modular circuit breakers. Procured models of arc chambers have been undergoing simulations concerning heating, electric potential distribution, electric charge velocity and traverse paths. The data acquired has been juxta-positioned against experimental data procured in the Short-Circuit Laboratory, Warsaw University of Technology. The reflection of the theoretical approach was clearly noted in the experimental results. Mutual areas of the modeled element expressed the same physical properties and robustness errors when tested under specific conditions – faithfully reflecting those which were experimented with. Moreover, the physical phenomena essential for electrical engineering could be determined already at the model stage. This procedure proved highly valuable during designing/engineering work in terms of material economy.

Key words: miniature circuit breaker (MCB), finite element method (FEM), computational fluid dynamics (CFD), arc chambers.

1. Introduction

Rapidly growing demand for electrical installations composed of high quality electrical components dictates new trends in designing low voltage circuit breakers. The main aim of designing and engineering electrical devices is to create solutions that can vastly improve their electrical and mechanical parameters as well as size and endurance for short-circuit conditions. Modern electrical apparatuses are built in accordance with current standards (e.g. European Standards; IEC 60947). These requirements concern low-voltage circuit breakers (LVCB; MCB). Despite the small sizes of the above-mentioned devices, these are adapted to effectively switch off the overload and short-circuit currents and protect the other elements of the electrical systems such as cables and wires. During the process of extinguishing the electric arc in the circuit breaker, complex physical phenomena occur such as heat released in the arc channel and the formation of electrodynamic forces causing stress affecting the contacts of the circuit breaker. This also affects the structural elements that the device is made of (copper, steel, ferromagnetic elements, bimetals, aluminum, polymers etc.). Those occurrences can cause damage to the breaker after exceeding the critical values of electrical durability or temperature. The key element of the circuit breakers' construction is the electric arc chamber. During switching off of the short-circuit current, the arc chamber is exposed to thermal and dynamic influences which can lead to permanent damage of this element or even the whole circuit breaker. Arc chambers vary in shape, size and the number of ferromagnetic plates from which they are constructed. The greater the number of ferromagnetic plates in the chamber, the greater its ability to extinguish the arc. The value of the minimum voltage upholding the electric arc is reduced between the plates, which in combination with the spatial charge created near the cathode (plates) of each ferromagnetic plate is directly causing its faster extinction. The number of plates in the arc chamber for alternating current is described by the following equation:

$$n \geq \frac{U}{\sqrt{3 \cdot \left(\dfrac{\delta^2 \cdot U_a^2}{1.5^2 \cdot \tau^2} + \dfrac{\pi^2 \cdot u_t}{4}\right)}}, \tag{1}$$

U is the voltage peak value between open contacts, U_a is the initial durability near the cathode, u_t is the voltage between a pair of consecutive plates, δ is the factor of irregularity between the plates – approx. 0.5, τ is the factor of amplitude (for power breakers – approx.: 1.7; for the motor breaker – approx.: 1.5).

In order to verify the construction guidelines and the necessity of the solutions chosen, many tests and simulations are carried out that allow for detection of defects and optimization of the arc chamber effectivity at the project stage. Those measures are essential for reducing material take-off and they help improve the arc chamber properties. The usage of FEM (finite element method) simulations is very effective for running multiple analysis concerning electrical, mechanical and material durability aspects. The huge advantage of this method lies in the ability to check complicated scenarios employing various boundary conditions. A good example is a simulation concerning gas pressure distribution on the FSI arc chamber surface by Lijun

*e-mail: mm.szulborski@gmail.com

Manuscript submitted 2019-07-13, revised 2019-11-20, initially accepted for publication 2019-11-26, published in February 2020

Wang and his team, which is shown in Fig. 1 below. In the cited case, the simulation was used for maintaining additional information subjected to measurements of the arc chamber housing deformations [1–6].

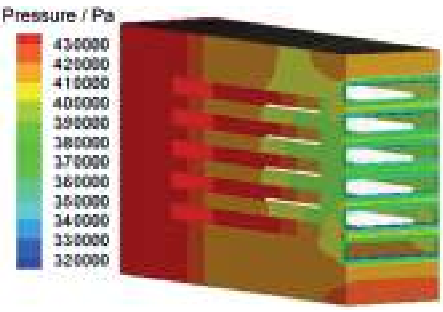

Fig. 1. Pressure distribution on the FSI arc chamber surface [2]

FEM is an essential and powerful numerical method that can explicitly optimize the designing process of electrical devices and proper employment of the finite element method itself. It is the key to arriving at the recipe for easy, fast and precise optimization of arc chamber parameters. This paper focuses on the juxtaposition of experimental data and simulations data in order to show FEM advantages and disadvantages concerning arc chambers modelling parameters – such as the number of plates and critical conditions (temperature, velocity of electrical charge, electrical charge flux in the chamber, electrical potential distribution and overall short-circuit conditions in regard to the materials used). For charge transversal analysis this work employs the usage of various FEM tools like: SolidWorks, Comsol, ANSYS and even computational fluid dynamics (CFD) [7–11].

2. FEM design guidelines

Prompt technological progress allowed for the use of modern software to support the process of designing and engineering electrical apparatuses. Currently constructed electrical appliances are designed and tested with the use of software such as CAD and CAE (Computer Aided Design, Computer Aided Engineering). Mathematical analysis is employed to predict the distribution of electrical fields, temperatures, stresses and other physical quantities. In order to perform such analyzes and simulations, each element is described by specific physical properties, such as: Young's modulus, Poisson's coefficient, thermal expansion ratio, thermal and electrical conductivity. These are the necessary physical properties needed to perform correct calculations during simulations that reflect the actual phenomena occurring in a constructed device. The results of these calculations allow for estimating whether the elements of a designed device, made of specified materials, meet the global standards [12–17].

2.1. AutoCAD (model procurement). AutoCAD software allows for creation of precise 2D technical drawings and 3D three-dimensional models. This functionality is essentially used for drawing elements of the arc chamber. The elements of the structure are matched, which helps generate a simplistic model that is easy to export to other programs, e.g. those that are FEM based. Parts created in the AutoCAD graphical environment are shown in Fig. 2.

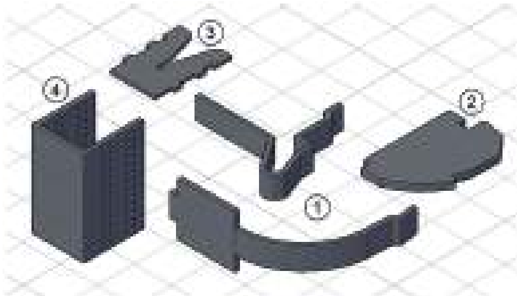

Fig. 2. Elements of the arc chamber created in AutoCAD: 1) tread electrodes; 2) rear sheath; 3) arc chamber plate; 4) arc chamber casing

2.2. COMSOL Multiphysics and SolidWorks (FEM analysis and model procurement). The COMSOL Multiphysics software is a tool with the ability to run and analyze the concurrent simulations of many physical phenomena. The software's key functionality is based on solving partial differential equations using the finite element method (FEM) and molecular dynamics. It is commonly used for electrical analysis concerning potential and electrical field distribution in medium and high voltage devices and systems [18–21].

a) b)

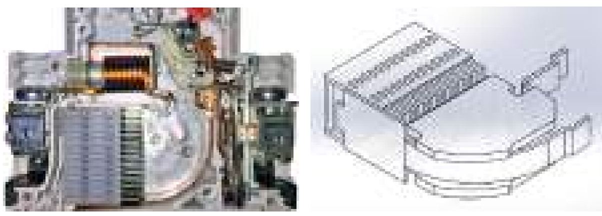

Fig. 3. Visual comparison of a real scale arc chamber (a) and its model drawn in SolidWorks (b)

2.3. ANSYS (advanced FEM analysis). ANSYS is an advanced FEM analytical tool built of various modules that merge into a major multiphysics engine. The use of several conjugate fields makes it possible to visualize the current flow and its effects – not only thermal but also electrodynamic ones. This feature is referred to as "coupling" and it is used regularly for complex analysis of various connected and resulting phenomena [22–24].

The numerical fluid mechanics of the computational fluid dynamics module (CFD; ANSYS module) is a method of simulating the behavior of systems, processes and devices related to the flow of gases and fluids, heat and mass exchange, chemical reactions and other similar physical phenomena. The CFD module allows for obtaining the necessary information about fluid flow (velocity field distribution, pressure field), heat movement (temperature field) and other accompanying phenomena (including chemical reactions). Electrical analysis can employ CFD in order to simulate potential distribution, electrical charge velocity and its traverse routes inside the chosen element of the analyzed device (arc chamber) [25, 26].

3. FEM simulation results

Mandatory assumptions for all procured simulations were:

- Apparatus modeled: miniature circuit breaker B16/1,
- Number of plates in MCB arc chamber: a) 13 plates; b) 9 plates,
- Voltage parameters: rated voltage: $U_n = 230$ V; voltage,
- Frequency: $f = 50$ Hz; alternating current,
- Breaking capacity: $I_{cu} = 6$ kA; RMS value,
- Simulations were executed in an air surrounding,
- Dimensions of 13 plates in the arc chamber: $14 \times 19.7 \times 26$ mm,
- Dimensions of 9 plates in the arc chamber: $14 \times 19.7 \times 18$ mm,
- Dimensions of single plate: $14 \times 19.7 \times 0.8$ mm.

3.1. Heat distribution in the arc chamber. The simulations performed concerned two variants of the arc chamber, which are shown in Fig. 4 below. Main goal of the simulations was to determine if the distribution of heat in the tested arc chamber models is balanced over the entire element. That would provide data about the path of the electric arc inside the arc chamber during short circuit and its extinguishment. Case a) represents a model of the arc chamber that consists of 13 plates. The even temperature distribution implied that the electric arc was proportionally divided through the metal plates in the arc chamber. Energy dissipation along the metal plates is consistent with the assumptions. Moreover, on the basis of the regular temperature distribution, the proper dynamics of the electric arc propagation on the contact is assumed. The arc was stretched by the moving contacts of tread electrodes (actuator mechanism). It was forced into the arc chamber by tread electrodes and divided thereafter. De-ionization of the intermetallic gap is assumed. In addition, a much lower temperature of rear sheaths provides data about the proper extinguishment of the electric arc. Case b) represents a model of the arc chamber that consists of 9 plates. The temperature distribution is evidently not as balanced as in the case of the 13-plate model of the arc chamber [27, 29–36].

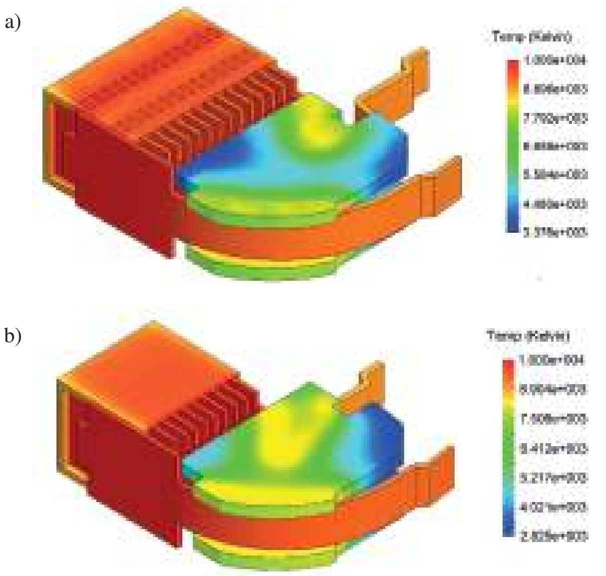

Fig. 4. Simulations of heat distribution (K) for two variants of MCB B16/1 arc chambers: a) arc chamber with 13 plates; b) arc chamber with 9 plates. Simulations were carried out in SolidWorks

Observation concerns mostly the edge of the plates and the tread electrode, where heat values are highest. Other regions of the arc chamber have lower temperatures, which indicate non-exhaustive functioning of the MCB-modeled element. Therefore, the following scenario was possible: the electric arc was not divided completely alongside the length of the modeled element. This may lead to re-ignition of the electric arc at the tread electrode and between the plates. Moreover it would result in welding contact with the arc chamber case, causing vast damage of the apparatus from overheating. The temperature distribution on the rear sheaths indicates that the electric arc was not pushed inside the arc chamber. It could be extinguished on the rear sheath and re-ignited, which applies to the above part, which in turn assumes that the arc was not divided and that the process caused vast damage to the apparatus.

3.2. Electric field and electric potential distribution in the arc chamber. The simulations performed concerned two variants of arc chambers, which are shown in Fig. 5 below. The goal of the simulations was to examine if the electric field distribution is homogenous for both variants and if the electric potential value does not exceed the critical value of 18 V per space located between the single pair of plates installed in the arc chamber, in accordance with experimental data [28].

Both cases present that the distribution of the electric field is not homogenous. The difference in the maximum critical value of the electric field is at least one order of magnitude with advantage on the part of the arc chamber with 13 plates. Moreover, in the 13 plates variant critical values occur on the tread electrodes far from the arc chamber casing, which results from the solution used in electrical connection engineering. It is also unlikely to expect welding of the electrodes. The simulation of the arc chamber with 9 plates shows a higher possibility of welding the electrodes. The critical values are localized much closer to the arc chamber case. It may be assumed that the problem is connected with the lack of control of the electric arc path on the tread electrodes, which is caused by smaller dimensions of the arc chamber. Therefore the distance between the first plate and the electrodes is different for both cases.

Electric potential distribution was valid for both cases and was not different for the 9 and 13 plate variants, as it should be for voltage value of 230 V. Figure 6 presents the electric potential distribution for the variant with 9 plates.

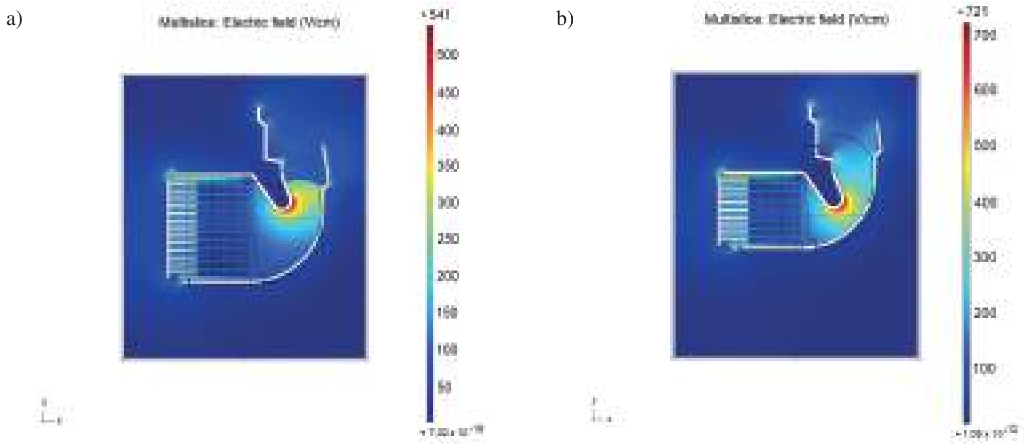

Fig. 5. Simulations of electric field distribution (V/cm) for two variants of MCB B16/1 arc chambers: a) arc chamber with 13 plates; b) arc chamber with 9 plates. Simulations were carried out in Comsol

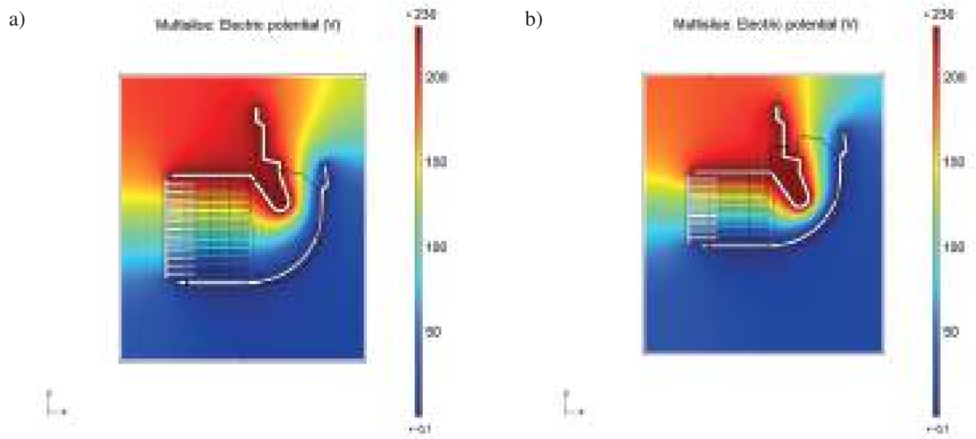

Fig. 6. Simulations of electric potential distribution (V) for two variants of MCB B16/1 arc chambers: a) arc chamber with 13 plates; b) arc chamber with 9 plates. Simulations were carried out in Comsol

Figure 7 shows a comparison of electric values potential between the pairs of plates for the arc chamber variant with 13 plates and 9 plates. The designation line shows the range for which potential was drafted on graphs. It is evident that the potential values for 9 plates are vastly exceeded (values around 26–29 V). Values for the arc chamber with 13 plates are valid

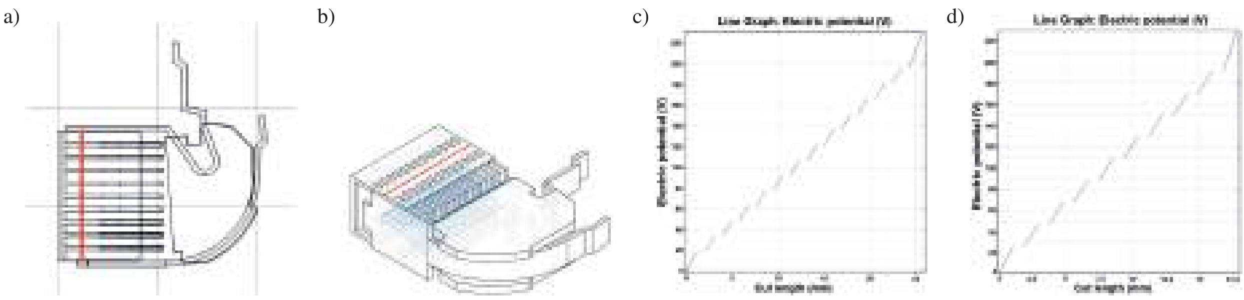

Fig. 7. Graphs presenting values of electric potential (V) dependent on cut length (mm) between the pairs of plates in the arc chambers: a) electric potential designation line (9 plates); b) electric potential designation line (13 plates); c) graph for the arc chamber with 13 plates; d) graph for the arc chamber with 9 plates

(values around 16–18 V). Therefore the applied reduction in the number of plates lacks any physical sense as it may, and probably will, cause errors.

3.3. Velocity and traverse paths of electric charge. The ANSYS analysis was based on the reverse engineered elements drafted in the SolidWorks software. The area representing air present in the gap between the electrodes was generated as a grid of points in which calculations were carried out. For calculation purposes, the source and destination target were defined as surfaces of electrodes facing each other. The initial flow velocity was set as $1.07 \cdot 10^7$ m/s, which is the magnitude of velocity for the elementary charge accelerated at the voltage rate of 230 V. The outcome was the distribution of routes and partial velocities of charges inside the arc chamber in the form of a visualization superimposed on the model. Figure 8 presents particle velocity field distribution and Fig. 9 presents particle flow lines (traverse paths) of the electric charge.

Figure 8 and Fig. 9 indicate highest velocity at areas where the arc is mostly expected. Partial charges colliding with the plates move at a lower velocity before they strike the surface of the other electrode. The combination of traverse paths with the velocity of the electric charge is determinant for the probability of the arc presence in the specific area of the arc chamber.

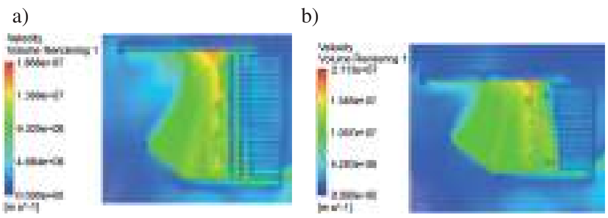

Fig. 8. Particle velocity field distribution for electric charge inside the arc chamber (m/s) for two variants of MCB B16/1 arc chambers: a) arc chamber with 13 plates; b) arc chamber with 9 plates. Simulations were carried out in ANSYS CFD module

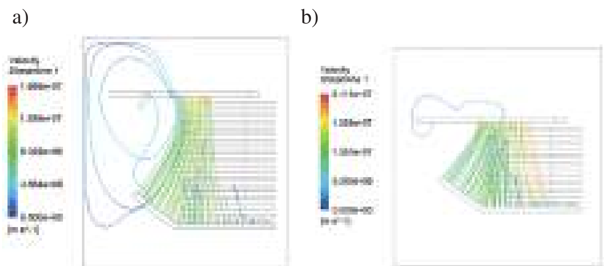

Fig. 9. Traverse paths of electric charge inside the arc chamber for two variants of MCB B16/1 arc chambers: a) arc chamber with 13 plates; b) arc chamber with 9 plates. Simulations were carried out in ANSYS CFD module

The CFD calculation module is originally used to simulate the flow of fluids, therefore obtaining results from it provides interpretation of the electromagnetic phenomena.

The traverse paths of the electric charge in the cross-section of the arc chamber are continuous for the circuit breaker with 13 plates (Fig. 9a). As a result, despite the slightly lower velocity of the particles (in comparison with the chamber with 9 plates), their distribution is regular.

The higher gas pressure in the arc chamber with 9 plates results in higher particle velocity. Bearing in mind the triggering system (electromagnetic coil), this variation of the chamber achieves greater dynamics in relation to the larger, 13-plate arc chamber. The key to effective use of the inter-cathode effect takes the form of even distribution of particles and regular velocity. The studied case shows that it is not fulfilled. This is clearly visible at the arc chamber outset. Numerous discolorations are visible, representing the heterogeneity of electric charge velocity.

4. Laboratory test results

Laboratory tests concerning the two types of the arc chambers were conducted at the Short-Circuit Laboratory forming part of the Electrical Faculty, Warsaw University of Technology. The tests were carried out in accordance with the IEC 60898-1 standard – Electrical accessories – Circuit-breakers for overcurrent protection for household and similar installations – Part 1: Circuit-breakers for a.c. operation. The above-mentioned standard applies to the air circuit breakers for rated voltage not exceeding 440 V, rated current not exceeding 125 A and rated short-circuit breaking capacity not exceeding 25 kA.

In accordance with the standard, two types of overcurrent circuit breakers were tested. The first contained 13 plates in the arc chamber and the second contained 9 plates in the arc chamber, as it was depicted in previous chapter, which concerned FEM simulations. The short-circuit system used during the tests was also shown in Fig. 10.

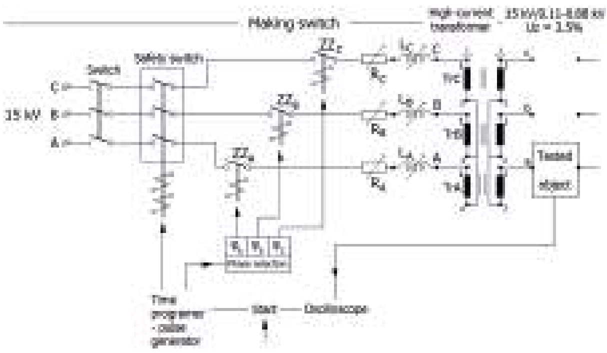

Fig. 10. Short-circuit system used for laboratory tests. Short-Circuit Laboratory, Electrical Faculty, Warsaw University of Technology

4.1. Short-circuit tests. The overcurrent circuit breakers have been tested in accordance with IEC 60898-1. The tests were carried out using single phase from the laboratory short-circuit system. The effective value of the reference current was 6 kA (ref-

a) b)

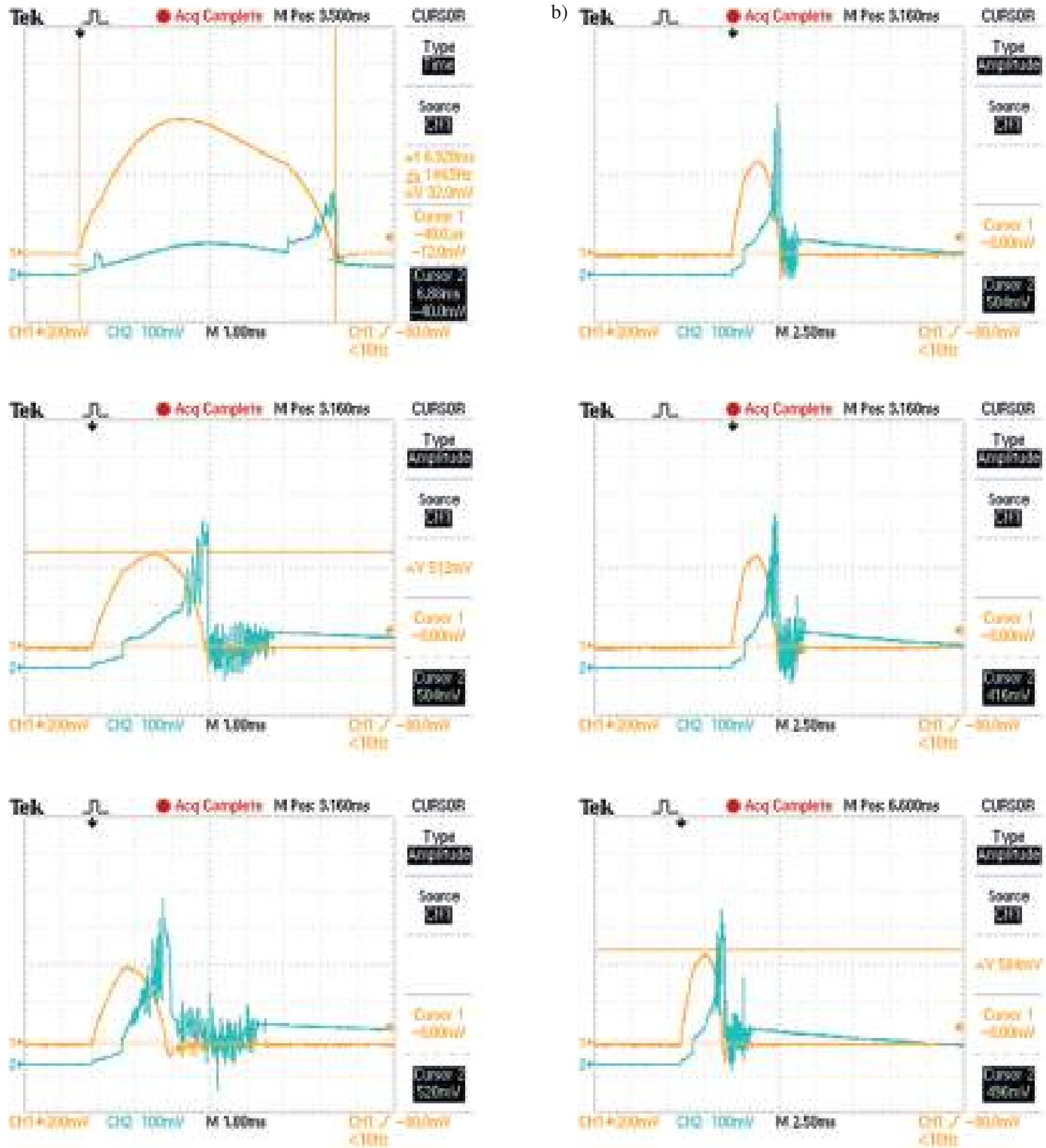

Fig. 11. Exemplary result characteristics of current and voltage during switching off of short-circuit current (screens from the oscilloscope): a) MCB with an arc chamber with 9 plates (negative result); b) MCB with an arc chamber with 13 plates (positive result). The measuring shunt is of our own construction. The shunt is manganese concentric and of resistance equal to 157 μΩ]

erence current characteristic is shown in Fig. 11a); rated voltage equal to 230 V and power factor $(\cos\varphi)$ equal to 0.65–0.70. Circuit breakers with arc chamber containing 13 plates disabled the short-circuit current in accordance with the standard in all iterations. 5 iterations were conducted (one iteration for one MCB, total of 25 short-circuit tests). All iterations rendered positive results. Therefore the MCB type with an arc chamber containing 13 plates passed the short-circuit test. Circuit breakers with the arc chamber containing 9 plates did not disable the short-circuit current in accordance with the standard in all iterations. None of the tested devices withstood a full iteration (5 short-circuit tests per MCB). The devices were damaged on the second or third short-circuit test (outcome did not comply with the standard). Therefore the MCB type with the arc chamber containing 9 plates did not pass the short-circuit test. Exemplary results concerning the iterations chosen have been tabularized (Table 1). Exemplary result characteristics saved during the tests are presented in Fig. 11.

Table 1. Exemplary short-circuit tests results for single iterations (pairs of devices from each type). Results for circuit breakers containing 13 and 9 plates in the arc chamber.

Table 1
Short-circuit test results

No.	MCB arc chamber with 13 plates		MCB arc chamber with 9 plates	
	Off time duration [ms]	Value of the short-circuit current [kA]	Off time duration [ms]	Value of the short-circuit current [kA]
1	1.5	1.950	2.0	2.090
2	1.5	3.490	4.5	1.990
3	2.1	2.460	11	2.710*
4	1.5	2.640	–	–
5	1.5	1.900	–	–

* damaged circuit breaker contacts

4.2. Overcurrent protection test. In order to conduct the tests, the TW-1a type transformer was used with a rated voltage of 220 V, frequency equal to 50 Hz and rated power equal to 1 kVA. According to the standard in force (IEC 60898-1), the circuit breakers were tested with the set value of the current equal to 2.8 in for 60 seconds. Five devices from each type were tested. A total of 10 tests was performed. The circuit breakers that contained the arc chamber with 9 plates did not pass the test in any iteration. The circuit breakers that contained the arc chamber with 13 plates passed the test in all iterations.

4.3. Dielectric strength tests. In order to perform the dielectric strength tests, the AP-5 device was used, with the rated test voltage of 5 kV. Circuit breakers were tested using the voltage value of 900 V within 5 seconds. Tests did not indicate the insulation breakdown of the tested MCB containing the arc chamber with 13 plates. In addition, there was no breakthrough of the air gap between the main contacts of the circuit breakers. Therefore the device passed the test. Tests also indicated the insulation breakdown of the tested MCB containing the arc chamber with 9 plates. Breakthrough of the air gap between the main contacts was indicated. Therefore the device did not pass the test.

5. Switching-off cycle procedure and results validation

Switching-off cycle procedure and results were carried out in accordance with standard IEC 60898-1, subsections 9.7.6.3; 9.12.7.1; 9.12.7.3; 9.12.11.2; 9.12.11.3; 9.12.11.4; 9.12.12.1 and 9.12.12.2.

5.1. Test of rated short-circuit breaking capacity (I_{cn}). The tested circuit is scaled accordingly. The test is performed on three samples in the appropriate circuit. If the supply and receiving terminals of the circuit breaker are not properly marked under the test conditions, two samples are connected in one direction and the third in the opposite direction. The switching cycle is being executed: O–t–CO (switch-off; time; switch- on). If 'O' is switched off and the auxiliary switch 'A' synchronizes with the voltage waveforms in such a manner that the circuit closes before switching off the first sample at the moment corresponding to the 15° phase angle. It is made in accordance with standard 67 – EN 60898-1: 2003 + A1: 2004 + A11: 2005. In the case of switching off the second sample, the moment of switching on the circuit is shifted by a phase angle of 30°, and in the case of switching off the third sample – by a further 30° of a phase angle. Sync tolerance should be ±5°. For multi-pole circuit breakers, synchronization should be performed in relation to the same reference pole.

In the case of switching off single-pole switches with rated voltage 230/400 V, the test is performed in the circuit on an additional set of four samples. Three of these samples are included in the test circuit, one in each phase; closing synchronization of the short circuit with auxiliary switch 'A' is not performed. It is forbidden to connect the neutral point of the power supply system to the common point on the load side of the breakers.

5.2. Circuit breaker check after short-circuit testing. Reduced short-circuit currents, at 1 500 A and with operational short-circuit capacity. After each test the switches should not exhibit any damages affecting their further operation and should pass with a positive result, and without maintenance, the tests listed below:

a) Checking the leakage current between open contacts;
b) Checking the dielectric strength, performed from 2 h to 24 h after short-circuit tests, but with the testing voltage reduced by 500 V without prior influence of humidity.

During these tests, it should be checked whether after performing the test under the conditions concerning the specified item the indicators are in the state of opening, and after the test under these conditions their closing status should be verified.

c) In addition, the circuit breakers should not trip when all of the poles are in the cold state under influence of a current equal to 0.85 of the conventional failure current.

At the end of this check, the current should be gradually increased so that it reaches 1.1 times the value of the conventional tripping current within 5 s. The switch should trip within conventional time.

5.3. Circuit breaker check after short-circuit testing. Short-circuit tests at rated short-circuit capacity. After the tests, the polyethylene film should not have holes visible with normal or corrected vision without additional enlargement, and the switches should not show any damages affecting their further operation. Likewise, they should, without maintenance and prior influence of humidity, have positive results of the following tests:

a) Checking the leakage current between open contacts;
b) Checking the dielectric strength, performed from 2 h to 24 h after short-circuit tests, but with 900 V voltage value and without prior humidity influence.

During these tests, it should be checked whether after performing the test under the conditions concerning the specified item the indicators are in the state of opening, and after the test under these conditions their closing status should also be verified.

c) In addition, these switches should trip under a load of a current equal to 2.8 in on all poles during the time corresponding to the test. The lower operating time limit is 0.1 s instead of 1 s but not exceeding 60 s.

MCB detailed dimensions were shown in Fig. 12a.

6. Juxtaposition of theoretical and empirical results

The most important and interesting data concerning empirical work were derived from the short-circuit tests. Negative results manifested themselves in evaporation of contacts, evaporation of the rear sheaths and evaporation of the arc chamber elements. Moreover, those were caused by errors in MCB construction such as: poorly designed arc chamber, incorrect shape of tread electrodes, contact defects and defects of electromagnetic release. The faults listed above are the direct cause for the occurrence of a large amount of very hot gases and soot. They are the reasons for the huge increase in temperature inside the device. The moment the deionizing properties are constrained, reignition of the electric arc occurs, caused directly by returning voltage. Finally, physical damage to the electromagnetic release or to the thermo-bimetallic release occurs. That can be observed in Fig. 12b.

Hence an unsuccessful attempt to switch off the short-circuit current was observed repeatedly for the MCB with the arc chamber containing 9 plates (no overcurrent function).

An important question emerges: how were the theoretical results derived from the FEM simulations reflected in the empirical results? In this case, the contact system was not the object of calculations. Nevertheless, calculations of the distribution of electric potential could prove helpful in the selection and placement of the right solution concerning the engineering of the arc chamber. Simulations showed places which exhibited heterogeneity of the electric field, and thus electric arc exposure (Fig. 5). In Fig. 7, the value of the potential is exceeded for the MCB with the arc chamber that contains 9 plates. Potential in the gap between the consecutive plates always exceeds 20 volts. Judging from the analytical calculations (Eq. (1)) and the engineering empirical data – 18 Volts and 0.5 Ampere are the limiting values for the possibility/restriction of electric arc occurrence. The FEM model reacts correctly to the nominal voltage. The simulations indicated the areas of the device where the arc was not properly extinguished and that is fully reflected in the empirical results (Fig. 12b). The electrical calculations derived in this manner may prove extremely helpful in the optimization process of the construction of modular apparatuses for all ranges of voltage (e.g. vacuum arc chambers solutions).

It would seem that the voltage calculations are most valuable for low voltage modular devices optimization. However, they are not. Heating simulations clearly indicated that the arc chamber is experiencing faults.

a)

b)

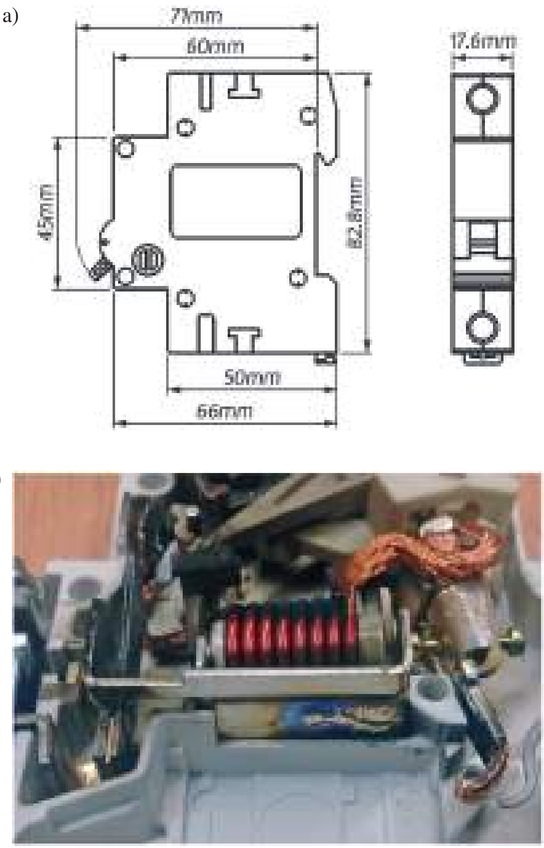

Fig. 12. Empirical results and dimensions of an MCB: a) detailed dimensions of an MCB; b) photo of an MCB with the arc chamber that contained 9 plates. The electric arc has welded the arc chamber to the tread electrodes. The gases generated as a result of electric arc reignition were accumulated in the upper part of the apparatus and then destroyed the thermo-bimetallic plate

The most characteristic is the temperature rise on rear sheaths (Fig. 4b). Moreover, the peak temperature on the plates dividing the arc chamber is indicating electric arc ignition in front of it – this is abnormal. The arc chamber with 13 plates has regular heat distribution. Simulations of this type provide the opportunity to optimize not only the arc chamber but also the other elements of low voltage electrical apparatuses. The possibilities are immense.

An interesting approach was the usage of computational fluid dynamics in terms of electrical apparatuses analysis. Based on the simulations, the functioning and physical phenomena occurring inside the electrical device can be analyzed thoroughly. The CFD module provided not only knowledge about velocity and the distribution of electrically charged particles, but was also useful for the determination of the arc channel placement and therefore the electric arc occurrence.

It is very important to note that the multiple FEM tools used indicated the possibility of electric arc occurrence in the specific areas of the studied circuit breakers. Those areas were common. They also matched those indicated during experimental studies. Therefore it can be stated that the modeled simulations are emulating and reflecting faithfully the reality and the actual empirical tests that were conducted.

7. Summary

This paper revolves around the construction of an FEM model that could fully and faithfully recreate conditions from reality. The mentioned approach is inestimable when it comes to modelling electrical apparatuses. The approach of using several FEM tools for designing the arc chambers was chosen rightly. However, the optimum possibilities of these tools have been exploited for which they are dedicated in order to receive a valuable and full image of the modelled object. Indeed, this was achieved. The presented model as well as the procedure was verified by empirical studies that confirm the validity of such proceedings. An important feature coming from this work is the possibility of reconstructing the arc chamber models and, in the case of structural changes, avoiding costly and time-consuming laboratory tests or at least reducing the expenses. This approach follows the currently prevailing trend of time and cost reduction in the design and manufacture of electrical equipment. Optimization can be applied to existing solutions using the proposed procedure. Such a process might not only increase the users' safety/service, but also reduce the use of materials, positively affecting the environment. Besides, FEM modeling can be used for designing apparatuses for different conditions, voltage ranges and applications. The above-stated creates vast possibilities for safe, fast and highly economical creation of new trends and solutions in electrical apparatuses engineering. Obviously, the disadvantage of FEM modeling is still an urge to perform experimental tests, as per all the standards in force. Moreover, it should be stressed that in the case of the arc chambers, the modeling is simple and the layout is not complicated. More complex solutions may generate additional errors that can easily lead to major mistakes in designing. This is expected in particular in a boundary conditions setting. Still the proposed modelling procedure is worth employing.

References

[1] R. Bini, B. Galletti, A. Iordanidis, and M. Schwinne, 1st International Conference on Electric Power Equipment – Switching Technology, Xi'an, 2011, pp. 375–378.

[2] L. Wang, H. Liu, W. Zheng, R. Guan, Ch. Ge, L. Chen, and Sh. Jia, "Numerical Simulation of Impact Effect of Internal Gas Pressure on Chamber Housing in Low-Voltage Circuit Breaker", *IEEE Transactions on Components, Packaging and Manufacturing Technology* 4(4), (2014).

[3] X. Ye, M.T. Dhotre, J.D. Mantilla, and S. Kotilainen, "CFD Analysis of the Thermal Interruption Process of Gases with Low Environmental Impact in High Voltage Circuit Breakers", 2015 Electrical Insulation Conference (EIC), Seattle, 2015.

[4] M.T. Dhotre, X. Ye, M. Seeger, M. Schwinne, and S. Kotilainen, "CFD Simulation and Prediction of Breakdown Voltage in High Voltage Circuit Breakers", 2017 Electrical Insulation Conference (EIC), Baltimore, 2017.

[5] B. Qi, X. Zhao, Sh. Zhang, M. Huang, and Ch. Li, "Measurement of the electric field strength in transformer oil under impulse voltage", *IEEE Transactions on Dielectrics and Electrical Insulation* 24, 1256–1262 (2017).

[6] C. Rumpler, H. Stammberger, and A. Zacharias, "Low-voltage arc simulation with out-gassing polymers", *Proc. IEEE 57th Holm Conf. Electr. Contacts*, 2011, pp. 1–8.

[7] V.V. Ryzhov, O.N. Molokanov, P.A. Dergachev, N.A. Vedechenkov, E.P. Kurbatova, and P.A. Kurbatov, "Simulation of the Low – Voltage DC Arc", Intenational Youth Conference on Radio Electronics, Electrical and Power Engineering (REEPE), 2019, Russia.

[8] N.D. Geetha, P. Rasilo, and A. Arkkio, "Sensitivity Analysis of Inverse Thermal Modeling to Determine Power Losses in Electrical Machines", *IEEE Transactions on Magnetics* 54(11), (2018).

[9] J. Li, Y. Cao, M. Y., Sh. Liu, Z. Du, and Y. Feng, "Research on the Effect of Magnetic Field on Micro-Characteristics of Vacumm Arc During Arc Formation Process", 28^{th} International Symposium on Discharges and Electrical Insulation in Vacuum (ISDEIV), 2018, Germany.

[10] P. Tarnowski and W. Ostapski, "Pulse powered turbine engine concept – numerical analysis of influence of different valve timing concepts on thermodynamic performance", *Bull. Pol. Ac.: Tech.* 66 (3), 373–382 (2018).

[11] V.S. Nagarajan, V. Kamaraj, and S. Sivaramakrishnan, "Geometrical sensitivity analysis based on design optimization and multiphysics analysis of PM assisted synchronous reluctance motor", *Bull. Pol. Ac.: Tech.* 67 (1), 155–163 (2019).

[12] R. Bini, N.T. Basse, and M. Seeger, "Arc-induced Turbulent Mixing in a Circuit Breaker Model", *J. Phys D Appl Phys* 44 (2), (2011).

[13] R. Holm, *Electric Contacts – Theory and Application*, NewYork, NY, USA: Springer.

[14] N.P.T. Basse, R. Bini, and M. Seeger, "Measured turbulent mixing in a small-scale circuit breaker model", *Appl. Optics* 48 (32), 6381–6391 (2009).

[15] F.P. Incropera, D.P. DeWitt, T.L. Bergman, and A.S. Lavine, *Introduction to Heat Transfer*, 5th ed. Hoboken, NJ, 2006, USA: Wiley.

[16] P.T. Muller, ' 'Macroscopic electro thermal simulation of contact resistances, Bachelor thesis", RWTH, 2016, Aachen, Germany.

[17] W. Biao, L. Yanyan, and Z. Xiaojun, "Study on detection technology of the contact pressure on the electrical contacts of relays", 26th International Conference on Electrical Contacts (ICEC), 2012, pp. 161 – 164.

[18] X. Sun, B. Su, L. Chen, Z. Yang, and K. Li, "Design and analysis of interior composite-rotor bearingless permanent magnet synchronous motors with two layer permanent magnets", *Bull. Pol. Ac.: Tech.* 65 (6), 833-843 (2017).

[19] M. Kriegelet, X. Zhu, H. Digard, S. Feitoza, M. Glinkowki, et al., "Simulations and Calculations as verification tools for design and performance of high voltage equipment", CIGRE, Paris, France, , A3-210 (2008).

[20] P. Kumar and A. Kale, "3-Dimensional CFD simulation of an internal arc in various compartments of LV/MV Switchgear", Ansys Convergence Conference, 2016.

[21] D.J. Hartland, "Electric contact systems – passing power to the trains", IET Professional Development Course on Electric Traction Systems, 2010, pp. 25–37.

[22] G. Chen, L. Lan, Z. Pan X. Wen, Y. Wang, and Y. Wu, "Electrical erosion test and condition assessment of SF6 CB contact sets", *IET Generation, Transmission & Distribution* 11 (8), 1901–1909 (2017).

[23] J.D. Mantilla, N. Gariboldi, S. Grob, and M. Claessens, "Investigation of the insulation performance of a new gas mixture with extremely low GWP", Electrical Insulation Conference, Philadelphia, 2014.

[24] A.A. Iordanidis and C.M. Franck, "Self-consistent radiation based simulation of electric arcs: Application to gas circuit breakers", *Journal of Physics D: Applied Physics* 41, 135206, (2008).

[25] X. Ye and M.T. Dhotre, "CFD Simulation of Transonic Flow in High Voltage Circuit Breaker", *International Journal of Chemical Engineering*, 2012, Article ID 609486.

[26] H. Kim, I. Chong, and S. Lee, "Analysis of SLF Interruption Performance of Self-Blast Circuit Breaker by Means of CFD Calculation", *Journal of Electrical Engineering & Technology* 9 (1), 254–258 (2014).

[27] M. Lindmayer and H. Stammberger, "Application of numerical field simulations for low-voltage circuit breakers", *IEEE Transactions on Components, Packaging, and Manufacturing Technology: Part A* 18 (3), (1995).

[28] P.U. Frei and H.O. Weichert, "Advanced Thermal Simulation of a Circuit Breaker", *Proceedings of the 50th IEEE Holm Conference on Electrical Contacts and the 22nd International Conference on Electrical Contacts Electrical Contacts* (2004).

[29] S. Ito, Y. Takato, Y. Kawase, and T. Ota, "Numerical analysis of electromagnetic forces in low voltage AC circuit breakers using 3-D finite element method taking into account eddy currents", *IEEE Transactions on Magnetics* 34 (5), (1998).

[30] Ch. Degui, L. Xingwen, J. Liang, and Z. Xin, "Numerical Simulation of Arc Motion During Interruption Process of Low-Voltage Circuit Breakers", ICEC 2012.

[31] P. Kačor and P. Bernat, "Analysis of force characteristic of short-circuit release in low voltage circuit breaker", *Proceedings of the 2014 15th International Scientific Conference on Electric Power Engineering*, (2014).

[32] M. Conecici-Lucian, C. Munteanu, and I.M. Purcar, "3D finite element analysis of a miniature circuit breaker", 6th International Conference on Modern Power Systems MPS2015, Cluj-Napoca, 2015.

[33] L. Chunlei, W. Dong, Z. Bing, L. Jin, and Z. Wenjun, "On Novel Methods for Characterizing the Arc/Contact Movement and Its Relation With the Current/Voltage in Low-Voltage Circuit Breaker", *IEEE Transactions on Plasma Science* 45 (5), 882–888 (2017).

[34] N. Vasiraja and P. Nagaraj, "The effect of material gradient on the static and dynamic response of layered functionally graded material plate using finite element method", *Bull. Pol. Ac.: Tech.* 67 (4), 828–838 (2019).

[35] 1. D. Pop, L. Neamt, R. Tirnovan, and D. Sabou, ' "3D Finite Element Analysis of a Miniature Circuit Breaker", HE 8th International Symposium on Advanced Topics in Electrical Enginnering, Bucharest, 2013.

[36] Ch. Degui, D. Ruicheng, Z. Jingshu, and T. Weixiong, "Dynamic Simulation of Operating Mechanism for Molded Case Circuit Breaker", *Electrical Contacts*, 2007.

A3. *Mechanical and Electrical Simulations of Tulip Contact System*

energies

MDPI

Article

Mechanical and Electrical Simulations of the Tulip Contact System

Sebastian Łapczyński [1], Michał Szulborski [1,*], Karol Gołota [2], Łukasz Kolimas [1] and Łukasz Kozarek [3]

1 Institute of Electrical Power Engineering, Warsaw University of Technology, 00-662 Warsaw, Poland; seb.lapczynski@gmail.com (S.Ł.); lukasz.kolimas@ien.pw.edu.pl (Ł.K.)
2 KGMG Sp. Z O. O., 22-100 Warsaw, Poland; karolgolota@gmail.com
3 ILF Consulting Engineers Polska Sp. Z.O.O., 02-823 Warsaw, Poland; lukaszkozarek@gmail.com
* Correspondence: mm.szulborski@gmail.com; Tel.: +48-662-119-014

Received: 19 August 2020; Accepted: 23 September 2020; Published: 25 September 2020

check for updates

Abstract: The purpose of this work is to discuss the tulip contact behavior during mechanical and electrical simulations in a Finite Element Method (FEM) environment using ANSYS and COMSOL software. During the simulations, the full contact movement was analyzed. During the contact movement, the individual behavior of the contact components was taken into consideration. the motion simulation was carried out at different velocities and forces acting on the contact. the obtained results were compared to each other and discussed. Relatively, the angles of the contact surfaces to each other were also changed, which meant that we could conduct a more in-depth analysis. the other approach of simulation research was a field analysis of physical phenomena occurring in the tulip contact. This analysis was performed in COMSOL Multiphysics. Parametric analysis allowed an observation of the electric field in the tulip contact at different contact distances with respect to each other. This work is important in terms of the cost effectiveness for design procedures concerning tulip contacts and fault avoidance, which both result from mechanical and electrical conditions throughout contact exploitation and optimization of the working conditions for the tulip contact.

Keywords: tulip contact; electrical contacts; FEM; simulation; mechanical analysis; electrical parameters

1. Introduction

Digital calculation methods such as the Finite Element Method (FEM) allow many calculations to be performed in parallel. This can significantly accelerate the whole design process of the chosen components. Digital techniques are also used in designing structures of electrical apparatuses. Using CAD software, it is possible to design devices from a single element to whole complex assemblies [1,2]. Simulations of such structures are also possible in a further stage, as part of a project using specialized software [3,4]. These can be employed in order to simulate the movement of elements relative to each other, exclude collisions, and end by observing the drafted system in conditions simulating a natural work environment [5,6].

The contacts of electrical apparatuses belong to the most loaded elements of current circuits [7,8]. Therefore, they should be designed, constructed, and operated in such a way that the permissible limitations of their technical parameters, resulting from relevant regulations and standards, are not exceeded [9]. the parameters of the electrical apparatus connecting process strictly depend on the parameters and kinematic, dynamic, and structural properties of the mechanism that is responsible for the movement of the electrical contact. the tasks of this mechanism include reliable movement of the set of movable contacts in an intended manner and maintaining contact pressure in their contact state [10]. the mechanical part of the switching contacts is required to reliably maintain the contact state, regardless of the rated parameters of the apparatus. the temperature of the entire structure must be maintained at a level that allows stable working conditions, which are also specified in the relevant standards. the mechanism should be resistant to the phenomenon of contact clogging when connecting, operating, and exposed to fault currents, as well as when conducting analysis under short circuit conditions [11]. This is directly related to the working temperature of the contacts and the phenomenon of contact bounce. It is also important to minimize contact expenditure while switching on currents. a number of forces act on the contacts during the bonding process [12,13]. These can be divided according to the source of origin. If there were no difference in electrical potential between the contacts, the current would not flow while the contacts touched, and therefore, the associated forces would not appear.

The combination of two types of analyzes—motion analysis and analysis of the electric field distribution—gives the image closest to the real environment of the system in which tulip contact is usually employed. This allows the entire contact to be designed in the most optimal way. the optimization applies to both the design time and the costs and quantity of the prototype construction. Therefore, our team executed a number of simulations in order to prove that proper simulations can aid the design process of electrical contacts, fault detection, and optimization [14].

This work is novel as it focuses on an analysis of the operation of the fixed contact. Nevertheless, movable contact analysis was also taken into consideration and executed whilst discussing the simulation results. the following points highlight the impact of this work:

- the ability to observe the behavior, operation, forces, and energy of all lamellas of the stationary (fixed) contact;
- Observation of the influence of the eccentricity of the movable contact mounting on the possibility of switching on;
- Mechanical analysis of the contact as for a real physical system;
- Determination of electrical parameter values during the switching operation;
- Contact development in other extinguishing environments (future work on the procured model).

2. State of the Art

The rapidly growing demand for electrical devices (the main elements are the contact system and the extinguishing chamber) consisting of high-quality electrical components has led to a new approach to designing switches. the main goal of designing and constructing electrical devices is to create solutions that can significantly improve their electrical and mechanical parameters, size, and short-circuit resistance [15]. Modern electrical apparatus is built in accordance with applicable standards (e.g., European standards). These requirements also apply to high-voltage circuit breakers (SF_6 insulated). Despite the increasingly smaller sizes of the devices mentioned, they are adapted to the effective breaking of short-circuit currents and protection of other elements of the power system. Complex mechanical phenomena occur in the circuit-breaker during the closing and opening process. This affects the structural components of the switch (copper, tungsten, steel, and aluminum) [16].

Competing authors have mostly concentrated on only simulating the contact system from a single, uniform material [17–19]. In fact, with a small number of cuts, the stationary contact is massive and no overall mechanical analysis may be required [20]. Therefore, the analysis of phenomena can be reduced to only a single lamella [21]. Nevertheless, the example of a multi-lamella contact system, consisting of a large number of elements, requires a different approach. the importance of mutual displacements of lamellas that mutually interact was observed. This results in a change in the total energy, torque, and mechanical stresses that must be taken into account. It is worth noting that high-current tulip contact systems are also commonly used in the vacuum technique. It is true that in the vacuum technique, multi-lamella contact systems are always closed without voltage (the vacuum circuit breaker is inserted into the distribution box on the grid). Nevertheless, the mechanical stress and the associated risks, including damage, failure, and destruction, are very similar to the systems in the extinguishing environment with SF_6 gas.

The FEM model presented in this paper is applicable to contact systems in various environments and geometric configurations. the results enable the proper construction of complex contact systems for high-voltage conditions (heavy duty). the presented solution enables the validation of advanced analytical calculations, and the implementation of different, often complicated, geometries in relation to the simplified models of contacts. the model enables the determination of values for scientific and research calculations.

3. Contacts in Electrical Apparatuses and Current Circuits

3.1. Non-Connecting and Connecting Contacts

Current circuits and contact systems allow the conductive operating of currents, and contact systems of electrical connectors are used to make connections in electrical circuits. a contact is a part of the current circuit in which the current flow is made possible by the conjunction of two conductors. Due to their function in the current circuit, a distinction can be made between connecting and non-connecting contacts [22]. Connecting contacts consist of movable and fixed elements, while non-connecting contacts are only made of fixed elements. an example of connecting and non-connecting contacts is shown in Figure 1 below.

(a)

(b)

Figure 1. The view of exemplary contacts from families: (**a**) Non-connecting contacts (own study) and (**b**) connecting contacts [23].

Non-connecting contacts are fixed, and their elements cannot move with respect to each other. Figure 1a shows typical non-connecting contacts used in low-voltage switchgears. the movable contacts are used in contact switches and enable switching on and off of the current in a given circuit (such a contact is shown in Figure 1b). These can be divided into normally open (closed in the forced position of the movable contact) and normally closed (open in this position) contacts. Due to the shape of the contact surfaces, the contacts are divided into point, line, and surface contacts. a point contact is a contact in which contact takes place on a surface with a very small radius (through which current flows). the surface contact is characterized by a relatively large apparent (nominal) contact surface, while the actual contact surface of such a contact is a small percent of the apparent surface.

The contacts of electrical apparatuses belong to the most loaded elements of current circuits. Therefore, they should be designed, constructed, and operated in such a way that the permissible limits of their technical parameters resulting from relevant provisions and standards are not exceeded.

3.2. Tulip Contacts

Tulip contacts are an example from the group of connecting contacts. These contacts are also classified as coronary contacts and are often used in medium-voltage switchgears [23].

4. Construction of a Tulip Contact Used in Finite Element Method Analysis

The tulip contact which was used was patented under the number US 2012/0129374 A1/B2. the view of the tulip contact on which the three-dimensional modeling was based is shown in Figures 2 and 3 below.

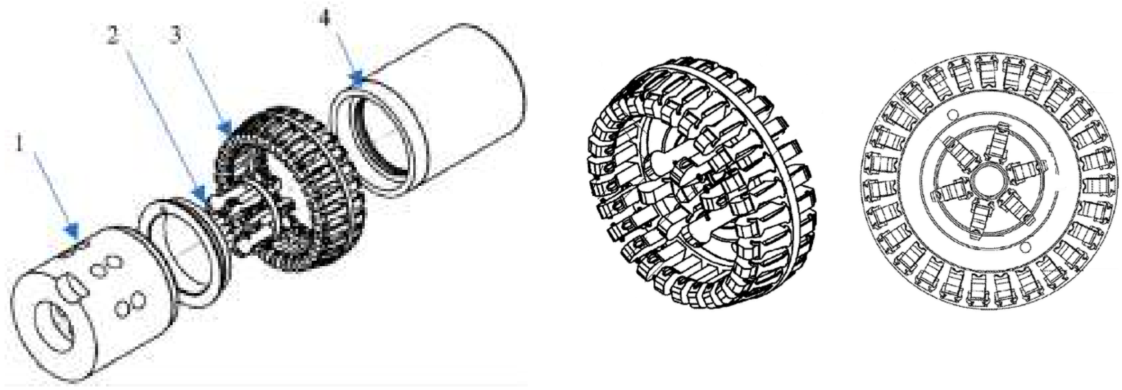

(**a**) (**b**)

Figure 2. Structural view of the tulip contact: (**a**) 1—movable part of the contact, 2—inner crown lamellas, 3—outer crown lamellas, and 4—lamella seating, and (**b**) detailed view of tulip contact lamellas [24].

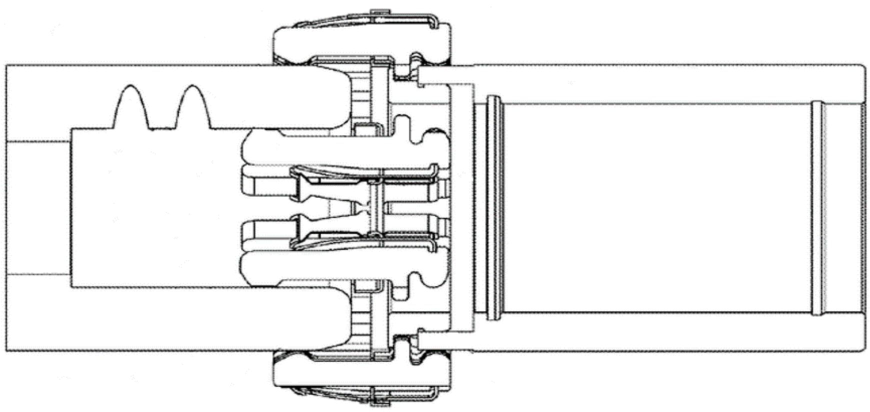

Figure 3. Longitudinal section of a closed tulip contact [24].

3D modeling was carried out in SolidWorks software. This software provides the ability to perfectly map the elements that were selected for simulation. Figure 4 was derived based on the materials proposed by the manufacturers of electrical apparatus and engineering experience. Three-dimensional models were mapped, which were used for further simulations in the ANSYS FEM software.

The movable contact element during the simulation of contact motion in the ANSYS software was assigned the physical and mechanical properties of a copper alloy. the same properties were also assigned to all lamellas. However, both fastening crowns (large crowns and small crowns) were defined as steel. Each electrical contact must be designed to meet electrical conditions in the open position and electro-mechanical conditions while closing and opening. All of the material data used in the simulation are described in Table 1.

(a)

(b)

Figure 4. 3D model of the tulip contact: (**a**) View of a designed tulip contact model and (**b**) view of the lamellas in the tulip contact model.

Table 1. Table of the material data used in the procured model.

Engineering Data	Copper	Steel	Unit
Density	8300	7850	(kg/m^3)
Young's Modulus	1.10×10^{11}	2.00×10^{11}	(Pa)
Poisson's Ratio	0.34	0.3	
Bulk Modulus	1.15×10^{11}	1.67×10^{11}	(Pa)
Shear Modulus	4.10×10^{10}	7.69×10^{11}	(Pa)

5. Physical Properties of Tulip Contact Systems

5.1. Insulation Strength of Contact Systems

The insulation strength mainly depends on the distribution of the electric field and the medium between the contacts. the layout of the contact and the materials used directly affect the electric field distribution. the electric medium should be air, gases, gas mixtures, and various types of oils.

Air is the most common gas dielectric used in practical high-voltage insulation systems. Its dielectric strength depends on many parameters. the most important are the construction of the insulation system and the electric field distribution, depending on the spark gap, type and course of voltage over time, air density, temperature, and humidity.

Sulfur hexafluoride has a number of properties that make it great as dielectric fluid. It is a very good insulating medium. It has a 2.5 times higher puncture strength than air, and at a pressure above three bar, its puncture strength is higher than that of mineral oil. Due to the high electron affinity of fluorine, the use of SF_6 increases the initial voltage of partial discharges. It is a very good extinguishing medium. For SF_6, the high electron affinity of fluorine combined with the abundance of fluorine on each discharge path ensures a strong interaction with high-energy electrons. This makes SF_6 almost 100 times more efficient at extinguishing than air. SF_6 is an inert and non-flammable gas. Only temperatures of 500 °C or electrical discharge can initiate dissociation and possible reactions. Fortunately, in the absence of other compounds, the dissociation products of SF_6 naturally combine with each other to regenerate SF_6. SF_6 is characterized by its unique ability to self-regenerate among dielectric fluids. Sulfur hexafluoride is an excellent heat carrier. the thermal conductivity coefficient of SF_6 is higher than that of air. Moreover, it grows with an increasing pressure. However, for sufficiently high pressures or flows, the SF_6 heat transfer coefficient is better than that of mineral oil. SF_6 is a non-toxic gas. This increases its attractiveness from the point of view of health and safety.

In practice, there is usually a channel mechanism for the development of discharge, because the electrode spacing usually ranges from 1 to 2 cm, which, at the atmospheric pressure and temperatures encountered in practice, is the border separating the two discharge mechanisms: Townsend and channel mechanisms.

Practical systems should usually be treated as blade systems, because the ratio of the distance to the dimensions of the electrodes is generally large and even avoiding sharp edges does not eliminate the unevenness of the electric field distribution. the dependence of the blade system strength on the electrode distance is shown in Figure 5 below.

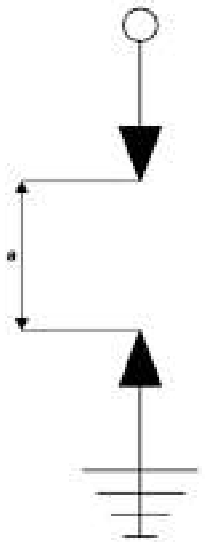

(**a**)

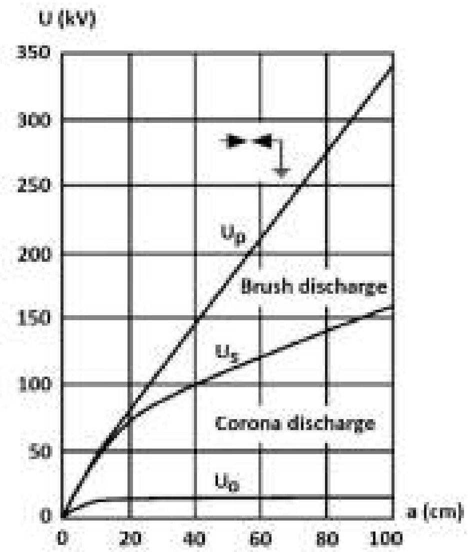

(**b**)

Figure 5. View of a blade-type insulation system: (**a**) Blade with insulation distance a and (**b**) dependence of voltage U_o, U_s, and U_p on the distance between the electrodes for the blade system, where U_o—initial voltage, U_s—shearing voltage, and U_p—jump voltage.

During the flow of electric current, electromagnetic forces occur in the contact system. These forces largely depend on the ratio between the radius of the external contact-R and the radius of the narrowing r, as well as on the position of the tangent point in relation to the entire system. As the number of contact points increases, the electrodynamic forces acting on the contacts decreases. the increasing distance between the contact points also lowers the force value. the solution used in the tulip contact is therefore a perfect example of dividing the contact points and providing a gap between them to counteract the electrodynamic force. When no current flows through the contact system, forces are still present in the process of closing and opening the movable contact. Along with the driving force closing and opening the movable contact, resistance forces occur. They result from movement of the movable contact surface against the stationary contact surface. the value of the resistance force depends on the contact material, the shape of the contacting elements, and the number of lamellas. an electrical apparatus installed in the power grid should cause the least losses, i.e., its contact resistance should be as low as possible. This requires the closed contact force to be maintained at a sufficiently high value. On the other hand, it is expected that the value of the resistance force when closing the contacts is low and as close as possible to that while opening the contact layout.

5.2. Continuous, Variable and Short-Circuit Current Carrying Capacity

In the process of designing and testing current apparatus, the only aim is to determine the current carrying capacity. the current carrying capacity in the process of electrical apparatus construction is a set value and also a design assumption. However, during the testing of existing switching devices, the heat dissipation capability at rated and short-circuit currents must be checked. the load capacity of the cables largely depends on the intensity of heat dissipation from the heated body. Due to the conditions of heat dissipation from apparatus currents and switchgears, the following main calculation cases can be distinguished:

- Unprotected current circuits placed in air or an SF_6 environment, where heat is mainly released into the environment through radiation and lifting;
- Homogeneous current paths, surrounded by a layer of solid insulation, where all forms of heat transfer are significant;
- Heterogeneous current circuits, in which, in a steady state, an important role in heat transfer is carried out by axial heat flow.

In electric apparatuses and current circuits, the elements in which the resistance changes show the greatest heat gain. Such a change is usually observed at the contact points or narrowing of the current circuit. Figure 6 shows the heating of the current circuit from the point of electrical contact.

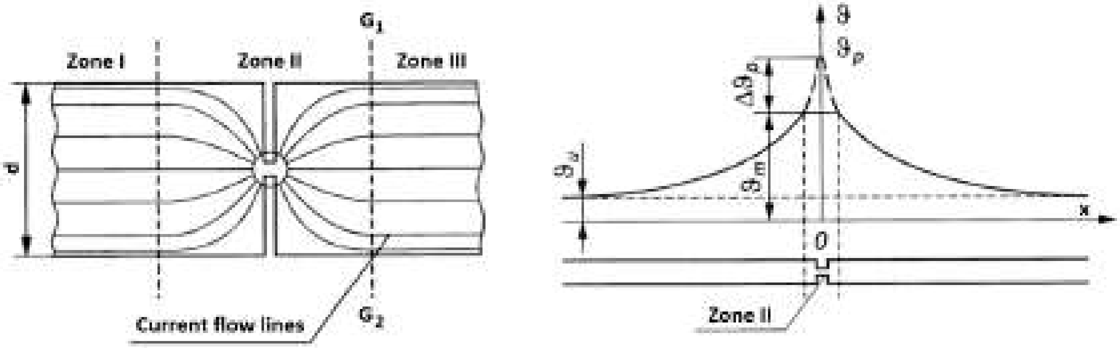

(**a**) (**b**)

Figure 6. Heating of the current circuit with a single point contact: (**a**) Contact model and (**b**) temperature distribution along the current path, where ῠ—maximum temperature present at the contact point.

The heating constant of a given current circuit or contact system should also be determined. Several calculation methods can be employed for determining the characteristics. Below are some of the basic mathematical relationships used to determine the characteristics and the temperature waveforms as a function of time. the current circuit heating characteristic is shown in Figure 7.

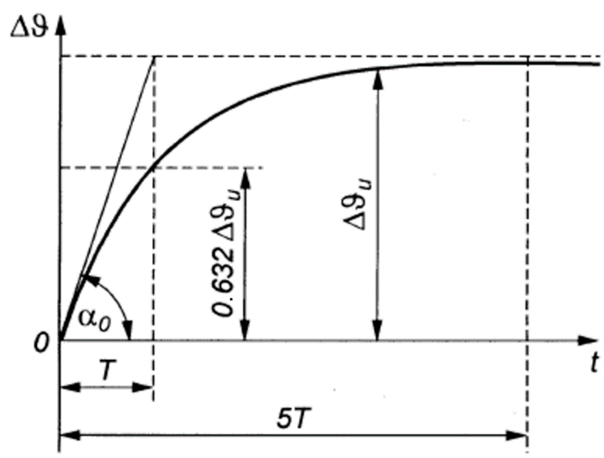

Figure 7. Typical characteristic of current circuit heating.

Current circuits can be subjected to continuous, occasional, and intermittent current loads. In all cases, the heating of the current circuits begins with the value of the ambient temperature.

the temporary and intermittent loads last for too short a period of time to determine the temperature rise. the interrupted load is a variable load with repeated periods and interruptions in a current flow. During load breaks, the conductor does not cool down to the ambient temperature because the no-current periods are too short compared to the value of time constant T.

6. Motion Simulations of the Tulip Contact System

Simulation studies were focused on by examining the dynamics of movement and physical phenomena in the tulip contact system. the analysis of the contact operation in the form of simulations was carried out in the ANSYS software. During the simulation, forces and times prevailing in existing tulip contacts were used. This resulted in obtaining values that are as close as possible to engineering experimental data. Several simulations were carried out relative to reference values. Both the forces arising from the release from constraints and the closing velocity of the contact were changed.

6.1. Environment for Simulation Research

ANSYS software was the tool used to perform motion analysis. the program used the Explicit Dynamics module, which is used to study the movement of fast-changing and short-lived events. the module analyzes phenomena and forces with non-linear characteristics. the internal structure of materials is analyzed during the interactions between elements and surface effects of motion dynamics. the tool used to perform the electrical analysis was COMSOL Multiphysics version. One of the calculation modules employed was the AC/DC module, which is used to simulate the electric, magnetic, and electromagnetic fields for static and low-frequency applications.

6.2. Discretization of the Procured Model

Extracting elements in area V, in which the solution is searched for, is a very important stage in creating the FEM calculation model. the method of discretization depends on the geometry of the area, physical properties, and certain general premises regarding the results of the solution, as well as the expected efficiency of calculations.

The method of discretizing the area determines the number of unknowns and the size and shape of the elements, and this affects the accuracy of the task solution. In order to obtain the required accuracy of the solution sought, the elements used should be small enough that the approximated functions inside them can be rough by means of polynomials. However, reducing the elements leads to an increase in the number of values of the nodal value function sought, and this simultaneously results in a longer calculation time. Most often, an uneven division into elements is used. While predicting where the function changes rapidly allows the element mesh to be compacted, where the function changes slowly, the element mesh should be diluted.

The accuracy of the solution primarily depends on the accuracy of the approximation of physical quantities inside the element using interpolation functions, hereinafter referred to as shape functions. With the correct mapping of the physical quantities of the element, reducing the areas of the elements (increasing their number) causes the nodal values of the sought function, which are an approximate solution of the task. the mesh process of the procured model is shown in Figure 8.

6.3. Analysis of the Tulip Contact Motion Dynamics—Variant I

The figures below show the mechanical stresses resulting from the motion analysis performed. By means of color spots, the force values are graphically represented, which can be read from the scale on the left side of each drawing. Graphical presentation of the results significantly speeds up the analysis of the results and facilitates the work. Figure 9 shows the entire tested tulip contact from two calculation views. Each of them unambiguously showed the highest loads in this type of tested structure. Thee mechanical loads appear in small movable elements, i.e., small and large lamellas and crown fixing of these lamellas. It should be remembered that in commercially produced contacts, each lamella is pressed towards the contact axis by springs surrounding the entire tulip or through direct spring pads that press against a single frame. In the analyzed contact, such elements were replaced by pressing forces applied in appropriate places, allowing the system to be released from such constraints.

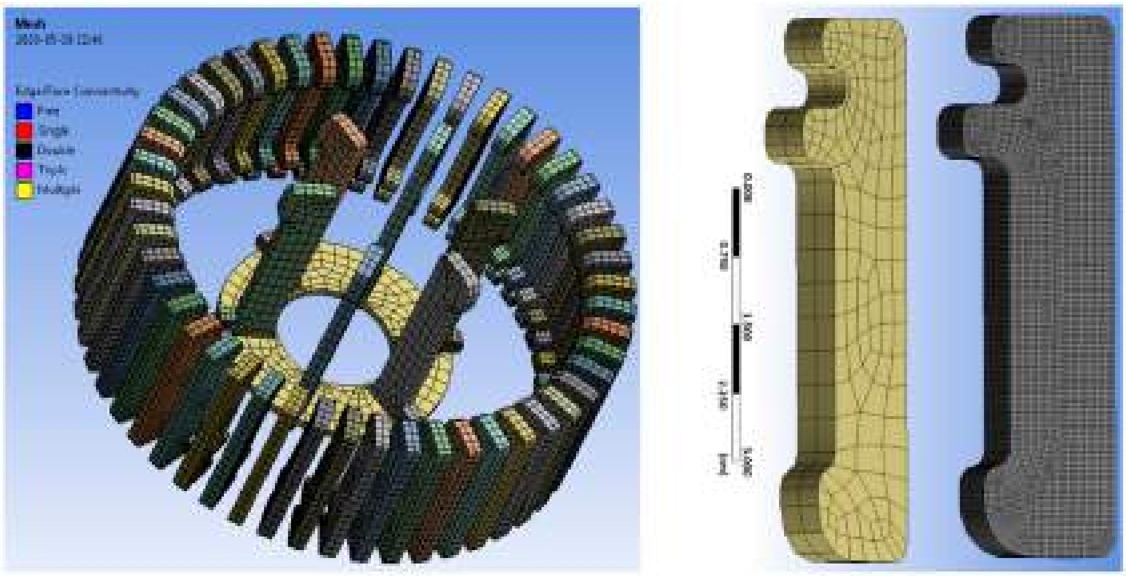

(a) (b)

Figure 8. Meshing procedure of tulip contact system elements: (**a**) Tulip contact and (**b**) lamella with different rates of mesh during the discretization process.

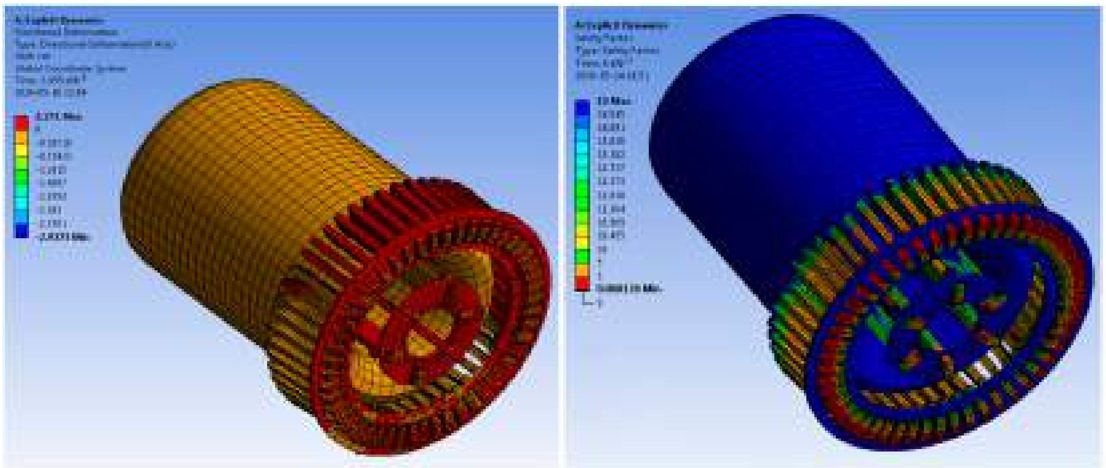

(a) (b)

Figure 9. View of the tulip contact analyzed in ANSYS: (**a**) View of the direct values of contact deformation and (**b**) the safety factor.

In a further part of the analysis, individual elements of the tested system were discussed. In Figure 10, the discretization grid (mesh) and results of deformation analysis can be seen for lamellas. the mesh was compacted with fragments, requiring more detailed analysis. the views of the lamellas show that the places where they are attached in the crowns are exposed to high overload. In these places, deformation of the material occurs very often. the ANSYS program showed red loose dots in the output. In this way, it represents the crumbled lamella or crown material. Chips of this type occur as a result of two elements hitting each other with significant force. During further work on a given lamella, the connection between the lamella and the crown should be rebuilt by reducing friction and optimizing the distribution of forces and movement of the element.

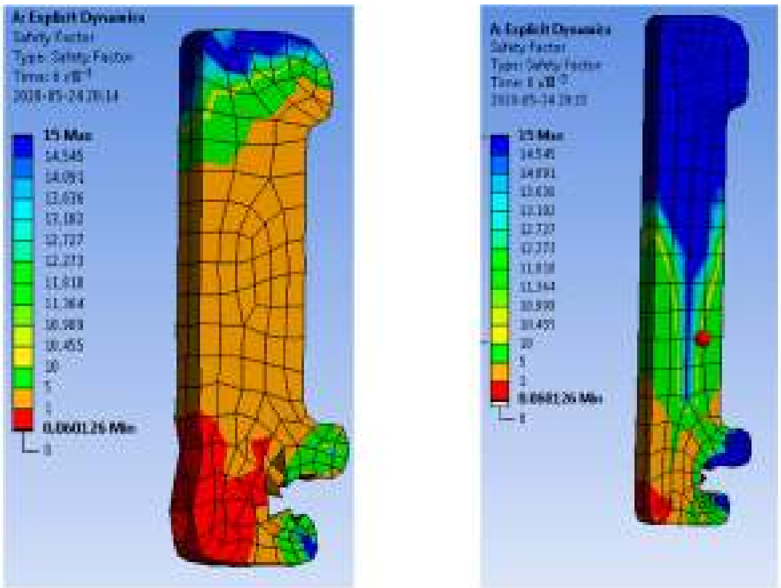

(**a**) (**b**)

Figure 10. View of the lamellas used in the tulip contact: (**a**) Small (external) lamella in the deformation value view and (**b**) large (internal) lamella in the deformation view.

Crowns were the next element observed to be more susceptible to deformation. Figure 11 shows that the crowns carry high mechanical loads through them. It should be remembered that the crowns rest on the lamellas, which, in turn, are hit by the moving part of the contact. In a later phase of movement, the lamellas deviate from the contact axis and, being fixed in the lower part, exert torque on the crown. This causes the force of the crown to become deformed. In the small crown, the principle of movement and the type of forces are the same, but the direction of the slat deflection is the opposite, due to its setting. When considering the construction of the crown, it should be remembered that it must support the lamellas longitudinally in relation to the contact axis and prevent them from deflecting sideways.

6.4. Results of Motion Dynamics—Variant I

All of the above-mentioned results were read from colored scales next to the elements of the tulip contact system. These were also presented graphically as the course of the functions of force, moment, and energy. Color maps of forces marked on the contact elements facilitate quick analyses of the tested value. an hourglass effect can be seen in Figure 12. In order to analyze all of the movement, it is significant to refer to the graphs below Figures 13 and 14. In the first graph—Figure 15—the course of kinetic energy, internal energy, and the hourglass effect (Hourglass Energy) is shown. It can be noticed that from the first moment of time, the input has the highest kinetic energy. This proves that the moving part of the contact was activated at the beginning of the simulation. With the flow of time in the motion analysis, it can be clearly seen that the kinetic energy value is decreasing. This is the moving part of the contact that moves downwards. As a result, the distance between the elements decreases. In accordance with the formula for kinetic energy, its value decreases. In the same diagram, the course of the internal energy of the system can be viewed. This energy increases as the simulation runs, reaching the maximum values just after the movable contact hits all of the lamellas. the red line in the same figure shows the hourglass effect. This is a false deformation of the finite element mesh resulting from the stimulation of the freedom degrees of zero energy. It usually manifests itself in a cluster of zigzag lines or shapes in which the individual elements have strongly deformed edges.

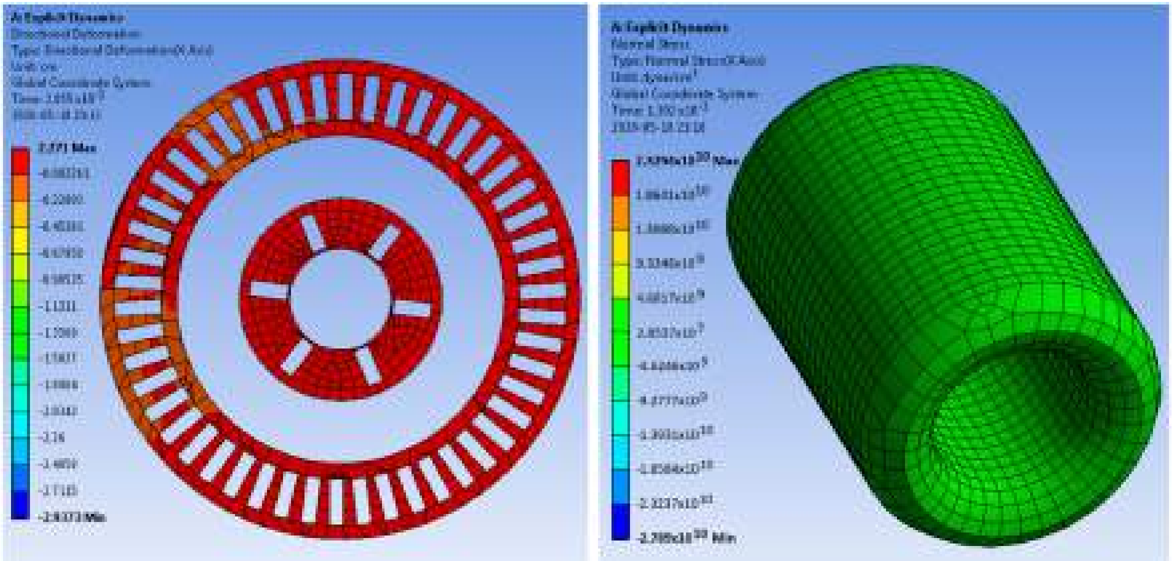

(**a**) (**b**)

Figure 11. Crown analysis: (**a**) View of the lamella fastening crowns and (**b**) view of the movable part of the contact.

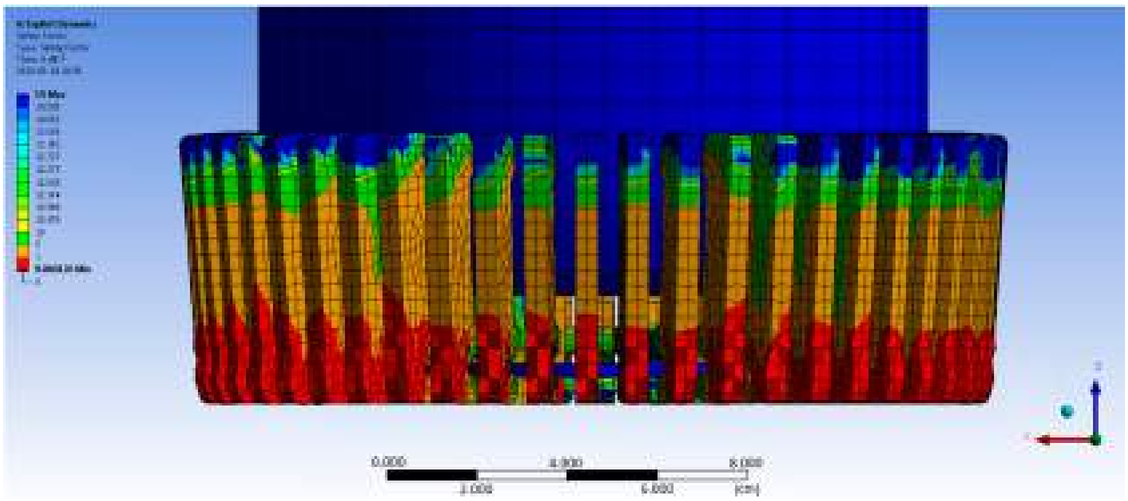

Figure 12. View showing the hourglass effect.

Therefore, the red line in Figure 15a runs below the value of the internal energy of the contact until the collision of the movable part and the small lamellas. This proves that this effect is of negligible value. However, after hitting the small lamellas, this value increases and reaches its maximum as soon as the motion of the moving part is finished and the small lamellas stop keying. During the impact, the small lamellas detach from the axis of the system, and thanks to the pressing forces, they hit the external part of the contact and begin to press on its surface. De-keying and keying cause compressive stresses in the rear parts of the lamellas, which, for a given discretization grid, result in the effect of glass-gluing. To prevent this effect in subsequent iterations, the discretization mesh should be increased locally. This will directly contribute to increasing the density of calculations and reduce the phenomenon of false deformation of the material. the next step was to increase the pressure of the lamella. This can reduce the angle of the throw and the keying itself.

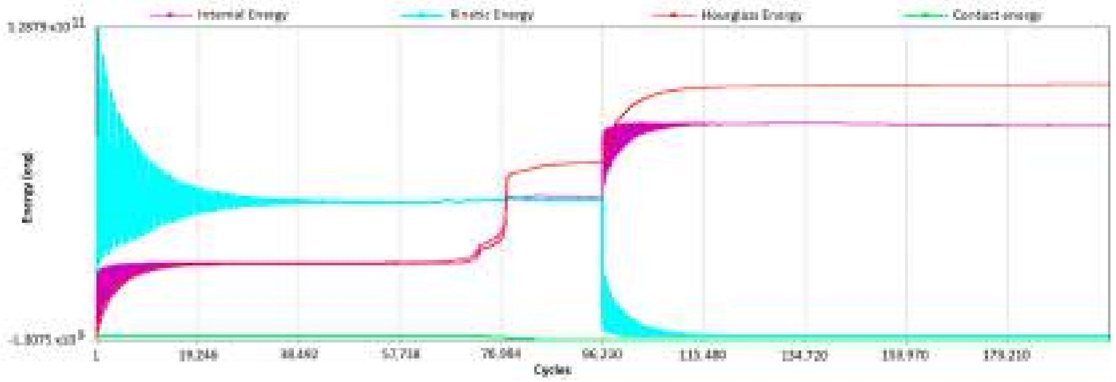

(**a**)

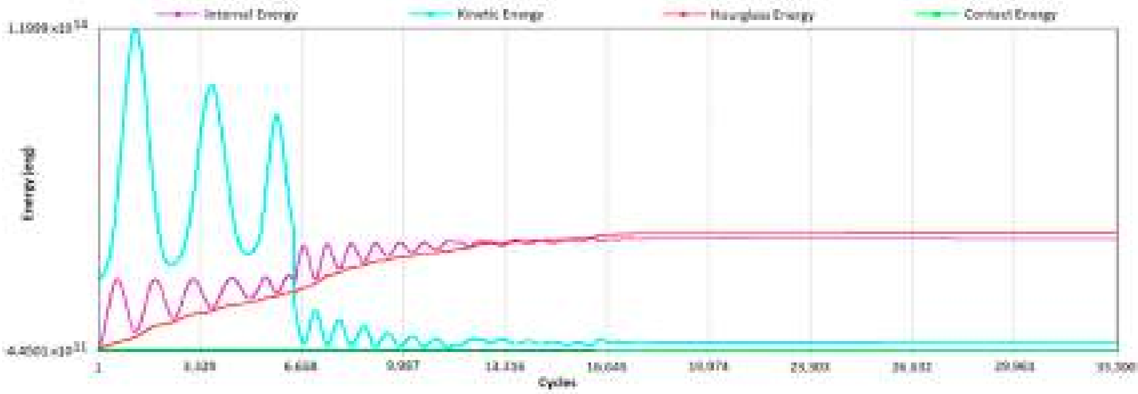

(**b**)

Figure 13. Diagrams of the tulip contact motion analysis: (**a**) Energy summary—normal operation and (**b**) energy summary—contact destruction.

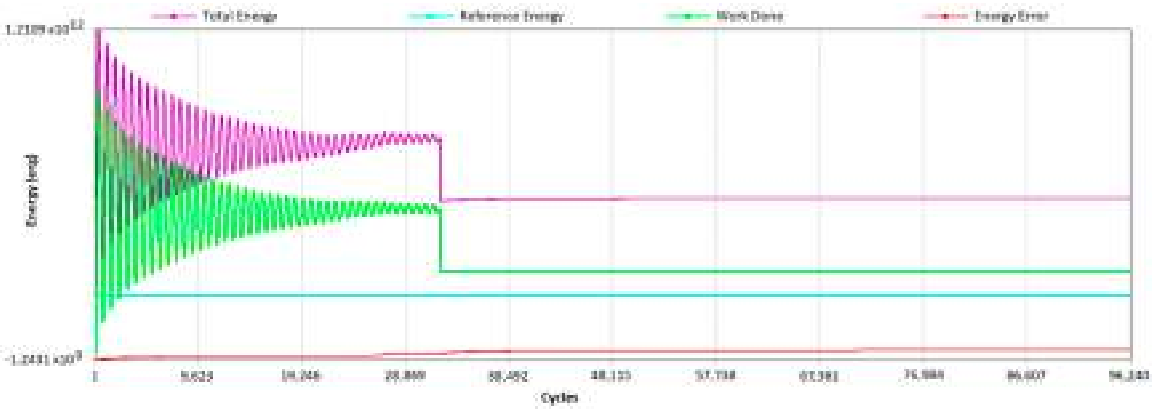

Figure 14. Graphs produced from the analysis of the motion of the tulip contact, energy consumption, and energy conservation.

The graph in Figure 15b shows the values of two parameters: the total energy and work. It can be seen that energy and work follow the same course. This means that the calculations are consistent with real conditions. With the passage of motion time analysis, a decrease in the value of both energies can be noticed, which is caused by the movement of the contact. After moving the movable part of the contact to a lower position, there is still a moment of vibration on the small blades. the energy and work drop to low values. Note that the error value increased at the end of the move. Nevertheless, it was still significantly below the assumed error limit.

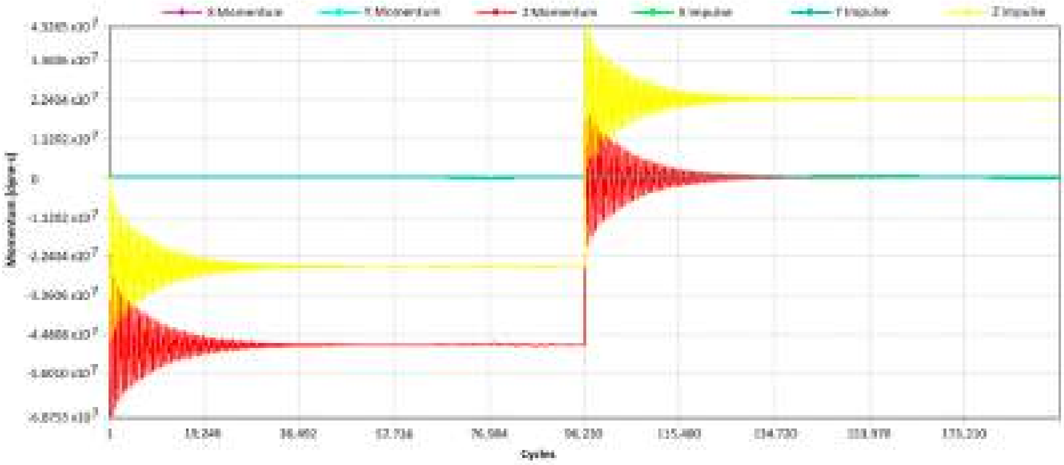

(**a**)

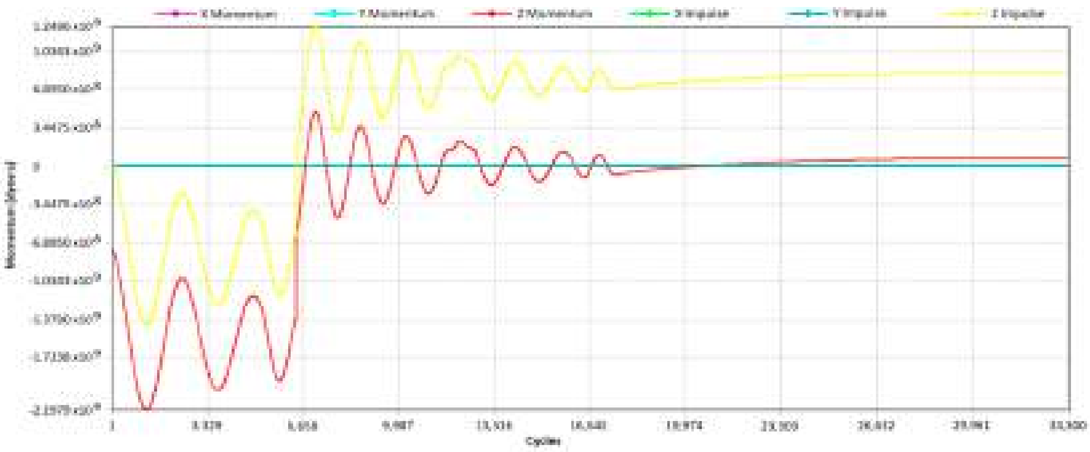

(**b**)

Figure 15. Graphs produced from the analysis of the motion of a tulip contact, presenting a summary of moments: (**a**) Normal operation and (**b**) contact destruction.

The main torque and energy impulse runs along the axis of the tulip contact. It can be noticed that the greatest moment exists at the time of the maximum velocity and force of the moving part of the contact. Then, this value decreases as the elements collide with each other. the moment value then returns to its original value. This is due to the fact that the movement of the cylindrical part of the contact is negative in relation to the main reference system. the lamellas, on the other hand, deviate in positive directions. At the time of reading the lamellas, an increase in the moment was noticed, which also, after a while, began to stretch across the frictional forces and stresses inside the elements.

6.5. Analysis of the Tulip Contact Motion Dynamics—Variant II

The second variant revolved around an analysis of the nearly exact contact system, but the radius of the lamellas with the moving part of the contact was modified. Figure 16 shows the difference in the radius of the lamellas and therefore, the change in contact parts' geometry.

Figures 16 and 17 show the modified lamellas. Figure 17 additionally shows the results of the analysis. Two fundamental differences were noted. In the upper part of the lamella, the force distribution, namely the yellow line representing the value 10, has a completely different course. the movable parts of the contact strike the lamellas at different angles in both cases. In the first case, when the lamella radius is greater, the point of impact is closer to the edge of the internal contact axis. This translates into a lower deflection force of the lamella from the moving contact compared to the second case. the reduction of the generating radius in the second case increased the friction during the impact, which implied the creation of higher force values in the entire lamella. the yellow lines of force values reflect how the direct impact is distributed to the stresses inside the material. It was observed that a larger radius also translated into greater forces in the upper part of the lamella. the stress distribution in the middle is identical in both cases. However, the lower part of the lamellas, which was fixed in the crown, shows considerable damage in the reduced radius version. the greater recoil force of the lamellas resulted in greater stresses of the lamellas in relation to the crown, and thus deformation of the material.

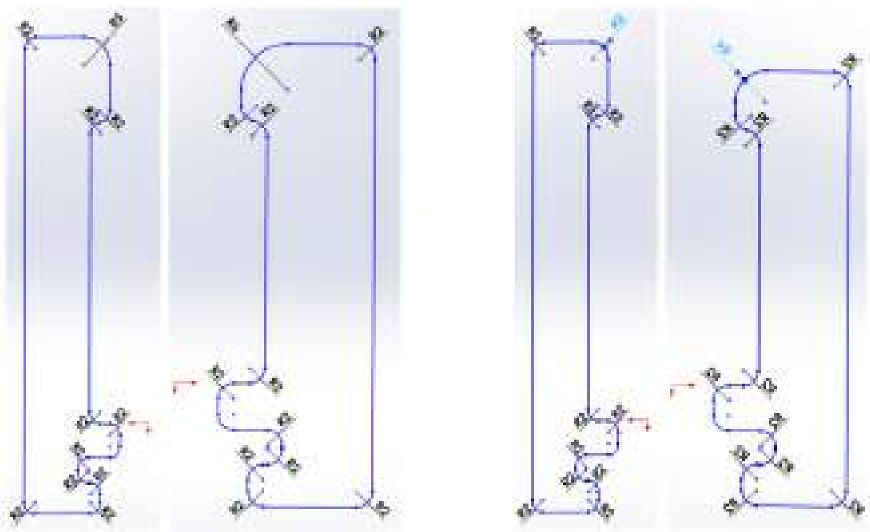

(**a**) (**b**)

Figure 16. Lamella views: (**a**) First variant and (**b**) second variant.

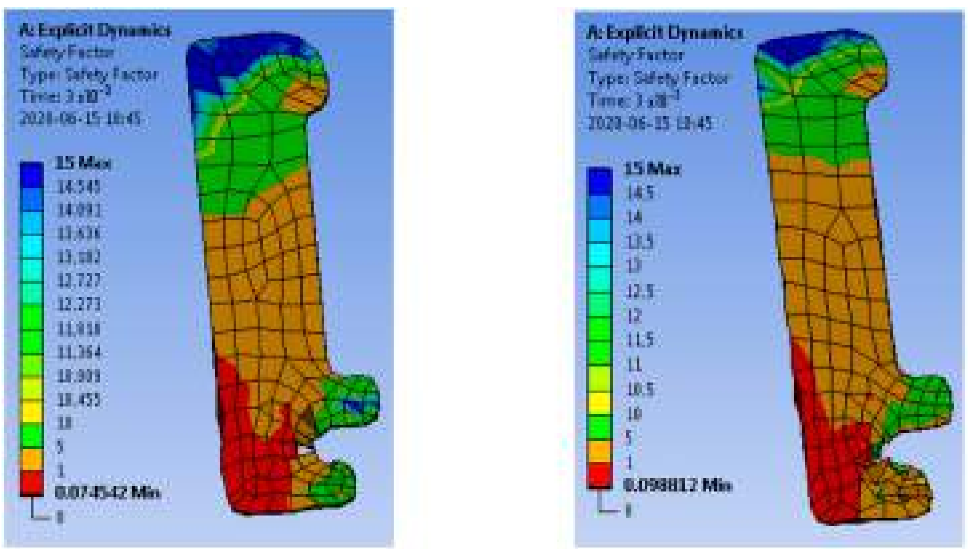

(**a**) (**b**)

Figure 17. View of small lamellas: (**a**) Old lamellar radius R6—Variant I and (**b**) new lamellar radius R4—Variant II.

Figure 18 shows large lamellas with the same modification as described above. In these lamellas, it is harder to notice significant deformations than for smaller lamellas. This is due to the fact that the total length of the lamella is greater compared to the small lamellar, which was translated into greater plasticity of the entire element.

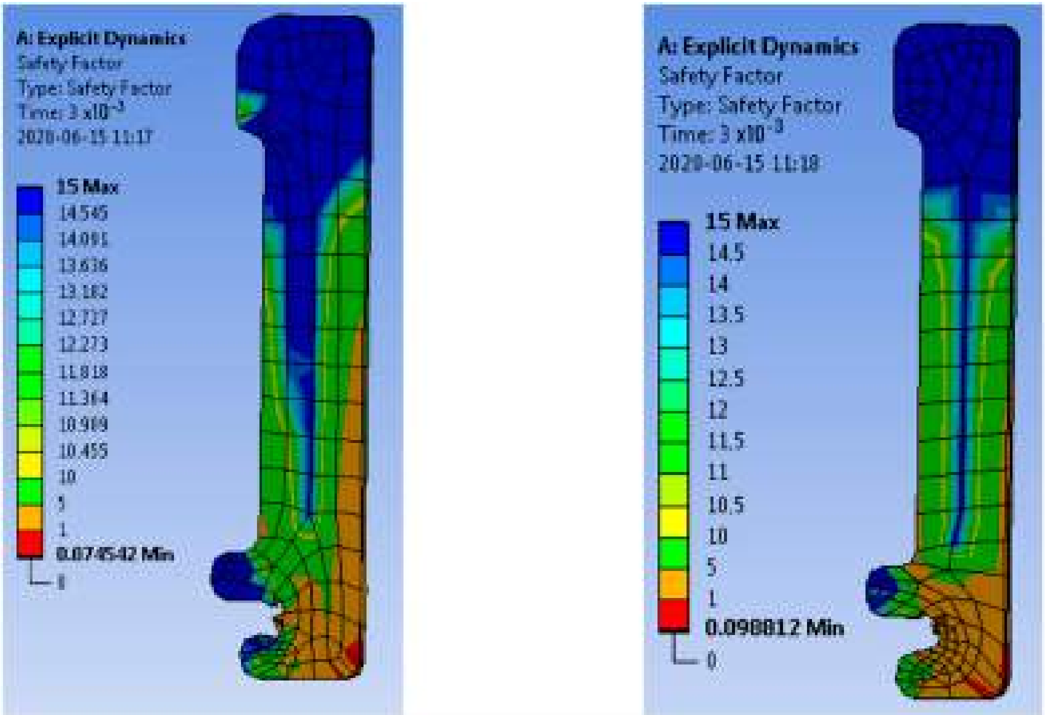

(**a**) (**b**)

Figure 18. View of large lamellas: (**a**) Old lamellar radius R5—Variant I and (**b**) new lamellar radius R3—Variant II.

The results show a comparison of the values of the first analysis and the analysis performed after the modification of the lamella. Figure 18 shows the velocity of deflection of the lamella in each plane, and the values are expressed in cm/s. It was noticed that the velocity values of the lamellas after modifying their contact part with the moving contact were lower. Comparative charts of the velocity in a given plane before and after the modification clearly show the impact of changing the structure of the contact surface and impact on the behavior of the lamella. It turns out that after the modification, the lamellas move slower, with smaller oscillations, and with slower velocities in each of the planes.

The energy and torque values presented in Figure 19 show the values of the above-mentioned parameters in relation to the system with rebuilt lamellas. the above diagram should be read in combination with Figures 13a and 15a. Then, it can be seen that the energy values in the second analysis were much higher. It was also noted that a much lower hourglass effect was achieved. Additionally, the energy values reached higher values, whilst their shape and form remained unchanged. Figures 19 and 20 are presented below.

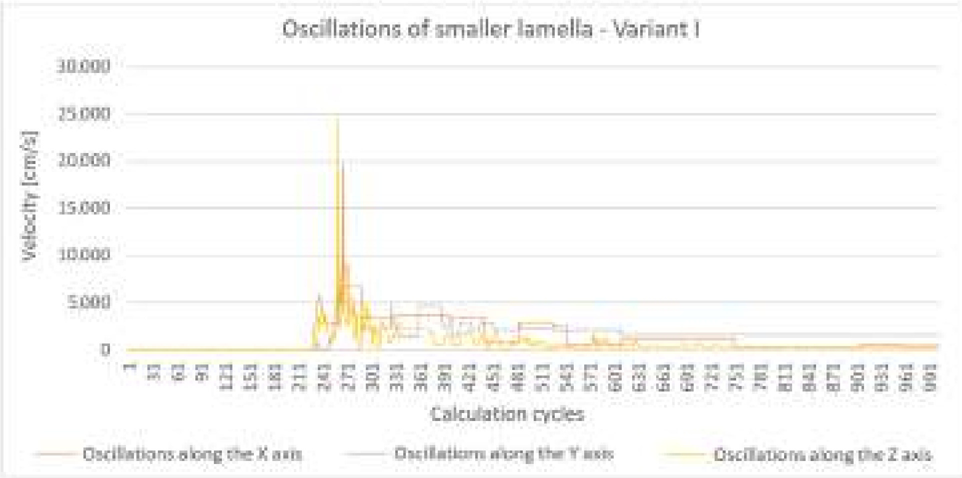

(**a**)

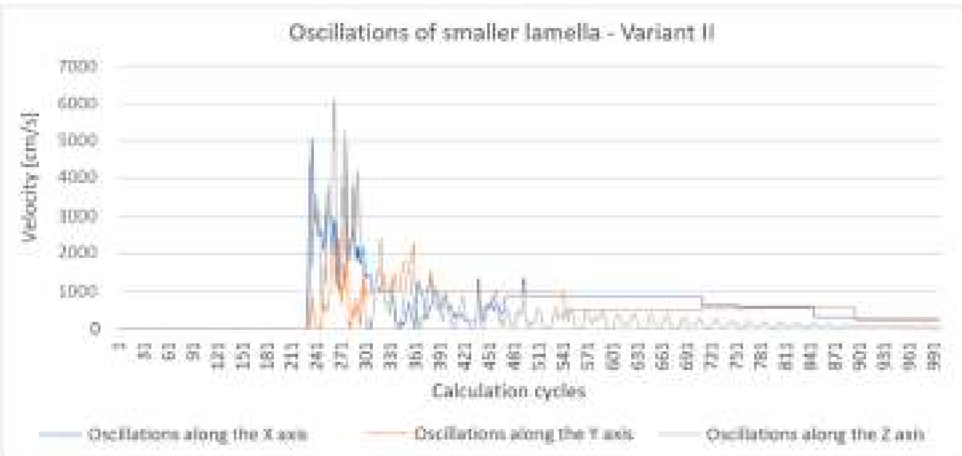

(**b**)

Figure 19. View of the small lamellas' oscillations before and after modification in each plane: (**a**) Variant I and (**b**) Variant II.

6.6. Defects Study in Motion Dynamics Analysis

During the preparation of the dynamic motion analysis, a number of simulations were performed. In the initial phase of developing the tested model, the execution of a three-dimensional representation in the SolidWorks environment was conducted and the model was prepared in the ANSYS software. In the course of releasing parameters from constraints, replacing forces, assigning contacts, and determining the friction area, their coefficients' influence of various weak and weakened points on the correct operation of the system was observed. These types of observations, despite the fact that they resulted from complete randomness, uncovered significant assets. Thanks to such analyzes, which type of failure of a single element may affect the operation and generate faults and aging correlated with certain parameters of the apparatus was observed.

Figure 21 shows the damaged crown of the small lamellas. This damage occurred as a result of several factors. One of them was the wrong kind of contact between the moving part of the lamellas and the large crown. This resulted in too much torque exerting pressure on the crown and thus in its deformation while deflecting the lamellas from the axis of the camera. In real conditions, this type of case may occur when the contact is not maintained. This can result in jamming of the moving parts on the contact parts. Another reason was the insufficient forces pressing the lamellas against the contact axis. These forces were due to the release of the constraints against the springs surrounding the contact. As a result, when the movable part hit the lamellas, the crowns were significantly deformed. In extreme situations, the lamellas tear the crown apart and fall outside their area and the contact is completely destroyed. Such a situation is shown in Figures 22 and 23.

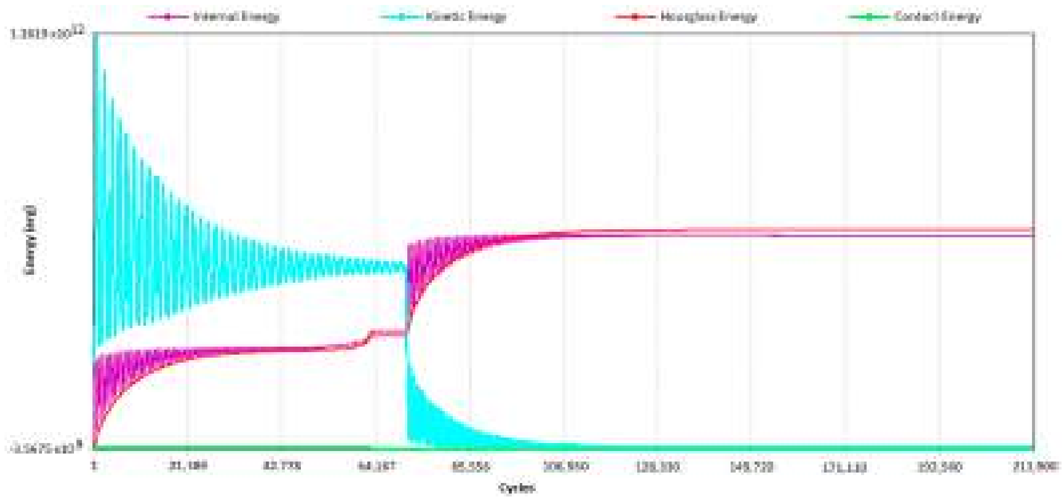

(**a**)

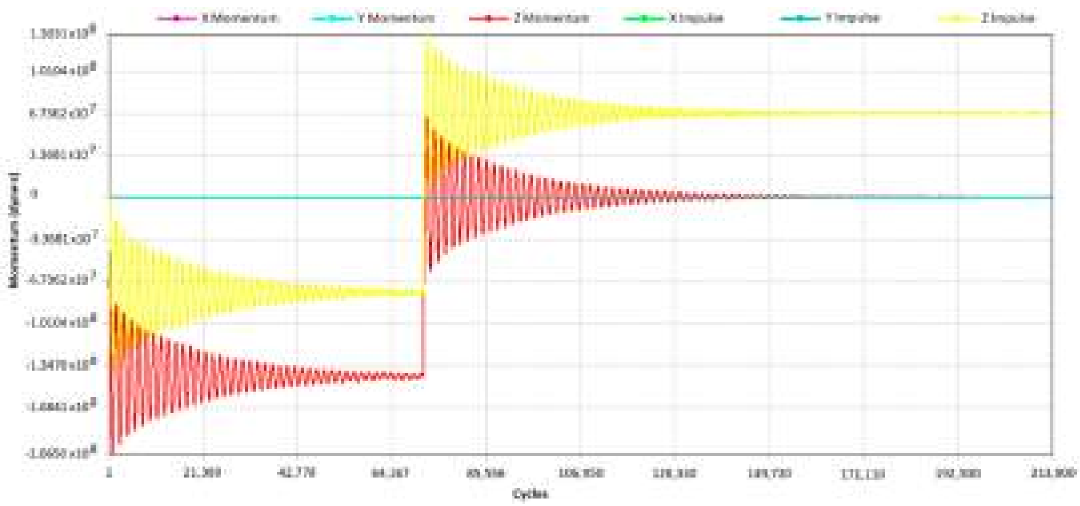

(**b**)

Figure 20. Tulip contact motion analysis charts: (**a**) Sum of energy—Variant II, and (**b**) torque value—Variant II.

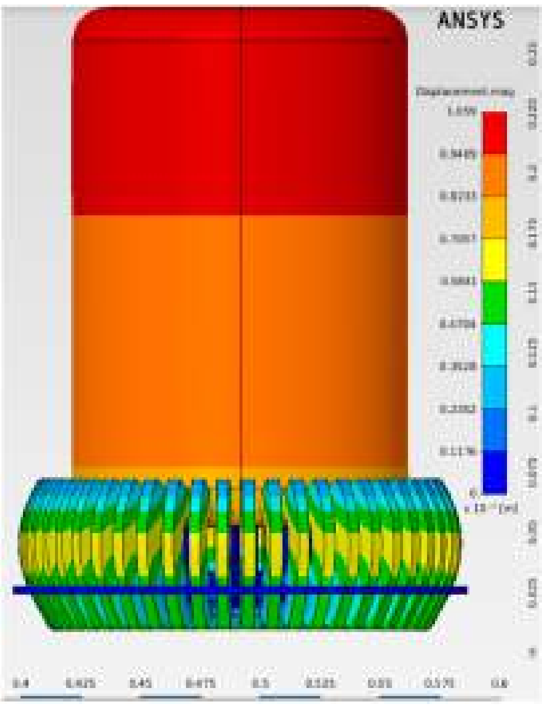

Figure 21. Deformation of small lamellas.

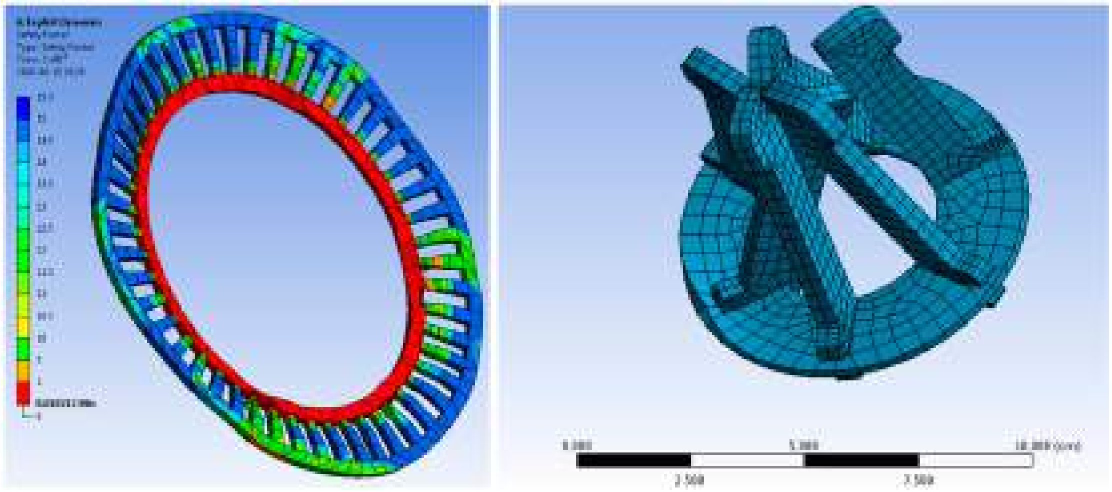

(**a**) (**b**)

Figure 22. Deformation of the crowns: (**a**) Outer crown and (**b**) inner crown.

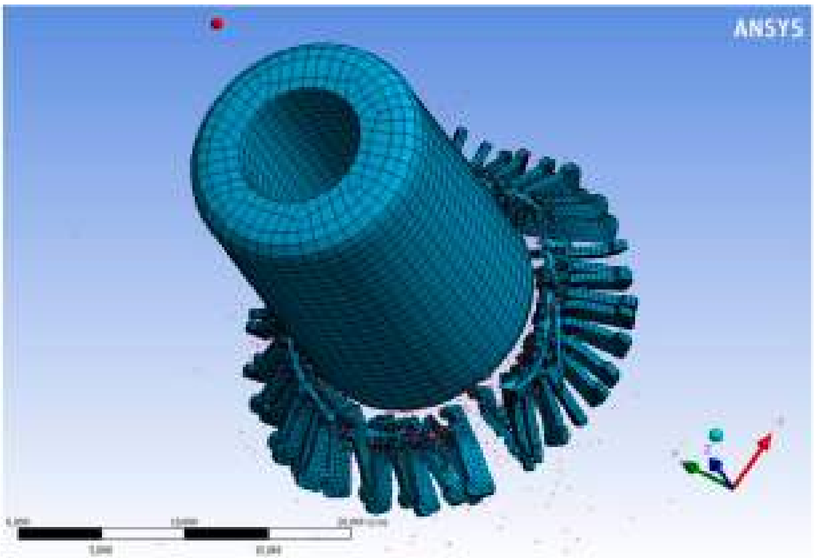

Figure 23. Destruction of the entire contact system.

7. Electrical Simulations of the Tulip Contact System

7.1. Electric Field Distribution in a Tulip Contact System

The first considered case concerns the contact in the open position (NO). the ground potential *V* was equal to 0 V and was assigned to all lamellas and both crowns. the movable part of the contact was assigned a potential of V equal to 110 kV. the color maps below show the distribution of the potential and the electric field. Thanks to these values, the points that will first form the opening of the plasma channel and the burning of the electric arc were observed. This information is extremely important when designing a contact system.

Figure 24a above shows the electric potential distribution around a contact. It is worth noting that a given distribution is symmetrical along the "z" axis. Such data provide information about evenly distributed potential, which translates into switching parameters. Each of the contact elements at the same level, with the same distance from the movable part of the contact, are at the same voltage level. During the operation of the tulip contact, this will cause an even distribution of the electric field, which will have a direct impact on the formation of sheaf and partial discharge phenomena. Uniformity of the field distribution ensures greater switching properties and a longer exploitation time for the contact system.

Considering the field phenomena further, it should be mentioned how the results will be presented. Figure 24b above shows the plane inside the computational cuboid. the plane creates an intersection through the model and represents the distribution of the studied value over the plane. the location of a given surface is freely defined.

Figures 25 and 26 present the distribution of the electric field with the exact space between the large lamellas and the moving part of the contact. In line with the assumptions, it was noticed that the greatest electric field gradient occurred between elements with different potential and close to each other considering sharp edges of the elements. It was observed that the field distribution between the right and left side of the contact was symmetrical. This proves the central axial location of the elements in relation to each other. Maintaining the alignment brings not only mechanical benefits, but also visibility during the movement of the contact and electric potential in both open and closed positions. a uniform field distribution in the open position of the electrical apparatus results in the appearance of partial discharges. Thanks to this, it is known which sites of the contact will be constantly exposed to this type of discharge and consequently, to the appearance of a temperature source and slow burning of the surface in a given place. However, from the moment of starting the contact closing procedure, the field gradient begins to increase rapidly until the formation of a plasma channel, ignition of the electric arc, and the collision of lamellas. the uniformity of the electric field also produces an even distribution of electrodynamic forces, in accordance with the Biot–Savart and Ampere standard laws.

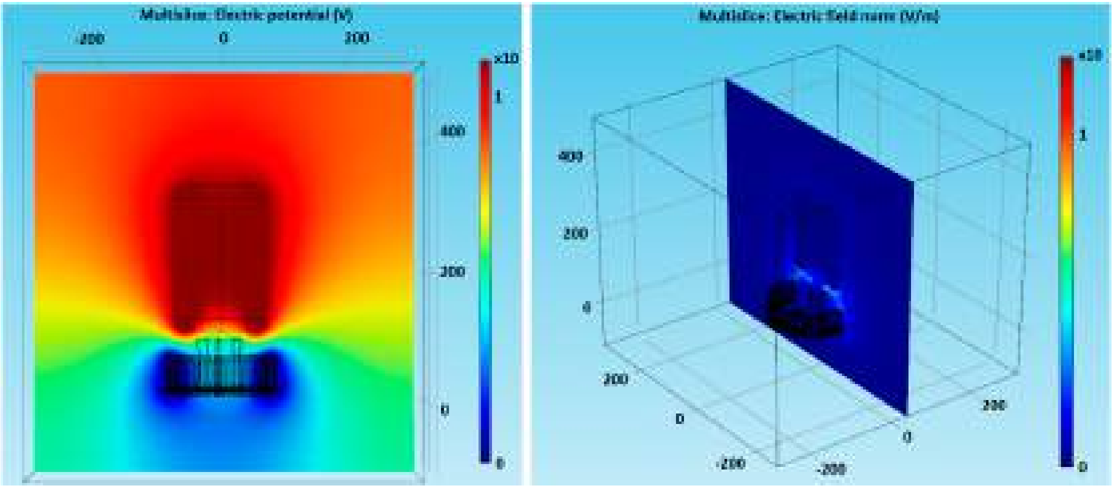

(**a**) (**b**)

Figure 24. Electric potential distribution: (**a**) Potential distribution around the tulip contact (*V/V*) and (**b**) plane showing the calculated values.

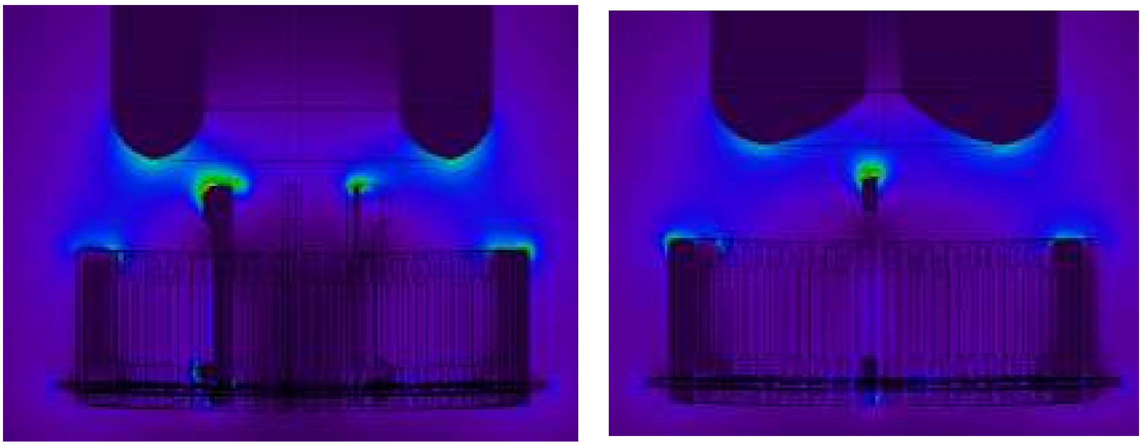

Figure 25. Electric field intensity distribution of large lamellas (*V/m*).

The movement of the moving part of the contact towards the lamellas causes a greater intensity of the electric field. If any of the lamellas have a different distance or angle than the others in relation to the working part of the contact, this would cause electrodynamic forces to appear in the contact lamellas at different times. This would translate into a resultant force different from zero acting transversely to the direction of movement of the working part. the appearance of this type of force can cause the moving part to deflect by several degrees. Small lamellas may hit at the wrong angle, and the appearance of electrodynamic forces may thus differ in time for distinct lamellas. Repeated connections with this type of fault will lead to destruction of the contact.

The electric field in switching systems can be managed in a number of ways. One of them is the use of field diffusing materials. Another way is to use contact elements with an appropriate geometry, so that the field gradient is highest in the right places.

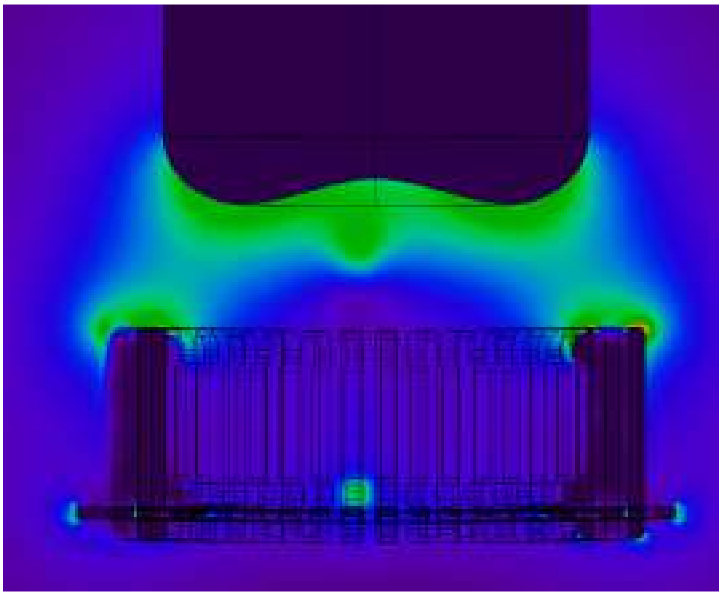

Figure 26. Electric field intensity distribution of large lamellas (*V/m*).

7.2. Parametric Analysis of the Electric Field

The further part of the electrical analysis was carried out in several steps determining the position of the movable part of the contact in relation to the lamellas. In this approach, the natural work of the tulip contact was studied. During each position, the field distribution between two large lamellas and between several small lamellas was tested. the analysis was conducted as follows. a line was drawn between the lamellas, indicating between which elements the measurements were made. the positions of both lines are shown in Figure 27 below. the obtained results are presented graphically on the charts in Figures 28–30. the results of individual analyzes were compared and discussed.

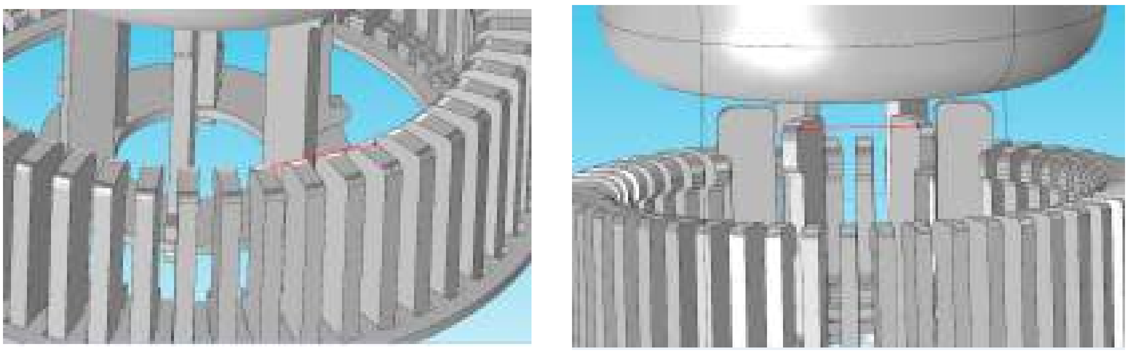

(a) **(b)**

Figure 27. View of the measurement lines: (**a**) Small lamellas and (**b**) large lamellas.

Figure 27 shows the distribution of the field along the measurement lines. According to the legend, the blue line represents the distribution of the electric field. It was noticed that the distribution character was repeatable and symmetrical in relation to the adjacent lamellas. This proves the uniformity of the field distribution on the individual contact elements at the same distance from the movable part of the contact. the moving part is a hollow cylinder with chamfered edges. the purpose of chamfering is not only to reduce the friction and obtain an appropriate angle between the connecting surfaces, but also to reduce the sharp edges and limit the electric field gradient. This leads to an even distribution and an increase in the dielectric strength of the system. There were also differences in potential between the edges of the same lamella. However, this does not indicate an actual difference in potential at the edge of the element, but highlights how to measure a given parameter. the measurement line is a chord between several elements. Therefore, the normal distance on both sides of the lamella to the chord is different, as observed in potential differences.

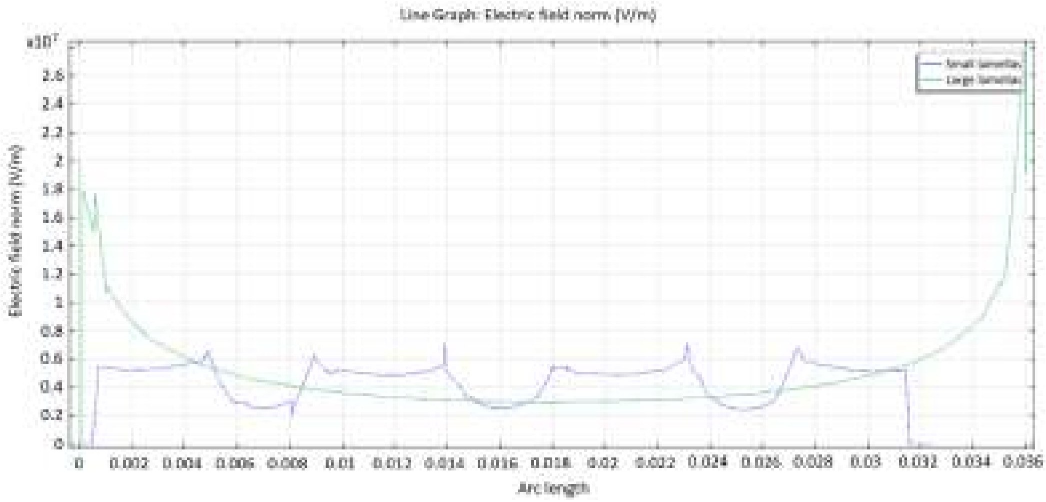

Figure 28. Results of the electric field distribution along the measurement lines.

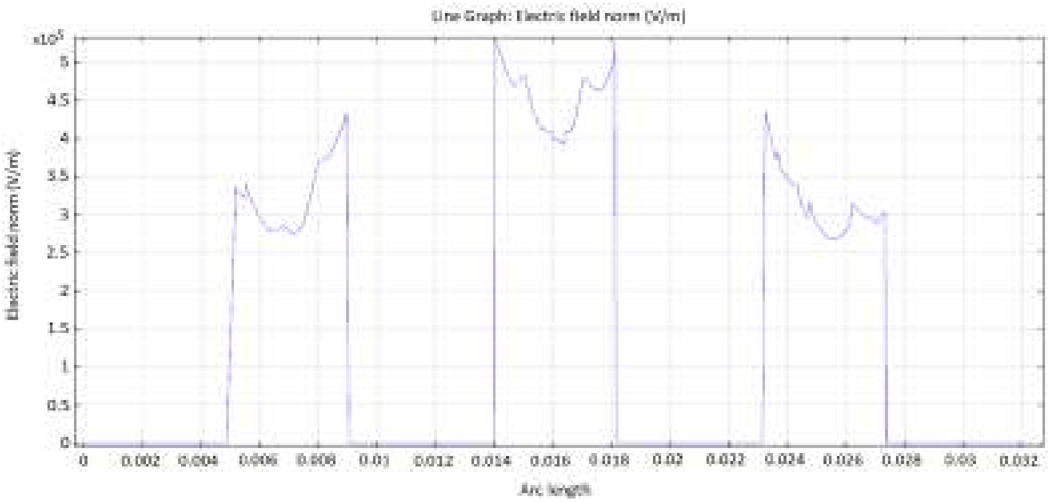

Figure 29. Results of the electric field distribution along the measurement lines for small lamellas.

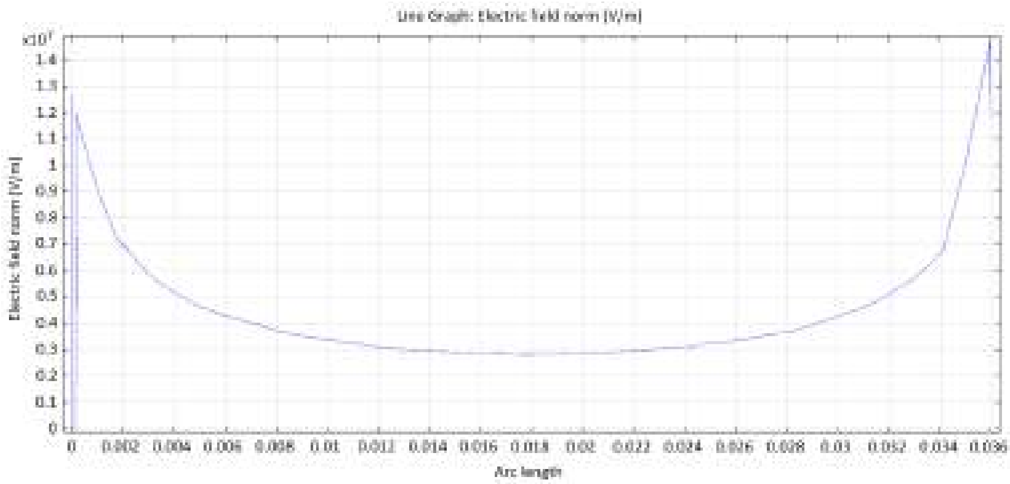

Figure 30. Results of the electric field distribution along the measurement lines for large lamellas.

In Figures 29 and 30, the field distribution can be observed with the moving part displaced by 5 mm towards the lamellas. Figure 30 represents the distribution of the electric field, along the measurement line placed next to the large lamellas. a decrease in the intensity value can be observed. This is due to the proximity of the moving element and the reduction of the field distribution gradient. There was also a reduction in the difference between the value on the left side of the chart and on the right side. the lower difference is also due to the more uniform field. the same applies to the measuring line next to the small lamellas which were presented in Figure 29 above.

8. Validation of the Procured Simulations

The validation was carried out on a tulip contact made in the short-circuit laboratory of the Warsaw University of Technology. It was not a construction like in the presented simulations. Nevertheless, it exactly reflects the nature of physical phenomena witnessed in simulations.

In practical solutions, the inner surface of the contact point differs significantly from a completely flat one. Depending on the solution, the active part may only be located in the closest vicinity of the pressure spring. In other words, there may be distinct grooves to prevent welding of the contacts. To determine the initial spacing between the contacts, it is suggested that a limiting ring is used (Figure 31). the upward movement of the contact should also be blocked in the first moment after hitting the movable contact—a bumper is used for this purpose.

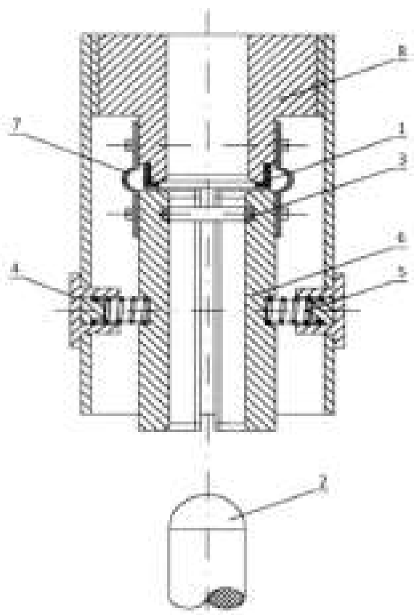

Figure 31. Tulip contact: 1—impactor; 2—movable contact with an arcing tip; 3—limiting ring; 4—compression spring guide; 5—compression spring; 6—pins; 7—flexible connection; 8—body of fixed contact.

The operation of a high-voltage tulip contact in a dynamic system was analyzed on the test stand, taking into account the welding currents. the tests were carried out with the use of a short-circuit system. the laboratory stand is presented in Figure 32 below.

On the oscillograms shown in Figure 33, the following negative phenomena occurring in the contacts during closing were observed. First of all, a bounce phenomenon was observed on the graph showing the puss—the point of contact of the contacts—Figure 33a. It is visible in the form of oscillations. It is a disadvantageous phenomenon because it causes the formation of an electric arc, which in turn deteriorates the electrical properties by gradual burning of the contacts. In order to prevent this phenomenon, the contact pressure force should be changed.

(**a**)

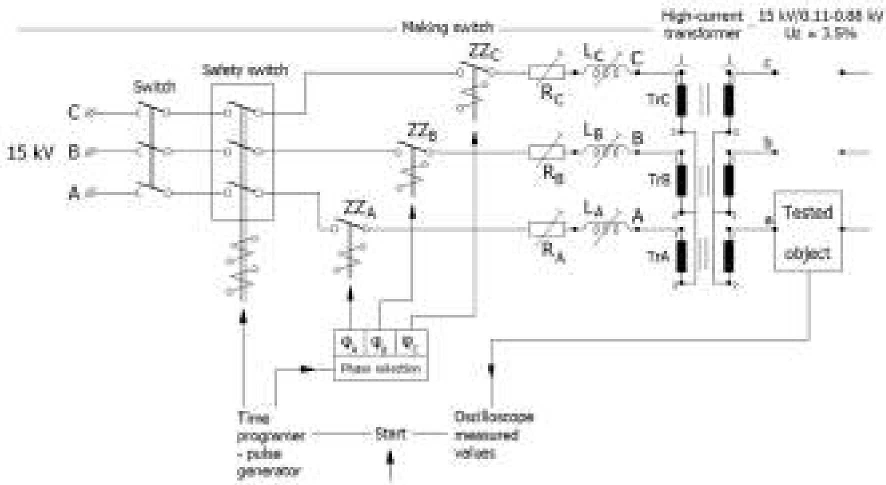

(**b**)

Figure 32. Laboratory setup for simulation validation: (**a**) Laboratory stand and (**b**) short-circuit system in the Short Circuit Laboratory, Electrical Faculty, Warsaw University of Technology.

Another disadvantageous phenomenon is the friction force between the contact elements. It is perfectly visible, also in the form of oscillations in the course of acceleration and speed. the last observed phenomenon is the welding of contacts. Welding the contacts together leads to the necessity to increase the value of the force needed to open the contacts. In this case, there is also the possibility of an electric arc appearing between the contacts. On the basis of the tests performed and the recorded velocity waveforms, it was possible to determine the speed of the contacts' convergence. Full validation was executed in the Warsaw University of Technology Laboratory.

Figure 34 shows the characteristics of the movable contact velocity for two cases: Without bounce and with movable contact bounce. Characteristics derived from the simulation were compared to those which had been captured during laboratory tests.

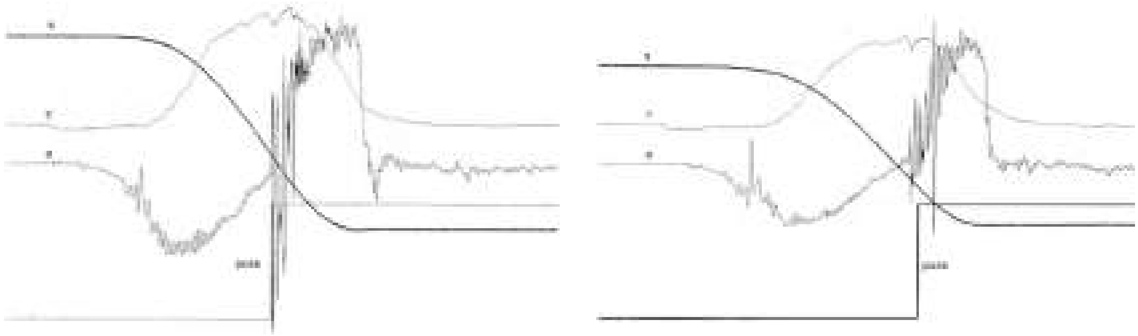

(**a**) (**b**)

Figure 33. Exemplary laboratory results of the tested tulip contact system: *v*—speed, *a*—acceleration, *s*—path, and puss—characteristic that indicated contact between system elements. (**a**) With bounce and (**b**) without bounce.

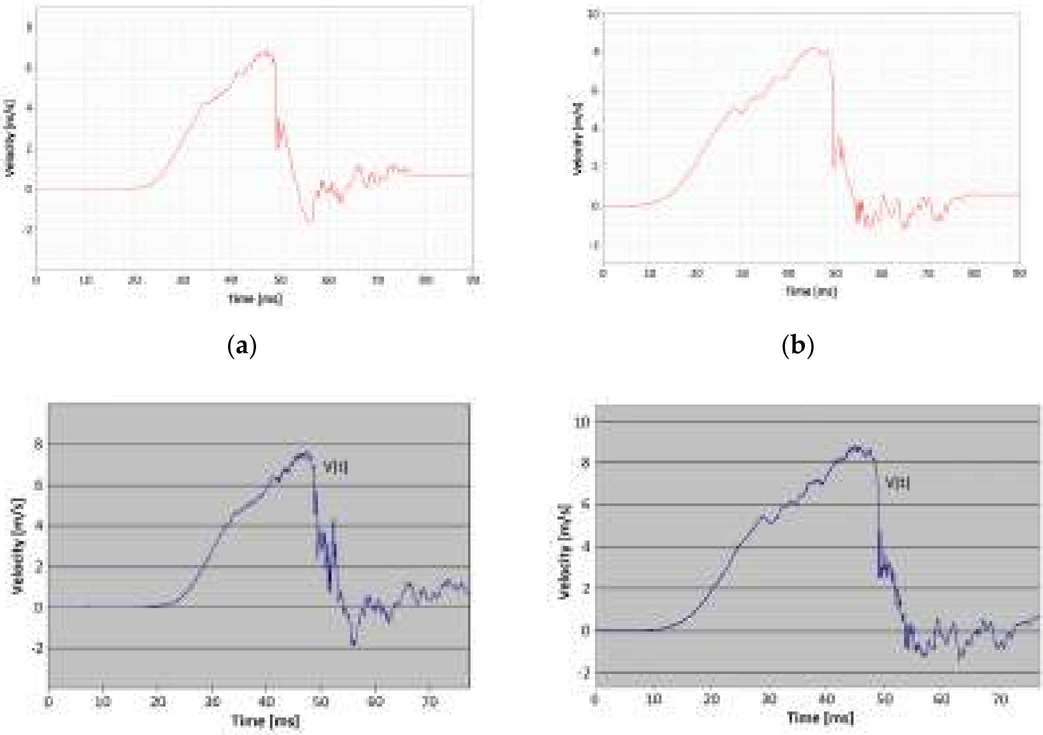

(**a**) (**b**)

(**c**) (**d**)

Figure 34. Juxtaposition of characteristics derived from the simulation in comparison to those captured during laboratory tests. Ansys characteristics (**a**) without movable contact bounce and (**b**) with movable contact bounce. Laboratory test characteristics (**c**) without movable contact bounce and (**d**) with movable contact bounce.

9. Summary

Each described case of analysis should be considered individually, remembering that a contact is a system of many elements cooperating with each other. By improving one factor, the optimal values of the other may deteriorate. When defining the project, which is the design of the switching system, it is essential to define the conditions, purpose, and natural working environment of a given electrical apparatus. In the considered cases, the change in the geometry of the contact surface and the contact angle of the elements with each other affected the work of the entire contact system. This started from the forces required to close the system, through the vibration speeds of the lamellas after closing the contacts, to damage and contact destruction by fault usage. the damage described showed examples of faults that can occur in tulip contacts.

The field distribution simulation studies show the symmetry of the charge distribution with respect to the axis of the tulip contact. Due to the observation of such regularity, several approximations were made in a further analysis. the described cases should be treated as homogeneous movement of the apparatus. Performing such an observation allows the influence of the electric field on individual elements to be observed.

10. Conclusions

The procured simulations have shown that the tulip contact is a complex structure and its design for given electrical parameters is the sum of compromises between the individual component values of the entire operating system. the combination of two types of analyzes—motion analysis and analysis of the electric field distribution—gives the image most similar to the real operating environment of the system. This allows the entire contact to be designed in the most optimal way. Optimization concerns both the design work time and the cost and quantity of prototyping. the advantage of simulation analysis is not only the speed of the obtained result, but also the possibility of a very quick modification, either in the model or the set parameters. the obtained results confirm the operation and maintenance documents (DTR) regarding the proper servicing and diagnosis of switching devices. the issue of analyzing the operation of a tulip contact has certainly not been exhausted.

The tulip contact is a very well-designed contact system for switching high-intensity currents and high voltages. Due to the large connection area resulting from many individual elements, the system allows the application of high closing forces, which translates into velocity of the operation. a very good electric field distribution promotes the dielectric properties of the system and improves its electrical parameters. Undoubtedly, numerical analyzes help to select materials and parameters for the system operation very quickly. the tulip contact is a construction that is still used in the professional power industry. It is modified according to current needs. These elements work in an environment of chambers filled with both air and technical gases, such as SF_6. the gases allow the operating voltage of the system and the rated and fault currents to be increased thanks to the higher heat dissipation coefficient.

Unfortunately, the current computing environments do not allow analyzes to be carried out as one analysis—analysis of the movement of connections with the applied potentials and material permeabilities. This would reproduce the working environment of the contacts. the official response from ANSYS says that it is currently not possible to combine Explicit Dynamics' high-speed analysis module with ANSYS MAXWELL's field analysis. the procured model of the tulip contact system is complex and as the validation results showed, it can be used for a cost effective method of testing and designing such systems.

Figure 34 clearly showed the significant convergence of results derived from simulations and those captured during laboratory tests. Therefore, the design modifications and further work projects can already be implemented using the proposed simulation. It has been demonstrated that the derived simulation is useful for the rapid changing of modules used in the analysis of the dynamics of tulip contact elements' movement.

Author Contributions: Conceptualization, Ł.K. (Łukasz Kolimas), S.Ł., M.S., Ł.K. (Łukasz Kozarek), K.G.; Data curation, Ł.K. (Łukasz Kolimas), S.Ł., M.S., Ł.K. (Łukasz Kozarek); Formal analysis, Ł.K. (Łukasz Kolimas), S.Ł., M.S., Ł.K. (Łukasz Kozarek), K.G.; Investigation, Ł.K. (Łukasz Kolimas), S.Ł., M.S., Ł.K. (Łukasz Kozarek), K.G.; Methodology, Ł.K. (Łukasz Kolimas), S.Ł., M.S., Ł.K. (Łukasz Kozarek), K.G.; Project administration, Ł.K. (Łukasz Kolimas), S.Ł., M.S., Ł.K. (Łukasz Kozarek), K.G.; Resources, Ł.K. (Łukasz Kolimas), S.Ł., M.S., Ł.K. (Łukasz Kozarek), K.G.; Supervision, Ł.K. (Łukasz Kolimas), S.Ł., M.S., Ł.K. (Łukasz Kozarek), K.G.; Validation, Ł.K. (Łukasz Kolimas), S.Ł., M.S., Ł.K. (Łukasz Kozarek), K.G.; Visualization, Ł.K. (Łukasz Kolimas), S.Ł., M.S., Ł.K. (Łukasz Kozarek), K.G.; Writing—original draft, Ł.K. (Łukasz Kolimas), S.Ł., M.S., Ł.K. (Łukasz Kozarek), K.G.;

Writing—review & editing, Ł.K. (Łukasz Kolimas), S.Ł., M.S., Ł.K. (Łukasz Kozarek), K.G.; All authors have read and agreed to the published version of the manuscript.

Funding: This research received no external funding.

Conflicts of Interest: The authors declare no conflict of interest.

References

1. Bini, R.; Galletti, B.; Iordanidis, A.; Schwinne, M. Arc-induced Turbulent Mixing in a Circuit Breaker Model. In Proceedings of the 1st International Conference on Electric Power Equipment–Switching Technology, Xi'an, China, 23–27 October 2011; pp. 375–378.
2. Wang, L.; Liu, H.; Zheng, W.; Ge, C.; Guan, R.; Chen, L.; Jia, S. Numerical Simulation of Impact Effect of Internal Gas Pressure on Chamber Housing in Low-Voltage Circuit Breaker. *IEEE Trans. Compon. Packag. Manuf. Technol.* **2014**, *4*, 632–640. [CrossRef]
3. Ye, X.; Dhotre, M.T.; Mantilla, J.D.; Kotilainen, S. CFD Analysis of the Thermal Interruption Process of Gases with Low Environmental Impact in High Voltage Circuit Breakers. In Proceedings of the 2015 Electrical Insulation Conference (EIC), Seattle, WA, USA, 7–10 June 2015.
4. Dhotre, M.T.; Ye, X.; Seeger, M.; Schwinne, M.; Kotilainen, S. CFD Simulation and Prediction of Breakdown Voltage in High Voltage Circuit Breakers. In Proceedings of the 2017 Electrical Insulation Conference (EIC), Baltimore, MD, USA, 11–14 June 2017.
5. Chen, D.G.; Li, Z.P.; Li, X.W. Simulation of pressure rise in arc chamber of MCCB during its interruption process. In Proceedings of the 53rd IEEE Holm Conference on Electrical Contacts, Pittsburgh, PA, USA, 16–19 September 2007; pp. 43–47.
6. Rumpler, C.; Stammberger, H.; Zacharias, A. Low-voltage arc simulation with outgassing polymers. In Proceedings of the IEEE 57th Holm Conference on Electrical Contacts, Minneapolis, MN, USA, 11–14 September 2011; pp. 1–8.
7. Li, Z. Research of Gas Dynamic Problems in Arc Chamber of Low-Voltage Circuit Breaker. Ph.D. Dissertation, Department Electrical Engineering, Xi'an Jiaotong University, Xi'an, China, 2006.
8. Lindmayer, M. Complete simulation of moving arc in low voltage switchgear. In Proceedings of the 14th International Conference Gas Discharge Applications, Liverpool, UK, 2–6 September 2002; pp. 318–324.
9. Nordborg, H.; Iordanidis, A. Self-consistent radiation based modelling of electric arcs. Part I: Efficient radiation approximations. *J. Phys. D Appl. Phys.* **2008**, *41*, 135205. [CrossRef]
10. Iordanidis, A.; Franck, C.M. Self-consistent radiation based simulation of electric arcs. Part II: Application to gas circuit breakers. *J. Phys. D Appl. Phys.* **2008**, *41*, 135206.
11. Holm, R. *Electric Contacts-Theory and Application*; Springer: New York, NY, USA, 1958.
12. Basse, N.P.T.; Bini, R.; Seeger, M. Measured turbulent mixing in a small-scale circuit breaker model. *Appl. Opt.* **2009**, *48*, 6381–6391. [CrossRef] [PubMed]
13. Incropera, F.P.; DeWitt, D.P.; Bergman, T.L.; Lavine, A.S. *Introduction to Heat Transfer*, 5th ed.; Wiley: Hoboken, NJ, USA, 2006.
14. Muller, P.T. Macroscopic Electro Thermal Simulation of Contact Resistances. Bachelor's Thesis, RWTH Aachen University, Aachen, Germany, 2016.
15. Kumar, P.; Kale, A. 3-Dimensional CFD simulation of an internal arc in various compartments of LV/MV Switchgear. In Proceedings of the ANSYS Convergence Conference 2016, Pune, India, 23 August 2016.
16. Wu, Y.; Li, M.; Rong, M.; Yang, F.; Murhpy, A.B.; Wu, Y.; Yuan, D. Experimental and theoretical study of internal fault arc in a closed container. *J. Phys. D Appl. Phys.* **2014**, *47*, 505204. [CrossRef]
17. Kulas, S.; Kolimas, Ł.; Piskała, M. Electromagnetic forces on contacts. In Proceedings of the 2008 43rd International Universities Power Engineering Conference, Padova, Italy, 1–4 September 2008.
18. Christen, T. Radiation and nozzle ablation models for CFD simulations of gas circuit breakers. In Proceedings of the 1st International Conference on Electric Power Equipment–Switching Technologies, Xi'an, China, 23–27 October 2011.
19. Bini, R.; Basse, N.T.; Seeger, M. Arc-induced Turbulent Mixing in a Circuit Breaker Model. *J. Phys. D Appl. Phys.* **2011**, *44*, 025203. [CrossRef]

20. Biao, W.; Yanyan, L.; Xiaojun, Z. Study on detection technology of the contact pressure on the electrical contacts of relays. In Proceedings of the 26th International Conference on Electrical Contacts (ICEC 2012), Beijing, China, 14–17 May 2012; pp. 161–164.
21. Shing, A.W.C.; Pascoschi, G. Contact wire wear measurement and data management. In Proceedings of the IET International Conference on Railway Condition Monitoring, Birmingham, UK, 29–30 November 2006; pp. 182–187.
22. Kriegel, M.; Zhu, X.; Digard, H.; Feitoza, S.; Glinkowski, M.; Grund, A.; Kim, H.K.; Roldan, J.L.; Robin-Jouan, P.; Sluis, L.; et al. Simulations and Calculations as verification tools for design and performance of high voltage equipment. In Proceedings of the CIGRE Conference 2008, Paris, France, 25–28 August 2008; p. A3-210.
23. Siemens Product Catalogs. Available online: https://publikacje.siemens-info.com (accessed on 21 June 2020).
24. Tu, Z.; Zhu, K.; Lv, Y. Tulip Contact and Electrical Contact System for Switching Device. U.S. Patent 8,641,837 B2, 4 February 2014.

A4. *Control System and Measurements of Coil Actuators Parameters for Magnetomotive Micropump Concept*

BULLETIN OF THE POLISH ACADEMY OF SCIENCES
TECHNICAL SCIENCES, Vol. 68, No. 4, 2020
DOI: 10.24425/bpasts.2020.134171

CONTROL, INFORMATICS AND ROBOTICS

Control system and measurements of coil actuators parameters for magnetomotive micropump concept

Ł. KOLIMAS[1], K. BIEŃKOWSKI[2], S. ŁAPCZYŃSKI[1], M. SZULBORSKI[1*], Ł. KOZAREK[3], and K. BIREK[3]

[1] Institute of Electrical Power Engineering, Warsaw University of Technology, 75 Koszykowa Street, 00-662 Warsaw, Poland
[2] Astronika Sp. z o.o., 18 Bartycka Street, 00-716 Warsaw, Poland
[3] ILF Consulting Engineers sp. z o.o., 12 Osmańska Street, 02-823 Warsaw, Poland

Abstract. This paper presents an approach to the construction and measurements of electrodynamic and reluctance actuators. Executive elements were used as drives in a novel concept of a magnetomotive micropump. The paper discusses various aspects concerning the designation of parameters, control system, the explanation of physical phenomena, and the optimization of the basic elements for coil units. The conducted work describes the measurement system and the analysis of the derived values. The actuators were compared and the pros/cons of building the conceptual device were highlighted. The best solution to be used in the upcoming work concerning the construction of a magnetomotive micropump was chosen based on measurements, engineering aspects, layout control, and key parameters such as the piston velocity, energy stored in capacitors, and efficiencies.

Key words: control system, micropump, electrodynamic induction, magnetic acceleration.

1. Introduction

Electromagnetic field can generate force by acting on a given magnetic body and accelerating it to a high velocity. There are two ways to achieve that. The first is based on a coil with a ferromagnetic core. While the coil is energized, a strong magnetic field is formed [1]. Then the core magnetizes itself, which in turn causes the core to move toward the center of the coil. The second way involves a conductor placed in the magnetic field. From the moment the current flows through the conductor, a force is generated, causing displacement [2]. The force generated is described as the Lorentz force [3–7]:

$$F = I \cdot l \times B, \tag{1}$$

$$F = I \cdot l \cdot B \cdot \sin\alpha \tag{2}$$

where: F is force; I is current intensity; B is magnetic flux density; l is the length of the part of the conductor in the magnetic field; α is the angle between the conductor's direction and magnetic induction B.

The phenomena described above can be successfully implemented to create a drive in a linear flow micropump for industrial applications. A huge advantage of such a solution is the elimination of friction elements, which enables the pump operations in a hazardous (explosive) environment, and an expected lower failure rate and usage concerning special applications, e.g. medical and chemical. The concept of the micropump is shown in Fig. 1.

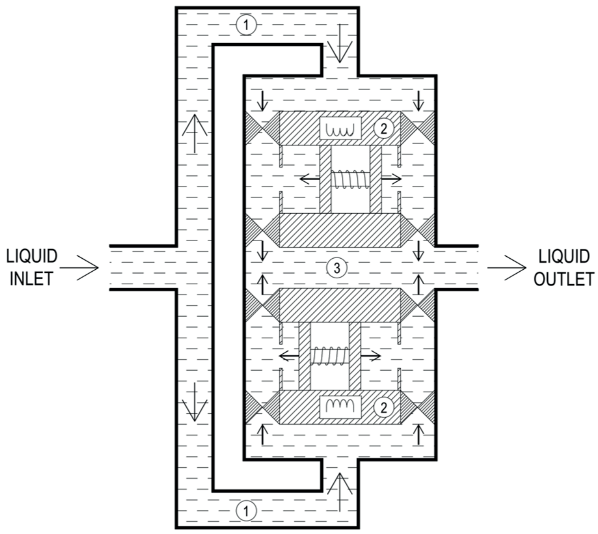

Fig. 1. The concept of the novel magnetomotive micropump: 1) inlet lines; 2) coil units; 3) collector

This micropump consists of two sections. Each section is equipped with a coil unit. The coil units are synchronized by the control system, which is discussed in this paper. The accurate control of those units is essential for guaranteeing the linear flow on the pump outlet which is directly acquired by the piston synched movement. The applied one-way valves ensure the

*e-mail: mm.szulborski@gmail.com

Manuscript submitted 2019-12-11, revised 2020-05-03, initially accepted for publication 2020-06-06, published in August 2020

medium flow in one direction. The schematic diagram of the solution is shown in Fig. 2.

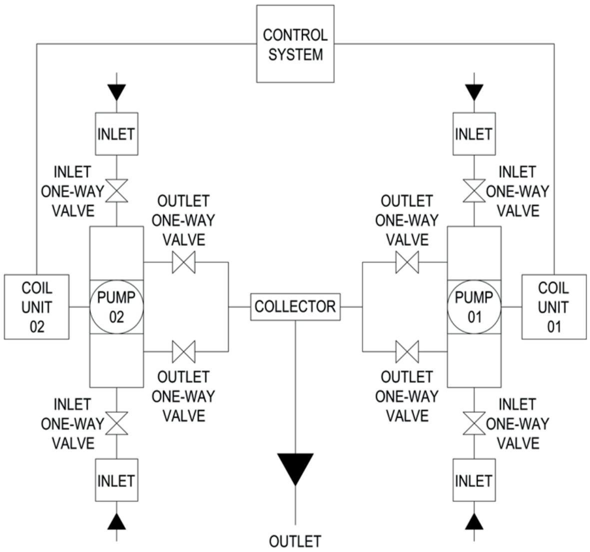

Fig. 2. The schematic diagram of the magnetomotive micropump

This paper focuses on proposing the most efficient and accurate control system for coil units being a key element of the application – magnetomotive micropump. Two variants of coil actuators were taken into consideration: a reluctance actuator and an electrodynamic actuator. The measurements of the electrical and mechanical parameters (piston velocity, energy) were made. For those two variants of the coil, actuators were considered. Moreover, the control and measurement systems were constructed and tested on a laboratory scale for two variants of actuators along with software (program code) obtained for achieving the desired functionality of the control system. The selection of the necessary components was justified and explained by the theoretical and practical calculations.

2. Review of technical solutions

Pumps are used as machines necessary for the proper functioning of industrial plants with different business profiles. Their diversity is impressive, so they are applicable in a variety of pumping installations for almost any medium. While pumping, the device receives mechanical energy from the drive motor, and then transfers it to the medium flowing through the device using a rotor, piston, shaft, etc. As a result, the energy of the medium is lifted and increases. It should be added that pumps are passive hydraulic devices since those devices draw energy from the outside. Electric motors, internal combustion engines, and steam turbines are most often used drives in such devices. Importantly, the pump drive can be controlled directly or indirectly via gears. However, the solutions used often have a significant size (even for low power devices) and no compact construction. Most of them have numerous friction elements (easily perishable). There are difficulties in expansion with an existing application and a problem with ensuring a linear flow of the medium. The authors were guided by the idea of building a pump that provides:

- increased durability (no friction elements),
- guarantee of a linear flow of the medium (not only liquids but also gases),
- full scalability in the range of active power from four to hundreds of watts,
- the opportunity to work in a specialized environment (gas, chemical),
- easy expansion – connecting pumps,
- unique way of working (the precise way of switching sections).

An analysis of the physical phenomena associated with the work of these systems was conducted in the work on the construction of the actuators for the magnetomotive micropump. This was considered in research and tests and a lot of attention was paid to the proper control of the reluctance and electrodynamic actuator piston (determining the optimal moment of switching on the next coil). Research and tests concerning the employment of the actuator were conducted to give an answer on the type and the scope of the device implementation. Studies of physical phenomena and literature concerning an electromagnetic actuator have already made it possible to optimize the parameters of the capacitance of capacitors, the number of capacitors, and the number of coils. The guidelines were as follows: possibly high kinetic energy, constant piston length, possibly low mass of the piston itself, and thus a cylinder, compact design.

Currently, presented solutions are often one-coil section structures and most likely classical electromagnet designs. Therefore, the analysis of the time and place of enclosing individual sections is unnecessary. There are constructions with high tare masses and limited operating frequency [8]. Obviously, the presented results are ordered and used by the authors to determine the direction of work. As far as calculations and methodology are concerned, a comprehensive description can be found in [9]. This paper presents the design study of a lightweight inertial actuator with an integrated velocity sensor, for the implementation of velocity feedback control, i.e. active damping, in lightly damped panels. However, in the literature, the model presented does not clearly combine analytical and numerical calculations for actuators with linear fluid flow. A transparent way of designing and testing such executive elements by building a repeatable test stand was not found. There are still constructions with high tare masses and limited operating frequency, e.g. in [10]. A half-practical solution was presented by a team of Chinese researchers [11]. The authors used several excellent studies on electromagnetic structures, where they presented methods for calculating electrical machines [12–16]. Undoubtedly, the presented model also shows how to control the flow so that it is linear, which is often key in applications in the medical and chemical industries.

3. Reluctance actuator

A reluctance actuator consists of a coil and a ferromagnetic piston. When the current passes through the coil, the force acts on the piston on its periphery. It pulls the piston inside the solenoid and tends to hold it in the middle of the coil. However, if the current is cut off at the proper moment of piston moving toward the center of the coil, the piston acquires kinetic energy. The velocity of the ferromagnetic body would be high enough to exit the coil through the other end. It does not matter on which side of the coil the body is placed. The element always attains the opposite polarity and as a result is magnetized by the energized solenoid and pulled inside the coil. In this paper certain parameters of the reluctance actuator elements were determined via proper calculations and analysis [17].

3.1. Coil geometry (length and diameter). A properly designed coil geometry can increase the efficiency of the actuator, reduce kinetic energy losses, and thus increase the velocity of the piston. To determine the maximum efficiency of the coil, the Fabry method was used with variables describing the designed solenoid geometry. Two parameters have been defined: $\alpha = \alpha_2/\alpha_1$ (α_1 is the inside coil radius; α_2 is the outside coil radius), and $\beta = b/\alpha_1$ (b is the half of the coil length). The dimensionless geometric coefficient, also known as Febry's factor, is a function of these two parameters. It is not dependent on the size of the coil but only on its shape:

$$G(\alpha,\beta) = \frac{\sqrt{2\pi}}{5} \cdot \sqrt{\frac{\beta}{\alpha^2-1}} \cdot \ln\left(\frac{\alpha+\sqrt{\alpha^2+\beta^2}}{1+\sqrt{1+\beta^2}}\right). \tag{3}$$

The value of the Febry's factor $G(\alpha,\beta)$ ranges from 0 to $\sim$0.179. The maximum value is reached for $\alpha = 3.1$ and $\beta = 1.875$, which means that the solenoid with the shape defined by such parameters generates the highest magnetic field intensity for the given power load. The dependency describing the value of the magnetic field strength in the center of the coil, considering the Febry's factor $G(\alpha,\beta)$ is shown below [1]:

$$H_0 = \sqrt{\frac{P\cdot\lambda}{\alpha_1\cdot\rho}} \cdot G(\alpha,\beta) \tag{4}$$

where: H_0 is the intensity of the magnetic field in the center of the coil; P is power taken by the coil; λ is the space factor (for a wire with a circular cross-section $\lambda = \pi/4$); ρ is the resistivity of the winding wire.

For a constant internal diameter and an assumed power of 50 W, the coil shape was optimized for different values of the outside diameter and the length of the coil. The plane that represents maximum efficiency is shown in Fig. 3. Optimal results for the designed coil: length (L) – 1.5 cm, radius (α_2) – 2.48 cm. Values were derived for the highest magnetic field intensity value: $G(\alpha,\beta) = 0.179$.

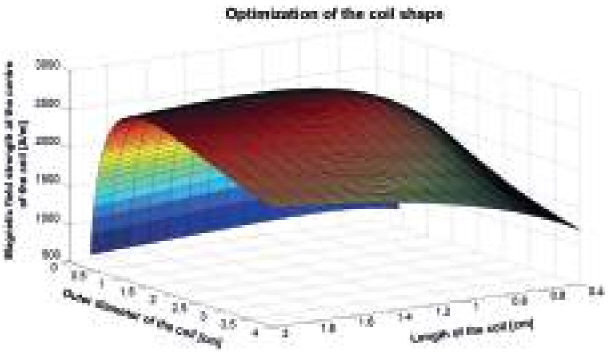

Fig. 3. The intensity of the magnetic field in the center of the coil as a function of the length and the diameter of the designed coil

3.2. Thickness of the coil winding The next parameter affecting the efficiency of the reluctance actuator is the thickness of the winding wire. The change in the wire diameter is related to the change in the number of coils and the resistance of the entire coil unit. The first step was to determine the resistance. The space factor λ, which has already been used, is the ratio of the cross-sectional area of the wire S_d to the surface area S_z that takes up one roll and is equal to $\pi/4$. Assuming that the space factor is a constant in the entire coil, the volume of the winding wire V_d is expressed in relation to the total volume V_c [18, 19]:

$$V_c = \pi \cdot \left(a_2^2 - a_1^2\right) \cdot L, \tag{5}$$

$$V_d = \lambda \cdot V_c, \tag{6}$$

$$V_d = \pi \cdot \lambda \cdot \left(a_2^2 - a_1^2\right) \cdot L. \tag{7}$$

With the total volume of the wire, its length L_d was determined by dividing the wire volume by the cross-sectional area of the coil [1]:

$$L_d = \frac{V_d}{S_d}, \tag{8}$$

$$L_d = \frac{4\cdot\lambda\cdot\left(a_2^2 - a_1^2\right)\cdot L}{\phi^2}. \tag{9}$$

Using the wire length L_d, its cross-sectional area S_d, the resistivity ρ of the material and angle ϕ for the contour curve s, the coil resistance R_c was determined:

$$R_c = \rho \cdot \frac{L_d}{S_d}, \tag{10}$$

$$R_c = \frac{16\cdot\rho\cdot\lambda\cdot\left(a_2^2 - a_1^2\right)\cdot L}{\pi\cdot\phi^4}. \tag{11}$$

The current density in the winding J is given by the equation:

$$J = \frac{I_c}{S_d}. \tag{12}$$

To obtain the current density J_c for the coil, the dependence is multiplied by the space factor λ:

$$J_c = \lambda \cdot \frac{I_c}{S_d}. \tag{13}$$

The value of the current I_c flowing in the coil depends on the resistance of the coil R_c, the external resistance R_z and voltage U (the sum of resistances of all circuit elements except for the coil).

$$I_c = \frac{U}{R_c + R_z}. \tag{14}$$

The combination of this dependency with the formula describing the resistance facilitated determining the current density in the coil:

$$J_c = \lambda \cdot \frac{U}{\frac{1}{4} \cdot \pi \cdot \phi^2 \cdot R_z + \frac{4 \cdot \lambda \cdot \rho \cdot \left(a_2^2 - a_1^2\right) \cdot L}{\phi^2}}. \tag{15}$$

The above dependencies were implemented and the J_c values were derived for several different wire diameters. The result is shown in Fig. 4. Derived calculations uncovered that the highest current density occurs in a wire with a diameter of 1.1 mm.

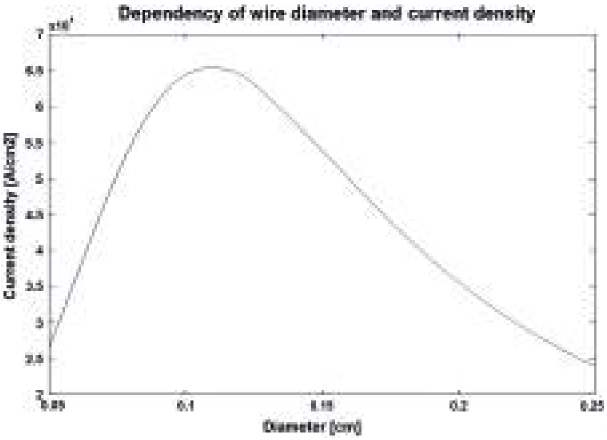

Fig. 4. Dependency between the current density and the diameter of the winding wire

3.3. Piston material. In the case of a reluctance actuator, the construction material of the piston is of high importance. The best efficiency is achieved when the core is demagnetized as fast as possible after exiting the coil. Carbon steel, which was assigned as a piston material, has the best properties in this respect. The non-linear magnetization characteristics of steel were also considered during the material selection.

4. Electrodynamic actuator

The electrodynamic actuator is also equipped with a coil and a piston. However, the piston is a non-ferromagnetic conductor – it can be a copper tube, a cylinder, or even a second coil. The piston is pushed out by the force generated as a result of the eddy currents induced in it. Currents interact with the radial component of the magnetic field, thereby causing the piston to move. However, the piston does not work with the force that causes it to accelerate only. The circuit that accelerates the piston consists of a capacitor with a capacity of C charged to a certain voltage level. The driving element is the inductance L which produces a magnetic field inducing the current in the piston. The resistance of the current in the circuit with the capacitor is affected by its resistance and the resistance of the wire from which the coil is built. The important parameter is M_{cp} – mutual inductance between the coil and the piston. The parameter determines the electrical energy conversion into the kinetic energy of the piston. The most important parameters for electrodynamic actuators were described below [20].

4.1. Voltage. The influence of voltage has been tested in the range from 0 V to 800 V, taking the 100 V step between successive values. With increasing voltage, the equivalent capacity was always equal to 250 μF. In contrast, the effect of the volume was tested in the range of 0 V to 500 μF, taking the 100 μF step between the successive values. While increasing the capacity, the voltage was equal to 700 V. The diagram is presented in Fig. 5.

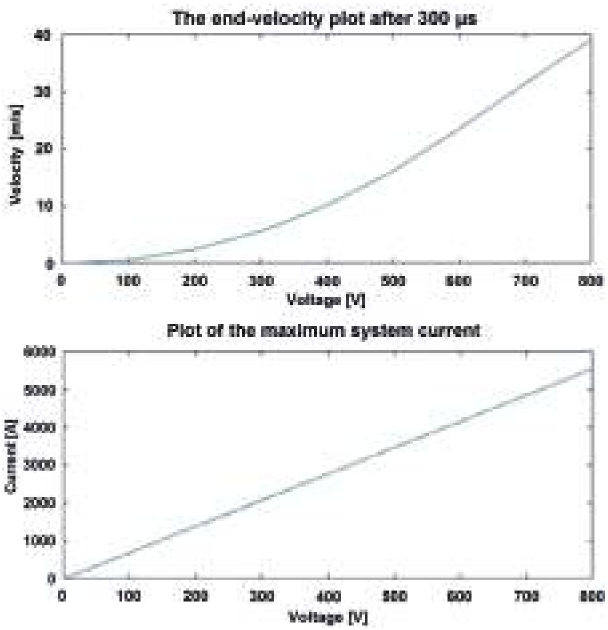

Fig. 5. Dependency between the force and the velocity over time and the capacitor voltage value for a 14-mm quadrilateral coil

The speed increased exponentially with the voltage. Electrical energy was converted into the kinetic energy of the piston.

4.2. Mutual inductance. The piston in the electrodynamic actuator is a copper tube. The tube has a lower mass compared to the full cylinder and, due to very short times of inducting the currents, the whole phenomena is observed on the surface of the piston. Therefore, reducing the weight by using a tube does not affect the energy losses, and increases the acceleration. The external circuit was characterized by a 700 V capacitor with a capacity equal to 250 μF. The coil had an internal diameter of 8.2 mm, a length of 30 mm, and a thickness of 3 mm. The obtained graphs are presented in Fig. 6.

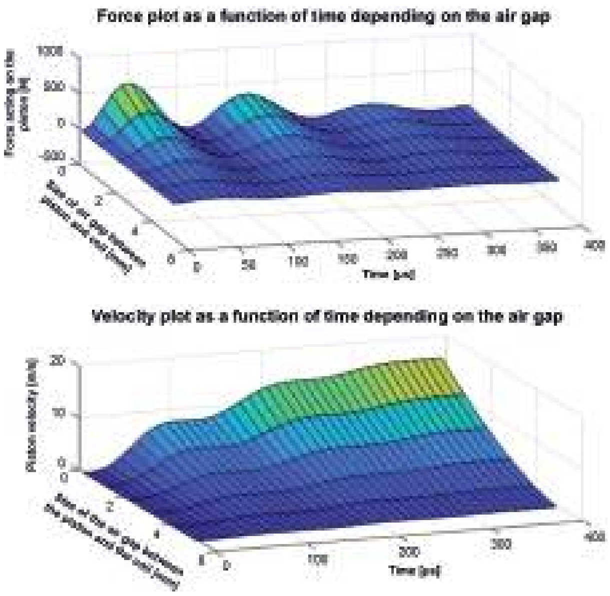

Fig. 6. Dependency between the force and the velocity over time depending on the air gap for the coil

A smaller gap causes greater magnetic coupling between the coil and the piston, which results in a better energy conversion in the system. Looking at the graphs, it is clear that reducing the gap definitely increases the force acting on the piston. The greater the force, the higher the speed of the piston, and, as a result, the greater its kinetic energy is.

4.3. Coil geometry and dimensions. To determine the optimal parameters of the coils, dependencies like those for the reluctance actuator were used, except for the formulation of Febry's factor (layer coil) [1]:

$$G = \frac{\sqrt{\pi a_1}}{5} \cdot \sqrt{\int_{a_1}^{a_2} \frac{\lambda^+}{\rho^+} \frac{z}{rs^2}\, dr} \tag{16}$$

where: dr is the cylinder thickness in cm; z is the length in cm; a_1 is the inside coil radius in cm; a_2 is the outside coil radius in cm; ρ is resistance in ohm·cm; r is the half-cylinder height in cm; s is the cylinder diagonal in cm.

Based on the previous simulations, a vast number of fixed parameters was assumed. The coil unit is set to be supplied with two capacitors of capacity 250 μF connected in a series and charged to 700 V. The piston is determined as a 1 mm thick copper tube, 20 mm long, with the weight of 2.00 g and an external diameter of 8 mm. The coil will be wound up from a wire with a cross-section of 2 mm × 1 mm.

5. Actuators setup

During the work concerning the construction of the coil actuators for the magnetomotive micropump, an analysis of the physical phenomena associated with the optimization of these systems was conducted. Research has clearly indicated that in the reluctance actuator, due to the disappearance of the current in the preceding coil, the piston can decelerate. This occurrence had direct impact on the overall piston velocity. With the electrodynamic actuator, electromagnetic and physical mechanics tended to push the piston without deceleration. Moreover, it was assumed that the electrodynamic actuator piston will eventually have a higher kinetic energy. It was decided to construct a reluctance actuator consisting of three coil sections, while the electrodynamic actuator consisted of only two coil sections. Another feature that should be emphasized is the weight of the piston. The reluctance actuator piston was a ferromagnetic core. The weight of the piston was slightly higher than in the electrodynamic actuator (2.00 g) and was equal to 3.33 g. In our research and trials, a lot of attention was paid to the proper control of the reluctance actuator piston (determination of the optimal moment of switching on the next coil section). This did not change the fact that larger capacitance of the capacitor than for the electrodynamic actuator was used. Naturally, this resulted in an increase in the input energy of the system. Research data and attempts to use such an actuator setup were to give an answer concerning the type and scope of use in the final design of the magnetomotive micropump.

The study of the physical phenomena and literature regarding an electrodynamic actuator already facilitated lowering such parameters as the capacity of the capacitors, their quantity, and the number of coil sections.

5.1. Reluctance actuator. The heart of the control system was an 8-bit microprocessor from the AVR family – Atmega32A, clocked at 16 MHz, the microcontroller with enough digital inputs and outputs required for this project and the SPI interface allowing programming without urge to physically remove the component from the fixed system. The whole system was powered by 230 V AC mains voltage, the blue electroluminescent diode signaled the power switching status. The first stage implemented by the controller was the charging process of the capacitors. 230 V AC/110 V AC transformer and small rectifying bridges DF08 were used. Connecting and disconnecting the charging circuits of subsequent sections were conducted by PE014005 relays. The microcontroller controlled their coils through the BC547 NPN transistors, which were protected against overvoltage by the UF4007 extinguishing diodes. Capacitors were charged by 100 Ω resistors of power rating equal to 220 W. This solution reduced the charging current, which extended the life of the capacitors and made it easier to control the circuit. In parallel with capacitors: 2780 μF, 1805 μF and 860 μF, low impedance capacitors (Low ESR)

330 μF/500 V, 290 mΩ/100 Hz were used. Elements designed for high-frequency operation were not damaged by fast charging and discharging thanks to the presented solution. Such a solution would make standard impedance capacitors less vulnerable to damage resulting from the high discharge current pulse after the coil circuits were turned on. IGBT transistors were chosen as executive control elements for each coil section since they are more resistant to surge currents. Moreover, the voltage drops across the connector did not grow with the current in those transistors. After controlling the input, the voltage $U = 15$ V will be given to the gate of the IGBT transistor connected in a low-side configuration. The coil sections, connected on one side to the high capacitor bank capacitance, were shorted to the zero potential on the second end. The current pulse generated an electromagnetic field that set the piston in motion. Synchronization of the coils was set in such a way that the capacitors were discharged at the right time – so that the piston did not slow down after crossing the center of the coil (or slowed marginally). The described actuator and its control system were shown in Fig. 7.

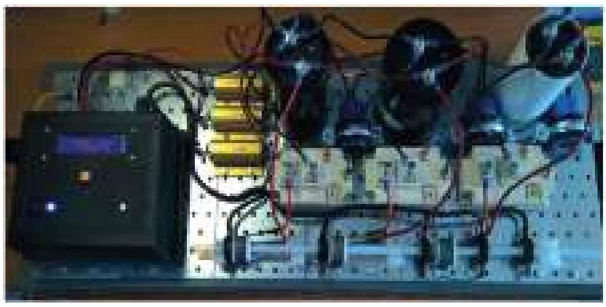

Fig. 7. Reluctance actuator and its control system

Three subsequent coil sections were controlled in the described way. Phototransistors for velocity measurement were placed on the third section at a distance of 50 mm from each other. A dedicated circuit board was created for this system to assure the best control of the described elements. A circuit board was designed considering the appropriate housing, from which four connectors, the LCD display and the LED diode would be outputted and a button initiating the successive stages of the program would be executed. Connectors would connect in sequence: IEC 320 C14 – 230 V AC power supply, DB15 – IR luminescent diodes, phototransistors and IGBT gate control signals, Molex 4P – charged of three capacitor banks, IDC 10P – ISP/KANDA standard programmer.

5.2. Electrodynamic actuator. The FR5739 microcontroller from Texas Instruments, a member of the MSP430 family, was selected for the role of the main control system component. Microcontrollers from this family were compatible with the von Neumann architecture, whose most important feature is energy efficiency. In addition, the microcontroller is equipped with FRAM memory (Ferroelectric Random Access Memory), which was characterized by high data writing speed. The clock frequency of 24 MHz was sufficient for the system. Due to the different supply voltages of components included in the control and measurement system, it was necessary to use voltage stabilizers to obtain a voltage of 3.3 V and 5 V. Stabilizers LM78xx were chosen. To realize the measurement of the piston velocity in the solenoid, photodiode BPW34 was chosen. These photodiodes react to light waves in a wide spectral range. Photodiodes were placed on the second section at a distance of 50 mm from each other. Essential elements in the system were also capacitors that filter signals and provide a reserve of energy at a sudden demand. Each section consisted of two capacitors with a value of 125 μF (single capacitor) and a voltage equal to 400 V. The controller also used resistors, ARK-2 connectors, a mini USB connector, a gold pin connector and signaling diodes as well as switches that enabled interaction. To charge the capacitors, miniature JQX-115F ZS3 power relays were used. The moment the high state appeared on the appropriate pin of the microcontroller, the coil was connected by 12 V pin with the LTV816 optocoupler. The coil attracted a contact that allowed the capacitor to be charged. When the desired voltage was reached on the capacitor, the signal on the microcontroller output changed to low and the coil was disconnected. Power supply was IEC 320 C14 – 230 V AC, as in the case of a reluctance actuator.

Moreover, as for a reluctance actuator, the custom circuit board was designed to control the described elements. The model of the electromagnetic actuator with control and measurement system are shown in Fig. 8. A schematic diagram of the control system is presented in Fig. 9.

(a)

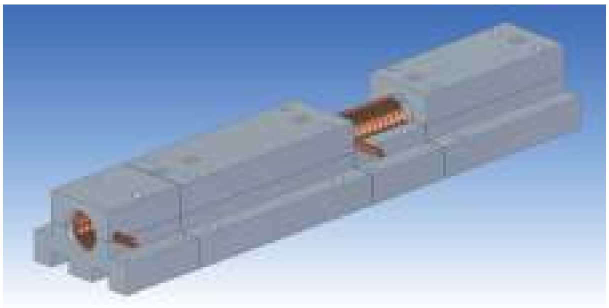

(b)

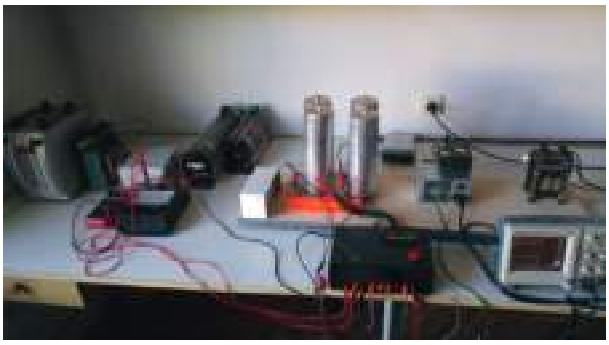

Fig. 8. Electrodynamic actuator and its control system: a) fragment of the electrodynamic actuator chassis; b) laboratory setup

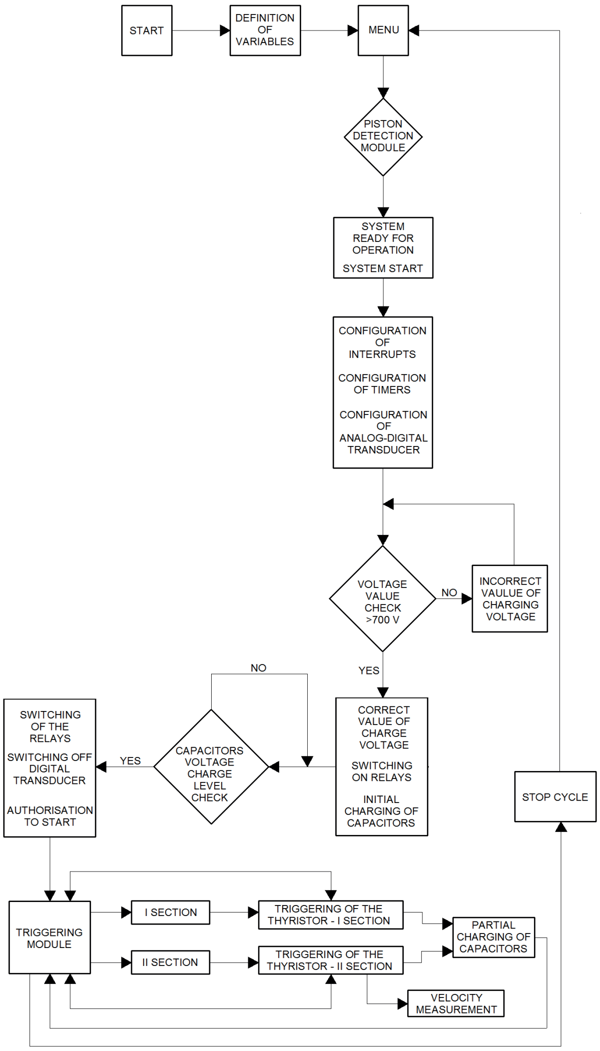

Fig. 9. Reluctance actuator and its control system

6. Measurements results

A series of measurements was arranged to determine the piston velocity after III coil section for the reluctance actuator and II coil section for the electrodynamic actuator. The five-measurement series for each actuator type was conducted. The results were presented in Table 1 and Table 2.

Oscillograph records taken from the detectors measuring the range for the reluctance actuator after III coil section and for the electrodynamic actuator after II coil section were presented in Figs. 10 and 11.

Table 1
Reluctance actuator – results of measurements

Actuator type	Reluctance actuator				
Description	Velocity measurements results after III coil section				
Series number	1	2	3	4	5
Time [ms]	1.323	1.339	1.336	1.335	1.335
Velocity [m/s]	37.326	37.530	37.425	37.439	37.453
Velocity average value [m/s]	37.435				
Average kinetic energy accumulated in capacitors [J]	77.312				
Average kinetic energy of the piston [J]	2.344				
Efficiency [%]	3.030				

Table 2
Electrodynamic actuator – results of measurements

Actuator type	Reluctance actuator				
Description	Velocity measurements results after II coil section				
Series number	1	2	3	4	5
Time [ms]	1.600	1.450	1.500	1.450	1.465
Velocity [m/s]	31.250	34.480	33.330	34.480	34.12
Velocity average value [m/s]	33.532				
Average kinetic energy accumulated in capacitors [J]	40.000				
Average kinetic energy of the piston [J]	1.124				
Efficiency [%]	2.810				

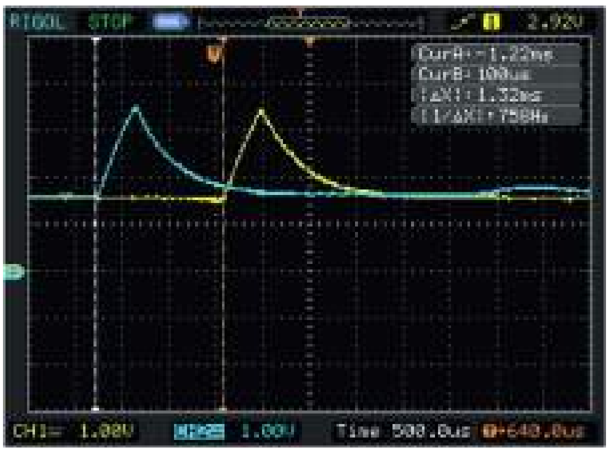

Fig. 10. ROscillograph record determining the piston velocity after the third section of the reluctance actuator. Detector: phototransistors

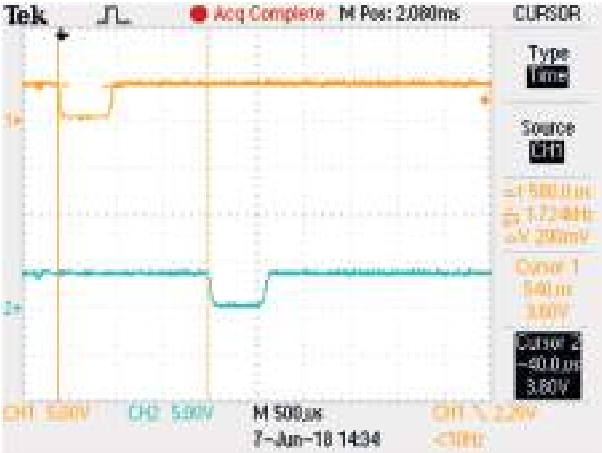

Fig. 11. ROscillograph record determining the piston velocity after the second section of the electrodynamic actuator. Detector: photodiodes

7. Discussion about measurements

The efficiencies of both actuators are acceptable during the prototype stage, as presented in Tables 1 and 2. Undoubtedly, attention should be paid to the mechanics of these devices. The coil units should be fast and precise – it was decided to use elements executive with pulse power supply. In electromagnetic micromachinery constructions developed worldwide, employing the aforementioned type of power supply, the expected efficiency is around 5%. Larger electromagnetic devices with pulse power supply reach 11% [21, 22]. The electrodynamic actuator reached an efficiency of 2.8%, while the reluctance actuator reached an efficiency of 3.0%. The constructed electrodynamic actuator consisted of two coil sections. The efficiencies were in the same range despite the fact the electrodynamic actuator piston is much lighter, and the entire construction is favorable in terms of quality, durability, versatility, and the best performance. The abovementioned depend strictly on the materials that were used to design and shape the element chassis and piston. The shape of the mentioned element is ideal for implementation. Moreover, smaller capacity and voltage are involved, which is also favorable. On the other hand, the reluctance actuator consisting of three coil sections is much heavier as the control system is also more complex, considering the control of residual stream caused by the current shift. That may lead to issues during the implementation.

Measuring systems employing different types of detectors were proposed to conduct measurements. The peak characteristic witnessed on the oscillograph record presented in Fig. 10 is the effect of piston partially covering the detector while moving towards it. The peak characteristic is standard for a phototransistor. The photodiodes that were used as detectors in the case of the electrodynamic actuator exhibit a wider peak than those observed in the series involving a phototransistor (Fig. 11). Measurement ranges were marked on the oscillograph records to present the variation of time values obtained during the measurements. The differences in the measured velocity values in the series can be associated with the factors that were not included in the simulations and laboratory work at the prototype stage, including friction and drag, initial piston position error, and also the difference and magnetization curve of the actual material. This means that the greatest losses occur while converting the electrical force into a magnetomotive force that sets the piston in motion.

Table 3
Electrodynamic actuator – results of measurements

Actuator type	Reluctance actuator		Electrodynamic actuator	
Description	Velocity measurement summary		Velocity measurement summary	
Method	Laboratory	FEM	Laboratory	FEM
Velocity [m/s]	37.530	42.120	34.480	39.47
Velocity difference [m/s]	4.59		4.99	
Average kinetic energy of the piston difference [J]	0.369		0.389	
Efficiency difference [%]	0.84		0.92	

Simulations employing the Finite Element Method were conducted to create reference results for both coil units. The summary of the laboratory results and simulation results is presented in Table 3. The FEM simulations represent ideal conditions. Therefore, the results are slightly better. However, the derived values still fall within the range of those obtained from the laboratory work.

8. Conclusions

The team of authors examined two types of actuators in terms of usage, by means of constructing the electromagnetic micropump. The subjects of the research presented in this paper were coil units in both reluctance and electrodynamic versions. Two actuators involving different control systems were designed, constructed, and compared. The results of the comparison are as follows:

- The electrodynamic actuator is more compact.
- The electrodynamic actuator exhibits better efficiency in comparison to the reluctance actuator.
- The control system for the electrodynamic actuator is easier to implement.
- The estimated length of service for the electrodynamic actuator is estimated as longer in comparison to the reluctance actuator (the control system, the complexity of the solution).
- The reluctance actuator requires a bigger and heavier chassis construction.
- The piston is heavier in the prototype of the reluctance actuator.

- A compensating residual stream caused by the current shift causes difficulties related to the reluctance actuator control system.

Finally, it was settled that the electrodynamic actuator will be implemented into the novel concept of a magnetomotive micropump. Some construction aspects may change during the intended and upcoming assignments concerning the described scientific and engineering work, for example, the dimensions of the basic elements that will be used for the actuator assembly.

The efficiency of the solution was shown by measuring the kinetic energy of the piston and the efficiency of the system. Naturally, the selection is made only by comparing the cylinders tested.

The added value of the work is the clearly presented model of conduct while selecting the actuators for the presented pump design. Optimization of place and time of switching on the individual coil sections of the actuator was tested and presented. Instrumentation was comprehensively presented so that the tests can be repeated as a transparent procedure. The best executive element for the structure was determined.

References

[1] W.F. Gauster, "Somerbasic concepts for magnet coil design", *Conference paper*, Illionois, pp. 1–17, 1959.

[2] J. Liu and T. Koseki, "3 degrees of freedom control of semi-zero-power magnetic levitation suitable for two-dimensional linear motor", *Proceedings of the Fifth International Conference on Electrical Machines and Systems*, Shenyang, China, pp. 976 – 981, 2001.

[3] Y. An, G. Liu, P. Wang, H. Wen, and Z. Meng, "Magnetic force analysis and experiment of novel permanent magnet axial thrust balance structure in canned motor pump", *IEEE 2nd International Conference on Advanced Computer Control*, Shenyang, China, vol. 1, pp. 1–8, 2010.

[4] J. Cai and Y. Deng, "Initial Rotor Position Estimation and Sensorless Control of SRM Based on Coordinate Transformation", *IEEE Trans. Instrum. Meas*. 64 (4), 1004–1018 (2015).

[5] A. Masi, A. Danisi, R. Losito, and R. Perriard, "Characterization of magnetic immunity of an ironless inductive position sensor", *IEEE Sens. J*. 13 (3), 941–948 (2013).

[6] K. Yongdae, H.Y. Choi, and Y.CH. Lee, "Design and preliminary evaluation of high-temperature position sensors for aerospace applications", *IEEE Sens. J*. 14 (11), 4018–4025 (2014).

[7] F. Khoshnoud, and C.W. Silva, "Recent advances in MEMS sensor technology-mechanical applications", *IEEE Trans. Instrum. Meas*. 15 (2), 14–24 (2012).

[8] G. Loussert, "An Efficient and Optimal Moving Magnet Actuator for Active Vibration Control", *15 th International Conference on New Actuators*, Bremen, Germany, pp. 1390–1420, 2016.

[9] C. Paulitsch, P. Gardonio, S.J. Elliott, P. Sas, and R. Boonen, "Design of a Lightweight, Electrodynamic, Inertial Actuator with Integrated Velocity Sensor for Active Vibration Control of a Thin Lightly-Damped Panel", *Proceedings of ISMA*, pp. 239–251, 2004.

[10] C. Paulitsch, P. Gardonio, and S.J. Elliott, "Active vibration damping using an interial, electrodynamic actuator", *J. Vib. Acoust.* 129, 39-47 (2007).

[11] X. Li, K. Tian, and Y. Zhou, "Linear Electromagnetic Oil Pumping Unit Based on the Principle of Coil Gun", *IEEE Conference*, China, 2008.

[12] P. Fang, F. Ding, and Q. Li, "Novel High-Response Electromagnetic Actuator for Electronic Engraving System", *IEEE Trans. Magn.* 42 (3), 460–464 (2006).

[13] Y. Nakanishi, T. Honda, K. Kasamura, Y. Nakashima, K. Nakano, K. Kondo, and H. Higaki, "Bio-inspired shaft seal in coolant pump for electric vehicles", *IEEE International Conference on Renewable Energy Research and Applications (ICRERA)*, 2016.

[14] R.E. Clark, G.W. Jewell, S.J. Forrest, J. Rens, and J. Maerky, "Design Features for Enhancing the Performance of Electromagnetic Valve Actuation Systems", *IEEE Trans. Magn.* 41 (3), 692–696 (2005).

[15] H. Hoshi, T. Shinshi, and S. Takatani, "Third-generation blood pumps with mechanical noncontact magnetic bearings", *Artif. Organs* 30 (5), 324–338 (2006).

[16] J.F. Antaki, B. Paden, G. Burgreen, and N.J. Groom, "Blood pump having a magnetically suspended rotor", US Patent, No: 6447266 B2, 2002.

[17] J. Albert, R. Banucu, W. Hafla, and W.M. Rucker, "Simulation based development of a valve actuator for alternative drives using BEM-FEM code", *IEEE Trans. Magn*. 45 (3), 1744–1747 (2009).

[18] M.P. Goldowsky, "Magnetic suspension blood pump", US Patent, No: 6527699 B1, 2003.

[19] D. Elata, "On the static and dynamic response of electrostatic actuators", *Bull. Pol. Ac.: Tech*. 53 (4), 373–384 (2005).

[20] S.M. Yang and M.S. Huang, "Design and Implementation of a Magnetically Levitated Single- Axis Controlled Axial Blood Pump", *IEEE Trans. Ind. Electron*. 56 (6), 2213–2219 (2009).

[21] M.B. Khamesee and E. Shameli, "Pole piece effect on improvement of magnetic controllability for noncontact micromanipulation", *IEEE Trans. Magn*. 43 (2), 533–542 (2007).

[22] B. Ozdalyan and O. Dogan, "Effect of a semi electro-mechanical engine valve on performance and emissions in a single cylinder spark ignited engine", *J. Zhejiang Univ., Sci. A*. 11 (2), 106–114 (2010).

A5. *Calculations of Electrodynamic Forces in Three-phase Asymmetric Busbar System with the use of FEM*

energies

MDPI

Article

Calculations of Electrodynamic Forces in Three-Phase Asymmetric Busbar System with the Use of FEM

Michał Szulborski [1,*], Sebastian Łapczyński [1], Łukasz Kolimas [1], Łukasz Kozarek [2] and Desire Dauphin Rasolomampionona [1]

[1] Institute of Electrical Power Engineering, Warsaw University of Technology, 00-662 Warsaw, Poland; seb.lapczynski@gmail.com (S.Ł.); lukasz.kolimas@ien.pw.edu.pl (Ł.K.); desire.rasolomampionona@ien.pw.edu.pl (D.D.R.)
[2] ILF Consulting Engineers Polska Sp. z o.o., 02-823 Warsaw, Poland; lukaszkozarek@gmail.com
* Correspondence: mm.szulborski@gmail.com; Tel.: +48-662-119-014

Received: 23 September 2020; Accepted: 14 October 2020; Published: 20 October 2020

Abstract: Proper busbar selection based on analytical calculations is of great importance in terms of power grid functioning and its safe usage. Experimental tests concerning busbars are very expensive and difficult to be executed. Therefore, the great advantage for setting the valid parameters for busbar systems components are analytical calculations supported by FEM (finite element method) modelling and analysis. Determining electrodynamic forces in busbar systems tends to be crucial with regard to subsidiary, dependent parameters. In this paper analytical calculations of asymmetric three-phase busbar system were carried out. Key parameters, like maximal electrodynamic forces value, mechanical strength value, busbar natural frequency, etc., were calculated. Calculations were conducted with an ANSYS model of a parallel asymmetric busbar system, which confirmed the obtained results. Moreover, showing that a model based on finite elements tends to be very helpful in the selection of unusually-shaped busbars in various electrotechnical applications, like switchgear.

Keywords: EIPB; asymmetric busbar system; electrodynamic forces; FEM; simulation; analytical calculations; design methods; analysis

1. Introduction

The development of realistic design procedures involving busbar systems, responding to the mechanical loads associated with fault current impact, was a recurrent problem throughout the history of the power industry. A large number of studies have been done in order to assess how the busbars will withstand a stress corresponding to the instantaneous peak force due to short circuit currents. The approach adopted by NEMA (National Electrical Manufacturers Association) neglects the dynamic aspects of the problem and assumed that the stresses acting on busbars are directly proportional to the prevailing forces according to the Standards for Power Switching Equipment (SG6). Classical methods involving calculations of electrodynamic interactions in current circuits were created with intent to manually calculate those values with help of auxiliary graphical methods [1]. These methods are mainly used in the case of one-dimensional, straight-line busbars. Furthermore they are very effective in accordance to busbar testing. The accuracy of these methods is particularly high for current circuits feeding high voltage devices, due to the transverse dimensions being significantly smaller than the distance between the wires.

During calculations, individual configurations of busbars can be distinguished:

- Layout of flat parallel busbars;
- Layout of flat perpendicular busbars;
- Layout of spatial perpendicular busbars.

The use of power distribution busbars in low voltage power system switchgears is highly advantageous. It is an exact way to conduct energy distribution with a problem-free possibility of its expansion in the case of adding additional apparatuses in place of reserves intended for additional devices. On the other hand, the installation of the main busbar at the rear of the switchgear allows for optimal heat dissipation resulting from the heating of the loaded busbars, as well as withstanding the greatest stresses in the event of a short circuit. To guide the busbars inside the switchgear, special insulators are used which are screwed to the supporting brackets of structures intended for this type of solution. In most cases, the rails are attached horizontally. Vertical busbar systems occurs when the rated current is below 4000 A and there are no movable and withdrawable elements. The distances between insulators are determined based on the requirements of the standards and short circuit currents that may occur in the switchgear. Busbars in switchboards with higher currents are a better choice than cables. This is due to the fact that the rails dissipate heat better and can conduct higher values of the load current. An important advantage is also the certainty of screw connections between the rails, as opposed to terminals crimped on the wires. Under the influence of electrodynamic forces, the conductor may break out of the cable terminal and touch other conductive parts, leading to a short circuit. The most commonly used busbar thicknesses for energy distribution in switchboards are 5 and 10 mm, while the widths are 20–100 mm. Most often, those are made of pure copper, which is reducing the skin effect and allows the conduction of higher currents by about 20%.

Unfortunately, analytical formulas used in classical methods can be very complex even in the case of investigating simple busbar layouts. A particular computational problem is the mathematical complexity of integrals. In order to make correct calculations, modern computer software and numerical methods (described below) are recommended. For example, the ANSYS environment is based on the finite element model (FEM) method [2]. FEM is characterized by a variational formulation, a discretization strategy, one or more solution algorithms and post-processing procedures. FEM is used, e.g., to calculate the electrodynamic force and its effect on the EIPB (enclosed isolated phase busbar) [3].

The second group of solutions used for calculations are called peripheral methods. These methods allow determining the electrodynamic interactions with regard to cross-section and current variability in both parallel and perpendicular layout of current circuits [4]. This method relies on replacing one busbar of heterogeneous current density by a series of separate smaller current circuits of constant current density [5]. The application of the Biot–Savart law gives the possibility of determining the magnetic induction at any point of space caused by the flow of current through the element of the conductor [6]. Furthermore, calculations of the magnetic induction value allow determining the electrodynamic forces acting in the conductor system [7], which is shown in Figure 1 below.

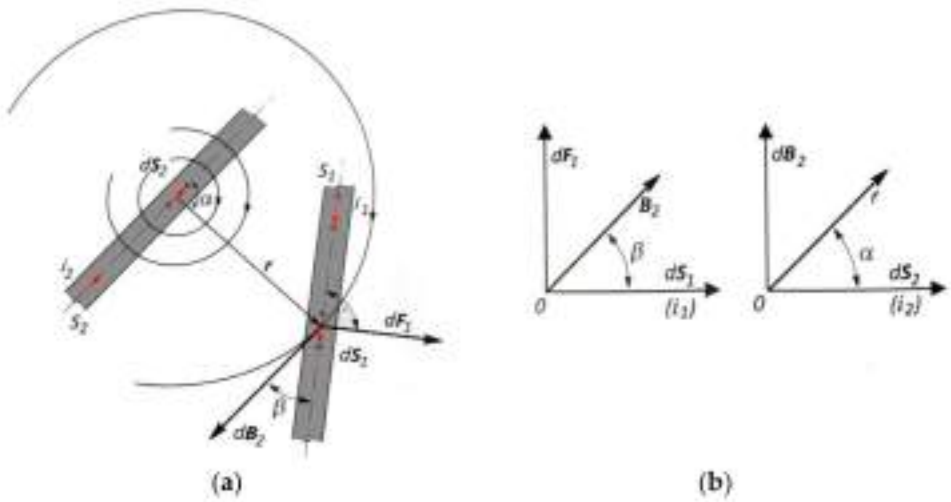

Figure 1. Determination of electrodynamic force value acting on the busbar. (**a**) the method of determining the direction and sense of magnetic induction; (**b**) Biot-Savart law.

The magnetic induction in the system shown in Figure 1 can be determined using the formula:

$$dB_2 = \frac{\mu \cdot i_2}{4 \cdot \pi \cdot r^2} \cdot \left[d\vec{s}_2 \cdot \vec{r} \right] \quad (1)$$

where i_2 is the current flowing through the current circuit; $d\vec{s}_2$ is a vector, the length of which corresponds to the length of the conductor element, with the direction of the conductor and the return consistent with the direction of the flowing current; r is the distance of the conductor element from the magnetic field point; $\vec{r}$ is a vector which origin is the source of the magnetic field and the end is the chosen point in space.

The third group of solutions are numerical methods, such as FEM, finite difference method, finite volume method, boundary element method, etc. In a simplified manner, these methods rely on the division of the contemplated continuous area into a finite number of subareas and searching for an outcome in those sectors [8]. The solution is obtained by interpolating the derived results in any point of space [9]. The main difference between these methods is the way of searching for a solution by analysis and definition of boundary conditions. FEM is an approximate method for solving partial differential equations. In FEM, the studied area is divided into many subareas. Finite elements with a simple shape are derived, for example for a two-dimensional space—a triangular or quadrangular element. This procedure allows calculating the values in a section of a given system/model. The functions sought are being solutions of partial differential equations [10]. Those functions are approximated locally in each finite element using special continuous test functions determined uniquely by their values at certain points called nodes (nodes lie inside or on the element's edge). An important coefficient for overall electrodynamic forces calculations (also natural frequency) is the Dwight factor [11]. The Dwight factor is used in case of parallel busbar arrangement with rectangular cross-section [12].

This work is consisted of analytical model (derived by classic calculations of electrodynamic forces) and numerical model (made using FEM) were compared in order to determine the best solutions for designing three-phase busbar system considering electrodynamic forces impact on the tested layout.

This manuscript includes the brief summary of work done by other scientist that was essential for concluded research in Section 2. The properties of busbar systems are mentioned in Section 3. Analytical calculations were procured for the chosen busbar layout and are presented in Section 4. Those calculations were confronted with the main part of the manuscript—the FEM simulations of an asymmetric three phase busbar system, which are presented in Section 5. The last section concludes the work gathering all of the knowledge coming from this research.

2. State of Art

Due to the increasing threats posed to human health, life and devices like switchgears, short circuit currents have been investigated with an emphasis on electrodynamic forces.

How important it is to build simulation models of busbars and distribution bars can be proved, inter alia, in publications [13]. Based on the thermal results, the authors calculate the dynamic stability of the EIPB (enclosed isolated phase busbar) to analyze the electrodynamic force under short circuit conditions [14]. A 2-D model was used for this purpose. In our discussion, a 3-D model is presented taking into account all electromechanical hazards (stresses of supporting insulators, natural frequency of the system and electrodynamic forces) [15]. Many scientists have studied the thermal stability of EIPB under short circuit current conditions [16]. Various scientists propose a method of calculating the busbar conductor temperature using the heat network analysis [17]. Analyses of the contact resistance of the busbar parts and calculations concerning the temperature rise generated by the resistance could be witnessed [18]. Other authors used experimental methods to check the reliability of busbar contacts and predicted the contact state on the basis of theoretical models [19,20]. Therefore, considering the effects of electrodynamic forces, temperature rise, and other factors, such as mechanical strength and the effect of a short circuit conditions on the busbar is analyzed [21–23].

However, most of these methods are based on the very small size of the rails which are no longer than 5 m, the test object is small and has a simple structure. In this work, the validation of the analytical model using the 3-D model of busbars with contacts and load bars is presented. Due to the complex structure of the power system network, actual EIPBs are often large with complex structures and it is difficult to directly calculate the dynamic stability. The finally presented FEM model is applicable to insulated rails in various environments. On this basis, the design and implementation of low-voltage switchgear was successfully carried out. The presented results enable a correct selection of the rails not only from the point of view of the current carrying capacity, but also considering the electrodynamic capacity. A solution enabling the validation of analytical calculations, the implementation of different, often complicated current circuits in relation to the calculations of simple rectangular or circular current circuits were presented. The model enables the determination of values for scientific and engineering calculations. It has been shown that the selection of power supply and receiving current circuits can be performed not only from the current load side. Not only was the skin effect taken into account, but also the current displacement and the natural frequency of the system.

In low voltage switchgears, small insulation gaps between the busbars of individual phases are sufficient, and the level of short circuit currents is similar to that in high voltage switchgears. The problem of electrodynamic stresses on rails is therefore more pronounced in the former, although the mitigating circumstance is the smaller distances between the rail fixing points. The rules for dimensioning rigid rails with regard to electrodynamic loads in short circuits are specified in the standard (IEC 865-1 Short circuit currents—Calculation of effects). The calculations are quite complex and based on such simplifications that their practical usefulness is too low. When developing the concept of a new series of switchgears, these calculations form the basis for initial design solutions, which are then verified in the short circuit laboratory. The author's team works on a daily basis in the short circuit laboratory of the Warsaw University of Technology, Institute of Electrical Power Engineering, and conduct work in the field of design and testing of switchgear devices. Multicore cables and other insulated conductors, suitably selected for their thermal short circuit capability, generally also withstand the electrodynamic forces associated with the flow of short circuit current. Due to the small thickness of the insulation, and therefore smaller distances between the axles of the conductors, the electrodynamic forces in cables and other low-voltage cables—with the same value of short circuit current—are greater than in high-voltage cables. Validation may be needed in the case of extremely high short circuit currents (over 60 kA) that are switched off in a short time (less than 20 ms), but without any limiting effect, i.e., with passing the expected value of the surge short circuit current [24]. Electrodynamic exposures must also be taken into account when choosing the construction principle and assembly technique of the heads and cable joints.

In the absence of a simulation model, a number of laborious and time-consuming works related to the determination of the maximum withstand forces are performed. This applies to both the current circuits and the insulators (Figure 2).

It is worth noting that with such an approach, additional tests are carried out by designing current circuits and switchgear devices. The analytical model is the correct application of the dependencies from the electromagnetic fields supported by the dependencies from the IEC 60609 standard for short circuit currents. The novelty of the procured work is presented in the following:

- Global approach to the model of electrodynamic forces in switchgears (model not only is presenting parallel current circuits, but a real system of rails with contacts);
- Consideration of an unfavorable case (the currents contains asymmetries), analytically countable only with a high approximation (not meeting the design requirements for such currents in practice). Therefore the numerical model is a novelty that is able to omit tedious calculations with better results;
- Reference to the design of switchgears from the angle of calculating electrodynamic forces, not only the current carrying capacity of the busbars, which is very rare.

- Limitation of oversizing (in the case of the cross-section of the current circuits) and frequent underestimating in calculations (in the case of supporting insulations), or vice versa, in the case of low-, medium-, and high-voltage secondary circuits of the switchgear.

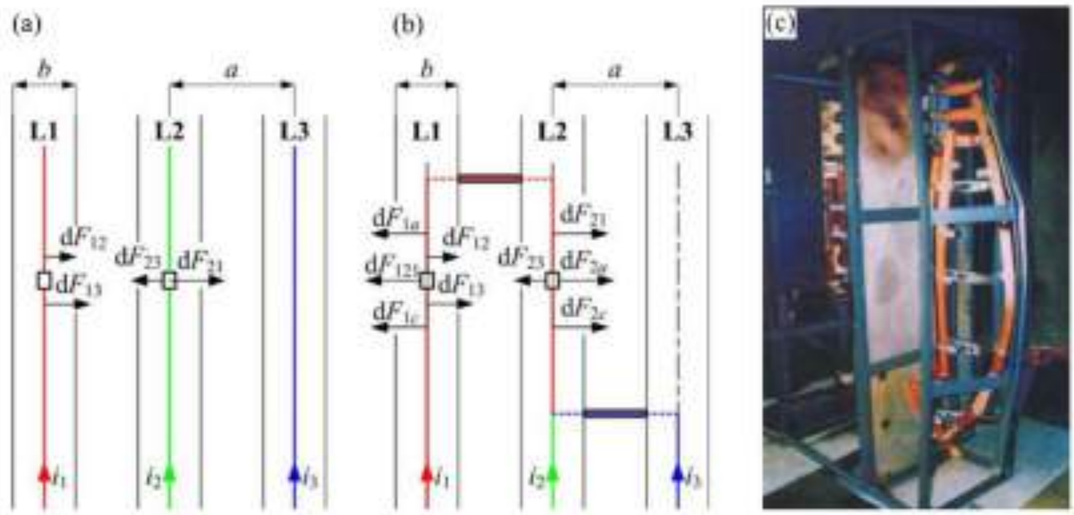

Figure 2. Busbar system in the switchgear after arc fault tests with the distribution of electrodynamic forces acting on individual rails of the flat busbar system at the time of: (**a**) metallic fault; (**b**) arc fault (**c**) damage of the busbar system after arc fault tests in the switchgear [25].

3. Properties of Busbar Systems

3.1. Mechanical Vibrations in Busbar Systems

Busbars exposed to electrodynamic forces are also exposed to mechanical vibrations also occurring during this phenomenon. The amplitude of these vibrations depends on many factors, which include, among others: the way the busbars are placed, the type of material they are made of and the number of insulation supports installed. The worst case that could happen is when the natural frequency of the busbars coincides with the frequency of changes in forces affecting their system. For this reason, the natural frequency of the busbar should be offset from the frequency of mechanical excitations resulting from electrodynamic forces. The most dangerous case may occur during the appearance of resonance characterized by the system's own vibrations equal to [26]:

$$f_o = 2 \cdot f \tag{2}$$

where f_o is the system natural vibration; f is the frequency of current change; $2f$ is the frequency of changes in periodic (non-disappearing) components.

In order to determine the permissible natural frequency of the busbar system the following dependency (3) shall be used. Furthermore it is obligatory to choose a frequency value that is outside the following interval:

$$f_o = (1.7 - 2.4) \cdot f \tag{3}$$

The properly determined busbar natural frequency should be outside the specified incorrect ranges. In case the calculated frequency does not correspond to the above assumptions, the system parameters should be adjusted in such a way as to detune the natural frequency of the tested rail from the resonance frequency. Table 1 presents the relevant formulas for determining the correct operating frequency for busbars firmly fixed at both ends. After substituting parameters related to the cross-section of the busbar, the natural frequency of the current circuit is obtained. Different calculations are made for multi-frequency systems where the mounting of rails and brackets is flexible.

Table 1. Formulas for determining the frequency of natural vibrations concerning the wire shape and material.

BusbarCross-Section / **Material**	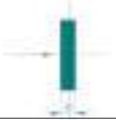			
Copper	$3.62\frac{b}{l^2}\cdot 10^5$	$3.62\frac{b}{l^2}\cdot 10^5$	$3.13\frac{d}{l^2}\cdot 10^5$	$3.13\frac{d_z^2+d_w^2}{l^2}\cdot 10^5$
Aluminum	$5.17\frac{b}{l^2}\cdot 10^5$	$5.17\frac{b}{l^2}\cdot 10^5$	$4.48\frac{d}{l^2}\cdot 10^5$	$4.48\frac{d_z^2+d_w^2}{l^2}\cdot 10^5$

It is possible to determine the natural frequencies of a given rail by taking into account the coefficients responsible for the particularities concerning the shape of the current circuits analyzed. In this case the following formula is used [27]:

$$f_o = f_{oo}\cdot c_1\cdot c_2\cdot c_3 \quad (4)$$

where f_{oo} is a natural frequency of a simplified system; c_1 is a coefficient that allows to take into account the influence of spacers used to connect individual rails in a multi-strip system; c_2, c_3 is a factor that allows stiffness, weight, and cable routing to be taken into account.

3.2. Short Circuit Currents

While studying electrodynamic forces, the possibility of short circuit occurrence must be considered. An accidental connection between individual phase conductors or between a phase conductor and earth is called an electrical short circuit. A short circuit may occur directly through an electric arc or through a component with low resistance. This phenomenon is generally harmful and/or undesirable. There are several types of short circuits, including symmetrical (for example three-phase or three-phase with earth) and asymmetrical (single-phase, two-phase, and two-phase with earth) short circuits. We can also classify certain short circuits according to their frequency of occurrence in given power systems. However, when calculating the electrodynamic forces, regardless of the frequency of occurrence, we must take as the basic scenario the short circuit, which has the most harmful effect on the system. The occurrence of a short circuit is usually associated with a current that is much higher than the current under normal operating conditions. The increasing value of electric current contributes to the heating of the devices and to the increase of interactions derived from electrodynamic forces. Therefore, it is necessary to use devices with increased protection values against short circuits, resistant to the risks of mechanical damage in the event of a much higher current flow than in normal periods.

The course of the short circuit current is variable both during the direct current flow and in the case of AC circuits, so it is particularly important to take into account the impact of changes in the value of short circuit currents in the transient state during calculations. The short circuit current contains two very distinct components: a periodic component i_{ok} and a non-periodic component n_{os}. The RMS value of the periodic component is constant throughout the duration of the short circuit, assuming that the RMS value of the electromotive force of the circuit and the value of the short circuit impedance do not change significantly. The non-periodic component, on the other hand, has a certain initial value that disappears exponentially with the circuit time constant of $T = L/R$. Figure 3 is an example of a short circuit current waveform showing the shape of the characteristic, taking into account the periodic and non-periodic components (assuming constant amplitude of the periodic component).

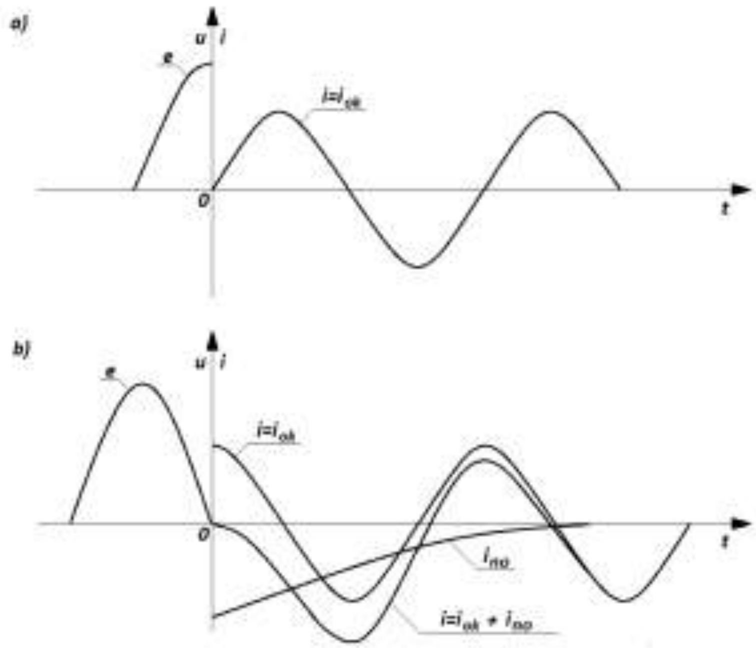

Figure 3. Example of short circuit current waveform: (**a**) without non-periodic component, (**b**) with the highest rate of non-periodic component, i_{no}—non-periodic component, i_{ok}—periodic component.

3.3. Short Circuit Current Calculations

In order to determine the circuit parameters that allow safe operating conditions to be maintained during a short circuit, calculations of electrodynamic forces should be made assuming the most unfavorable short circuit scenario associated with the currents with the highest possible intensity. In general, such conditions occur during a symmetrical three-phase short circuit and in this case the basic diagrams are shown in Figure 2. The initial symmetrical short circuit current I_k'' that represents rms value of the AC symmetrical component of a prospective short circuit current can be calculated from the formula [27]:

$$I_k'' = \frac{c \cdot U_n}{\sqrt{3} \cdot (Z_k + \Delta Z)} \tag{5}$$

where U_n is rated voltage; c is voltage factor that represents ratio between the equivalent voltage source and the nominal system voltage U_n divided by $\sqrt{3}$; Z_k is an abbreviated expression for the positive-sequence short circuit impedance for the calculation of three-phase short circuit while ΔZ = 0.

Based on the determined value, the so-called initial current can be calculated. Maximum initial symmetrical short circuit depends strictly on highest voltage for equipment (line to line RMS value) and can be describes as [27]:

$$U_m = c_{max} \cdot U_n \tag{6}$$

where c_{max} is a voltage factor that represents maximum short circuit current for a three-phase short circuit.

Assuming the value $c_{max} = 1.1$, the value of the initial symmetrical short circuit current can be expressed as [27]:

$$I_k'' = \frac{1.1 \cdot U_n}{\sqrt{3} \cdot Z_1} \tag{7}$$

Due to the occurrence of a non-periodic component, the peak short circuit current can reach much higher values than the peak value of the periodic component. In the event that the short circuit occurs when voltage passes through zero (for phase angle voltage equal to 0), the peak value of the short circuit current reaches the highest possible value and is called the surge current. The surge current is the maximum achievable short circuit current used in electrodynamic calculations. The spoken value can be determined from the following formula, taking into account the calculated initial short circuit current value [27]:

$$i_p = \kappa \cdot \sqrt{2} \cdot I_k'' \tag{8}$$

where i_p is maximum possible instantaneous value of the prospective short circuit current; κ is a surge factor for the R/X ratio obtained from Figure 3 or calculated by the following expression [27]:

$$\kappa = 1.02 + 0.98 \cdot e^{-3 \cdot R/X} \tag{9}$$

The use of the surge factor κ in the formula makes it possible to include in the calculations the attenuation of the non-periodic short circuit current component over time until the appearance of the overvoltage current. The value of this coefficient can be selected on the basis of the following characteristics shown in Figure 4 below.

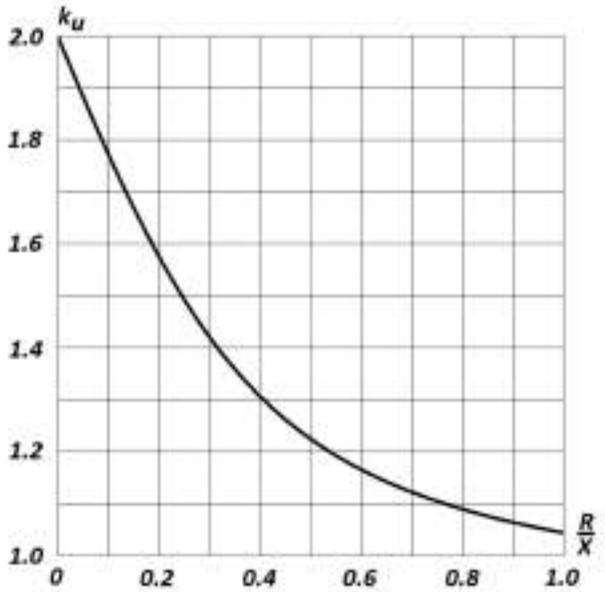

Figure 4. Surge factor characteristics.

3.4. Impact of Short Circuit Current Variability on Electrodynamic Force Values

The analysis concerning the operation of electrodynamic forces in the current circuits of electrical apparatuses is usually carried out taking into account the flow of short circuit currents through the busbars. The force values are then the largest. Short circuit currents are characterized by variability as a function of time, so it is important to check how the change in the value of these currents affects the time courses of electrodynamic forces. Among the forces acting on a given system, individual components can be distinguished:

- Periodic, disappearing and non-disappearing;
- Periodic decay of a frequency equal to the frequency of the voltage source; and
- Periodic non-disappearing frequencies with twice the frequency of the voltage source.

For single-phase and two-phase short circuits, variation curves of electrodynamic forces are related with the value of the squares of currents: symmetrical or asymmetrical (Figure 5). In the case of symmetrical current, the following equation applies:

$$F(t) = \frac{\mu}{4 \cdot \pi} \cdot k_F \cdot \frac{I_m^2}{2} - \frac{\mu}{4 \cdot \pi} \cdot k_F \cdot \frac{I_m^2}{2} \cdot \cos 2\omega t \tag{10}$$

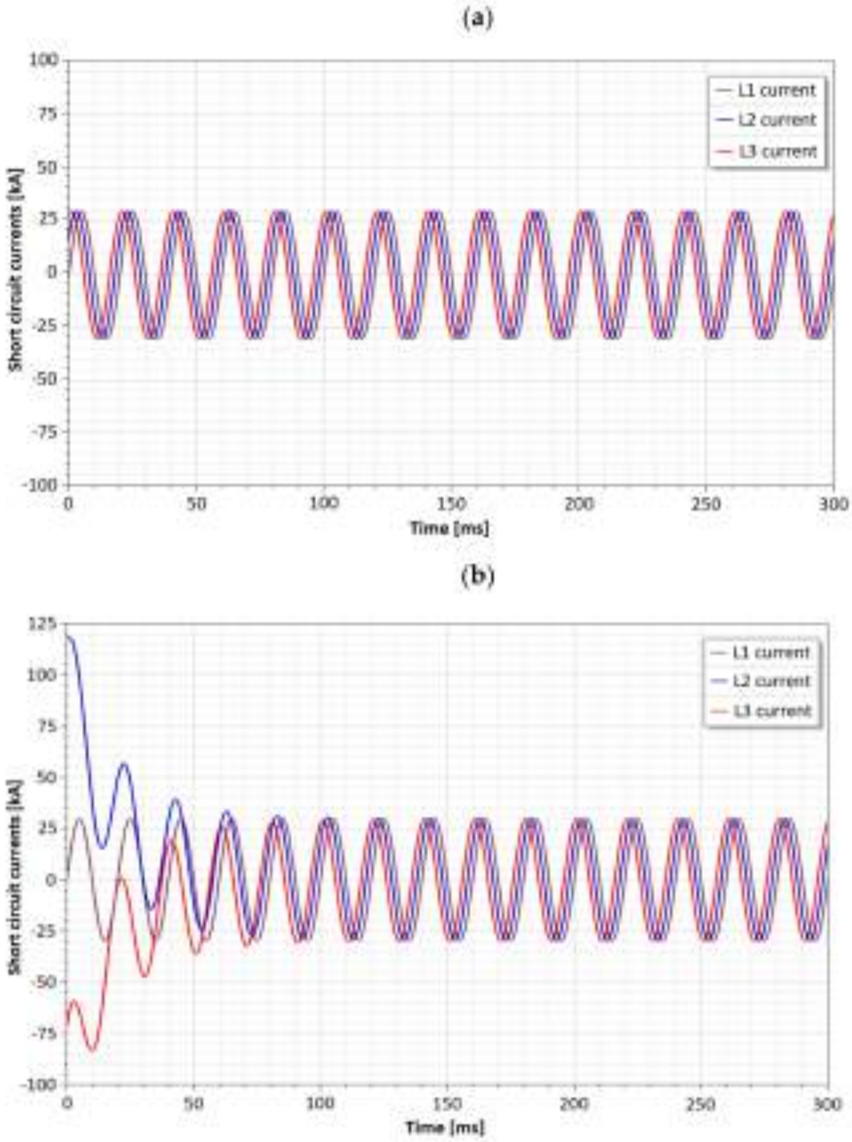

Figure 5. Current waveforms and their squares in the case of a single-phase short circuit current in the circuit: (**a**) symmetrical, (**b**) asymmetrical.

However, for an asymmetrical short circuit current:

$$F_1 = \frac{\mu}{4 \cdot \pi} \cdot k_F \cdot I_m^2 \cdot \sin\left(\omega t + \frac{2}{3} \cdot \pi\right)\left[\sin \omega t + \frac{1}{2} \sin\left(\omega t - \frac{2}{3} \cdot \pi\right)\right] \tag{11}$$

where α is the current phase at the moment of short circuit $\alpha = \psi - \phi$; ψ is the voltage phase at the moment of short circuit.

When determining the electrodynamic interactions at the level of three-phase faults, two cases can be distinguished, taking into account or not the non-periodic components. If the influence of non-periodic components is not taken into consideration and also assuming that the individual phase currents are out of phase by 120 g, the short circuit currents can be described by the following formulas [27]:

$$ci_A = I_m \cdot \sin(\omega t + \frac{2}{3} \cdot \pi) \tag{12}$$

$$i_B = I_m \cdot \sin\ \omega t \tag{13}$$

$$i_C = I_m \cdot \sin(\omega t - \frac{2}{3} \cdot \pi) \tag{14}$$

In order to correctly determine the value of the mutual interaction of electrodynamic forces, it is necessary to find their largest values, which in this case will take place when the multiplication of the two currents will produce a maximum value. Therefore, in a flat single three-pole system, where the external current circuits are arranged symmetrically with respect to the middle busbar, the electrodynamic forces acting on individual conductors can be described by the following equations [27]:

$$F_A = \frac{\mu}{4 \cdot \pi} \cdot k_F \cdot i_A \cdot (i_B + \frac{i_c}{2}) \tag{15}$$

$$F_B = \frac{\mu}{4 \cdot \pi} \cdot k_F \cdot i_B \cdot (i_A + i_C) \tag{16}$$

$$F_C = \frac{\mu}{4 \cdot \pi} \cdot k_F \cdot i_C \cdot (-\frac{i_A}{2} - i_B) \tag{17}$$

After having made a substitution of the above formulas, we obtain an equation which makes it possible to determine the value of the electrodynamic forces acting on the external current circuits through which the current i_A flows:

$$F_1 = \frac{\mu}{4 \cdot \pi} \cdot k_F \cdot I_m^2 \cdot \sin(\omega t + \frac{2}{3} \cdot \pi)\left[\sin \omega t + \frac{1}{2}\sin(\omega t - \frac{2}{3} \cdot \pi)\right] \tag{18}$$

In order to obtain the maximum value of the above-mentioned force it is necessary to determine the extrema of the function $f\ (wt)$:

$$f(\omega t) = \sin(\omega t + \frac{2}{3} \cdot \pi)\left[\sin \omega t + \frac{1}{2}\sin(\omega t - \frac{2}{3} \cdot \pi)\right] \tag{19}$$

After having made the appropriate substitution the following equations are obtained:

$$F_{1max} = -\frac{\mu}{4 \cdot \pi} \cdot k_F \cdot I_m^2 \cdot 0.808 \tag{20}$$

$$F_{1min} = \frac{\mu}{4 \cdot \pi} \cdot k_F \cdot I_m^2 \cdot 0.058 \tag{21}$$

The maximum values of electrodynamic forces for the external current circuit through which the current i_c flows are exactly the same as for the conductive busbar i_a and could be determined from the following formulas:

$$F_{3max} = -F_{1max} = \frac{\mu}{4 \cdot \pi} \cdot k_F \cdot I_m^2 \cdot 0.808 \tag{22}$$

$$F_{3min} = -F_{1min} = -\frac{\mu}{4 \cdot \pi} \cdot k_F \cdot I_m^2 \cdot 0.058 \tag{23}$$

The value of electrodynamic forces acting on the center busbar of the system is slightly different. After substituting the current formulas, the following equation is obtained:

$$F_2 = \frac{\mu}{4 \cdot \pi} \cdot k_F \cdot I_m^2 \cdot \sin \omega t\left[-\sin(\omega t + \frac{2}{3} \cdot \pi) + \sin(\omega t - \frac{2}{3} \cdot \pi)\right] \tag{24}$$

After determining the maximum values, the above-mentioned formula can be described as:

$$F_{2max} = \frac{\mu}{4 \cdot \pi} \cdot k_F \cdot I_m^2 \cdot 0.866 \tag{25}$$

The force of the same value acts in the opposite direction (towards the *C* phase rail). Based on the analysis of the above relationships determined for each busbar of the three-wire system it can be stated that the largest load of electrodynamic forces concerns the phase *B* busbar (middle rail). In this case, it is worth considering changing the parameters of the outer rails and adjusting their mechanical strength to a slightly lower load. However, calculations of mechanical strength are often made assuming loads that act on the middle current circuit. Therefore, the busbars with identical parameters are used. This is due to the small difference between the electrodynamic forces of the outer and middle tracks, which are just over 7%. Similarly, calculations are made when the occurrence of non-periodic short circuit currents is taken into account. Then slightly higher values of electrodynamic forces will be obtained, however, the relationships between individual phase conductors remain unchanged (the middle current path will be most loaded).

4. Analytical Calculations for Three-Phase Busbar SYSTEM

4.1. Calculations of A Single-Wire Three Phase Busbar System—Parameters of the Tested System

This subsection will present examples of calculations allowing determining: the maximum value of the electrodynamic force, the value of arising mechanical stress, the breaking force of the supporting insulators and the system's natural frequency.

The busbar arrangement under test is a three-phase, one-wire system, in which the external current circuits are symmetrical with respect to the middle path. The system is composed of rectangular copper bus bars. All the busbars have been stacked. It is also assumed that the electric currents in each phase have the same direction and equal values. The calculations presented in this subsection have been carried out on the basis of the theoretical information previously discussed and allow the determination of the individual parameters associated with the occurrence of electrodynamic forces, the proper adjustment of which allows maintaining safe and stable operation of the entire system. The calculations concerning the maximum value of the electrodynamic force were carried out taking into account the mathematical relations mentioned above, according to which the central current path of the system is the most loaded. In order to determine the parameters enabling safe operation of devices, tests should be carried out under the most unfavorable operating conditions of the system, which, in this case, means calculations under short circuit conditions (three-phase short circuit).

The tested busbar system is characterized by the following parameters:

- i_{uIII} = 60 kA—surge current value at three phase short circuit;
- *S: b* = 10 × h—current busbar cross section (rectangular cross section);
- l = 50 cm—distance between support insulators of a given phase;
- d = 12 cm—distance between the centers of the wires;
- material used: copper; and
- σ_{dop} = 1400 daN/cm^2—allowable material stress.

The arrangement of busbars, their support insulators and their dimensions are shown in Figure 6.

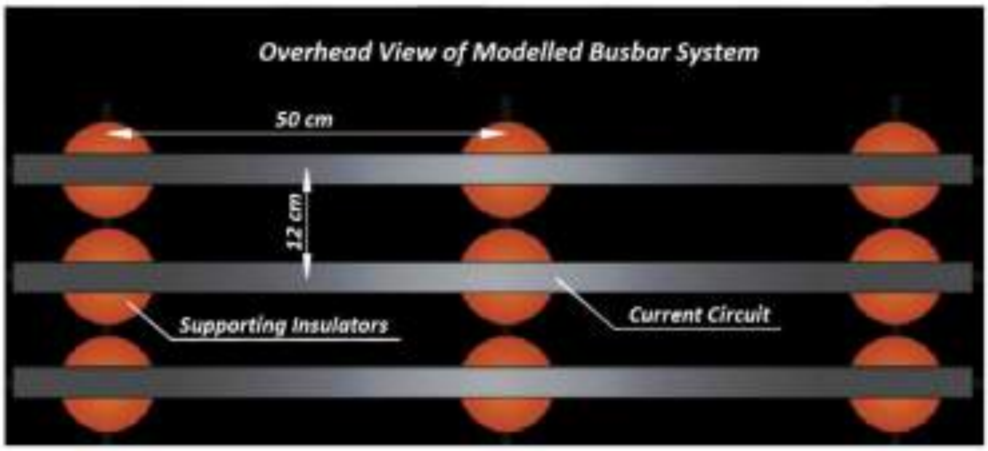

Figure 6. Graphical representation of modelled busbar system.

4.2. Determination of the Maximum Electrodynamic Force Value

Taking into account the relationships previously determined concerning the impact of the variability of the short circuit current on the values of the electrodynamic forces, it can be assumed that the most important forces act on the average current circuit. Correct calculations of the values concerning electrodynamic forces acting under three-phase short circuit conditions can be obtained using the following formula:

$$F_{2\max} = \frac{\mu}{4 \cdot \pi} \cdot k_F \cdot k_D \cdot \frac{\sqrt{3}}{2} \cdot \left(i_u^{III}\right)^2 \tag{26}$$

where k_F is the shape factor of the current circuit system; k_D is the Dwight coefficient based on the characteristics from ($i_u{}^{III}$)—surge current at three-phase short circuit.

Based on the available circuit parameters, the k_F factor value can be determined using the following formula:

$$k_F = 2 \cdot \frac{l}{d} = 2 \cdot \frac{50}{d12} = 8.34 \tag{27}$$

where l is the distance between the axles of individual phase conductors; d is the distance between the axles of individual phase conductors.

The Dwight coefficient value (k_D) can be derived from the charts [27]:

$$\frac{d-b}{h+b} = \frac{12\text{cm} - 1\text{cm}}{4\text{cm} + 1\text{cm}} = 2.2 > 2 \tag{28}$$

$$\frac{b}{h} = \frac{1}{5} = 0.2 \tag{29}$$

The Dwight coefficient value is equal: k_D = 1. After substitution to Equation (26), the values of the surge current and the values of the determined coefficients make it possible to obtain the maximum electrodynamic force acting on the middle current circuit and it is equal to:

$$F_{2max} = \frac{4 \cdot \pi \cdot 10^{-7}}{4 \cdot \pi} \frac{H}{m} \cdot 8.34 \cdot \frac{\sqrt{3}}{2} \cdot 36 \cdot 10^8 \cdot A^2 = 2600.16 \text{ N} = 260.016 \text{ daN} \tag{30}$$

4.3. Calculations of Natural Frequency for the Tested System

Due to the occurrence of interactions of electrodynamic forces in the examined system, mechanical vibrations also appear in the described system. In order to determine the natural frequency of the tested busbar layout, it is mandatory to use the equations described in Table 1.

$$n = 3.67 \cdot \frac{b}{l^2} \cdot 10^5 \tag{31}$$

After substituting the appropriate values, the following value is obtained:

$$n = 3.67 \cdot \frac{1}{50^2} \cdot 10^5 = 146.8 \text{ Hz} \tag{32}$$

To avoid resonance phenomena, the natural frequency of the busbars—f must be outside the range (1.7–2.4). For an operating frequency of f = 50 Hz, the following equation can be used:

$$n = 146.8 \text{ Hz} > 2.4f = 120 \text{ Hz} \tag{33}$$

The natural frequency of the system determined previously meets the condition expressed above. Based on the above-mentioned formulas regarding the determination of the natural vibrations of the busbars, it can be stated that the factor that can be adjusted to avoid the occurrence of the resonance phenomenon is the distance 'l' at which the phase insulators are placed.

4.4. Selection of Support Insulators

Based on the above calculations, it can be concluded that each support insulator of the tested busbar system is subject to a static force equal to $R = F_{2max} = 260.016$ daN. In order to correctly select support insulators with an appropriate breaking force capacity, the force applied in the axis of the busbar R should be reduced to the force applied at the height of the upper edge of the insulator fitting R'. To this end, the response factor vF should be determined according to the characteristics presented in Figure 7.

$$R' = \vartheta_F \cdot R = 1.2 \cdot 260.016 \text{ daN} = 312.019 \text{ daN} \tag{34}$$

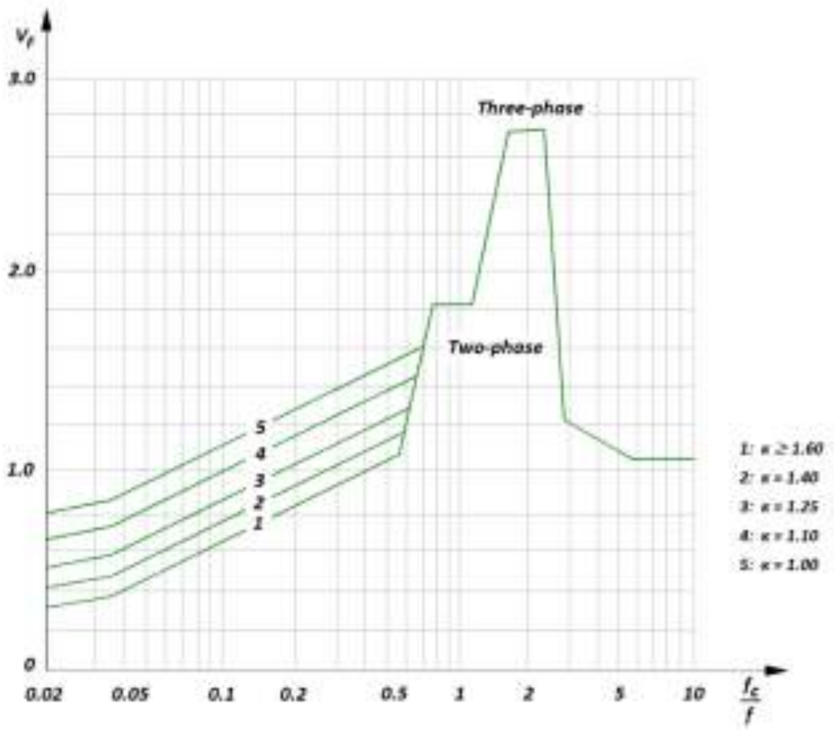

Figure 7. Characteristics used to determine the value of the reaction coefficient of the supports.

For some selected support insulators, it is mandatory to respect the safe operating conditions, formulated by the following inequality:

$$R' < F_{Nz} R' < F_{Nz} \tag{35}$$

It is therefore necessary to select support insulators with a rated breaking strength capacity expressed as follows $-F_{Nz} > 312.019$ daN .

4.5. Mechanical Strength

The busbars operating in the system under test have a certain, characteristic resistance to mechanical stress for a particular type of material. Table 2 shows the maximum stress data for different types of copper and aluminum busbars in accordance with the guidelines contained in the PN-72/E-05025 standard.

In order to check whether the effect of electrodynamic forces will not be associated with excessive mechanical stress of the conductors, it is necessary to check whether the bending stress values described by the following equations do not exceed the allowable stress values specified in the standards:

$$\sigma_g = v_\sigma \cdot k_\sigma \cdot \frac{M_g}{W} \le \sigma_{dop} \tag{36}$$

where σ_g is the bending stress value acting on the cable; v_σ is the dynamic bending stress factor; k_σ is a factor related to the increase in material strength at loads equal to k_σ = 0.5 for cables with a rectangular cross-section; M_g is the bending moment; W is the bending strength of the rail cross-section; σ_{dop} is the allowable value of mechanical stress for a given material.

In order to check the strength of the busbars, it is necessary to know the maximum bending moment of the rail, which can be determined from the following relationships for articulated rail fastening:

$$M_g = \frac{1}{8} F_{\max} \cdot l \tag{37}$$

However, in the case of rigid mounting of busbars:

$$M_g = \frac{1}{12} F_{\max} \cdot l \tag{38}$$

In the tested system it was assumed that the busbars are rigidly fastened at both ends:

$$M_g = \frac{1}{12} \cdot 260.015 \text{ daN} \cdot 50 \text{ cm} = 1083.39 \text{ daN} \cdot \text{cm} \tag{39}$$

Table 2. Permissible mechanical stress values for busbars with specific shapes made of copper and aluminum.

Current Busbar Material	Type of Current Busbar	Permissible Stress σ_{max} (daN/cm^2)
Copper	All types	1400
Aluminum	Rectangular, round or tubular current busbar	700
	C-section current busbar	500

To determine the dynamic coefficient of bending stress *ns*, it is necessary to know the ratio of the natural frequency of the conductor to the frequency of the flowing current *n*/*f*.

$$\frac{n}{f} = \frac{146.8}{50} = 2.936 \tag{40}$$

Based on the above calculations, v_σ = 1 was selected from the chart below in Figure 8.

The bending strength index of a rectangular section can be calculated as based on the relationships given in Table 3.

Table 3. Graphs for determining the dynamic bending stress coefficient.

Cross-Section System of Current Bars	Strength Index
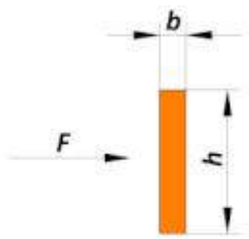	$W = \frac{hb^2}{6} \approx 0.167\ bh^2$

In the tested system it was assumed that there is one conductor per phase and that all busbars are set to edge. Thus, it can be written that:

$$W = \frac{h \cdot b^2}{6} = \frac{1\text{cm} \cdot 16\text{cm}^2}{6} = 2.67\ \text{cm}^3 \tag{41}$$

After substituting the determined parameters for Equation (32), the value of mechanical stress acting on the tested system is obtained:

$$\sigma_g = 0.5 \cdot \frac{1083.396\ \text{daN/cm}}{2.67\ \text{cm}^3} = 202.883\ \text{daN/cm}^2 \leq \sigma_{dop} = 1400\ \text{daN/cm}^2 \tag{42}$$

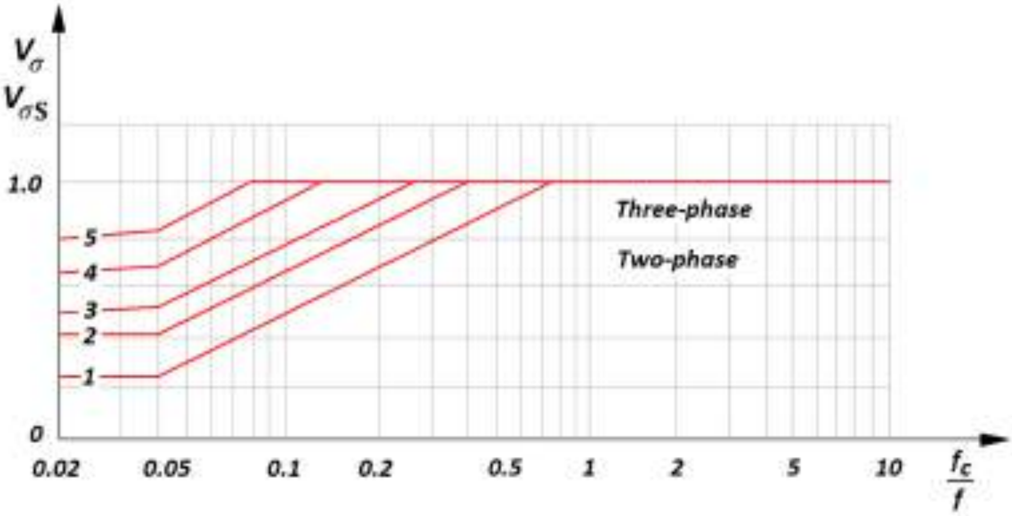

Figure 8. Graphs for determining the dynamic bending stress coefficient.

4.6. Summary of Analytical Calculations

The interactions arising from electrodynamic forces is related to the electric current flowing through the busbars in the magnetic field. These interactions can occur not only between current circuits but also near the ferromagnetic masses (for example between the concerned circuit and the ferromagnetic material). Among the methods for determining the electrodynamic forces acting on a given system, classical methods are used, one can enumerate, among others, the methods used in the case of one-dimensional busbars as well as the methods allowing to take into account the section of busbars and the variability of the electrodynamic forces passing through them in the calculations.

Basic equations were used for this purpose, the sources of electrodynamic forces and the means to select the appropriate system parameters allowing safe operation of the devices under conditions compatible with the assumptions presented above are considered. The most unfavorable operating conditions possible have always been assumed during the tests of correct operation of a given system. As in the same way as for the cases enumerated before, in the case of electrodynamic forces acting on busbars, such conditions will occur during the flow of short circuit currents. When designing current circuits that are to operate correctly even during high short circuit current flow, individual parameters should be taken into account:

1. Determination of the maximum value of electrodynamic force.

The value of the calculated electrodynamic force is used to determine the remaining parameters that affect the proper operation of the entire system. The determination of the maximum possible value of the electrodynamic force makes it possible to select the parameters of the system so that its operational safety is maintained under all conditions, including the most unfavorable conditions.

2. Determination of the natural system frequency.

The magnitude of mechanical vibrations resulting from electrodynamic forces is affected, among other things, by factors such as how the busbars are arranged, the type of material used in their construction, as well as the number of supporting insulators and the distance at which they are attached. In the case where the frequency of the vibrations caused by the force is equal to the frequency of the natural vibrations of the system, an unwanted resonance phenomenon may appear.

3. Determination of mechanical stress.

Under the influence of electrodynamic forces, the current circuits are subjected to mechanical stresses, the maximum size of which is determined for each material.

4. Selection of the material used to construct busbars.

The exact choice of the right material has a very large impact on the proper operation of the entire system due to a number of parameters related to thermal load and mechanical strength. However, for electrodynamic forces, the most important factor is the value of allowable stress σ_{dop}. According to the data presented in Table 1, the allowable stress is σ_{dop} = 1400 daN/cm^2 for copper and σ_{dop} = 700 daN/cm^2 for aluminum. In the case where the stresses resulting from electrodynamic forces exceed the permissible value for a given material, a mechanical deformation of the busbars may occur.

5. Selection of support insulators of appropriate strength.

Support insulators are often made of stiff, brittle materials, which means those are not very not very flexible or malleable. If the bracket is overloaded, it may break. Under the influence of electrodynamic forces, conductors in which current flows in the same direction attract each other, on the contrary, if currents flow in opposite directions, conductors repel each other. In particular cases during a short circuit electrodynamic forces reach such high values that their impact on a given electrical system can even lead to mechanical damage and deformation of the busbars. The dependencies (Equations (20), (22), and (25)) show that during electrodynamic forces presence, the average current circuit is subjected to the greatest stress. This is due to the fact that in a system in which the busbars are arranged symmetrically with respect to the middle current circuit, the interaction of the external busbars is slightly smaller due to the greater distance. In practice, however, identical parameters are often used for the center busbar and external rails. Sample calculations allowed determining how individual parameters of the busbar system affect the value of arising electrodynamic forces and how their proper adjustment affects the safety of current circuits.

Based on the formulas and dependencies presented, it can be stated that the maximum value of electrodynamic forces depends on:

- Surge current values. The surge current i_u is the maximum short circuit current that can be reached. This current occurs when the voltage crosses zero, i.e., for a phase angle of voltage equal to 0 or π. In the case of calculations the surge current (reaching very large values) rose to the square is taken into account, this is the main parameter that has the greatest impact on the value of electrodynamic forces (the higher the electric current, the greater the interaction between conductors).
- Distances between two supporting insulators of one phase. The distance at which two support insulators of one phase are laid, which was determined in the calculations as 'l' may affect both the value of electrodynamic forces and the natural frequency of the system. If the calculated natural frequency of the system is within the range defined as dangerous, a modification of the parameter 'l' can be performed to offset the value of natural frequency from an undesirable resonant frequency. The distance between the brackets is also used when determining the bending moment of the rail, which is necessary to calculate the mechanical stress acting on the system.

- Distance between the axles of individual phase conductors. The distance between the axles of the conductors marked as *'d'* is used in the formula expressing the shape factor of the current circuit system—k_F. The greater the distance *'d'*, the smaller the k_F value is, which directly reduces the value of interacting electrodynamic forces.
- Busbar cross-section shape. In the case of circular conductors, calculations are carried out in the same way as for conductors with a negligible cross-section. Using conductors with a rectangular cross-section, it is necessary to take into account the influence of the cross-sectional shape on the values of arising electrodynamic forces. This influence is expressed in simplified formulas for engineering calculations by using a special coefficient called the Dwight coefficient.

Based on the information discussed, it can be concluded that the operational safety of the system exposed to electromagnetic forces depends on many different factors, the values of which are often related to each other. The most important of these factors, however, is the maximum short circuit current that may flow in the circuit. Therefore, in order to maintain stable operation of the system, methods should be used to limit the frequency of short circuits and their duration.

5. Simulations Results for Three-Phase Busbar System

The subject of the simulations was the analysis of the high-current circuit model in the FEM environment. The study aimed to determine electrodynamic interactions in the high-current circuits. The current circuits have been modeled as part of the busbar models of the medium voltage switchgear. The software (2019 R2, Ansys® Academic Research, Pittsburgh, PA, USA) was used to perform the analysis. The program uses FEM and gives a very wide spectrum of possibilities for simulating phenomena in the field of mechanics, electrothermics, and electromagnetism.

5.1. Simulation Results

The results showing the maximum values were compared. The most interesting values obtained are the values of the mechanical stresses and electrodynamic forces within the insulators' mountings and the middle part of the busbars between the insulators. Not only were the allowable resistance of the conductor and the selection of insulators checked, but also the convergence with the analytical calculations. Sample results are shown below. The differences obtained as deviations of the maximum values of the electrodynamic forces are equal to 5.5%. In the event of an error at this level, the maximum calculated value of allowable stress in the insulator and conductor is still not exceeded. The simulations were made for the system shown in Figure 9.

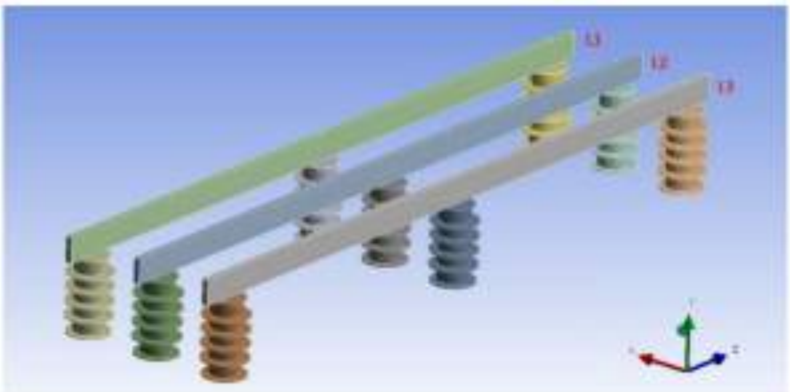

Figure 9. EIPB system drawn in ANSYS with the same geometry as for analytical calculations.

In the simulation tests, the currents as shown in Figure 10, were implemented. In the system of parallel rails, the maximum deviation was expressed in mm, reduced mechanical stresses and their time characteristics expressed in MPa (von Mises). The characteristics of the electrodynamic forces are expressed in N. Those results are presented in Figures 11 and 12 below.

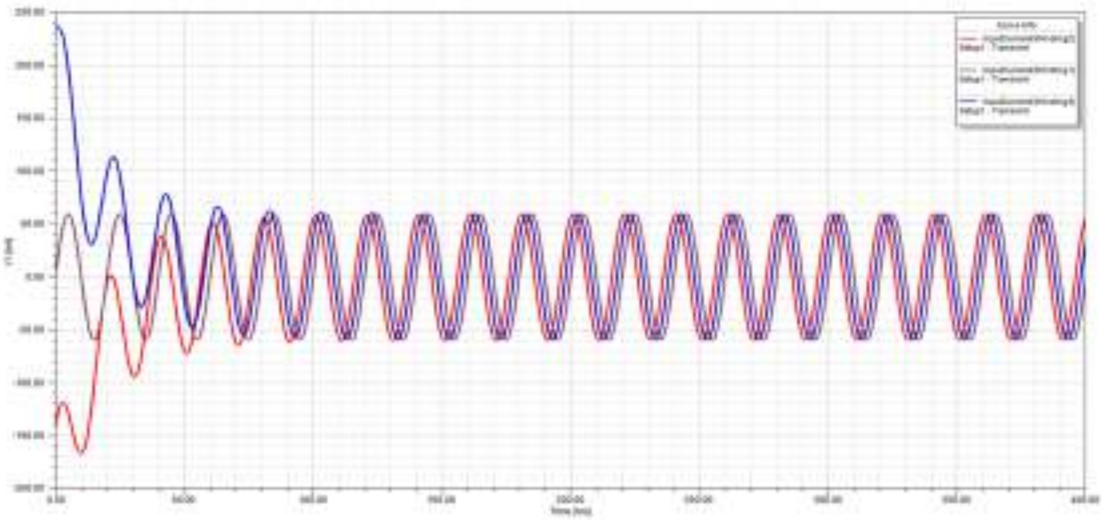

Figure 10. Short-circuit current characteristics that were implemented for simulation analyses.

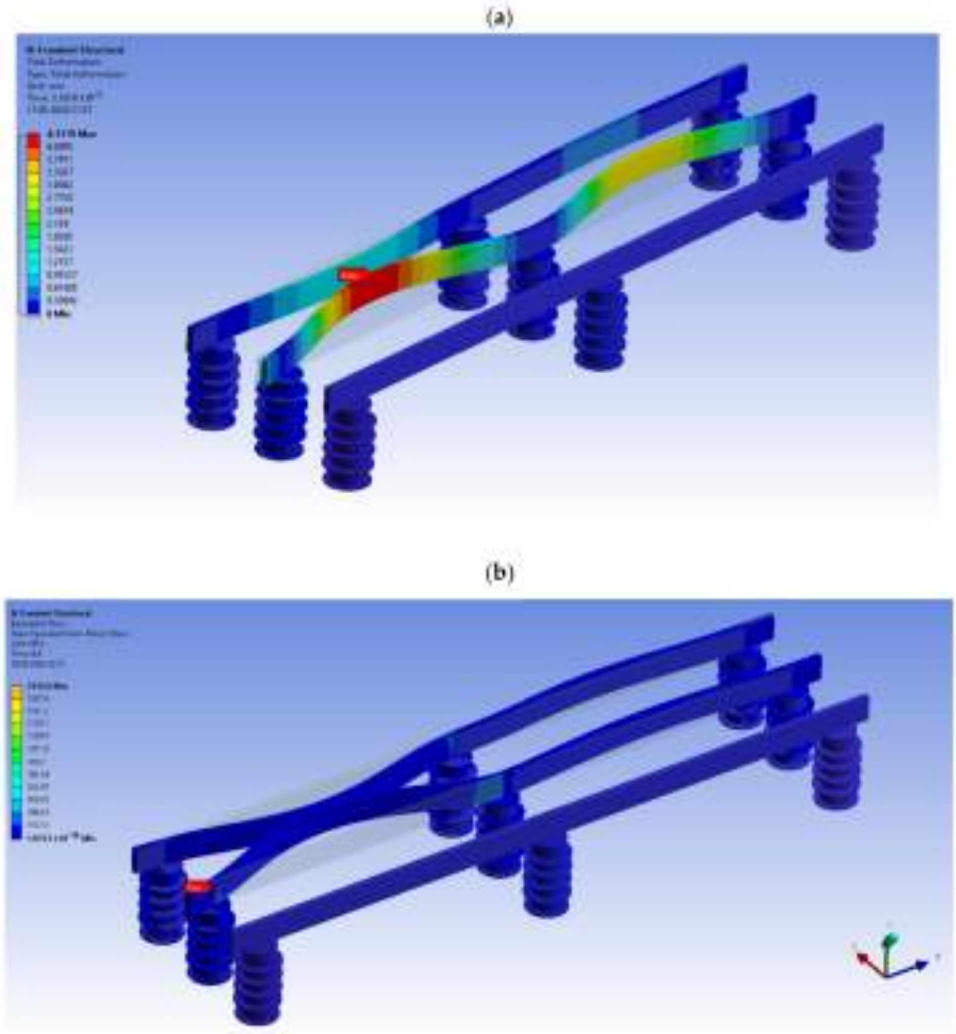

Figure 11. Simulation results for studied EIPB system (graphical): (**a**) Deformation in mm; (**b**) deformation in MPa (von Mises).

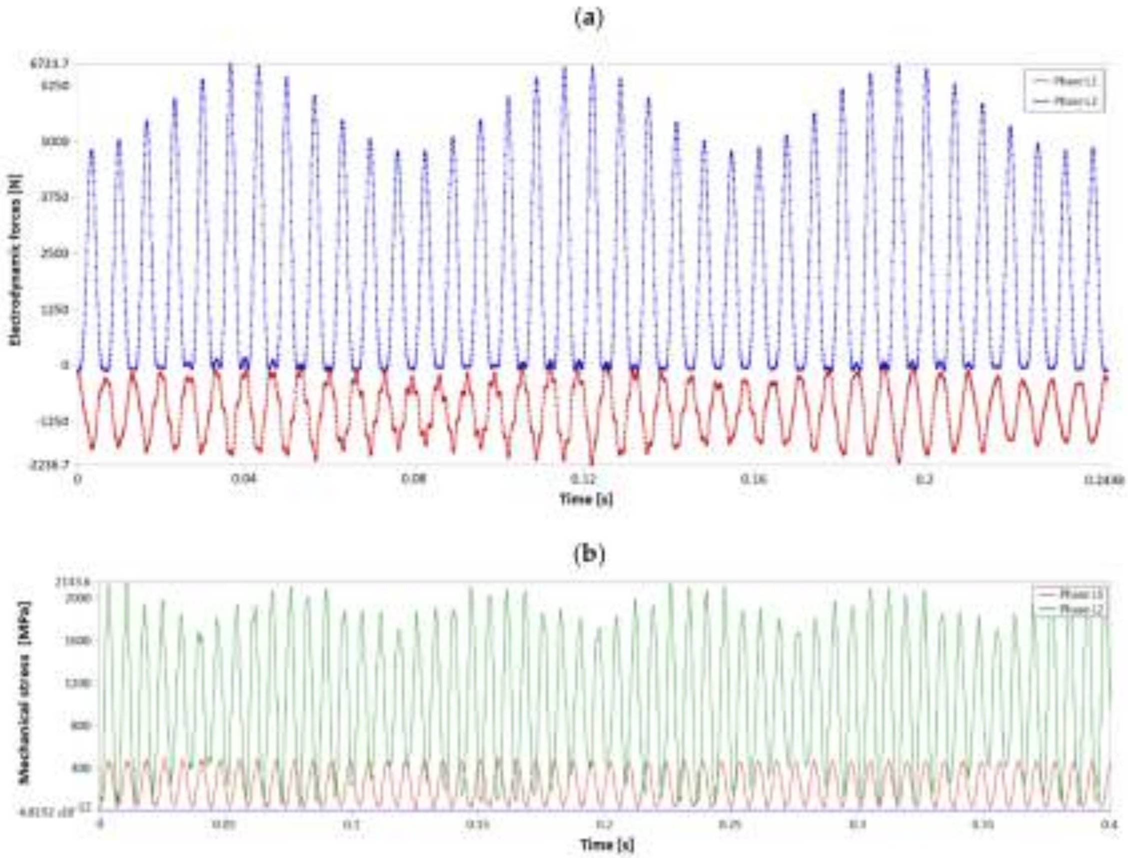

Figure 12. Simulation results for studied EIPB system (characteristics): (**a**) Electrodynamic forces characteristic; (**b**) mechanical stress characteristics.

Only parallel current circuits (round or rectangular) were considered in this publication. Alternatively, an electrical apparatus was selected for consideration. However, it is a disconnector, i.e., a system of parallel rails (cross-sectional area). Exemplary results are presented in Figures 13 and 14.

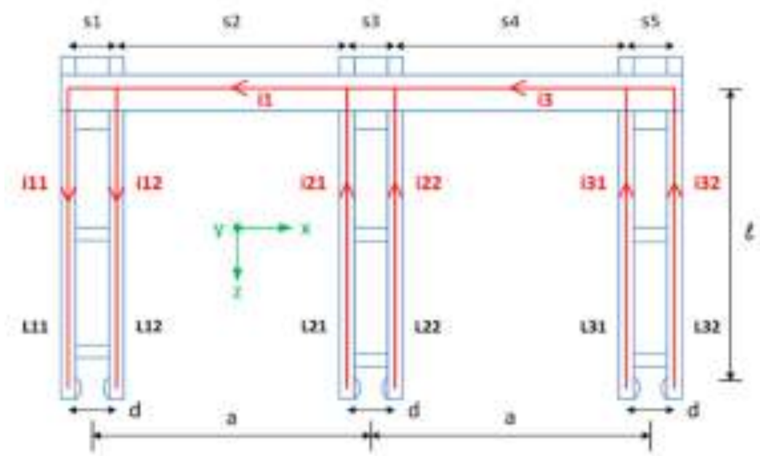

Figure 13. Top view of the earthing switch—red lines represent current lines; s1–s5 represent segments for force calculation on conductors at right angles; L11-L32 represent designations of each earthing knife [26].

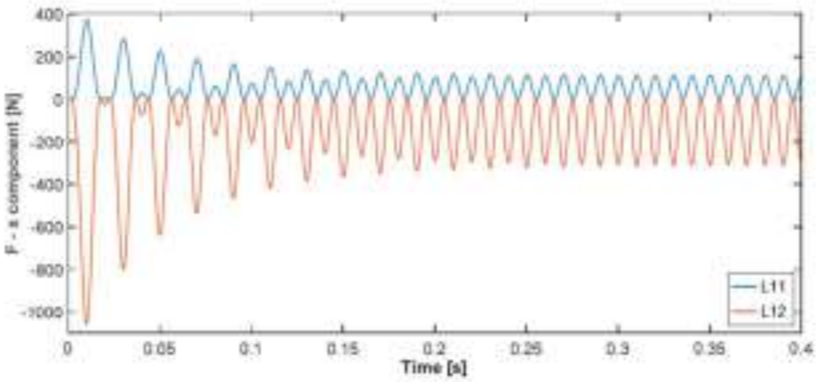

Figure 14. Electrodynamic forces on earthing knifes L11 and L12 [26].

In terms of the nature of the electrodynamic forces for time up to 0.24 s, a very large convergence of results can be noticed. This confirms the correctness of the implemented methodology. Correctly specified:

- Material features;
- Boundary conditions; and
- Type and kind of simulation.

It is also worth noting that the results concerning the value of the electrodynamic forces are consistent between the analytical and numerical calculations. Table 4 shows a comparison of the results for selected short circuit currents.

Table 4. Comparison of the results for selected short circuit currents.

Short Circuit Current I (kA)	Electrodynamic Forces (N)—Analytical Calculations	Electrodynamic Forces (N)—Numerical Calculations	Percentage Difference (%)
20	890	806	9.4
40	1936	1785	7.8
60	2600	2384	8.3

The results in Table 4 show that the differences between the analytical and numerical calculations that are not exceeding 10%. It is worth noting the differences between quite unusual short-circuits from the point of view of analytical calculations are presented here. It is a situation in which the currently used dependencies (not only in standards, but also in the world of science) treat the asymmetric short circuit current as symmetrical. Hence, current circuits may often be oversized (despite the lack of indications from the current and hence thermal exposure), and at the same time underestimating the quantity and quality of insulating supports. The opposite situations are also possible, when the current carrying capacity indicates the correct selection of the cross-sections, but those will not ensure the correct electrodynamic forces value. Hence, building dynamic FEM models in the manner shown above guarantees the correctness of calculations in the construction of not only low voltage switchgears, but also medium voltage and high-voltage secondary circuits. The confirmation of the presented considerations is the implementation into mass production of low voltage switchgear using the above-mentioned model.

5.2. Model Employment in Electrotechnical Analyzes

The model prepared in such a way was successfully used to calculate the power supply and busbars for low voltage switchgear. A series of numerical calculations related to the designation and mechanical checking of current circuits cross-sections, as well as the quantity and quality of insulators were performed. Figure 15 shows the deformations in mm for the four selected times in short circuit conditions.

(a)

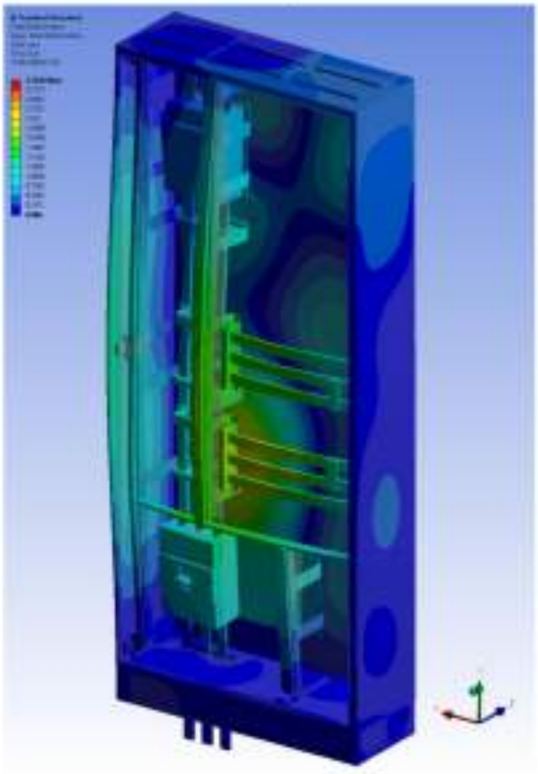

(b)

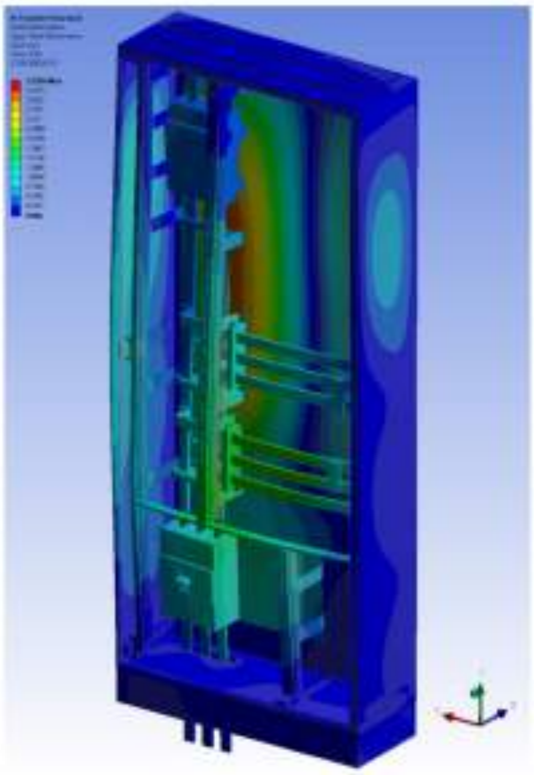

Figure 15. *Cont*.

(c)

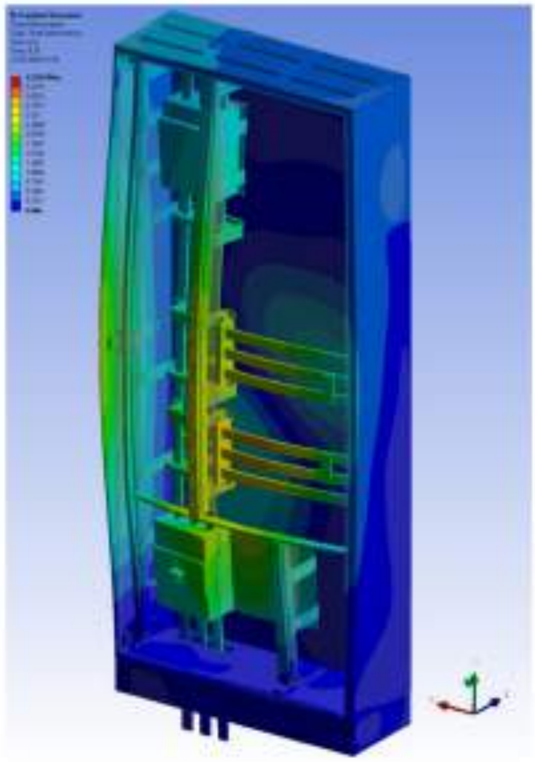

(d)

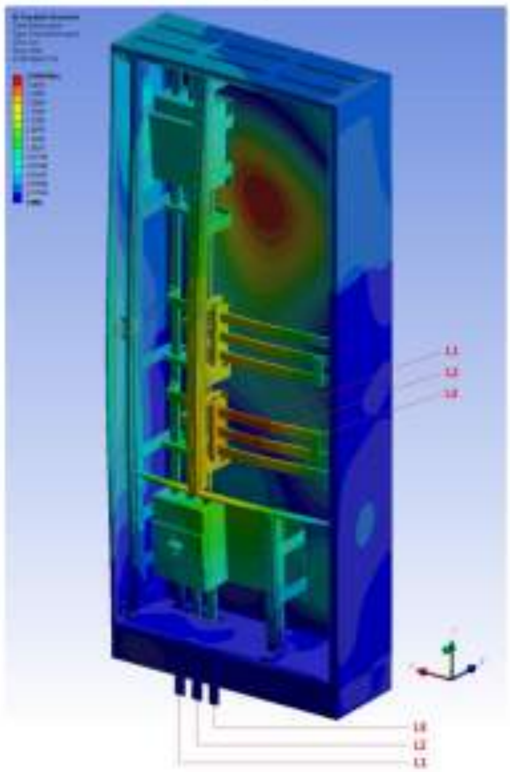

Figure 15. Results of deformations made for the low voltage switchgear at four different short circuit times: (**a**) T = 0.21 s; (**b**) T = 0.28 s; (**c**) T = 0.35 s; (**d**) T = 0.5 s.

Figure 16 shows the waveforms of electrodynamic forces for the points in Figure 15d.

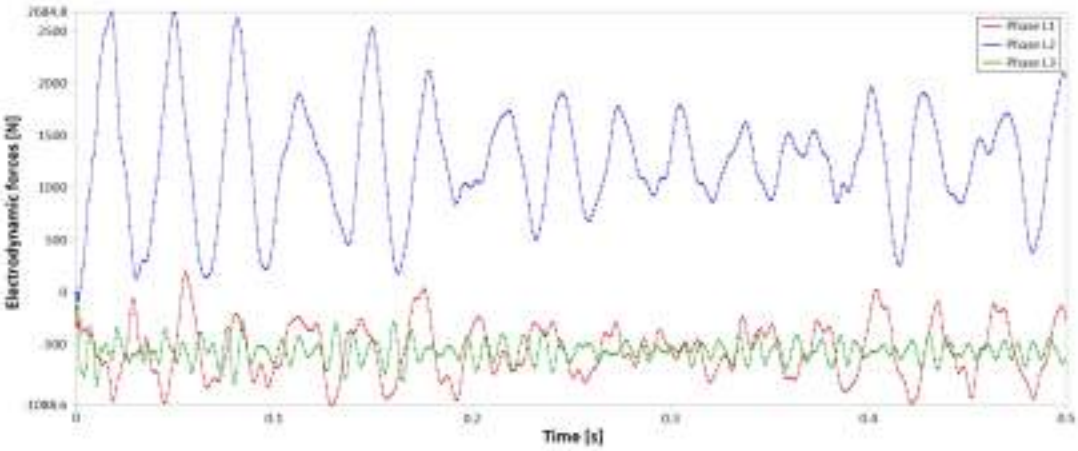

Figure 16. Results of tested quantities for low voltage switchgear: electrodynamic forces (points for L1, L2, L3 from the bottom).

Figure 17 shows the waveforms of electrodynamic forces in parallel, flat low-voltage current circuits. These are representations of the results of analytical calculations for the short circuit current, the course of which is shown in Figure 18 [24]. It has been noticed that the rate of the electrodynamic forces value on the exposed rail is twice as high.

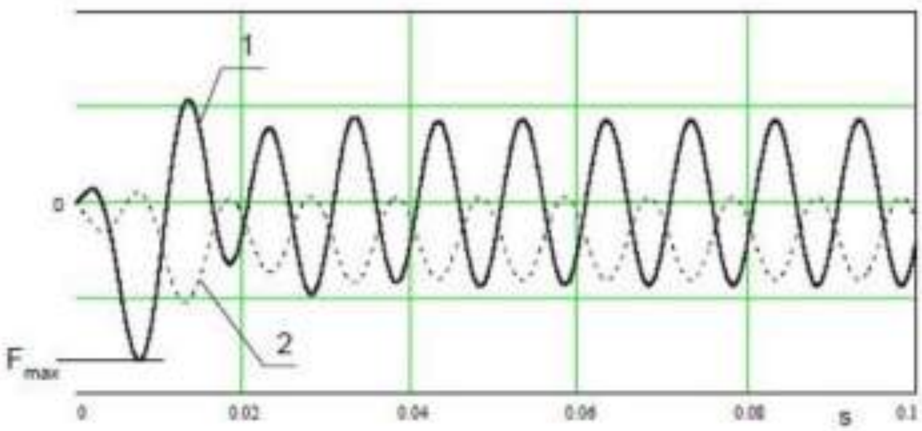

Figure 17. An example of the course of electrodynamic forces at a three-phase short circuit in a flat busbar system (the current in phase 1 runs as shown in Figure 15): 1—force acting on the middle rail L2, 2—force acting on the busbars L3 and L1 [24].

The simulation results presented in Figures 12a and 16 show a high convergence with the results of analytical calculations as to the value and nature of changes. Of course, in the case of current circuits in the switchgear, waveforms are caused by the occurrences (especially Figure 16):

- Contacts (flat connections);
- Current circuit system (these are not only parallel current circuits);
- Influence of switchgear operation (natural housing vibrations).

It is worth noting and emphasizing that the results of the calculations were used in the construction of the switchgear. Type tests according to specific subject standards were successful. The presented model and approach to the calculation of electrodynamic forces in high-current circuits can, therefore, be used to build similar switchgears.

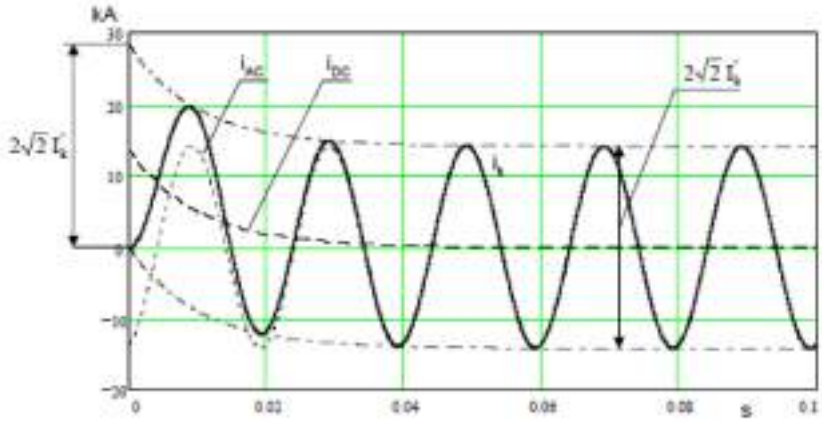

Figure 18. An example of the prospective short circuit current waveform at a remote short circuit in a low-voltage circuit, i_{AC}—periodic component, i_{DC}—non-periodic component, i_k—peak current [24].

6. Conclusions

The results are consistent not only with the theory and examples of normative calculations for asymmetric short circuit currents (IEC 60609 standard), but also with the analytical calculations presented in this work. The discrepancies are the result of simplifications in the case of analytical calculations for asymmetric short circuit currents. Additionally, the analysis of the maximum values of the electrodynamic forces and reduced stresses for certain other short circuit currents for the same rail system were also performed.

The presented results clearly show that it is worth stabilizing the current circuits by choosing proper supporting insulators. Despite the large electrodynamic forces occurring in power supply lines and the mechanical stresses stabilization on the receiving lines is achieved. Not only are the maximum values much lower than those allowed for copper tracks, but also their waveforms are very similar. The work was performed by simulating a three-phase busbar system in a similar way. Hence the force is distributed over the entire discharge system. The risk of transmission of vibrations to the power supply devices was also reduced, which is especially important in the case of a rigid connection.

The work is essential in order to provide the highlights for constructing the new types of medium- and low-voltage switchgears and their simulations, which is considered as future works. This work is also part of electrical contact systems research which are the main subject of this team's scientific interest.

Author Contributions: Conceptualization, M.S., S.Ł., Ł.K. (Łukasz Kolimas), Ł.K. (Łukasz Kozarek), D.D.R.; Data curation, M.S., S.Ł., Ł.K. (Łukasz Kolimas), Ł.K. (Łukasz Kozarek), D.D.R.; Formal analysis, M.S., S.Ł., Ł.K. (Łukasz Kolimas), Ł.K. (Łukasz Kozarek), D.D.R.; Investigation, M.S., S.Ł., Ł.K. (Łukasz Kolimas), Ł.K. (Łukasz Kozarek), D.D.R.; Methodology, M.S., S.Ł., Ł.K. (Łukasz Kolimas), Ł.K. (Łukasz Kozarek), D.D.R.; Project administration, M.S., S.Ł., Ł.K. (Łukasz Kolimas), Ł.K. (Łukasz Kozarek), D.D.R.; Resources, M.S., S.Ł., Ł.K. (Łukasz Kolimas), Ł.K. (Łukasz Kozarek), D.D.R.; Supervision, M.S., S.Ł., Ł.K. (Łukasz Kolimas), Ł.K. (Łukasz Kozarek), D.D.R.; Validation, M.S., S.Ł., Ł.K. (Łukasz Kolimas), Ł.K. (Łukasz Kozarek), D.D.R.; Visualization, M.S., S.Ł., Ł.K. (Łukasz Kolimas), Ł.K. (Łukasz Kozarek), D.D.R.; Writing—original draft, M.S., S.Ł., Ł.K. (Łukasz Kolimas), Ł.K. (Łukasz Kozarek), D.D.R.; Writing—review & editing, M.S., S.Ł., Ł.K. (Łukasz Kolimas), Ł.K. (Łukasz Kozarek), D.D.R.; All authors have read and agreed to the published version of the manuscript.

Funding: This research received no external funding

Conflicts of Interest: The authors declare no conflict of interest.

References

1. Wang, S.; Wang, S.; Li, H.; Yuan, D.; Wang, S. Mechanical characteristics analysis of defective transformer windings under short-circuit fault using 3-D FEM. In Proceedings of the 2017 20th International Conference on Electrical Machines and System (ICEMS), Sydney, Australia, 11–14 August 2017.
2. Kadkhodaei, G.; Sheshyekani, K.; Hamzeh, M.; Tavakoli, S.D. Multiphysics analysis of busbars with various arrangements under short-circuit condition. *IET Electr. Syst. Transp.* **2016**, *6*, 237–245. [CrossRef]

3. Vladimir, N.; Ančić, I.; Šestan, A. Effect of ship size on EEDI requirements for large container ships. *J. Mar. Sci. Technol.* **2018**, *23*, 42–51. [CrossRef]
4. International Electrotechnical Commission. *High-Voltage Switchgear and Controlgear—Part 102: Alternating Current Disconnectors and Earthing Switches*; IEC 62271-102:2012; International Electrotechnical Commission: Geneva, Switzerland, 2018.
5. International Electrotechnical Commission. *Short-Circuit Currents—Calculation of Effects—Part 1: Definitions and Calculation Methods*; IEC 60865-1:2011; International Electrotechnical Commission: Geneva, Switzerland, 2012.
6. Kulas, S.; Kolimas, Ł.; Piskała, M. Electromagnetic forces on contacts. In Proceedings of the IEEE Confrerence, Padova, Italy, 1–4 September 2008.
7. Kolimas, Ł.; Łapczyński, S.; Szulborski, M. Tulip contacts: Experimental studies of electrical contacts in dynamic layout with the use of FEM software. *Int. J. Electr. Eng. Educ.* **2019**, *1*, 1–4. [CrossRef]
8. Kolimas, Ł.; Łapczyński, S.; Szulborski, M.; Świetlik, M. Low voltage modular circuit breakers: FEM employment for modelling of arc chambers. *Bull. Pol. Acad. Sci. Tech. Sci.* **2020**, *68*, 1–10.
9. Jiaxin, Y.; Yang, W.; Lei, W.; Xiaoyu, L.; Huimin, L.; Longqing, B. Thermal dynamic stability analysis for the enclosed isolated-phase bus bar based on the subsegment calculation model. *IEEE Trans. Compon. Packag. Manuf. Technol.* **2018**, *8*, 626–634. [CrossRef]
10. Williams, D.M. Human factors affecting bolted busbar reliability. In Proceedings of the 2016 IEEE 62nd Holm Conference on Electrical Contacts (Holm), Clearwater Beach, FL, USA, 9–12 October 2016; pp. 86–93.
11. Yang, J.; Liu, Y.; Hu, D.; Wu, B.; Li, J. Transient vibration study of GIS bus based on FEM. In Proceedings of the IEEE PES Asia–Pacific Power and Energy Engineering Conference (APPEEC), Xi'an, China, 25–28 October 2016; pp. 1092–1095.
12. Triantafyllidis, D.G.; Dokopoulos, P.S.; Labridis, D.P. Parametric short-circuit force analysis of three-phase busbars-a fully automated finite element approach. *IEEE Trans. Power Deliv.* **2003**, *18*, 531–537. [CrossRef]
13. Yang, J.; Liu, Y.; Hu, D.; Wu, B.; Che, B.; Li, J. Transient electromagnetic force analysis of GIS bus based on FEM. In Proceedings of the International Conference on Condition Monitoring and Diagnosis (CMD), Xi'an, China, 25–28 September 2016; pp. 554–557.
14. Guan, X.; Shu, N. Electromagnetic field and force analysis of three-phase enclosure type GIS bus capsule. In Proceedings of the IEEE PES T&D Conference and Exposition, Chicago, IL, USA, 14–17 April 2014; pp. 1–4.
15. Popa, I.C.; Dolan, A.I. Numerical modeling of three-phase busbar systems: Calculation of the thermal field and electrodynamic forces. In Proceedings of the International Conference on Applied and Theoretical Electricity (ICATE), Craiova, Romania, 6–8 October 2016; pp. 1–9.
16. Jiaxin, Y.; Ruichao, W.; Huimin, L.; Longqing, B.; Hongjian, W. Research on the calculation methods of enclosed isolated phase busbar in short-circuit condition. In Proceedings of the IEEE 62nd Holm Conference on Electrical Contacts (Holm), Clearwater Beach, FL, USA, 9–12 October 2016; pp. 111–114.
17. Park, S.W.; Cho, H. A practical study on electrical contact resistance and temperature rise at at the connections of the copper busbars in switchgears. In Proceedings of the IEEE 60th Holm Conference on Electrical Contacts (Holm), New Orleans, LA, USA, 12–15 October 2014; pp. 1–7.
18. Gatherer, J.; Jackson, R.L. A multi-variable parametric study on the performance of bolted busbar contacts. In Proceedings of the IEEE 61st Holm Conference on Electrical Contacts (Holm), San Diego, CA, USA, 11–14 October 2015; pp. 124–131.
19. Farhana, M.; Jamil, M.K.M.; Dahaman, I.; Syafrudin, M. Study on the electromagnetic force affected by short-circuit current in vertical and horizontal arrangement of busbar system. In Proceedings of the International Conference on Electrical, Control and Computer Engineering 2011 (InECCE), Pahany, Malaysia, 21–22 June 2011; pp. 1–8.
20. Kadkhodaei, G.; Sheshyekani, K.; Hamzeh, M. Coupled electric– magnetic–thermal–mechanical modelling of busbars under shortcircuit conditions. *Generat. Transmiss. Distrib.* **2016**, *10*, 955–963. [CrossRef]
21. Zhong, J.Y.; Wu, S.J.; Wang, Z.; Guo, Y.J.; Qin, X.Y. A 3-D steady-state analysis of thermal behavior in EHV GIS busbar. *J. Electr. Eng. Technol.* **2016**, *11*, 781–789.
22. Khademi-Zahedi, R.; Alimouri, P. Finite element analysis to the effect of thermo-mechanical loads on stress distribution in buried polyethylene gas pipes jointed by electrofusion sockets, repaired by PE patches. *Energies* **2018**, *11*, 2818. [CrossRef]

23. Wang, Q.; Li, Y.; Yang, W.; Jiang, Z.; Song, Y.; Jiang, S.; Luo, Q.; Liu, D. Finite element simulation of multi-scale bedding fractures in tight sandstone oil reservoir. *Energies* **2020**, *13*, 131. [CrossRef]
24. Musiał, E. Rated currents in low-voltage AC installations and equipment. *Biul. SEP* **2011**, *40*, 3–50.
25. Kowalak, D. The Dynamic of the Low-Voltage Emergency Arc. Ph.D. Thesis, Gdańsk University of Technology, Gdańsk, Poland, 2013.
26. Krčum, M.; Zubčić, M.; Dlabač, T. Electromechanical analysis of the medium voltage earthing switch due to short-time and peak withstand current test. *Energies* **2019**, *12*, 3189. [CrossRef]
27. IEC 60609—Short Circuit Current Standard. Available online: https://pdf.wecabrio.com/iec-60609.pdf (accessed on 15 May 2020).

A6. *Transient Thermal Analysis of NH000 gG 100A Fuse Link Employing Finite Element Method*

energies

Article

Transient Thermal Analysis of NH000 gG 100A Fuse Link Employing Finite Element Method

Michał Szulborski [1,*], Sebastian Łapczyński [1], Łukasz Kolimas [1], Łukasz Kozarek [2], Desire Dauphin Rasolomampionona [1], Tomasz Żelaziński [3] and Adam Smolarczyk [1]

[1] Faculty of Electrical Engineering, Electrical Power Engineering Institute, Warsaw University of Technology, 00-662 Warsaw, Poland; seb.lapczynski@gmail.com (S.Ł.); lukasz.kolimas@ien.pw.edu.pl (Ł.K.); desire.rasolomampionona@ien.pw.edu.pl (D.D.R.); adam.smolarczyk@ien.pw.edu.pl (A.S.)

[2] ILF Consulting Engineers Polska Sp. z o.o., 02-823 Warsaw, Poland; lukaszkozarek@gmail.com

[3] Institute of Mechanical Engineering, Warsaw University of Life Sciences, 02-787 Warsaw, Poland; tomasz_zelazinski@sggw.edu.pl

* Correspondence: mm.szulborski@gmail.com; Tel.: +48-662-119-014

Abstract: In this paper, a detailed three-dimensional, transient, finite element method of fuse link NH000 gG 100 A is proposed. The thermal properties during the operation of the fuses under nominal (100 A) and custom conditions (110 and 120 A) are the main focus of the analyses that were conducted. The work concerns both the outside elements of the fuse link (ceramic body) and the elements inside (current circuit). Both the distribution of the electric current and its impact on the temperature of the construction parts of the fuses during their operating mode have been described. Temperature distribution, power losses and energy dissipation were measured using a numerical model. In order to verify and validate the model, two independent teams of scientists executed experimental research, during which the temperature was measured on different parts of the device involving the rated current. Finally, the two sets of results were put together and compared with those obtained from the simulation tests. A possible significant correlation between the results of the empirical tests and the simulation work was highlighted.

Keywords: fuse links; low voltage fuses; transient thermal analysis; design methods; FEM; modeling and simulation; ANSYS coupled analysis

Citation: Szulborski, M.; Łapczyński, S.; Kolimas, Ł.; Kozarek, Ł.; Rasolomampionona, D.D.; Żelaziński, T.; Smolarczyk, A. Transient Thermal Analysis of NH000 gG 100A Fuse Link Employing Finite Element Method. *Energies* **2021**, *14*, 1421. https://doi.org/10.3390/en14051421

Academic Editor: Anna Richelli

Received: 27 January 2021
Accepted: 26 February 2021
Published: 4 March 2021

1. Introduction

Currently, there are many fuse design solutions available on the market for various applications, for example, in the construction industry and other branches. Fuses are very efficient short-circuit protection devices. These are distinguished by a high short-circuit capacity (equal to 120 kA). Fuse links are often installed with circuit breakers, e.g., in series connection upstream of the circuit breaker. In this configuration, the inserted fuse significantly reduces the short-circuit current appearing on the circuit-breaker contacts and reduces the duration of a short-circuit. Fuse links are among the fastest-acting short-circuit protection means of relatively not-large dimensions. These devices are able to remove currents quickly and efficiently without risk of disturbance. Fuses are irreplaceable as a preventive measure of last resort in the event of failure or the spread of failure. Their advantages are also visible in many other applications that make replacement completely impossible in some situations. A model of a fuse link is shown in Figure 1 below.

Designing of NH fuse links often revolves around adaptation to comply with the guidelines contained in the standards (PN-EN 60269-1, PN-HD 60269-2) that allow to design and market a product that meets all requirements necessary and does not compromise safety protocols. NH-type fuses consist of a ceramic body to which the silver blades of the fuse are screwed on both sides. For fuse knives located inside the body, a perforated fuse is soldered, usually made of a strip of copper or its alloy. In the past, straight wire was used as flux. Currently, the shape of the topic element depends on the fuse link purpose. In order to improve cooling, thin tapes, usually copper or silver, are used to reduce the cross-section of the fuse as these metals have very good material properties and allow the dimensions of the fuses to be minimized. They are also quite resistant to the aging process.

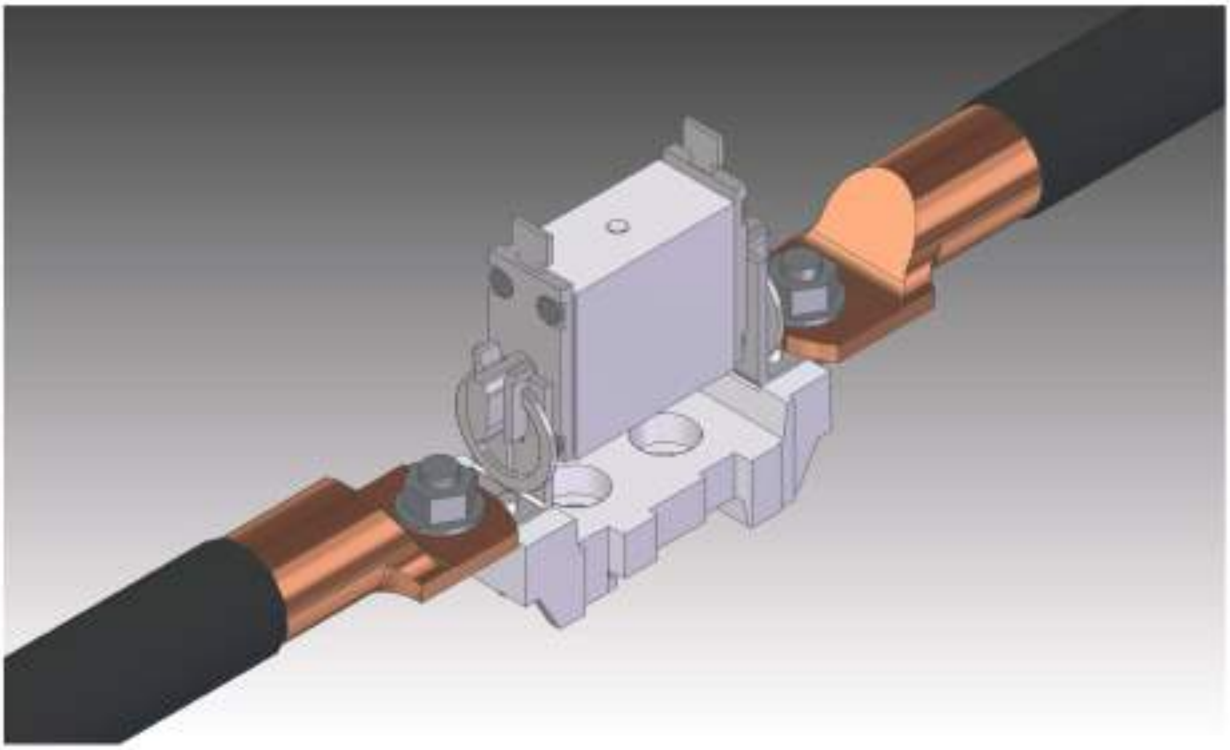

Figure 1. Model of a fuse link mounted in a fuse base during simulation research.

The width of the fuse and the number of constrictions made in it depend on the rated current of the fuse and type of its characteristic. During cumulative flow overload currents, the heat generated in the central tapering of the fuse dissolves from the center on both sides to the fuse knives; in this case, a fuse burnout occurs in the middle. It is different in the case of a short-circuit current, during the flow of which all the elements of the subject are burnt at the same time.

At this point, a technique called the Metcalf effect (M-Effect) should be mentioned. It consists in creating a eutectic alloy of an element's material with another metal (usually mounted as a solder ball on a fusible element). The temperature of the eutectic is below the temperature of the melting point of the fusible link. In the event of an overload, the fuse heats up and the solder diffuses with the fuse element. Due to this phenomenon, the fusible link exhibits greater resistance and, thus, shortens the time required to burn out the fuse in the feature around where the solder has been applied.

The main goal of this research was to construct and launch a fully operational and accurate transient thermal model of fuse link NH000 gG 100A on the basis of empirically derived results.

As indicated, thermal analysis aspects are mandatory to fully understand and improve the construction of fuses. This paper brings some novelties to the thermal analysis of fuse links by deriving a functional 3D finite element model (FEM):

- Introduction of a detailed, realistic model with exact physical properties;
- The digital model used a in transient state can also be used for analyzing a steady state;

- The studied models can be used to calculate power losses and energy dissipation during operation under various conditions;
- The model was validated by two independent sources;
- Shortening of the design and implementation time of new electrical devices by solving the validated FEM—in this case, fuses;
- Versatility of the employed model for modeling fuse links involving other current–voltage parameters in terms of other electrical apparatuses. Tests of heating with rated current are necessary for every electrical apparatus and switchgear;
- A transparent and elastic method to describe thermal physical phenomena, which result in a reduction concerning the number of prototypes, thus increasing economic efficiency and reducing the impact on the natural environment;
- The publications available so far are vital, and the authors of the manuscript have analyzed those. However, the available literature does not deal with issues related to an organized and formalized approach concerning the construction of thermal models of fuse links. The study may be used in scientific and research institutes, in the process of designing or enhancing the structure of electrical devices.

2. State of the Art

The problem of building a universal model of a fuse as a protective element of electrical devices is an important task. The importance of this research is evidenced by numerous publications. Nevertheless, many researchers choose only starting energy as a basic parameter. The publication [1] presents the calculation of the fuse melting point on the basis of the starting energy. The test layout was designed as a case study.

Fuse links are widely used to provide surge protection in many types of wiring systems and electrical equipment. In view of the short operating time of the fuse during certain disturbances under overcurrent conditions, the publication [2] presents a system for testing the low-voltage fuse operation time.

The authors of [3] treat the fuse link as one of the most important safeguards in a power system. Of course, knowing the thermal behavior of a fuse is an important aspect for an optimized design of the protection system of a particular element as part of a given power system as well as for the correct selection of a fuse rating to protect this element. The designed fuse must operate properly at rated and instantaneous overcurrent (e.g., at motor starting) and interrupt the short-circuit current. In the article, a two-dimensional thermal model was developed in order to study the temperature distribution on the fuse using the ANSYS program. This paper presents a summary of the results of this work.

First of all, we should mention a model of peripheral electrical apparatus [4]. The article presents the procedure of creating an energy-based fuse link model. A fuse model which takes into account both the pre-arc and arc characteristics of any time current characteristic curve has been developed in this paper. The fuse model developed was based on the energy from the fuses. The curve fitting technique allows to accurately determine the fuse's melting time. A MATLAB/Simulink simulation model in which the fuse parameters can be entered from the user interface was designed and run in order to test and verify the model conception.

To build an optimal fuse model, the authors used some of the results from the publication [5]. The article describes a new model that can calculate the melting time and fuse current only on the basis of the catalogue value of the Joule's integral given by the manufacturer. The calculated value on the fuse is compared to the catalog value, so that the circuit is open when the two values are equal. Two features allow us to easily and accurately obtain the value of the Joule's integral in the fuse for different circuits. One of them is a method of detecting the current in the fuse at any time, so that the fuse current can be accurately calculated. Regarding the second feature, the diffusion coefficient is taken into account so that the melting time can be accurately calculated, even when the fuse current is relatively small. It is not necessary to perform many fuse blowing experiments.

The fuse melting time and current can be calculated accurately and easily when the fuse is part of a large circuit of the power system [6,7].

The publications so far are vital, and the authors of this manuscript have used them. However, the available literature does not deal with issues related to an organized and formalized approach concerning the construction of fuse links thermal models.

The study may be used in scientific and research institutes in the process of designing or enhancing the structure of electrical devices. The presented results of simulation and empirical studies concern the analysis of non-linear physical phenomena. Such a model was also developed. The proposed method does not eliminate other thermal simulation models. The presented method (modeling method) may be a support for other methods. Hence, when looking at publications, the method can be based on, for example, the proposed innovative stepwise response matrix identification procedure, which is based on the combination of external non-linear least squares iteration for relocating time constants. The publication presents the structure of the algorithm, the connection of its main functions, describes those in detail and comments on the mathematical features of the proposed formulation concerning the identification problem. The model presented by the team has the possibility of cooperation among others with this method. To a great advantage, this can improve the accurate method of determining the temperature from only a partial result (approximation).

3. Theoretical Model

3.1. Fuse Link Thermal Energy

Thermal energy in a fuse link is generated by the rated current or the short-circuit current flowing through the main current circuit, being part of the fuse link structure and wires connected to the base of the fuse. The thermal energy from the current busbars is dissipated to the environment by convection, conduction and radiation [8].

The value of the electrical power generated on a given busbar length is the sequence of current and resistance, described below by means of the equation:

$$P = I^2 \times R \tag{1}$$

where P is the power dissipated per unit length (W), I is the current in the conductor (A) and R is the resistance per unit length of the conductor (Ω).

All calculations related to the current flow in the fuse links are possible using the following Maxwell equations [9]:

$$\nabla\ x\ \{H\} = \{J\} + \left\{\frac{\partial D}{\partial t}\right\} = \{J_s\} + \{J_e\} + \{J_v\} + \left\{\frac{\partial D}{\partial t}\right\} \tag{2}$$

$$\nabla\ x\ \{E\} = -\left\{\frac{\partial B}{\partial t}\right\} \tag{3}$$

$$\nabla\ \times\ \{B\} = 0 \tag{4}$$

$$\nabla\ \times\ \{D\} = \rho \tag{5}$$

where ∇x is the curl operator, $\nabla \cdot$ is the divergence operator, $\{H\}$ is the magnetic field intensity vector, $\{J\}$ is the total current density vector, $\{J_s\}$ is the applied source current density vector, $\{J_e\}$ is the induced eddy current density vector, $\{J_v\}$ is the velocity current density vector, $\{D\}$ is the electric flux density vector, t is the time, $\{E\}$ is the electric field intensity vector, $\{B\}$ is the magnetic flux density vector and ρ is the electric charge density.

For the calculation concerning the coupled heat transfer process between the carrier fluid (air) and the solid domains the, Navier–Stokes equation is used alongside the energy equations, described below [10].

The continuity equation is given by:

$$\frac{\partial u}{\partial x} + \frac{\partial v}{\partial y} + \frac{\partial w}{\partial z} = 0 \tag{6}$$

The momentum equation:

$$\rho \vec{v} \times \vec{\nabla} \vec{v} = -\vec{\nabla} p + \mu \vec{\nabla}^2 \vec{v} + \vec{F} \tag{7}$$

The expression of the energy equation is as follows:

$$\rho c_p \left(\frac{\partial Tu}{\partial x} + \frac{\partial Ty}{\partial y} + \frac{\partial Tw}{\partial z} \right) = \frac{\partial}{\partial x} \left(k \frac{\partial T}{\partial x} + u\tau \right) + \frac{\partial}{\partial y} \left(k \frac{\partial T}{\partial y} + v\tau \right) + \frac{\partial}{\partial z} \left(k \frac{\partial T}{\partial z} + w\tau \right) \tag{8}$$

where x, y and z are the Cartesian coordinates; u, v and w are the velocities in x, y and z, directions, respectively; $\vec{v}$ is the velocity vector, p is the pressure, ρ is the density, μ is the dynamic viscosity, $\vec{F}$ is the body force vector, T is the temperature, k is the thermal conductivity of air and τ is the viscous shear stress.

3.2. Heat Transfer during Fuse Link Operation

During heat transfer from fuse links, the following types of heat transfer to the environment can be distinguished [11]:

- Through radiation;
- By convection;
- By conduction.

All types of heat dissipation that may occur during physical phenomena must be taken into account in the fuse calculations. The heat transferred by the conductive material or the insulating material is implemented by conduction. On the other hand, in the case of a heated device in the air environment, e.g., unenclosed switchgear, heat is transferred to the environment by both radiation and convection [12]. While calculating the thermal phenomena of electrical apparatus for the rated load, the share of heat transfer by radiation and natural convection is similar (for a temperature difference of several dozen Kelvins). The conditions of heat transfer to the environment in thermal calculations are often determined using the so-called heat transfer coefficient k, which defines the total amount of heat transferred to the environment from a given surface per unit time from the cooled body to the environment [13]. The total coefficient for the fuse link placed in the air is, therefore, the sum of the coefficients of heat transfer to the environment by convection and radiation, which is shown in the following relation [14]:

$$k = k_r + k_k \tag{9}$$

where k_r is a heat transfer coefficient by radiation; k_k is a heat transfer coefficient by convection.

During the radiation of a given fuse and, therefore, of a current circuit, electromagnetic waves of different lengths are emitted. However, not all of them are capable of transferring thermal energy. Depending on the wavelength, these radiate more or less thermal energy [15]. The wavelengths that most effectively transfer heat energy to the environment are the waves in the range of 0.4–10 μm, lying in the so-called reddened area. The energy that is radiated from a given body is partially reflected, partially absorbed and passed through another body. This phenomenon is described by the following equation [16]:

$$\frac{Q_o}{Q} + \frac{Q_w}{Q} + \frac{Q_p}{Q} = 1 \tag{10}$$

where Q_o is a wave reflection coefficient; Q_w is a wave absorption coefficient and Q_p is a wave transmission coefficient.

Using the Stefan–Boltzmann law, it is possible to determine the radiation power P_{pr} in relation to the surface of the radiating body [17]:

$$P_{pr} = \varepsilon \sigma_o \Theta^4 \tag{11}$$

where ε is a black radiation coefficient of the given body; σ_o is a Stefan–Boltzmann coefficient and Θ is the radiating body temperature expressed in Kelvins.

Examples of the ε coefficient values for various materials from which fuse link current circuits can be made are presented in Table 1.

Table 1. ε coefficient values for various materials.

Material	Surface Status	ϑ (°C)	ε Coefficient Value
Aluminum	Polished	20	0.05
Aluminum	Rough	20	0.07
Copper	Oxidized	20–60	0.5–0.6
Copper	Polished	60	0.04
Silver	Polished	20	0.02

In electrical apparatuses, one can also observe the phenomenon of convection, which takes place between the elements of the electric apparatus and the gas (air or SF_6) or liquid (oil) in the immediate vicinity of, for example, a current circuit [18]. The convective motion of a gas or liquid largely depends on the type of motion forced, the shape and dimensions of the surface of the heated body or the physical properties of the media, which makes the convection process a complex process dependent on many factors. There are two types of convection phenomena that release heat to the environment: natural and forced [19,20].

In the case of natural convection (free movement), the movement of gas or liquid is caused by the difference in the density of the heated and cool particles, which generates the forces of lifting. The lighter heated particles are lifted upwards [21–23]. The process of forced convection takes place when the movement of the liquid or gas is caused by external forces generated, for example, by fans or wind. In both cases, the movement of particles around the heated solid can be of a laminar or turbulent particle flow. Laminar flow of gas or liquid particles occurs at low particle velocities, and turbulent flow follows laminar movement after exceeding the so-called critical speed. The movement of particles during the convection phenomenon has a very significant impact on the heat transfer from the cooled current circuit of the apparatus [24–26]. During laminar flow, the amount of heat released depends on the thermal conductivity of the gas or liquid. In the case of turbulent motion, the heat transfer process depends mainly on the thermal resistance of the boundary layers with laminar flow. The thinner the layers, the greater the conditions for heat exchange from the cooled body. Heat transfer by convection to the environment also depends on the physical properties of gases and liquids. These are mainly heat capacity, thermal conductivity, specific mass or dynamic viscosity [27–30].

4. Laboratory Setup

Nowadays, the initial prototypes of electrical devices are designed using 3D computer software and coupled programs for performing mechanical, thermal and electrodynamic analyses. At a time when such tools did not exist, designers constructed electrical devices based on mathematical calculations, experience and on the basis of available standards in force.

Currently, fuse links are also designed by manufacturers in accordance with the standard PN-EN 60269-1, PN-HD 60269-2. The scope of the standard includes standardized methods of testing fuse links, which are used in accredited laboratories to conduct type tests and tests of conformity of the manufactured devices with the given requirements of the standard. The performed tests allow to check the operation and construction of the apparatus, which was previously designed in 3D software, the simulation analysis of which could include some simplifications. Additionally, type testing is necessary to obtain a certificate for the product that the manufacturer wants to introduce to the market. In this work, a fuse link with a rated current of 100 A was subjected to tests in order to check the temperature fluctuations in the current circuit elements. A schematic of the layout used for laboratory measurements is shown in Figure 2 below.

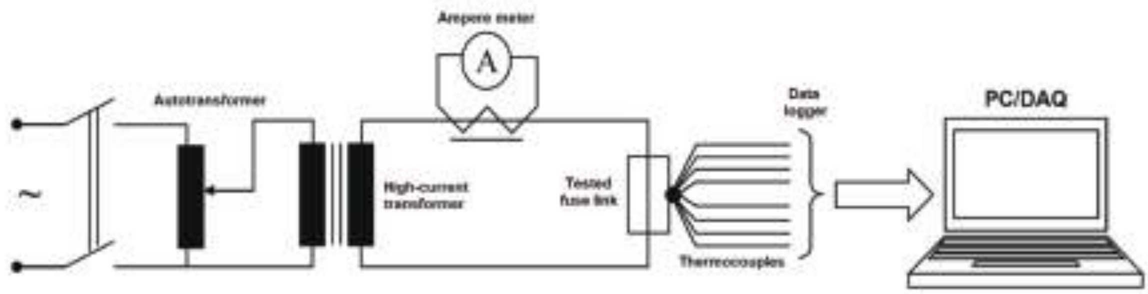

Figure 2. Diagram of the measuring system constructed for fuse link measurements.

Thermocouples were installed in different places of the device, as it is seen in Figure 3. This made it possible to perform the measurements in accordance with the above standard. Type K thermocouples were fixed using a special thermally conductive glue on the elements of the current circuit: upper and lower terminals (T1; T6); upper and lower electrical contacts (T2; T5—fuse link knives); on the fuse link body (T3; T4); T7 for measuring ambient temperature and T8 for measuring the power supply cable's temperature. The places where the thermocouples were installed depended on the previously performed computational analyses for the 3D model of this fuse link type in order to compare the obtained results.

After fixing the thermocouples, it was realized that their placement did not affect the operation of the device and did not cause any problems with its operation. No modifications were made to the fuse, which allowed the temperature fluctuations and rise to be measured correctly. In order to carry out the tests, it was necessary to prepare a test bench to record the temperature rise of the elements of the current circuit of the fuse link for specific currents: 100, 110 and 120 A. For this purpose, a single-phase autotransformer was used, to which a single-phase high-current transformer was connected. The autotransformer in this case was used to regulate the current at the output of the high-current transformer. In order to measure the current, a clamp meter (ammeter) was installed on the cable supplying the tested object—an overcurrent switch. In order to collect data from the installed thermocouples in the fuse link, two 4-channel temperature recorders with an accuracy of 0.1 °C were used, the sampling time of which was set to 1 s (temperature was measured on 6 thermocouples every second). Data from the recorder, via the USB communication interface, were sent online to the recorder software on a PC, where the heating charts of the tested elements were generated. That was depicted in Figure 2.

The length of the power supply cables powering the fuse link is precisely defined in the standard and those are respectively equal to 1 m from the bottom of the fuse link and 1 m from the top of the fuse link. These recommendations were followed during the tests, and the actual layout is shown in Figure 3.

The ambient temperature was measured using two other thermocouples immersed in the oil reservoir—the temperature oscillated around 22 °C.

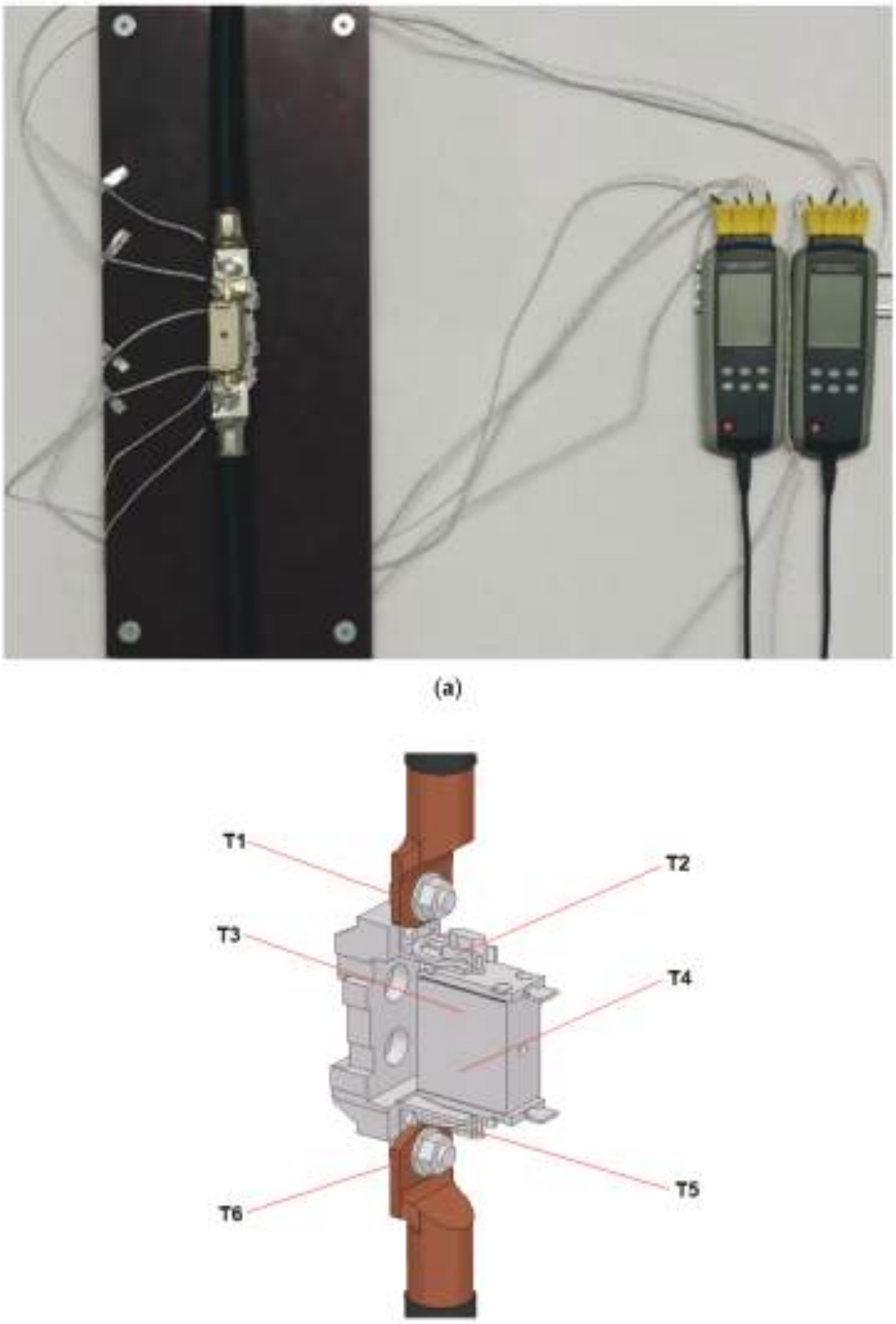

(**a**)

(**b**)

Figure 3. Fuse link with glued thermocouples (type K): (**a**) photo of the laboratory stand layout; (**b**) placement of thermocouples on the 3D fuse link model—T1, upper terminal; T2, upper electrical contact; T3, T4, fuse link body; T5, lower electrical contact; T6, lower terminal.

5. Experimental Work

5.1. Assumptions

As previously indicated, empirical work was conducted by two independent teams of researchers—Team A and Team B. In order to perform the thermal analysis, two stands, described in Section 4, were constructed. The fuse link NH000 gG 100 A has been verified with a rated current equal to 100 A. It is worth noting that according to the results presented in the tables below (Tables 2 and 3), temperature results for the thermocouples refer to the temperature fixed values. The measurements were recorded after the lab stand had been operating for two hours (7200 s). The measurements were taken each time for 10 fuse links—five fuse links per team.

Table 2. Results obtained by Team A for fuse link type NH000 gG 100 A.

Order Number	Fuse Link Type	Resistance (mΩ)	Power Losses(W)	T1 (°C)	T2 (°C)	T3 (°C)	T4 (°C)	T5 (°C)	T6 (°C)
1	NH 000 gG 100 A	0.51	6.70	38	50	57	56	46	36
2	NH 000 gG 100 A	0.57	6.80	40	51	60	58	48	35
3	NH 000 gG 100 A	0.56	6.80	39	52	59	57	44	38
4	NH 000 gG 100 A	0.52	6.70	41	52	61	59	43	40
5	NH 000 gG 100 A	0.55	6.80	38	51	53	53	45	37

Table 3. Results obtained by Team B for fuse link type NH000 gG 100 A.

Order Number	Fuse Link Type	Resistance (mΩ)	Power Losses (W)	T1 (°C)	T2 (°C)	T3 (°C)	T4 (°C)	T5 (°C)	T6 (°C)
1	NH 000 gG 100 A	0.54	6.85	40	53	62	62	45	38
2	NH 000 gG 100 A	0.53	6.85	41	54	61	60	46	39
3	NH 000 gG 100 A	0.51	6.85	38	56	63	61	47	36
4	NH 000 gG 100 A	0.56	6.75	40	51	58	56	43	40
5	NH 000 gG 100 A	0.54	6.75	40	52	60	57	46	39

5.2. Empirical Results

The results obtained by Team A and Team B are juxtaposed in Tables 2 and 3 below. The results were derived from two independent laboratory stands.

The results are also depicted on the chart shown in Figure 4 below.

The results obtained for a nominal current of 100 A by the two teams were consistent. Therefore, it was possible to draw the conclusion that the results of the empirical work were confirmed by the simulations and vice versa.

Additionally, in order to check different conditions, the thermal analysis was procured for currents equal to 110 and 120 A. The empirical results are presented in Figures 5 and 6 below.

Figure 7 below depicts the screens captured from a thermal imaging camera during the experimental work performed.

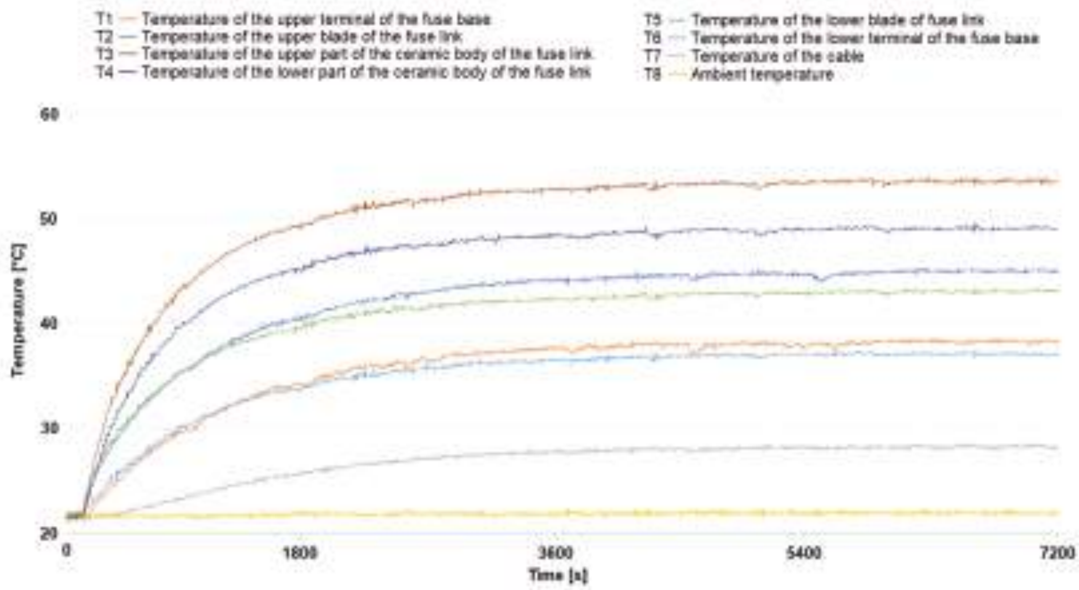

Figure 4. Chart showing results for thermocouples T1; T2; T3; T4; T5 and T6. The results were obtained for a time of 7200 s for a type of fuse NH000 gG 100 A and for a current of 100 A.

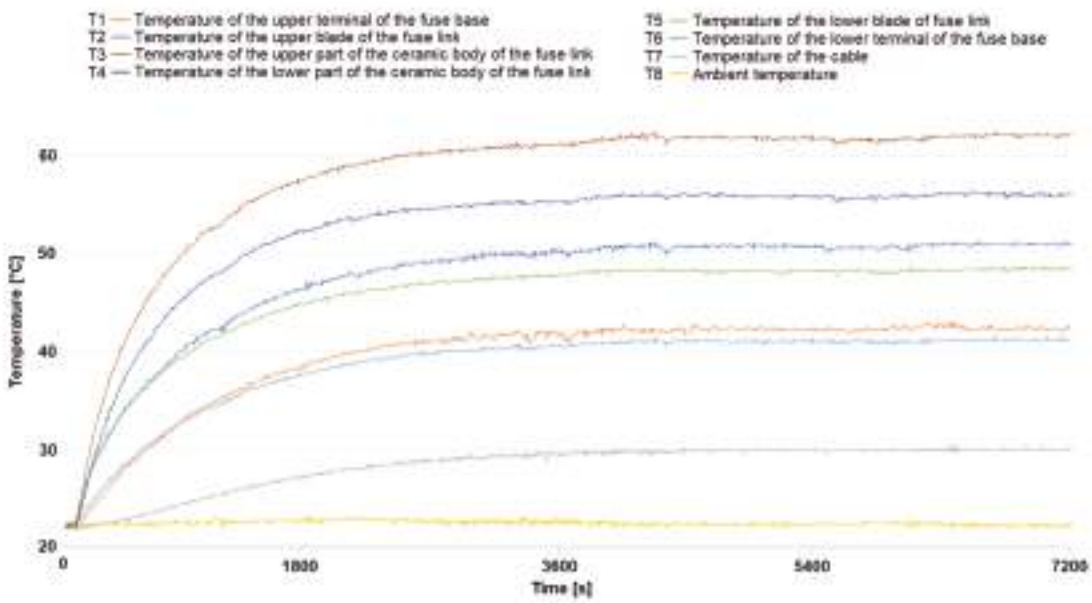

Figure 5. Chart showing results for thermocouples T1; T2; T3; T4; T5 and T6. The results were obtained for a time of 7200 s for a type of fuse NH000 gG 100 A and for a current of 110 A.

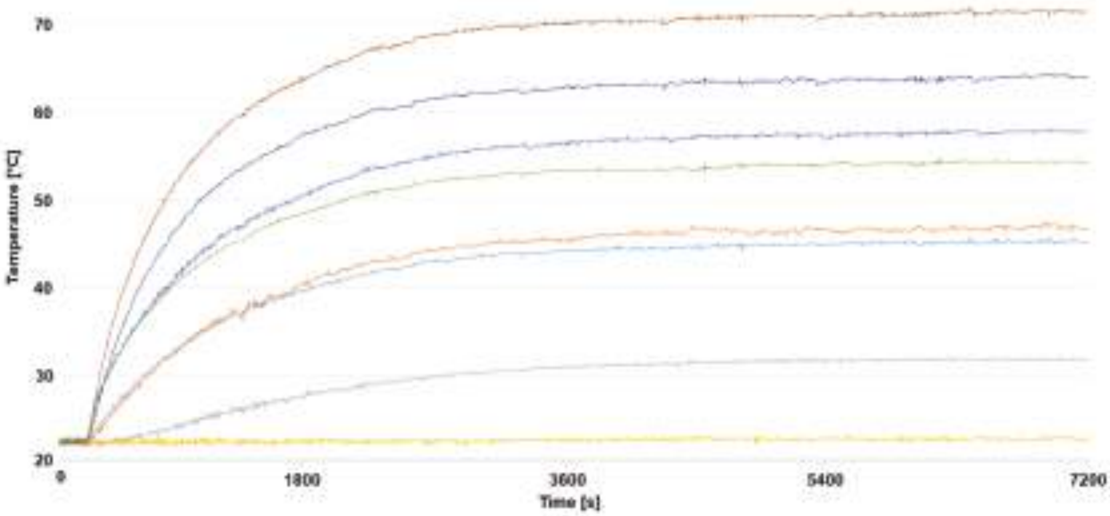

Figure 6. Chart showing results for thermocouples T1; T2; T3; T4; T5 and T6. The results were obtained for a time of 7200 s for a type of fuse NH000 gG 100 A and for a current of 120 A.

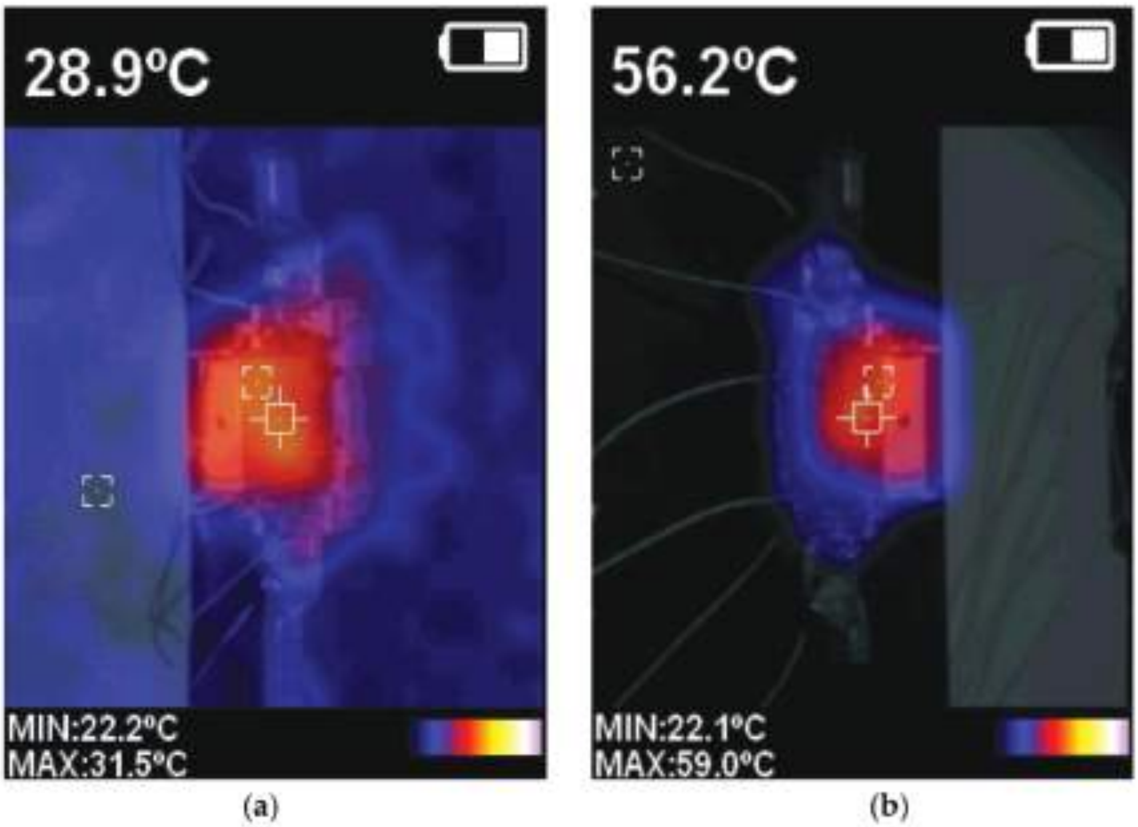

Figure 7. Screens captured from a thermal imaging camera during analysis: (**a**) after 5 min; (**b**) after maintaining the set temperature.

6. Simulations

6.1. Fuse Link Simulations for Rated Current of 100 A

The first coupled analysis was performed with the ANSYS Workbench using the coupled Maxwell 3D and Transient Thermal environments. This analysis made it possible to obtain precise results linked to the nominal current flowing through the fuse. The highest current density and ohmic losses in the fuse link, shown in Figure 8 below, were achieved on a fusible element inside the ceramic body. The effect of the current flow through the circuit breaker circuit was the generation of power losses in the form of released heat, presented in Figure 9 below. A thermal analysis was performed after the calculations related to the current flow. Further importation of data allowed calculating the temperature distribution obtained on the fuse link circuit. The highest temperature value, equal to 63 °C, was reached on the ceramic body.

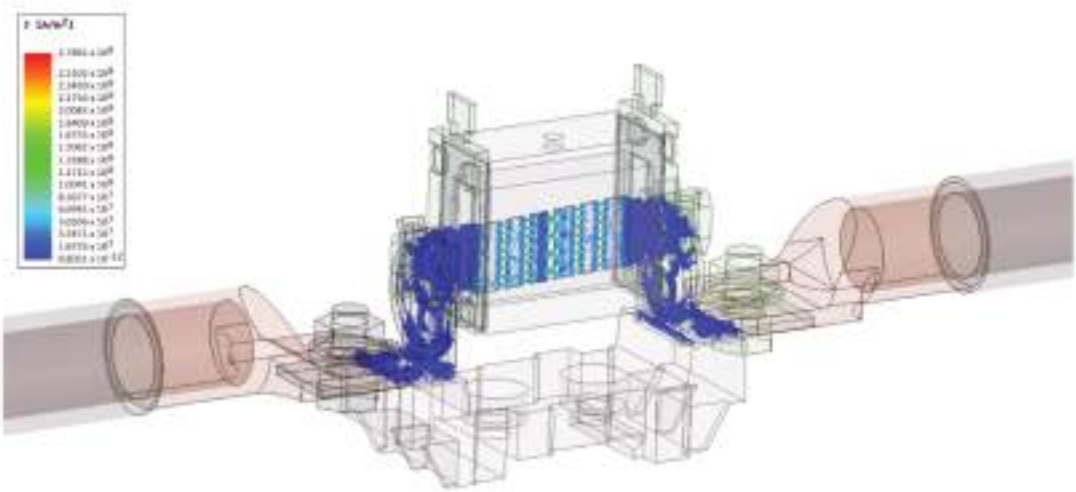

Figure 8. Distribution of the current density on the current circuit elements of the fuse model for a rated current of 100 A.

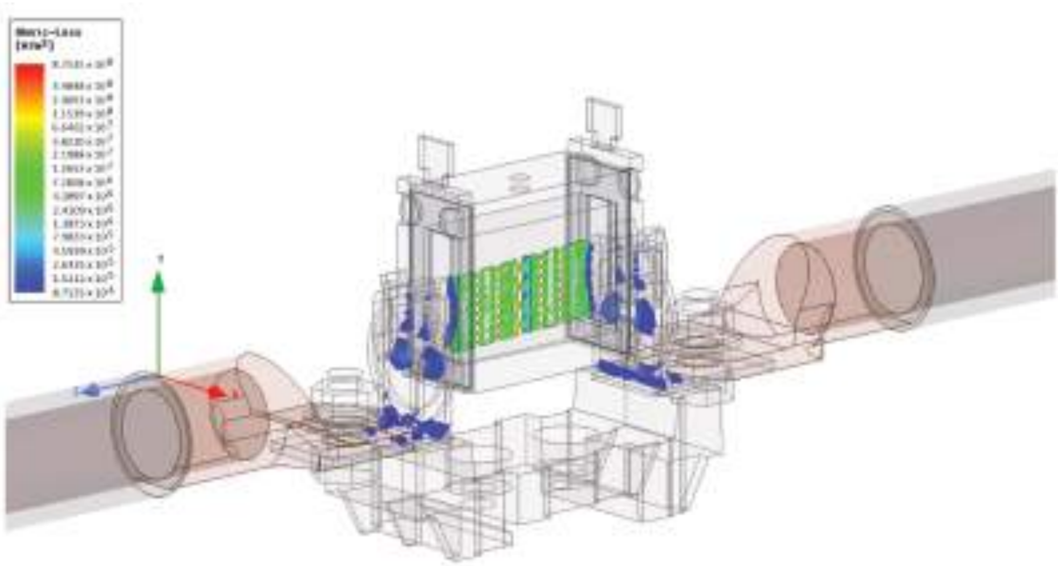

Figure 9. Ohmic losses on the current circuit elements of the fuse model for a rated current of 100 A.

Figure 10 below shows the graphical thermal analysis results for the tested fuse link.

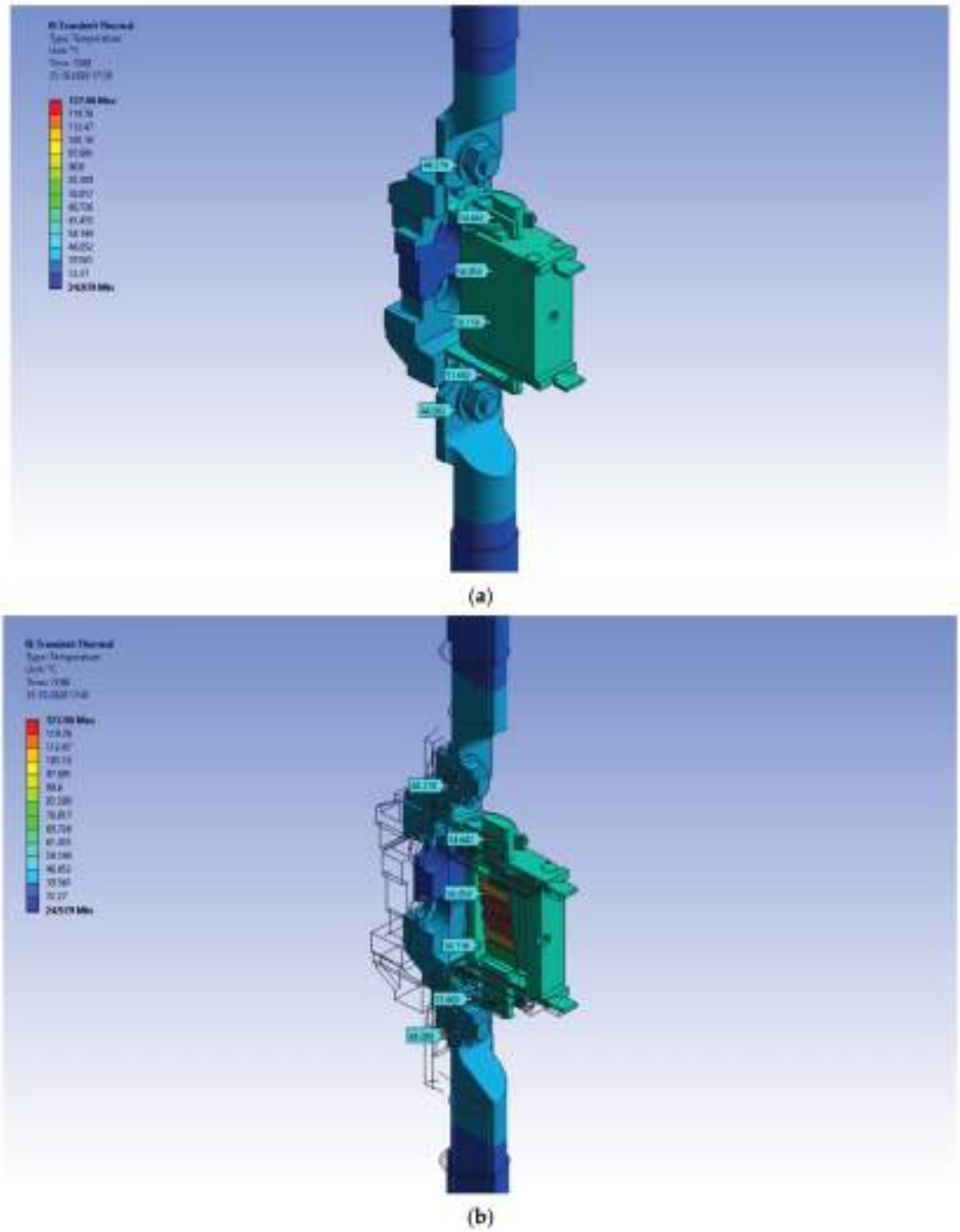

Figure 10. Graphical results of thermal analysis of the fuse link: (**a**) thermal analysis of the fuse link; (**b**) cross-section of the fuse link showing the fusible element.

For additional tests, a longer fuse link operating time has been defined. This test should prove that the temperature stabilized for a little longer. Despite this length, the measured time is still compatible with the standard.

For the purpose of validating the simulation results obtained with experimental tests, heating time histories were generated using the "Temperature Probe" option. Obtained waveforms were consolidated into one chart using the "Chart plot" function. Temperature charts are presented in Figure 11 below.

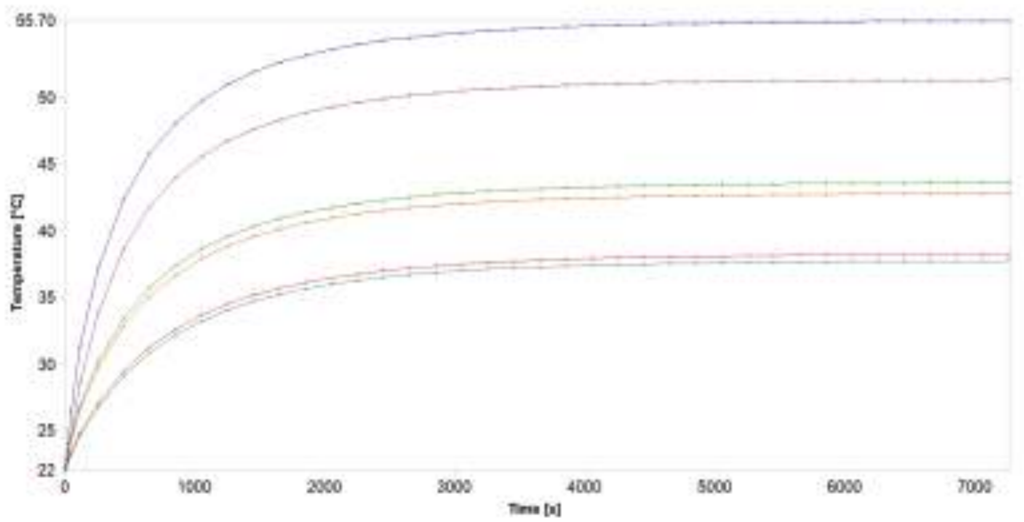

Figure 11. Chart showing results of ANSYS simulations for thermocouples T1; T2; T3; T4; T5 and T6. The results were obtained for a time of 7200 s for a type of fuse NH000 gG 100 A.

6.2. Fuse Link Simulations for Rated Current of 110 and 120 A

The results for simulations involving currents of 100, 110 and 120 A are juxtaposed in Table 4 below.

Table 4. Results for amperages of 100, 110 and 120 A for fuse link type NH000 gG 100 A. Results were obtained after 7200 s.

Order Number	Fuse Link Type	Simulation Amperage (A)	T1 (°C)	T2 (°C)	T3 (°C)	T4 (°C)	T5 (°C)	T6 (°C)
1	NH 000 gG 100 A	100	38	49	51	54	44	37
2	NH 000 gG 100 A	110	42	52	65	61	51	41
3	NH 000 gG 100 A	120	47	58	72	68	55	46

7. Results Summary

It has been shown, thanks to a numerical analysis confirmed by empirical work executed in parallel, that it is possible to develop a fuse link model taking into account the physical phenomena of temperature. Some of the most important tests of the constructed product type are thermal tests. The importance of such tests is indicated, inter alia, by standards, scientific publications and a number of operating experiences of electrical apparatus and switchgear devices.

The presented research showed a high convergence of the results obtained through simulation and empirical research. Therefore, the presented method for modeling electrical devices having a resistive power-breaking nature has been found to be correct. It should be noted that a similar approach can be used successfully in the design of fuse links operated in high-voltage networks. Thermal phenomena, regardless of the voltage level, have the same characteristics and could be analyzed in the same way as presented in this article. Application of the presented approach may also contribute to the work on DC fuses. This type of electrical device is currently experiencing a renaissance in connection with the development of smart networks based largely on renewable energy sources. Furthermore, in this type of network, the method of studying thermal phenomena may be similar to that presented in this article.

The authors did not reduce the thermal analysis only to the presentation of the results concerning the contact (insert knives). Six places on the apparatus were chosen for thermal analysis. The results were consistent across all comparative tables. The graphs (Figures 4 and 11) which show the waveforms from simulations and empirical tests indicate not only similar values of the set temperature but also the nature of the changes.

The aim of the simulation and research in the field of currents higher than the rated one was the fact that, in the case of fuse links, the current flow may be even up to several percent greater than the nominal current. Therefore, the simulation process for 110- and 120-A currents was repeated. The actual tests (Figures 5 and 6) were drafted to validate the results. In this case, the authors also obtained coherent results.

Undoubtedly, the added value of the presented approach to prototyping an electrical apparatus, which is a fuse link, is the ability to observe power losses and current density distribution over time. On this basis, already at the stage of preliminary assessments, it is possible to influence the shape of the fuse link and the outline dimensions of the apparatus body. The presented approach shortens the time between the conceptual work and product implementation. This allows for a quick response to the needs of consumers. In addition, it reduces material costs and environmental burden due to the construction of numerous prototypes.

The presented modeling method may be useful not only in scientific research but also in engineering. Looking at Figures 4 and 10, one can notice such a large convergence of characteristics that in the conditions of quick engineering check, a graphical method could be used. Figure 12 shows the idea of obtaining the temperature determined on the basis of only part of the test (the test shortened to the beginning of the formation of the temperature characteristics).

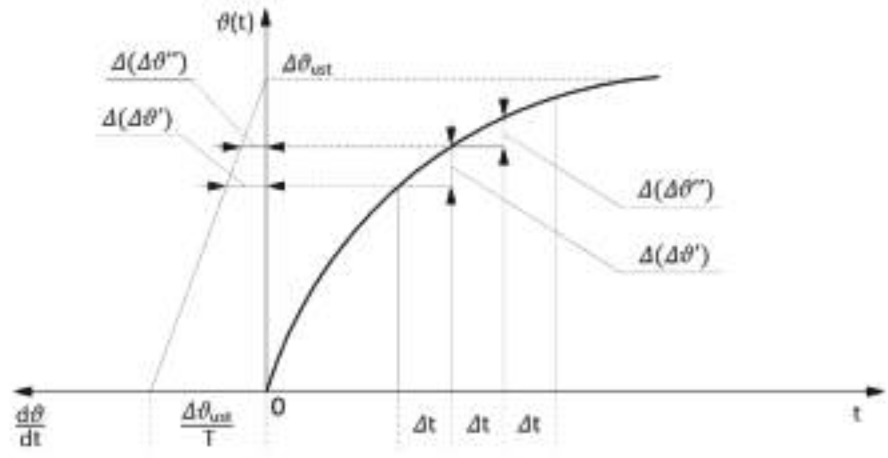

Figure 12. Graphical method of determining the value of the set temperature rise on the basis of a partial sample.

In order to quickly and precisely determine the set temperature, it is enough to use the presented modeling method. Shorten the simulation time to the necessary minimum (so as to be able to determine the temperature from the graphical method) and effectively use the presented approach.

8. Conclusions

Fuse links thermal analysis is an important aspect for scientific and engineering purposes. In order to better understand the phenomena occurring during fuse link thermal analysis, a detailed FEM was procured. The FEM was validated by empirical results. The validation showed that the derived results are valuable in terms of enhancing the design methods. The model itself can be described as functional and accurate in terms of the transient thermal analysis of fuse links. Therefore, it can be stated that the proposed model is a valuable asset that can reduce costs and simplify and accelerate works concerning research on new types of fuse links. An important aspect was the fact that validation was obtained from two independent sources, which makes this work significant. A crucial fact is that the introduced model is transient, but it can also be used for steady-state analysis. Electrical systems exploited in the world are focusing on power loss analysis. The fuse link FEM procured by our team was also made in order to calculate power losses for different conditions. This objective was not the primary one, but still it is essential in view of reducing electrical systems' exploitation costs.

Author Contributions: Conceptualization, M.S., S.Ł., Ł.K. (Łukasz Kolimas), Ł.K. (Łukasz Kozarek), D.D.R., A.S. and T.Ż.; data curation, M.S., S.Ł., Ł.K. (Łukasz Kolimas), Ł.K. (Łukasz Kozarek), D.D.R., A.S. and T.Ż.; formal analysis, M.S., S.Ł., Ł.K. (Łukasz Kolimas), Ł.K. (Łukasz Kozarek), D.D.R., A.S. and T.Ż.; investigation, M.S., S.Ł., Ł.K. (Łukasz Kolimas), Ł.K. (Łukasz Kozarek), D.D.R., A.S. and T.Ż.; methodology, M.S., S.Ł., Ł.K. (Łukasz Kolimas), Ł.K. (Łukasz Kozarek), D.D.R., A.S. and T.Ż.; project administration, M.S., S.Ł., Ł.K. (Łukasz Kolimas), Ł.K. (Łukasz Kozarek), D.D.R., A.S. and T.Ż.; resources, M.S., S.Ł., Ł.K. (Łukasz Kolimas), Ł.K. (Łukasz Kozarek), D.D.R., A.S. and T.Ż.; supervision, M.S., S.Ł., Ł.K. (Łukasz Kolimas), Ł.K. (Łukasz Kozarek), D.D.R., A.S. and T.Ż.; validation, M.S., S.Ł., Ł.K. (Łukasz Kolimas), Ł.K. (Łukasz Kozarek), D.D.R., A.S. and T.Ż.; visualization, M.S., S.Ł., Ł.K. (Łukasz Kolimas), Ł.K. (Łukasz Kozarek), D.D.R., A.S. and T.Ż.; writing—original draft preparation, M.S., S.Ł., Ł.K. (Łukasz Kolimas), Ł.K. (Łukasz Kozarek), D.D.R., A.S. and T.Ż.; writing—review and editing, M.S., S.Ł., Ł.K. (Łukasz Kolimas), Ł.K. (Łukasz Kozarek), D.D.R., A.S. and T.Ż. All authors have read and agreed to the published version of the manuscript.

Funding: This research received no external funding.

Institutional Review Board Statement: Not applicable.

Informed Consent Statement: Not applicable.

Data Availability Statement: Not applicable.

Conflicts of Interest: The authors declare no conflict of interest.

References

1. Demir, M.; Kahramanoğlu, G.; Yıldız, A.B. Calculating of fuse melting point for power electronics circuits by inrush energy and determination of the eligibility. In Proceedings of the 2016 18th European Conference on Power Electronics and Applications (EPE'16 ECCE Europe), Karlsruhe, Germany, 5–9 September 2016; pp. 1–6. [CrossRef]
2. Tong, J.; Zou, Y. Design of a fuse-time testing system on STM32. In Proceedings of the 2013 International Conference on Computer Sciences and Applications, Wuhan, China, 17–19 October 2013; pp. 406–409. [CrossRef]
3. Farahani, H.F.; Asadi, M.; Kazemi, A. Analysis of thermal behavior of power system fuse using finite element method. In Proceedings of the 2010 4th International Power Engineering and Optimization Conference (PEOCO), Shah Alam, Malaysia, 23–24 June 2010; pp. 189–195. [CrossRef]
4. Li, D.; Qi, L. Energy based fuse modeling and simulation. In Proceedings of the 2013 IEEE Electric Ship Technologies Symposium (ESTS), Arlington, VA, USA, 22–24 April 2013; pp. 487–492. [CrossRef]

5. Tanaka, T.; Yamasaki, M. Modeling of fuses for melting time and fusing current analysis; INTELEC 2004. In Proceedings of the 26th Annual International Telecommunications Energy Conference, Chicago, IL, USA, 19–23 September 2004; pp. 671–675. [CrossRef]
6. Pihler, J.; Stegne, M.; Kitak, P.; Glotic, A.; Fluher, B.; Ticar, I.; Voršic, J. Fuse application in medium voltage switchgear. In Proceedings of the 9th International Conference on Electric Fuses and their Applications (ICEFA), Maribor, Slovenia, 12–14 September 2011; pp. 110–118.
7. Grass, N. Protection of power electronic multi converter systems in AC and DC applications. In Proceedings of the 10th International Conference on Electric Fuses and their Applications, Frankfurt am Main, Germany, 14–16 September 2015; Dresden University of Technology: Dresden, Germany, 2015; pp. 1–5.
8. IEEE. *C37.42-2009—IEEE Standard Specifications for High-Voltage (>1000 V) Expulsion-Type Distribution-Class Fuses, Fuse and Disconnecting Cutouts, Fuse Disconnecting Switches, and Fuse Links, and Accessories Used with These Devices*; IEEE: New York, NY, USA, 2010. [CrossRef]
9. Kolimas, Ł.; Łapczyński, S.; Szulborski, M.; Świetlik, M. Low voltage modular circuit breakers: FEM employment for modeling of arc chambers. *Bull. Polish Acad. Sci. Techn. Sci.* **2020**, *68*, 61–70.
10. Gómez, J.C.; Tourn, D.H. gPV fuse: Special characteristics for photo voltaic cells protection. In Proceedings of the 9th International Conference on Electrical Fuses and their Applications (ICEFA), Maribor, Slovenia, 12–14 September 2011; pp. 1–9.
11. Gomez, J.C.; Tourn, D.; Nesci, S.; Zamarillo, G.R. PV cells protection by using class PV fuses. *IEEE Lat. Am. Trans.* **2013**, *11*, 531–537. [CrossRef]
12. Plesca, A.; Mihet-Popa, L. Thermal analysis of power rectifiers in steady-state conditions. *Energies* **2020**, *13*, 1942. [CrossRef]
13. Zhang, Y.; Su, J.; Zheng, L.; Li, R.; Yu, B.; Shang, W. Analysis of high-voltage DC fuse's ageing characteristics under the overload pulse current carrying mode and the caused short-circuit failure in series-resonant converter power source. *Int. J. Elect. Power* **2020**, *117*, 1–10. [CrossRef]
14. Pochanke, Z.; Daszczyński, T.; Kolimas, Ł. Uncertainty of the characteristics of electrical devices based on the measurements of the time-current characteristics of MV fuses. *Bull. Polish Acad. Sci. Tech. Sci.* **2020**, *68*, 751–757.
15. Gräf, T.; Kunze, A. Damage avoidance due to the use of high voltage fuses and temperature monitoring. In Proceedings of the 10th International Conference on Electric Fuses and their Applications, Frankfurt am Main, Germany, 14–16 September 2015; Dresden University of Technology: Dresden, Germany, 2015; pp. 1–7.
16. Plesca, A. Numerical analysis of thermal behaviour of DC fuse. *Energies* **2020**, *13*, 3736. [CrossRef]
17. Sarajlic, M.; Hribernik, M.; Kitak, P.; Pihler, J. LV melting fuse convection factor calculation using an optimization algorithm. In Proceedings of the 11th International Conference on Electric Fuses and their Applications, Egaleo, Greece, 16–19 September 2019; ICEFA: Athena, Greece, 2019; pp. 1–5.
18. Wilkins, R. Robust fuse design. In Proceedings of the 9th International Conference on Electrical Fuses and their Applications (ICEFA), Maribor, Slovenia, 12–14 September 2011; pp. 46–52.
19. Yang, C.P.; Ball, R.; Mcgordon, A.; Dhadyalla, G. Simulation methodologies to support novel fuse design for energy storage systems using COMSOL. In Proceedings of the IET Hybrid and Electric Vehicles Conference (HEVC 2013), London, UK, 6–7 November 2013; pp. 1–5.
20. Braga, G.; Zanin, A.; Peres, A.; Ghendy, C. Curve fitting analysis of expulsion fuse links through the cross-validation technique. In Proceedings of the 2018 IEEE PES Transmission & Distribution Conference and Exhibition—Latin America (T&D-LA); IEEE, Lima, Peru, 18–21 September 2018.
21. Łapczyński, S.; Szulborski, M.; Kolimas, Ł.; Kozarek, Ł.; Gołota, K. Mechanical and electrical simulations of tulip contact system. *Energies* **2020**, *13*, 5059. [CrossRef]
22. Wang, J.; Zhiyuan, L. Vacuum type high voltage fuse for external protection of shunt capacitors. In Proceedings of the 8th International Conference on Electric Fuses and their Applications, Clermont-Ferrand, France, 10–12 September 2007; IEEE: New York, NY, USA, 2007; pp. 98–102.
23. He, H.; Wang, J.A. High voltage vacuum type hybrid current limiting fuses for double protection of the shunt power capacitors. In Proceedings of the 8th International Conference on Electric Fuses and their Applications, Clermont-Ferrand, France, 10–12 September 2007; IEEE: New York, NY, USA, 2007; pp. 42–46.
24. Sakuraba, T.; Chen, S.; Gerlaud, A.; Milliere, L. Current distribution of high speed parallel dc fuses for hvdc protection. In Proceedings of the 10th International Conference on Power Electronics ECCE ASIA, Busan, Korea, 27–30 May 2019; pp. 3303–3308.
25. Szulborski, M.; Łapczyński, S.; Kolimas, Ł.; Kozarek, Ł.; Rasolomampionona, D.D. Calculations of electrodynamic forces in three-phase asymmetric busbar system with the use of FEM. *Energies* **2020**, *13*, 5477. [CrossRef]
26. Kühnel, C.; Schlegel, S.; Großmann, S. Investigations on the long-term behavior and switching function of fuse-elements for NH-fuse-links (gG) at higher thermal stress. In Proceedings of the 2017 6th International Youth Conference on Energy (IYCE), Budapest, Hungary, 21–24 June 2017.
27. De Tommasi, L.; Magnani, A.; De Magistris, M. Advancements in the identification of passive RC networks for compact modeling of thermal effects in electronic device s and systems. *Int. J. Num. Modell. Electron. Netw. Devic. Fields* **2018**, *31*, e2296. [CrossRef]
28. Kumar, A. Electro-thermal Characterizations, Compact Modeling and TCAD based De-vice Simulations of advanced SiGe:C BiCMOS HBTs and of nanometric CMOS FET. Micro andnanotechnologies/Microelectronics. Ph.D. Thesis, Université Bordeaux 1 Sciences et Technologie, Bordeaux, France, 2012.

29. Di Napoli, F.; Magnani, A.; Copola, M.; Guerriero, P.; D'Alessandro, V.; Codecasa, L.; Tricoli, P.; Daliento, S. On-line junction temperature monitoring of switching devices with dynamic compact thermal models extracted with model order reduction. *Energies* **2017**, *10*, 189. [CrossRef]
30. Zhan, Y.; Kumar, S.V.; Sapatnekar, S.S. *Thermal Aware Design*; Foundations and Trends®inElectronic Design Automation: Delft, The Netherlands, 2007; Volume 2, pp. 255–370.

A7. *Transient Thermal Analysis of the Circuit Breaker Current Path with the use of FEA Simulation*

energies

Article

Transient Thermal Analysis of the Circuit Breaker Current Path with the Use of FEA Simulation

Michał Szulborski [1,*], Sebastian Łapczyński [1], Łukasz Kolimas [1] and Daniel Zalewski [2]

[1] Faculty of Electrical Engineering, Electrical Power Engineering Institute, Warsaw University of Technology, 00662 Warsaw, Poland; seb.lapczynski@gmail.com (S.Ł.); lukasz.kolimas@ien.pw.edu.pl (Ł.K.)
[2] PGE Dystrybucja S.A. Division in Warsaw, 04470 Warsaw, Poland; Daniel.Zalewski@pgedystrybucja.pl
* Correspondence: mm.szulborski@gmail.com; Tel.: +48-662-119-014

Abstract: The finite element analysis (FEA) is an essential and powerful numerical method that can explicitly optimize the design process of electrical devices. In this paper, the employment of the finite element method (FEM) as ANSYS is proposed in order to aid electrical apparatus engineering and modeling of low voltage modular circuit breakers. The procured detailed model of a miniature circuit breaker (MCB) was undergoing transient thermal simulations of the current path. Acquired data were juxtapositioned with experimental data procured in the laboratory. The reflection of the simulation approach was clearly noted in the experimental results. Mutual areas of the modeled element expressed similar physical properties and robustness errors while tested in the specific conditions—faithfully reflecting those that were experimented with. Moreover, the physical phenomena essential for electrical engineering could be determined on the model stage. These types of 3D models can be used to analyze the thermal behavior of the current path during the current flowing condition.

Keywords: low voltage circuit breaker; current path; transient thermal analysis; design methods; FEM; modeling and simulation; ANSYS coupled analysis

Citation: Szulborski, M.; Łapczyński, S.; Kolimas, Ł.; Zalewski, D. Transient Thermal Analysis of the Circuit Breaker Current Path with the Use of FEA Simulation. *Energies* **2021**, *14*, 2359. https://doi.org/10.3390/en14092359

Academic Editor: Acha-Daza Enrique

Received: 9 March 2021
Accepted: 18 April 2021
Published: 21 April 2021

1. Introduction

Miniature circuit breakers (MCB) are constructed in accordance with current standards (e.g., European standards; IEC 60947). These requirements concern low voltage circuit breakers (LVCB; MCB). Despite the small sizes of the mentioned devices, they are adapted to effectively switch off the overload and short-circuit currents and protect the other elements of the electrical systems, such as cables and wires [1–3]. During the process of extinguishing the electric arc in the circuit breaker, complex physical phenomena occur, such as heat released in the arc channel and the formation of electrodynamic forces, causing stress, affecting the contacts of the circuit breaker [4]. These phenomena also affect the structural elements the device is made of (copper; steel; ferromagnetic; bimetals; aluminum; polymers, etc.). These occurrences can cause damage to the breaker after exceeding the critical values of electrical durability or temperature [5].

The crucial element of the circuit breaker construction is the current path of the circuit breaker. During the switching off of the short circuit current, the current path is exposed to the thermal and mechanical influences, which can lead to the permanent damage of the element or even the whole circuit breaker [6,7]. The current paths vary in shape and size of electrical contacts. The greater the rated current of a circuit breaker, the stronger (more massive) the electrical contacts are in the current path [8].

When the breaker contacts are closed, the operating current flows through the circuit breaker [9,10]. This results in Joule losses in current circuit elements that have very low resistances, such as contacts (transition resistance), short circuit breaker coils, and flexible connections of bimetal. Therefore, the breaker must effectively dissipate the heat generated in it by these elements [11,12].

In order to verify the construction guidelines and necessity of chosen solutions, many tests and simulations have been carried out that allow detection of defects and optimization of the current path at the project stage [13]. These measures are essential to determine the appropriate cross-section of the main current path inside the circuit breaker (Figure 1) and to check how the heat is dissipated from the current circuit by means of conduction, convection, and radiation [14].

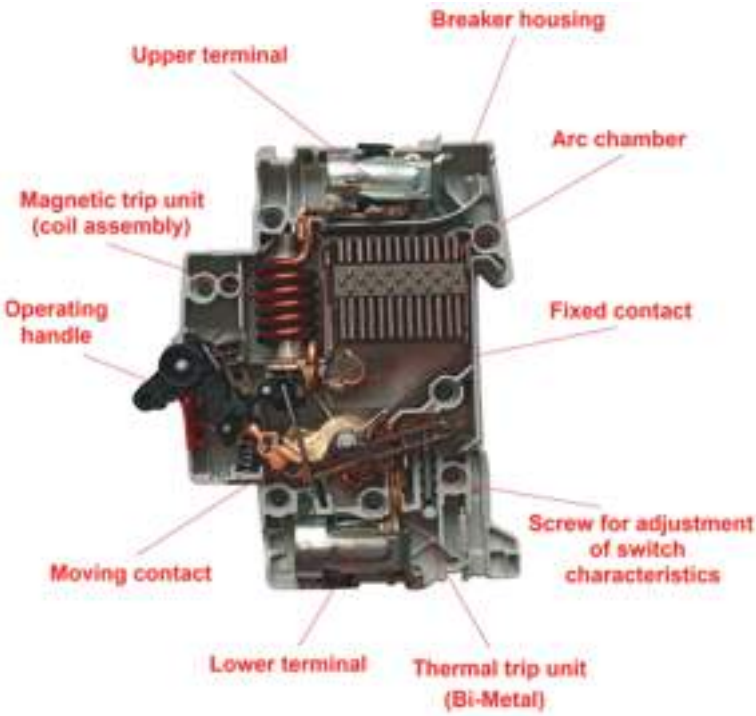

Figure 1. Basic construction elements of a miniature circuit breaker (MCB).

The usage of finite element method (FEM) coupled simulations is very effective for running a multiple analysis concerning electrical, thermal, and material durability aspects. The huge advantage of this method is the ability to check complicated scenarios employing various boundary conditions [15,16].

It is worth referring to the groundbreaking and important document "Grid 2030". The United States, through the Department of Energy (DOE), envisions the future power grid as a fully automated power transmission network with the ability to monitor and control each network node, ensuring a two-way flow of information and energy between all nodes in the transmission and distribution process from the power plant to the end user [17–20]. Optimization of the operation of the air circuit breaker (MCB) and the compact circuit breaker (MCCB) is currently being conducted [21]. Much of the research is focused on the optimization of extinguishing chambers [22–25]. Less frequently, the tests concern single and two-point contact systems, reducing the transition resistance [25–28]. In order to be able to fully prepare modular electrical devices for digitization understood as linking functions with intelligence in action, it is necessary to build, among others, FEM models and appropriate described electronics [28–30].

As mentioned, research works in the field of modular electrical devices are carried out, some of them quite advanced. The authors present dynamic voltage models [31,32] and CFD models [33–39].

The paper presents an advanced dynamic thermal model supporting research on:

- Current carrying capacity;
- Selection of the release system (short-circuit and overcurrent module);

- Shaping the contact system;
- Materials used.

The originality of the work is related to the capabilities of the model and its functionality (some of which is written above):

- Proper modeling of the current path, including the routing of the arc channel;
- Shaping the contact system, the entire transition resistance;
- Selection of materials;
- Introduction of a detailed, realistic model with exact physical properties;
- The studied models can be used to calculate power losses and energy dissipation during operation under various conditions;
- Shortening the design and implementation time of new electrical devices by solving the validated FEM model, in this case MCB;
- A transparent and elastic method to describe thermal physical phenomena, which results in a reduction concerning the number of prototypes, increasing economic efficiency and reducing the impact on the natural environment;
- The publications available so far are vital, and the authors of the manuscript have used them for analysis. However, the available literature does not deal with issues related to an organized and formalized approach concerning construction of thermal models of fuse-links. The study may be used in scientific and research institutes in the process of designing or enhancing the structure of electrical devices.

2. Assumptions for Theoretical Thermal Model

The thermal energy in the current path of MCB is generated by the rated current or short circuit current flowing through the current circuit, which is the main part of the circuit breaker construction with wires connected to its terminals. The thermal energy from the current path is dissipated into the environment by convection, conduction, and radiation.

The value of the electric power generated on a given breaker current path length is the aftermath of current and resistance, described below by means of the equation:

$$P = I^2 \cdot R \tag{1}$$

where P is power dissipated per unit length (W), I is current in the conductor (A), and R is resistance per unit length of the conductor (Ω).

All calculations related to the current flow in the current path are possible using the following Maxwell equations:

$$\nabla\ x\ \{H\} = \{J\} + \left\{\frac{\partial D}{\partial t}\right\} = \{J_s\} + \{J_e\} + \{J_v\} + \left\{\frac{\partial D}{\partial t}\right\} \tag{2}$$

$$\nabla\ x\ \{E\} = -\left\{\frac{\partial B}{\partial t}\right\} \tag{3}$$

$$\nabla \cdot \{B\} = 0 \tag{4}$$

$$\nabla \cdot \{D\} = \rho \tag{5}$$

where $\nabla\ x$ is curl operator, ∇ is divergence operator, $\{H\}$ is magnetic field intensity vector, $\{J\}$ is total current density vector, $\{J_s\}$ is applied source current density vector, $\{J_e\}$ is induced eddy current density vector, $\{J_v\}$ is velocity current density vector, $\{D\}$ is electric flux density vector, t is time, $\{E\}$ is electric field intensity vector, $\{B\}$ is magnetic flux density vector, and ρ is electric charge density.

For the calculation concerning the coupled heat transfer process between the carrier fluid (air) and the solid domains, the Navier–Stokes equation is used alongside the energy equations; these are described below:

Continuity equation:
$$\frac{\partial u}{\partial x} + \frac{\partial v}{\partial y} + \frac{\partial w}{\partial z} = 0 \tag{6}$$

Momentum equation:
$$\rho \vec{v} \cdot \vec{\nabla} \vec{v} = -\vec{\nabla} p + \mu \vec{\nabla}^2 \vec{v} + \vec{F} \tag{7}$$

Energy equation:
$$\rho c_p \left(\frac{\partial Tu}{\partial x} + \frac{\partial Ty}{\partial y} + \frac{\partial Tw}{\partial z} \right) = \frac{\partial}{\partial x}\left(k\frac{\partial T}{\partial x} + u\tau \right) + \frac{\partial}{\partial y}\left(k\frac{\partial T}{\partial y} + v\tau \right) + \frac{\partial}{\partial z}\left(k\frac{\partial T}{\partial z} + w\tau \right) \tag{8}$$

where $x,\ y,\ z$ are the Cartesian coordinates; u, v, w are the velocities in x, y, z directions; $\vec{v}$ is the velocity vector; p is the pressure; ρ is the density; μ is the dynamic viscosity; $\vec{F}$ is the body force vector; T is the temperature; k is the thermal conductivity of air; τ is the viscous shear stress; and c_p is the specific heat.

During heat transfer from current paths, the following types of heat transfer to the environment can be distinguished:

- Through radiation (radiation);
- By convection (natural or forced);
- By conduction (conductivity).

In the case of performing calculations for the current paths of electrical apparatus, all types of heat dissipation may occur.

The heat transferred by the conductive material or the insulating material is carried out by conduction. On the other hand, in the case of a heated current path placed in the air, e.g., an unenclosed switchgear (in an open version), heat is transferred to the environment by both radiation and convection.

When calculating the thermal (thermal) current paths of electrical apparatus for the rated load, the share of heat transfer by radiation, and natural convection is similar (for a temperature difference of several dozen Kelvin).

The conditions of heat transfer to the environment in thermal calculations are often determined using the heat transfer coefficient k, which defines the total amount of heat given off to the environment from a given surface per unit time from the cooled body to the surroundings.

The coefficient for the current path placed in the air is, therefore, the sum of the coefficients of heat transfer to the environment by convection and radiation, which is illustrated by the following dependence:

$$k = k_r + k_k \tag{9}$$

where k_r is the coefficient of heat transfer by radiation and k_k is the coefficient of heat transfer by convection.

$$\frac{Q_o}{Q} + \frac{Q_w}{Q} + \frac{Q_p}{Q} = 1 \tag{10}$$

where Q_o is a wave reflection coefficient, Q_w is a wave absorption coefficient, and Q_p is a wave transmission coefficient.

Using the Stefan–Boltzman law, it is possible to determine the radiation power P_{pr} in relation to the surface of the radiating body:

$$P_{pr} = \varepsilon \sigma_o \Theta^4 \tag{11}$$

where ε is a black radiation coefficient of the given body, σ_o is a Stefan–Boltzman coefficient, and Θ is radiating body temperature expressed in Kelvins.

During radiation from a given current path, electromagnetic waves of different lengths are sent. However, not all of them are capable of transferring thermal energy. Depending on the wavelength, they radiate thermal energy to a greater or lesser extent. The wavelengths that most effectively transfer heat energy to the environment are the waves in the range 0.4–10 μm, lying in the so-called reddened area.

The energy that is radiated from a given body is partially reflected, partially absorbed, and passed through another body; this phenomenon is described by the following formula:

$$dQ = -\lambda S \; grad \; \vartheta \; dt \tag{12}$$

$$P_c = -\lambda S \; grad \; \vartheta \tag{13}$$

$$P = -\lambda \; grad \; \vartheta \tag{14}$$

where dQ is the amount of heat energy transferred by conduction through the surface S over time dt, grad ϑ is the temperature gradient normal to the surface S, λ is the material's thermal conductivity coefficient, P_c is the total heat power that has been transmitted through the section S by conduction, and P is the heat power transferred by a unit area by conduction.

The value of the λ coefficient for all bodies depends on their temperature. In addition, in the case of solids, it depends on the structure of the material, specific weight, pressure, and humidity. In the case of electrically insulating materials, the thermal conductivity is several orders of magnitude lower in relation to, for example, the copper current path.

Energy exchange between adjacent surfaces or between a surface and its surroundings can have a large impact on the overall heat distribution. Hence, although the radiation effects generally affect the heat transfer solution only through the boundary conditions, the coupling is particularly strong due to the non-linear temperature dependence of radiation. For this reason, the starting points are the equations below.

Extending the Stefan–Boltzmann law for the n-surface system, the energy balance for each surface can be described by the Siegal and Howell equation, which relates energy losses to surface temperatures:

$$\sum_{i=1}^{n} \left(\frac{\delta_{ji}}{\varepsilon_i} - F_{ji} \cdot \frac{1-\varepsilon_i}{\varepsilon_i} \right) \frac{1}{A_i} \cdot Q_i = \sum_{i=1}^{n} (\delta_{ji} - F_{ji}) \sigma \cdot T_i^4 \tag{15}$$

where n—number of surfaces, δ_{ji}—Kroneckers delta, ε_i—emisivity, F_{ji}—radiation factor, A_i—surface area, Q_i—energy losses, σ—Boltzman factor, and T_i—absolute temperature.

From the first law of thermodynamics, which speaks about conservation of energy, it is possible to find the physical basis in the form of the equation for conduction and convection:

$$\rho \cdot c \left(\frac{\partial T}{\partial t} + \{v\}^T \cdot \{L\} \cdot T \right) + \{L\}^T \cdot \{q\} = \dddot{q} \tag{16}$$

where ρ—density, c_p—specific heat, T—temperature, t—time, $\{L\}$—vector operator, $\{v\}$—velocity vector, $\{q\}$—heat flux vector, and $\dddot{q}$ —the rate of heat generation.

The heating of the contacts of the circuit breaker is generally considered by means of tests and calculations for two cases:

- Current paths heating up under continuous load with rated currents;
- Current paths heating up with the flow of short-circuit currents.

In the first case, the tested current paths reach the state of thermal equilibrium when the amount of heat released in the current path corresponds to the amount of heat given off to the environment. The duration of the temperature settling is five times the constant T.

In the case of heating of the current paths by the flow of instantaneous short-circuit currents, the amount of heat given off to the environment at the moment of their duration is negligibly small. The temperature achieved depends mainly on the amount of heat released during the passing short-circuit current.

In both considered cases, a very important parameter is the permissible temperature values of individual elements of the circuit breaker circuit. It is worth paying attention to the fact that the value of the permissible temperature during short-term heating in short-circuit current conditions may be higher than in the case of long-term heating with rated current. This is due to the fact that the effects of short-term thermal action, despite the higher value of the current, are smaller (not exceeding the permissible value).

Permissible temperatures for current paths are determined by taking into account the following factors:

- Contact resistance;
- Mechanical strength of track elements;
- Thermal resistance of the insulation surrounding the current path.

The increase in temperature of the conductive material reduces its mechanical strength. In the case of copper, under continuous rated load conditions, the temperature rises in the range of 20–100 °C, the tearing strength decreases by approx. 10%, for 150 °C by approx. 15%, and for 200 °C by 25%. However, in the case of heating the current path with a short-circuit current from the ambient temperature of 20 °C to 300 °C, it reduces the tear strength by 15%.

Taking into account the factors described above and on the basis of tests, the permissible limit temperature increases for the external parts of overcurrent switches were defined in the IEC 60898-1: 2015 standard.

3. Design Assumptions for Circuit Breaker 3D Model

Currently, designing electrical apparatus is based on the use of tools (programs) for computer-aided design and prototyping of computer-aided design (CAD) and computer-aided engineering (CAE) types. These programs perform complex computational operations allowing the distribution of electromagnetic induction density, temperatures, stresses, and other physical quantities in the prototype device (3D model) to be determined.

In order to perform the above-mentioned computer simulations, a 3D model of the overcurrent switch was made.

All the individual structural elements of the switch were modeled in the "SpaceClaim Geometry" software. The elements of the current circuit were made with the maximum possible precision, maintaining their dimensions, shape, and position in relation to each other inside the circuit breaker. The main components of the circuit breaker are:

- Short-circuit release coil combined with the switch's fixed contact;
- Moving contact;
- Thermobimetal combined with the "arc runner"—the element along which the electric arc is led to the extinguishing chamber;
- Arc chamber;
- Upper and lower terminal of the switch.

The modeled elements of the current path are shown in Figure 2 below. These are selected elements of the considered overcurrent circuit breaker.

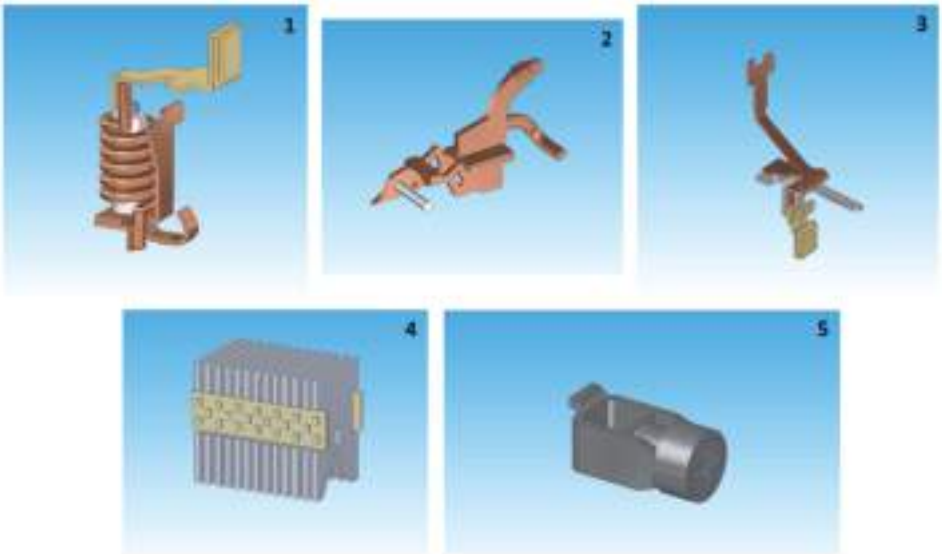

Figure 2. Main elements of the circuit breaker's current path modeled in 3D: **1**—short-circuit tripping coil with fixed contact, **2**—movable contact, **3**—thermobimetal with "arc runner", **4**—arc chamber, **5**—wire terminal.

After all the elements of the switch were made, it was possible to make a 3D assembly of the entire switch, as shown in Figure 3 below.

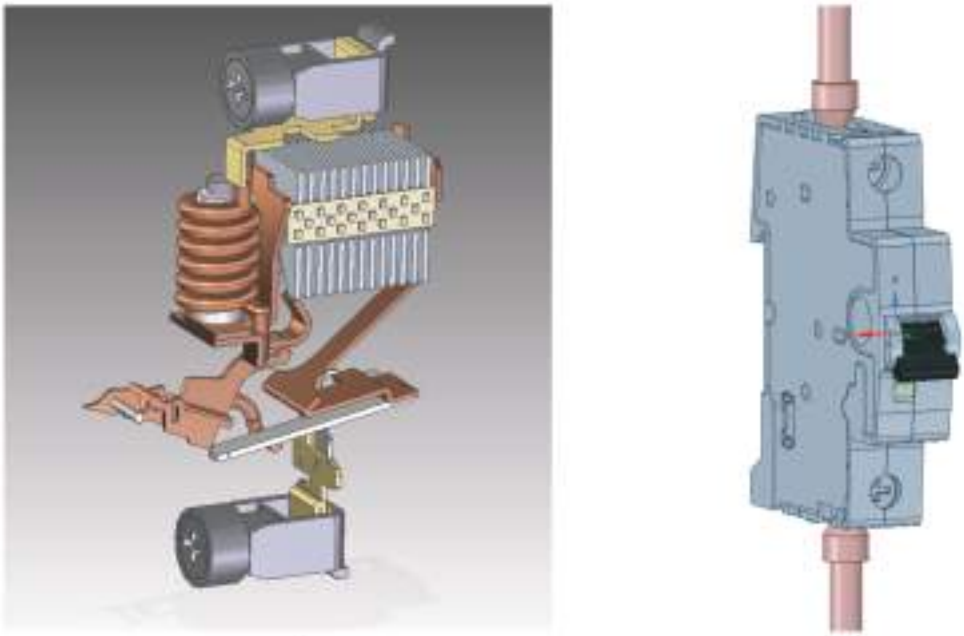

(a) (b)

Figure 3. Assembly of 3D model of the tested circuit breaker: (**a**) circuit breaker components of current path; (**b**) completed model of the circuit breaker.

The 3D model of the circuit breaker prepared in this way was ready to be loaded into solvers in ANSYS Workbench, which allowed for the performance of coupled analysis, which, after complex computational iterations, allowed us to check how different physical phenomena influence each other.

4. FEA Simulations

4.1. Simulations Assumptions and Settings

Coupled analysis was performed by coupling two solvers: Maxwell 3D and transient thermal. The computational simulations were performed for three cases: 0.8 × In, 1 × In, and for 2 × In. The results of coupled analysis for all three cases have been collected in Sections 5.1–5.3, where they have been thoroughly presented and described.

In the transient thermal module, as in the Maxwell module, material properties were assigned from the material library, a mesh was generated (densified, for example, on contacts), and then "loads" were imported from Maxwell in the form of Ohm losses, which allowed for the temperature distribution in transient thermal. Material data are presented in Table 1 below.

Table 1. Table of the material data used in procured model.

Engineering Data	Copper	Aluminum	ABS	Steel	Unit
Density	8300	2712	1024	7850	(kg/m^3)
Young's Modulus	1.10×10^{11}	1.1×10^{8}	1.25×10^{9}	2.00×10^{11}	(Pa)
Poisson's Ratio	0.34	0.33	0.40	0.30	
Bulk Modulus	1.15×10^{11}	2.15×10^{9}	2.27×10^{9}	1.67×10^{11}	(Pa)
Shear Modulus	4.10×10^{10}	2.55×10^{7}	8.75×10^{8}	7.69×10^{10}	(Pa)

Table 2 presents computational iterations for executed simulations:

Table 2. Table for details of computational iterations in ANSYS Maxwell 3D.

Pass	Tetrahedra	Energy Error (%)	Delta Energy (%)
1	697,411	20.015	N/A
2	910,039	1.6707	7.5067
3	1,187,597	1.0679	1.7898
4	1,549,876	0.72435	0.97035

The simulation calculation error can be related to the error described as "energy error", which in ANSYS Maxwell is reduced during the automatic compaction of the mesh during subsequent computational iterations by the function—"adaptive mesh refinement"—in areas where fields are of interest or the field gradients are high. The obtained convergence of calculations below 1% is a satisfactory result for this type of simulation; it often happens that the simulation cannot achieve convergence despite many computational iterations and a powerful generated computational mesh consisting of several million Tetrahedra elements.

Table 3 presents exemplary settings (transient thermal module) for executed simulations:

Table 3. Exemplary simulations setting for transient thermal module.

Number of Steps	Current Step Number	Step End Time (s)	Auto Time Stepping	Initial Time Step (s)	Min. Time Step (s)	Max. Time Step (s)
1	1	6000	Program Controlled	60	0.001	600

Moreover, it is worth mentioning the mesh size with the number of nodes amounting to 1,193,962 and number of elements amounting to 738,634. Ambient temperature in Maxwell 3D and transient thermal was set as 22 °C.

Forcing in Maxwell 3D Module was set as solid with current value of 32 A and phase equal to 0 degrees.

4.2. Current Flow Simulation for 0.8 × the Rated Current—25.7 A

The first coupled analysis performed with the ANSYS Workbench using paired Maxwell 3D and transient thermal environments allowed for obtaining precise results related to 0.8 × In current flow through the overcurrent circuit breaker.

The current density in the circuit breaker current path was highest in the part consisting of a movable contact and a fixed contact, as shown in Figure 4a below. The effect of the current flow through the circuit breaker current path was the generation of losses in the form of released heat, which is presented below (Figure 4b).

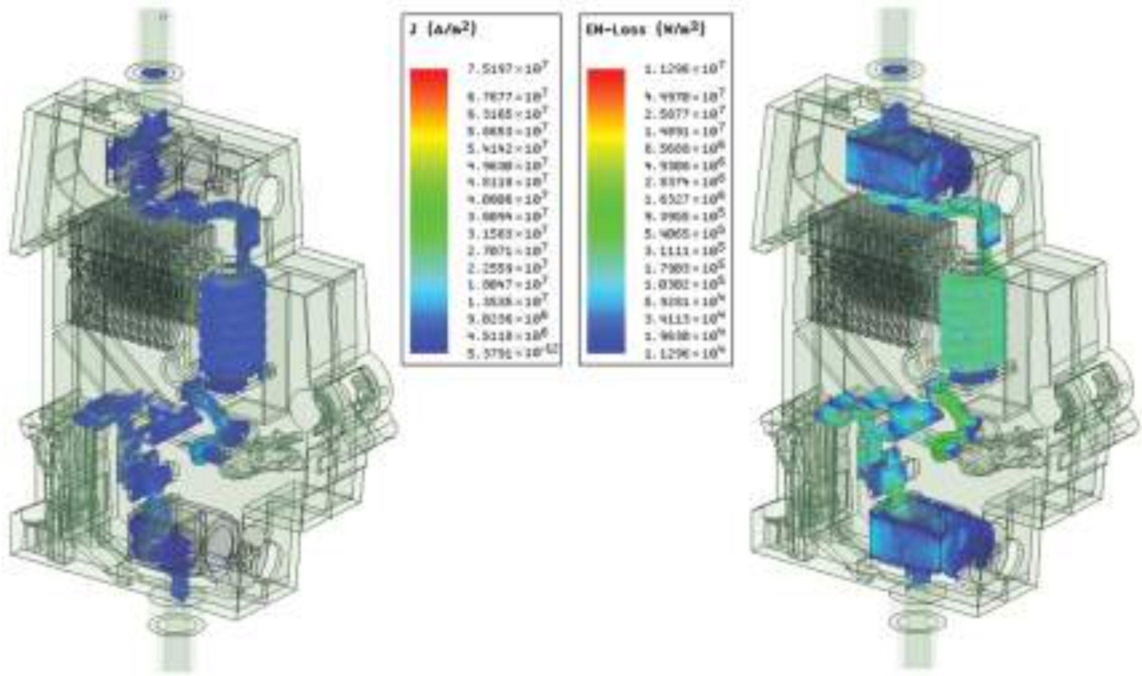

(a) (b)

Figure 4. Analysis of current flow 0.8 In through the circuit breaker current path: (**a**) distribution of current density in the current path; (**b**) distribution of energy losses in the current path.

Calculations related to the current flow were performed, and on their basis, a thermal analysis was executed. Temperature distribution on the circuit breaker's current path was obtained in form of graphical representation. The highest temperature value was reached on the solenoid release coil; it was equal to 47.37 °C. The higher temperature value on the coil in relation to the contact of the current path was caused by the high current density witnessed in the coil. Moreover, the presence of an aluminum housing inside the coil and a metal trigger pin, in which eddy currents were generated, caused additional losses in the form of generated heat. The temperature difference between the coil and the contact was less than 2 °C. The temperature distribution on the current path of the overcurrent circuit breaker is shown in detail in Figure 5 below.

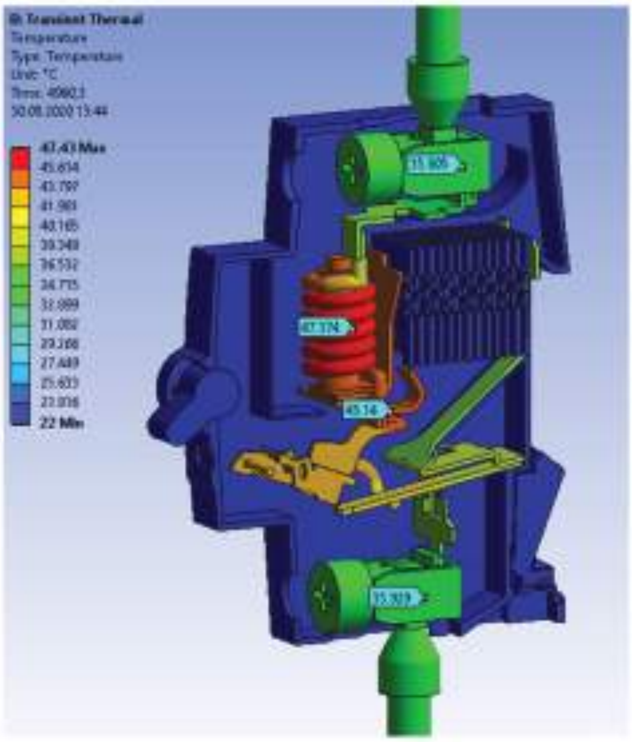

Figure 5. Temperature distribution on the elements of the circuit breaker for a current of 25.7 A.

For validation of the obtained simulation results with experimental tests, the time courses of heating the contact, coil, and upper and lower terminals were generated using the "temperature probe" option. All the obtained waveforms were consolidated into one chart using the "chart plot" function. Temperature charts are presented in Figure 6.

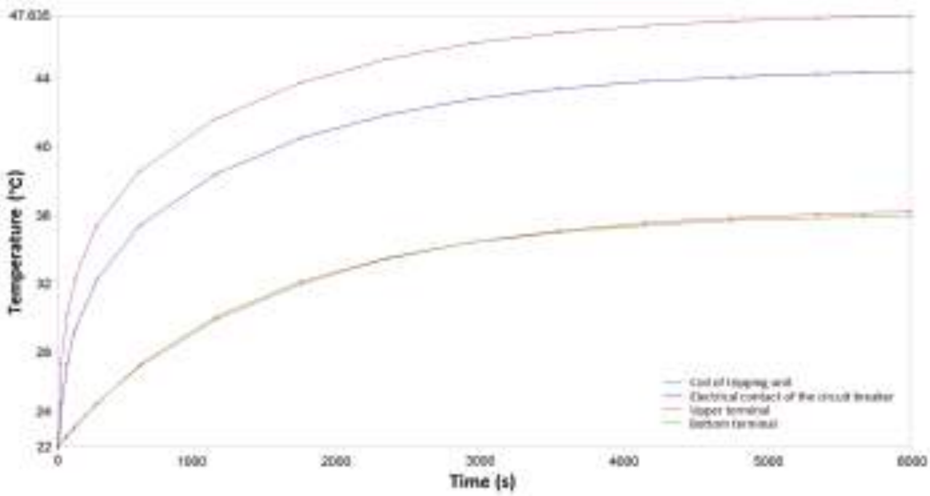

Figure 6. Temperature charts for contact, coil, and terminals of the upper and lower miniature circuit breaker for 0.8 × In.

4.3. Current flow Simulation for 1 × Rated Current—32 A

For the second coupled analysis, precise results were obtained related to the flow of In (32 A) through the overcurrent circuit breaker. The current density in the circuit breaker current path was highest in the contact, as shown in the following Figure 7a.

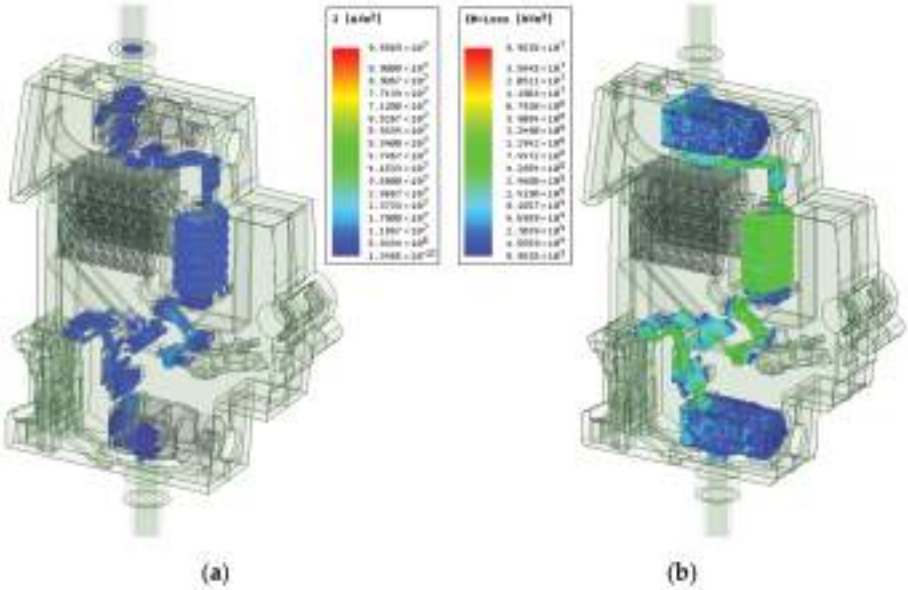

Figure 7. Analysis of the In current flow through the circuit breaker current path: (**a**) distribution of current density in the current path; (**b**) distribution of energy losses in the current path.

In this computational case, the value of generated losses related to the flow of rated current is similar in value both for the contact and for the coil. On the other hand, the total losses in the coil are greater, as shown in Figure 7b above.

As in the previous case, after performing the calculation operations related to the current flow, a thermal analysis was performed for the circuit breaker during the flow of the rated current where the highest temperature value was also reached on the short-circuit release coil. The exact temperature distribution is shown in Figure 8.

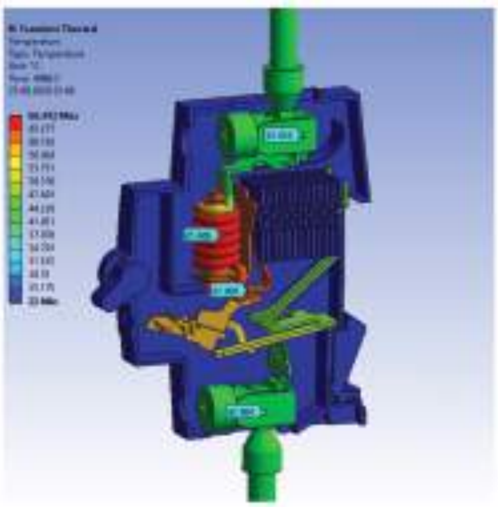

Figure 8. Temperature distribution on the elements of the circuit breaker for the rated current of 32 A.

Additionally, for the purposes of the experimental validation, graphs concerning heating of current path elements were generated for the rated current, as shown in Figure 9 below.

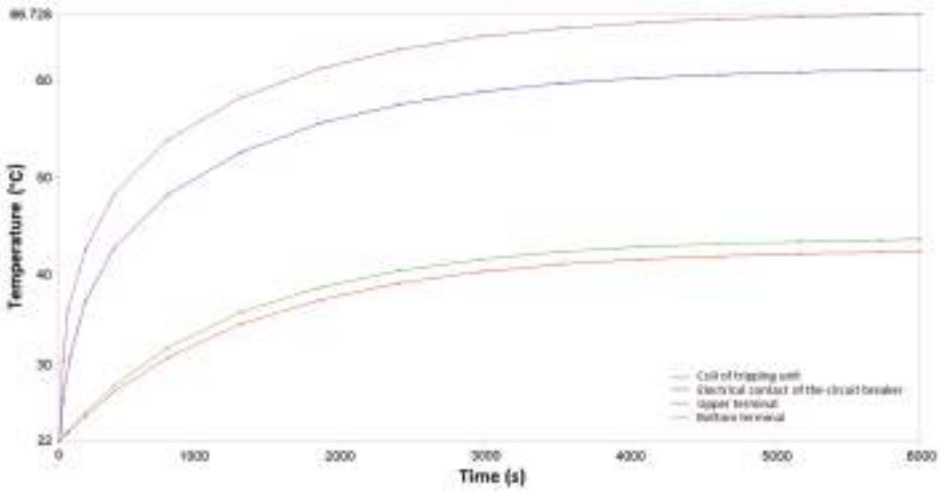

Figure 9. Temperature charts for the contact, coil, and terminals of the upper and lower miniature circuit breaker for In.

4.4. Current Flow Simulation for 2 × Rated Current—64 A

The third coupled analysis was performed for a double rated current of 2 × In (64 A). The current density in the circuit breaker circuit was much higher than in the previous cases; it achieved the highest value in the contact, as shown in Figure 10a below.

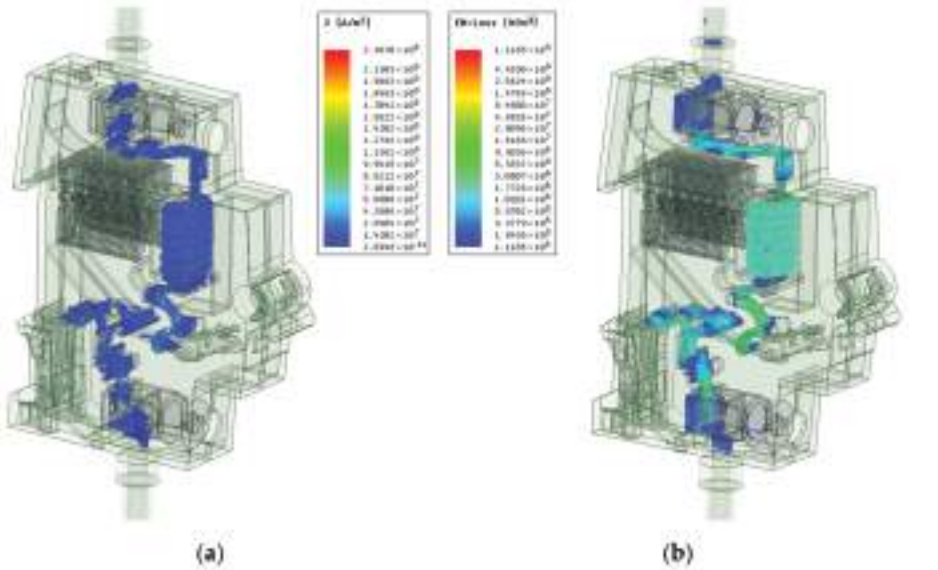

Figure 10. Analysis of the 64 A current flow through the circuit breaker current path: (**a**) distribution of current density in the current path; (**b**) distribution of energy losses in the current path.

As in the previous calculation case, the value of the generated losses related to the flow of rated current, in terms of value, was slightly higher for the contact than for the coil. On the other hand, the total losses in the coil were greater; this dependency is shown in Figure 10b above.

From the obtained calculation operations related to the current flow and the performed thermal analysis for the circuit breaker during the flow of double rated current, the highest temperature value was reached on the short-circuit release coil, which was equal to 196.41 °C. The temperature difference between the coil and the contact was 8.61 °C. The exact temperature distribution is shown in Figure 11.

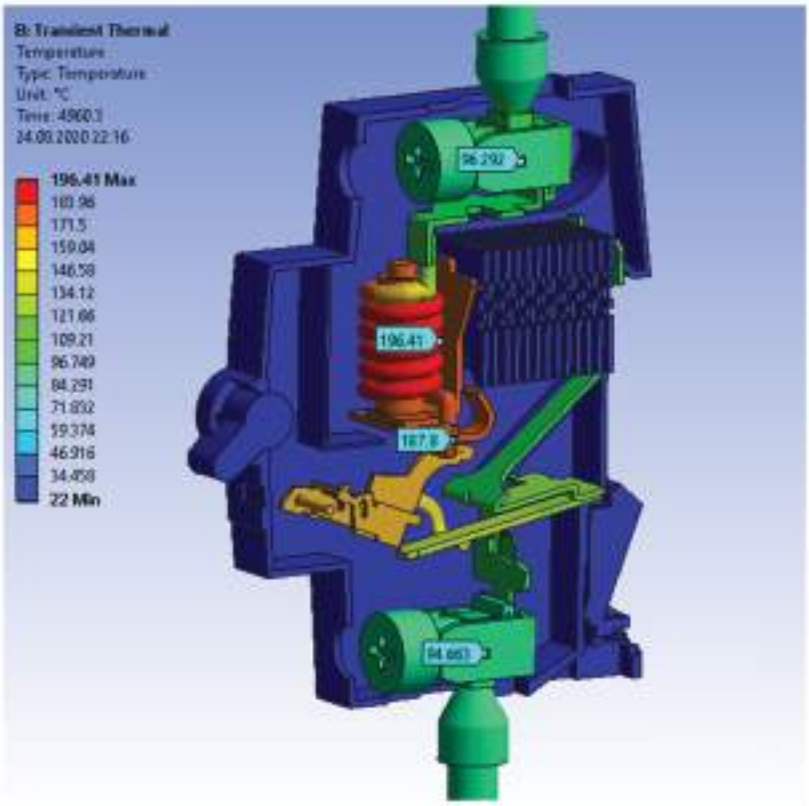

Figure 11. Temperature distribution on the elements of the circuit breaker for double the rated current of 64 A.

As in the previous cases, additionally, for the experimental validation, plots of heating of the current path elements for double rated current were generated, as shown in Figure 12 below.

Thermal analysis of the current path of the overcurrent circuit breaker were performed on a carefully prepared 3D model in ANSYS software, coupling two solvers: Maxwell 3D and transient thermal.

Each simulation performed in the first stage required calculations related to the flow of a given current through the current path (Maxwell 3D), which made it possible to determine the density of the current flowing through the current path and Ohm's losses. Then, it was possible to import the data into another solver (transient thermal), which made it possible to determine (after performing a certain number of computational iterations) the temperature distribution on the circuit breaker current path.

The analysis performed in this way for the currents: 0.8 × In, In, and for 2 × In and the results of the temperature distribution obtained in this way were the basis for the experimental validation of the heating concerning the current path in real conditions at the above-mentioned currents, which is presented in the next subsection of this work.

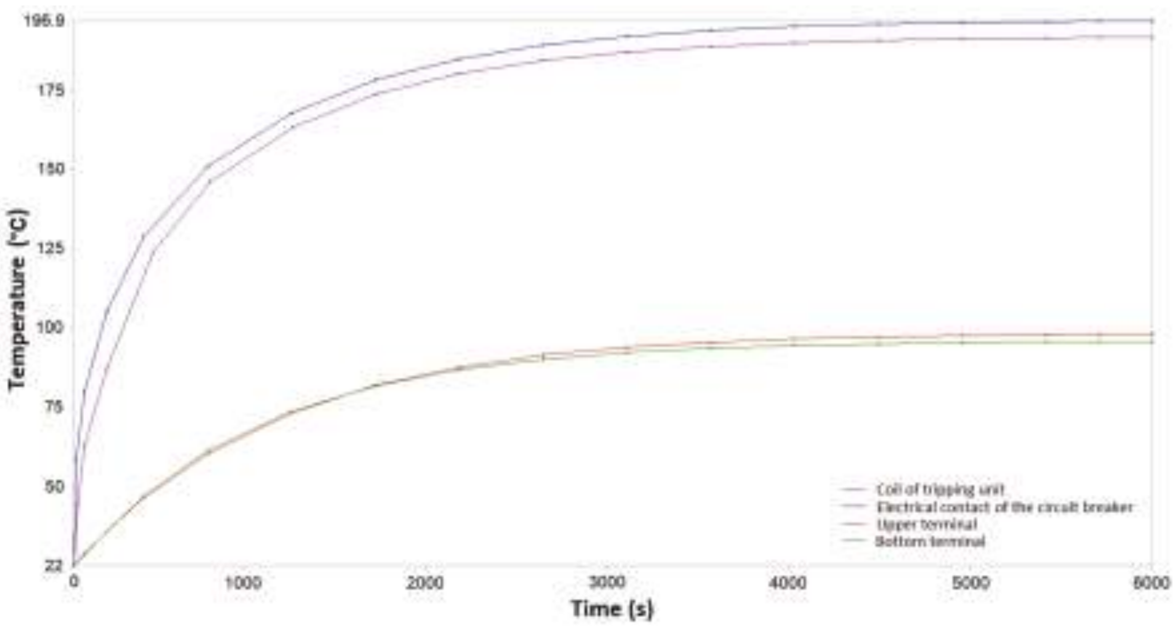

Figure 12. Temperature charts for contact, coil, and terminals: upper and lower circuit breaker for current 2 × In.

5. Experimental Work

Currently, preliminary prototypes of electrical devices are designed using 3D computer software and coupled analysis programs for performing mechanical, thermal, electrodynamic analyses, etc. At a time when such tools did not exist, designers constructed electrical devices on the basis of mathematical calculations, experience, and employing the standards in force.

Currently, the miniature circuit breakers are also designed by the manufacturers in accordance with the standards. One such standards is the European standard IEC 60898-1: 2015. The scope of the standard includes standardized methods of testing overcurrent circuit breakers that are used in accredited laboratories to conduct type tests and tests of conformity of the manufactured devices with the given requirements of the standard. The performed tests allow manufacturers to check the operation and construction of the apparatus, which was previously designed in 3D software, the simulation analyses of which could include some simplifications. Additionally, type testing is necessary to obtain a certificate for the product that the manufacturer wants to introduce to the market.

In this work, an overcurrent circuit breaker with a rated current of 32 A was subjected to tests in order to check the temperature rise on the current circuit elements. This made it possible to carry out measurements in accordance with the above standard, which states that, during the measurements, no cover of the switch housing may be removed or unscrewed as in Figure 13.

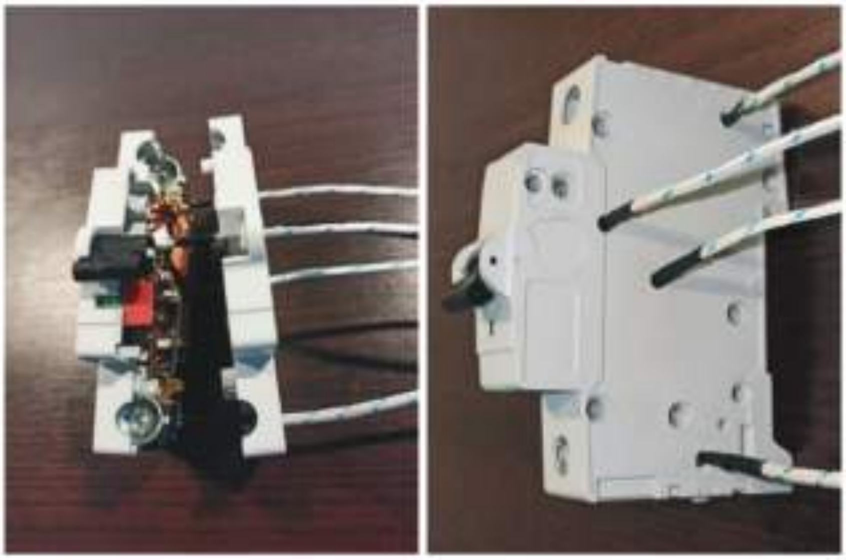

Figure 13. Overcurrent circuit breaker with openings in the casing allowing for trouble-free removal of thermocouples from the switch.

Type K thermocouples were glued with a special thermally conductive glue to the elements of the current path: coil, fixed contact, and upper and lower terminal. The spots of installation of the thermocouples depended on the previously performed computational analysis for the 3D model of this circuit breaker in order to juxtapose the obtained results. The glued thermocouples on the circuit breaker current path elements are shown in Figure 14.

Figure 14. Miniature circuit breaker with glued thermocouples (type K) on the main switch contact, the electromagnet coil, and on the upper and lower terminals.

After the thermocouples were glued, the switch was put back to its original state before disassembly, and the glued thermocouples did not affect the switch mechanism, which did not cause any problems during its operation. Apart from the technological openings for inserting the thermocouples, no other openings and changes were made in the switch, which allowed for the correct measurements of the temperature rise.

Characteristics of thermocouples are standardized, and the values of the thermoelectric force for individual materials and permissible deviations are included in the international standard IEC 60584 and ITS 90. The afore-mentioned standard IEC 60584 defines the formulas for calculating permissible measurement errors. Therefore, for the "K" type thermocouple (NiCr-Ni—this was used in the validation process), the errors are presented in the Table 4 below:

Table 4. Table of "K" thermocouples errors.

Thermocouple Class	Temperature Range	Permissible Error
1	−40 °C . . . + 375 °C +375 °C . . . + 1000 °C	±1.5 °C ±0.0040 × $\lvert t \rvert$
2	−40 °C . . . + 333 °C +333 °C . . . + 1200 °C	±2.5 °C ±0.0075 × $\lvert t \rvert$

The measurement sensitivity for such a thermocouple is 41 μV/°C, hence, the SEM dependence in the temperature range used, −200 to 1200 °C, was almost linear. It is shown in Figure 15 below.

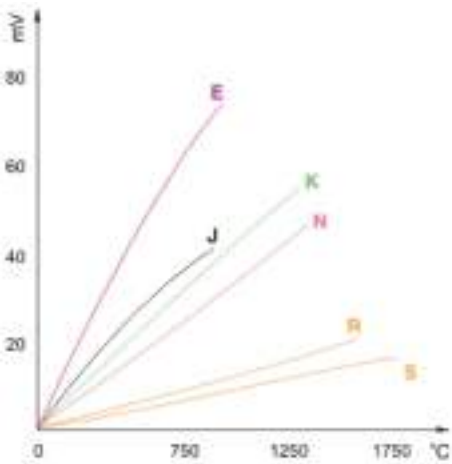

Figure 15. SEM characteristic for different type of electrodes and among others for "K" type thermocouple.

In order to perform the tests, it was necessary to prepare a test stand for recording the temperature rise of the circuit breaker current path elements for specific currents: 0.8 × In, In, and for 2 × In. For this purpose, a single-phase autotransformer was used, to which a single-phase high-current transformer was connected. The autotransformer was used to regulate the current at the output of the high-current transformer. In order to measure the current, a clamp meter (ammeter) was installed on the cable supplying the tested object—an overcurrent switch. In order to collect data from installed thermocouples in the switch, a four-channel temperature recorder with an accuracy of 0.1 °C was used, the sampling time of which was set to 1 s (temperature was measured every second on four thermocouples). Data from the recorder, via the USB communication interface, were sent online to the recorder software on a PC, where the heating charts of the tested elements for the overcurrent circuit breaker were generated. The diagram of the measuring system is presented below (Figure 16).

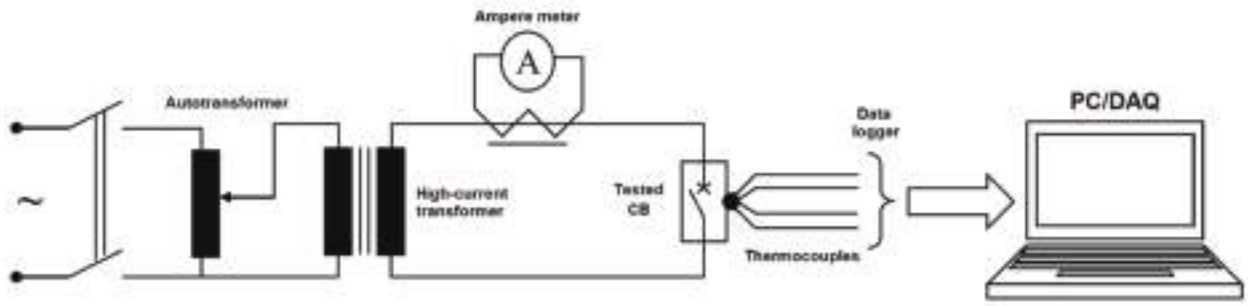

Figure 16. Diagram of the measuring system for the tested current circuit of the overcurrent circuit breaker.

The length of the power supply cables to the circuit breaker is precisely defined in the standard and those are, respectively, equal to 1 m from the bottom of the circuit breaker and 1 m from the top of the circuit breaker. These recommendations were followed during the tests; the actual layout is shown in Figure 17 below.

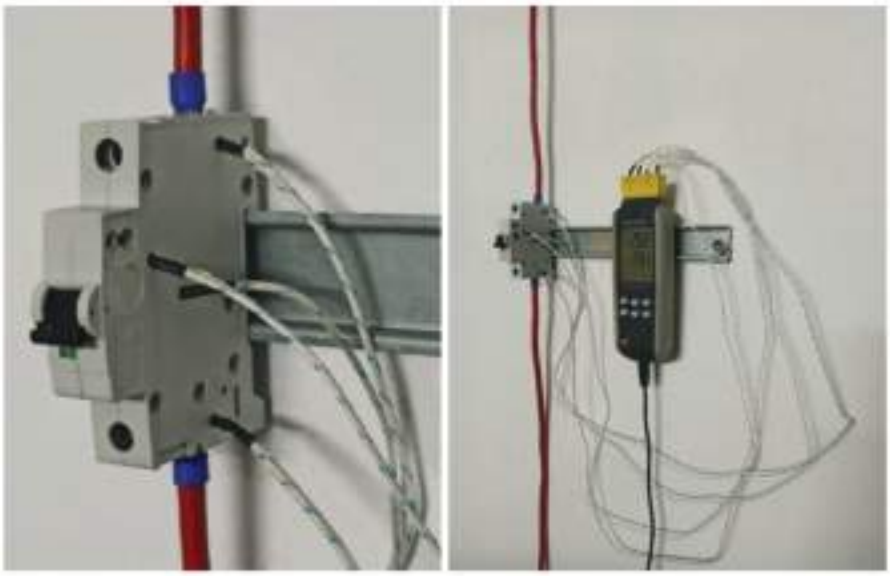

Figure 17. The measuring system of the tested overcurrent circuit breaker.

The ambient temperature was measured by means of two other thermocouples immersed in the oil reservoir—the temperature oscillated around 23 °C.

During the experimental tests, in order to illustrate the temperature distribution on the circuit breaker path and to, additionally, verify the obtained simulation and experimental results, at the end of the heating tests, photos were taken with a thermal imaging camera for each tested current.

5.1. Measurements of the Temperature rise Concerning the Circuit Breaker Current Path for 0.8 × In

During the test of the temperature rise of the contact and the remaining elements of the circuit breaker, the current of 0.8 × In (25.7 A) was set using an autotransformer.

The temperature recorded on the switch contact after its determination amounted to slightly over 44.9 °C. The highest temperature value was recorded for the electromagnetic release coil, which was heated to 46.8 °C after the temperature stabilized. Similar temperatures were recorded on the switch terminals: the lower terminal temperature was equal to 34.7 °C and the upper terminal to 35.0 °C. All recorded measurements are presented below in Figure 18 in the form of a graph.

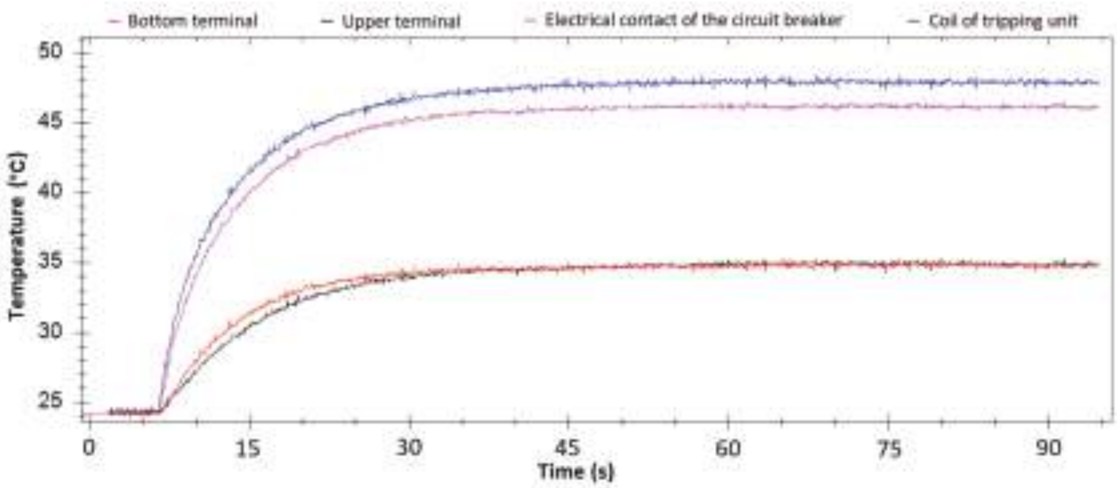

Figure 18. Graphs of heating the contact and other elements of the circuit breaker for the current 0.8 × In.

The obtained results of experimental tests were additionally compared with the measurement made with the use of a thermal imaging camera. Taking a photo with a thermal imaging camera allowed us to register the temperature distribution on the circuit breaker's current path elements for the tested value of the current flowing through the current circuit. Figure 19 shows and confirms that the highest temperature was released on the coil of the electromagnetic trigger. Measurements made with the use of a thermal imaging camera were consistent with the results obtained from tests with thermocouples.

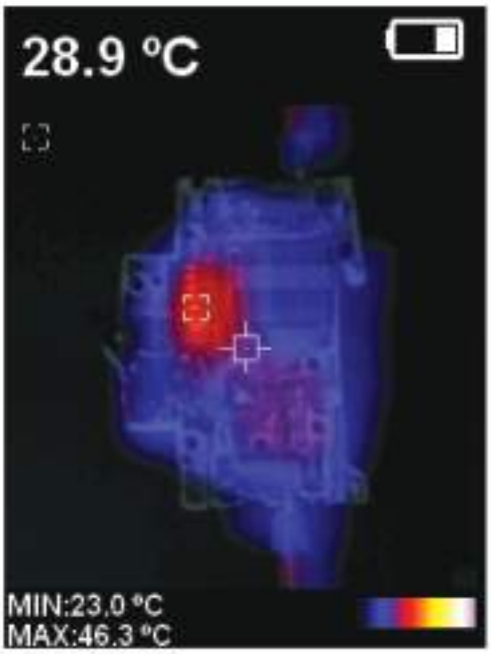

Figure 19. Temperature distribution on the elements of the circuit breaker current path for 0.8 × In.

5.2. Measurements of the Temperature Rise Concerning the Circuit Breaker Current Path for In

The tests of the temperature rise concerning the contact and the remaining elements of the circuit breaker for the current of In (32 A) were performed in the same way as in the previous point, giving the appropriate voltage value from the autotransformer to the high-current transformer in order to obtain the rated current of the circuit breaker.

The highest temperature value was recorded for the electromagnetic trigger coil, as in the previous measurement; following the test, it was determined to be equal to 64.1 °C. The temperature recorded on the switch contact, after it was established, amounted to slightly over 62.5 °C. The temperatures were recorded on the terminals: the lower terminal measured at −41.9 °C and the upper terminal −41.6 °C. All recorded measurements are presented in Figure 20 in the form of a graph.

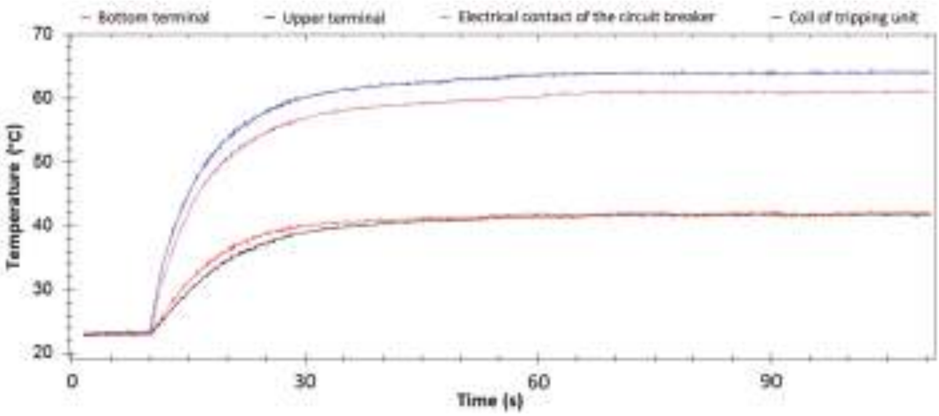

Figure 20. Temperature measurement curves for individual elements of the circuit breaker for rated current In = 32 A.

The obtained results of experimental tests, as in the previous case, were additionally compared with the measurement made with the use of a thermal imaging camera. Measurements made with the use of a thermal imaging camera were also consistent with the results obtained from tests with thermocouples (Figure 21).

Figure 21. Photo from the thermal imaging camera of the current path at the set temperature for the rated current of the circuit breaker In = 32 A.

5.3. Measurements of the Temperature Rise Concerning the Circuit Breaker Current Path for $2 \times In$

The temperature rise tests performed for the current of 2 × In (64 A) were performed similarly to the previous tests. In this case, the temperatures of the contacts and elements of the circuit breaker exceeded the allowable values of the temperature rise specified in the standard.

The highest temperature value was achieved on the electromagnetic release coil as in the previous measurements; following the test, it was determined to be 202.3 °C. The temperature recorded on the switch contact, after it was established, amounted to slightly over 192 °C. The temperatures were recorded on the switch terminals: the lower terminal measured at 93.9 °C and the upper terminal 96.8 °C. All recorded measurements are shown in Figure 22 in the form of a graph:

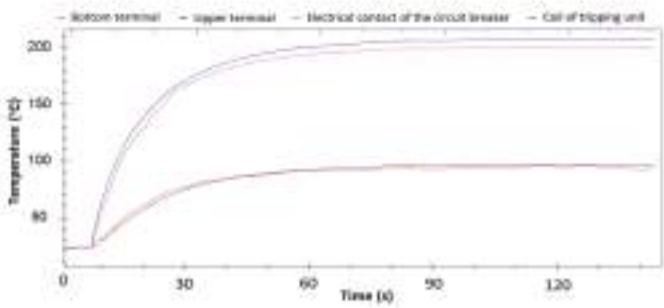

Figure 22. Temperature measurement curves for the individual elements of the circuit breaker for the current 2 × In = 64 A.

The results of experimental tests for the double rated current have also been additionally correlated with the measurement made with a thermal imaging camera. Taking a photo with a thermal imaging camera allowed us to check the exact temperature distribution on the circuit breaker current circuit elements for the tested value of the current flowing through the current circuit. Figure 23 shows and confirms that the highest temperature value evolved on the electromagnetic trigger coil. The measurements made with the thermal imaging camera were similar to the measurements made with the thermocouples. The temperature difference in the measurements taken, for example, on the trigger coil was almost 3 °C.

Figure 23. Photo from the thermal imaging camera of the current path at the set temperature for double the rated current of the 64 A circuit breaker.

6. Results Summary

The performed experimental tests in the form of measurements concerning the heating of the circuit breaker current path elements allowed us to determine the actual temperature values of the individual circuit breaker parts depending on the current flowing. The recorded results were collected in the form of plotted heating curves for the currents: 0.8 × In, In, and for 2 × In.

The overload release of low voltage modular circuit breakers is located in the main circuit of the electrical apparatus. Regardless of the type of time–current characteristic, the current of this release is between 1.13 and 1.45 of the rated current (In). Moreover, in accordance with the standard for testing and certification of circuit breakers IEC 60989, the overload element can conduct 2.8 × In for up to 60 s. Hence, it was decided to use this current range to validate the simulation model. An additional argument was the willingness to check the model due to the non-linear dependence of resistivity as a function of temperature. Having such a selected and wide research schedule, it was possible to obtain correct validation.

The temperature values in the case of the current 0.8 × In and In did not exceed the permissible values of temperature increases and the permissible long-term temperature. In the case of a current of 2 × In, the above-mentioned values were exceeded.

For a current of 0.8 × In (25.7 A), the maximum temperature was reached on the short-circuit release coil −46.8 °C and on the contact −44.9 °C. 34.7 °C was noted on the lower terminal of the switch and 35.0 °C on the upper terminal of the switch.

In the recorded results for the rated current In = 32 A, despite the increase in current by only 6.3 A compared to the previous measurement, a significant increase in temperature was noted on the elements of the current circuit. The highest value, as before, was recorded on the electromagnetic trigger coil and amounted to 64.1 °C. The temperature at the switch contact, after it was established, was slightly over 62.5 °C. The following predetermined temperature values were reached at the switch terminals: lower terminal −41.9 °C and upper terminal −41.6 °C.

In the case of the last measurement for the double rated current of the circuit breaker, equal to 64 A, the temperature on the coil increased more than three times compared to the measurement for the rated current and amounted to 202.3 °C. A similar temperature value was recorded for the switch contact −192.5 °C. On the terminals, the value of the recorded set temperature more than doubled and amounted to, respectively, −93.9 °C on the lower terminal, and −96.8 °C on the upper terminal.

The switch during and after measurements was still fully functional. The achieved high temperature value of 202.3 °C did not affect the structure (housing) and other elements of the circuit breaker in any way—no part of it was melted or deformed.

The experimental tests, carried out using thermocouples in the form of K-type thermocouples coupled online with a temperature recorder and a PC, were additionally validated using photos taken with a thermal imaging camera. Measurements made with the use of a thermal imaging camera were made for the set temperature value just before the end of each measurement. The obtained results, in the form of photos from the thermal imaging camera, are consistent with the measurements made with thermocouples.

7. Conclusions

This article presents the construction of the current path of a modular circuit breaker that protects low voltage network circuits against short-circuits and overloads.

The main purpose of the work was the thermal analysis of the current path of the overcurrent circuit breaker, which was performed with the use of computer simulations and validated by the performed experimental tests.

In order to perform simulation coupled analyses, an accurate 3D model of individual parts of the current path, as well as the entire circuit breaker with power cables, was developed. The ANSYS software was used to carry out simulation calculations, which enabled direct connection of various types of solvers, creating couplings that were enabling data import from one solver to another and vice versa, e.g., from Maxwell 3D to transient thermal.

The simulation tests were performed for three currents: 0.8 × In, In, and for 2 × In. During the simulation, the values of the current density and Ohm losses in the current path were determined, which in turn, allowed us to determine which elements heat up the most and how the heat spreads in the modeled current path of the circuit breaker. From the data obtained during the coupled analyses, the heating courses of selected elements of the circuit breaker were generated, which, in the subsequent stages of work, allowed for the comparison of the obtained courses with the experimental tests performed.

To perform the experimental tests, a specially prepared switch was used with installed (glued in) K-type thermocouples inside that did not affect the mechanical and electrical operation of the switch. They allowed for precise temperature measurements of selected elements: short-circuit release coil, contact, and terminals. From the data collected by means of a temperature recorder, exact heating courses of the above-mentioned elements were generated. In order to verify the obtained results, photos were additionally taken with a thermal imaging camera for each of the three tested currents after reaching the set temperatures.

The obtained results of simulation tests and experimental tests were similar. The temperature distributions in the circuit breaker current path in the calculation simulations made in the transient thermal solver were consistent with the performed thermal imaging measurements. In addition, the generated waveforms of heating the circuit breaker part in the simulation calculations were very similar to those obtained during experimental tests with thermocouples.

The conducted analyses allowed us to conclude that the development of accurate 3D models and the performance of advanced coupled analyses can be successfully used during the construction and prototyping of new devices by designers of electrical apparatus. Thanks to this type of analysis, it is possible to make more elaborate designs of switches and electrical devices. In addition, it allows for significant reduction of the costs associated with the production of prototypes and the performance of tests and research in laboratories, which are often time-consuming.

The knowledge acquired during the implementation of the above issue allowed the authors to understand in detail and learn about the processes related to the flow of current through the current paths of electrical devices.

Author Contributions: Conceptualization, M.S., S.Ł., Ł.K., and D.Z.; data curation, M.S., S.Ł., Ł.K., and D.Z.; formal analysis, M.S., S.Ł., Ł.K., and D.Z.; investigation, M.S., S.Ł., and Ł.K.; methodology, M.S., S.Ł., and Ł.K.; project administration, M.S., S.Ł., and Ł.K.; resources, M.S., S.Ł., Ł.K., and D.Z.; supervision, M.S., S.Ł., and Ł.K.; validation, M.S., S.Ł., and Ł.K.; visualization, M.S., S.Ł., and Ł.K.; writing—original draft, M.S., S.Ł., and Ł.K.; writing—review and editing, M.S., S.Ł., Ł.K., and D.Z. All authors have read and agreed to the published version of the manuscript.

Funding: This research received no external funding.

Institutional Review Board Statement: Not applicable.

Informed Consent Statement: Not applicable.

Data Availability Statement: Not applicable.

Conflicts of Interest: The authors declare, no conflict of interest.

References

1. Demir, M.; Kahramanoğlu, G.; Yıldız, A.B. Calculating of fuse melting point for power electronics circuits by inrush energy and determination of the eligibility. In Proceedings of the 2016 18th European Conference on Power Electronics and Applications (EPE'16 ECCE Europe), Karlsruhe, Germany, 5–9 September 2016; pp. 1–6. [CrossRef]
2. Bini, R.; Galletti, B.; Iordanidis, A.; Schwinne, M. CFD in Circuit Breaker Research and Development. In Proceedings of the 1st International Conference on Electric Power Equipment—Switching Technology, Xi'an, China, 23–27 October 2011; pp. 375–378.

3. Wang, L.; Liu, H.; Zheng, W.; Guan, R.; Ge, C.; Chen, L.; Jia, S. Numerical Simulation of Impact Effect of Internal Gas Pressure on Chamber Housing in Low-Voltage Circuit Breaker. *IEEE Trans. Compon. Packag. Manuf. Technol.* **2014**, *4*, 1–8. [CrossRef]
4. Ye, X.; Dhotre, M.T.; Mantilla, J.D.; Kotilainen, S. CFD Analysis of the Thermal Interruption Process of Gases with Low Environmental Impact in High Voltage Circuit Breakers. In Proceedings of the 2015 Electrical Insulation Conference (EIC), Seattle, WA, USA, 7–10 June 2015.
5. Dhotre, M.T.; Ye, X.; Seeger, M.; Schwinne, M.; Kotilainen, S. CFD Simulation and Prediction of Breakdown Voltage in High Voltage Circuit Breakers. In Proceedings of the 2017 Electrical Insulation Conference (EIC), Baltimore, MD, USA, 11–14 June 2017.
6. Qi, B.; Zhao, X.; Zhang, S.; Huang, M.; Li, C. Measurement of the electric field strength in transformer oil under impulse voltage. *IEEE Trans. Dielectr. Electr. Insul.* **2017**, *24*, 1256–1262. [CrossRef]
7. Rumpler, C.; Stammberger, H.; Zacharias, A. Low-voltage arc simulation with out-gassing polymers. In Proceedings of the 011 IEEE 57th Holm Conference on Electrical Contacts (Holm), Minneapolis, MN, USA, 11–14 September 2011; pp. 1–8.
8. Ryzhov, V.V.; Molokanov, O.H.; Dergachev, P.A.; Vedechenkov, N.A.; Kurbatova, E.P.; Kurbatov, P.A. Simulation of the Low—Voltage DC Arc. In Proceedings of the 2019 International Youth Conference on Radio Electronics, Electrical and Power Engineering (REEPE), Moscow, Russia, 14–15 March 2019.
9. Geetha, N.D.; Rasilo, P.; Arkkio, A. Sensitivity Analysis of Inverse Thermal Modeling to Determine Power Losses in Electrical Machines. *IEEE Trans. Magn.* **2018**, *54*, 1–5.
10. Li, J.; Cao, Y.; Yan, M.; Liu, S.; Du, Z.; Feng, Y. Research on the Effect of Magnetic Field on Micro-Characteristics of Vacumm Arc During Arc Formation Process. In Proceedings of the 28th International Symposium on Discharges and Electrical Insulation in Vacuum (ISDEIV), Greifswald, Germany, 23–28 September 2018.
11. Tarnowski, P.; Ostapski, W. Pulse powered turbine engine concept—Numerical analysis of influence of different valve timing concepts on thermodynamic performance. *Bull. Pol. Acad. Sci. Tech. Sci.* **2018**, *66*, 373–382.
12. Nagarajan, V.S.; Kamaraj, V.; Sivaramakrishnan, S. Geometrical sensitivity analysis based on design optimization and multiphysics analysis of PM assisted synchronous reluctance motor. *Bull. Pol. Acad. Sci. Tech. Sci.* **2019**, *67*, 155–163.
13. Bini, R.; Basse, N.T.; Seeger, M. Arc-induced Turbulent Mixing in a Circuit Breaker Model. *J. Phys. D Appl. Phys.* **2011**, *2*, 44.
14. Holm, R. *Electric Contacts—Theory and Application*; Springer: New York, NY, USA, 1967.
15. Basse, N.P.T.; Bini, R.; Seeger, M. Measured turbulent mixing in a small-scale circuit breaker model. *Appl. Opt.* **2009**, *48*, 6381–6391. [CrossRef] [PubMed]
16. Incropera, F.P.; DeWitt, D.P.; Bergman, T.L.; Lavine, A.S. *Introduction to Heat Transfer*, 5th ed.; Wiley: Hoboken, NJ, USA, 2006.
17. Muller, P.T. Macroscopic Electro Thermal Simulation of Contact Resistances. Bachelor's Thesis, Rheinisch-Westfälische Technische Hochschule Aachen, Aachen, Germany, 2016.
18. Biao, W.; Yanyan, L.; Xiaojun, Z. Study on detection technology of the contact pressure on the electrical contacts of relays. In Proceedings of the 26th International Conference on Electrical Contacts (ICEC 2012), Beijing, China, 14–17 May 2012; pp. 161–164.
19. Sun, X.; Su, B.; Chen, L.; Yang, Z.; Li, K. Design and analysis of interior composite-rotor bearingless permanent magnet synchronous motors with two layer permanent magnets. *Bull. Pol. Acad. Sci. Tech. Sci.* **2017**, *65*, 833–843. [CrossRef]
20. Kriegelet, M.; Zhu, X.; Digard, H.; Feitoza, S.; Glinkowki, M. Simulations and Calculations as verfication tools for design and performance of high voltage equipment. In Proceedings of the CIGRE Conference 2008, Paris, France, 25–28 August 2008. paper A3-210.
21. Kumar, P.; Kale, A. 3-Dimensional CFD simulation of an internal arc in various compartments of LV/MV Switchgear. In Proceedings of the Ansys Convergence Conference, Pune, India, 23 August 2016.
22. Hartland, D.J. Electric contact systems—Passing power to the trains. In Proceedings of the 5th IET Professional Development Course on Railway Electrification Infrastructure and Systems (REIS 2011), London, UK, 6–9 June 2010; pp. 25–37.
23. Tong, J.; Zou, Y. Design of a Fuse-Time Testing System on STM32. In Proceedings of the 2013 International Conference on Computer Sciences and Applications, Wuhan, China, 14–15 December 2013; pp. 406–409. [CrossRef]
24. Farahani, H.F.; Asadi, M.; Kazemi, A. Analysis of thermal behavior of power system fuse using finite element method. In Proceedings of the 2010 4th International Power Engineering and Optimization Conference (PEOCO), Shah Alam, Malaysia, 23–24 June 2010; pp. 189–195. [CrossRef]
25. Li, D.; Qi, L. Energy based fuse modeling and simulation. In Proceedings of the 2013 IEEE Electric Ship Technologies Symposium (ESTS), Arlington, VA, USA, 22–24 April 2013; pp. 487–492. [CrossRef]
26. Kolimas, Ł.; Łapczyński, S.; Szulborski, M.; Świetlik, M. Low voltage modular circuit breakers: FEM employment for modelling of arc chambers. *Bull. Pol. Acad. Sci. Tech. Sci.* **2020**, *68*, 61–70.
27. Gómez, J.C.; Tourn, D.H. gPV fuse: Special characteristics for photo voltaic cells protection. In Proceedings of the 9th International Conference on Electrical Fuses and Their Applications (ICEFA), Maribor, Slovenia, 12–14 September 2011; pp. 1–9.
28. Gomez, J.C.; Tourn, D.; Nesci, S.; Zamarillo, G.R. PV cells protection by using class PV fuses. *IEEE Lat. Am. Trans.* **2013**, *11*, 531–537. [CrossRef]
29. Plesca, A.; Mihet-Popa, L. Thermal Analysis of Power Rectifiers in Steady-State Conditions. *Energies* **2020**, *13*, 1942. [CrossRef]
30. Zhang, Y.; Su, J.; Zheng, L.; Li, R.; Yu, B.; Shang, W. Analysis of high-voltage DC fuse's ageing characteristics under the overload pulse current carrying mode and the caused short-circuit failure in series-resonant converter power source. *Int. J. Electr. Power* **2020**, *117*, 1–10. [CrossRef]

31. Łapczyński, S.; Szulborski, M.; Kolimas, Ł.; Kozarek, Ł.; Gołota, K. Mechanical and Electrical Simulations of Tulip Contact System. *Energies* **2020**, *13*, 5059. [CrossRef]
32. Szulborski, M.; Łapczyński, S.; Kolimas, Ł.; Kozarek, Ł.; Rasolomampionona, D.D. Calculations of Electrodynamic Forces in Three-Phase Asymmetric Busbar System with the Use of FEM. *Energies* **2020**, *13*, 5477. [CrossRef]
33. Kühnel, C.; Schlegel, S.; Großmann, S. Investigations on the long-term behavior and switching function of fuse-elements for NH-fuse-links (gG) at higher thermal stress. In Proceedings of the 2017 6th International Youth Conference on Energy (IYCE), Budapest, Hungary, 21–24 June 2017.
34. De Tommasi, L.; Magnani, A.; De Magistris, M. Advancements in the identification of passive RC networks for compact modeling of thermal effects in electronic device s and systems. *Int. J. Numer. Model. Electr. Netw. Dev. Fields* **2018**, *31*, e2296.
35. Kumar, A. Electro-thermal Characterizations, Compact Modeling and TCAD based De-vice Simulations of advanced SiGe:C BiCMOS HBTs and of nanometric CMOS FET. In *Micro Andnanotechnologies/Microelectronics*; Université Bordeaux 1 Sciences et Technologie: Talence, France, 2012.
36. Di Napoli, F.; Magnani, A.; Copola, M.; Guerriero, P.; D'Alessandro, V.; Codecasa, L.; Tricoli, P.; Daliento, S. On-Line Junction Temperature Monitoring of Switching Devices with Dynamic Compact Thermal Models Extracted with Model Order Reduction. *Energies* **2017**, *10*, 189. [CrossRef]
37. Szulborski, M.; Łapczyński, S.; Kolimas, Ł.; Kozarek, Ł.; Rasolomampionona, D.; Żelaziński, T.; Smolarczyk, A. Transient Thermal Analysis Of NH000 gG 100A Fuse Link Employing Finite Element Method. *Energies* **2021**, *14*, 1421. [CrossRef]
38. Bartosik, M.; Borkowski, P.; Wójcik, F. Ultra-Fast Hybrid Systems for Protecting Direct Current Circuits with High Magnetic Energy. *Bull. Pol. Acad. Sci. Tech. Sci.* **2021**, 1–14. [CrossRef]
39. Zhan, Y.; Kumar, S.V.; Sapatnekar, S.S. Thermal Aware Design. *Found. Trends Electron. Des. Autom.* **2007**, *2*, 255–370. [CrossRef]

A8. *Thermal analysis of heat distribution in busbars during rated current flow in low-voltage industrial switchgear*

energies

MDPI

Article

Thermal Analysis of Heat Distribution in Busbars during Rated Current Flow in Low-Voltage Industrial Switchgear

Michał Szulborski *, Sebastian Łapczyński and Łukasz Kolimas

Faculty of Electrical Engineering, Electrical Power Engineering Institute, Warsaw University of Technology, 00-662 Warsaw, Poland; seb.lapczynski@gmail.com (S.Ł.); lukasz.kolimas@ien.pw.edu.pl (Ł.K.)
* Correspondence: mm.szulborski@gmail.com; Tel.: +48-662-119-014

Abstract: The manuscript presents advanced coupled analysis: Maxwell 3D, Transient Thermal and Fluent CFD, at the time of a rated current occurring on the main busbars in the low-voltage switchgear. The simulations were procured in order to aid the design process of such enclosures. The analysis presented the rated current flow in the switchgear busbars, which allowed determining their temperature values. The main assumption of the simulation was measurements of temperature rise during rated current conditions. Simulating such conditions is a valuable asset in order to design better solutions for energy distribution gear. The simulation model was a precise representation of the actual prototype of the switchgear. Simulations results were validated by experimental research. The heat dissipation in busbars and switchgear housing through air convection was presented. The temperature distribution for the insulators in the rail bridge made of fireproof material was considered: halogen-free polyester. The results obtained during the simulation allowed for a detailed analysis of switchgear design and proper conclusions in practical and theoretical aspects. That helped in introducing structural changes in the prepared prototype of the switchgear at the design and construction stages. Deep analysis of the simulation results allowed for the development concerning the final prototype of the switchgear, which could be subjected to the full type tests. Additionally, short-circuit current simulations were procured and presented.

Keywords: heat distribution; thermal analysis; electromagnetic analysis; conduction; convection; radiation; CFD simulation; ANSYS coupled analysis; low-voltage switchgear; FEM simulations

Citation: Szulborski, M.; Łapczyński, S.; Kolimas, Ł. Thermal Analysis of Heat Distribution in Busbars during Rated Current Flow in Low-Voltage Industrial Switchgear. *Energies* **2021**, *14*, 2427. https://doi.org/10.3390/en14092427

Academic Editor: Fabio Polonara

Received: 1 March 2021
Accepted: 22 April 2021
Published: 24 April 2021

1. Introduction

Industrial low-voltage switchgears are electrical devices that allow power distribution. It is necessary to properly protect, control, and monitor the discharge lines from the switchgear to the energy receivers [1]. Low-voltage switchgears are manufactured based on the requirements specified in the IEC 61439 standard (low-voltage switchgear and controlgear assemblies). Therefore, they must meet all requirements for electrical, mechanical, and thermal parameters [2].

In order to meet the thermal requirements for the switchgear, the ratio of heat generated by the active elements in the switchgear must be smaller than the heat dissipation capacity of the entire layout (passive system). Heat transfer to the environment, in this case, is performed by convection, conduction, and radiation [3].

Skin effect, contact resistance, proximity effect occurring in the current circuits, and the resistivity of the material from which the current circuits are made (e.g., busbars) contribute significantly to the generation of increased heat [4–6]. After taking them into account, it is possible to determine active power losses according to Joule's law expressed in watts [7]. Thermal calculations of the current circuits are carried out by heating the busbars with operating currents of a continuous nature and heating from the short-circuit currents [8].

For both situations, the criterion of the permissible thermal condition of the circuit should not exceed the permissible temperature values. Those are standardized and depend on the properties of the circuit material and the environment in the immediate vicinity of the current circuit [9]. Properties were determined considering factors such as reduction of mechanical strength, loss of plasticity, and accelerated aging processes. Under short-circuit conditions, the permissible circuit temperature is higher due to the short-circuit current flow time.

The long-term power load of the busbars with the rated current in the switchgear is defined as the maximum power load of the busbars with the current, which effect does not exceed the temperature for the current circuit [10]. An important parameter describing this phenomenon is the time constant (T) of the current circuit heating. The calculation of the time value of the current circuit heating time (T) allows determining, with high accuracy, the time of heating to the set temperature [11]. After determining one time constant, the temperature increase reaches the value of 0.632 of the temperature in the steady-state of the current circuit. After calculating the five time constants (T), the calculated temperature rise reaches 0.98 of the permissible temperature in the steady-state of the current circuit. Heat transfer of the heated busbars in the switchgear can take place in three ways: by conductivity, convection, and radiation. In the calculation scenarios of electrical equipment current circuits, all or only some of these types of heating may occur [12–14].

The phenomenon of convection relates to the exchange of thermal energy between a solid and a gas or liquid in the immediate vicinity of the solid. It is related to the movement of gas or liquid and depends mainly on the physical properties of the media, the shape and dimensions of the solid surface, temperature difference, and the method of excitation [15]. An analytical determination of the amount of thermal energy transferred by convection is a difficult issue due to the large number of variables and the complexity of initial and boundary conditions.

Radiation is the process of transferring energy from the radiating body to other bodies in the vicinity. The radiating body is characterized by the emission of electromagnetic waves consisting of various wavelengths [16]. The wavelength range with the highest thermal energy transfer is from 0.4 to 10 μm. These can be observed in the infrared region, which is invisible to the human eye. The contribution of radiation to heat transfer and to the environment is primarily dependent on the temperature difference and emissivity between the radiating body and the environment [17]. With a small difference in the order of magnitude, a few or several degrees, radiation plays a small role. Heat is transferred practically by convection. With a temperature difference of several dozen degrees, the proportion of radiation increases significantly and amounts to about 50%. This is the temperature range that occurs in the design of current circuits, so the effect of radiating heat should be considered. Radiation is treated as the release of heat along straight lines perpendicular to the surface of the emitting body [18]. The degree of blackness (ε) of the body radiating heat also affects the radiation efficiency. Covering current circuits (especially with copper and aluminum) with various types of layers and varnishes helps increase the radiated heat flux. This is a widely recognized and affordable activity. This increases the current carrying capacity while maintaining the original heating temperature. In most cases, heat losses through radiation and convection determine the load capacity of the busbar system [19]. The share of heat losses by lifting and radiation depends on the geometrical dimensions of the rail system. In general, the proportion of convection decreases for smaller conductors, while it increases for larger structures [20].

During laboratory tests, specific points in the switchgear are examined where an increase in temperature is expected [21]. However, this does not fully reflect the entire temperature range witnessed in the current circuits present inside the switchgear [22]. In addition, performing these types of tests is a complicated operation, expensive and time-consuming. It requires several tests before developing the finished product. In order to reduce the costs of this type of research [23–27], it is possible to prepare a detailed 3D model of the switchgear and perform a computer simulation in the ANSYS Workbench environment. In addition, using coupled analyses: Maxwell 3D, Fluent CFD, Transient Thermal, allowing for an accurate temperature distribution on the busbars and inside the switchgear [28–31]. This type of calculation allows the structure to be optimized in terms of high temperature resistance, as well as heat dissipation from the switchgear to the environment [32–37]. The novelty of the approach is clearly the cost reduction concerning expensive experimental research and also the ability to reduce materials quantities that ought to be used for switchgear assembly.

The purpose of this work is to analyze the temperature distribution in busbars during rated current flow. A simulation model of physical-thermal phenomena occurring during the flow of current through current circuits in low-voltage switchgear was developed in work and experimentally validated. Additionally, the short-circuit currents simulations and analysis were added but not validated because of the humongous costs that those approaches would take.

The subject of theoretical analysis and simulation were the busbars of low-voltage switchgears and the associated contacts. The presented theoretical test results can be used by designers and manufacturers of switchgears, busbars, and low-voltage electrical apparatus. The paper examines in particular issues regarding:

- Load distribution in current paths;
- Temperature distribution in busbars.

These issues are analyzed in the case of selected systems, requirements, and adopted assessment criteria regarding values:

- Permanent load transfer;
- Failure elimination;
- The arrangement of current circuits and the devices supplied by them.

These criteria are the basis for assessing the proposed design solutions for current circuit systems and their selection in low-voltage switchgears. Taking into account these criteria, appropriate mathematical models have been created that are the basis for all analyzes and simulations of current circuits, their connections in low-voltage switchgears, as well as the implementation of these solutions for production.

In the current conditions of free competition, producers who want to stay on the market are forced to constantly reduce the duration of the launch of a new product, lower its price, increase its utility values, quickly respond to changing customer requirements and adapt to a constantly changing environment. The most effective way to cope with such pressure is to use various types of computer-aided engineering techniques related to it.

An indispensable theoretical base enabling the correct approach to the problem is the book concerning electrical contacts by P. Slade [26], which contains theoretical and practical information about physical phenomena occurring in current circuit contacts. In particular, issues related to the calculation of contact resistance and contact welding were discussed, and the problem of selecting contact materials was presented. Other publications used by Milenko Braunovic are publications [9,10]. The authors showed how important mechanical and electrical characteristics affect the overall reliability and performance of a current circuit contact system.

To date, many scientists have been involved in the analysis and research of busbars. Particular mention should be made of the works of A. Plesca, studies [1,8], in which thermal analyzes in busbars were presented and discussed. In both articles, the author presents simulations of current flow in current paths consistent with the results of experimental research.

The publication J. Lotiya [6] is valuable in the area of heating up high-current flat busbars. The author discusses screw connections of flat busbars commonly used in electrical systems of power stations. The paper presents the analysis of the influence of the clamping force of the screw connection on the value of temperatures achieved in contact with the flow of interference currents on the example of flat copper bars. The issue of heating the current circuits in switchgears is complemented by publications by M. Bedkowski and co-authors [3,18], in which the authors presented a simulation thermal analysis of current circuits for rated currents of prototype switchgears using a CFD solver.

Valuable publications are the works of D. Chapman and T. Norris [4] and R. Berrett [5], which accurately describe how calculations related to flow and heat dissipation from current circuits by convection and radiation should be performed, the authors thoroughly discuss in their works what should mathematical models look like for this type of thermal calculations.

Other works on the generation and dissipation of heat from current circuits during the current flow allowed for a precise reference to the problem in the presented publication [2,6,7,14–16].

2. The Mathematical Model

Thermal energy in the switchgear is generated by the rated current, or short-circuit current flowing through the main current busbars and wires leaving the switchgear. The thermal energy from the current busbars is dissipated to the environment by convection, conduction, and radiation. The relationships describing these phenomena are presented below in Figure 1.

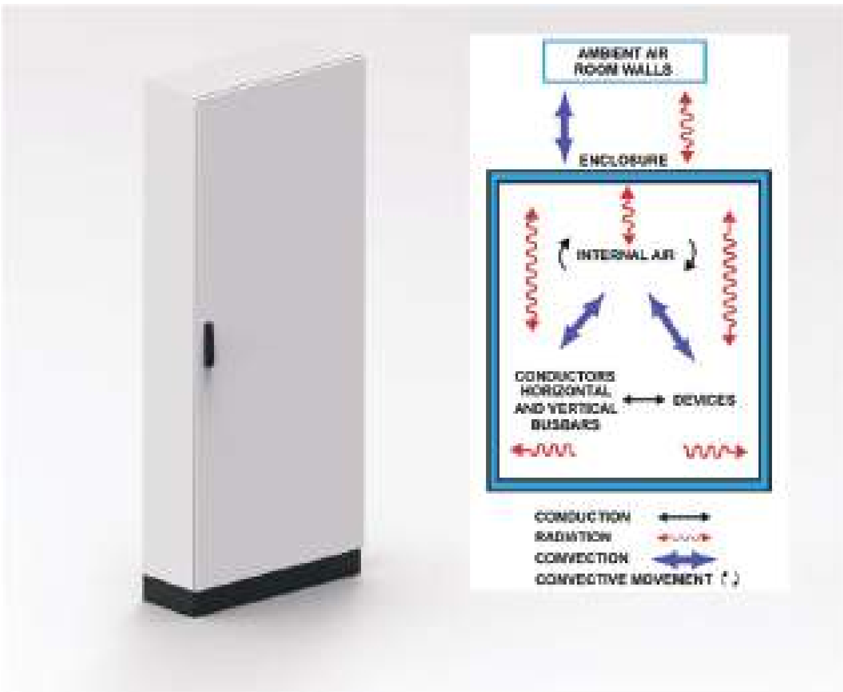

Figure 1. A scheme of heat dissipation in the switchgear by means of conduction, convection, and radiation.

The value of the electric power generated on a given busbar length is the aftermath of current and resistance, described below by means of the equation [38]:

$$P = I^2 x R \tag{1}$$

where P is the power dissipated per unit length (W), I is current in the conductor (A), and R is the resistance per unit length of the conductor (Ω).

All calculations related to the current flow in the busbars and the distributions of the electromagnetic field in the switchgear are possible using the following Maxwell equations [39]:

$$\nabla\ x\ \{H\} = \{J\} + \left\{\frac{\partial D}{\partial t}\right\} = \{J_s\} + \{J_e\} + \{J_v\} + \left\{\frac{\partial D}{\partial t}\right\} \tag{2}$$

$$\nabla x\{E\} = -\left\{\frac{\partial B}{\partial t}\right\} \tag{3}$$

$$\nabla \times \{B\} = 0 \tag{4}$$

$$\nabla \times \{D\} = \rho \tag{5}$$

where $\nabla\ x$ is the curl operator, ∇ is the divergence operator, *{H}* is the magnetic field intensity vector, *{J}* is the total current density vector, *{Js}* is the applied source current density vector, *{Je}* is the induced eddy current density vector, *{Jv}* is the velocity current density vector, *{D}* is the electric flux density vector, *t* is the time, *{E}* is the electric field intensity vector, *{B}* is the magnetic flux density vector, ρ the electric charge density.

For the calculation concerning the coupled heat transfer process between the carrier fluid (air) and the solid domains, the Navier–Stokes equation is used alongside the energy equations, and those were described below [40]:

The continuity equation is given by:

$$\frac{\partial u}{\partial x} + \frac{\partial v}{\partial y} + \frac{\partial w}{\partial z} = 0 \tag{6}$$

and the momentum equation:

$$\rho \vec{v} \cdot \vec{\nabla} \vec{v} = -\vec{\nabla} p + \mu \vec{\nabla}^2 \vec{v} + \vec{F} \tag{7}$$

The expression of the energy equation is as follows [40]:

$$\rho c_p \left(\frac{\partial Tu}{\partial x} + \frac{\partial Ty}{\partial y} + \frac{\partial Tw}{\partial z}\right) = \frac{\partial}{\partial x}\left(k_t \frac{\partial T}{\partial x} + u\tau\right) + \frac{\partial}{\partial y}\left(k_t \frac{\partial T}{\partial y} + v\tau\right) + \frac{\partial}{\partial z}\left(k_t \frac{\partial T}{\partial z} + w\tau\right) \tag{8}$$

where *x*,*y*,*z* are the Cartesian coordinates, *u*, *v*, *w* are the velocities in *x*, *y*, *z*, directions, $\vec{v}$ is the velocity vector, *p* is the pressure, ρ is the density, μ is the dynamic viscosity, $\vec{F}$ is the body force vector, *T* is the temperature, k_t is the thermal conductivity of air, and τ is the viscous shear stress.

2.1. Heat Dissipation by Convection in Busbar

The amount of heat dissipated by convection depends on the shape, size of the rail, and the temperature increase around the rail [4]. Heat dissipation from the busbar by convection is different for horizontal and vertical surfaces, as shown in Figure 2 and the equation below [38,39]:

$$q_{conv} = W_c A_c = W_v A_{Cv} + W_h A_{ch} \tag{9}$$

where W_c is heat dissipated per square meter due to convection (W/m^2), A_c is the surface area of the conductor (m^2), W_v is heat dissipated per vertical square meter due to convection (W/m^2), W_h is heat dissipated per horizontal square meter due to convection (W/m^2), A_{Cv} is the vertical surface area of the conductor (m^2), A_{ch} is the horizontal surface area of the conductor (m^2).

Convective heat exchange is influenced by: thermal conductivity coefficient, heat capacity, specific mass, kinematic viscosity, shape and dimensions of the cooled solid, and the nature of the cooling gas flow. In this paper, due to the lack of forced flow of the refrigerant, the issues concerning the forced convection are omitted. The thermal power transmitted to the environment by air convection is determined then by the formula [38,39]:

$$P_k = k_k S_k (T - T_o) \quad (10)$$

where, P_k is power transmitted by convection (W), k_k is the heat transfer coefficient by convection (W/m^{2}K), S_k is heat dissipation surface (m^2), T is the temperature of the cooled element (K), and T_0 is the ambient temperature (K).

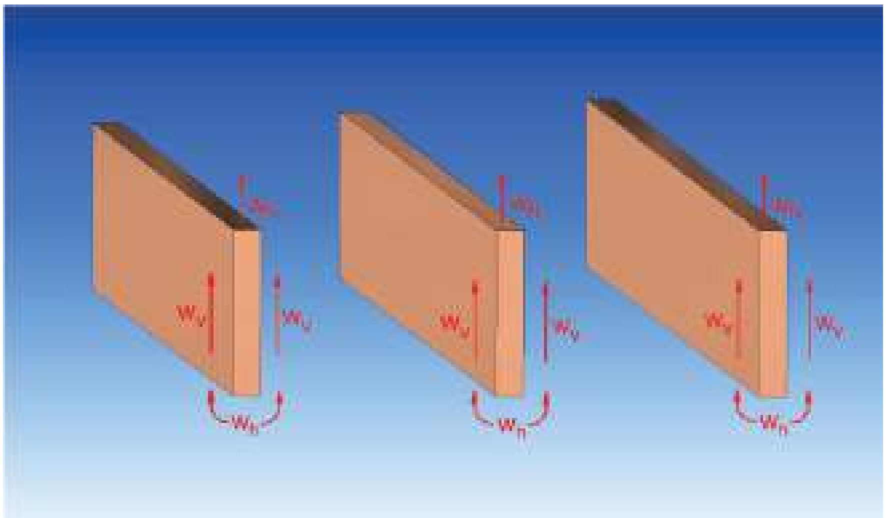

Figure 2. A scheme of heat dissipation in the switchgear.

Analytical determination of the amount of thermal energy transferred by convection is a difficult issue due to the large number of variables and the complexity of initial and boundary conditions. The coefficient values can be determined experimentally, with the proviso that the results obtained are valid only for the conditions occurring during the measurement. In the field of thermokinetics of electrical apparatuses, similarity theory is used to quantify the value of heat transfer that is causing hotter air to lift. Criterion numbers are described by the formulas below [38,39]:

$$Nu = \frac{k_k}{\lambda} l_w \quad (11)$$

$$Gr = \frac{g\beta\Delta T}{v_r^2} l_w^3 \quad (12)$$

$$Pr = \frac{v_r}{a_t} \quad (13)$$

$$Ra = \frac{V_{speed}}{v_r} l_w \quad (14)$$

where λ is the thermal conductivity of the heat-carrying gas *(W/mK)*, l_w is the characteristic dimension of the body giving off heat (for cylindrical shapes, this will be the diameter, for flat bars arranged vertically—height) *(m)*, g is gravity constant (9.8 m/s^2), β is the coefficient of thermal expansion *(1/K)*, v_r is the refrigerant lifting speed (m^2/s), a_t—temperature conductivity of the fliud [W/m·K], V_{speed}—cooling medium lifting spedd [m/s].

For the case of cooling current paths through free airflow, the following dependency is used [38,39]:

$$Nu = f(Gr \cdot Pr) = c_1 (Gr \cdot Pr)^{n_1} \quad (15)$$

The values of the coefficients c_1 and n_1 depend on the result of the numbers Gr and Pr, to which the respective shapes of current circuits can be assigned. Introducing the additional equation presented below allows the determination of the value of the coefficient k_k [38,39]:

$$A = \frac{g\beta}{v_r^2} Pr \tag{16}$$

$$k_k = \frac{\lambda \cdot c_1 \cdot \left[A \cdot l_w^3 \cdot (T - T_0)\right]^{n_1}}{l_w} \tag{17}$$

Table 1 presents examples of coefficient values for frequently analyzed calculation cases of this type.

Table 1. The list of c_1 and n_1 values for a given Gr and Pr range.

The Shape of the Cooled Element	Gr · Pr	c_1	n_1
Switchboard vertical plate	1.7×10^8–2×10^{10}	0.15	0.33
Horizontal plate (heat dissipation up top)	2.3×10^8–1.1×10^{10}	0.17	0.33
Cylindrical busbar	5×10^2–2×10^7	0.54	0.25
Rectangular busbar	9.4×10^4–4.6×10^6	0.60	0.25

For busbars with simple shapes, the practical calculations of the heat transfer coefficient in the air, the simplified formulas below are often used [38,39]:

- For vertical planes, the following relation applies:

$$k_k = 7.66 \left(\frac{\Delta T}{l_w}\right)^{0.25} \tag{18}$$

- For horizontal planes:

$$k_k = 5.92 \left(\frac{\Delta T}{l_w}\right)^{0.25} \tag{19}$$

- For circular busbars:

$$k_k = 7.66 \left(\frac{\Delta T}{l_w}\right)^{0.25} \tag{20}$$

2.2. Heat Dissipation by Radiation in Busbar

The distribution of heat by radiation from the busbar to the environment is shown in Figure 3 and described in the following equation [38,39]:

$$q_{rad} = W_R A_R = 5.70 \times 10^{-8} \times \mathrm{e} \left(T_1^4 - T_3^4\right) \times A_R \tag{21}$$

$$\mathrm{e} = \frac{\varepsilon_1 \varepsilon_2}{(\varepsilon_1 + \varepsilon_2) - (\varepsilon_1 \varepsilon_2)} \tag{22}$$

where W_R is heat dissipated per square meter due to radiation (W/m^2), A_R is the surface area of the conductor (m^2), e is relative emissivity, T_1 is the average temperature of busbar (K), T_3 is the average temperature of the inner surface (K), ε_1 is the absolute emissivity of busbar, ε_2 is the absolute emissivity of the enclosure's inner surface.

For internal opposite surfaces of rectangular busbars, it is assumed that there is no radiation. The temperatures of these surfaces are approximately equal.

2.3. Heat Absorption by Enclosure from Busbars

When the short-circuit current flows through the busbars, a very large amount of heat is generated. It is transferred from busbars to the enclosure by means of radiation and convection. The rate at which the heat generated by the busbars is absorbed by the enclosure is proportional to the rate at which this heat is generated in the busbars by the flow of short-circuit current. This relation is described by the equation:

$$P = q_{conv} + q_{rad} \tag{23}$$

where P is power dissipation per unit length of busbar (W), q_{conv} is heat dissipation due to convection (W), q_{rad} is heat dissipation due to radiation (W).

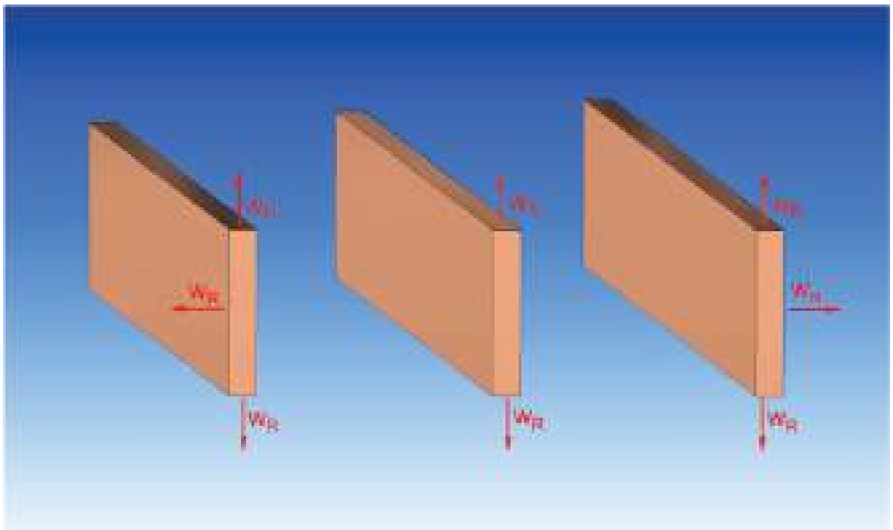

Figure 3. A scheme of heat dissipation from vertical busbars in the switchgear.

2.3.1. Heat Absorption by Enclosure from Busbars by Convection

The rate at which the heat dissipated by the busbars is absorbed to the enclosure via convection depends on the size, shape, and surface difference of the enclosure and busbars [5]. Heat absorbed by the enclosure via convection from busbars is different for vertical and horizontal surfaces of the copper busbars, as described in the equation [38,39]:

$$q_{conv} = k_{kvertical} A_v + k_{khorizontal} A_t \tag{24}$$

where $k_{kvertical}$ is average vertical convection heat transfer coefficient ($\mathrm{W/m^2}$), $k_{khorizontal}$ is average top convection heat transfer coefficient ($\mathrm{W/m^2}$), A_v is the vertical surface area of enclosure ($\mathrm{m^2}$), and A_t is the top surface area of enclosure ($\mathrm{m^2}$).

The heat absorbed via convection by the vertical plane can be calculated by means of equations [38,39]:

$$Ra_{vertical} = \frac{g\beta(T_1 - T_3)G_1^3}{v \cdot \alpha} \tag{25}$$

$$Nu_{vertical} = 0.22\left(\frac{Pr}{0.2 + Pr} Ra_{vertical}\right)^{0.28}\left(\frac{H}{G_1}\right)^{-1/4} \tag{26}$$

$$k_{kv1} = \frac{Nu_{vertical} k_t}{H} \tag{27}$$

where Nu is average Nusselt number, Ra is Rayleigh number, β is volumetric thermal expansion coefficient (K^{-1}), g is gravity constant ($9.8\ \mathrm{m/s^2}$), T_1 is the average temperature of busbar (K), T_3 is the average temperature of the inner surface (K), H is the height of the enclosure (m), G is the gap between the enclosure wall and busbar (m), v is kinematic viscosity ($\mathrm{m^2/s}$), α is thermal diffusivity ($\mathrm{m^2/s}$), k_t is thermal conductivity (W/mK), and Pr is the Prandtl number.

The same applies to the heat absorbed by the horizontal plane by convection when heated from below, which can be calculated using the following equations [38,39]:

$$Ra_{horizontal} = \frac{g\beta(T_1 - T_3)G_2^3}{v \cdot \alpha} \tag{28}$$

$$Nu_{horizontal} = 0.0069 Ra_{horizontal}^{1/3} \cdot Pr^{0.074} \tag{29}$$

$$k_{kt1} = \frac{Nu_{horizontal} \cdot k_t}{H} \tag{30}$$

2.3.2. Heat Absorption by Enclosure from Busbars by Radiation

The heat absorbed by the enclosure is equal to the dispersion of heat radiation from the busbars. This is described by the equation in point 2.2.

2.4. Heat Transfer via Conduction through the Enclosure Wall

Heat transfer through the sheets of the casing is carried out by means of conduction. This can be described in the following equations [38,39]:

$$P = q_{cond} \tag{31}$$

$$q_{cond} = k_t A \frac{\Delta T}{\Delta x} \tag{32}$$

$$\Delta = T_3 - T_4 \tag{33}$$

where P is power dissipation per unit length of busbar (W), q_{cond} is heat conducted through enclosure rear sheet (W), k_t is enclosure thermal conductivity (W/mK), A is the surface area of enclosure (m^2), T_3 is the average temperature of the outer enclosure surface (K), T_4 is the average temperature of the outer enclosure surface (K), and Δx is enclosure sheet thickness (m).

3. Three-Dimensional (3D) Model

In order to perform computational simulations, it was necessary to prepare an accurate 3D model of the chosen switchgear. For this purpose, Solid Edge software was used, where all components of the switchgear were modeled. The created 3D model focused on the exact mapping of the arrangement and dimensions of all structural elements of the switchgear. The external dimensions of the switchgear were 800 mm (width), 1950 mm (height), and 300 mm (depth). The L1, L2, and L3 vertical busbars, i.e., the main supply bridge in the switchgear, connected the other horizontal busbars with the main switch. Fuse disconnectors were installed on the horizontal rail bridges. All copper busbars in the switchgear were 30 × 10 mm in cross-section. On the horizontal rail bridges, metallic phase connections (jumpers) have been designed to withstand rated current flow in the switchgear busbars using short copper bars, also with a cross-section of 30 × 10 mm. In the prepared model, the requirement was to accurately reflect the busbar system, including insulators, brackets, and holders, because the results of simulations of current distribution, heat, and power losses are only then the closest to the results obtained in experimental conditions.

The prepared 3D model was modeled of many parts and assembled consisting of various shapes and different material parameters. Creating a very accurate 3D model of the switchgear was associated with a longer duration of calculations and more computational iterations. The main reason for the large number of calculations was the large number of surfaces, edges, and computational nodes in the generated mesh. The finished switchgear model was saved in the ". sat" format. This format is the most suitable for importing files in ANSYS.

In the simulations, the same detailed 3D model was used in the calculations with the Maxwell 3D and the Transient Thermal. The CFD solver used a 3D model cross-section that accurately reflected the location of the busbars and masking panels in the switchgear.

Creating a "mesh" was an extremely important process during the discretization of the 3D model.

In Maxwell 3D analysis, the solver used the adaptive grid generator option, which automatically compacted the mesh during calculations until the assumed convergence parameter, "Energy error" of 1%, was reached. The final amount of mesh elements for this solver was 379639. The Transient Thermal solver was made with a mesh of an appropriate density, which resulted in 513,304 mesh elements and 1,084,554 computational nodes.

In the CFD solver, due to the effects associated with boundary layers, e.g., between busbars and the surrounding air, the mesh was additionally condensed in these places. That made it possible to meet the requirements for the type of phenomenon simulated. Mesh size for CFD solver was 335,420 nodes and 331,140 elements, respectively.

The structural model of the switchgear is the most detailed 3D model. It contains all the details such as bolts, nuts, gaskets etc. Figure 4 shows different views of the structural model of the switchgear (prototype). The figure shows the open switchgear and the internal insert itself in the form of brackets, holders, and copper busbars, to which the main switchgear apparatuses were attached or connected with.

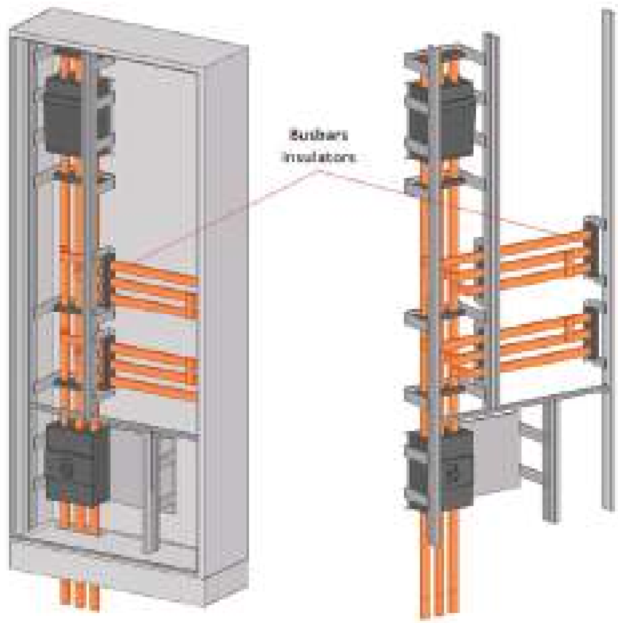

(**a**) (**b**)

Figure 4. Views of the finished construction 3D model of the switchgear: (**a**) open; (**b**) the internal part of the switchgear.

4. Coupled Electromagnetic, Transient Thermal and Fluid Flow Analysis (ANSYS Maxwell, Transient Thermal and Fluent CFD)

4.1. Simulation in Ansys Maxwell 3D—Rated Current Flow in Switchgear

In order to conduct the analysis, it was necessary to implement the prepared 3D model of the switchgear. ANSYS Maxwell 3D software managed to load a previously prepared 3D model in ". sat" format. After importing the model, the solver type was chosen: "Eddy Current" and material properties for busbars, insulators, switchgear metal elements, housing as well as switchgear surroundings were given; in this case, it was air. All material properties were shown in Table 2.

Table 2. Materials properties for electromagnetic and thermal analyses.

Material	Density (kg/m^3)	Specific Heat (J/kg*K)	Thermal Conductivity (W/m*K)	Electric Conductivity (S/m)	Magnetic Permeability (H/m)
Air	1.205	1005	0.0257	3.00×10^{-15}	1.256×10^{-6}
Copper	8960	385	401	5.81×10^{7}	1.256×10^{-6}
Structural Steel	7850	434	60.5	6.21×10^{6}	1.256×10^{-6}
Galvanized Steel	7833	481	52.0	5.88×10^{6}	1.256×10^{-6}
Polyethylene	950	2300	0.28	6.3×10^{-14}	1.256×10^{-6}

The values of rated currents were added to the main busbars supplying the switchgear. Busbars were entering the interior of the switchgear before the main switch. This is precisely reflected in the following Table 3 and Figure 5, where current excitation values for each phase of the L1, L2, and L3 switchgear current circuits were given and marked.

Table 3. Current excitations in 3-phase busbar in "Eddy Current" solution type.

Phase of Busbar	Value (A)	Phase (deg)
L1	630	0
L2	630	120
L3	630	240

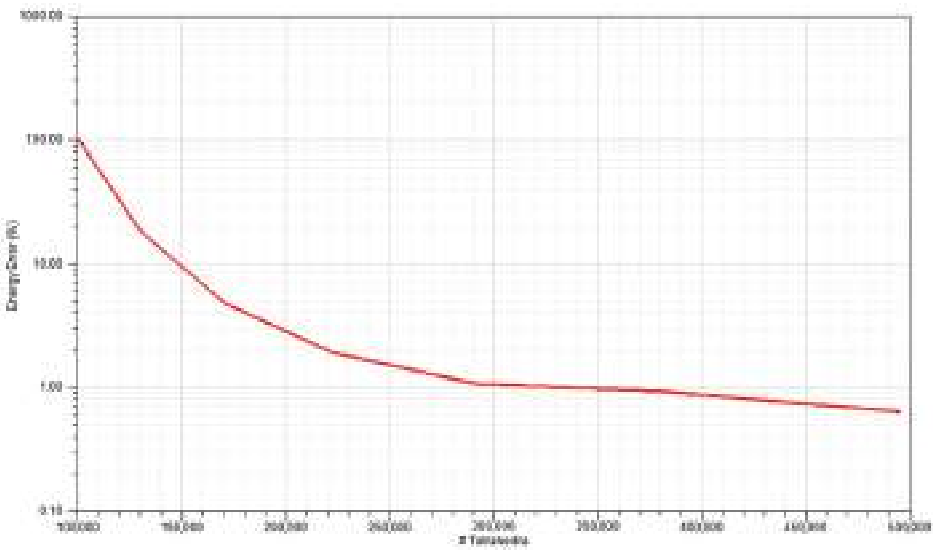

Figure 5. Convergence plot—energy error in relation to the number of "Tetrahedra".

After determining all boundary conditions for the simulation, it was possible to start the solver, which performed calculations for a three-phase rated current of 630 A in each of the busbar phases inside the switchgear.

Our calculations showed that the number of "Tetrahedra" components was equal to 379,639 elements with the assumed "Energy Error" below 1%. Mesh density can be applied in the solver using an energy error estimation. The energy error is calculated by comparing the difference between the final averaged node value flux value for each node throughout the model. This error is then multiplied by the conductivity matrix for each node and integrated on each element to determine the energy error for that element. The energy error for the entire model is the sum of the energy errors for each element. Large energy error values mean that the flux field is very discontinuous, and small energy error values mean a more continuous flux field. While there are no absolute values for the energy error limits, a maximum percentage error of 1% is the recommended value [25]. To perform this analysis, the solver needed six computational iterations. Figure 5 illustrates the above amount of increased mesh elements with each subsequent calculation iteration.

Table 4 below shows the results of each iteration step for the number of Tetrahedra. Total Energy, Energy Error and Delta Energy elements. These are parameters which values determine whether the simulation results coincide. In the analyzed case, it can be seen that in the last six computational iterations, an "Energy Error" of 0.68203% was obtained, which is a satisfactory result.

Table 4. Number of iterations of calculation with the Energy Error accepted for calculation.

Pass	Tetrahedra	Total Energy (J)	Energy Error (%)	Delta Energy (%)
1	100,267	429.44	104.34	N/A
2	130,859	390.37	18.278	9.0977
3	170,789	378.11	4.8174	3.1413
4	222,883	373.48	1.9065	1.2243
5	290,877	370.84	1.0733	0.70696
6	379,639	369.51	0.68203	0.35688

After using the post-processing function in ANSYS Maxwell 3D, the calculation results were generated in the form of drawings showing the current flow in the rails counting in Ohm losses or the distribution of electromagnetic induction in the body and metal parts of the housing. Ohm losses arising during the flow of currents through the busbars are expressed in (W/m^3). In the metal housing and metal elements of the switchgear, under the influence of induced eddy currents, Ohm losses in the form of heat generated also arose. Figure 6 shows the exact distribution of Ohm's losses on a logarithmic scale in both busbars and metal components of the switchgear.

Another simulation result in the Maxwell 3D solver was the distribution of current density in current circuits expressed as (A/m^2) and the distribution of the electromagnetic induction field expressed in Tesla. The highest value of current density was achieved in the sections of the busbars through which the rated currents flowed. In the case of electromagnetic induction field distribution, the highest values were generated in the bottom and rear sheet of the switchgear housing near the vertical rail bridge through which the rated currents for three phases flowed.

After analyzing the distribution of the electromagnetic induction field in each metal element, one can find the relationship between Ohm losses generated by eddy currents in the metal elements of the switchgear (bypassing copper bars). This relationship is extremely important because, in some cases, the local temperature may increase in the metal elements of the switchgear. It is caused by the induced eddy currents, which were not the desired phenomenon. The value of current density and electromagnetic induction field distribution was shown in Figure 7.

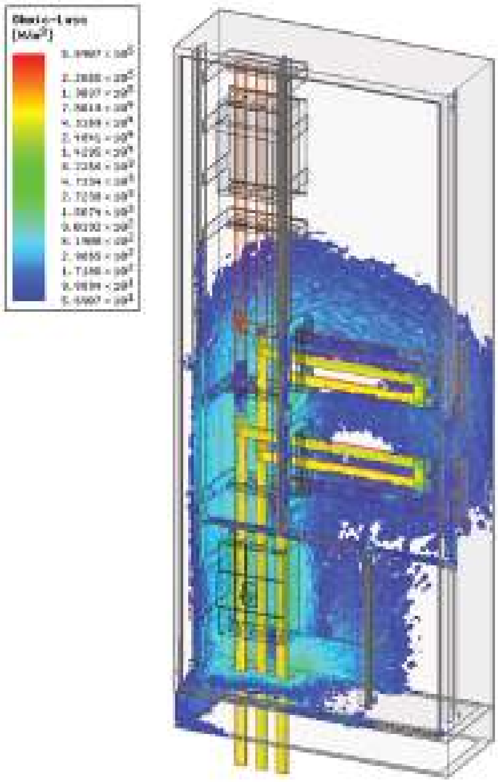

Figure 6. Ohm's loss distribution presented on a logarithmic scale in the switchgear.

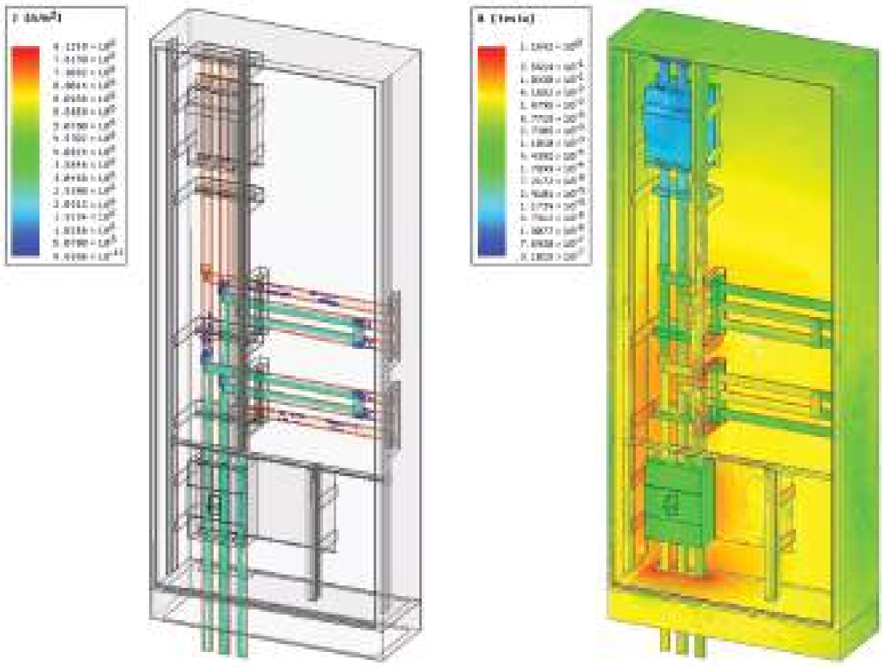

Figure 7. Current density distribution in busbars **(on the left)**, electromagnetic induction field distribution in the switchgear **(on the right)**.

4.2. Simulation in Transient Thermal—Heat Generation under the Influence of Rated Current Flow in the Switchgear Busbars

After performing the computational operations related to the rated currents in Maxwell 3D, it was possible to start a coupled analysis consisting of the imported calculation results from the previous solver to the next calculation module, “Transient Thermal”. To achieve this, the “Transient Thermal” solver was selected in the Workbench workspace and added to the “Maxwell 3D” solver, after which the two solvers were properly combined.

The next stage of the coupled analysis initiation was selecting the appropriate material data from the “Engineering Data” tab, which was used after opening the “Transient Thermal” solver to assign them to individual structural parts of the switchgear. Then the “mesh” was generated with the appropriate accuracy for this type of calculation.

After making a high-quality computational grid, the parameters for convection (film coefficient and ambient temperature) and radiation (emissivity and ambient temperature) for copper busbars were added to the solver. The ambient temperature of the switchgear was assumed as 22 °C. It was possible to import the heat generation sources from the Maxwell 3D solver. To achieve this, the “Imported Load” option was used, the data were imported, and calculations were made.

At this stage, it was already possible to make calculations related to heat distribution in current circuits. The calculations were made for 7200 s, which obtained the theoretical characteristics of the temperature values for the busbars placed in the housing, Figure 8. In addition, it was assumed that the insulators and switchgear construction withstood the resulting electrodynamic forces and mechanical stresses associated with them. It is known that in short-circuit conditions, it is not possible to achieve because, under the influence of electrodynamic forces and stresses, the switchgear structure could be disturbed, insulators could be destroyed, and rails could bend and melt after exceeding the Curie temperature.

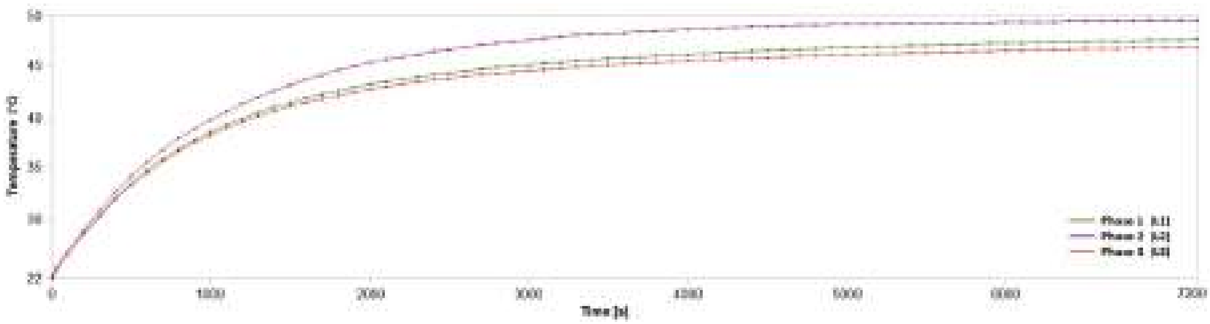

Figure 8. The characteristics of the theoretical establishment of the temperature value in the current busbars.

The characteristics obtained allowed for an assessment of when the maximum operating temperature of the current insulators used would be exceeded. In the analyzed case, the flame-retardant material used for insulators was a fireproof halogen-free polyester, which has a maximum operating temperature of 960 °C. The busbar temperature distribution for 7200 s was shown in Figure 9.

The above temperature distribution on the insulator ensures that the use of flame-retardant material for support insulators for busbars allows to significantly extending the insulator’s resistance to high temperature. At the same time, it increases the strength and reliability of the entire switchgear in the event of a short circuit, when a very high temperature can occur in the busbars during short-circuit conditions that are not the main objective of this work.

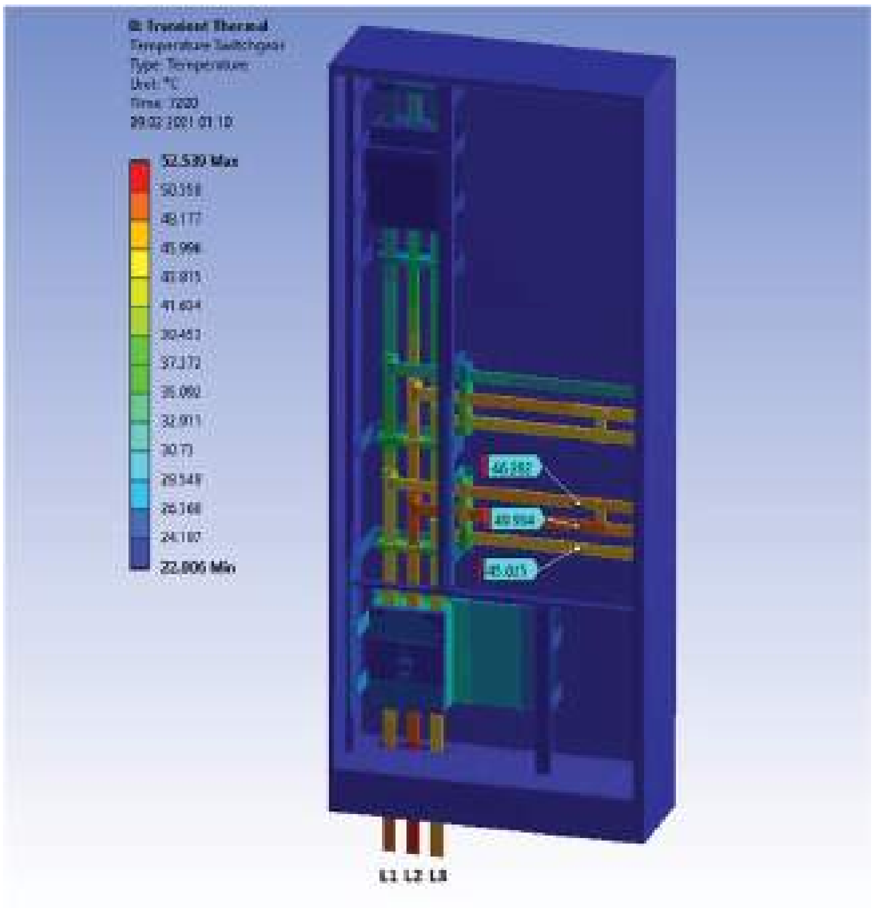

Figure 9. The temperature distribution in busbars and insulators during 7200 s simulation.

4.3. Simulation in ANSYS Fluent CFD—Heat Distribution from Busbars Inside the Enclosure under the Influence of Rated Current Flow in Switchgear Busbars

In order to investigate the impact of heat inside the low-voltage switchgear more widely at the operation at rated current conditions, another Fluent CFD (Computational Fluid Dynamic) solver was used. The CFD calculation module is originally used to simulate the flow of fluids, therefore obtaining results from it is an interpretation of the electromagnetic phenomena. The current carrying capacity of the busbars depends on the temperature discharge. Multiphysical simulations are now used to predict flow field and energy distribution. Using the 2D module, we can quickly orientate heat convection even from point sources (connections, mounting holes that reduce the conduction surface). This solver allows simulating the distribution of hot air through current rails using conduction, convection, and radiation inside the switchgear. This method is labor-intensive in preparation for calculations and requires large memory resources (high-end computer), such as a large random-access memory (RAM) and hard disk capacity, as well as a fast processor. This method allows you to perform the simulations for complex 3D models, thanks to which it is possible to analyze in detail the heat flow inside the developed and complicated construction of the low-voltage switchgear.

In order to use this method, it was necessary to properly prepare the geometric model of the switchgear model. An important task before making the calculations was the proper preparation of geometry and mesh, which in the CFD solver must be carefully refined.

In the analyzed case, it was decided to use the Fluent CFD 2D solver, which required proper preparation of the 2D model of the modeled switchgear. For the purposes of simulation, a cross-section was made from the 3D structural model of the switchgear so as to obtain a preliminary 2D model of the switchgear. This process is thoroughly illustrated in Figure 10.

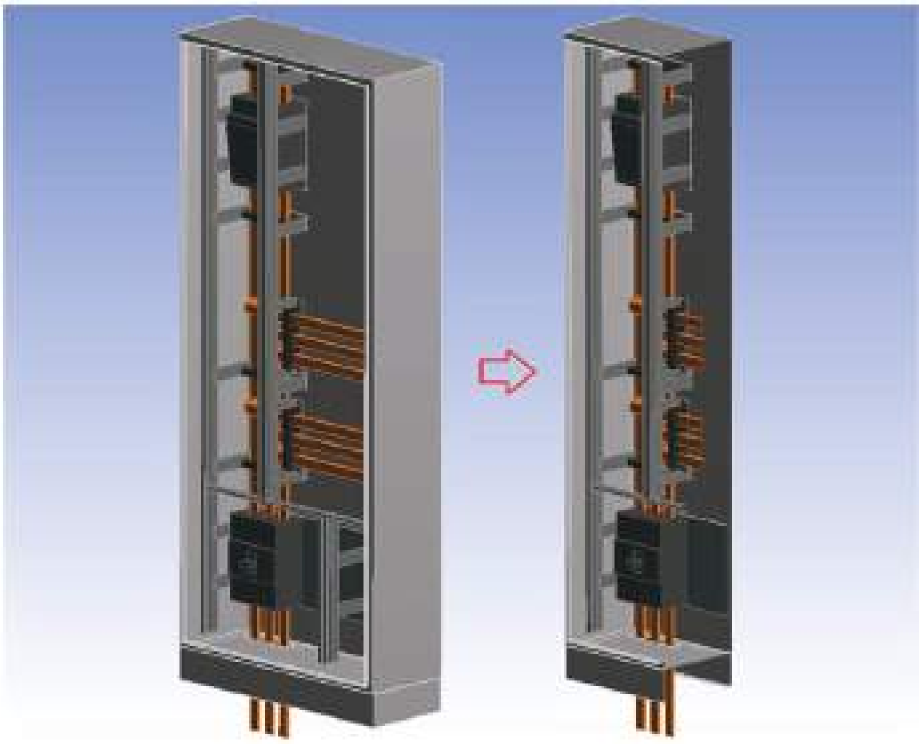

Figure 10. The switchgear cross-section necessary for calculations in Ansys Fluent 2D.

After importing the model into the solver, a mesh was prepared with properly concentrated places in the boundary layers, between the busbars, shields, and air. At this stage, all necessary parameters and conditions necessary to perform the simulation were set. Material properties have been defined for switchgear and air components. The same ambient temperature was used as for the simulation in Transient Thermal −> 22 °C. Parameters have been defined in "Boundary Conditions" and "Cell Zone Conditions". Then, the simulation time steps were defined at the level of 1 s and the simulation length, which was assumed to be 7200 s. After all the simulation settings, it was possible to start calculations in the Fluent CFD solver.

The simulation results are presented in Figure 11, where the convective distribution of heated air from current bars inside low-voltage switchgear is illustrated. The simulation results were presented for: 15, 30, 45, 60, 600, 1800, 3600, and 7200 s of simulation time. The Fluent CFD solver needed 7200 computational iterations to perform a full simulation.

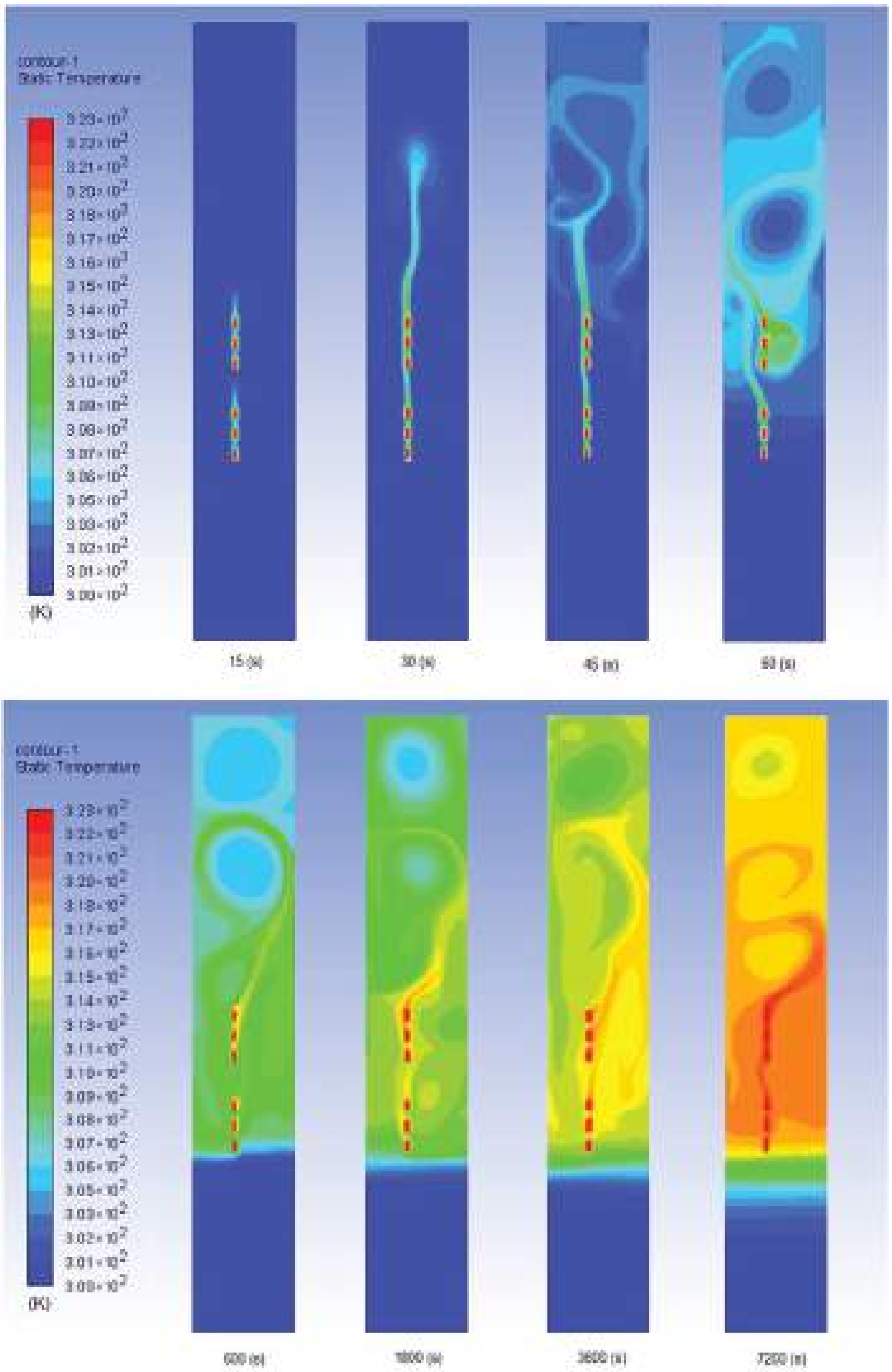

Figure 11. The convective distribution of heated air inside the switchgear.

Further concluding the calculations in the Fluent CFD solver, it was possible to observe how the air heated intensively by the busbars behaves. In addition, the phenomenon of natural convection fueled the process of mixing cool and hot air inside the switchgear. As observed in the simulation results, the air temperature in the upper part of the interior of the switchgear that was up to 15 s of simulation duration would not threaten the wires and electrical apparatuses, while in the further part of the simulation, the temperature increased significantly. At these temperatures, the insulation of the wires and the housing of the switchgear melt. For 7200 s, the temperature inside the switchgear exceeded 50 °C, the temperature of this volume would not cause the inside of the switchgear to ignite.

4.4. Additional Theoretical Short-Circuit Simulations

Additionally, simulations in short-circuit conditions were procured in order to show thermal impact on the transmission elements of the switchgear (busbars, insulators). As it can be witnessed in Figures 12 and 13, the temperature during short circuits conditions, which involved the short-circuit current equal to 25 kA, exceeded 960 °C. Taking into account the temperature and electrodynamic forces influence the conditions may cause a fire in the switchgear, insulators fault, and even busbar destruction.

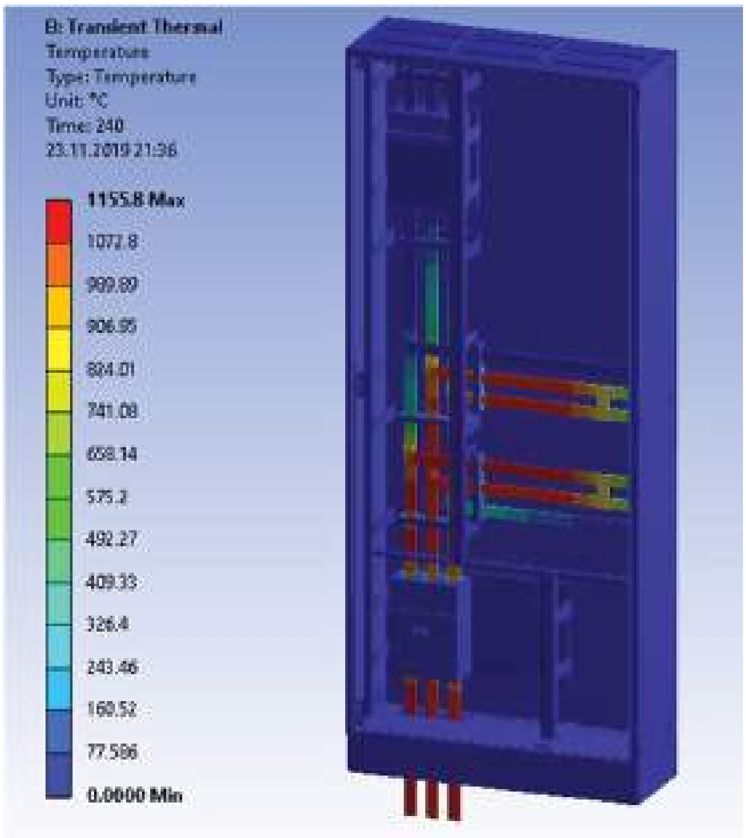

Figure 12. The convective distribution of heated air inside the switchgear in short-circuit conditions.

For short-circuit simulation, validation was not executed because of the very high costs of experimentation measures. Those simulations are theoretical and should be treated as additional content for this work. Those may be validated in future works.

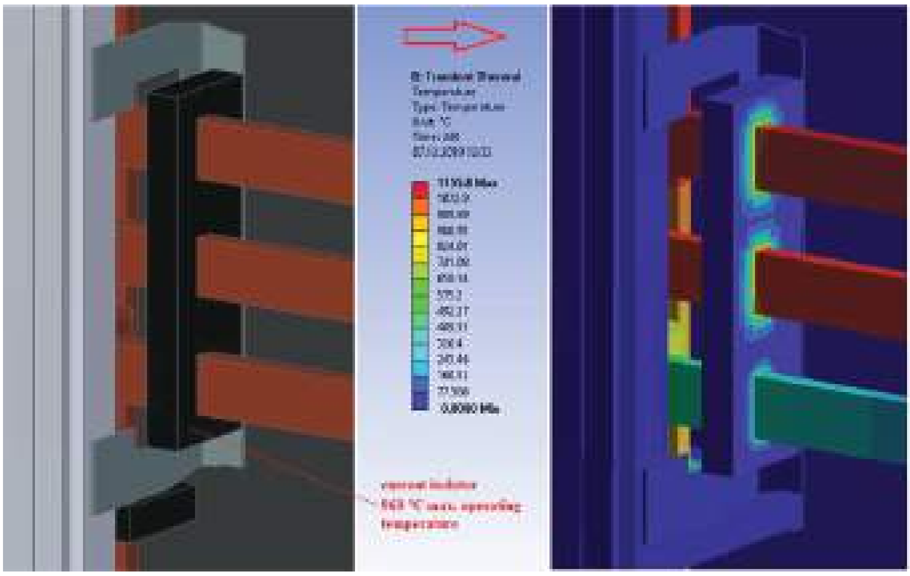

Figure 13. The temperature distribution in busbars and insulators during 240 s simulation in short-circuit conditions.

5. Laboratory Setup

5.1. Elements of the Test Stand

The laboratory layout was consisting of:

- The power supply device, i.e., a regulated mains current source and a three-phase transformer of these phase currents with values up to 1 kA and output voltages adjustable with jumpers (Figure 14);
- Flexible cables of type LGY 2 × 1 × 150 mm^2 connecting the above-mentioned transformer with switchgear busbars screw joints;
- Tested switchgear equipped with fuse switch disconnectors; thermocouples were glued to the switchgear temperature measuring points;
- Screen recorder with a 16-channel waveform measuring device, which, among other things, conducts the acquisition of measurements.

(**a**) (**b**)

Figure 14. Power supply system used for tests: (**a**) three-phase regulated mains current source; (**b**) three-phase adjustable power transformer.

The preparation of the measuring system in the laboratory was not complicated and relatively short, while the measurements took about 2 h. The acquired practical knowledge makes it possible to state unequivocally that in order to obtain objective results, the stand should be expanded with additional measuring devices, for example, the possibility of measuring voltage drops on fuse-links and entire devices along with temperature increase. However, those were not obligatory for the means of results validation.

5.2. Experimental Results

Thermocouples were mounted in the contact space of the disconnectors being inside the switchgear—one for each apparatus. The results are graphically represented by curves. One of the thermocouples was placed in the upper part of the switchgear, above the tested disconnectors. The results of air temperature measurement in the switchgear are shown in Figure 15 below:

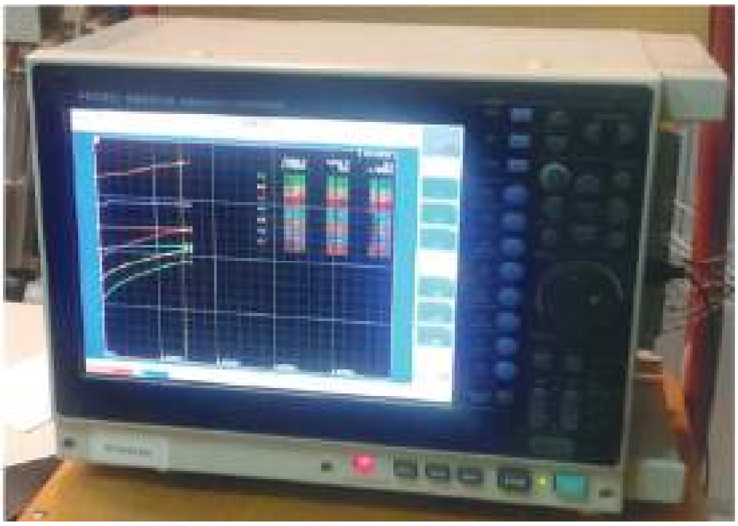

(**a**)

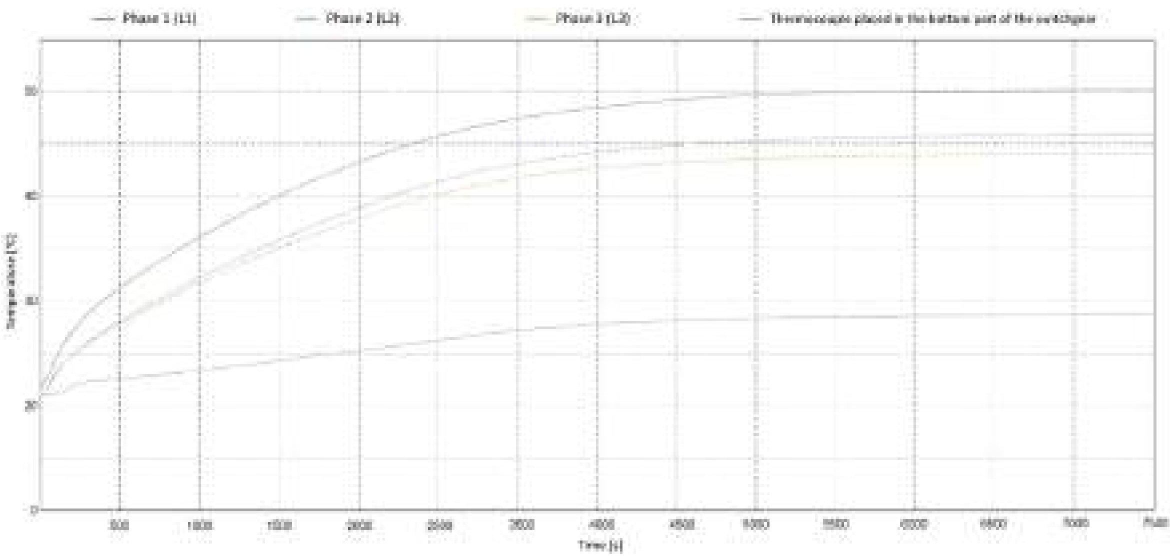

(**b**)

Figure 15. Experimental results: (**a**) measurement results; (**b**) measurement results for phase currents of approximately 630 A.

Results values derived from simulations were significantly similar to those derived from experimental work. Therefore, those are validating positively 3D model functionality during rated current simulations.

6. Conclusions

The preparation of a detailed 3D model of low-voltage switchgear and the use of the coupled analyzes Maxwell 3D ⇔ Transient Thermal ⇔ Fluent CFD, is helpful and necessary when performing the thermal design of the low-voltage switchgears. It is essential in order to save time and resources during the design process. That mostly concerns the shape of busbars inside the switchgear and their placement, as it is essential for proper heat distribution.

The results of the Fluent CFD solver calculations are consistent with the calculations in the Transient Thermal solver and have been carried out correctly. The busbar temperature in both analyzes is confirmed and valid. The simulation in Fluent CFD provided additional information regarding heat distribution inside the switchgear associated with air convective movement models concerning conditions inside the switchgear.

The simulation results obtained proved that such simulations are an ideal tool for correctly designing the construction of low-voltage switchgear. This type of simulation verification of the prototype of the switchgear structure allows reducing potential construction errors and avoiding expensive experimental tests, which in the case of testing the heat flow inside the switchgear during a short circuit, are very complicated and require advanced equipment. Moreover, the simulation results were validated for rated conditions of employing currents equal to 630 A. Validation for a value of 25 kA was not possible due to the aspect of conducting very expensive research work. Nevertheless, the approximation is enough in order to evaluate FEM model functionality and accuracy.

The advantage of this analysis is that the creation of a 3D model of the switchgear and simulation are much faster than experimental research. Moreover, those are significantly reducing costs, which allows for rapid product development. The performed analyzes prove that this solution can be used in the case of complex projects involving the generation and distribution of heat inside switchgears.

These types of simulation solutions allow refining the design of low-voltage switchgears and obtaining more reliable construction solutions.

Author Contributions: Conceptualization, M.S., S.Ł., and Ł.K.; Data curation, M.S., S.Ł., and Ł.K.; Formal analysis, M.S., S.Ł., and Ł.K.; Investigation, M.S., S.Ł., and Ł.K.; Methodology, M.S., S.Ł., and Ł.K.; Project administration, M.S., S.Ł., and Ł.K.; Resources, M.S., S.Ł., and Ł.K.; Supervision, M.S., S.Ł., and Ł.K.; Validation, M.S., S.Ł., and Ł.K.; Visualization, M.S., S.Ł., and Ł.K.; Writing—original draft, M.S., S.Ł., and Ł.K.; Writing—review and editing, M.S., S.Ł., and Ł.K. All authors have read and agreed to the published version of the manuscript.

Funding: This research received no external funding.

Institutional Review Board Statement: Not applicable.

Informed Consent Statement: Not applicable.

Data Availability Statement: Not applicable.

Conflicts of Interest: The authors declare no conflict of interest.

References

1. Plesca, A. Thermal Analysis of Busbars from a High Current Power Supply System. *Energies* **2019**, *12*, 2288. [CrossRef]
2. Kim, M.; Bak, S.; Jung, W.; Hur, D.; Ko, D.; Kong, M. Improvement of Heat Dissipation Characteristics of Cu Bus-Bar in the Switchboards through Shape Modification and Surface Treatment. *Energies* **2019**, *12*, 146. [CrossRef]
3. Bedkowski, M.; Smolka, J.; Banasiak, K.; Bulinski, Z.; Nowak, A.J.; Tomanek, T.; Wajda, A. Coupled numerical modeling of power loss generation in busbar system of low-voltage switchgear. *Int. J. Therm. Sci.* **2014**, *82*, 122–129. [CrossRef]
4. Chapman, D.; Norris, T. *Copper for Busbars*; Copper Development Association Copper Alliance: Hertfordshire, UK, 2014.

5. Barrett, R. Operating Temperature of Current Carrying Copper Busbar Conductors. Bachelor's Thesis, University of Southern Queensland, Toowoomba, Australia, 2013.
6. Lotiya, J. Thermal analysis and optimization of temperature rise in busbar joints configuration by FEM. In Proceedings of the 2014 6th IEEE Power India International Conference (PIICON), Delhi, India, 5–7 December 2014; pp. 1–5.
7. Smirnova, L.; Juntunen, R.; Murashko, K.; Musikka, T.; Pyrhönen, J. Thermal analysis of the laminated busbar system of a multilevel converter. *IEEE Trans. Power Electron.* **2016**, *31*, 1479–1488. [CrossRef]
8. Plesca, A.; Scintee, A. 3D thermal analysis of a power supply busbar structure. In Proceedings of the 2010 ASME 10th Biennial Conference on Engineering Systems Design and Analysis, Istanbul, Turkey, 12–14 July 2010; pp. 695–702. [CrossRef]
9. Barcikowski, F.; Lindmayer, M. Simulations of the heat balance in low-voltage switchgear. In Proceedings of the 20th Int. Conf. Elect. Contacts (ICEC 2000), Stockholm, Sweden, 19–23 June 2000.
10. Callegaro, A.D.; Guo, J.; Eull, M.; Danen, B.; Gibson, J.; Preindl, M.; Emadi, A. Bus bar design for high-power inverters. *IEEE Trans. Power Electron.* **2018**, *33*, 2354–2367. [CrossRef]
11. Wang, L.; Chiang, H.D. Toward online bus-bar splitting for increasing load margins to static stability limit. *IEEE Trans. Power Syst.* **2017**, *32*, 3715–3725. [CrossRef]
12. Geng, C.; He, F.; Zhang, J.; Hu, H. Partial stray inductance modeling and measuring of asymmetrical parallel branches on the bus-bar of electric vehicles. *Energies* **2017**, *10*, 1519. [CrossRef]
13. Kim, J.W.; Park, J.Y.; Sohn, J.M.; Ahn, K.Y. A study on thermal characteristics for D.C. molded cased circuit breaker busbar. *Korean Inst. Electr. Eng.* **2014**, *11*, 252–254.
14. Yaman, G. A thermal analysis for a switchgear system. *J. BAUN Inst. Sci. Technol.* **2019**, *21*, 72–80.
15. Yu, E.; Joshi, Y.K. Natural convection air cooling of electronic components in partially open compact horizontal enclosures. *IEEE Trans. Compon. Packag. Technol.* **2000**, *23*, 14–22. [CrossRef]
16. Delgado, F.; Renedo, C.J.; Ortiz, A.; Fernández, I.; Santisteban, A. 3D thermal modeland experimental validation of a low voltage three-phase busduct. *Appl. Ther. Eng.* **2017**, *110*, 1643–1652. [CrossRef]
17. Singh, S.; Summer, R. A novel approach for the thermal analysis of air insulated switchgear. In Proceedings of the 21st International Conference on Electricity Distribution, Frankfurt, Germany, 6–9 June 2011.
18. Bedkowski, M.; Smolka, J.; Bulinski, Z.; Ryfa, A.; Ligeza, M. Experimentally validated model of coupled thermal processes in a laboratory switchgear. *IET Gener. Transm. Distrib.* **2016**, *10*, 2699–2709. [CrossRef]
19. Guo, B.; Song, Z.; Fu, P.; Jiang, L.; Wang, M.; Dong, L. Prediction of Temperature Rise in Water-Cooling DC Busbar Through Coupled Force and Natural Convection Thermal-Fluid Analysis. *IEEE Trans. Plasma Sci.* **2016**, *44*, 3346–3352. [CrossRef]
20. Popa, I.C.; Dolan, A.I.; Ghindeanu, D.; Bolta¸su, C. Thermal modeling and experimental validation of an encapsulated busbars system. In Proceedings of the 2014 18th International Symposium on Electrical Apparatus and Technologies (SIELA), Bourgas, Bulgaria, 29–31 May 2014; pp. 1–4.
21. Muhammood, M.; Kamarol, M.; Ishak, D.; Masri, S. Temperature rise prediction in 3-phase busbar system at 20 °C ambient temperature. In Proceedings of the 2012 IEEE International Conference on Power and Energy (PECon), Kota Kinabalu, Malaysia, 2–5 December 2012; pp. 736–740.
22. Risdiyanto, A.; Arifin, M.; Khayam, U. Study on temperature distribution at busbar connection based on contact resistance of dierent plating contact surface. In Proceedings of the 2013 Joint International Conference on Rural Information Communication Technology and Electric-Vehicle Technology (rICT & ICeV-T), Bandung, Indonesia, 26–28 November 2013; pp. 1–6.
23. Jung, H.S. Study for temperature rise on busbar of the switchgear and controlgear assemblies. *Korea Inst. Inf. Commun. Eng.* **2017**, *21*, 379–385.
24. Park, S.W.; Cho, H. A practical study on electrical contact resistance and temperature rise at at the connections of the copper busbars in switchgears. In Proceedings of the 2014 IEEE 60th Holm Conference on Electrical Contacts (Holm), New Orleans, LA, USA, 12–15 October 2014; pp. 1–7. [CrossRef]
25. Thompson, M.K.; Thompson, J.M. *ANSYS Mechanical APDL for Finite Element Analysis*; Butterworth-Heinemann: Oxford, UK, 2017; ISBN 978-0-12-812981-4.
26. Slade, P. *Electrical Contacts: Principles and Applications*; CRC Press: Boca Raton, FL, USA, 2014; ISBN 978-1-4398-8130-9.
27. Braunovic, M.; Myshkin, N.; Konchits, V. *Electrical Contacts: Funamentals, Applications and Technology (Electrical and Computer Engineering)*; CRC Press: Boca Raton, FL, USA, 2006; ISBN 978-3642335723.
28. Braunovic, M. Characterization Techniques for Nanostructured Contact Materials. In Proceedings of the 56th IEEE Holm Conference on Electrical Contacts (HOLM 2010), Charleston, SC, USA, 4–7 October 2010. [CrossRef]
29. Szulborski, M.; Łapczyński, S.; Kolimas, Ł.; Kozarek, Ł.; Rasolomampionona, D.D. Calculations of Electrodynamic Forces in Three-Phase Asymmetric Busbar System with the Use of FEM. *Energies* **2020**, *13*, 5477. [CrossRef]
30. Łapczyński, S.; Szulborski, M.; Kolimas, Ł.; Kozarek, Ł.; Gołota, K. Mechanical and Electrical Simulations of Tulip Contact System. *Energies* **2020**, *13*, 5059. [CrossRef]
31. Kolimas, Ł.; Łapczyński, S.; Szulborski, M.; Świetlik, M. Low voltage modular circuit breakers: FEM employment for modeling of arc chambers. *Bull. Pol. Acad. Sci. Tech. Sci.* **2020**, *68*, 61–70.
32. Kühnel, C.; Schlegel, S.; Großmann, S. Investigations on the long-term behavior and switching function of fuse-elements for NH-fuse-links (gG) at higher thermal stress. In Proceedings of the 2017 6th International Youth Conference on Energy (IYCE), Budapest, Hungary, 21–24 June 2017.

33. De Tommasi, L.; Magnani, A.; De Magistris, M. Advancements in the identification of passive RC networks for compact modeling of thermal effects in electronic device s and systems. *Int. J. Numer. Model. Electron. Netw. Devices Fields* **2018**, *31*, e2296. [CrossRef]
34. Kumar, A. Electro-thermal Characterizations, Compact Modeling and TCAD Based Device Simulations of Advanced SiGe:C BiCMOS HBTs and of nanometric CMOS FET. Ph.D. Thesis, Micro andnanotechnologies/Microelectronics, Université Bordeaux 1 Sciences et Technologie, Talence, France, 2012.
35. Di Napoli, F.; Magnani, A.; Copola, M.; Guerriero, P.; D'Alessandro, V.; Codecasa, L.; Tricoli, P.; Daliento, S. On-Line Junction Temperature Monitoring of Switching Devices with Dynamic Compact Thermal Models Extracted with Model Order Reduction. *Energies* **2017**, *10*, 189. [CrossRef]
36. Zhan, Y.; Kumar, S.V.; Sapatnekar, S.S. Thermal Aware Design. *Found. Trends Electron. Des. Autom.* **2007**, *2*, 255–370. [CrossRef]
37. VanGilder, J.; Tian, W.; Bean, J. Transient Thermal Analysis of an Air-Conditional IT Rack with a Thermal Buffering Unit. In Proceedings of the 19th IEEE Intersociety Conference on Thermal and Thermomechanical Phenomena in Electronics System (ITerm), IEEE, Orlando, FL, USA, 21–23 July 2020.
38. Ciok, Z. *Switching Processes in Electric Power Systems*; OWPW: Warsaw, Poland, 2001.
39. Frei, U.P.; Weichert, O.W. Simulation of electrical field and breakdown phenomena in low voltage circuits breakers. In Proceedings of the 23th Int. Conf. on Electrical Contacts, ICEC, Sendei, Japan, 6–9 June 2006; pp. 577–582.
40. Available online: https://www.ansys.com (accessed on 5 January 2021).

A9. *Increasing magnetic blowout force by using ferromagnetic side plates inside MCB*

energies

Article

Increasing Magnetic Blow-Out Force by Using Ferromagnetic Side Plates inside MCB

Michał Szulborski *, Sebastian Łapczyński and Łukasz Kolimas

Faculty of Electrical Engineering, Electrical Power Engineering Institute, Warsaw University of Technology, 00-662 Warsaw, Poland; seb.lapczynski@gmail.com (S.Ł.); lukasz.kolimas@ien.pw.edu.pl (Ł.K.)
* Correspondence: mm.szulborski@gmail.com; Tel.: +48-662-119-014

Abstract: The paper presents a modern method of computer modeling, concerning the low-voltage extinguishing chambers employed in modular apparatuses. The focus was put on presenting the phenomenon of increasing the blow-out, through the use of ferromagnetic plates, dividing the electric arc inside the electrical apparatus. The use of ferromagnetic material for the production of extinguishing chambers results in the distortion of the magnetic field generated by the electric arc. This creates a magnetic force that draws the arc towards the plate area of the extinguishing chamber. The authors presented a modern tool for the analysis of physical phenomena inside the extinguishing chamber. The presented material makes it possible to examine the influence of changes in the geometry and materials of the mentioned components on the process of switching off the current. The applied approach can be used to analyze physical phenomena in devices, not only for alternating current, but also for direct current. Moreover, the model is scaled to the various parameters of these devices.

Keywords: magnetic blow-out force; MCB; ferromagnetic side plates; ANSYS; FEM

Citation: Szulborski, M.; Łapczyński, S.; Kolimas, Ł. Increasing Magnetic Blow-Out Force by Using Ferromagnetic Side Plates inside MCB. *Energies* **2022**, *15*, 2776. https://doi.org/10.3390/en15082776

Academic Editors: Issouf Fofana, Andrea Mariscotti and Mauro Feliziani

Received: 8 January 2022
Accepted: 6 April 2022
Published: 10 April 2022

1. Introduction

Technological progress in the field of designing electrical apparatus manifested itself in the use of computer-aided design and prototyping tools. Circuit breakers are designed and tested employing computer methods, e.g., CAD and CAE (computer-aided design, computer-aided engineering) software. This tool exploits mathematical analysis to predict field distribution, temperatures, stresses, and other physical quantities. Thanks to such calculations, it is known whether the designed apparatus and materials it will be built of will withstand the working conditions. Examples of such software are SolidWorks by Dassault Systems, COMSOL Multiphysics by COMSOL Inc. (Stockholm, Sweden), and ANSYS from ANSYS, Inc. (Canonsburg, PA, USA) [1]. Every MCB (miniature circuit breaker) is equipped with an extinguishing chamber capable of breaking short-circuit currents of 6 kA [2,3]. This component is one of the most important, as it is directly responsible for interrupting the electric arc. The arc chamber is often made of 13 metal plates. The tested internal elements of the circuit breaker were mapped in three dimensions, maintaining their proportions, sizes, and mutual position. Arc chambers vary in the shape, size, and number of ferromagnetic plates from which they are constructed. The greater the number of ferromagnetic plates in the chamber, the greater its ability to extinguish the arc.

The elements considered for the analysis purposes were:

- Metal plates dividing the electric arc;
- Plastic or metal mold with embedded metal plates.

The main objective of the procured work, for the means of this paper, was the analysis of the calculations that described the electric arc motion on, and through, the arc chamber ferromagnetic plates during short-circuit conditions. Calculations were executed by the use of FEM (finite element method software).

2. State of the Art

Paper [4,5] discusses various methodologies for assessing and improving the performance of a miniature circuit breaker (MCB) at higher voltage and short-circuit currents. Experimental studies were conducted to investigate the effect of different types of coating on deionization plates, in order to obtain higher breaking capacity at higher voltage. At higher voltage, the operation of the circuit breaker becomes a challenge, based on the efficiency of the arc extinguishing system performance. The authors investigated the effect of various coatings on the deionization plate, in order to increase performance at higher voltage and current. The result of their work is a general improvement of the arc extinguishing system, thanks to the nickel and copper coating on the deionization plates. The performance improvement was assessed on the basis of parameters such as arc time and pass energy, which determine the behavior of the circuit breaker under various short-circuit conditions. The above research is valuable. Manufacturers of low-voltage modular equipment are sensitive to such suggestions. Previously, a slightly expanded team of authors discussed [6–8] the different methodologies used to increase the MCB breaking capacity. The authors conducted experimental studies to investigate the effect of various types of plating on deionization plates. The influence of various parameters, such as plating and deionization materials, were determined. The general phenomenon of introducing an electric arc into the extinguishing chamber is aided by nickel plating and the use of permeable steel baffles (attached to the surrounding walls). The performance improvement was assessed on the basis of parameters such as run time and energy passed, which indicate the response of the current-limiting circuit breaker to a fault.

In the work [9–11], it was proposed to use permanent magnets inside the arc chamber, in order to improve the arc extinguishing efficiency. Permanent magnets create a magnetic field in which the electric arc behaves differently to the deionization plates. The authors of the study presented a comparison of the test data of the circuit breakers with the configuration of the deionization plate and permanent magnets, taking into account different polarities and arrangement. The purpose of this work was to understand the arc behavior inside circuit breakers when permanent magnets are used to extinguish the arc in an arc chamber. This work will present a comprehensive behavioral study for subsequent designs and technologies. Interesting works were executed by the authors in the publication [12–15]. Their work focused on the plasma arc problem. The article focuses on the effects of various polymer vapors, such as PA66, POM, PTFE, PMMA, etc., on arc behavior, as well as the effect of venting on pressure distribution. The ablated polymer vapors generated by the strong radiation of the arc change the thermodynamic and transport properties of the arc plasma. The CFD simulation showed arc plasma cooling and improved gas flow. Three different generations of vents (baffles, perforated plates, and mesh wires) were tested to obtain their pressure drop characteristics. A three-dimensional CFD analysis of these vents was performed, evaluating the porous jump coefficients and parameters of the vents. Investigating the venting system helped to better design vents with optimal pressure drop and gas deionization characteristics [16–20].

The methodology of modifying the behavior of the electric arc in the extinguishing process has been the subject of investigation for several researchers. The use of deionization plates to extinguish an electric arc is very well researched in the literature. Nevertheless, the aim of the material presented in this manuscript was to draw attention to modern tools dedicated to simulating physical phenomena in low-voltage modular apparatus. The simulation work was positively validated. The proposed construction of the electric arc model, in the area of the contact systems and extinguishing chambers, can be used in apparatuses with deionization plates and permanent magnets. The presented approach can be an interesting material for manufacturers of low-voltage electrical apparatus [20–25].

3. Theoretical Part

The presence of ferromagnetic elements or plates of a specific shape has a significant impact on the distribution of the magnetic flux density and value of the force affecting the electric arc appearing in their vicinity [25–30]. The use of V-shaped ferromagnetic plates (Figure 1) increases the arc attraction force by the factor $[(360°/a) - 1]$, compared to the use of flat plates.

$$B = \frac{\mu_0}{4\pi}\frac{\mu_r - 1}{\mu_r + 1}\frac{I}{a} \tag{1}$$

where B is electromagnetic induction, a is arc distance from ferromagnetic plate, μ_0 is air permeability, and μ_r is the tile permeability.

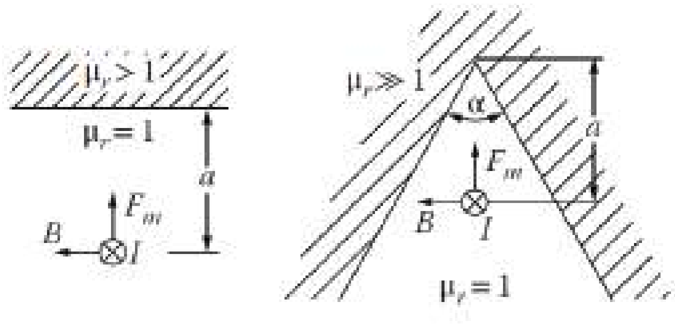

(**a**) (**b**)

Figure 1. Principle of arc attraction by ferromagnetic plates: (**a**) straight front side; (**b**) V-shaped front side [3].

The phenomenon concerning the formation of electrodynamic forces acting on the electric arc was used in the process of constructing extinguishing chambers. The specific shapes of openings during the development of extinguishing chambers depend mainly on the type of extinguished current AC or DC (Figure 2). The use of alternately arranged tiles, with an additional side cutout, allows for additional extension of the arc flowing into the chamber before it is divided into several arcs between the tiles, by the formation of new anode and cathode stains [30–34].

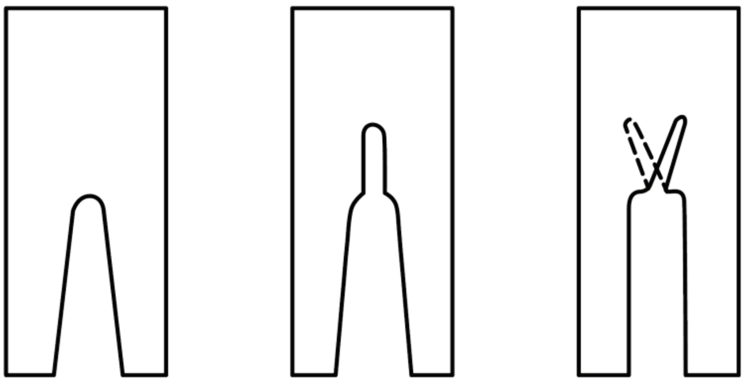

(**a**) (**b**) (**c**)

Figure 2. Deion plates for low-voltage circuit-breakers: (**a**) standard U- or V-shaped recess (AC applications); (**b**) with central slot; (**c**) with staggered slots (DC applications).

The use of ferromagnetic plates, placed inside the arc chamber, allows the arc to be divided into smaller arcs. This allows to increase the arc voltage and facilitate its extinguishing, while ferromagnetic plates enhance the process of extinguishing the arc by its additional cooling.

The plates made of a ferromagnetic material, in the structure of the extinguishing chamber, distort the magnetic field generated by the arc, causing the appearance of an electrodynamic force, which attracts the arc towards the plate area. Figure 3 shows the principle described above.

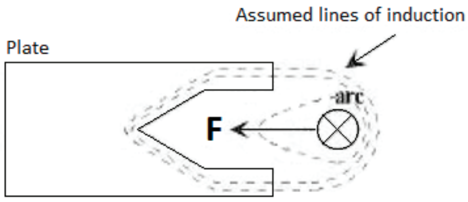

Figure 3. Principle of electrodynamic forces acting on the electric arc in arc chambers [2].

The magnetic flux density and electrodynamic force vary, depending on the position of the arc, in relation to the plates. Figure 4 shows an example of the distribution of the magnetic field for different positions of the arc, in relation to the extinguishing chamber metal plates.

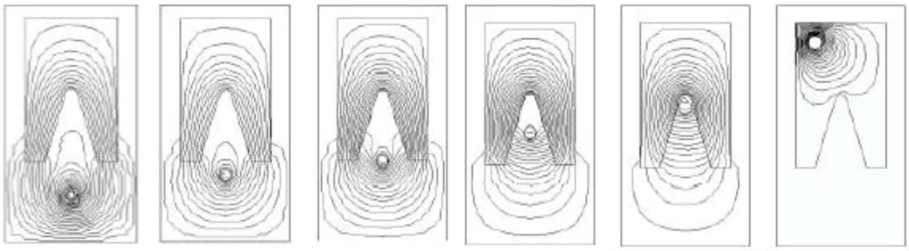

Figure 4. Magnetic field distribution for different positions of the arc in the Deion plate [2].

Most air circuit breakers use the intrinsic magnetic field created by the chamber's ferromagnetic plates to move the arc past the contacts towards the extinguishing chamber. This field can be increased by additional ferromagnetic flux concentrators, such as side plates isolated from the arc chute, as shown in Figure 5 below. The generated lines of magnetic flux tend to flow in areas of minimal magnetic resistance, and the arc is subjected to an electrodynamic force that moves it upwards into the extinguishing chamber.

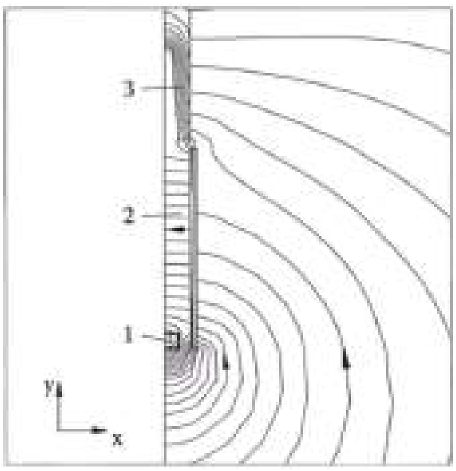

Figure 5. Increase of magnetic blow-out force by ferromagnetic side plates: 1—arc; 2—ferromagnetic side plates; 3—ferromagnetic plates [2].

The contact force (F_c) necessary to counteract the blow-off force is proportional to the square of the peak current (I):

$$F_C \geq K_2 \cdot I^2 \tag{2}$$

where K_2 is coefficient that contains the geometry and also material properties.

Equation (2) below presents the dependency for blow-out force (F_w):

$$F_w = K \cdot W_c^{2/3} \tag{3}$$

where $W_c = \int V_c \cdot Idt$, V_c is the voltage measured across the contacts.

Hence, great forces are needed to overcome the static and attraction forces from the point contact. In order to limit the complexity of contact layout it is viable to employ the electrodynamic forces. This is necessary, in order to limit the short-circuit current in a brief amount of time. Here, an approved method is to use the magnetic repulsion of two anti-parallel and closely spaced current paths (Figure 6). This force can be considerably increased by concentrating the self-field of the current path to the moving contact part where the force is needed [2].

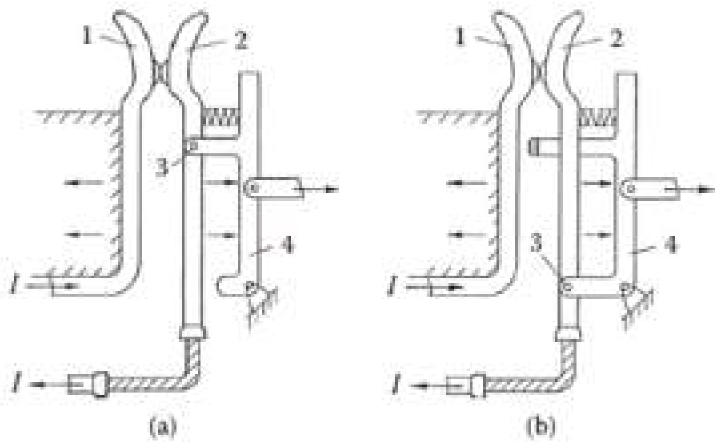

Figure 6. Dynamic intensification of: (**a**) contact force; (**b**) blow-out force. 1—fixed contact; 2—moving contact; 3—pivot point of moving contact; 4—switching lever [2].

The arc-switching magnetic extinguishing chamber is used, in principle, for switching off all magnitudes of currents and powers. The effect of cooling, dividing, and stretching of the arc on the internal resistance of the arc column is used here. In the magnetic blow-out mechanism, the electric arc between the switch contacts is being pushed by the forces of electromagnetic induction into the extinguishing chamber [2]. The greatest electrical resistance of the arc occurs in the area near the electrode; therefore, such a division significantly increases the electrical resistance of the arc column. The arc chamber interrupts an electric arc, producing an arc voltage instead of a supply voltage. This voltage can be defined as the smallest voltage that is necessary to maintain the arc. The arc voltage can be increased by cooling the arc plasma. After reducing the temperature of the arc plasma and movement of the particles, an additional voltage gradient is needed to maintain the arc. It is possible to increase the arc voltage while increasing the arc path. As soon as the arc path length is increased, the resistance will also increase the arc voltage that is used across the current path. In a single-point contact system, AgCu material is often used, mainly for the fixed contact, as well as copper (it can be silver-plated, which reduces the flash-on resistance value and, thus, reduces the transition resistance, which should not exceed 1 mΩ) [2]. Figure 7 shows a system where an electric arc burns between a fixed and moving contact. The movable part of the contact system is, thus, relieved of the stresses of the arc, and the electric arc can be better adapted to the shape of the stack of deionization plates. It is worth noting that this is additional time that can be source of delays. There are also solutions where the fixed guide is not connected to the movable contact, but this connection must be made and held with an additional arc.

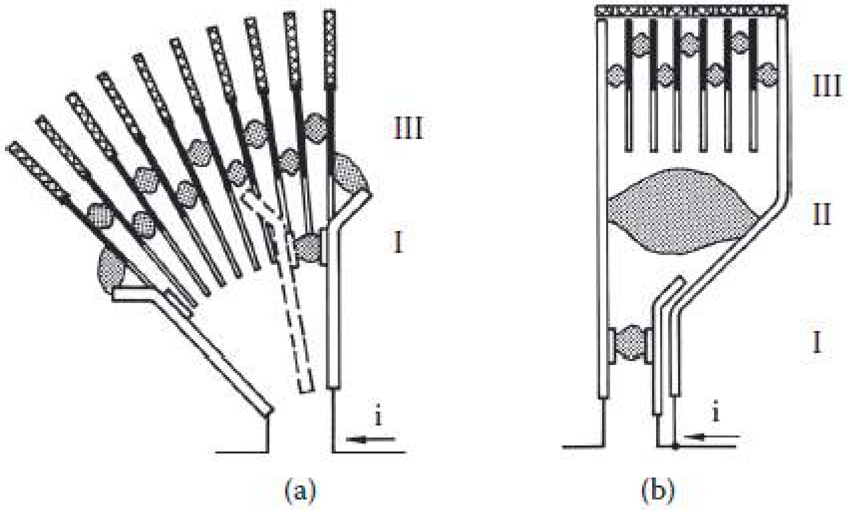

Figure 7. Schematic circuit breaker arrangements: (**a**) without commutation to a stationary arc runner; (**b**) with commutation to arc runner connected with the moving contact. I—arc between contacts; II—arc in intermediate position; III—arc split up between de-ion plates [2].

4. Simulation Part

In order to verify the above-mentioned theoretical assumptions and determine the return of the acting electrodynamic force, a very detailed 3D model of the ABB overcurrent circuit breaker—S201 C32 was made. Using the software "SpaceClaim Geometry", all the individual structural elements of the MCB were modeled.

The drawn elements of the overcurrent switch were made with the maximum possible precision, while maintaining their dimensions, shape, and position, in relation to each other. The main parts of the circuit breaker drafted structure are:

1. Short-circuit release coil combined with the fixed contact of the circuit-breaker;
2. Moving contact;
3. Thermobimetal combined with the "arc runner"—the element along which the electric arc is led to the extinguishing chamber;
4. Arc chamber;
5. Upper and lower terminal of the switch.

The modeled elements of the current path are shown in Figure 8 below, which shows the main elements of the overcurrent circuit breaker.

After modeling all the structure elements of the circuit breaker, it was possible to make a 3D assembly for the entire device (Figure 9 below).

The 3D model of the circuit breaker was loaded into the ANSYS Workbench environment. Numerical analysis for the prepared model was performed using the Maxwell 3D calculation module. After generating the calculation region for numerical simulation, individual parts of the model were assigned material properties from the material library. Then, a current excitation was applied, simulating the flow of a short-circuit current of 6 kA through the analyzed current circuit.

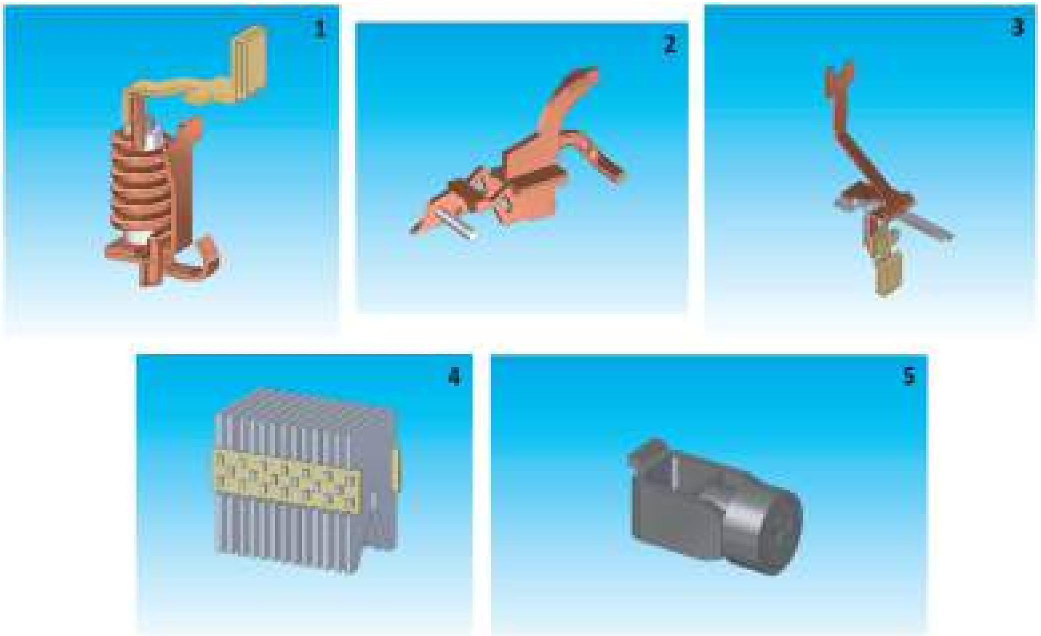

Figure 8. The main elements of the tested circuit breakers current path drawn in 3D.

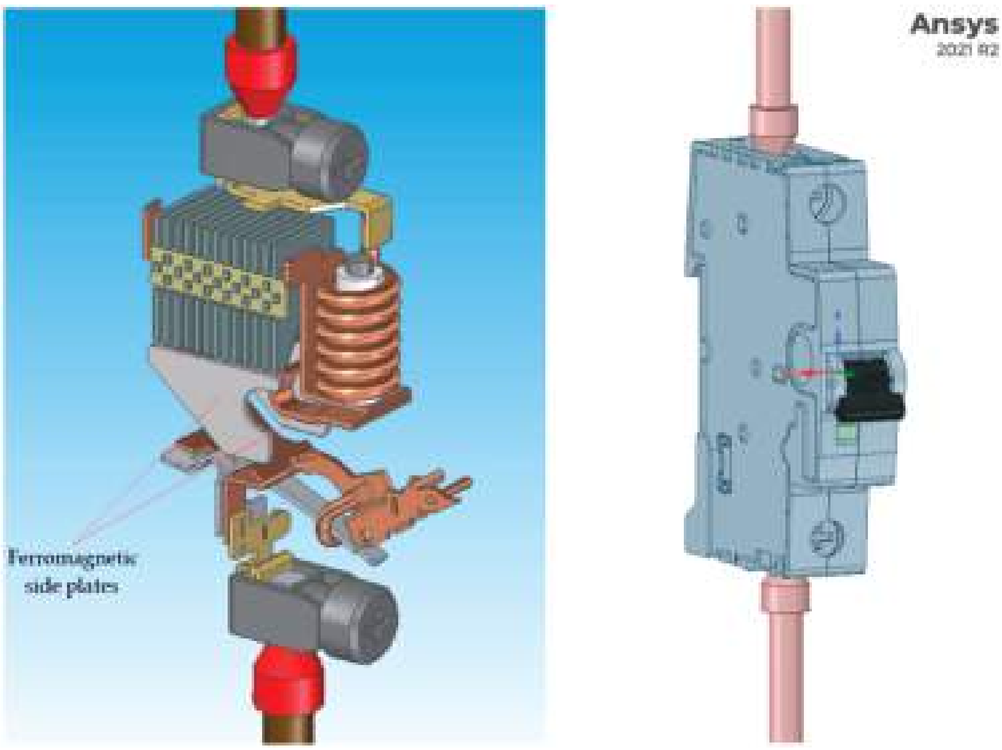

Figure 9. Precise 3D model of the circuit breaker prepared for numerical analysis conducted by the ANSYS software.

The preliminary mesh for the analysis was defined, where the initial value of the number of elements was set to 1,000,000 elements. When generating the mesh, the solver additionally densified the mesh. The final value of the mesh elements was 1,315,154 elements.

The set simulation time was assumed at the level of 200 ms. Additionally, the time steps of the performed calculations were defined for each 1 ms of the specified simulation time. After that, the computational simulation was launched.

It was possible to generate the distribution of the electromagnetic induction line density in the side ferromagnetic plates and plates of the extinguishing chamber at the moment of opening the contacts and appearance of an electric arc, as shown in Figure 10 below.

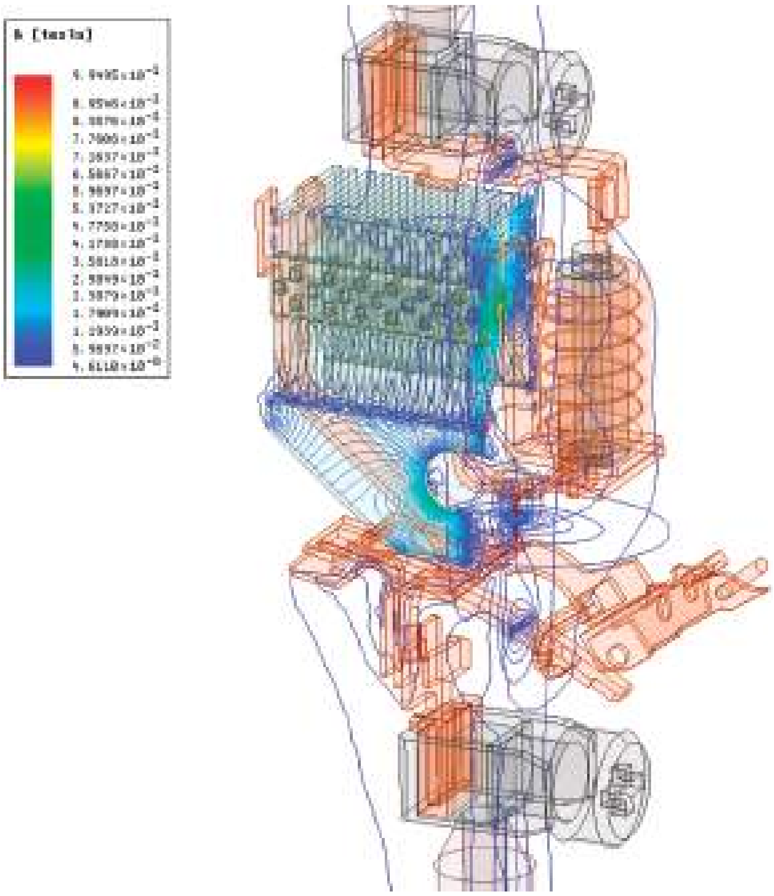

Figure 10. The distribution of electromagnetic induction density in the side ferromagnetic plates and in the plates of the extinguishing chamber at the moment of opening the contacts and the appearance of an electric arc.

The performed calculations also made it possible to analyze the value of the electrodynamic force acting on the electric arc resulting from the refraction of the electromagnetic arc field line in the side plates. The resulting magnetic flux is closed by the side plates and plates of the extinguishing chamber, causing the electric arc to be forced into the extinguishing chamber. The vector of electrodynamic force interaction on the arc, at the moment of opening the circuit breaker contacts, is shown in Figure 11 below.

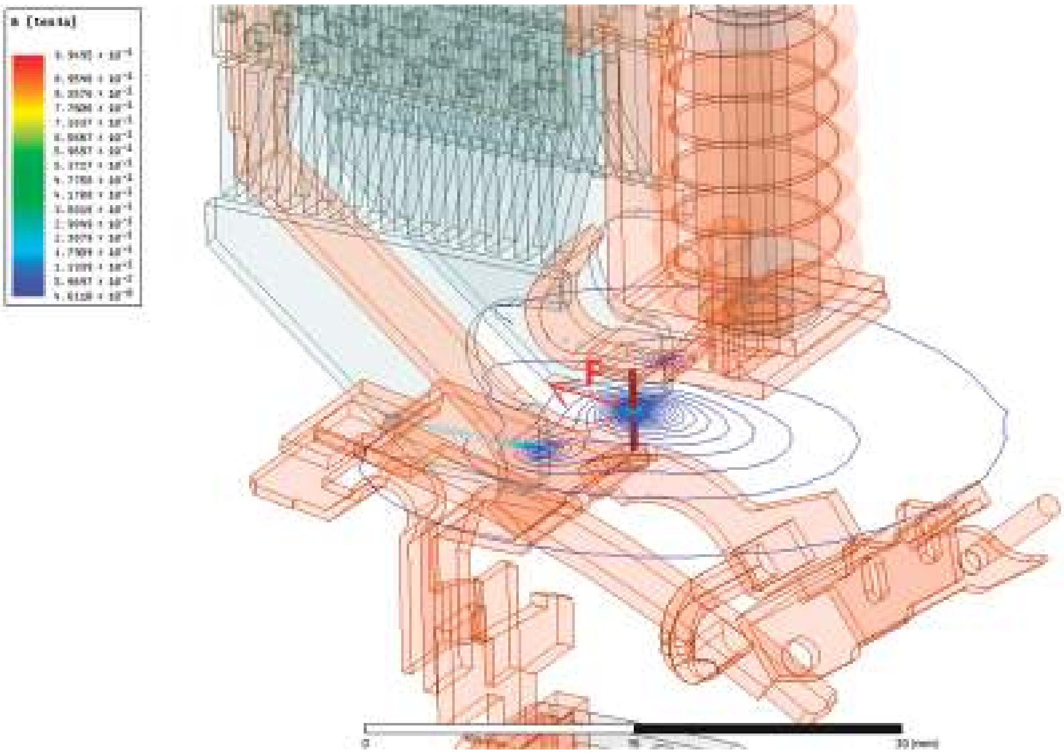

Figure 11. Distribution of the arc electromagnetic induction lines and the return of the electrodynamic force acting on the arc pushing it between the side ferromagnetic plates.

The influence of the electrodynamic force pushes the electric arc formed between the side ferromagnetic plates of the switch, moving it upwards into the extinguishing chamber. The resulting electromagnetic flux from the electric arc is closed in the plates of the extinguishing chamber. Depending on the position of the electric arc, in relation to the plates, the value of the electrodynamic force pushing the arc between the special cuts in the plates of the extinguishing chamber increases. This is due to the thickening of the electromagnetic induction lines in the triangular slots of the plates. In order to analyze this phenomenon in detail, additional induction value distributions were generated, with the resultant electrodynamic force vectors marked for several positions of the electric arc, in relation to the gap of the extinguishing chamber plate (Figure 12 below).

The simulation calculations of the analyzed electric arc motion were fully consistent with the theoretical assumptions presented by P. Slade for various arc positions in the plate of the extinguishing chamber, presented and described at the beginning of this chapter.

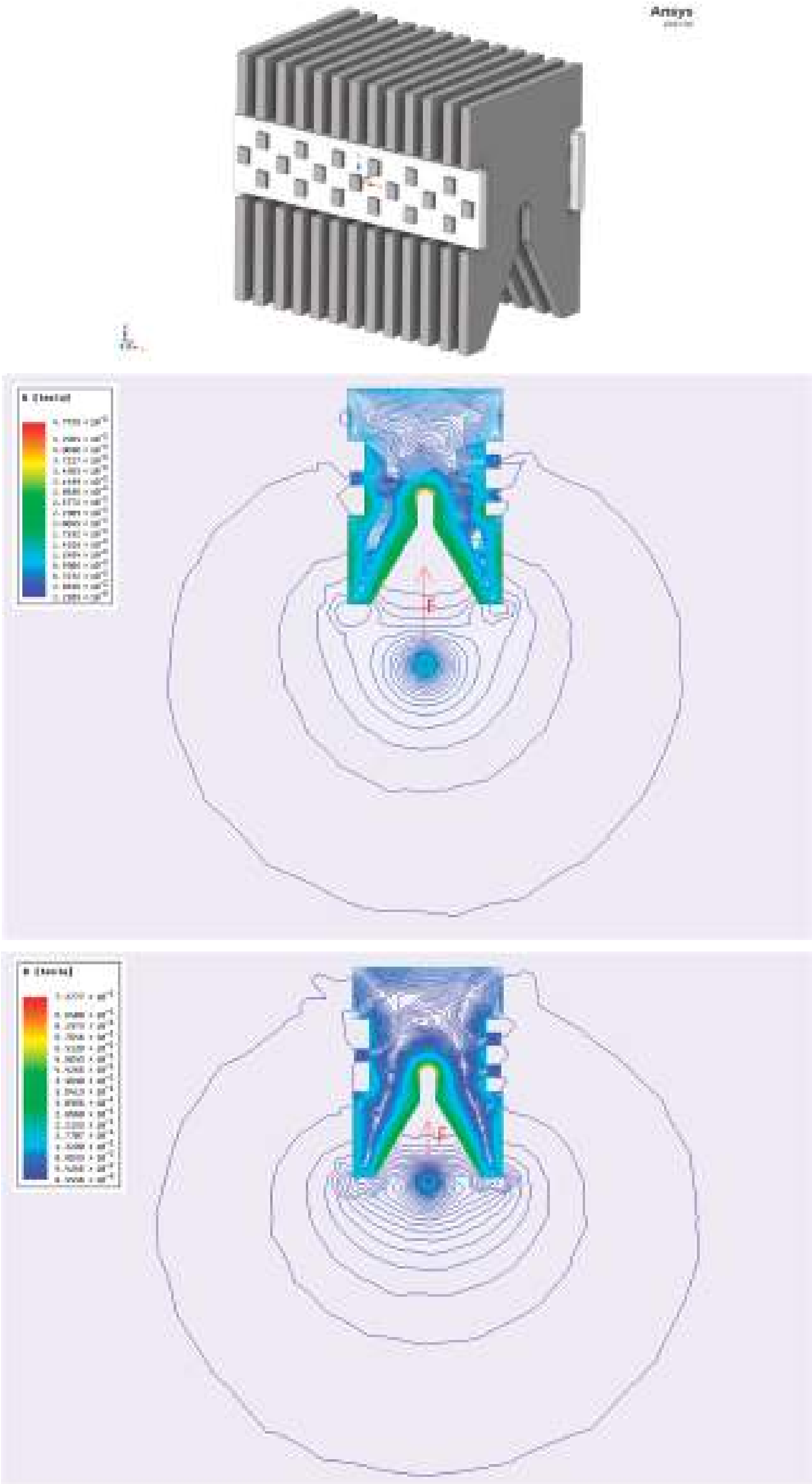

Figure 12. *Cont*.

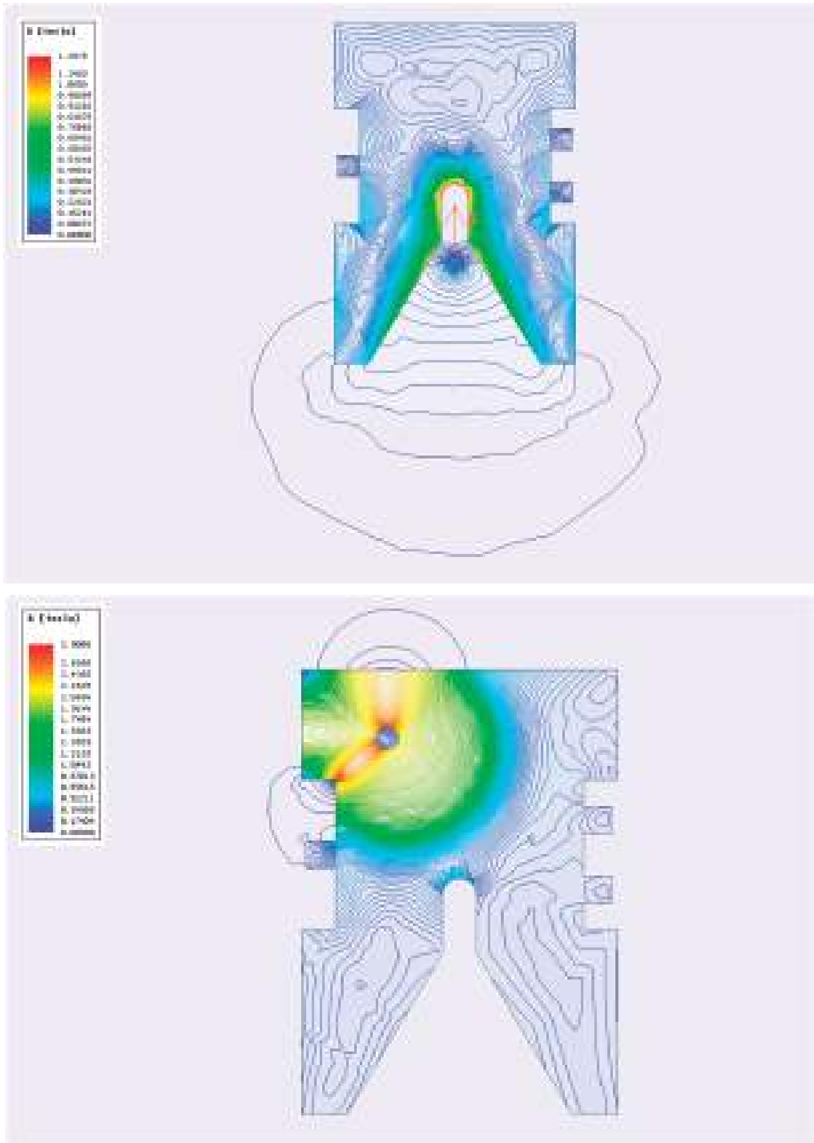

Figure 12. The distributions of the electromagnetic induction values for different positions of the electric arc in the cutouts of the extinguishing chamber plate determined by the use of the ANSYS software.

5. Results Validation

The computational simulation, performed in this way, was the basis for conducting the experimental validation of determining the electric arc displacement path inside the extinguishing chamber and between its plates, including the impact of electrodynamic forces on the arc.

In order to perform the experimental tests, the High-Current Laboratory of the Warsaw University of Technology was used. A diagram of the short-circuit system in the High-Current Laboratory is shown below in Figure 13 below.

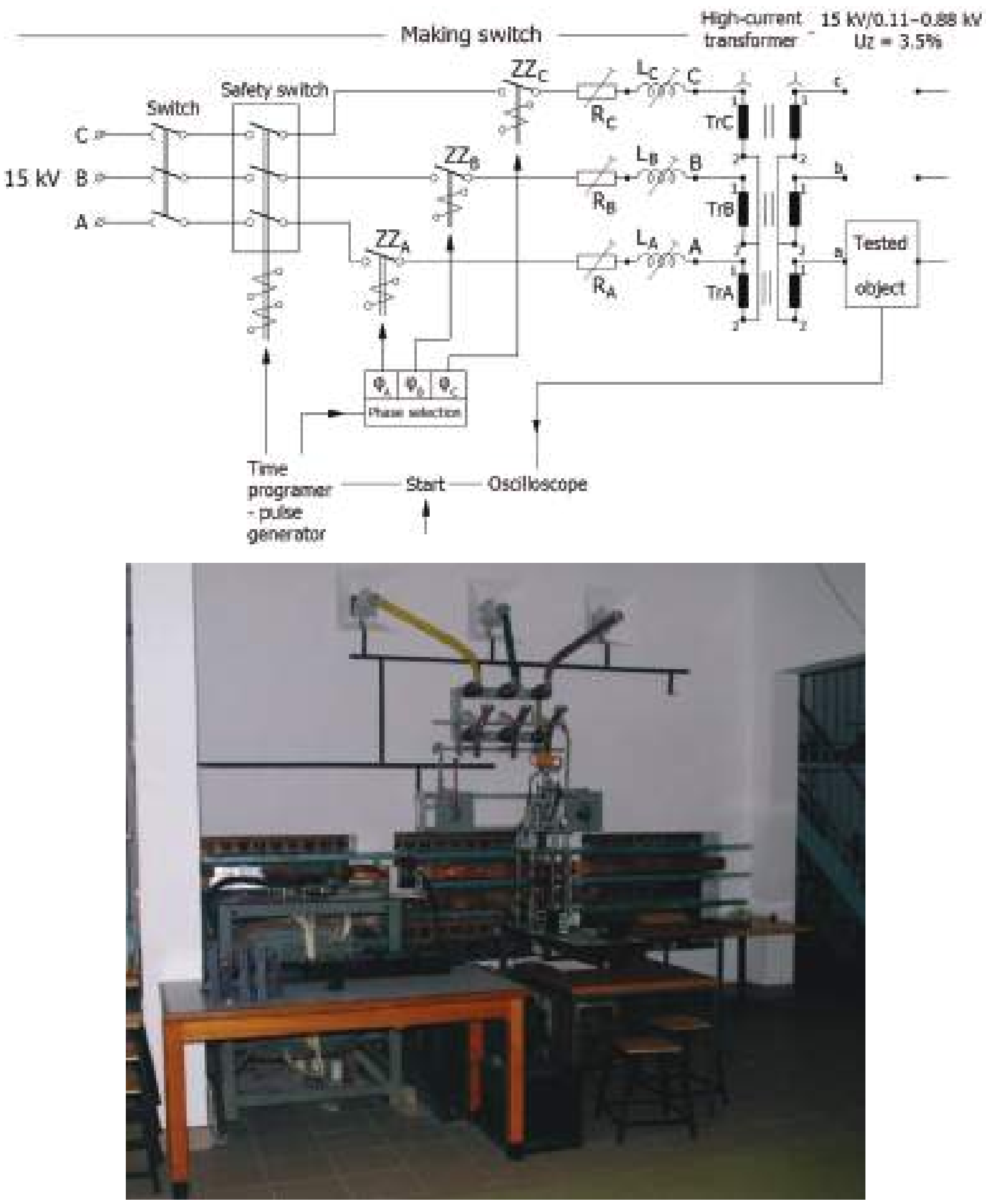

Figure 13. Short-circuit system used for laboratory tests. The Short-Circuit Laboratory, Electrical Faculty, Warsaw University of Technology.

In order to obtain visible paths of the electric arc motion on the plates of the extinguishing chamber, eight short-circuit tests were performed on eight samples of overcurrent circuit breakers with the C characteristic and 32 A rated current (Figure 14 below).

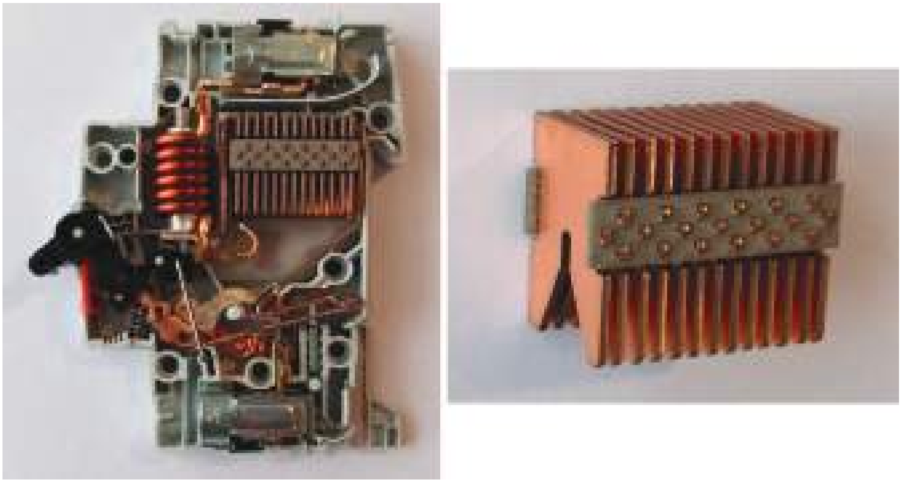

Figure 14. The interior of the tested circuit breaker with ferromagnetic side plates and an extinguishing chamber with ferromagnetic plates used as test objects.

The tests were performed on one of the short-circuit system lines, as presented in the diagram above. The waveforms obtained from the experimental tests for short-circuit currents of 6 kA for individual tests are presented below (Figure 15).

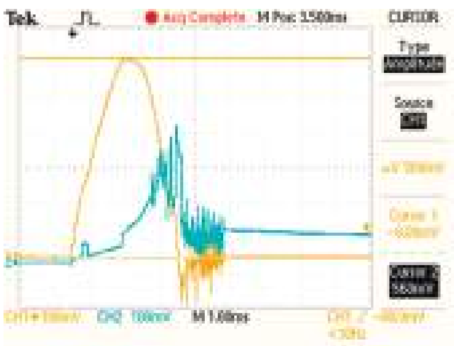

(**a**)

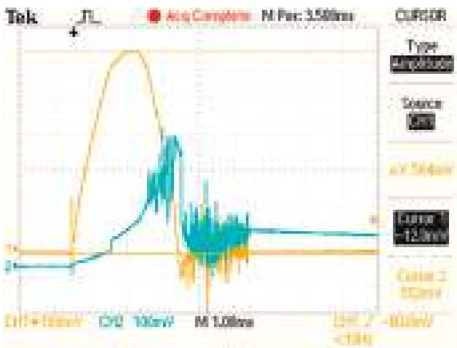

(**b**)

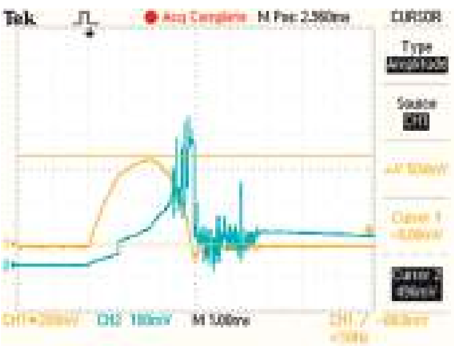

(**c**)

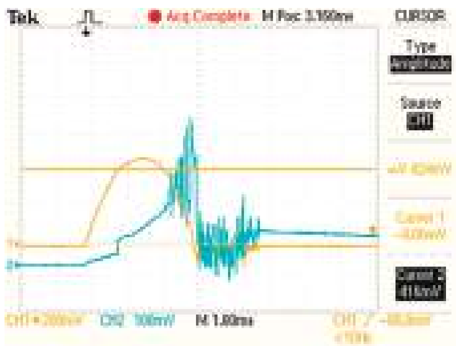

(**d**)

Figure 15. *Cont.*

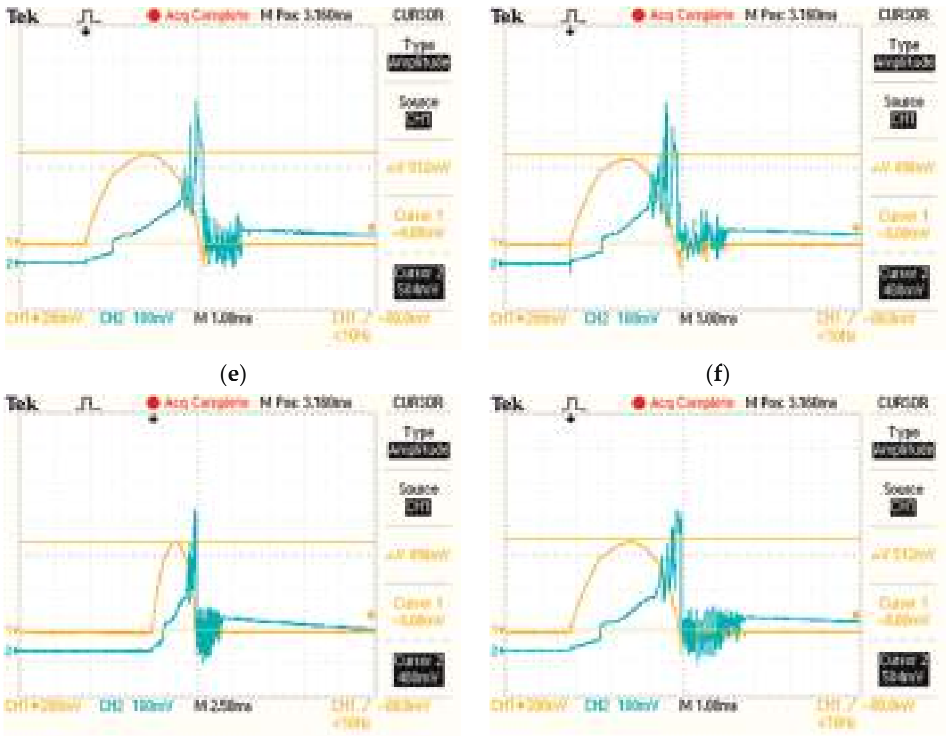

(e) (f)

(g) (h)

Figure 15. A recorded sample of short-circuit current and recovery voltage waveforms during short-circuit tests performed in the High-Current Laboratory at the Warsaw University of Technology. Different cases from (**a**–**h**).

The short-circuit tests performed made it possible to obtain and visualize the paths of the electric arc moving along the ferromagnetic plates inside the tested extinguishing chambers. The circuit breakers, after short-circuit tests, had their rivets removed and were dismantled. The extinguishing chambers of the switches were pulled out, unpackaged, and photographed. The photos taken of the plates from the extinguishing chamber were collected and presented below in Figure 16.

(**a**) (**b**) (**c**)

Figure 16. *Cont.*

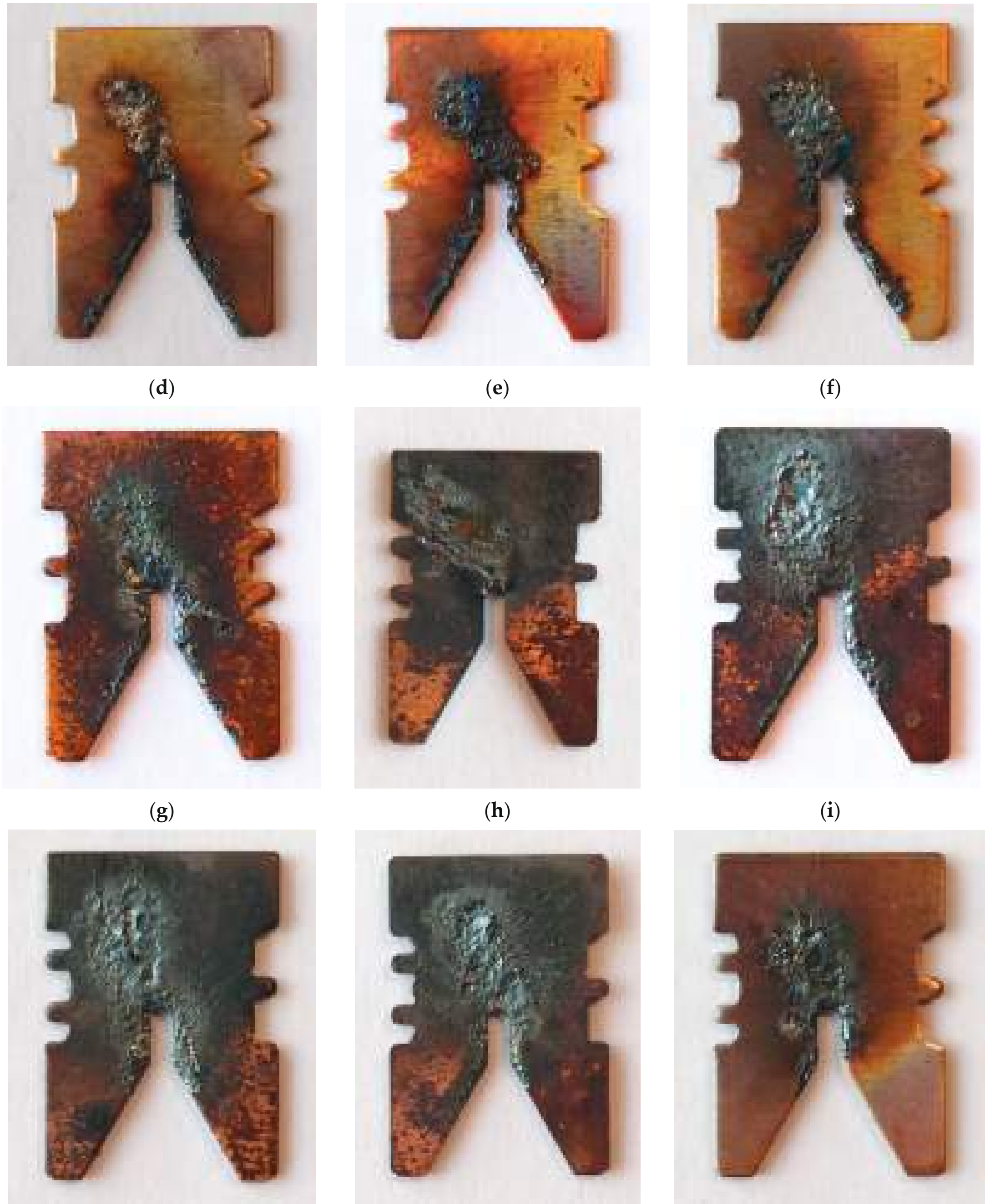

(**d**) (**e**) (**f**)

(**g**) (**h**) (**i**)

(**j**) (**k**) (**l**)

Figure 16. The plates of the extinguishing chamber of the tested circuit breaker with the visible effect of the electric arc inside the extinguishing chamber. Different cases from (**a**–**l**).

The figures above show the path of the electric arc pushed through the side ferromagnetic plates into the extinguishing chamber. The presented plates of extinguishing chamber show that, through the use of special triangular notches, the electric arc is received from the side plates through the generated electrodynamic forces and directed centrally to the center of the notches in the plates of the extinguishing chamber. The electric arc, after falling into the center of each of the plates, is divided into smaller arcs—their number depends on the number of plates used in the structure of the extinguishing chamber. As the electric arc splits, electrodynamic forces push the arc towards the upper left of each plate. This is precisely represented by the traces on the chamber plates, resulting from the movement of the electric arc on each of them.

The correlation between the oscillograms and plate photographs are depicted in Table 1 below.

Table 1. Correlation chart between oscillograms and the plates photographs.

Correlation Chart	MCB B16
Figure 15	**Figure 16**
a	h
b	i
c	k
d	j
e	l
f	g
g	f
h	a

The waveforms of current and voltage are presented in Figure 13. The results of switching off times and values of switched off currents are presented in Table 2 below.

Table 2. Juxtaposition of switching off results.

Lp.	MCB B16	
	Switch-off Time [ms]	**The Value of the Breaking Current [A]**
a	3	3670
b	3	2790
c	2.8	2820
d	3.1	2670
e	3.1	2770
f	3.1	2840
g	2.8	2760
h	3	2810

The investigated effect was demonstrated on the basis of a single-phase overcurrent circuit breaker B16. The tests were executed in accordance with the subject standard PN-IEC 60898. A switching test was conducted in the scope of the tests. The test site was the Short-Circuit Laboratory of the Institute of Electrical Power Engineering, Warsaw University of Technology. The Figure 17 below shows a reference short-circuit current waveform with an RMS value of 6400 A.

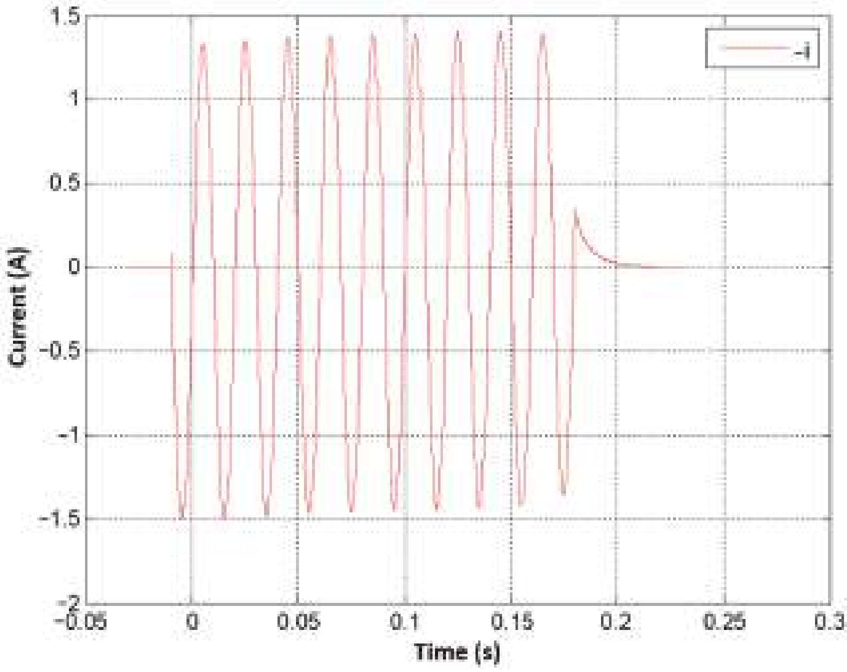

Figure 17. The waveform of the current for which the test was executed. RMS current value—6400 A.

6. Summary and Conclusions

The short-circuit tests performed confirmed the theoretical assumptions included in the literature. Additionally, the simulation results are consistent with the results obtained from the performed experimental tests. The performed computational simulations confirmed that performing numerical analyzes on accurate 3D construction models can be a significant facilitation during the construction and prototyping of extinguishing chambers. Thanks to this type of analysis, designers of electrical apparatus are able to create devices that are more refined at the design stage. By making appropriate design changes, such as refining the shape of the cutouts in the plates of the extinguishing chamber, it is possible to increase the electrodynamic force acting on the arc falling into the chamber and by appropriately stretching it inside the chamber—e.g., DC current extinguishing chambers in modular circuit breakers. During this work, the execution of the following objectives was achieved:

- Analysis of physical phenomena related to the flow of short-circuit current;
- Building a 3D model of a low-voltage modular apparatus, which can be used for further work in the field of switching power off. Especially now, where NEMA has issued a directive in which modular apparatuses by 2030 will have to, inter alia, communicate with control devices.
- Building a model that is useful not only for researchers, but also designers;
- The usefulness of the 3D model made in the ANSYS Maxwell environment for the analysis of physical phenomena, during the flow of rated current, but also during the flow of short-circuit current, was confirmed;
- The theoretical assumptions and simulation considerations, based on 2D models, regarding the use of the electrodynamic phenomenon with the use of ferromagnetic plates, were confirmed;
- It has been shown that the derived model can be useful in the design of low-voltage modular apparatuses.

The use of coupled analyzes in the process of developing the structure of extinguishing chambers and electrical devices allows to significantly reduce the costs associated with prototypes construction or performing expensive research and tests in research laboratories.

Author Contributions: Conceptualization, M.S., S.Ł. and Ł.K.; data curation, M.S., S.Ł. and Ł.K.; formal analysis, M.S., S.Ł. and Ł.K.; investigation, M.S., S.Ł. and Ł.K.; methodology, M.S., S.Ł. and Ł.K.; project administration, M.S., S.Ł. and Ł.K.; resources, M.S., S.Ł. and Ł.K.; supervision, M.S., S.Ł. and Ł.K.; validation, M.S., S.Ł. and Ł.K.; visualization, M.S., S.Ł. and Ł.K.; writing—original draft preparation, M.S., S.Ł. and Ł.K.; writing—review and editing, M.S., S.Ł. and Ł.K. All authors have read and agreed to the published version of the manuscript.

Funding: This research received no external funding.

Institutional Review Board Statement: Not applicable.

Informed Consent Statement: Not applicable.

Data Availability Statement: Not applicable.

Acknowledgments: The English proofreading of the text was done by Iwona Elżbieta Kolimas and Eric Maclean.

Conflicts of Interest: The authors declare no conflict of interest.

References

1. Wang, L.; Liu, H.; Zheng, W.; Guan, R.; Ge, C.; Chen, L.; Jia, S. Numerical Simulation of Impact Effect of Internal Gas Pressure on Chamber Housing in Low-Voltage Circuit Breaker. *IEEE Trans. Compon. Packag. Manuf. Technol.* **2014**, *4*, 632–640. [CrossRef]
2. Slade, P.G. *Electrical Contacts*; CRC Press: Boca Raton, FL, USA, 16 April 2017.
3. Lindmayer, M. The influence of Contact Materials and Chamber Wall Material on the Migration and the Splitting of the Arc in Extrinction Chamber. *IEEE Trans. Parts Hybrids Packag.* **1973**, *9*, 45–49. [CrossRef]
4. Degui, C.; Ruicheng, D.; Jingshu, Z.; Weixiong, T. Dynamic Simulation of Operating Mechanism for Molded Case Circuit Breaker. In Proceedings of the 53rd IEEE Holm Conference on Electrical Contacts, Pittsburgh, PA, USA, 16–19 September 2007.
5. Ye, X.; Dhotre, M.T.; Mantilla, J.D.; Kotilainen, S. CFD Analysis of the Thermal Interruption Process of Gases with Low Environmental Impact in High V oltage Circuit Breakers. In Proceedings of the 2015 Electrical Insulation Conference (EIC), Seattle, WA, USA, 7–10 June 2015.
6. Bura, V.S.; Diptisikha, R. Effect of different Deion plate surface finishes on arc mobility at higher voltage and fault currents. In Proceedings of the 2018 IEEMA Engineer Infinite Conference, New Delhi, India, 13–14 March 2018.
7. Dhotre, M.T.; Ye, X.; Seeger, M.; Schwinne, M.; Kotilainen, S. CFD Simulation and Prediction of Breakdown Voltage in High Voltage Circuit Breakers. In Proceedings of the 2017 Electrical Insulation Conference (EIC), Baltimore, MD, USA, 11–14 June 2017.
8. Qi, B.; Zhao, X.; Zhang, S.; Huang, M.; Li, C. Measurement of the electric field strength in transformer oil under impulse voltage. *IEEE Trans. Dielectr. Electr. Insul.* **2017**, *24*, 1256–1262. [CrossRef]
9. Bura, V.S.; Satbir, S.; Medhora, R.; Legha, A. Effect of Different De-ion Plate Surface Finishes on Arc Mobility. In Proceedings of the 2008 JIC on Power System Technology and IEEE Power India Conference, New Delhi, India, 12–15 October 2008.
10. Rumpler, C.; Stammberger, H.; Zacharias, A. Low-voltage arc simulation with out-gassing polymers. In Proceedings of the 2011 IEEE 57th Holm Conference on Electrical Contacts (Holm), Minneapolis, MN, USA, 11–14 September 2011; pp. 1–8.
11. Ryzhov, V.V.; Molokanov, O.N.; Dergachev, P.A.; Vedechenkov, N.A.; Kurbatova, E.P.; Kurbatov, P.A. Simulation of the Low–Voltage DC Arc. In Proceedings of the Intenational Youth Conference on Radio Electronics, Electrical and Power Engineering (REEPE), Moscow, Russia, 14–15 March 2019.
12. Galvan, E.; Rodrigues, J.J. Study of the influence of permanent magnets in the interruption process of the electrical arc in MCB. In Proceedings of the 2017 IEEE Holm Conference Electrical Contacts, Denver, CO, USA, 10–13 September 2017.
13. Geetha, N.D.; Rasilo, P.; Arkkio, A. Sensitivity Analysis of Inverse Thermal Modeling to Determine Power Losses in Electrical Machines. *IEEE Trans. Magn.* **2018**, *54*, 1–5.
14. Li, J.; Cao, Y.; Yan, M.; Liu, S.; Du, Z.; Feng, Y. Research on the Effect of Magnetic Field on Micro-Characteristics of Vacumm Arc During Arc Formation Process. In Proceedings of the 28th International Symposium on Discharges and Electrical Insulation in Vacuum (ISDEIV), Greifswald, Germany, 23–28 September 2018.
15. Tarnowski, P.; Ostapski, W. Pulse powered turbine engine concept—Numerical analysis of influence of different valve timing concepts on thermodynamic performance. *Bull. Pol. Acad. Sci. Tech. Sci.* **2018**, *66*, 373–382.
16. Nagarajan, V.S.; Kamaraj, V.; Sivaramakrishnan, S. Geometrical sensitivity analysis based on design optimization and multiphysics analysis of PM assisted synchronous reluctance motor. *Bull. Pol. Acad. Sci. Tech. Sci.* **2019**, *67*, 155–163.
17. Bini, R.; Basse, N.T.; Seeger, M. Arc-induced Turbulent Mixing in a Circuit Breaker Model. *J. Phys. D Appl. Phys.* **2011**, *44*, 25203. [CrossRef]
18. Holm, R. *Electric Contacts—Theory and Application*; Springer: New York, NY, USA, 2013.
19. Basse, N.P.T.; Bini, R.; Seeger, M. Measured turbulent mixing in a small-scale circuit breaker model. *Appl. Opt.* **2009**, *48*, 6381–6391. [CrossRef] [PubMed]
20. Incropera, F.P.; DeWitt, D.P.; Bergman, T.L.; Lavine, A.S. *Introduction to Heat Transfer*, 5th ed.; Wiley: Hoboken, NJ, USA, 2006.

21. Muller, P.T. Macroscopic Electro Thermal Simulation of Contact Resis—Tances. Bachelor's Thesis, RWTH Aachen University, Aachen, Germany, 2016.
22. Biao, W.; Yanyan, L.; Xiaojun, Z. Study on detection technology of the contact pressure on the electrical contacts of relays. In Proceedings of the 26th International Conference on Electrical Contacts (ICEC 2012), Beijing, China, 14–17 May 2012; pp. 161–164.
23. Sun, X.; Su, B.; Chen, L.; Yang, Z.; Li, K. Design and analysis of interior composite-rotor bearingless permanent magnet synchronous motors with two layer permanent magnets. *Bull. Pol. Acad. Sci. Tech. Sci.* **2017**, *65*, 833–843. [CrossRef]
24. Kriegelet, M.; Zhu, X.; Digard, H.; Feitoza, S.; Glinkowki, M.; Grund, A.; Kim, H.K.; Lopez Roldan, J.; Robin-Jouan, P.; van der Sluis, L.; et al. Simulations and Calculations as verfication tools for design and performance of high voltage equipment. In Proceedings of the Cigre Conference 2008, Paris, France, 25–28 August 2008; paper A3-210.
25. Kumar, P.; Kale, A. 3-Dimensional CFD simulation of an internal arc in various compartments of LV/MV Switchgear. In Proceedings of the ANSYS Convergence Conference, Pune, India, 23 August 2016.
26. Hartland, D.J. Electric contact systems—Passing power to the trains. In Proceedings of the IET Professional Development Course on Electric Traction Systems, London, UK, 6–9 June 2011; pp. 25–37.
27. Chen, G.; Lan, L.; Wen, Z.P.X.; Wang, Y.; Wu, Y. Electrical erosion test and condition assessment of SF_6 CB contact sets. *IET Gener. Transm. Distrib.* **2017**, *11*, 1901–1909. [CrossRef]
28. Mantilla, J.D.; Gariboldi, N.; Grob, S.; Claessens, M. Investigation of the insulation performance of a new gas mixture with extremely low GWP. In Proceedings of the Electrical Insulation Conference, Philadelphia, PA, USA, 8–11 June 2014.
29. Iordanidis, A.A.; Franck, C.M. Self-consistent radiation-based simulation of electric arcs: II. Application to gas circuit breakers. *J. Phys. D Appl. Phys.* **2008**, *41*, 135206. [CrossRef]
30. Ye, X.; Dhotre, M.T. CFD Simulation of Transonic Flow in High-Voltage Circuit Breaker. *Int. J. Chem. Eng.* **2012**, *2012*, 609486. [CrossRef]
31. Kim, H.; Chong, I.; Lee, S. Analysis of SLF Interruption Performance of Self-Blast Circuit Breaker by Means of CFD Calculation. *J. Electr. Eng. Technol.* **2014**, *9*, 254–258. [CrossRef]
32. Lindmayer, M.; Stammberger, H. Application of numerical field simulations for low-voltage circuit breakers. *IEEE Trans. Compon. Packag. Manuf. Technol. Part A* **1995**, *18*, 708–717. [CrossRef]
33. Frei, P.U.; Weichert, H.O. Advanced Thermal Simulation of a Circuit Breaker. In Proceedings of the 50th IEEE Holm Conference on Electrical Contacts and the 22nd International Conference on Electrical Contacts, Seattle, WA, USA, 23–23 September 2004.
34. Ito, S.; Takato, Y.; Kawase, Y.; Ota, T. Numerical analysis of electromagnetic forces in low voltage AC circuit breakers using 3-D finite element method taking into account eddy currents. *IEEE Trans. Magn.* **1998**, *34*, 2597–2600. [CrossRef]

A10. *Electrodynamic Forces in a High Voltage Circuit Breakers with Tulip Contact System – FEM simulations*

IEEE Access

Received 2 August 2022, accepted 9 September 2022, date of publication 19 September 2022, date of current version 26 September 2022.

Digital Object Identifier 10.1109/ACCESS.2022.3207768

RESEARCH ARTICLE

Electrodynamic Forces in a High Voltage Circuit Breakers With Tulip Contact System–FEM Simulations

MICHAŁ SZULBORSKI[1,2], SEBASTIAN ŁAPCZYŃSKI[1], ŁUKASZ KOLIMAS[1], AND MYKHAILO TYRYK[3]

[1]Institute of Electrical Power Engineering, Warsaw University of Technology, 00-662 Warsaw, Poland
[2]Symkom Sp. z o.o., Ansys Channel Partner, 02-639 Warsaw, Poland
[3]Faculty of Power and Aeronautical Engineering, Warsaw University of Technology, 00-665 Warszawa, Poland

Corresponding author: Michał Szulborski (mm.szulborski@gmail.com)

ABSTRACT Paper concerns the effects of electrodynamic forces that act on the contacts of the tulip contact system that is often implemented in high voltage circuit breakers. The high voltage circuit breaker often consists of two such systems. One of the systems is treated as an arcing one - made of tungsten coated elements. Capable of implementing the phenomenon of thermal-expansion. The second is made of one or two crown laces. The first system consists of a single piece of large mass, cut in such a way as to obtain the effect of increasing the contact surface. The second is a system, often of several dozen contacts, so as to increase the contact area and reduce the transition resistance. The main problem of actual validation through dynamic measurements (electrodynamic forces) is the specificity of the circuit breaker operation. The contact system is located directly in the switch chamber filled with CO_2 or SF_6 gas. Hence, tests under normal working conditions are very difficult - even impossible. Therefore, the authors proposed employment of FEM (Finite Element Method) in order to obtain values of electrodynamic forces acting on the contact system by executing the detailed 3D coupled simulation. The analysis of the results brought interesting conclusions that concerned operation of such contact layouts in short circuit conditions.

INDEX TERMS Electrodynamic forces, FEM, tulip contact, high voltage, circuit breakers.

I. INTRODUCTION

The formation of electrodynamic forces in the contacts of electrical devices is related to the flow of high currents, mostly short-circuit currents. Depending on the design of the contact system, the occurrence of electrodynamic forces is undesirable, as it can lead to welding of the contacts during electrodynamic bounces or even to their rupture and destruction. On the other hand, the electrodynamic recoil force is used to increase the speed of contact propagation in circuit breakers by employing appropriate loop shaping of the contact current paths. Due to the complexity concerning the occurrence of electrodynamic forces in contacts, in order to verify the structure in terms of resistance to electrodynamic contact bounces, tests are performed with the use of special devices under model conditions. Model systems for testing contact welding should reflect the real conditions in the circuit breakers to the greatest extent and should allow for adjustment of mechanical contact parameters, e.g. spring pressure. The phenomenon of electrodynamic bounce is revealed in two cases:

- when contact is closed during the flow of short-circuit current;
- at the moment of switching.

The phenomenon of electrodynamic contact bounce can lead to the formation of metallic bridges at the point of contact. It is caused by condensation of current streams which was shown in Figure 1 above. As a result of the high current flow at the point of contact, the contact material may evaporate. This creates additional forces and pressures greater than the generated electrodynamic forces, which can lead to the opening of the contacts and their damage by an electric arc.

The associate editor coordinating the review of this manuscript and approving it for publication was Giambattista Gruosso.

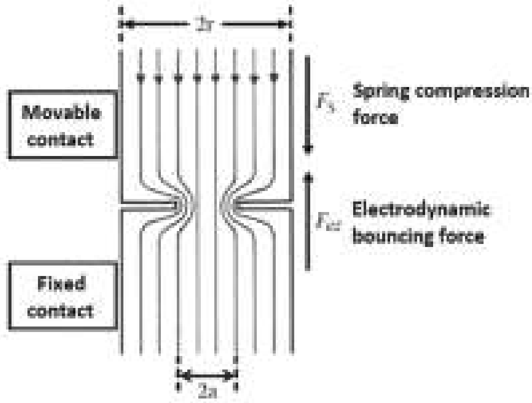

FIGURE 1. Generation of electrodynamic forces at the contact point caused by the condensation of current streams.

According to the complexity of the electrodynamic contact bouncing mechanism it is very hard to experimentally measure forces and phenomena occurring. Therefore authors propose to employ FEM in order to execute advanced coupled analysis and highlight values of electrodynamic forces and their influence that acts on high voltage circuit breaker tulip contact systems in two different versions. Moreover, this publication presents an approach for simulating electrodynamic forces in a tulip contact system that concerns the whole inner and outer crown not only one contactor (single lamella).

II. ANALYSIS OF ELECTRODYNAMIC FORCES PHENOMENA IN ELECTRICAL APPARATUSES

The phenomenon of electrodynamic contact bounce occurring in the contacts of high current electrical devices is related to the narrowing of the current lines at the point of the actual contact of conductors during the current flow. The microstructure of the contact surfaces is not perfectly even, there are specific current conduction zones in it, precisely illustrated below in the Figure 2.

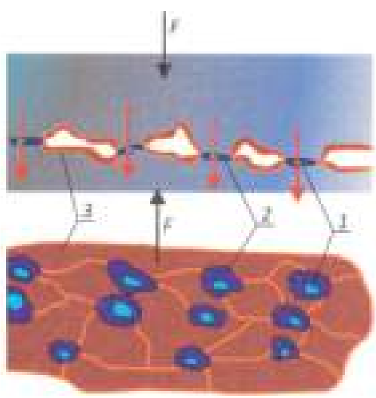

FIGURE 2. Conduction zones in the microstructure of contact surfaces; 1) electrically conductive zones, 2) semi-conductive zones - tunnel electric conduction, 3) non-conductive zones with coating layers [5].

When performing analytical calculations concerning the determination of electrodynamic contact bouncing forces that result in contacts abrupt repulsion, the main difficulty is determining the actual points of conductors contact. It is often the case that there are many zones of contact, which results in the formation of several parallel densities of the current lines as in the Figure 1 above. As a result, the electrodynamic contact bounce force is reduced. In the case of a single point of actual contact between the conductors surfaces, the force value can be determined from the dependency:

$$F_{ez} = 10^{-7} \cdot i^2 \cdot ln\frac{D}{2a} \tag{1}$$

where: i is instantaneous current value; D is outer diameter of the contact and a is radius of the actual contact surface.

In the case of contacts with a cross-section other than cylindrical, e.g. rectangular, of the equivalent diameter (D) the circular cross-section is determined. An example may be rectangular contact strips for which in practice the equivalent diameter D is determined. In the case of frontal loop contacts, apart from the F_{ez} force, there is also a loop electrodynamic force F_{ep} resulting from the loop shape of the contact, which additionally increases the effect of electrodynamic bounce. In some constructions it is used to accelerate the opening velocity of moving contacts during short-circuit currents. An example of this type of solution with a contact system for a low voltage circuit breaker is shown in the Figure 3 below.

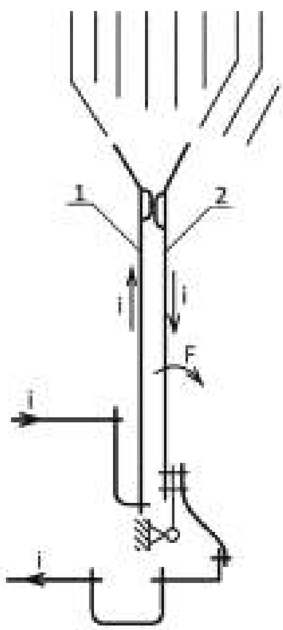

FIGURE 3. An example diagram of a LV switch contact, where the electrodynamic bounce force was used to accelerate the opening of the moving contact during the flow of short-circuit current.

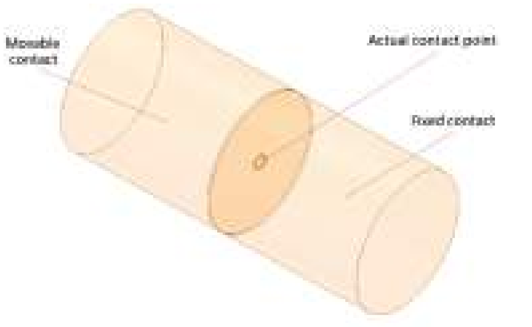

FIGURE 4. Initial 3D model of a contact geometry consisting of a movable and fixed contact.

The electrodynamic bouncing force between the contacts can be determined from the formula:

$$F_{ep} = 2 \cdot 10^{-7} \cdot i^2 \cdot \frac{l}{b} k_D \tag{2}$$

where: l, b are dimensions of the equivalent rectangular current loop of the contact, k_D is Dwight coefficient which value is depending on the cross-section of the contact arms.

It is assumed that the electrodynamic bouncing of the contacts starts when the electrodynamic force is greater than the values of the pressure springs which is expressed by relation (3):

$$F_e = F_{ez} + F_{ep} \geq F_s \tag{3}$$

where: F_s is contact spring pressure force.

In practice, it turns out that the propagation of the contacts and the appearance of an electric arc start already with the resultant electrodynamic force F_e lower than the pressure force of the springs pressing the contacts - F_s. This is due to the force generated by the rapid heating of the contact point and the explosive liquid decomposition of the formed metallic bridge. The extra force had impulse characteristics.

III. ELECTRODYNAMIC FORCES IN FEM SIMULATIONS

In order to determine the value of the electrodynamic force for the contact system, a 3D model was made for numerical analysis. The model was made for one actual point of surface contact. Initial stage of model geometry was shown in Figure 4 below.

After preparing the model and loading it into the Ansys Maxwell 3D environment, it was possible to assign boundary conditions, assign material properties and impose a current of 6 kA on the analyzed contact, in this case without a non-periodic component. Waveform of the short-circuit current in a single-point contact used during this analysis was shown in Figure 5 below.

The computational simulation of the short-circuit current flow through the contacts allowed to determine the current density at the actual point of contact and it was shown below in Figure 6.

As can be seen from the waveform in Figure 7 below, the interaction of the components in the Y direction is responsible for the repulsion of one contact from the other. In order to illustrate this phenomenon even better, the Y components of the two contacts are summarized on the waveform below. The presented forces in this case can lead to electrodynamic bounces in the case when the spring pressing the moving contact has a lower value than the sum of the forces presented as in equation (3) above and in the waveform in Figure 8 below.

In order to determine the vectors of the generated electrodynamic forces in the analyzed single-point contact, the results of calculations from Maxwell 3D were imported to the Ansys Transient Structural calculation module. On the basis of the performed analyses, it was possible to generate the values of the electrodynamic force vectors, which reached the highest value in the contraction of the contact, with the highest short-circuit current density.

Two components of electrodynamic forces can be distinguished from the analysis of electrodynamic forces in a contact system layout presented above:

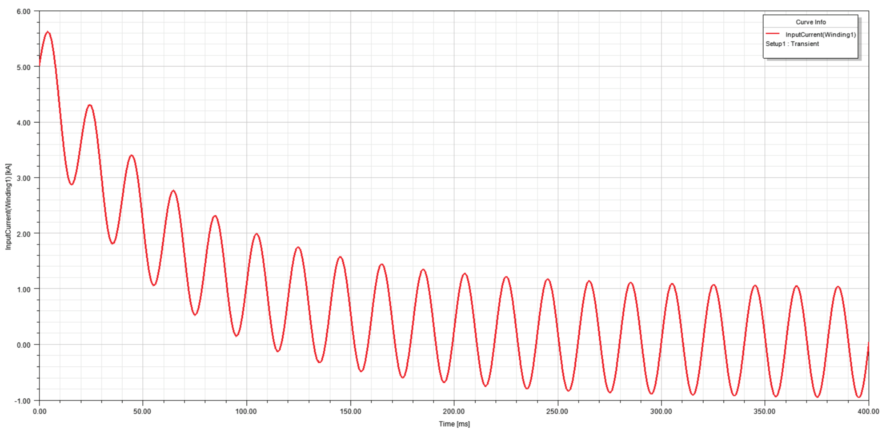

FIGURE 5. Short-circuit current waveform in a single-point contact layout—6 kA.

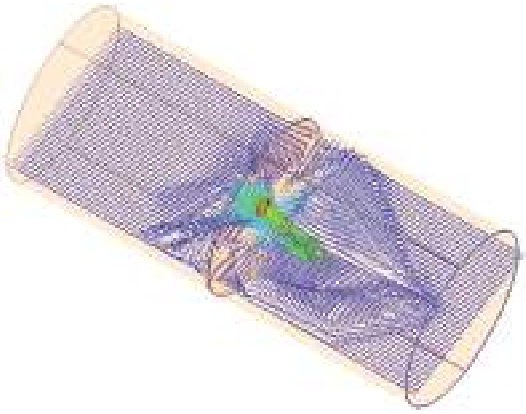

FIGURE 6. Distribution of the short-circuit current line flowing through a contact consisting of a movable and fixed contact with one point of actual contact.

- adial component,
- axial component.

Radial component of the generated electrodynamic forces causing compression of the contact material at the point of contact. Axial component of the resulting electrodynamic forces tending to break the contacts. The phenomenon from the analysis performed is illustrated in detail in the Figure 9 below.

The occurrence of electrodynamic forces in the contacts of electrical devices is a generally unfavorable phenomenon, which significantly reduces the contact pressure force, or at high values of the short-circuit current it leads to their abrupt opening. In order to prevent this phenomenon, electrodynamic force compensation systems are used. This is done by increasing the contact pressure force by applying the special cuts in the current paths or appropriate shaping of the current path inside an electrical apparatus, e.g. a circuit breaker. While current is flowing, forces are pressing the movable contacts or any contact elements to the fixed contact, compensating the electrodynamic bounce force. In tulip contacts, due to the uniform distribution of the contacts in relation to each other, with unidirectional current flow, the contacts are pressed against the pin, which in this case is a favorable phenomenon.

IV. INFLUENCE OF ELECTRODYNAMIC BOUNCES ON THE CONTACT WELDING

Due to the flow of short-circuit currents, electrodynamic forces influence in the contacts may result in bouncing and erosive changes on the contact surfaces. During the opening of the contacts, bridges of the molten metal may form, which may lead to permanent grafting of the connector contacts while the contacts are closing.

During the closing of the electrical device contacts, the movable contact collides with the fixed contact. The movable contact of the apparatus is influenced by the forces from the pressure spring of the connector, electrodynamic forces and forces from the generated intra-arcuate pressure (directed against the forces coming from the connector drive). After the contacts collide, the kinetic energy is converted into potential energy in the form of elastic stress in the movable contact of the switch, and then the potential energy is again converted into kinetic energy of the

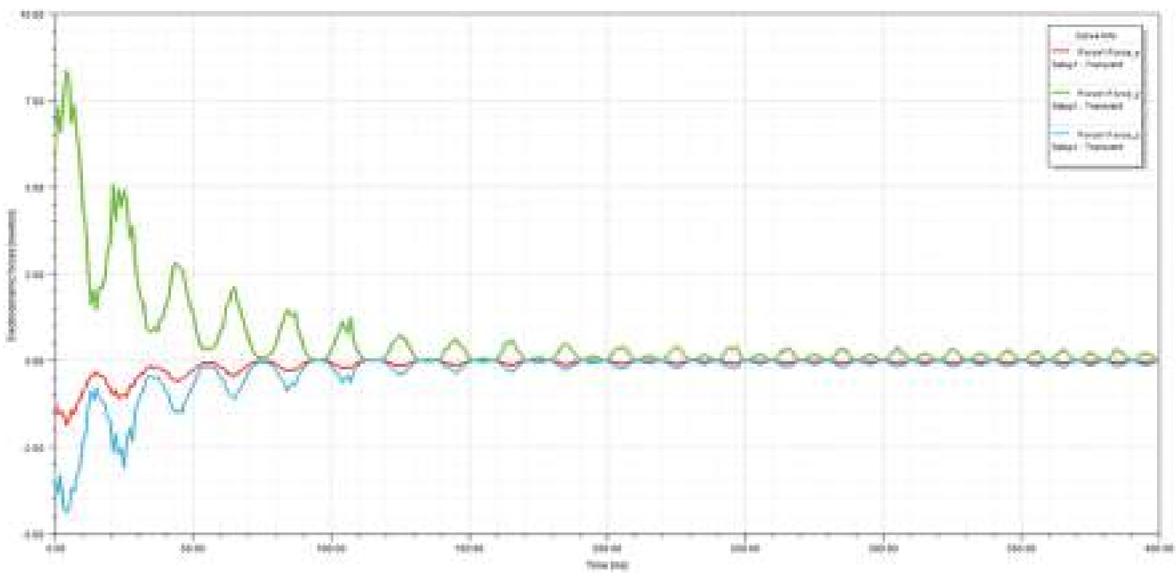

FIGURE 7. Determined X, Y and Z components of electrodynamic forces in a contact with one actual point of contact.

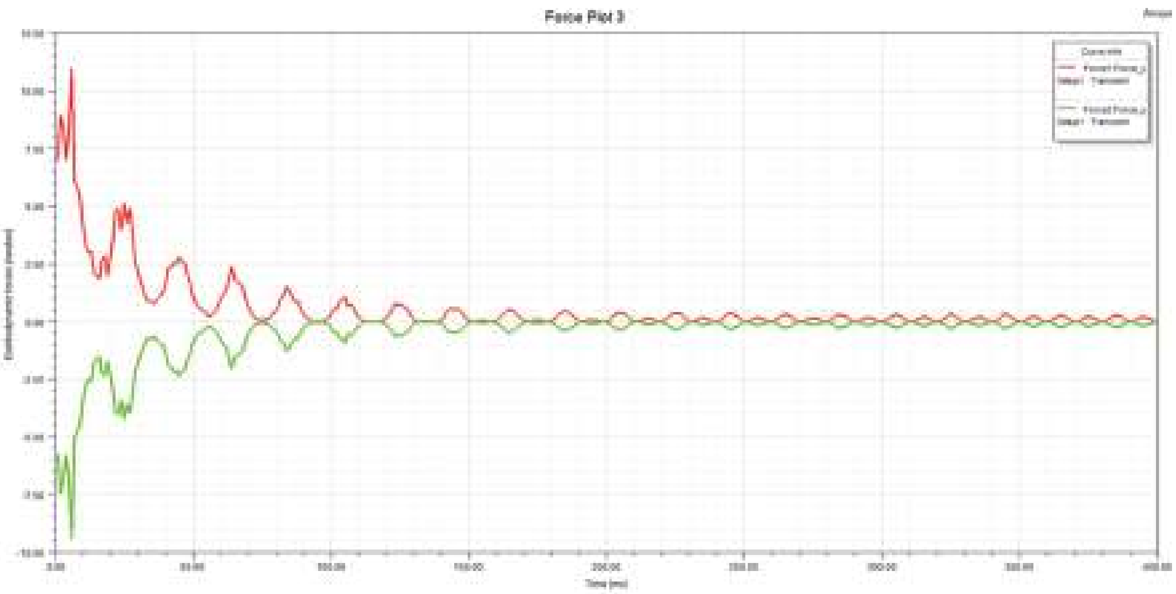

FIGURE 8. Determined *Y* components of the generated electrodynamic forces in the analyzed contact system with one actual point of contact.

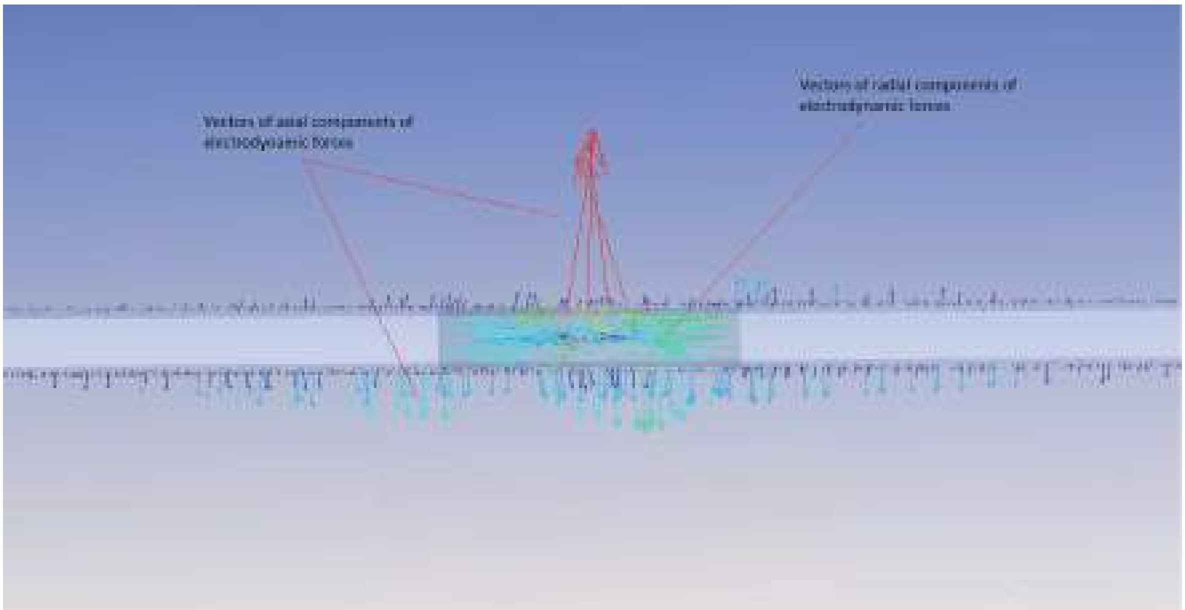

FIGURE 9. Components of electrodynamic forces in an analyzed contact system.

contact movement of the opposite sense. The reciprocal motion is magnified by the value of the generated electrodynamic forces.

The state without electrodynamic bounces usually occurs only after several bounces with decreasing amplitude and a shorter time of loss between the moving contact and the fixed contact.

Over the years, various methods have been developed to measure the duration of electrodynamic bounces. The simplest direct measurement of a single and total bounce time is the recording of the voltage on a bouncing moving contact, from which the obtained data allow to draw a curve describing changes in the gap between the contacts while electrodynamic bounce occurs.

Another direct method is to use the laser beam as an optical probe to measure the length of the gap between the contacts placed between the light source (laser), the photosensor. In this case, the light source must be set so that the generated contact movement during electrodynamic bounces causes a change in the amount of light reaching the sensor. This method, however, requires optical access to the contacts and is not applicable in the case of an electric arc between the contacts.

Due to the above-mentioned difficulties, it is recommended to use indirect optical methods to measure electrodynamic bounces, including the method of recording light by a CCD (charge-coupled device) camera, which allows for the recording and then reading of an electrical signal proportional to the amount of incident light that lights on it. An example of a system for measuring electrodynamic springs of the method using a CCD camera is shown in the Figure 10 below.

It should be noted that it is not enough to register only the movement of the movable contact, because also the fixed contact is usually subject to elastic vibrations caused by the hitting of the movable contact against it.

Mechanical models for studying the phenomena of electrodynamic bounce as shown in Figure 11. Below.

Those can be used to study impact phenomena or to determine the coefficient of impact for a certain material.

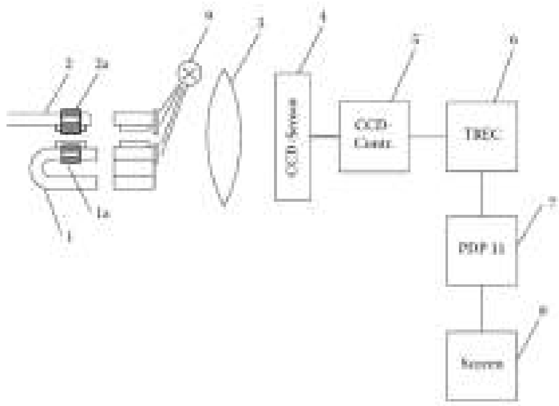

FIGURE 10. Recording of light reflected from contacts by CCD camera (1 - fixed contact; 2 - moving contact; 1a, 2a - contrast strips connected with contacts; 3 - lens; 4 - CCD sensor; 5 - CCD driver; 6 - transient recorder; 7 - computer; 8 - graphic screen; 9 - light source [5]).

In the designed contact, the clamping force value of the movable contact should be selected in such a way that in the case of the peak current of the connector, the spring pressure forces are greater than the expected electrodynamic force. In order to analyze the kinematic system that checks the time and amplitude of electrodynamic bounces, various contact models with specific degrees of contacts freedom are used,

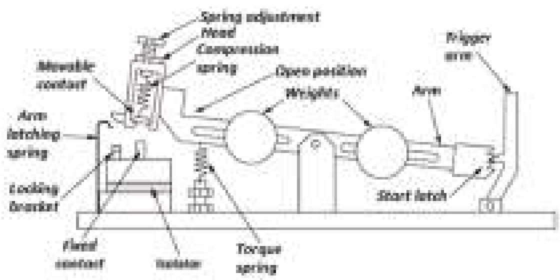

FIGURE 11. Shaw's contact bouncing control mechanism [5].

a model with two degrees of freedom will be reflected and will vibrate, causing bounces of smaller amplitude in turn, until those stop.

Due to the problematic effects of electrodynamic interactions in the form of bounces and electrodynamic repulsion force, various methods of limiting electrodynamic phenomena in contacts have been developed. These are among others listed below.

1. Setting the working surfaces of contacts at an angle an adynamic shaping shown in Figure 12:

$$F_e = F'_{ez} + F_{ek} \tag{4}$$

$$F'_{ez} = 2 \cdot F_{ez} \cdot cos\frac{\alpha}{2} \tag{5}$$

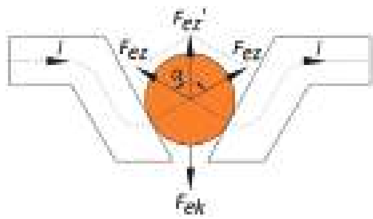

FIGURE 12. Setting the contact surfaces at an angle and electrodynamic compensation by means of adynamic shaping of the contact.

2. Contact sharing shown in Figure 13:

$$F_e = n \cdot F_{ez} \tag{6}$$

$$F_{ez} = k \cdot (1,3 \cdot \frac{i}{n})^2 \tag{7}$$

$$F_e = \frac{1,69}{n} \cdot k \cdot i^2 \tag{8}$$

$$F_e = 0,84 \cdot 5 \cdot k \cdot i^2 \text{ for } n = 2 \tag{9}$$

3. Electrodynamic compensation by dividing one contact into more parallel contacts (tulip contact) shown in Figure 14:

$$F_e = F_{ez} - \frac{F_{ek}}{2} \tag{10}$$

$$F_{ek} = 0,25 \cdot k_1 \cdot i^2 \cdot l \tag{11}$$

4. Compensation by shaping the current path in the form of a loop (single-loop, two-loop, multi-loop contacts)

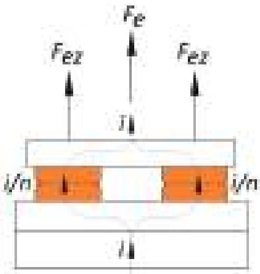

FIGURE 13. Sharing of a contact into several parallel contacts.

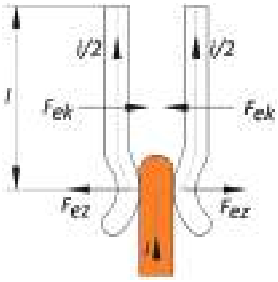

FIGURE 14. Electrodynamic compensation by splitting one contact into more parallel contacts (tulip contact system).

shown in Figure 15:

$$F_e = F_{ez} - F_{ek} \tag{12}$$

$$F_{ek} = k_1 \cdot i^2 \cdot l \tag{13}$$

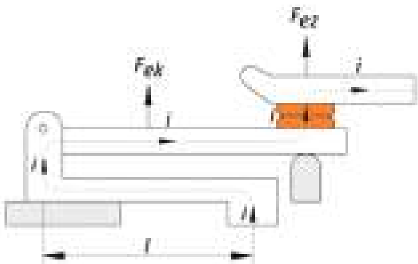

FIGURE 15. Compensation by shaping the current path in the form of a loop (single-loop, two-loop, multi-loop contacts).

5. Setting the working contact surfaces at an angle – for that scenario equations (4), (5) and (14) are employed. That was shown in Figure 16:

$$F'_{ez} < 2F_{ez} \tag{14}$$

In circuit-breakers with high current-carrying capacity of contacts, the system shown in Figure 16 is often used, in which the working surfaces of the contacts are set at an angle α in relation to the direction of interaction of the contact forces. In this case, the resultant force F'_{ez} is smaller than the sum of the electrodynamic forces F_{ez}, which is more

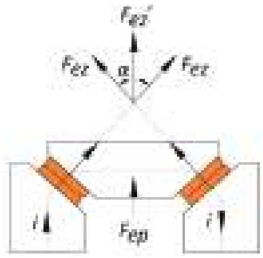

FIGURE 16. Setting the working contact surfaces at an angle.

favorable than in a typical contact. The circuit shown in Figure 12 has additional, more advantageous features due to the adynamic shape of the contact allowing for additional electrodynamic compensation of the forces that push the contacts away from each other. For contactors and circuit breakers, the example shown in Figure 13 is used, which is employed to separate the flowing current by using several parallel contacts. In this case, the arising electrodynamic forces in the contact have smaller values because the current value in a given contact is lower. Example shown in Figure 16 is found in medium voltage circuit breakers which are equipped with tulip contacts. Evenly spaced contacts are pressed against the pin by compression springs. In this case, during the flow of rated or short-circuit currents, the contact pressure force through the pressure springs is increased by the additional action of electrodynamic forces F_{ek} compensating the electrodynamic forces F_{ez} acting at the contact point of the contact system.

The above-mentioned theoretical methods of the compensation of electrodynamic forces in the contacts of electric devices were used by the authors in order to perform simulation calculations to verify the presented methods.

For this purpose, a 3D model presenting the geometry of the system 5 (Figure 16) was made, where the working surfaces of the contacts were positioned at an angle α in relation to the direction of interaction of contact forces, in accordance with the theoretical assumptions. After importing the model to the software, the boundary conditions were assigned and a simulation for a short-circuit current of 40 kA was performed.

After the computational simulation was performed, the current density distribution in the analyzed contact system was derived. The highest values of the short-circuit current density were found at the contact points, as shown in Figure 17 below.

The determined values of the electrodynamic forces in the executed simulation reached the average of 10 – 40 $\boldsymbol{N/m^3}$. The maximum value achieved was witnessed in the right contact of the current path shown and it amounted to 50 $\boldsymbol{N/m^3}$. This was shown in Figure 18 below.

The performed calculations confirmed the presented return of the electrodynamic forces $\boldsymbol{F_{ez}}$ acting in the contact, which at the same time confirms the thesis that the angular arrangement of the contacts allows for the reduction of the

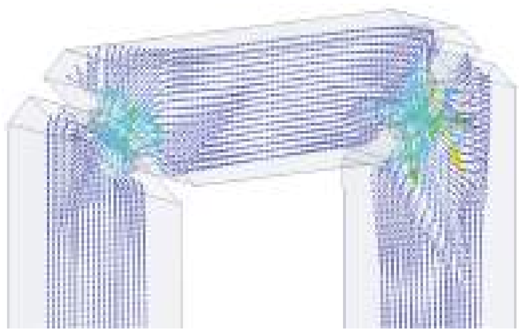

FIGURE 17. Current density distribution in the system compensating the effect of electrodynamic forces—arrangement of the contacts at an angle.

electrodynamic forces value that ought to open the analyzed contact. Force F'_{ez} value was smaller than force F_{ez} value. It is worth noting that the highest stresses in the computational simulation performed occurred in the center of the contact strips, where the radial component of the generated electrodynamic forces was revealed, causing the contact material to compress at the point of actual contact of. The stress distribution in the analyzed contact system is presented in Figure 19 below.

V. ELECTRODYNAMIC FORCES IN CLASSIC TULIP CONTACT LAYOUT

Analyzing furtherly the theoretical assumptions concerning the compensation of electrodynamic interactions in contacts, a 3D model of a tulip contact with specially elongated contacts of the contact crown was prepared. In this case, the generated force pressing the tulip lamellas against the arcing contact and the forces pushing the contacts at the point of contact with the pin were analyzed. In order to determine the interaction of electrodynamic forces in the tulip contact, a short-circuit current of 40 kA was passed through the contact along with the non-periodic component of the current raising it to 50 kA in the initial phase of its duration. The obtained waveform is shown below in Figure 20. The voltage level value for those simulations was set at 72,5 kV. For this voltage, the device can be filled with CO_2 or SF_6 gas. Of course, the extinguishing medium determines the current carrying capacity. And so for CO_2 gas this load capacity is, for example, 2750 A, and for the same cross-sections when filled with SF6 gas it is equal to 4000 A. Undoubtedly, it is related to the ability to receive energy from the electric arc and deionizing the contact gap. The key decision related to the selection of the contact system for research and analysis was the trend:

- restrictions on the use of SF_6 gas,
- developing the process and mechanism of thermal exposure to the next generations,
- research on the use of CO_2 gas and its mixtures and also other gases.

Current flowing through the tulip contact was analyzed, the highest current density was demonstrated at the contact points between the lamellas and the contact pin inserted into the crown formed by the system. Additionally, the distribution of the short-circuit current density flowing through the contact is presented in the Figure 21 above.

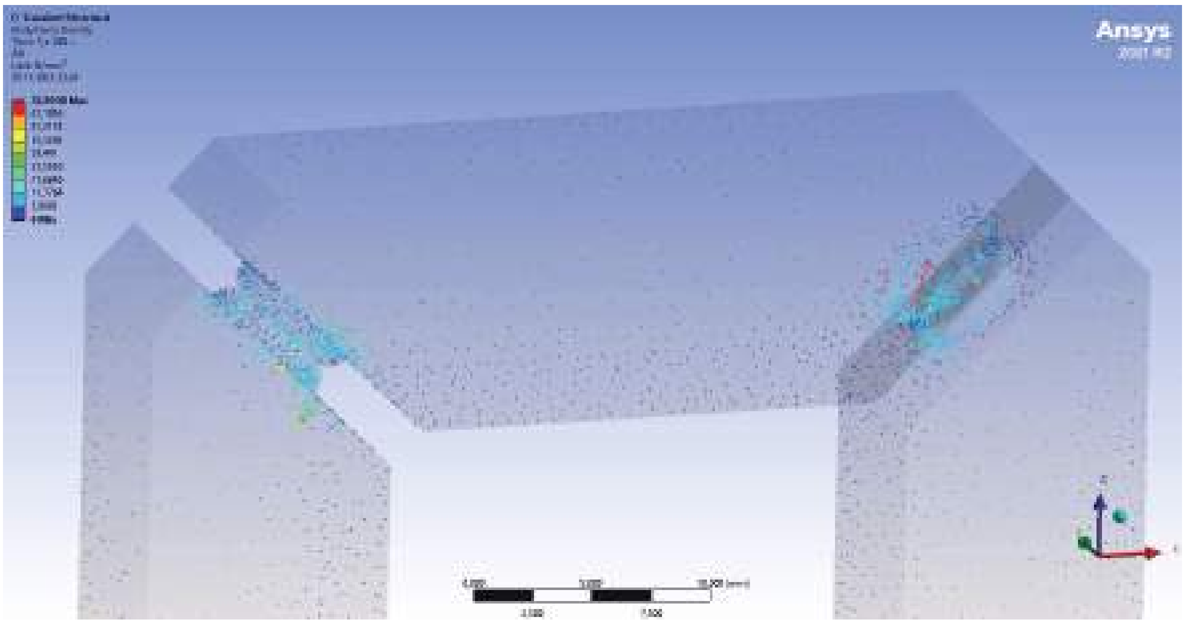

FIGURE 18. Distribution of electrodynamic forces in a contact - arrangement of contacts at an angle.

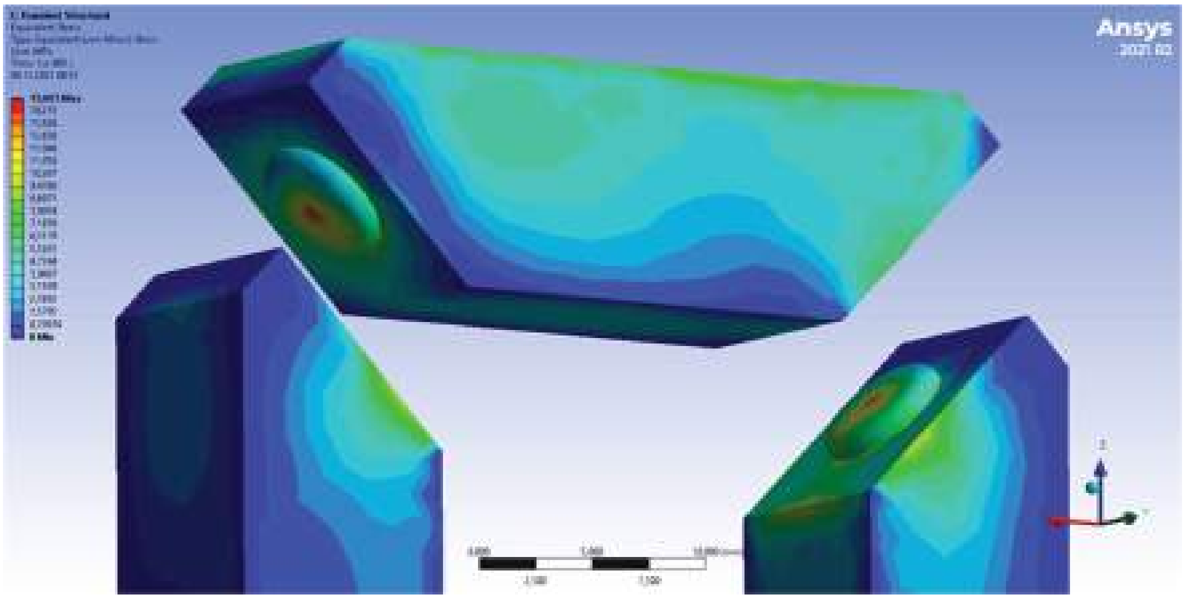

FIGURE 19. Distribution of electrodynamic forces in a contact - arrangement of contacts at an angle.

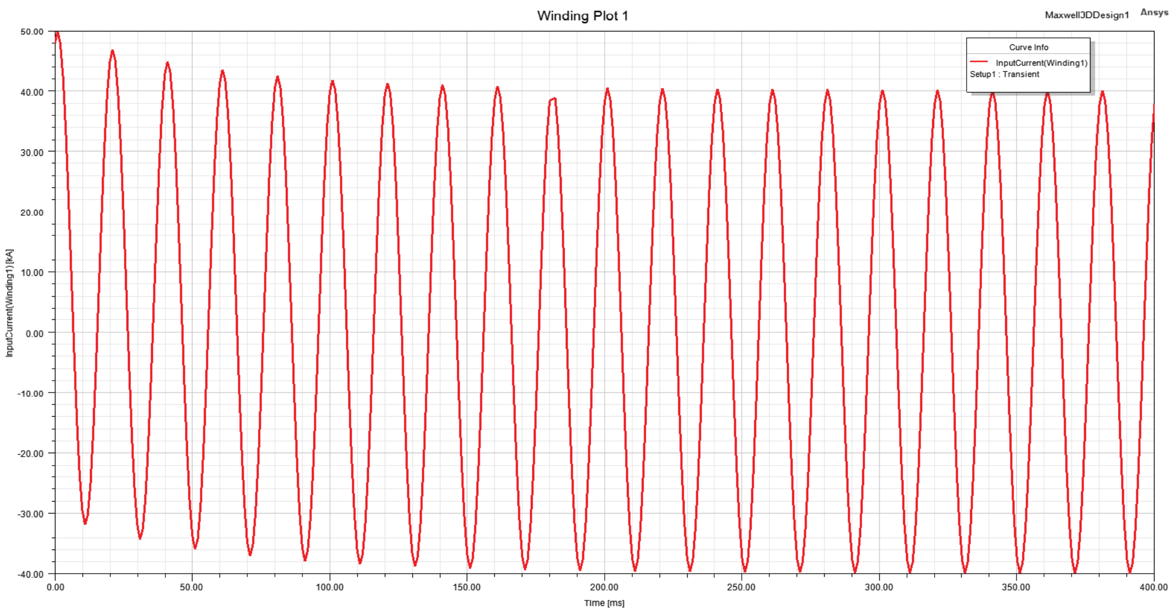

FIGURE 20. Generated simulation of the short-circuit current passed through the analyzed tulip contact.

After exporting the obtained computational data to the mechanical solver, it was possible to generate the distribution of the resulting electrodynamic forces in the analyzed tulip contact. In this case, the theoretical assumptions were confirmed, where forces $\boldsymbol{F}_{ez}$ were generated at the contact points, repelling the contacts of the contact crown from the contact pin. In the remaining parts of the contactor, electrodynamic forces $\boldsymbol{F}_{ek}$ were created, pressing all the contacts inwards, thus eliminating the impact of the forces repulsing the lamellas. The generated electrodynamic force vectors are shown below in the Figure 22 above.

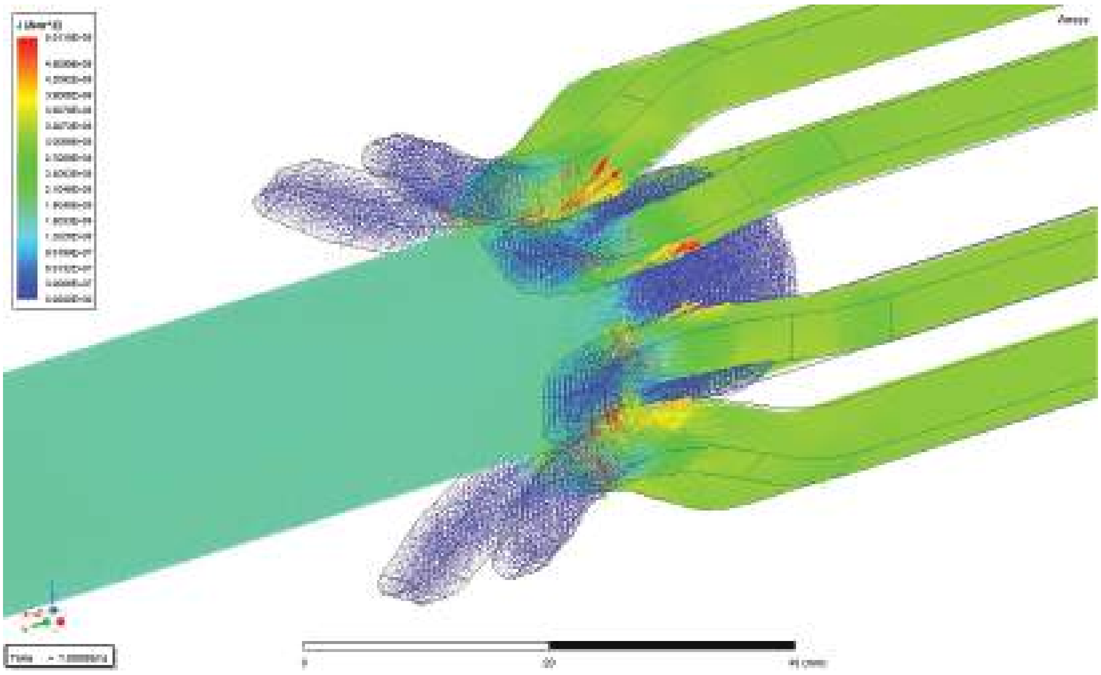

FIGURE 21. Short-circuit current density flowing through the tulip contact.

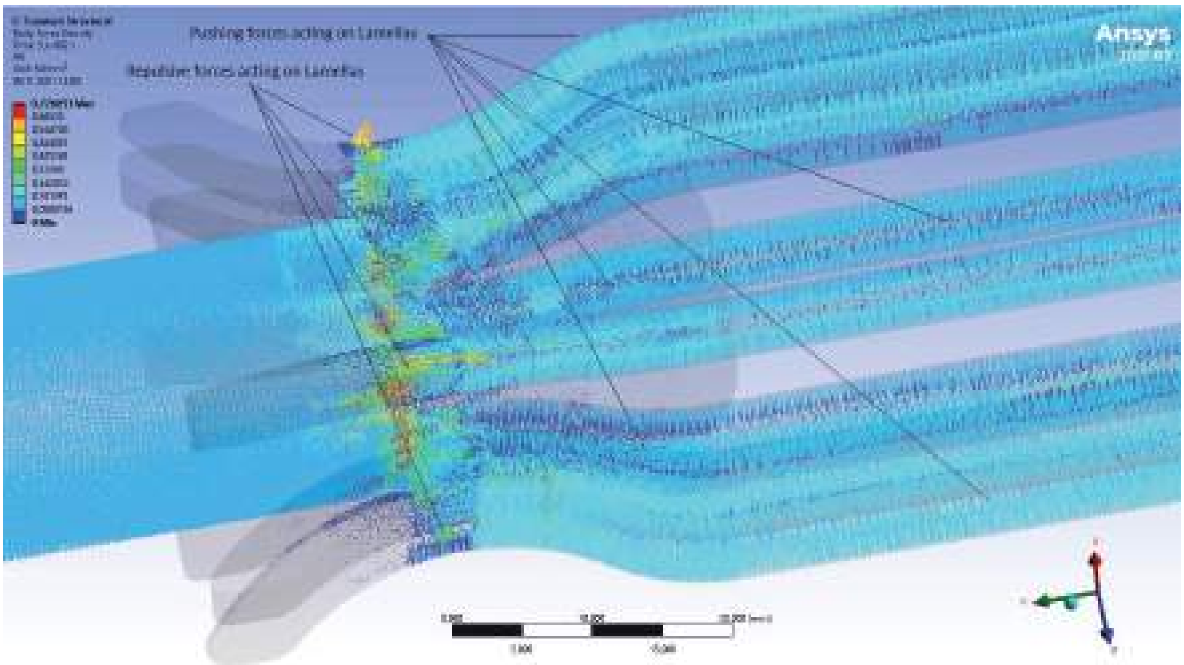

FIGURE 22. Distribution of the interacting electrodynamic forces at the actual contact points and the entire tulip contact body.

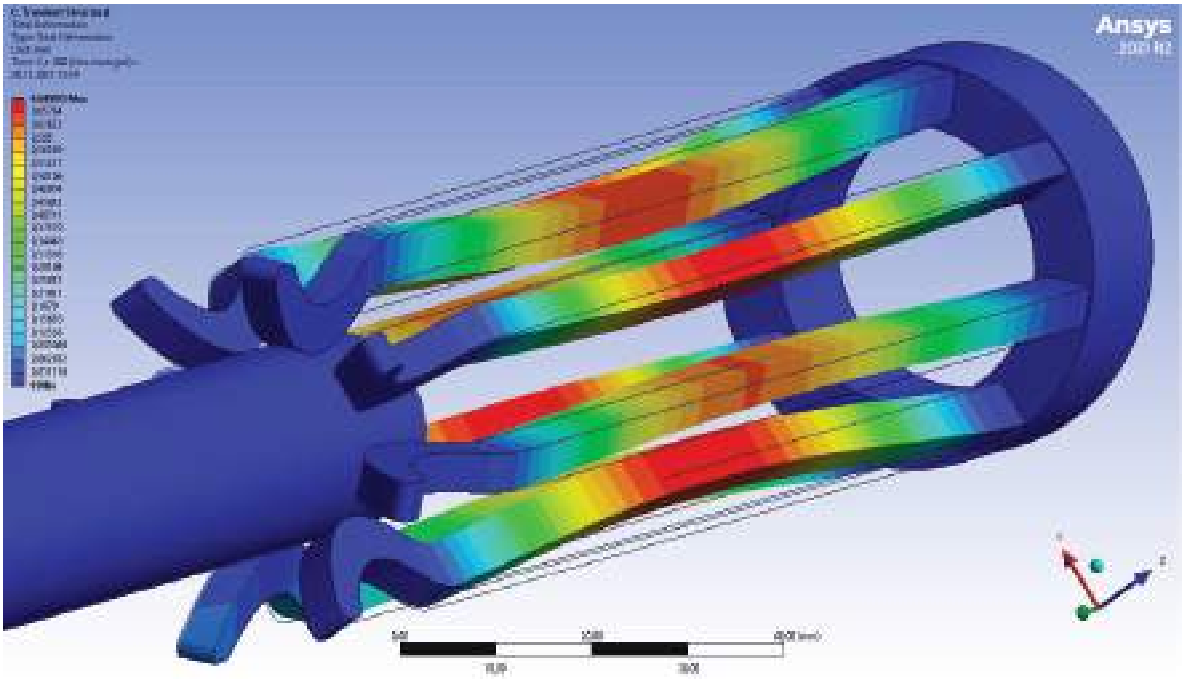

FIGURE 23. **Contact mechanical deformations in a tulip contact related to the interaction of electrodynamic forces.**

In order to verify which electrodynamic forces are greater, an additional mechanical analysis was performed to check where the greatest mechanical deformations occur. In the computational simulation, it turned out that the electrodynamic forces at the point of contact have a much lower value than the forces pressing the contactors. This is illustrated in detail in Figure 23 above, where the deformations related to the occurrence of the discussed forces in the tulip contact are presented.

VI. ELECTRODYNAMIC FORCES IN HIGH VOLTAGE APPARATUSSES–LIVE TANK CIRCUIT BREAKER

High voltage electrical apparatuses such as circuit breakers and disconnectors are connected in series to the protected circuit. When disturbances in the form of short-circuits occur, the flowing short-circuit currents can be greater multiple times than the rated currents of these devices. In effect, generation of mechanical stresses is a result of electrodynamic interactions.

Manufacturers of alike devices can successfully use modern numerical methods in order to design and manufacture apparatuses resistant to the impact of electrodynamic forces. Simulation analyses allow to determine the value of electrodynamic forces originating from peak short-circuit currents and mechanical stresses resulting in the developed layouts of high voltage electrical apparatuses. The electrodynamic force of the designed device is defined by the peak value of the current switched off, for example, by a high-voltage switch without depriving it of its ability to be used further (it is not causing its damage).

One of the most important high voltage apparatuses are circuit breakers. Those allow for switching off fault currents, e.g. short-circuit currents in a protected circuit after receiving a signal from the protection automatics in order to start the circuit breaker drive. An example of the design of a circuit-breaker with three poles mounted on a common supporting beam with a common operating mechanism is shown below in Figure 24.

Development of the structure and production of a high-voltage circuit breaker requires from the manufacturer not only constructional knowledge and ''know-how'', but also a large technical base and machinery park. Global manufacturers such as ABB, SIEMENS or ALSTOM produce overhead circuit breakers for voltages up to 300 kV and for currents up to 50 kA in a single-break version, i.e. with one set of connection chambers for a particular pole of the HV switch. In the case of higher voltages, systems with a double set of switching chambers (420 kV) and with a four set of switching chambers (800 kV) are used.

There are two typical designs of SF_6 gas overhead switches in the circuit breaker design. The first type are the live-tank circuit breakers, the connection chamber of which is built into a porcelain or composite insulator at high potential

FIGURE 24. **LTB-D high voltage Live-Tank circuit breaker by ABB.**

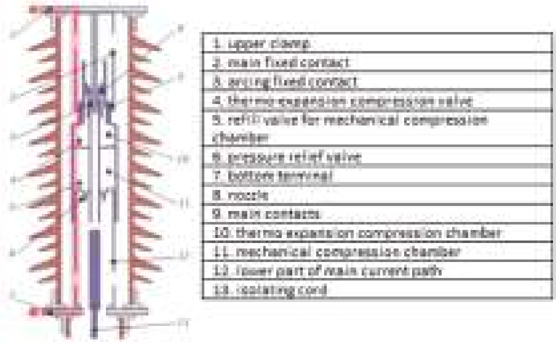

FIGURE 25. **Longitudinal section of the HV circuit breaker connection chamber with SF_6 - third generation thermo-expansion.**

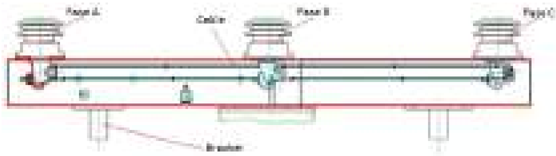

FIGURE 26. **Schematic drawing of cables connecting the mechanisms of HV switch for 3 poles.**

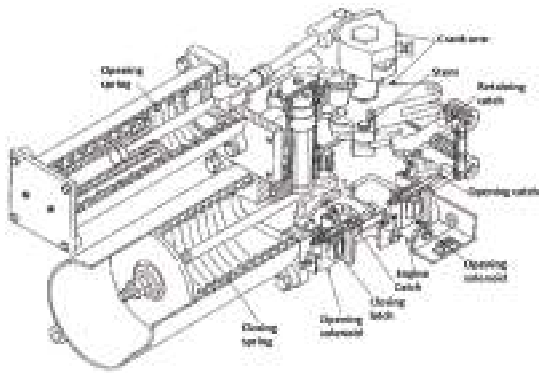

FIGURE 27. **The pictorial drawing of a common drive for HV storage circuit breaker.**

during operation. The second type of switches are dead-tank constructions, the tank of which, together with the connection chamber, works at the ground potential.

In this type of SF_6 circuit-breakers, the switching chambers are equipped with a puffer type, in which the gas is compressed by a piston or a cylinder directly coupled with the contact system. In the third generation of switches in the switching chambers, the thermal expansion effect is additionally used. The energy generated by the burning of the electric arc helps to extinguish it. During the opening or closing operation of the switch, the gas is compressed by a piston moving in a cylinder. The forced SF_6 gas into the extinguishing chamber flows around and cools the burning electric arc.

Currently used high-voltage circuit breakers are equipped with two-stream structures of extinguishing chambers, where SF_6 gas from the compression chamber is forced into a double system of nozzles with arcing contacts made of the main and auxiliary nozzles. Development work on the use of electric arc energy to increase the arc extinguishing efficiency during the zero crossing of the current, enabled the development of compression chambers consisting of two smaller chambers: thermal-expansion compression and mechanical compression. An example of the compression chambers built into the circuit breaker switching chamber is presented below in Figure 25.

The arcing contacts built into the switching chamber are most exposed to the effects of an electric arc during switching operations. The arcing contact system and the main contact system in the switching chamber operate in a specific switching sequence. When switching off e.g. fault currents, first the main contact of the switch opens without arcing, and then the arcing contact opens, taking over the erosive processes related to the action of the electric arc for which it is adapted (made of an alloy of tungsten or molybdenum with copper). When closing the circuit-breaker, the arc sequence of the arcing contact and the main contact are reversed.

FIGURE 28. Modeled 3D assembly of the HV switch according to the executed measurements.

VII. LIVE TANK CIRCUIT BREAKER 3D MODEL AND ELECTRODYNAMIC FORCES SIMULATIONS

To create a 3D simulation model of a live tank high voltage circuit breaker, the dimensions were taken from a real object. From the outside, the switch pole was made of a supporting insulator to which the extinguishing chamber of a single-break switch is screwed. The circuit-breaker has connections for screwing high-voltage cables and screw fittings for mounting the pole on the support beam of the three-pole system. Inside the circuit breaker, at the height of the supporting insulator, there is a string coupled with a piston moving inside the cylinder in the connection chamber. The traction layer is mechanically stressed with the mechanism of the entire circuit breaker. The power from the drive is transferred by means of strings to individual poles, where the contacts of the switch are closed or opened. An illustrative drawing of the mechanical system of the traction layers is presented in Figure 26 below. The traction layers are driven from the switch storage drive located under the middle pole of the switch (phase B). The energy from the closing and opening springs is transferred to the circuit-breaker poles by means of the strings. The main components of the storage drive of the high-voltage circuit breaker are described in Figure 27 below.

In the switching chamber, on the moving piston, there is a movable part of the arcing contact in the form of six lamellas and a movable part of the main contact of the analyzed circuit breaker (sleeve). The fixed elements of the arcing contact and the main switch, due to the fact that the circuit breaker was of the single-motion type, are the main crown with the main contact contacts and the arcing contact in the form of a bar overlapping the crown.

The circuit breaker components have been accurately measured and dimensioned. This allowed for the preparation of 3D models of individual elements of the high-voltage circuit breaker connection chamber, including: main contacts, arcing contact, nozzle, cylinder and other elements. The prepared 3D assembly of modeled elements of the high-voltage switch structure is shown in Figure 28 above and in

The 3D modeled simplified structure of the high-voltage circuit breaker chamber made it possible to perform simulation analyses of electrodynamic forces for the short-circuit

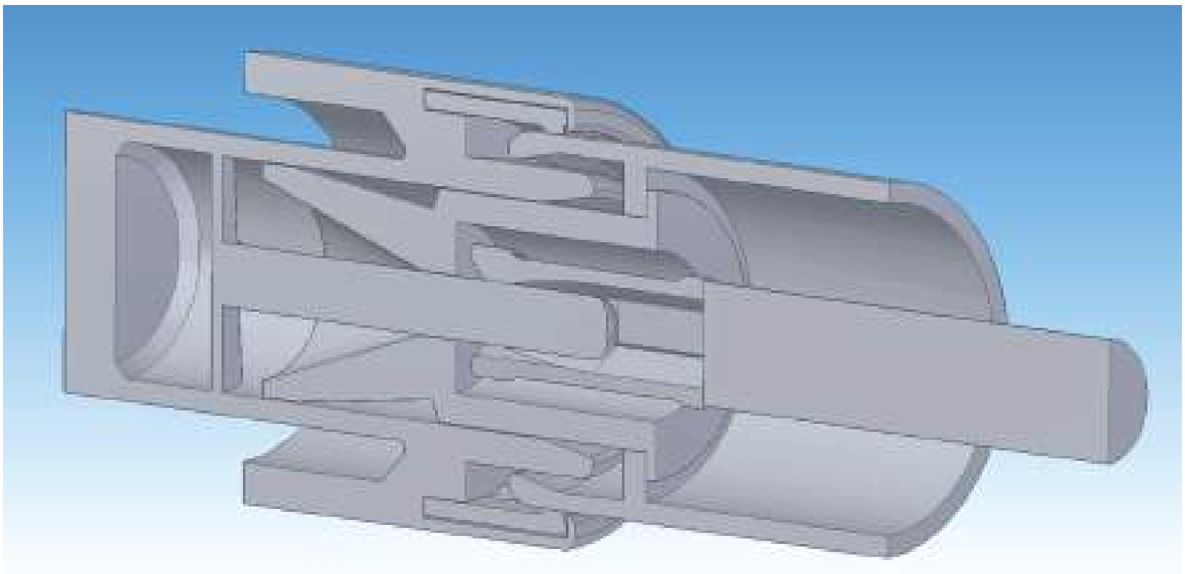

FIGURE 29. Modeled 3D assembly of the HV switch according to the executed measurements–cross section.

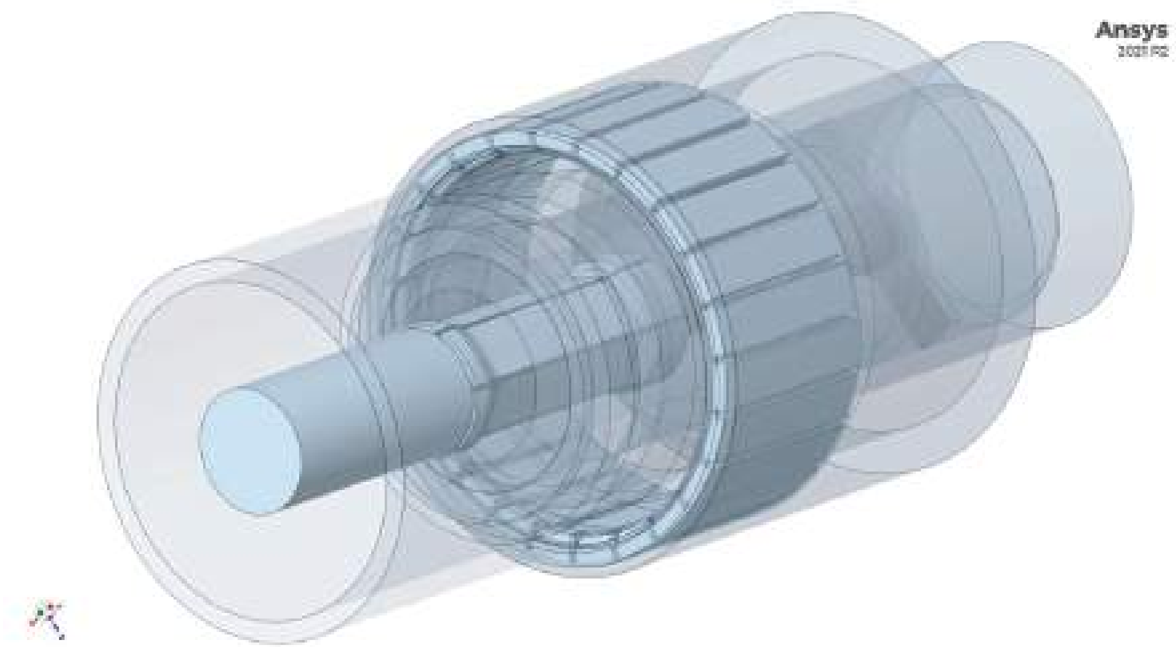

FIGURE 30. Optimized geometry of HV breaker in Ansys space claim module.

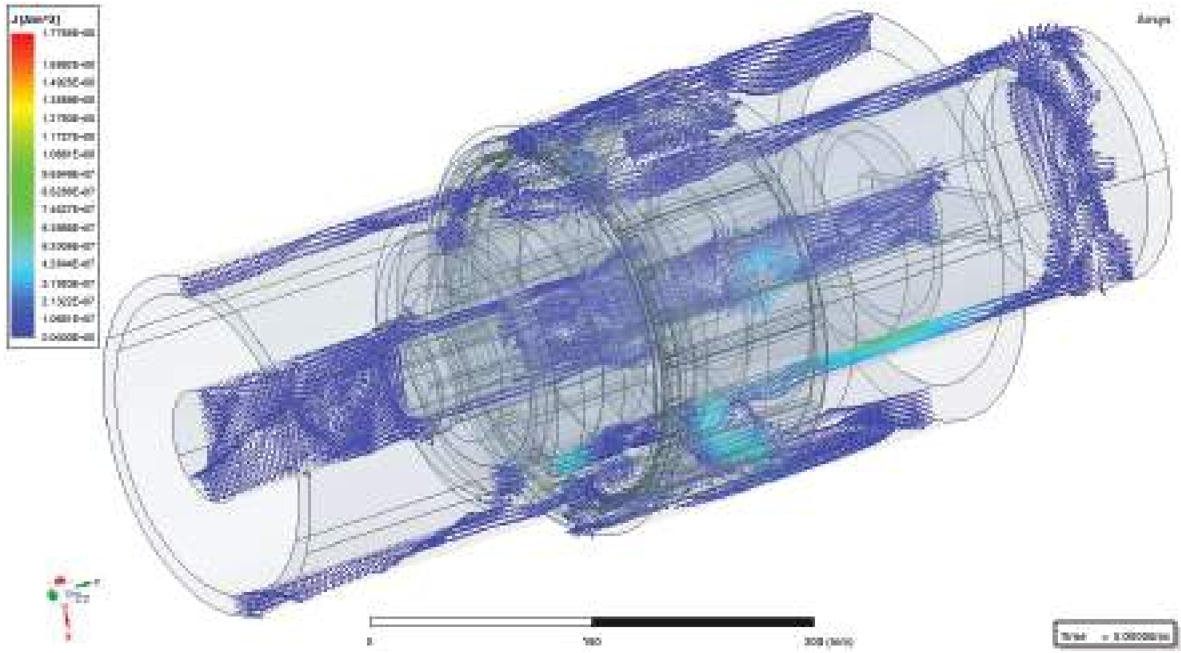

FIGURE 31. Density distribution of the short-circuit current flowing through the contacts of the switching chamber of the high-voltage circuit breaker.

conditions declared by the manufacturer in the form of 40 kA of rated short-circuit breaking current.

For this purpose, the prepared 3D model of the circuit breaker connection chamber was imported into the Ansys

Workbench software, where in the Space Claim Geometry module, the geometry was thoroughly checked and simplified in terms of the quality of modeled parts - redundant surfaces and duplicated unnecessary edges. The geometry was prepared in this way, devoid of any non-linearities and inaccuracies causing problems during calculations. It was shown in Figure 30 above.

In order to prepare a computational simulation, the 3D model was exported to the Ansys Maxwell 3D computational module. The simulation analysis to determine the electrodynamic forces in the contacts of the circuit breaker at the moment of the short-circuit current occurrence was performed for the closed main and arcing contacts of the circuit breaker. The imported 3D model of the circuit breaker into the Ansys Maxwell 3D environment was properly prepared for simulation. For the calculations, environmental conditions in the form of SF_6 gas were adopted and material properties were assigned to individual parts of the analyzed assembly of the HV switch. Examples of material properties for tungsten adopted for the arcing contact pin are shown in the Table 1 below.

After setting the material properties, the model was given current forces in the form of specific short-circuit currents. The initial direction of current flow for calculations was assumed from the fixed contacts to the moving contacts of the circuit breaker. Simulation analyses to determine the value of electrodynamic interactions in the circuit breaker contacts were performed for two cases of short-circuit current:

- 40 kA without non-periodic component,
- 40 kA with a non-periodic component increasing the short-circuit current up to 60 kA.

Boundary conditions for the prepared simulation were properly determined, it was necessary to determine the simulation time, the duration of which was assumed to be 200 ms. The time step for the computational iterations performed was assumed every 0.5 ms, which gave a total of 400 iteration steps that the solver had to perform.

In the case of the ''mesh'' calculation, elements of the ''tetrahedra'' type were used. On the contact points of the crown of the main contact and the arcing contact, the computational grid was additionally densified in order to obtain greater accuracy of calculations. In the first computational iteration, the number of mesh elements was 534379, the ''Adaptive Mesh Refinement'' function was employed, the mesh was compacted by a solver in places where it was additionally required.

Numerical calculations were started, the total time of which was 10.5 hours. From the obtained results, it was possible to check which elements of the switching chamber are most exposed to electrodynamic influences generated by the flow of short-circuit currents. At this stage of the calculations, it was also possible to analyze the generated approximate Ohm losses in each of the analyzed active parts of the circuit breaker. Additionally, the software made it possible to view the density distribution of the short-circuit current flowing through the closed contacts of the high-voltage switch, an example of the density distribution in the contact system is shown below in Figure 31. In the case of the simulation analysis performed, particular attention was paid to the forces occurring in the contacts of the main and arcing contacts.

TABLE 1. Examples of material properties for tungsten used for calculations in the simulation analysis for the switching chamber of the high-voltage circuit breaker.

Name	Type	Value	Units
Relative Permittivity	Simple	1	
Relative Permeability	Simple	1	
Bulk Conductivity	Simple	$182 \cdot 10^5$	siemens/m
Dielectric Loss Tangent	Simple	0	
Magnetic Loss Tangent	Simple	0	
Electric Coercivity	Vector		
Magnitude	Vector Mag	0	
Magnetic Coercivity	Vector		
Magnitude	Vector Mag	0	A per meter
Thermal Conductivity	Simple	174	W/m·C
Magnetic Saturation	Simple	0	tesla
Lande G Factor	Simple	2	
Delta H	Simple	0	A per meter
Measured Frequency	Simple	9.4e+09	Hz
Core Loss Model		None	w/m^3
Mass Density	Simple	19300	kg/m^3
Composition		Solid	
Specific Heat	Simple	132	j/kg·C
Young's Modulus	Simple	$375 \cdot 10^9$	N/m^2
Positions Ratio	Simple	0.3	
Thermal Expansion Coefficient	Simple	4.6e-06	1/C
Magnetostriction	Custom		
Inverse Magnetostriction	Custom		
Thermal Material Type		Solid	
Solar Behavior	Simple	0	

For the first numerical simulation, for an undistorted short-circuit current of 40 kA, the values of electrodynamic forces in the main contact were similar to the order of magnitude for all 24 main contactors (lamellas) (force values in kN). However, the calculated values of electrodynamic forces for

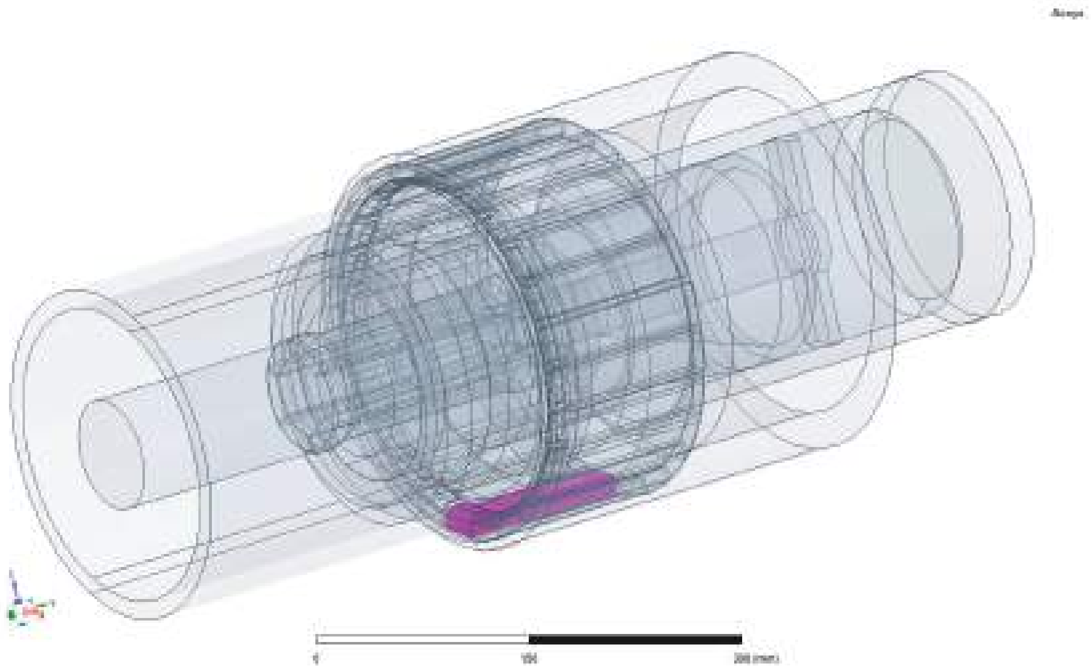

FIGURE 32. 1 of 24 lamellas (contactors) of the main contact in high voltage circuit breaker before simulation.

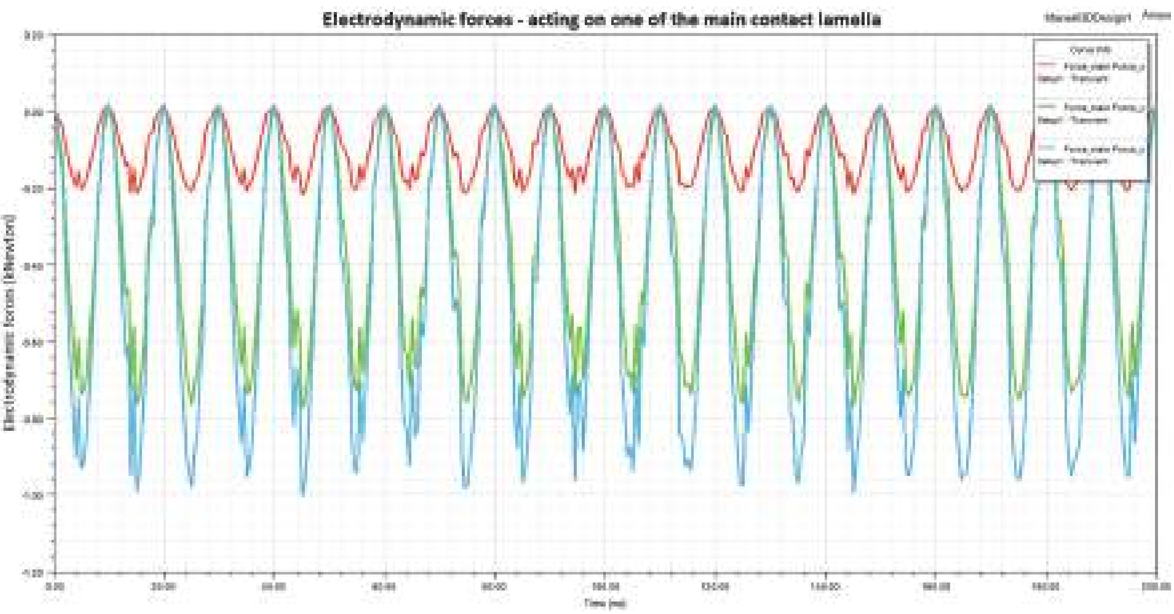

FIGURE 33. Values of electrodynamic forces acting on one of the main contact lamella for 40 kA without non-periodic component.

the contact points were different and ranged from 0.01 to 1.2 kN. An example of the generated electrodynamic forces for 1 of the 24 main lamellas is presented in Figure 32 above and Figure 33 below.

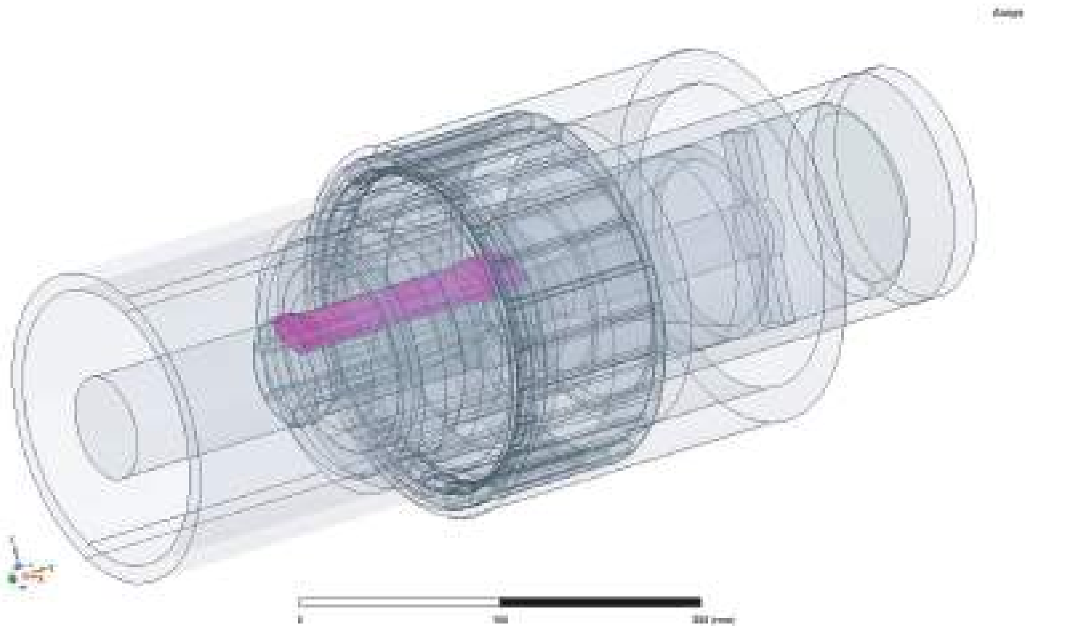

FIGURE 34. 1 of 6 lamellas (contactors) of the arcing contact in high voltage circuit breaker before simulation.

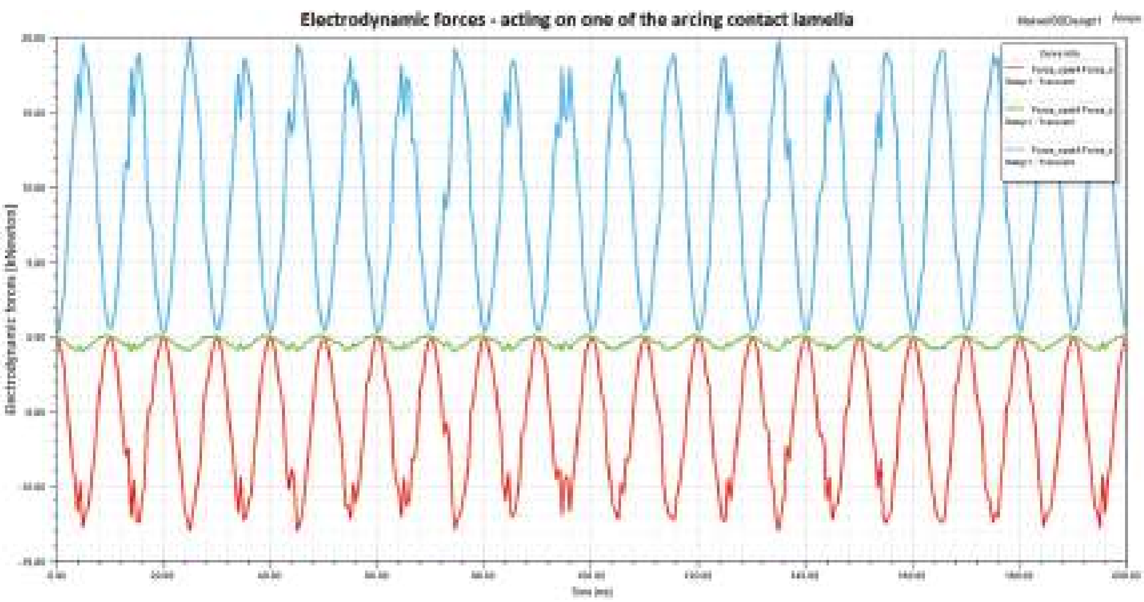

FIGURE 35. Values of electrodynamic forces acting on one of the arcing contact lamella for 40 kA without non-periodic component.

In Figures 34 above and Figure 35 below the simulation for 1 of 6 lamellas of the arcing contact were depicted for the 40 kA current without non-periodic component.

The results of the second computational simulation for the current with a non-periodic component shown that contacts were under influence of significant electrodynamic loads. It was dependent on the presence of a non-periodic component boosting the short-circuit current in the initial phase of its duration. The momentary boost of the short-circuit current value resulted in higher electrodynamic loads in the

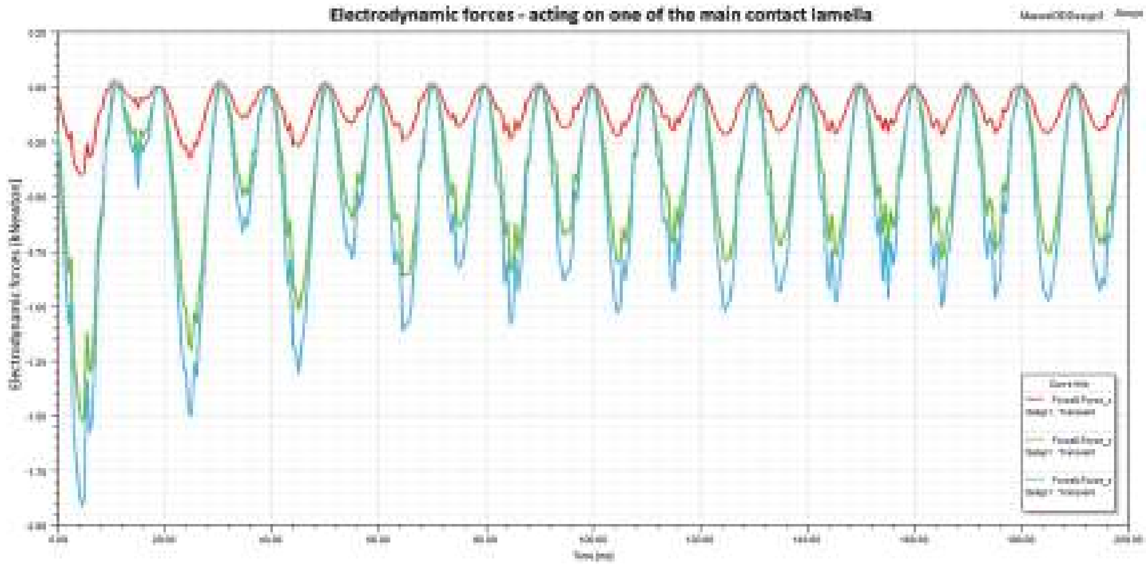

FIGURE 36. Values of electrodynamic forces acting on one of the main contact lamella for 40 kA with a non-periodic component increasing the short-circuit current up to 60 kA.

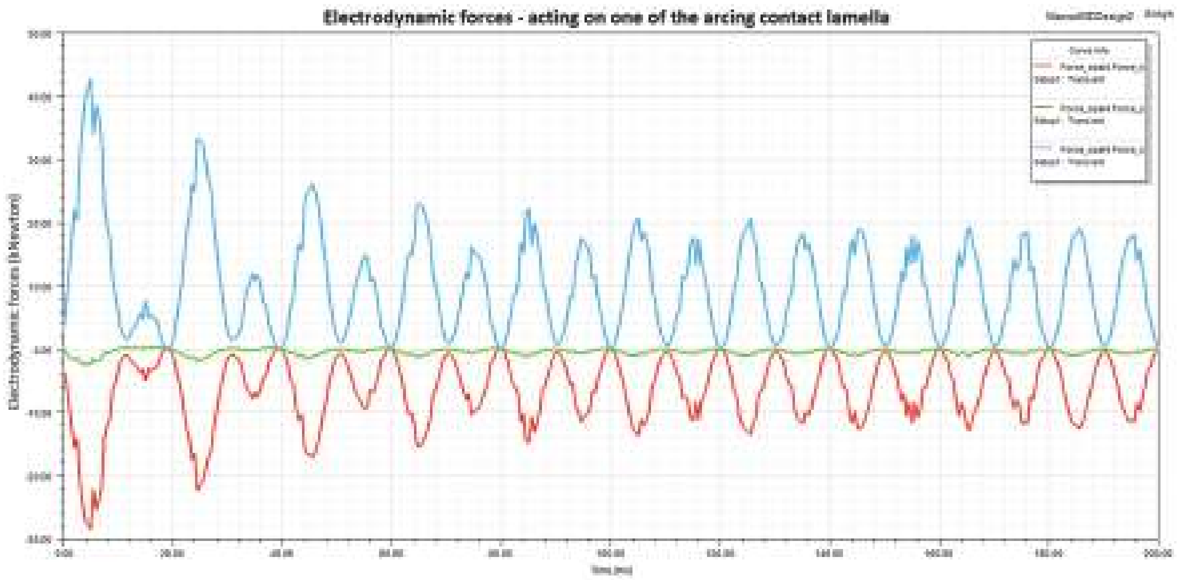

FIGURE 37. Values of electrodynamic forces acting on one of the arcing contact lamella for 40 kA with a non-periodic component increasing the short-circuit current up to 60 kA.

circuit breaker contacts. In the case of the main contact, the maximum value of the electrodynamic forces reached twice the value of about 2.5 kN, and then at the time of the decay of the non-periodic component, these values decreased to the level of the results from the previous calculations. Sample waveforms for a selected contactor are shown in Figure 36 below.

The electrodynamic effects for 40 kA current with a non-periodic component in the arcing contact are much greater. In relation to the simulation results for the arcing contact loaded with a current without a non-periodic component the calculated values are twice as high, reaching over 40 N. The values for the selected arcing contactor are shown in Figure 37 below.

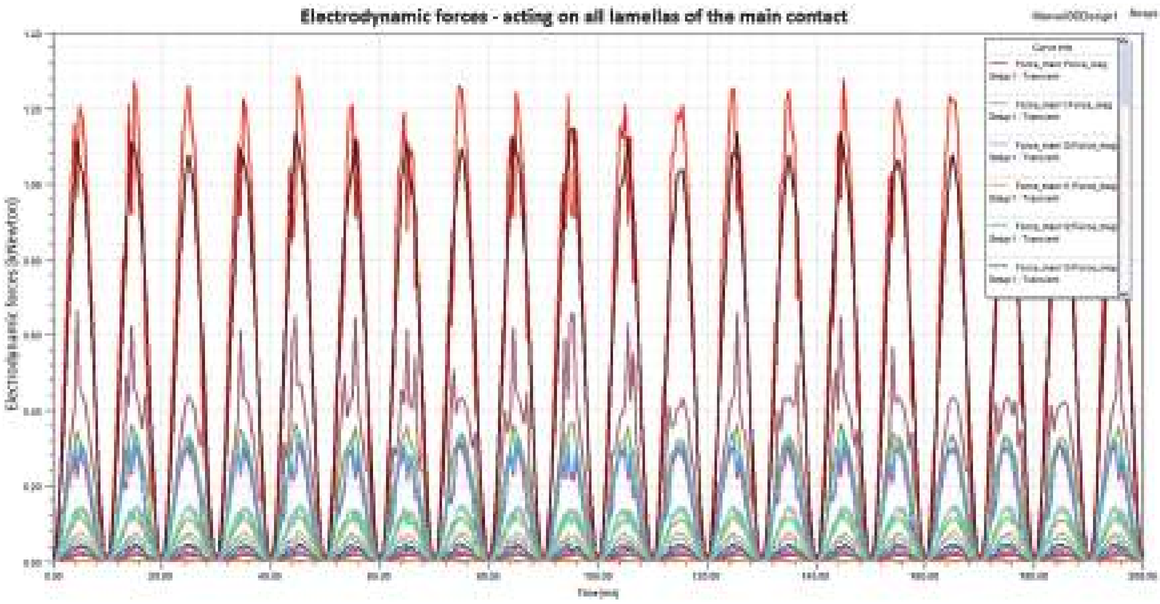

FIGURE 38. Values of electrodynamic forces acting on all lamellas of the arcing contact of the Live Tank high-voltage circuit breaker for short-circuit current without non-periodic component–arcing contact.

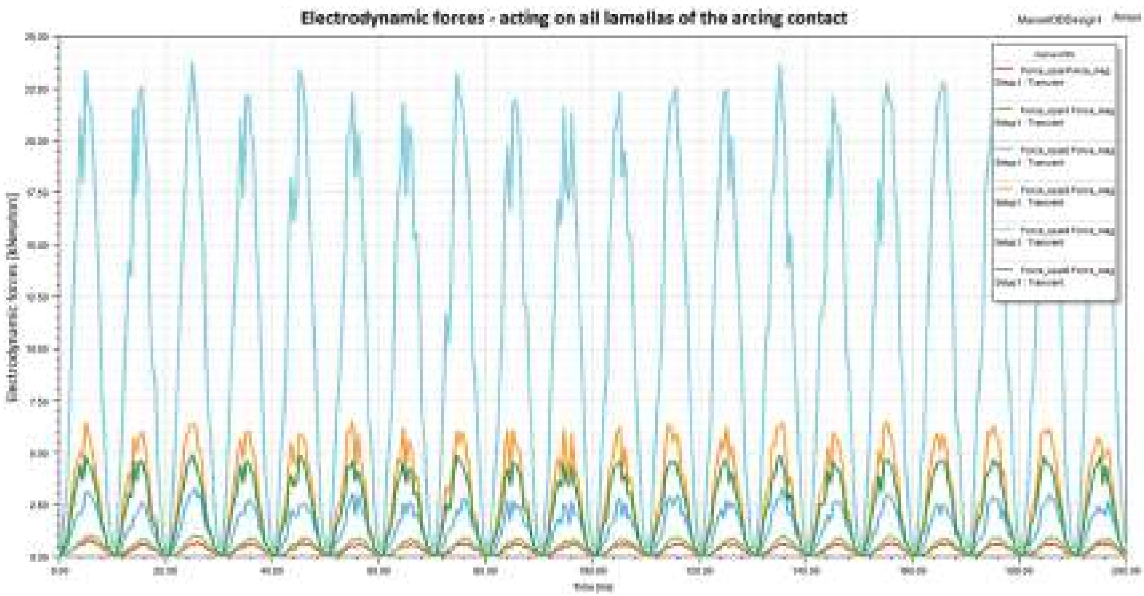

FIGURE 39. Values of electrodynamic forces acting on all lamellas of the main contact of the Live Tank high-voltage circuit breaker for short-circuit current without non-periodic component–main contact.

The obtained values illustrate the formation of momentary significant increases in electrodynamic interactions in the initial phase of the current flow in relation to the previous calculations for the short-circuit current without the non-periodic component.

The use of the 3D model of the circuit breaker switching chamber made it possible to perform very time-consuming calculations aimed at determining the electrodynamic interactions on all contacts. This unique approach made it possible to verify that all contacts in the contact system are evenly

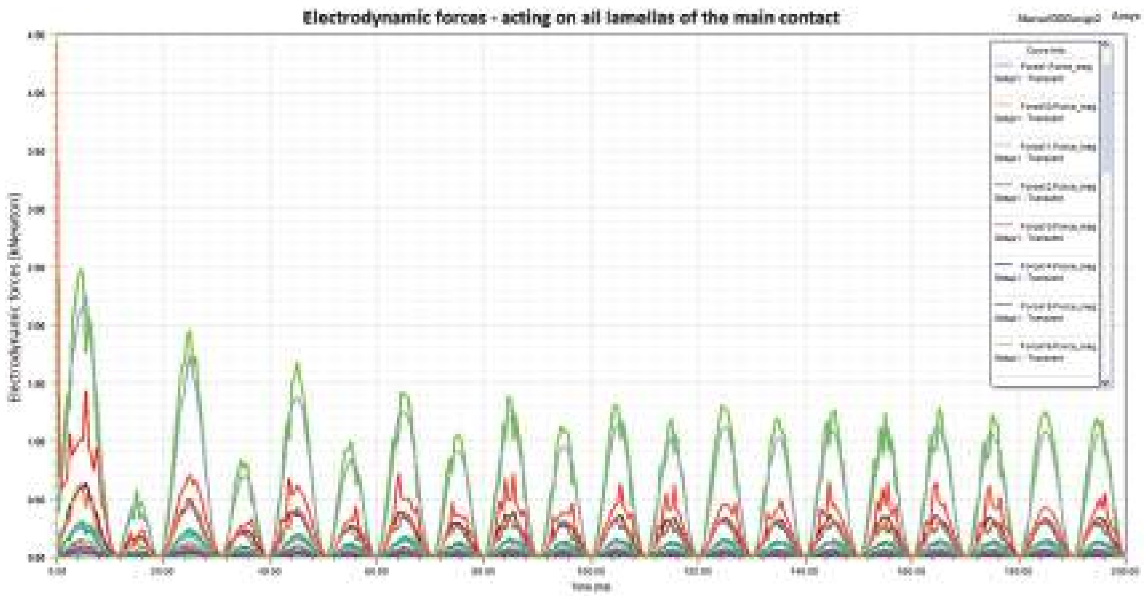

FIGURE 40. Values of electrodynamic forces acting on all lamellas of the main contact of the Live Tank high-voltage circuit breaker for short-circuit current with non-periodic component—arcing contact.

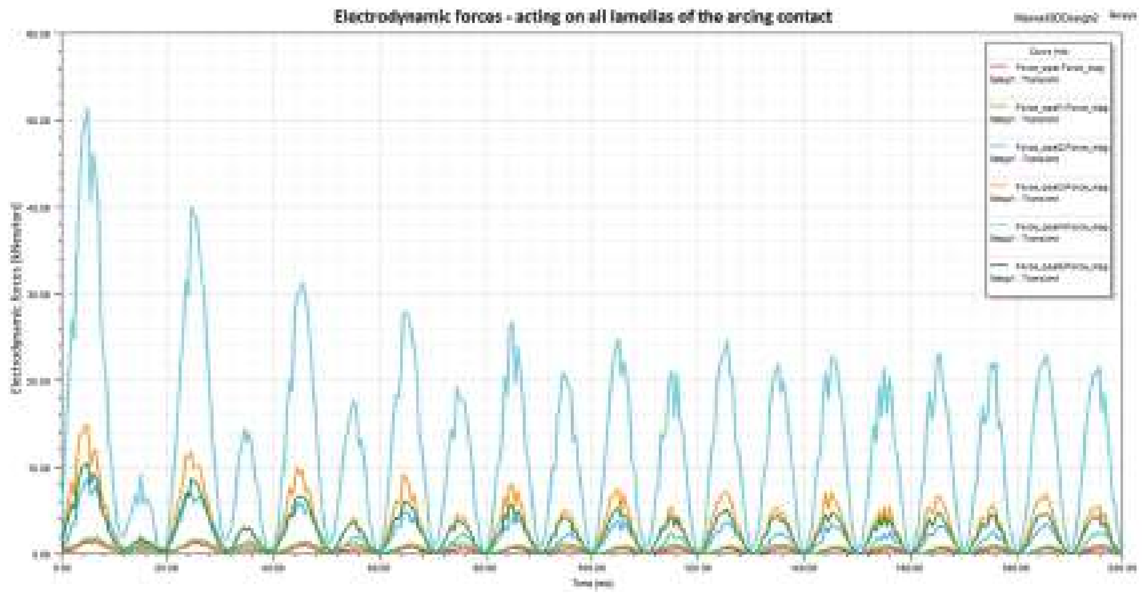

FIGURE 41. Values of electrodynamic forces acting on all lamellas of the main contact of the Live Tank high-voltage circuit breaker for short-circuit current with non-periodic component—arcing contact.

loaded. Calculations were executed for 1.265.243 generated computing nodes. As a result, it was possible to generate the resultant waveforms of electrodynamic interactions affecting the main and arcing contacts. It was presented in Figures 38-41 below.

VIII. SIMULATION RESULTS SUMMARY

The generated waveforms allowed for the analysis and conclusions that the main and arcing contacts are not uniformly electrodynamically loaded during a 40 kA short-circuit with a course not deformed by a non-periodic component. The same computational approach was performed for the short-circuit current much more unfavorably from the point of view of electrodynamic exposures, which contains a non-periodic component. This type of short-circuit current is much more harmful from the point of view of mechanical stresses - deformation or even contact damage. The calculations made in the form of generated waveforms for the main and arcing contact contacts for a more unfavorable short-circuit current were collected on the waveforms depicted in Figures 38-41.

In the case of the conducted analysis concerning the determination of the electrodynamic forces affecting the contacts of the main and arcing contact, the simulation approach presented by the authors may now be one of the simpler and very useful methods for determining the approximate values of the electrodynamic forces. Depending on the accuracy of the 3D model adopted for calculations, the obtained results are much more reliable than simplified analytical methods. In the case of such a complex structure as a high-voltage circuit breaker, and more precisely in the case of the performed analysis of its switching chamber, it is not possible to determine the exact values of the interacting electrodynamic forces in an analytical manner with the use of formulas and simplifications. Even if such computational steps were taken, the obtained results were subject to error and uncertainty.

IX. CONCLUSION

In the performed simulation, authors used an accurate 3D model prepared on the basis of measurements of individual parts of the dismantled pole of the high-voltage circuit breaker. The 3D model obtained in this way allowed for the performance of reliable simulation analyses, which helped to visualize how the contacts of the HV circuit breaker can actually behave in the event of the flow of short-circuit currents and to what electrodynamic exposures those are subjected to.

Interestingly, on the basis of the obtained results, the authors illustrated that the individual contacts of both the main contact and the arcing contact are not evenly electrodynamically loaded. From the generated electrodynamic force waveforms for each contact point, doubts were raised as to the possibility of using simplifications and performing calculations only for 1 contact point, which can be found in the literature. The obtained results show that the values of the electrodynamic forces can differ even from 2 kN, which in turn may initiate the deformation of the contact or even the damage of the whole contact system. Performing this type of numerical analysis on even more accurate 3D models in the form of structural models in R&D departments allows for obtaining precise data on electrodynamic exposures. Each improvement or change in design can be quickly simulated, which in the process of creating a prototype, e.g. of current circuits and contacts of a high-voltage circuit breaker, is extremely important in terms of cost reduction and limiting the number of prototypes for experimental tests in research laboratories.

Authors conducted thorough research of the literature which confirms the lack of information on the study of electrodynamic forces in high voltage contact systems. In the R&D manufacturers departments of contact systems and static breakers, static tests can be found [x]. The works concern only the contact system made of one element, cut in an appropriate manner. Then, outside the circuit breaker chamber, it is possible to conduct tests by pulling out one of the contacts and determining the force statically. It is not a force related to the flow of current. It is a mechanical force obtained through the elasticity of the material, sometimes also by pressure springs.

The authors referred to the global trend in the research of contact systems of high-voltage devices and focused on the correct selection of:

- materials,
- boundary conditions,
- physics issues.

Authors tried to recreate some of the research in laboratory conditions, in a short-circuit laboratory.

REFERENCES

[1] S. Wang, H. Li, and D. Yuan, "Mechanical characteristics analysis of defective transformer windings under short-circuit fault using 3-D FEM," in *Proc. 20th Int. Conf. Electr. Mach. Syst. (ICEMS)*, Sydney, NSW, Australia, Aug. 2017, pp. 1–4.

[2] G. Kadkhodaei, K. Sheshyekani, M. Hamzeh, and S. D. Tavakoli, "Multiphysics analysis of busbars with various arrangements under short-circuit condition," *IET Electr. Syst. Transp.*, vol. 6, no. 4, pp. 237–245, Dec. 2016.

[3] N. Vladimir, I. Ančić, and A. Šestan, "Effect of ship size on EEDI requirements for large container ships," *J. Mar. Sci. Technol.*, vol. 23, no. 1, pp. 42–51, Mar. 2018.

[4] *High-Voltage Switchgear and Controlgear—Part 102: Alternating Current Disconnectors and Earthing Switches*, Standard IEC 62271-102:2012, International Electrotechnical Commission, Geneva, Switzerland, 2018.

[5] *Short-Circuit Currents—Calculation of Effects—Part 1: Definitions and Calculation Methods*, Standard IEC 60865-1:2011, International Electrotechnical Commission, Geneva, Switzerland, 2012.

[6] S. Kulas, Ł. Kolimas, and M. Piskała, "Electromagnetic forces on contacts," in *Proc. 43rd Int. Univ. Power Eng. Conf.*, Padova, Italy, Sep. 2008, pp. 1–4.

[7] Ł. Kolimas, S. Łapczyński, and M. Szulborski, "Tulip contacts: Experimental studies of electrical contacts in dynamic layout with the use of FEM software," *Int. J. Electr. Eng. Educ.*, vol. 1, pp. 1–4, Dec. 2019.

[8] L. Kolimas, S. Łapczyński, M. Szulborski, and M. Świetlik, "Low voltage modular circuit breakers: FEM employment for modelling of arc chambers," *Bull. Polish Acad. Sci. Tech. Sci.*, vol. 68, no. 1, pp. 61–70, Feb. 2020.

[9] Y. Jiaxin, W. Yang, W. Lei, L. Xiaoyu, L. Huimin, and B. Longqing, "Thermal-dynamic stability analysis for the enclosed isolated-phase bus bar based on the subsegment calculation model," *IEEE Trans. Compon., Packag., Manuf. Technol.*, vol. 8, no. 4, pp. 626–634, Apr. 2018.

[10] D. M. Williams, "Human factors affecting bolted busbar reliability," in *Proc. IEEE 62nd Holm Conf. Electr. Contacts (Holm)*, Clearwater Beach, FL, USA, Oct. 2016, pp. 86–93.

[11] J. Yang, Y. Liu, D. Hu, B. Wu, and J. Li, "Transient vibration study of GIS bus based on FEM," in *Proc. IEEE PES Asia–Pacific Power Energy Eng. Conf. (APPEEC)*, Xi'an, China, Oct. 2016, pp. 1092–1095.

[12] D. G. Triantafyllidis, P. S. Dokopoulos, and D. P. Labridis, "Parametric short-circuit force analysis of three-phase busbars—A fully automated finite element approach," *IEEE Trans. Power Del.*, vol. 18, no. 2, pp. 531–537, Apr. 2003.

[13] J. Yang, Y. Liu, D. Hu, B. Wu, B. Che, and J. Li, "Transient electromagnetic force analysis of GIS bus based on FEM," in *Proc. Int. Conf. Condition Monit. Diagnosis (CMD)*, Xi'an, China, Sep. 2016, pp. 554–557.

[14] X. Guan and N. Shu, "Electromagnetic field and force analysis of three-phase enclosure type GIS bus capsule," in *Proc. IEEE PES TD Conf. Expo.*, Chicago, IL, USA, Apr. 2014, pp. 1–4.

[15] I. C. Popa and A.-I. Dolan, "Numerical modeling of three-phase busbar systems: Calculation of the thermal field and electrodynamic forces," in *Proc. Int. Conf. Appl. Theor. Electr. (ICATE)*, Craiova, Romania, Oct. 2016, pp. 1–9.

[16] Y. Jiaxin, W. Ruichao, L. Huimin, B. Longqing, and W. Hongjian, "Research on the calculation methods of enclosed isolated phase bus-bar in short-circuit condition," in *Proc. IEEE 62nd Holm Conf. Electr. Contacts (Holm)*, Clearwater Beach, FL, USA, Oct. 2016, pp. 111–114.

[17] S. W. Park and H. Cho, "A practical study on electrical contact resistance and temperature rise at at the connections of the copper busbars in switchgears," in *Proc. IEEE 60th Holm Conf. Electr. Contacts (Holm)*, New Orleans, LA, USA, Oct. 2014, pp. 1–7.

[18] J. Gatherer and R. L. Jackson, "A multi-variable parametric study on the performance of bolted busbar contacts," in *Proc. IEEE 61st Holm Conf. Electr. Contacts (Holm)*, San Diego, CA, USA, Oct. 2015, pp. 124–131.

[19] F. M. Yusop, M. K. M. Jamil, D. Ishak, and S. Masri, "Study on the electromagnetic force affected by short-circuit current in vertical and horizontal arrangement of busbar system," in *Proc. Int. Conf. Electr., Control Comput. Eng. (InECCE)*, Pahany, Malaysia, Jun. 2011, pp. 1–8.

[20] G. Kadkhodaei, K. Sheshyekani, and M. Hamzeh, "Coupled electric–magnetic–thermal–mechanical modelling of busbars under short-circuit conditions," *IET Gener., Transmiss. Distrib.*, vol. 10, no. 4, pp. 955–963, Mar. 2016.

[21] J. Lei, J.-Y. Zhong, S.-J. Wu, Z. Wang, Y.-J. Guo, and X.-Y. Qin, "A 3-D steady-state analysis of thermal behavior in EHV GIS busbar," *J. Electr. Eng. Technol.*, vol. 11, no. 3, pp. 781–789, May 2016.

[22] M. Krcum, M. Zubčić, and T. Dlabač, "Electromechanical analysis of the medium voltage earthing switch due to short-time and peak withstand current test," *Energies*, vol. 12, no. 16, pp. 1–17, 2019.

[23] *IEC 60609-Short Circuit Current Standard*. Accessed: May 15, 2020. [Online]. Available: https://pdf.wecabrio.com/iec-60609.pdf

[24] R. Bini, B. Galletti, A. Iordanidis, and M. Schwinne, "Arc-induced turbulent mixing in a circuit breaker model," in *Proc. 1st Int. Conf. Electr. Power Equip.-Switching Technol.*, Xi'an, China, Oct. 2011, pp. 375–378.

[25] L. Wang, H. Liu, W. Zheng, C. Ge, R. Guan, L. Chen, and S. Jia, "Numerical simulation of impact effect of internal gas pressure on chamber housing in low-voltage circuit breaker," *IEEE Trans. Compon., Packag., Manuf. Technol.*, vol. 4, no. 4, pp. 632–640, Apr. 2014.

[26] X. Ye, M. T. Dhotre, J. D. Mantilla, and S. Kotilainen, "CFD analysis of the thermal interruption process of gases with low environmental impact in high voltage circuit breakers," in *Proc. IEEE Electr. Insul. Conf. (EIC)*, Seattle, WA, USA, Aug. 2015, pp. 7–10.

[27] M. T. Dhotre, X. Ye, M. Seeger, M. Schwinne, and S. Kotilainen, "CFD simulation and prediction of breakdown voltage in high voltage circuit breakers," in *Proc. IEEE Electr. Insul. Conf. (EIC)*, Baltimore, MD, USA, Jun. 2017, pp. 11–14.

[28] D. Chen, Z. Li, X. Li, L. Ji, and Z. Song, "Simulation of pressure rise in arc chamber of MCCB during its interruption process," in *Proc. 53rd IEEE Holm Conf. Electr. Contacts*, Pittsburgh, PA, USA, Sep. 2007, pp. 43–47.

[29] C. Rumpler, H. Stammberger, and A. Zacharias, "Low-voltage arc simulation with out-gassing polymers," in *Proc. IEEE 57th Holm Conf. Electr. Contacts*, Minneapolis, MN, USA, Sep. 2011, pp. 1–8.

[30] M. Lindmayer, "Complete simulation of moving arc in low-voltage switchgear," in *Proc. 14th Int. Conf. Gas Discharge Appl.*, Liverpool, U.K., Sep. 2002, pp. 318–324.

[31] H. Nordborg and A. A. Iordanidis, "Self-consistent radiation based modelling of electric arcs: I. Efficient radiation approximations," *J. Phys. D, Appl. Phys.*, vol. 41, no. 13, Jul. 2008, Art. no. 135205.

[32] A. Iordanidis and C. M. Franck, "Self-consistent radiation-based simulation of electric arcs: II. Application to gas circuit breakers," *J. Phys. D, Appl. Phys.*, vol. 41, no. 13, 2008, Art. no. 135206.

[33] N. P. T. Basse, R. Bini, and M. Seeger, "Measured turbulent mixing in a small-scale circuit breaker model," *Appl. Opt.*, vol. 48, no. 32, pp. 6381–6391, 2009.

[34] F. P. Incropera, D. P. DeWitt, T. L. Bergman, and A. S. Lavine, *Introduction to Heat Transfer*, 5th ed. Hoboken, NJ, USA: Wiley, 2006.

[35] P. T. Müller, "Macroscopic electro thermal simulation of contact resistances," Bachelor's thesis, Center Comput. Eng. Sci.-Math. Division, RWTH Aachen Univ., Aachen, Germany, 2016.

[36] P. Kumar and A. Kale, "3-dimensional CFD simulation of an internal arc in various compartments of LV/MV Switchgear," in *Proc. ANSYS Converg. Conf.*, Pune, India, Aug. 2016, pp. 236–241.

[37] Y. Wu, M. Li, M. Rong, F. Yang, A. B. Murphy, Y. Wu, and D. Yuan, "Experimental and theoretical study of internal fault arc in a closed container," *J. Phys. D, Appl. Phys.*, vol. 47, no. 50, Dec. 2014, Art. no. 505204.

MICHAŁ SZULBORSKI received the B.S. and M.S. degrees in electrical engineering from the Warsaw University of Technology, Warsaw, Poland, in 2015 and 2018, respectively, and the B.S. degree in power engineering from the University of Warmia and Mazury in Olsztyn, Olsztyn, Poland, in 2016. He is currently pursuing the Ph.D. degree with the Department of Electrical Apparatus, Warsaw University of Technology. He is also an Engineer in the research and development of electrical equipment. In addition, he is an Application Engineer at ANSYS. His current research interest includes the design of electrical apparatus using FEA simulations.

SEBASTIAN ŁAPCZYŃSKI received the Graduate degree from the Warsaw University of Technology, Warsaw, Poland, in 2016, where he is currently pursuing the Ph.D. degree with the Department of Electrical Power Apparatus. He is also an Analyst, an Engineer, and an Editor specializing in the construction of electrical apparatuses, in aspects related to medium and low voltage electrical devices. His research interests include the construction of electrical apparatuses, electromechanical devices, contact systems, the numerical analysis of electrodynamic interactions, and thermal phenomena in current paths by means of finite element method.

ŁUKASZ KOLIMAS received the Graduate and Ph.D. degrees from the Warsaw University of Technology, Warsaw, Poland, in 2005 and 2008, respectively. He has been as the Doctor of Electrical Apparatus with the Warsaw University of Technology, where he is currently a Research Worker with the Division of Electrical Power Apparatus, Protection and Control. He is also a Constructor of low voltage apparatus, an Expert for Polish Centre for Accreditation in terms of short circuit laboratory, and a member of the Polish Agency for Enterprise Development.

MYKHAILO TYRYK received the bachelor's degree in hydropower engineering from the National University of Water and Management Resources Use, Rivne, Ukraine, in 2018, the Graduate degree in electrical engineering from Lviv Polytechnic National University, Lviv, Ukraine, in 2020, and the second Graduate degree in power engineering from the Warsaw University of Technology, Warsaw, Poland, in 2022. He is currently working as a Continuing Airworthiness Engineer with the Warsaw University of Technology.

A11. *Examination of Electrodynamic Forces in High Voltage Disconnector Related to the Short-Circuit Current Using the Digital Twin Technology*

IEEE Access

Received 21 March 2024, accepted 16 May 2024, date of publication 23 May 2024, date of current version 4 June 2024.

Digital Object Identifier 10.1109/ACCESS.2024.3404828

RESEARCH ARTICLE

Examination of Electrodynamic Forces in High Voltage Disconnector Related to the Short-Circuit Current Using the Digital Twin Technology

MICHAŁ SZULBORSKI[1,2,3], SEBASTIAN ŁAPCZYŃSKI[1], ŁUKASZ KOLIMAS[1], ŁUKASZ KOZAREK[1,4], HUBERT CICHECKI[5], PRZEMYSŁAW SUL[6], MACIEJ OWSIŃSKI[1], PRZEMYSŁAW BEROWSKI[7], DARIUSZ BACZYŃSKI[1], AND MARCIN WESOŁOWSKI[1,8]

[1]Faculty of Electrical Engineering, Electrical Power Engineering Institute, Warsaw University of Technology, 00-662 Warsaw, Poland
[2]Symkom Sp. z o.o.–ANSYS Channel Partner, 02-639 Warsaw, Poland
[3]ETI Elektroelement d.o.o., 1411 Izlake, Slovenia
[4]Energix Renewable Energies, 00-066 Warsaw, Poland
[5]Vortex Energy Polska Sp. z o.o., 70-479 Szczecin, Poland
[6]Institute of Theory of Electrical Engineering, Measurement and Information Systems, 00-661 Warsaw, Poland
[7]Institute of Power Engineering, 01-330 Warsaw, Poland
[8]Polish Society of Theoretical and Applied Electrical Engineering (PTETiS), 00-661 Warsaw, Poland

Corresponding author: Michał Szulborski (mm.szulborski@gmail.com)

ABSTRACT Paper concerns the novel modelling technology called digital twin in aspect of physical phenomenon simulation analysis. Digital twin model concerning electrodynamic forces in three-phase high voltage disconnector was presented, validated and discussed. Experiences related to laboratory work and measurement of electrodynamic forces clearly showed that often, despite the use of modern computing machines, the research process is hard, very expensive and values of electrodynamic forces are almost impossible to measure in real scale conditions. Hence the idea to use very advanced field models minimized to a reduced order model (ROM), using the digital twin technology seemed valid and rendered possibilities for advancements concerning this type of research. Due to the large weight of devices (chokes, transformers, disconnectors) on high-voltage networks it is often time-consuming or even impossible to perform the entire simulation. Proposed modelling approach helps to obtain results from very complex models also for long-term thermal tests. The reduced order model can be used not only by researchers, but also in the development departments of enterprises. Digital twin model results were compared and validated with values derived from short-circuit tests made in Institute of Power Engineering, Research Institute.

INDEX TERMS Electrodynamic forces, FEM, simulation, current paths, experiment.

I. INTRODUCTION

The modern power system is a set of high end distribution electrical devices (switchgears, apparatuses, energy storage facilities). Not only type tests, but above all construction and implementation tests are laborious and time-consuming. The series of PN-EN IEC 61439 standards is an important tool for implementing the essential requirements for designing electrical equipment, low-voltage switchgears and control gear assemblies (concerns low-voltage directives and electromagnetic compatibility). An important aspect of the work is, among others, the effects of the limit temperature increase in switchgears, control gears, electrical apparatuses, and this is a significant change, which is also the greatest challenge for manufacturers of electrical equipment. Mentioned standard describes the requirements and testing procedures for assemblies of different devices installed in an enclosure under various operating conditions compared to the product

The associate editor coordinating the review of this manuscript and approving it for publication was Su Yan.

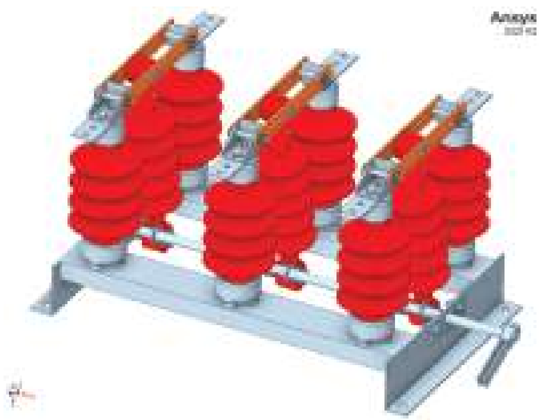

FIGURE 1. Optimized 3D model of medium voltage three-phase disconnector structure in SpaceClaim Geometry software constructed for this work by authors team.

standard. The actual temperature inside the switchgear is a factor that significantly limits the rated parameters of the equipment, especially in relation to current values. For example, a device with a rated current of 100 A, when installed in a switchgear, may have a current limit of 82 A. The development of the power industry puts more and more demands on electrical devices and components cooperating with them. They are sought for their optimal constructions both in terms of electrical and mechanical, guaranteeing at the same time high durability and reliability of their operation. In order to fully investigate the physical phenomena occurring in switchgear and electrical apparatus, more than one analytical or field model should be proposed. During the flow of currents of several to several tens of kiloamperes through the device, it is subjected to many processes, not only electrical but also mechanical. With the development of technology, a rapid increase in the rated power of electrical power equipment is observed. The development trend is to further increase the value of conducted currents. At the same time, the switchgear is subject to ever greater demands on the reliability and reliability of its operation. Digital calculation methods allow to perform many calculations in parallel. This solution significantly speeds up the entire process of designing selected elements. Digital techniques are successfully used in the design of the construction of electrical apparatus and switchgear (including contacts and current paths). Using CAD software, devices can be designed from a single component to entire complex assemblies. Those can be used to simulate the movement of elements relative to each other, exclude collisions, and end with the observation of the designed system in conditions simulating the natural working environment. In Figure 1 below, the detailed 3D model prepared for FEM (Finite Element Method) analysis was shown.

The requirements for switchgear devices differ from the typical requirements for devices with a small current load not only in that those possess much more complex structure, but also in the fact that there are new requirements resulting from the fact that the dimensions of the designed power devices and systems, their extent and diversity are constantly growing. In these systems, for high currents (of the order of kiloamperes), the following become important:

- analysis of electric current distribution in parallel current paths and contacts;
- analysis of temperature distribution in high-current circuits and contacts, in various configurations;
- analysis of electrodynamic interactions in high-current circuits and contacts;
- analysis of electromagnetic interactions in electrical apparatuses;
- increasing the permanent, transferred load in switching devices, electrical apparatus;
- failure elimination;
- correction of the arrangement of high-current tracks and devices powered by them;
- selection of optimal outline dimensions;
- analysis of the impact of the shape of contacts on the transition resistance and contact temperature;
- analysis of the impact of the clamping force on the transition resistance and the value of the welding current;
- synthetic process of modeling and designing contact systems, high-current circuits.

The most effective way to meet the requirements imposed on electrical devices is the use of various types of computer-aided research and development techniques, as well as the development of appropriate procedures and algorithms for research and implementation activities. The rapidly growing demand for electrical devices consisting of high-quality components imposes a new approach to the analysis of physical phenomena occurring during the flow of rated and short-circuit current. The main purpose of the analyzes of physical phenomena and design tests of electrical devices is to build solutions that can significantly improve their electrical (including short-circuit strength) and mechanical parameters. For this reason, the design of electrical apparatus, current circuits, contact systems is preceded by the development of accurate, reliable simulation models. Analyzes of physical phenomena performed on the basis of the aforementioned models are used to develop new concepts and constructions of basic elements of the power system. Based on the literature review, analysis of the directions of development of the power industry, the authors' research experience, implementation and construction studies are crucial for the correct introduction of the final product to the market. Such tests are important not only from the point of view of manufacturers of electrical devices, but also customers. It is the rapidly changing customer needs that often force design changes. The requirements of power operators, who even require safety certificates confirming construction tests, are not without significance. Often also the results of the tests themselves, and not just the certificate. Hence the increased interest in algorithms supporting the research process and identification of results. Especially in time-consuming, complex laboratory trials [1].

The aim of the project was to develop reduced order model of three-phase disconnector using the digital twin technology capable of simulating electrodynamic tests during one- and three-second short-circuit current flow and also thermal interactions during flow of rated current. Novelty of this project can be assumed as electrodynamic tests are very expensive and hard to conclude by means of standard laboratory tests, therefore the tool for precisely simulating those interactions would be asset concerning examination of physical phenomenon in electrical apparatuses. Moreover tests necessary to determine the current level of operational safety of devices often require costly shutdowns or, due to the mechanisms present in them – operational degradation, the test itself requires appropriate preparation and significant expenditures or interference in the construction of the device, e.g. when taking samples from the construction material for their laboratory examination [1]. Digital twin technology makes possible to run very complex simulation – that is hardly possible while taking into account classical FEM modelling software. The implementation of the research problem is possible, among others, by developing a reduced order model based on the finite element method with the use of artificial intelligence. Modules of artificial intelligence, neural networks, machine learning and additive manufacturing implemented in numerical programs give the opportunity to build the DT [1]. The use of adaptive algorithms makes it possible to obtain a numerical model that reduces the calculation time by several dozen times. At the same time, the results are highly consistent with the classical numerical models. Moreover the model was validated on the basis of short circuit tests done in Institute of Power Engineering, Research Institute.

The added value of the obtained results is the opportunity to observe the distribution of electrodynamic interactions in the electrical apparatus. Current path blades and disconnector terminals are the elements of the disconnector structure that are most exposed to damage. Making each design change in the process of building a prototype of current paths, contacts, and arc-extinguishing chambers can significantly reduce the costs associated with the number of prototypes and experimental tests performed in research laboratories. This is related to the possibility of a deeper understanding of physical phenomena, and this is proved by the presented results.

II. STATE OF THE ART

The digital twin technology is being used more and more widely. In the article [2], [3], [4], the authors analyze the electromagnetic characteristics, mechanical characteristics, thermodynamic characteristics and mutual coupling of a DC machine. The authors construct a mathematical model of ‘‘electrical-mechanical-thermal’’ integration, taking into account the digital twin. The presented model [2], [3], [4] was built on the basis of experimental data in order to increase the accuracy of the model. The results show that the digital twin model is a very reasonable approach that can well represent the different conditions of a real DC machine. The authors' statement is that it is not always possible to conduct an experiment under all conditions. The digital twin technology meets precisely such situations. Though not only. It is possible to shorten the computation time, reduce costs and time. The authors showed the possibilities of applying the digital twin in electromechanical constructions.

Successive authors in the field of electrical power engineering presented the idea of fully intelligent power stations [5], [6], [7], [8]. According to the authors, currently the station is not fully intelligent. The article presents a multi-level method of building a digital twin of the station. In this method, the digital twin technology provides the structure framework to manage the substation, and the multi-agent system realizes the intelligent function of the substation. First, the architecture of the station's digital twin technology is described in detail. Then, the framework of the multi-agent system for the station's digital twin was proposed and the function was presented in detail.

A very interesting publication is [5], [6], [7], and [8]. The authors show that digital twin technology is an excellent way to integrate electromechanical devices with various information technologies. The first part of the article presents the theoretical development process and the practice of using digital twin technologies. Then the authors focus on the use of the digital twin in the power industry. Including the fundamentally digital twin in the construction of the power grid, the construction of the digital twin of the power plant structure, the digital twin of the power equipment and other aspects. Finally, the characteristics of the digital twin in the power industry are summarized and some application perspectives are presented.

In publication [9], [10], [11], [12], the authors presented the technology of the digital twin itself in an interesting way. The authors show that with the advent of the digital age, the digital twin is a new potential Technology. It enjoys growing interest in both academic and industry circles. digital twin technology paves the way for cost-effective trials and optimal performance management by creating a digital representation of a virtual physical network for simulation and prediction. In this article, the authors propose a new network paradigm, called Digital Twin Network (DTN) architecture. Predictions are made for the future network, which consists of a physical network, a digital twin layer and a network application layer. The Sketch acquisition algorithm has been introduced to meet the demand for data collection in real-time on a large scale in the Data Lake. A method was developed to build digital twin networks based on a knowledge graph that can represent entity attributes and different topologies depending on the physical network. Finally, a proposed DTN was introduced to realize self-healing in the future network.

Another publication in which the authors deal with the potential and possibilities of using the digital twin technology is [13], [14], [15], and [16]. The authors point out that with the development of information technology, building safety management requires an urgent and intelligent digital modernization. Construction-oriented digital twin technology can improve the efficiency and safety of construction site management. Designing a construction-oriented digital twin system is a complex process, requiring the design of modules that implement the digital twin to ensure the viability of the system. In addition, it is necessary to design the system's functions and interactions according to the user's needs to ensure the humanization of the system. This article starts from these two aspects, constructs a theoretically construction-oriented digital twin module, pre-designs a system prototype and experimentally tests its usability. The innovations of this document include the following points: a) combine digital twin technologies with infrastructure construction safety management; b) gain insight into the issues and needs of security officers to study the design principles and specifications of digital twin technologies in new scenarios; c) familiarize user with the UX (User Experience) project of the interactive interface of the digital twin system. The research results of this article are of reference value for the practice of digital twin interaction design.

The scenario of operation of the digital twin technology [10], [17], [18], [19] was presented in the process of analyzing the construction and operation of the smart metro system. The examined aspects concerned those that are difficult to verify in real life. The digital twin achieves digitization of metro facilities, interface with related control systems, operation like simulating a real metro system, and a validation platform based on the digital twin can be used to check most of the smart metro scenarios. The article [10], [17], [18], [19] focuses on the smart metro and its scenario validation platform with digital twin technology, covering concept, architecture, modeling and data processing.

III. DIGITAL TWIN TECHNOLOGY

A digital twin refers to a digital replica of physical objects, processes and systems. The digital twin model is a combination of a physical object and its digital representation in virtual space, implemented thanks to the possibility of real-time data processing and constant updating of the state of model elements and processes. The greatest benefits of having a digital twin arise when there is limited access to the real object, its elements or parameters, e.g. for diagnostic tests. This is the case both in the case of objects in space and in the case of objects whose study significantly affects their functioning. Two main directions/technologies of DT construction can be distinguished: models based on data stream analytics and physical models based on properties and physical parameters of a real object. General diagram showing the principle for digital twin operation was shown in Figure 2 below.

Models based on the analysis of data streams, machine learning algorithms and solutions resulting from the use of artificial intelligence are aimed at searching for patterns of correctness and irregularities in data streams from a real object, learning patterns of "behavior" of a real object

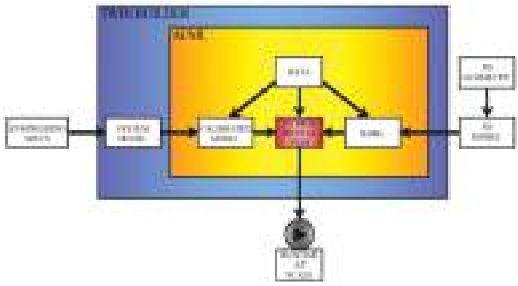

FIGURE 2. Diagram showing general principle of digital twin technology operation.

assessed as correct and incorrect in the learning process and improving algorithms for assessing states other than the model ones thanks to the possibilities of artificial intelligence.

Physical models based on the properties and physical parameters of a real object, such as geometric, material and technological data – both based on mathematical relationships/formulas and digital models such as: FEM (Finite Element Method), FDM (Finite-Difference Method) or CFD (Computational Fluid Dynamics), etc., working under the control of people and/or algorithms performing iterative calculations modeling the states of a physical object. Depending on the expected application and expected effects, they use one or both methods, working as different components of the digital twin of the object. An optimum design is sought, which would provide both the speed of AI (artificial intelligence) solutions and the precision and predictability of physical models. A digital twin can consist of multiple nested twins that provide narrower or broader views of equipment and resources based on a process or use case. DT modeling is an iterative process. The model should be characterized by high standardization, modularization, lightness and solidity. These virtual models, in order to be digital twins and best reflect real objects, must depend on real-world data and reproduce, as far as possible in real time, the parameters, boundary conditions and dynamics of a given object. A digital twin will only perform its tasks well if it is created with a full understanding of the real object and the data flowing from it. Otherwise, the virtual model could not effectively cooperate with the real object, and the inference would be burdened with unacceptable errors.

The model is created and works mainly thanks to data. One of the biggest challenges on the way to creating a digital twin is sensor data, which is usually locked in historical data systems and stored in a usually flat format – without context, i.e. without information about process changes or disturbances. This leads to the fact that analytics based on this data is almost impossible. The data must contain the state of the relationship with the associated asset. Digital twin data is both real-world object data and digital model data.

IV. MATHEMATICAL MODEL

The values of electrodynamic forces depend on the parameters and configuration of the systems and the product

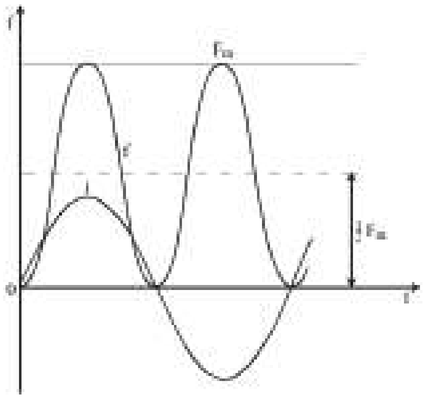

FIGURE 3. The dependance of force f with single phase alternating current.

of the currents (i_1, i_2) flowing through the conductors. It can be showed by relation (1) below (relations 1-17 from IEC 60865 concerning electrodynamic interactions during short-circuit current flow):

$$f = C \cdot i_1 \cdot i_2 \tag{1}$$

where: C - constant value depending on the parameters and configuration of the system; i_1, i_2 - currents flowing.

Concerning the single-phase alternating current systems, the following relation is usually met:

$$f = \frac{1}{2} C \cdot I_m^2 \cdot (1 - \cos 2\omega t) \tag{2}$$

where: I_m- maximum current value.

The above relation shows that the value of the electrodynamic force occurring in any system of conductors through which alternating current flows is not constant. This force changes from zero to the maximum value of the force (Fm) with twice the frequency of the current. It was shown in Figure 3 below.

$$F_m = C \cdot I_m^2 \tag{3}$$

While calculating the electrodynamic forces occurring at short-circuit currents, the influence of the non-periodic current component should be taken into account:

$$i = I_m \cdot e^{-\frac{R}{L} \cdot t} - \cos \omega t \tag{4}$$

The highest instantaneous current value is described by following equation:

$$i = I_m \cdot k_u \tag{5}$$

$$k_u = 1 + e^{-0{,}01 \cdot \frac{R}{L}} \tag{6}$$

where: R, L – resistance and inductance of the short-circuit circuit, k_u – impact factor.

The highest value of the force determining the destructive electrodynamic effects of a short-circuit current can be presented as dependency below:

$$F_m = C \cdot {i_u}^2 \tag{7}$$

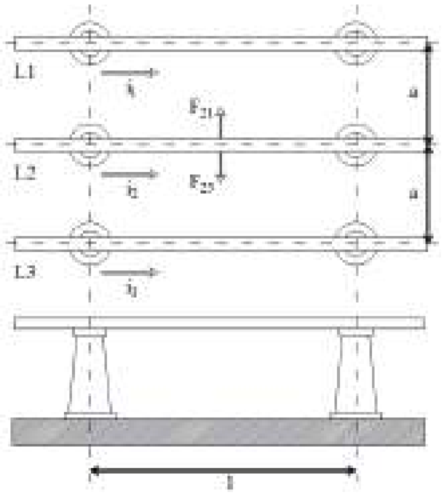

FIGURE 4. General principle for calculating electrodynamic forces occurring in three-phase systems.

Three-phase system is a system of three conductors in which currents of the same or similar RMS value, shifted in phase, flow. The maximum values of the forces acting on the conductors of individual phases, depending on the configuration of the system, may be different, and the forces are shifted in phase. In the simplest three-phase system consisting of three parallel conductors in one plane, the forces acting on individual conductors are:

$$F_1 = F_3 = F_{12} + F_{13} \tag{8}$$

$$F_2 = F_{21} + F_{23} \tag{9}$$

where: F_{ij} – force acting on the conductor due to the current flowing in the conductor j.

It can be shown that the greatest value of the force F when the conductors are laid flat occurs in the middle conductor:

$$\boldsymbol{i_1 = I_m \cdot \sin\omega t} \tag{10}$$

$$\boldsymbol{i_2 = I_m \cdot \sin(\omega t - \frac{2}{3}\pi)} \tag{11}$$

$$\boldsymbol{i_3 = I_m \cdot \sin(\omega t - \frac{4}{3}\pi)} \tag{12}$$

Therefore the force f2 and with further transformations the force F2m can be defined by the relations:

$$\boldsymbol{f_2 = \frac{2l}{a} \cdot I_m^2 \cdot sin(\omega t - \frac{2}{3}\pi) \cdot [sin\omega t - sin(\omega t - \frac{4}{3}\pi)] \cdot 10^{-7}} \tag{13}$$

$$\boldsymbol{F_{2m} = \sqrt{3} \cdot \frac{l}{a} \cdot I_m^2 \cdot sin(2\omega t - \frac{1}{3}\pi) \cdot 10^{-7}} \tag{14}$$

Practical calculations, while determining the maximum values of forces occurring during a short-circuit can be expressed by the below dependence:

$$\boldsymbol{F = \sqrt{3} \cdot \frac{l}{a} \cdot i_u^2 \cdot 10^{-7}} \tag{15}$$

FIGURE 5. An example of the construction of a three-phase disconnector.

The value of the force calculated from the relation (15) is determined with an excess because the peak values of the surge current do not occur simultaneously in all three phases. The forces acting on the extreme conductors can be described by the dependency presented below:

$$\boldsymbol{F_{1m} = F_{3m} \approx 0,93 \cdot F_{2m}} \tag{16}$$

$$F_{1m} = F_{3m} \approx 0,93 \cdot F_{2m} \tag{17}$$

Since the differences in the mechanical load of individual phases are relatively small, in practical calculations the stress in the current path most exposed to electrodynamic impacts is determined and the same components are selected for all three phases of designed apparatus or distribution system

V. GEOMETRICAL MODEL OF THEMEDIUM VOLTAGE DISCONNECTOR

Disconnectors with a rated voltage of 24 and 36 kV and a rated current of 400 – 2000 A are used to disconnect electrical circuits in the current less state in medium voltage overhead installations. The developed construction of disconnectors is capable of closing and opening medium voltage electrical circuits – overhead in the current less state. In the open position, the disconnectors create a safe and visible isolating distance that cuts off the voltage on the downstream side. Integrated designs of disconnectors with earthing switches are adapted to earthing previously disconnected electrical network. An example disconnector was shown in Figure 5 below.

The structure of the disconnector presented above is mounted on a metal frame to which porcelain support insulators are screwed. Fixed and movable contacts of the disconnector as well as movable contacts with pressure springs are screwed to the insulators. The insulation between the poles of the disconnector is air, in the case of solutions with a smaller inter-pole pitch, additional barriers are installed to increase the surface and air distances between the poles of the disconnector. Disconnectors are opened and closed by means of manual or electric (motor) drives, which allows the disconnectors to be installed and operated both in vertical

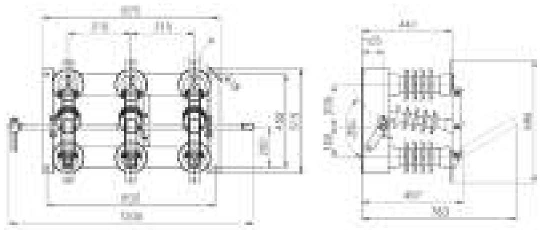

FIGURE 6. Dimensional drawing of three-phase disconnector structure used for simulations [30].

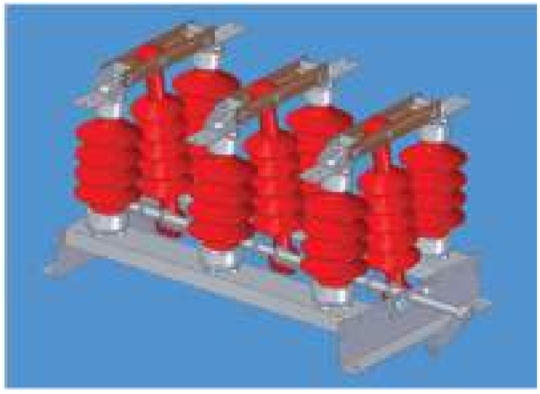

FIGURE 7. Developed 3D structural model of a threephase disconnector according to the dimensions from technical documentation and the dimensions from the physical object.

and horizontal position [20]. The design of the disconnectors allows for screwing additional earthing switches to the frame on both sides of the separable and non-separable fixed contacts, thus creating disconnectors with upper and lower earthing switches. The authors were basing measurements on the manufacturer's documentation and measurements of real dimensions on a physical device, developed a 3D model of the disconnector in question for the purposes of the simulation. This was the basis for analyzing the electrodynamic interactions in the moving contacts and current paths of the disconnector and for verifying the values of electrodynamic forces affecting the porcelain support insulators of the disconnector [21], [22], [23].

A properly prepared 3D structural model of the disconnector, taking into account the dimensions and construction details, is shown in the Figure 7 below.

A 3D model of a three-phase disconnector prepared in this way, all structural parts of which were reconstructed on the basis of available materials, could be imported into the working environment [24], [25]. In the simulation calculations, the modeled disconnector was subjected to exposures related to the impact of two short-circuit current values included in the manufacturer's specification:

- rated short-circuit current 1-sec of the disconnector equal to 20 kA;
- rated peak current of the disconnector equal to 50 kA.

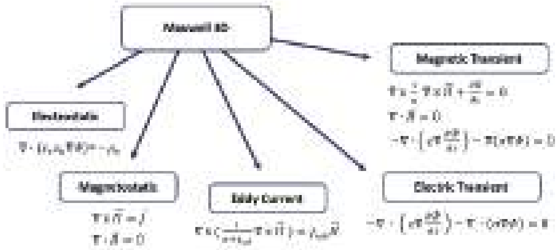

FIGURE 8. Functions for analyzing physical phenomena of Maxwell module and mathematical formulas behind them.

TABLE 1. Properties used for simulations.

Simulation Properties	
Stop time	250 ms
Time step	0.25 ms
Type of simulation	Transient
Nonlinear Residual	0.005
Scalar potential	Second Order
Nonlinear iterations	1-100
Time decomposition	General Transient
Solver DRS3 Matrix	59355
Solver Progress	0-25 s
Solve TD3 Tetrahedra	919 749
Stady State Stop Crit.	0.005
Voltage Source Freq.	50 Hz
RAM limit	Not Set
HPC	Enabled
Design Validation	Full Validations
Com Engine Memory	84.2 M
Mesh TAU3 Tetrahedra	1 508 183
Mesh Post Tetrahedra (TAU)	477 958
Mesh Post Tetrahedra	468 641
Mesh Volume, Seed Tetrahedra	919 749

In order to enforce these current values, it was necessary to use the recording of the short-circuit current waveform in the form of a.csv file, obtained during the tests of the disconnector in the High-Current Laboratory at the Institute of Power Engineering in Mory. The loaded data reconstructed the actual waveforms of short-circuit currents during the numerical simulation. Before starting the calculations, it was necessary to check and modify the disconnector modeled in 3D. For this purpose, the 3D model was loaded into the SpaceClaim Geometry module, where all edges and planes in the developed geometry of the disconnector were modified. This approach allows avoiding errors during the calculations related to the generation of the ''mesh'' computational grid.

VI. SIMULATION MODEL AND RESULTS

A. SIMULATIONS ENVIRONMENT

In order to perform simulation work on behalf of this manuscript the coupled Finite Element Method analysis was executed. Coupled FEM analysis is technique that allows to study the interactions of various physical phenomena, including structural, mechanical and electromagnetic. It is done by corelating various nodes of numerical program in order to fulfil specific conditions and recreate physical phenomena

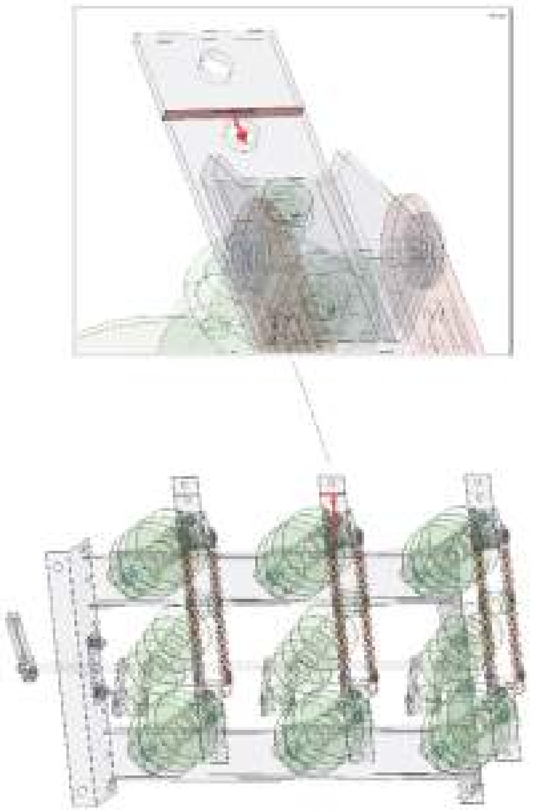

FIGURE 9. Marked terminal on the middle current path of a three-phase disconnector.

in digital environment that can be witnessed by concluding experiment. Coupled FEM analysis is based on transformation of conjugate partial differential equations in a set of unrelated ordinary differential equations using the modal decomposition technique. Module used for simulating the physical phenomena was ANSYS Maxwell 3D. In Figure 8 below the most important equations that were inserted into module solver during calculations were presented.

Depending on which Maxwell 3D solver is used, the calculations performed allow the determination of electrodynamic forces. Calculations are performed for implemented short-circuit current, where the results obtained for electrodynamic forces have a close relationship with the shape of the flowing short-circuit currents in the each current path. Boundary conditions used as at least one of the following sources of magnetic field:

- stranded or solid windings with voltage or current supply;
- a permanent magnet.

Outer boundary conditions were defined as:

- the default boundary conditions;
- an odd symmetry boundary;
- an even symmetry boundary.

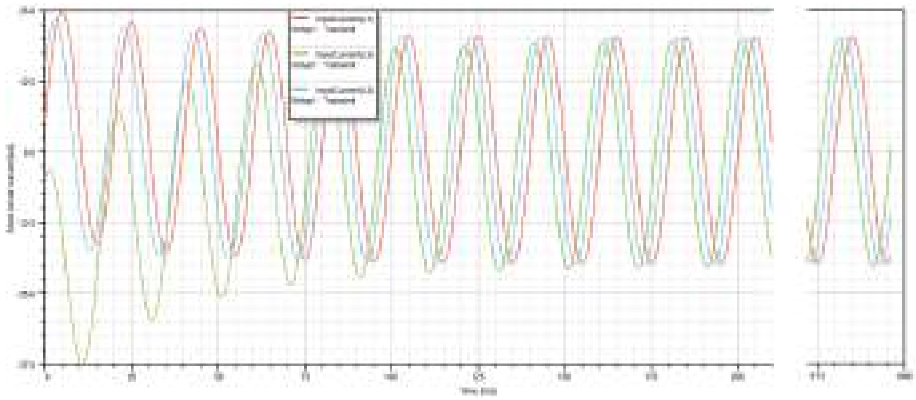

FIGURE 10. Imported waveform of the 1-sec short-circuit current of the disconnector equal to 20 kA for the analyzed disconnector.

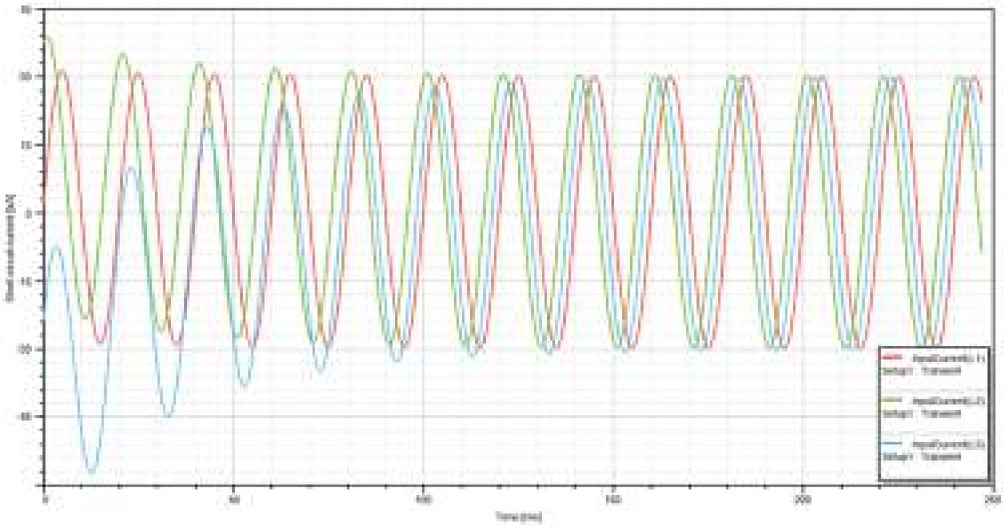

FIGURE 11. Imported waveform of the rated peak short-circuit current of the disconnector equal to 50 kA for the analyzed disconnector.

B. SIMULATIONS PROPERTIES

Conditions in which the simulation was executed were shown in Table 1 below. Data in Table 1 is valid for full scale model and reduced order model (DT).

After importing the disconnector model to the mentioned module, the appropriate calculation solver of the "Transient" type was selected. Then, boundary conditions and material properties were assigned to the constructed structural parts of the disconnector, such as air, steel, porcelain, and copper. Then, the appropriate terminals were added to the current circuits of the disconnector, in which the waveforms of short-circuit currents obtained in the laboratory were added (Figure 9).

Then, using the "Add Winding" option, the values of short-circuit currents previously generated from the.csv file, obtained in the high-current laboratory for the given pole of the disconnector, were assigned.

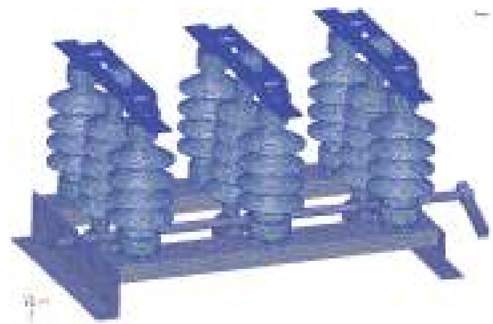

FIGURE 12. Generated "mesh" calculation grid on a 3D model of a three-phase disconnector.

The waveforms of the rated 1-sec short-circuit current of the disconnector equal to 20 kA to Maxwell 3D are shown in the waveform (Figure 10).

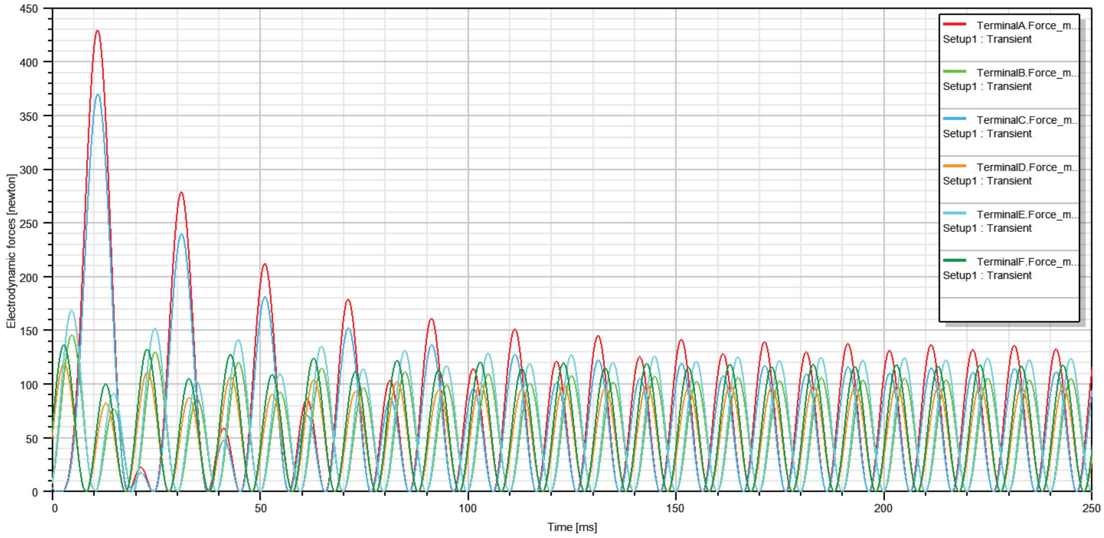

FIGURE 13. Values of electrodynamic forces at the disconnector terminals for short-circuit current 1 second equal to 20 kA.

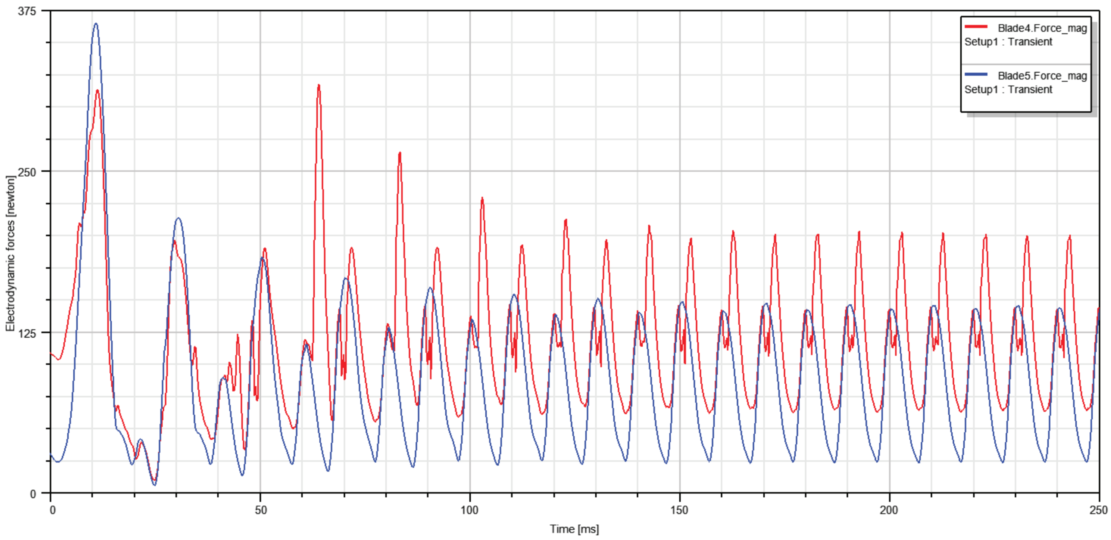

FIGURE 14. Values of electrodynamic forces on the blades of the current paths of the L2 phase of the disconnector for a 1-sec short-circuit current equal to 20 kA.

The mesh was compacted on the support insulators in order to more accurately calculate the value of the electrodynamic forces acting on the individual support insulators. The calculation grid for the model was 4,281,994 tetrahedra elements. In order to illustrate the grid distribution on the developed disconnector model, the calculation grid presented in the Figure 12 below was generated. Using the "Add solution setup" function, the time for the first computational simulation for the flow of the rated short-circuit current of 20 kA was defined as 1000 ms. In order to obtain accurate waveforms for the calculated values of electrodynamic forces, the iterative step was defined every 0.25 ms. As a result such settings made it possible to perform 4000 calculation iterations for the prepared computational simulation. At this stage of analysis settings, it was possible to start calculations.

C. ELECTRODYNAMIC FORCES SIMULATIONS

Using the "Add solution setup" function, the time for the first computational simulation concerning the flow of the rated short-circuit current of 20 kA was defined as 1000 ms.

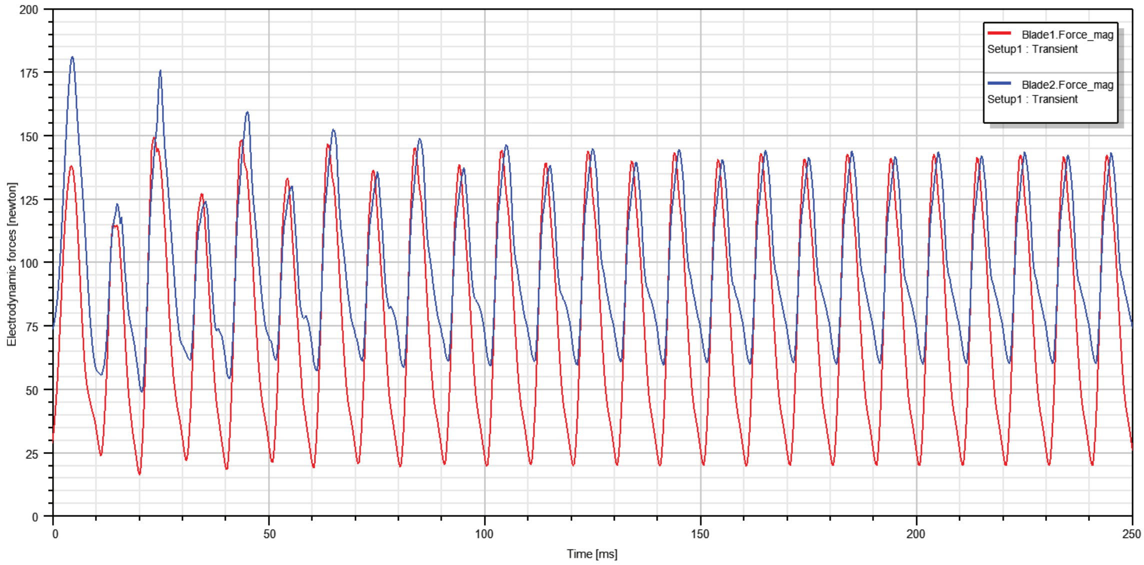

FIGURE 15. Values of electrodynamic forces on the blades of the current paths of the L1 phase of the disconnector for a 1-sec short-circuit current equal to 20 kA.

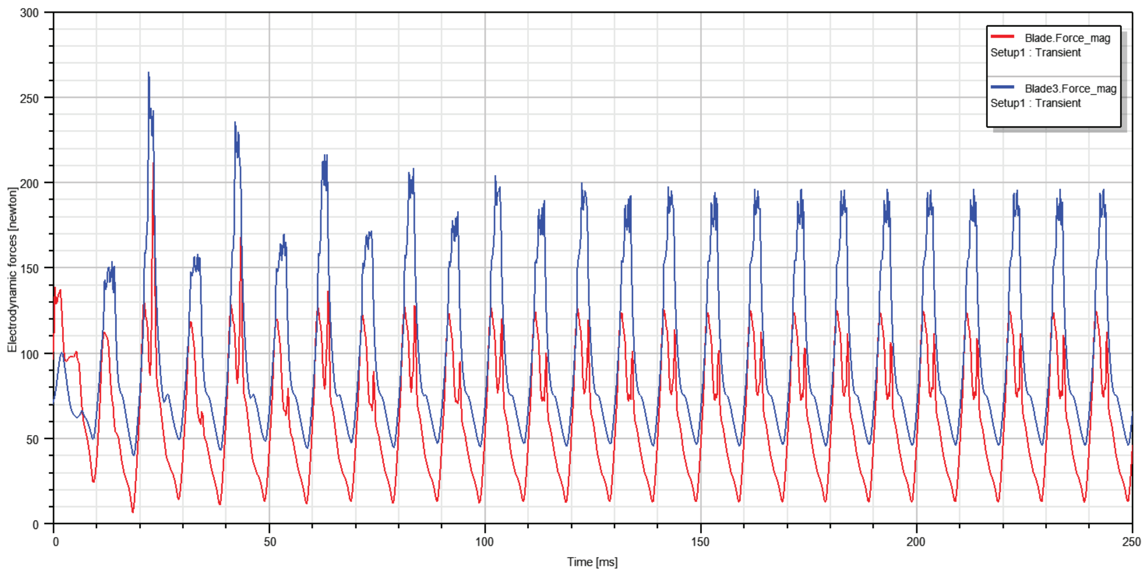

FIGURE 16. Values of electrodynamic forces on the blades of the current paths of the L3 phase of the 1-sec short-circuit current disconnector equal to 20 kA.

TABLE 2. Maximum values of deformations for selected points of the current path of the tested disconnector determined in the coupled analysis.

Measuring Point Number	Measuring Point 1	Measuring Point 2	Measuring Point 3	Measuring Point 4	Measuring Point 5	Measuring Point 6
Numerical analysis	1 mm	2 mm	0.8 mm	1.2 mm	2.5 mm	1 mm

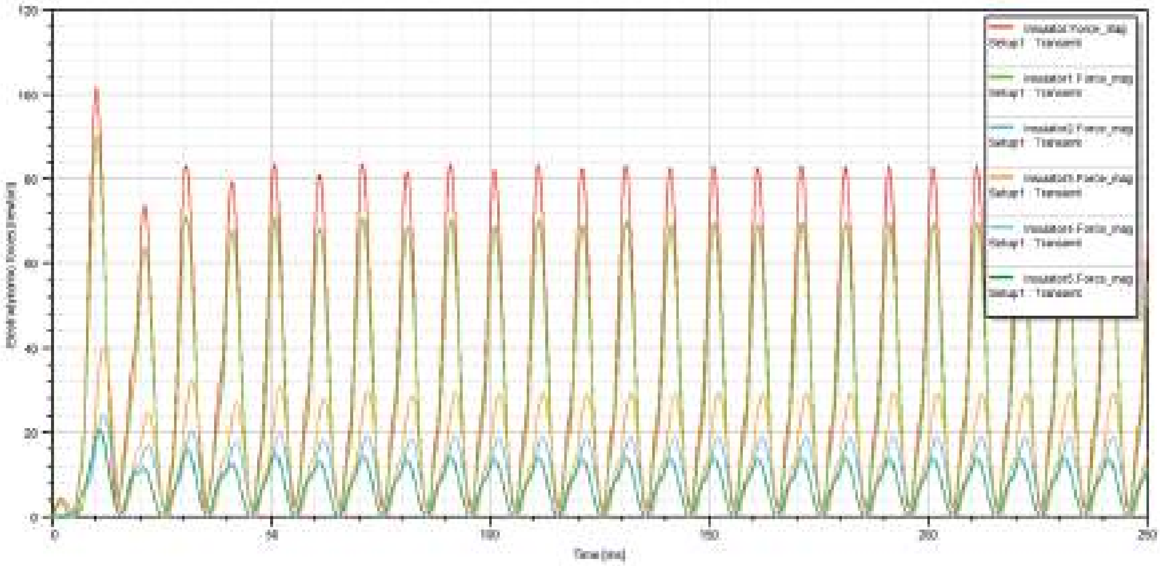

FIGURE 17. Values of electrodynamic forces on disconnector insulators for rated 1-sec short-circuit current equal to 20 kA.

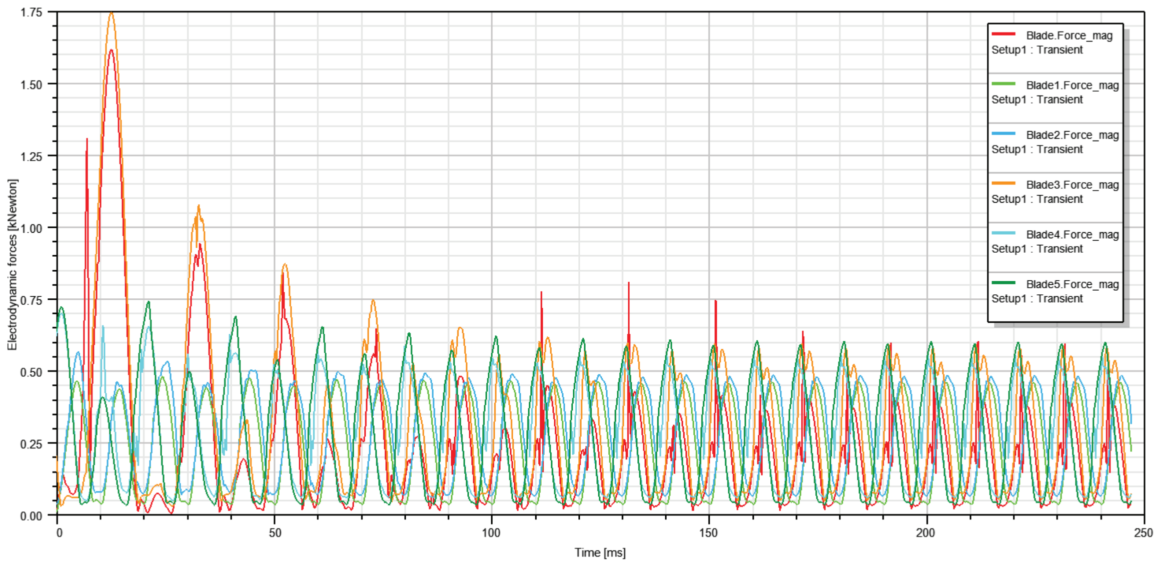

FIGURE 18. Values of electrodynamic forces on the blades of the disconnector's current paths for peak short-circuit currents.

In order to obtain accurate waveforms for the calculated values of electrodynamic forces, the iterative step was defined every 0.25 ms. As a result, such settings made it possible to perform 4000 calculation iterations for the prepared computational simulation. At this stage of analysis settings, it was possible to start calculations. The duration of the calculations in the Maxwell 3D module for the 1-sec short-circuit current of the disconnector equal to 20 kA lasted 9 days 5 hours. The duration of the calculations in the Maxwell 3D module for the peak short-circuit current of the disconnector equal to 50 kA lasted 4 days 8 hours. These calculations took less time due to the fact that the calculations were made for 200 ms. In the case of the analysis, it was crucial to determine the electrodynamic forces for the peak currents obtained during short-circuit tests. Waveforms of currents from laboratory tests were used. After performing the calculations using the

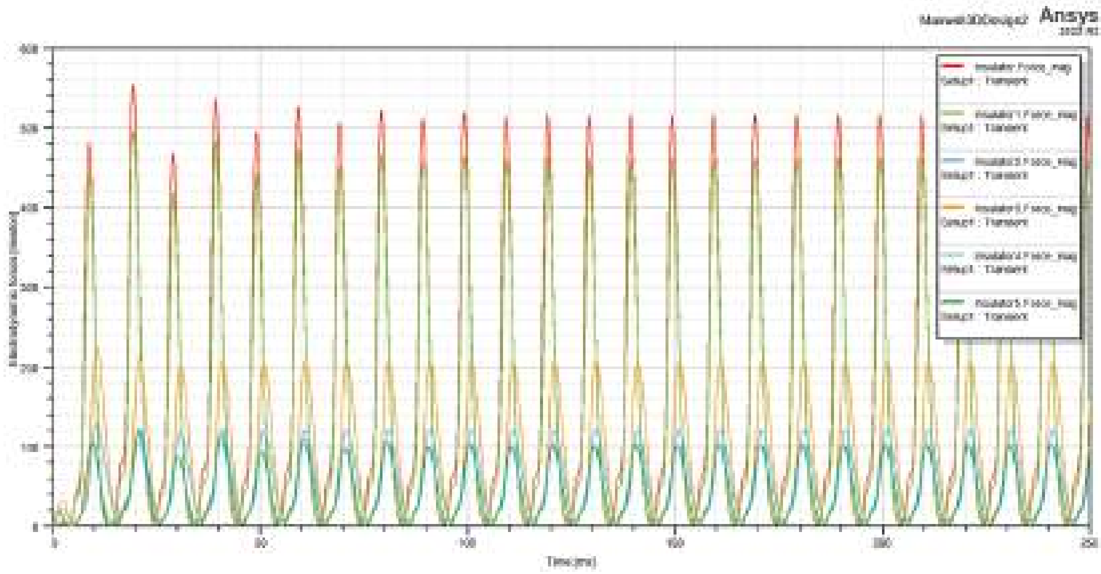

FIGURE 19. Values of electrodynamic forces on the support insulators of the disconnector for peak short-circuit currents.

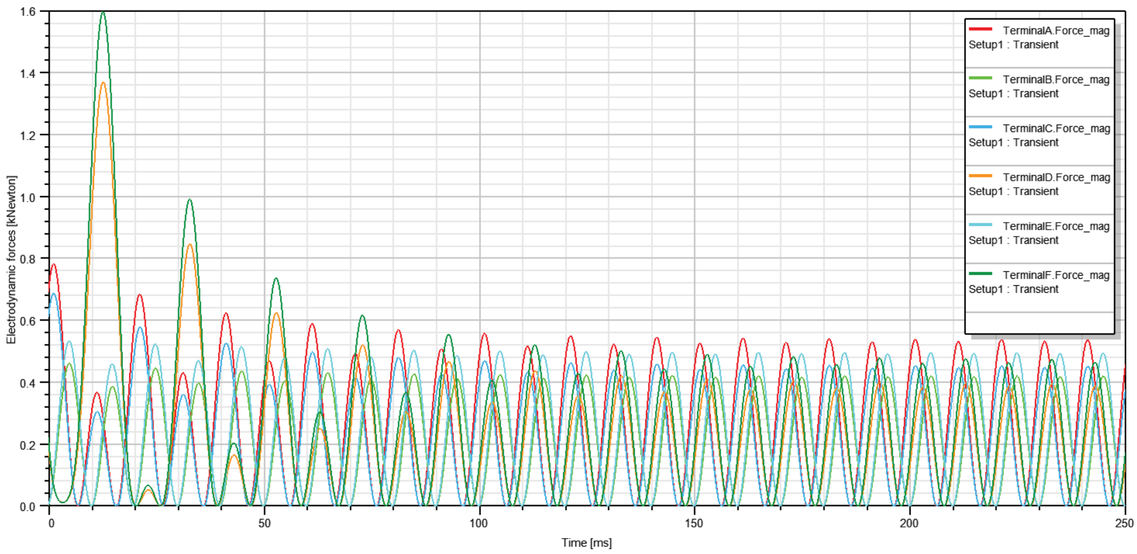

FIGURE 20. Values of electrodynamic forces at the terminals of the disconnector's current paths for peak short-circuit current.

"Results -> Rectangular plot -> Force" option, the values of electrodynamic forces affecting the individual elements of the disconnector's current path and the supporting structure were generated. In the case of the disconnector, the forces acting on the disconnector terminals, blades and support insulators were analyzed. In the first analysis of the waveforms of electrodynamic forces obtained for a 1-sec short-circuit current equal to 20 kA in the disconnector, it was noticed that the electrodynamic forces determined at the disconnector terminals were different for each pole. The highest values of electrodynamic forces at the terminals were obtained in the middle current path. The obtained force values were 430 N for terminal A and 370 N for terminal C, respectively. The waveform diagram of the obtained values for all disconnector terminals for the imported short-circuit current is shown in Figure 13. It should be noted that with the disappearance

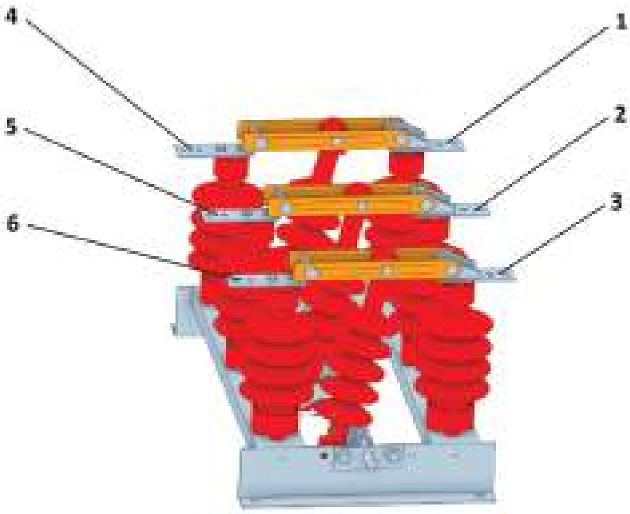

FIGURE 21. Selected points of the disconnector's current path for which maximum elastic deformations were determined during the flow of peak short-circuit currents.

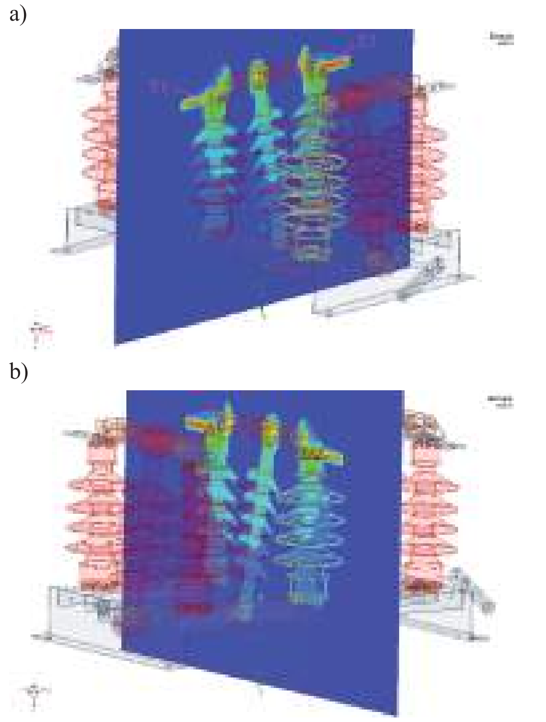

FIGURE 22. Selected points of the disconnector's current path for measuring during thermal experiment and simulation. Subpoints a) and b) – results of thermal simulation with rated current.

of the non-periodic components of individual short-circuit currents, the values of electrodynamic forces decrease and for the RMS value of 20 kA short-circuit current those reach

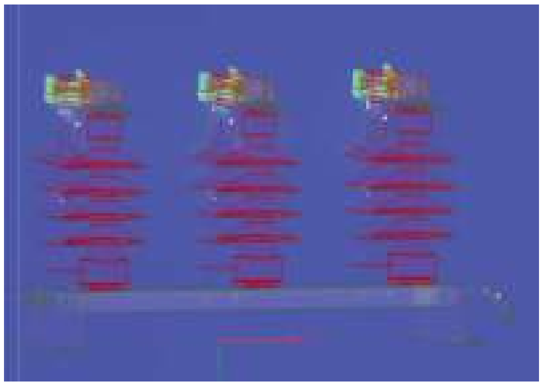

FIGURE 23. Additional angle - results of thermal simulation with rated current.

about 120 – 140 N in each terminal (after the complete disappearance of the non-periodic component).

The next elements of the disconnector structure that were tested in order to determine the values of the interacting electrodynamic forces were the blades of the disconnector's current paths in its individual poles. The highest values of electrodynamic forces were obtained on the blades of the second pole of the disconnector – phase L2. The peak values obtained were 365 N on the left knife and 315 N on the right knife from the supply side of the disconnector, respectively. The graph is shown below in the figure below (Figure 14).

The values calculated for the L1 phase are shown in Figure 15 below, where the maximum value of electrodynamic forces of 181 N was obtained on the left pick, and 149 N on the second pick. This phase had the lowest electrodynamic interactions in relation to the L2 and L3

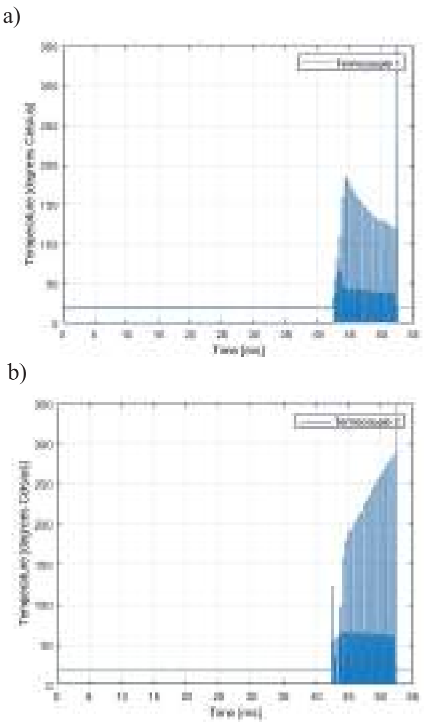

FIGURE 24. Experimental results for T1 and T2 – thermal analysis with rated current.

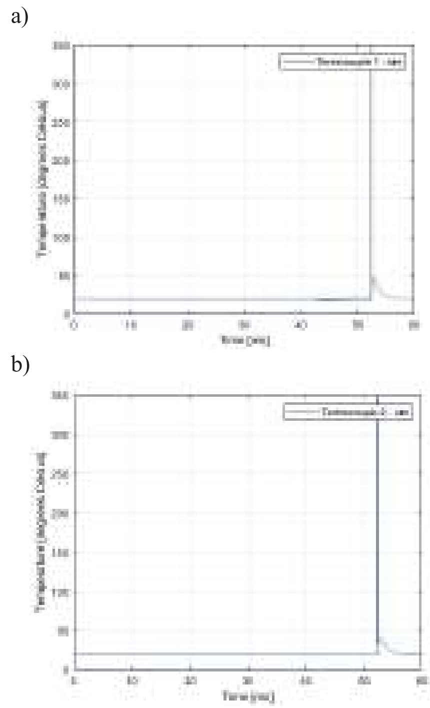

FIGURE 25. Simulation results for T1 and T2 – thermal analysis with rated current.

phases. At the last phase of the L3 disconnector, the impact values obtained were intermediate in relation to the values obtained for L1 and L2, where the peak values were 264 N and 211 N, respectively.

The waveforms for the electrodynamic forces in this pole of the disconnector are shown below in Figure 16.

It should be noted that the waveforms of the calculated electrodynamic forces for individual disconnector blades are deformed. It is caused by electromagnetic couplings acting between the blades in a given pole as well as by couplings coming from the adjacent poles of the disconnector.

The next elements of the disconnector structure for which the electrodynamic forces were determined were the support insulators. The highest values of electrodynamic interactions were obtained on the support insulators for the middle pole of the disconnector, the obtained values were equal to 101 and 90 Newtons, respectively. In the pole of the L1 phase, the obtained values were on average 3 times lower, and for the pole of the L3 phase of the disconnector, 4 times lower. The waveforms obtained for individual support insulators are presented in detail below in Figure 17. The obtained values of electrodynamic forces for individual elements of the medium voltage disconnector structure for a 1-second short-circuit current equal to 20 kA. Those allow for a precise assessment of the electrodynamic effects to which the current circuits and the supporting structure of the disconnector are subjected at the moment of flow of short-circuit currents. The disconnector is not capable of breaking short-circuit currents. Nevertheless, its construction must withstand electrodynamic, mechanical and thermal exposure in this type of emergency.

The calculations for the 1-sec short-circuit current equal to 20 kA show that the most exposed element of the disconnector structure to electrodynamic impacts were its terminals in the middle current path. In addition, for illustrative purposes, the values of forces have been converted into loads to which terminals A and C were subjected – it was 43.84 kg for terminal A and 37.72 kg for terminal C, respectively.

The results obtained are consistent with the short-circuit tests executed for these short-circuit current ratings. Both in the case of tests and numerical analyses, the disconnector was not damaged, and in the case of simulations it did not exceed the critical values that would cause its damage. Then, simulations were done for a peak short-circuit current of 50 kA. In this case, the highest values of electrodynamic interactions were achieved on the blades of the L3 phase of the disconnector pole. This is due to the occurrence of the highest value of the peak short-circuit current in this pole. The obtained values of electrodynamic forces were equal to 1.74 kN and 1.61 kN, respectively. These are very high values, but during short-circuit tests in the High-Current Laboratory at the Institute of Power Engineering in Mory, those did not cause damage to the disconnector. The remaining values in the other poles were: 742 N; 701 N in L2 and 568 N; 481 N in the L1 phase. This was shown in detail in the Figure 18 below.

The electrodynamic interactions on the support insulators of the disconnector were determined for the given peak short-circuit currents. The highest achieved values of electrodynamic forces were obtained for the insulators in the middle pole of the disconnector, which amounted to 553 N and 495 N. In the remaining supporting insulators in the poles of the L1 and L3 phases, the values obtained were more than half lower, as shown in the Figure 19 below.

The values of electrodynamic forces obtained at the disconnector terminals for peak short-circuit currents were slightly lower than the forces obtained at the current circuit blades. The maximum values were obtained at the terminals of the L3 phase (third pole) and were respectively: terminal D – 1.36 kN and terminal F – 1.59 kN. In the remaining peaks, the values in the initial phase were also more than half as low. With the disappearance of non-periodic components of short-circuit currents, the values of electrodynamic forces decreased to about 500 Newtons. This is precisely illustrated in the Figure 20.

D. ELECTRODYNAMIC DEFORMATIONS

The executed short-circuit tests were dummy tests, checking whether the structure would withstand electrodynamic exposure. During the work, deformations from short-circuit tests were analyzed in relation to the simulation results for peak short-circuit currents for various points in the disconnector. The maximum strain values were determined for the peak short-circuit currents at selected points of the disconnector current path, which are presented below in Figure 21. The maximum elastic deformations during the experimental tests were subtle, they could not be measured due to the fact that they were not plastic deformations (measurements after the laboratory tests). The current circuits of the disconnector were not deformed during the short-circuit tests. Hence, there were no visible effects of electrodynamic interactions. The maximum deformations were determined in the numerical analysis for the indicated points of the current path in Figure 21. The collected results are summarized below in Table 2.

In the analyzed points, the highest values of elastic deformations occurred on the middle current path of the disconnector on the connecting terminal of the outgoing line - measurement point no. 5. These results are consistent with the determined maximum values of electrodynamic forces for these elements of the current path. The results of the maximum values of electrodynamic forces in the current paths of the disconnector coincide with their maximum elastic deformations.

E. THERMAL SIMULATIONS

Thermal simulations were done using the Transient Thermal module. It was achieved simulating rated current with voltage level of 20 kV. Contact system was closed during analysis it means the voltage level has marginal influence on analysis results. Different situation would be taken into account if contact system would be open.

Procured simulations were validated by experimental thermal analysis. Results were showcased in Figure 24 and Figure 25 above.

VII. CONCLUSION

Presented numerical calculations concerning the determination of the electrodynamic forces affecting the current paths and the supporting structure of the medium voltage disconnector showed that the simulation approach proposed by the authors may be a helpful method of determining the exact values of the electrodynamic forces. Performing numerical calculations on very precise structural models is time consuming. However, the currently intensively developed digital twin technology can significantly reduce the computation time from several days to several hours. In case of this work the full scale simulation took approximately 12 hours while simulating the reduced order model around 2 minutes. The difference was significant and results were very comparable. The use of precise computational models allows for obtaining very accurate results practically at every point of the construction of the medium voltage disconnector. It is possible to determine waveforms and obtain accurate values of electrodynamic forces. Under physical conditions during short-circuit tests, it is not possible to read and measure the exact values of the measured electrodynamic forces. This will always be burdened with measurement errors and the influence of ambient conditions on the installed strain gauges. The added value of the obtained results is the opportunity to observe the distribution of electrodynamic interactions in the disconnector. Current path blades and disconnector terminals are the elements of the disconnector structure that are most exposed to damage. Making each design change in the process of building a prototype of current paths, contacts, and arc-extinguishing chambers can significantly reduce the costs associated with the number of prototypes and experimental tests performed in research laboratories. This is related to the possibility of a deeper understanding of physical phenomena, and this is proved by the presented results.

REFERENCES

[1] Accessed: Feb. 15, 2024. [Online]. Available: https://przemyslprzyszlosci.gov.pl/tag/digital-twin

[2] Q. Wu, B. Hou, S. Di, and Y. Bao, "Construction of digital twin model of other-excited DC motor and application of simulation experiments," in *Proc. 9th Int. Forum Electr. Eng. Autom. (IFEEA)*, Nov. 2022, pp. 155–159.

[3] J. Yuan, M. Sun, J. Xie, D. Su, J. Guo, Y. Guo, and S. Wang, "A multi-agent system construction method for substation digital twin," in *Proc. 2nd Int. Conf. Electr. Eng. Mechatronics Technol. (ICEEMT)*, Jul. 2022, pp. 397–402.

[4] Y. Fu, Y. Huang, F. Hou, and K. Li, "A brief review of digital twin in electric power industry," in *Proc. IEEE 5th Int. Electr. Energy Conf. (CIEEC)*, May 2022, pp. 2314–2318.

[5] Y. Zhu, D. Chen, C. Zhou, L. Lu, and X. Duan, "A knowledge graph based construction method for digital twin network," in *Proc. IEEE 1st Int. Conf. Digit. Twins Parallel Intell. (DTPI)*, Jul. 2021, pp. 362–365.

[6] Y. Liu, "Research on the design of digital twin system for construction safety," in *Proc. 2nd Int. Signal Process., Commun. Eng. Manage. Conf. (ISPCEM)*, Nov. 2022, pp. 254–258.

[7] X. Wang, H. Song, W. Zha, J. Li, and H. Dong, "Digital twin based validation platform for smart metro scenarios," in *Proc. IEEE 1st Int. Conf. Digit. Twins Parallel Intell. (DTPI)*, Jul. 2021, pp. 386–389.

[8] Y. Kong, Y. Wang, and L. Ren, "A cloud-edge collaborative security architecture for industrial digital twin systems," in *Proc. IEEE Smartworld, Ubiquitous Intell. Comput., Scalable Comput. Commun., Digit. Twin, Privacy Comput., Metaverse, Auton. Trusted & Vehicles (SmartWorld/UIC /ScalCom/DigitalTwin/PriComp/Meta)*, Dec. 2023, pp. 15–18.

[9] R. Bun and A. Krzyszkowski, "Mathematical models of electrodynamic influences on an example of the flat inductor," in *Proc. Modern Problems Radio Eng., Telecommun. Comput. Sci.*, Feb. 2002, pp. 24–25.

[10] D. G. Triantafyllidis, P. S. Dokopoulos, and D. P. Labridis, "Parametric short-circuit force analysis of three-phase busbars-a fully automated finite element approach," *IEEE Trans. Power Del.*, vol. 18, no. 2, Apr. 2003, pp. 531–537.

[11] B. Shen, X. Zhang, and D. Zhou, "Analysis and calculation of short-circuit electro-dynamic forces on rectangular bus bars," in *Proc. IEEE 6th Int. Power Electron. Motion Control Conf.*, May 2009, pp. 2618–2621.

[12] F. M. Yusop, M. K. M. Jamil, D. Ishak, and S. Masri, "Study on the electromagnetic force affected by short-circuit current in vertical and horizontal arrangement of busbar system," in *Proc. Int. Conf. Electr., Control Comput. Eng. (InECCE)*, Jun. 2011, pp. 196–200.

[13] M. Mouhamad, C. Elleau, F. Mazaleyrat, C. Guillaume, and B. Jarry, "Short-circuit withstand tests of metglas 2605SA1-based amorphous distribution transformers," *IEEE Trans. Magn.*, vol. 47, no. 10, pp. 4489–4492, Oct. 2011.

[14] G. Komurgoz and T. Gundogdu, "Effect of the tap winding configurations on the electromagnetic forces acting on the concentric transformer coils," in *Proc. 3rd Int. Conf. Electr. Power Energy Convers. Syst.*, Oct. 2013, pp. 1–6.

[15] I. C. Popa and A.-I. Dolan, "Numerical modeling of three-phase busbar systems: Calculation of the thermal field and electrodynamic forces," in *Proc. Int. Conf. Appl. Theor. Electr. (ICATE)*, Oct. 2016, pp. 1–9.

[16] G. Kadkhodaei, K. Sheshyekani, and M. Hamzeh, "Coupled electric-magnetic-thermal-mechanical modeling of busbars under shortcircuit conditions," *IET Gener., Transmiss. Distrib.*, vol. 10, pp. 955–963, Mar. 2016.

[17] B. Aprahamian, M. Marinova, and T. Dimova, "Assessment of the influence of magnetron sputtered coatings on the electrodynamic forces of current-carrying busbars," in *Proc. 20th Int. Symp. Electr. App. Technol. (SIELA)*, Jun. 2018, pp. 1–4.

[18] I. V. Popov, G. A. Evdokunin, and A. V. Syutkin, "Computation modelling of electrodynamic forces in transformers and reactors," in *Proc. IEEE Conf. Russian Young Researchers Electr. Electron. Eng. (EIConRus)*, Russia, Jan. 2020, pp. 1093–1097.

[19] I. V. Popov, G. A. Evdokunin, and V. V. Popov, "Influence of transformer's operating mode for value of electrodynamic force," in *Proc. Ural Smart Energy Conf. (USEC)*, Nov. 2020, pp. 88–92.

[20] J. Yang, Y. Liu, D. Hu, B. Wu, B. Che, and J. Li, "Transient electromagnetic force analysis of GIS bus based on FEM," in *Proc. Int. Conf. Condition Monit. Diagnosis (CMD)*, Xi'an, China, Sep. 2016, pp. 554–557.

[21] Y. Jiaxin, W. Ruichao, L. Huimin, B. Longqing, and W. Hongjian, "Research on the calculation methods of enclosed isolated phase busbar in short-circuit condition," in *Proc. IEEE 62nd Holm Conf. Elect. Contacts (Holm)*, Clearwater Beach, FL, USA, Oct. 2016, pp. 111–114.

[22] S. W. Park and H. Cho, "A practical study on electrical contact resistance and temperature rise at at the connections of the copper busbars in switchgears," in *Proc. IEEE 60th Holm Conf. Electr. Contacts (Holm)*, New Orleans, LA, USA, Oct. 2014, pp. 1–7.

[23] A. Jamali-Abnavi and H. Hashemi-Dezaki, "Evaluating the electromagnetic forces on the electric arc furnaces power cables under various operation conditions," *Electr. Power Syst. Res.*, vol. 201, Dec. 2021, Art. no. 107553.

[24] J. Gatherer and R. L. Jackson, "A multi-variable parametric study on the performance of bolted busbar contacts," in *Proc. IEEE 61st Holm Conf. Electr. Contacts (Holm)*, San Diego, CA, USA, Oct. 2015, pp. 124–131.

[25] P. Borkowski, M. Bartosik, M. Rodak, A. Sienicki, F. Wójcik, B. Panev, F. Rodriguez-Mateos, and A. Siemko, "Ultrafast, redundant, and unpolarized DC energy extraction systems for the protection of superconducting magnet circuits," *IEEE Trans. Ind. Electron.*, vol. 69, no. 10, pp. 9895–9904, Oct. 2022.

[26] M. Szulborski, S. Lapczynski, L. Kolimas, and M. Tyryk, "Electrodynamic forces in a high voltage circuit breakers with tulip contact system—FEM simulations," *IEEE Access*, vol. 10, pp. 99299–99320, 2022.

[27] J. Y. Zhong, S. J. Wu, Z. Wang, Y. J. Guo, and X. Y. Qin, "A 3-D steady-state analysis of thermal behavior in EHV GIS busbar," *J. Electr. Eng. Technol.*, vol. 11, no. 3, pp. 781–789, 2016.

[28] A. F. Nematollahi and B. Vahidi, "3D FEM analysis of induced current in the shield of the buried cable by non-vertical channel," *Electr. Power Syst. Res.*, vol. 212, Nov. 2022, Art. no. 108256.

[29] M. Szulborski, S. Łapczyński, and Ł. Kolimas, "Increasing magnetic blow-out force by using ferromagnetic side plates inside MCB," *Energies*, vol. 15, no. 8, p. 2776, Apr. 2022.

[30] *ABB Catalogue ONIII—Outdoor Disconnector*, ABB Sp. z o.o. ul. Leszno, Poland, 2020.

MICHAŁ SZULBORSKI received the B.Sc. degree in electrical engineering from Warsaw University of Technology, Warsaw, Poland, in 2015, the B.Sc. degree in power engineering from the University of Warmia and Mazury in Olsztyn, Olsztyn, Poland, in 2016, the M.Sc. degree in electrical engineering from Warsaw University of Technology, in 2018, and the Ph.D. degree from the Department of Electrical Power Apparatus, Warsaw University of Technology, in 2023. He is currently an experienced Designer of LV and MV electrical apparatus. In addition, he is a certified Application Engineer with Symkom Sp. z o.o.–ANSYS Channel Partner, responsible for electromagnetic, thermal, and mechanical calculations. His current research interests include the design of electrical apparatus using FEA simulations and digital twin technology.

SEBASTIAN ŁAPCZYŃSKI received the degree from Warsaw University of Technology, Warsaw, Poland, in 2016, where he is currently pursuing the Ph.D. degree with the Department of Electrical Power Apparatus. He is an Analyst, an Engineer, and an Editor specializing in the construction of electrical apparatuses, in aspects related to medium and low voltage electrical devices. His research interests include mostly construction of electrical apparatuses, electromechanical devices, contact systems, numerical analysis of electrodynamic interactions, and thermal phenomena in current paths by means of finite element method.

ŁUKASZ KOLIMAS received the degree from Warsaw University of Technology, Warsaw, Poland, in 2005, and the Ph.D. degree, in 2008. Since 2008, he has been the Doctor of Electrical Apparatus with Warsaw University of Technology. He is currently a Research Worker with the Division of Electrical Power Apparatus, Protection and Control. He is the constructor of low voltage apparatus, an Expert with Polish Centre for Accreditation in terms of Short Circuit Laboratory, and a member of Polish Agency for Enterprise Development.

ŁUKASZ KOZAREK received the B.Sc. and M.Sc. degrees in electrical engineering from Warsaw University of Technology, Warsaw, Poland, in 2011 and 2014 respectively. Since 2014, he has been involved in various areas as a certified Electrical Designer, an Inspector, an Auditor, and an Owner's Engineer. He is currently an employee of the private company whose main interest is placed in the field of renewable energy sources and distribution systems. He is also a member of association of Polish Electricians (Specialist) and a member of the District Chamber of Engineers.

HUBERT CICHECKI received the B.Sc. and M.Sc. degrees in electrical engineering from Warsaw University of Technology, Warsaw, Poland, in 2016 and 2018, respectively. He is currently an Experienced Designer of MV and HV electrical power systems, especially in grid integration with power plants. In addition, he is a qualified Cost-Technical Engineer with ability to determine cost-optimization quality factors. His current research interest includes the design of electrical power systems in terms of technical optimizations.

PRZEMYSŁAW SUL received the Ph.D. degree in electrical engineering from Warsaw University of Technology, Poland, in 2013. Since 2005, he has been a Researcher (an Assistant/Assistant Professor since 2013) with Warsaw University of Technology. He has been a Specialist, a Product Evaluation Inspector, and an Auditor with the Certification Department, Energy Institute, Warsaw, since 2015. He represents Warsaw University of Technology in Polish Committee for Standardization-work in the KT-55 Technical Committee. His scientific and research work in the field of electrical engineering: high voltage techniques-lightning and overvoltage protection, tests of surge arresters, tests and computer simulations of high-voltage phenomena, and tests of magneto-accumulation generators-FCG. His research interests include numerical simulation of electrical discharges in gases in short and long gaps, lightning protection, high voltage engineering, space charge analysis, partial discharges, and scientific computing methods.

MACIEJ OWSIŃSKI is currently with the Institute of Power Engineering, Warsaw. He is the long-term Manager of the Accredited High Current Laboratory. He is also with the Certification and Inspection Department. For many years, he has been involved in research and type tests in the field of cable accessories and devices used in the power industry.

PRZEMYSŁAW BEROWSKI received the M.Sc. Eng. degree from Warsaw University of Technology, Warsaw, Poland, in 1997, and the Ph.D. degree from the Electrotechnical Institute, Warsaw. He has many years of experience in the field of testing of electrical apparatus and devices. He also carried out work related to the design of medium voltage switchgears and apparatus, as the Research and Development Manager of a private company. He is currently the Head of the Accredited Equipment Distribution Laboratory, Institute of Power Engineering, Warsaw.

DARIUSZ BACZYŃSKI received the M.Sc., Ph.D., and D.Sc. degrees in electrical engineering from Warsaw University of Technology, in 1996, 1999, and 2014, respectively. He is currently the University Professor with the Electrical Power Engineering Institute, Faculty of Electrical Engineering, Warsaw University of Technology. He also cooperated with IT companies, as an Expert. His research interests include optimization, forecasting, and applications of computer systems in broadly understood electrical power engineering.

MARCIN WESOŁOWSKI received the Ph.D. degree from Warsaw University of Technology (WUT), Warsaw, Poland, in 2009. Since 2006, he has been with the Power Engineering Institute, WUT, and the Tele and Radio Research Institute, from 2004 to 2014. For many years, he was a Designer of many electrothermal devices, especially resistance and induction heating systems. His current research interests include wide known thermal-management systems, modeling and simulation of electromagnetic and thermal problems, and design of temperature controllers.

P1. *Urządzenie i sposób zmniejszania czasu wyłączenia łuku elektrycznego w wyłącznikach wysokiego napięcia*

NUMER REJESTRU PATENTOWEGO Pat.243768					NUMER ZGŁOSZENIA PCT/
Rubryka	Nr kolejny wpisu	Nr zgłoszenia: P.437864	Patent nr: Pat.243768	Data wydania decyzji o udzieleniu patentu: 2023-07-18	Data wpisu i podpis
		Data zgłoszenia: 2021-05-14	Pierwszeństwo:		
		Nr zgłoszenia macierzystego:		O udzieleniu patentu ogłoszono w WUP nr 41 rok 2023	
		Data ogłoszenia o zgłoszeniu: 2022-11-21	Numer i data zgłoszenia patentu głównego:		
		Int. Cl(8): H01H, 33/74			
A		**Nazwisko i imię albo nazwa, miejsce zamieszkania albo siedziba uprawnionego z patentu (miejscowość, kraj) oraz numer identyfikacyjny REGON - jeżeli został on wskazany**			
	1	POLITECHNIKA WARSZAWSKA, Warszawa, Polska, 000001554			2023-10-17 Agnieszka Bąkowska
B		**Tytuł wynalazku**			
	1	Urządzenie i sposób zmniejszania czasu wyłączenia łuku elektrycznego w wyłącznikach wysokiego napięcia			2023-10-17 Agnieszka Bąkowska
C		**Nazwisko i imię twórcy wynalazku oraz jego miejsce zamieszkania (miejscowość, kraj)**			
	1	KOLIMAS ŁUKASZ, Natolin, Polska ŁAPCZYŃSKI SEBASTIAN, Warszawa, Polska SZULBORSKI MICHAŁ, Pułtusk, Polska KOZAREK ŁUKASZ, Warszawa, Polska			2023-10-17 Agnieszka Bąkowska
D		**Prawa ograniczające patent, zajęcia dokonane przez uprawniony organ**			
E		**Wpisy uzupełniające stan prawny patentu (w szczególności patenty dodatkowe, zamiana patentu dodatkowego na patent oraz informacje o zmianie zakresu ochrony)**			
F		**Wnioski o unieważnienie, sprzeciwy oraz decyzje dotyczące patentu**			
G		**Data unieważnienia lub data i przyczyna wygaśnięcia patentu**			

P2. *Pompa oraz sposób sterowania pompy*

<table>
<tr><td colspan="5">NUMER REJESTRU PATENTOWEGO Pat.239155</td><td>NUMER ZGŁOSZENIA PCT/</td></tr>
<tr><td rowspan="5">Rubryka</td><td rowspan="5">Nr kolejny wpisu</td><td>Nr zgłoszenia: P.430873</td><td>Patent nr: Pat.239155</td><td rowspan="2">Data wydania decyzji o udzieleniu patentu: 2021-08-17</td><td rowspan="5">Data wpisu i podpis</td></tr>
<tr><td>Data zgłoszenia: 2019-08-16</td><td rowspan="2">Pierwszeństwo:</td></tr>
<tr><td>Nr zgłoszenia macierzystego:</td><td rowspan="3">O udzieleniu patentu ogłoszono w WUP nr 32 rok 2021</td></tr>
<tr><td>Data ogłoszenia o zgłoszeniu: 2021-02-22</td><td rowspan="2">Numer i data zgłoszenia patentu głównego:</td></tr>
<tr><td>Int. CI(8): F04B, 17/00
F04B, 17/04
F04B, 15/00
F04B, 13/00</td></tr>
<tr><td rowspan="2">A</td><td></td><td colspan="3">Nazwisko i imię albo nazwa, miejsce zamieszkania albo siedziba uprawnionego z patentu (miejscowość, kraj) oraz numer identyfikacyjny REGON - jeżeli został on wskazany</td><td></td></tr>
<tr><td>1</td><td colspan="3">POLITECHNIKA WARSZAWSKA, Warszawa, Polska, 000001554</td><td>2021-11-09 Agnieszka Bąkowska</td></tr>
<tr><td rowspan="2">B</td><td></td><td colspan="3">Tytuł wynalazku</td><td></td></tr>
<tr><td>1</td><td colspan="3">Pompa oraz sposób sterowania pompy</td><td>2021-11-09 Agnieszka Bąkowska</td></tr>
<tr><td rowspan="2">C</td><td></td><td colspan="3">Nazwisko i imię twórcy wynalazku oraz jego miejsce zamieszkania (miejscowość, kraj)</td><td></td></tr>
<tr><td>1</td><td colspan="3">KOLIMAS ŁUKASZ, Natolin, Polska
BIEŃKOWSKI KRZYSZTOF, Warszawa, Polska
ŁAPCZYŃSKI SEBASTIAN, Warszawa, Polska
SZULBORSKI MICHAŁ, Pułtusk, Polska
KOZAREK ŁUKASZ, Warszawa, Polska
BIREK KAROL, Włocławek, Polska</td><td>2021-11-09 Agnieszka Bąkowska</td></tr>
<tr><td>D</td><td></td><td colspan="3">Prawa ograniczające patent, zajęcia dokonane przez uprawniony organ</td><td></td></tr>
<tr><td>E</td><td></td><td colspan="3">Wpisy uzupełniające stan prawny patentu (w szczególności patenty dodatkowe, zamiana patentu dodatkowego na patent oraz informacje o zmianie zakresu ochrony)</td><td></td></tr>
<tr><td>F</td><td></td><td colspan="3">Wnioski o unieważnienie, sprzeciwy oraz decyzje dotyczące patentu</td><td></td></tr>
<tr><td>G</td><td></td><td colspan="3">Data unieważnienia lub data i przyczyna wygaśnięcia patentu</td><td></td></tr>
</table>

P3. *Wyzwalacz elektromagnetyczny*

<table>
<tr><td colspan="5">NUMER REJESTRU PATENTOWEGO Pat.239158</td><td>NUMER ZGŁOSZENIA PCT/</td></tr>
<tr><td rowspan="5">Rubryka</td><td rowspan="5">Nr kolejny wpisu</td><td>Nr zgłoszenia: P.431529</td><td>Patent nr: Pat.239158</td><td rowspan="2">Data wydania decyzji o udzieleniu patentu: 2021-08-10</td><td rowspan="5">Data wpisu i podpis</td></tr>
<tr><td>Data zgłoszenia: 2019-10-21</td><td rowspan="2">Pierwszeństwo:</td></tr>
<tr><td>Nr zgłoszenia macierzystego:</td><td rowspan="3">O udzieleniu patentu ogłoszono w WUP nr 32 rok 2021</td></tr>
<tr><td>Data ogłoszenia o zgłoszeniu: 2021-05-04</td><td rowspan="2">Numer i data zgłoszenia patentu głównego:</td></tr>
<tr><td>Int. Cl(8): H01H, 71/24
H01H, 33/38
H01H, 47/32</td></tr>
<tr><td rowspan="2">A</td><td></td><td colspan="3">Nazwisko i imię albo nazwa, miejsce zamieszkania albo siedziba uprawnionego z patentu (miejscowość, kraj) oraz numer identyfikacyjny REGON - jeżeli został on wskazany</td><td></td></tr>
<tr><td>1</td><td colspan="3">POLITECHNIKA WARSZAWSKA, Warszawa, Polska, 000001554</td><td>2021-11-09
Agnieszka
Bąkowska</td></tr>
<tr><td rowspan="2">B</td><td></td><td colspan="3">Tytuł wynalazku</td><td></td></tr>
<tr><td>1</td><td colspan="3">Wyzwalacz elektromagnetyczny</td><td>2021-11-09
Agnieszka
Bąkowska</td></tr>
<tr><td rowspan="2">C</td><td></td><td colspan="3">Nazwisko i imię twórcy wynalazku oraz jego miejsce zamieszkania (miejscowość, kraj)</td><td></td></tr>
<tr><td>1</td><td colspan="3">KOLIMAS ŁUKASZ, Natolin, Polska
BIEŃKOWSKI KRZYSZTOF, Warszawa, Polska
ŁAPCZYŃSKI SEBASTIAN, Warszawa, Polska
SZULBORSKI MICHAŁ, Pułtusk, Polska
KOZAREK ŁUKASZ, Warszawa, Polska
BIREK KAROL, Włocławek, Polska</td><td>2021-11-09
Agnieszka
Bąkowska</td></tr>
<tr><td>D</td><td></td><td colspan="3">Prawa ograniczające patent, zajęcia dokonane przez uprawniony organ</td><td></td></tr>
<tr><td>E</td><td></td><td colspan="3">Wpisy uzupełniające stan prawny patentu (w szczególności patenty dodatkowe, zamiana patentu dodatkowego na patent oraz informacje o zmianie zakresu ochrony)</td><td></td></tr>
<tr><td>F</td><td></td><td colspan="3">Wnioski o unieważnienie, sprzeciwy oraz decyzje dotyczące patentu</td><td></td></tr>
<tr><td>G</td><td></td><td colspan="3">Data unieważnienia lub data i przyczyna wygaśnięcia patentu</td><td></td></tr>
</table>

P4. *Reluktancyjny mechanizm udarowy ze stabilizacją drgań*

NUMER REJESTRU PATENTOWEGO Pat.241143

NUMER ZGŁOSZENIA PCT/

Rubryka	Nr kolejny wpisu			Data wpisu i podpis
		Nr zgłoszenia: P.434726 Data zgłoszenia: 2020-07-20 Nr zgłoszenia macierzystego: Data ogłoszenia o zgłoszeniu: 2022-01-24 Int. Cl(8): B25D, 13/00 B25D, 17/24	Patent nr: Pat.241143 Pierwszeństwo: Numer i data zgłoszenia patentu głównego:	Data wydania decyzji o udzieleniu patentu: 2022-05-06 O udzieleniu patentu ogłoszono w WUP nr 32 rok 2022
A		**Nazwisko i imię albo nazwa, miejsce zamieszkania albo siedziba uprawnionego z patentu (miejscowość, kraj) oraz numer identyfikacyjny REGON - jeżeli został on wskazany**		
	1	POLITECHNIKA WARSZAWSKA, Warszawa, Polska, 000001554		2022-08-08 Agnieszka Bąkowska
B		**Tytuł wynalazku**		
	1	Reluktancyjny mechanizm udarowy ze stabilizacją drgań		2022-08-08 Agnieszka Bąkowska
C		**Nazwisko i imię twórcy wynalazku oraz jego miejsce zamieszkania (miejscowość, kraj)**		
	1	KOLIMAS ŁUKASZ, Natolin, Polska BIEŃKOWSKI KRZYSZTOF, Warszawa, Polska ŁAPCZYŃSKI SEBASTIAN, Warszawa, Polska SZULBORSKI MICHAŁ, Pułtusk, Polska KOZAREK ŁUKASZ, Warszawa, Polska BIREK KAROL, Włocławek, Polska		2022-08-08 Agnieszka Bąkowska
D		**Prawa ograniczające patent, zajęcia dokonane przez uprawniony organ**		
E		**Wpisy uzupełniające stan prawny patentu (w szczególności patenty dodatkowe, zamiana patentu dodatkowego na patent oraz informacje o zmianie zakresu ochrony)**		
F		**Wnioski o unieważnienie, sprzeciwy oraz decyzje dotyczące patentu**		
G		**Data unieważnienia lub data i przyczyna wygaśnięcia patentu**		

P5. *Mufa elektrotechniczna*

<table>
<tr><td colspan="5">NUMER REJESTRU PATENTOWEGO Pat.241142</td><td>NUMER ZGŁOSZENIA PCT/</td></tr>
<tr><td rowspan="5">Rubryka</td><td rowspan="5">Nr kolejny wpisu</td><td>Nr zgłoszenia: P.434020</td><td>Patent nr: Pat.241142</td><td>Data wydania decyzji o udzieleniu patentu: 2022-05-12</td><td rowspan="5">Data wpisu i podpis</td></tr>
<tr><td>Data zgłoszenia: 2020-05-20</td><td rowspan="2">Pierwszeństwo:</td><td rowspan="4">O udzieleniu patentu ogłoszono w WUP nr 32 rok 2022</td></tr>
<tr><td>Nr zgłoszenia macierzystego:</td></tr>
<tr><td>Data ogłoszenia o zgłoszeniu: 2021-11-22</td><td rowspan="2">Numer i data zgłoszenia patentu głównego:</td></tr>
<tr><td>Int. Cl(8): H02G, 15/04</td></tr>
<tr><td rowspan="2">A</td><td></td><td colspan="3">Nazwisko i imię albo nazwa, miejsce zamieszkania albo siedziba uprawnionego z patentu (miejscowość, kraj) oraz numer identyfikacyjny REGON - jeżeli został on wskazany</td><td></td></tr>
<tr><td>1</td><td colspan="3">POLITECHNIKA WARSZAWSKA, Warszawa, Polska, 000001554</td><td>2022-08-08
Agnieszka
Bąkowska</td></tr>
<tr><td rowspan="2">B</td><td></td><td colspan="3">Tytuł wynalazku</td><td></td></tr>
<tr><td>1</td><td colspan="3">Mufa elektrotechniczna</td><td>2022-08-08
Agnieszka
Bąkowska</td></tr>
<tr><td rowspan="2">C</td><td></td><td colspan="3">Nazwisko i imię twórcy wynalazku oraz jego miejsce zamieszkania (miejscowość, kraj)</td><td></td></tr>
<tr><td>1</td><td colspan="3">KOLIMAS ŁUKASZ, Natolin, Polska
BIEŃKOWSKI KRZYSZTOF, Warszawa, Polska
ŁAPCZYŃSKI SEBASTIAN, Warszawa, Polska
SZULBORSKI MICHAŁ, Pułtusk, Polska
KOZAREK ŁUKASZ, Warszawa, Polska
BIREK KAROL, Włocławek, Polska</td><td>2022-08-08
Agnieszka
Bąkowska</td></tr>
<tr><td>D</td><td></td><td colspan="3">Prawa ograniczające patent, zajęcia dokonane przez uprawniony organ</td><td></td></tr>
<tr><td>E</td><td></td><td colspan="3">Wpisy uzupełniające stan prawny patentu (w szczególności patenty dodatkowe, zamiana patentu dodatkowego na patent oraz informacje o zmianie zakresu ochrony)</td><td></td></tr>
<tr><td>F</td><td></td><td colspan="3">Wnioski o unieważnienie, sprzeciwy oraz decyzje dotyczące patentu</td><td></td></tr>
<tr><td>G</td><td></td><td colspan="3">Data unieważnienia lub data i przyczyna wygaśnięcia patentu</td><td></td></tr>
</table>

P6. *Urządzenie do pomiaru rezystywności gruntu*

<table>
<tr><td colspan="5">NUMER REJESTRU PATENTOWEGO Pat.244861</td><td>NUMER ZGŁOSZENIA PCT/</td></tr>
<tr><td rowspan="5">Rubryka</td><td rowspan="5">Nr kolejny wpisu</td><td>Nr zgłoszenia: P.437401</td><td>Patent nr: Pat.244861</td><td rowspan="2">Data wydania decyzji o udzieleniu patentu: 2023-12-12</td><td rowspan="5">Data wpisu i podpis</td></tr>
<tr><td>Data zgłoszenia: 2021-03-25</td><td rowspan="2">Pierwszeństwo:</td></tr>
<tr><td>Nr zgłoszenia macierzystego:</td><td rowspan="3">O udzieleniu patentu ogłoszono w WUP nr 12 rok 2024</td></tr>
<tr><td>Data ogłoszenia o zgłoszeniu: 2022-09-26</td><td rowspan="2">Numer i data zgłoszenia patentu głównego:</td></tr>
<tr><td>Int. Cl(8): G01R, 27/02
G01R, 27/14
G01R, 27/08
G01R, 27/20</td></tr>
<tr><td rowspan="2">A</td><td></td><td colspan="3">Nazwisko i imię albo nazwa, miejsce zamieszkania albo siedziba uprawnionego z patentu (miejscowość, kraj) oraz numer identyfikacyjny REGON - jeżeli został on wskazany</td><td></td></tr>
<tr><td>1</td><td colspan="3">POLITECHNIKA WARSZAWSKA, Warszawa, Polska, 000001554</td><td>2024-03-18
Agnieszka
Bąkowska</td></tr>
<tr><td rowspan="2">B</td><td></td><td colspan="3">Tytuł wynalazku</td><td></td></tr>
<tr><td>1</td><td colspan="3">Urządzenie do pomiaru rezystywności gruntu</td><td>2024-03-18
Agnieszka
Bąkowska</td></tr>
<tr><td rowspan="2">C</td><td></td><td colspan="3">Nazwisko i imię twórcy wynalazku oraz jego miejsce zamieszkania (miejscowość, kraj)</td><td></td></tr>
<tr><td>1</td><td colspan="3">KOLIMAS ŁUKASZ, Natolin, Polska
ŁAPCZYŃSKI SEBASTIAN, Warszawa, Polska
SZULBORSKI MICHAŁ, Pułtusk, Polska
KOZAREK ŁUKASZ, Warszawa, Polska</td><td>2024-03-18
Agnieszka
Bąkowska</td></tr>
<tr><td>D</td><td></td><td colspan="3">Prawa ograniczające patent, zajęcia dokonane przez uprawniony organ</td><td></td></tr>
<tr><td>E</td><td></td><td colspan="3">Wpisy uzupełniające stan prawny patentu (w szczególności patenty dodatkowe, zamiana patentu dodatkowego na patent oraz informacje o zmianie zakresu ochrony)</td><td></td></tr>
<tr><td>F</td><td></td><td colspan="3">Wnioski o unieważnienie, sprzeciwy oraz decyzje dotyczące patentu</td><td></td></tr>
<tr><td>G</td><td></td><td colspan="3">Data unieważnienia lub data i przyczyna wygaśnięcia patentu</td><td></td></tr>
</table>